TPB

International Symposium

TOPICAL PROBLEMS OF BIOPHOTONICS – 2015

PROCEEDINGS

Optical Bioimaging

Nanobiophotonics

Novel Laser Applications in Biomedicine

Clinical Biophotonics

Tumor and Stem Cells Biology

Nizhny Novgorod, Russia
20-24 July, 2015

Russian Academy of Sciences
Institute of Applied Physics

V International Symposium

TOPICAL PROBLEMS OF BIOPHOTONICS

20 – 24 July, 2015

Nizhny Novgorod, Russia

P R O C E E D I N G S

Nizhny Novgorod, 2015

Organized by

Institute of Applied Physics of the Russian Academy of Sciences
www.iapras.ru

Nizhny Novgorod State Medical Academy
www.gma.nnov.ru

University of Nizhny Novgorod
www.unn.ru

in cooperation with

GYCOM Ltd
www.gycom.ru

Government of the Nizhny Novgorod Region
www.government.nnov.ru

Russian Federal Nuclear Center – VNIIEF
www.vniief.ru/

Skoltech
www.skoltech.ru/

Supported by

www.biovitrum.ru/

www.becker-hickl.de

www.optecgroup.com

www.coherent.com

www.lasertrack.ru

www.stanfordcomputeroptics.com

V International Symposium

TOPICAL PROBLEMS OF BIOPHOTONICS

Topical Conferences

Optical Bioimaging

Nanobiophotonics

Novel Laser Applications in Biomedicine

Workshops

Clinical Biophotonics

Tumor and Stem Cells Biology

P R O C E E D I N G S

The electron version of the Symposium proceedings
is published by the decision of the Editorial Board
of the Institute of Applied Physics of the Russian Academy of Sciences

Scientific Advisory Board

Symposium Web site: http://www.biophotonics.sci-nnov.ru

ISBN 978-5-8048-0105-3

CONTENTS

PLENARY TALKS

OPTICAL BIOIMAGING

NANOBIOPHOTONICS

NOVEL LASER APPLICATIONS IN BIOMEDICINE

WORKSHOPS

CLINICAL BIOPHOTONICS

TUMOR AND STEM CELLS BIOLOGY

SPONSORS

Plenary Talks

ULTRAFAST LASER DRIVEN ELECTRON ACCELERATION AND X-RAY COHERENT IMAGING FOR BIOMEDICAL APPLICATIONS

J.-C. Kieffer

[1] INRS-EMT, Université du Québec, Québec, Canada, kieffer@emt.inrs.ca

Abstract. I will present an overview of our experimental effort in high field science (up to 10^{23} W/cm^2) with the high peak power laser system (>200 TW) at the Advanced Laser Light Sources facility (ALLS). Results on electron acceleration (by laser wakefield and by direct laser field) and on the generation of ultrafast hard x-rays (betatron emission) obtained with the actual 200 TW ALLS laser system (30 fs, 5J) will be presented and discussed.

In one part of our program, electrons are accelerated through laser wakefield and generate betatron emission. The x rays produced by the accelerated electrons were measured by several diagnostics. The measured angular spreads of the x-ray beams were 25 and 31 mrad (FWHM) in the horizontal and the vertical directions (averaged over 10 successive laser shots). We currently have 2.2×10^8 photons/0.1% bandwidth/sr/shot at 10 keV. The total number of photons over the whole spectrum, obtained from the synchrotron fit distribution, is $N=10^9$ ph. The x-ray spot size was measured to be 1.7 μm (FWHM). Single shot phase contrast images of complex objects have been obtained with the 10keV betatron X-ray source in different geometries, and are interpreted with a comprehensive model of x-ray propagation integrating the properties and geometries of the imaging beam line. Many approaches have been presented for the optimization of image quality and phase information retrieval in various geometries with micro-focus X-ray and synchrotron sources. Simple rules have been derived for the parameters of projection images of a generic phase edge. However, there is still a need for a semi-quantitative method enabling an easy extraction of information on interfaces inside inhomogeneous media and allowing a characterization of the quality of an imaging set up. I will discuss a Figure of Merit (FOM), which looks promising for mapping and characterizing interfaces inside complex inhomogeneous media. Applications of this betatron phase contrast Imaging Beam line to Biophotonics, Agriculture and Forestry will be presented and discussed.

In a second part of our program, we are studying the acceleration of electrons directly by the laser field. A maximum intensity of 10^{22} W/cm^2 has been achieved on target and electron have been accelerated to multi-MeV energies directly by the laser field (DLFA) using radially polarized TM_{01} modes. Our most recent experiments with TE_{01} and TM_{01} mode in the ultrarelativistic regime will be presented and discussed.

We are currently upgrading our high peak power laser facility. I will describe our progress towards a 500 TW facility, the perspectives of electron acceleration beam lines based on wakefield and direct laser acceleration (TM_{01} mode) and the potential of the betatron beam line for biomedical imaging with our new facility. template is a set of styles and page layout settings that determine the appearance of a document.

References

1. S. Fourmaux et al. *Optics Letters*, 2011, **36**(13), 2426-2428.
2. S. Payeur et al. *Appl. Phys. Lett.*, 2012, **101**(4), 041105.
3. S. Fourmaux et al. *Appl. Phys. Lett.*, 2012, **101**(11), 111106.
4. P. E. Masson-Laborde et al. *Phys. Plasmas*, 2014, **21**(12), 123113.

NOVEL FLUORESCENT PROTEINS FOR MULTIPARAMETER LIVE-CELL IMAGING

K.A. Lukyanov

Institute of Bioorganic Chemistry, Miklukho-Maklaya 16/10, 117997 Moscow, Russia
Nizhny Novgorod State Medical Academy, Minin Sq. 10/1, 603005 Nizhny Novgorod, Russia
kluk@ibch.ru

Abstract. Genetically encoded fluorescent probes – fluorescent proteins – enable dynamic visualization of target structures and processes in live models. Multiparameter imaging requires many probes with distinct spectral properties such as excitation and emission wavelengths or fluorescence lifetimes. In this talk, focus will be on our recent developments in the field of fluorescent proteins and sensors that open new possibilities for multiparameter fluorescence imaging.

Due to unique mechanism of self-catalyzed chromophore formation fluorescent proteins are widely used in biology as fully genetically encoded fluorescent probes to visualize various structures and events in live cells and organisms [1]. Simultaneous observation of several different processes (multiparameter imaging) is very important to decipher their interrelationship in time and space.

The most straightforward way for multiparameter imaging is to use a combination of probes of different fluorescence colors. Wide spectral diversity of fluorescent proteins enables imaging in several color channels. Yet, imaging in far-red region (which is especially important for imaging in animal models due to minimal light absorption and scattering in this spectral range) suffers from low brightness of available fluorescent proteins. We developed an improved variant of far-red protein Katushka – Katushka2S, which shows superior performance in animal models compared to other far-red fluorescent proteins [2]. Moreover, we found that various far-red fluorescent proteins can be spectrally unmixed providing the possibility of multiplexed imaging.

Most currently available genetically encoded sensors fluoresce in blue-green-yellow. Thus, red fluorescent sensors are in a high demand for multiparameter imaging [3]. We constructed far-red sensor for activity of caspase-3 – an effector caspase, which plays a key role in apoptosis – using FRET between far-red fluorescent protein mKate2 as a donor and bacteriophytochrome-based infrared fluorescent protein iRFP as an acceptor. This sensor was used for simultaneous monitoring of caspase-3 activation (in far-red and near-infrared channels) and translocation of Bax-EGFP (in green channel). Potentially, the new sensor is perspective for whole body animal imaging due to its red-shifted spectra.

Spectral diversity of fluorescent proteins, crucial for multiparameter imaging, is based mainly on chemical diversity of their chromophores. Recently we demonstrated that tryptophan-based chromophore of a cyan fluorescent protein can exist in a previously unknown anionic state with red-shifted (green) fluorescence [4]. We developed a new green fluorescent protein NowGFP with anionic tryptophan chromophore that possesses long fluorescence lifetime. Signals of NowGFP and EGFP can be clearly distinguished by their fluorescence lifetimes. Thus, NowGFP provides an additional channel for multiparameter FLIM microscopy of green fluorescent proteins.

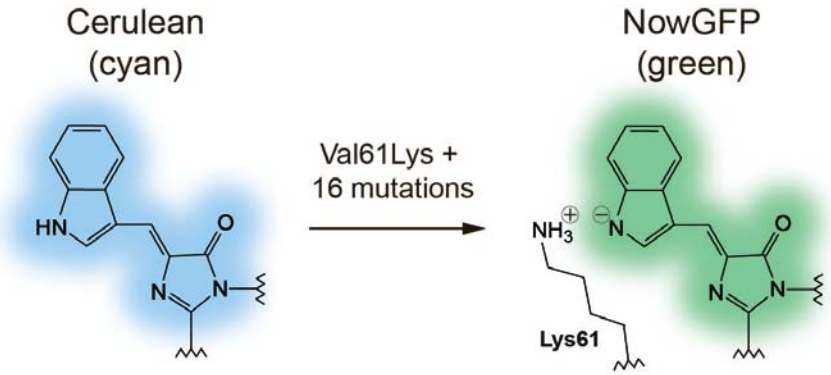

Fig. 1. The proposed structure of anionic tryptophan-based chromophore in green fluorescent protein NowGFP obtained by mutagenesis of cyan fluorescent protein Cerulean. Key substitution (valine 61 to lysine) results in stabilization of negative charge on the chromophore

Phototoxic red fluorescent protein KillerRed is a fully genetically encoded photosensitizer [5]. In response to green-orange light illumination, KillerRed generates local oxidative stress, which damages nearby intracellular targets (proteins, lipids or DNA), resulting in cell death or target protein inactivation. We constructed a blue-shifted variant of this protein – KillerOrange, which is phototoxic under blue light. Due to distinct activating light wavelengths, KillerRed and KillerOrange can be used together for killing two independent cell populations.

A significant problem of fluorescence microscopy is photobleaching of the probes. Such applications as time-lapse and 3D microscopy, single-molecule detection, and fluorescence correlation spectroscopy strongly suffer from insufficient photostability of fluorescent proteins. An important step forward in understanding and overcoming of the GFP photobleaching was discovery of oxidative green-to-red photoconversion ("redding") based on electron transfer from excited GFPs to intracellular electron acceptors [6]. It was realized that oxidative redding can represent a major pathway of GFP photobleaching in live cells [7]. We found that suppression of redding by optimization of imaging media composition is a simple and efficient way to increase GFP photostability [8].

Acknowledgements

Generous support from by Russian Science Foundation (14-25-00129) is greatly acknowledged.

References

1. D.M. Chudakov, M.V. Matz, S. Lukyanov, and K.A. Lukyanov, *Physiol. Rev.*, 2010, **90**, 1103-1163.
2. K.E Luker, P. Pata, I.I. Shemiakina, A. Pereverzeva, A.C. Stacer, D.S. Shcherbo, V.Z. Pletnev, M. Skolnaja, K.A. Lukyanov, G.D. Luker, I. Pata, and D.M. Chudakov, *Sci. Rep*., 2015, in press.
3. Y.G. Ermakova, D.S. Bilan, M.E. Matlashov, N.M. Mishina, K.N. Markvicheva, O.M. Subach, F.V. Subach, I. Bogeski, M. Hoth, G. Enikolopov, and V.V. Belousov, *Nat. Commun.*, 2014, **5**, 5222.
4. K.S. Sarkisyan, I.V. Yampolsky, K.M. Solntsev, S.A. Lukyanov, K.A. Lukyanov, and A.S. Mishin, *Sci. Rep*., 2012, **2**, 608.
5. M.E. Bulina, D.M. Chudakov, O.V. Britanova, Y.G. Yanushevich, D.B. Staroverov, T.V. Chepurnykh, E.M. Merzlyak, M.A. Shkrob, S. Lukyanov, and K.A. Lukyanov, *Nat. Biotechnol.*, 2006, **24**, 95-99.
6. A.M. Bogdanov, A.S. Mishin, I.V. Yampolsky, V.V. Belousov, D.M. Chudakov, F.V. Subach, V.V. Verkhusha, S. Lukyanov, and K.A. Lukyanov, *Nat. Chem. Biol.*, 2009, **5**, 459-461.
7. A.M. Bogdanov, E.A. Bogdanova, D.M. Chudakov, T.V. Gorodnicheva, S. Lukyanov, and K.A. Lukyanov, *Nat. Methods.*, 2009, **6**, 859-860.
8. A.V. Mamontova, A.M. Bogdanov, and K.A. Lukyanov, *Biotechniques*, 2015, **58**(5), 258-261.

BIOMEDICAL OPTOACOUSTIC IMAGING: 22 YEARS OF DEVELOPMENT FROM FIRST IDEAS TO CLINICAL TRIALS

A.A. Oraevsky

TomoWave Laboratories, Houston, Texas, USA
AAO@tomowave.com

Abstract. This lecture will discuss history of optoacoustic imaging from pioneering works that set the basic principles of the technology to the first *in vivo* images, to the most recent advances, and finally to the future medical imaging modalities and their applications in the main stream medicine and surgery. We also present the design features and technical parameters of the optoacoustic imaging systems required for clinically viable devices.

In early 1880, Alexander Bell submitted a patent application and then presented and published a number of lectures describing his newly invented photophone. At the reception side of this device there was light-to-sound transducer made of light absorbing cell made of crystalline selenium with high thermal expansion and electrically connected to a speaker. When illuminated with a sun beam modulated by sound, the selenium cell reproduced acoustic vibration of the sound [1]. About 100 years later, combination of optical spectroscopy and piezoelectric transducers revealed that detection of sound resulting from the optical absorption represents a very sensitive means for detection of absorbing molecules in gases and liquids and absorbing layers in solids, and photoacoustic spectroscopy was born [2]. In 1970s-80s there were several proposals to make optoacoustic images, but no systems were developed and no images were produced. Only after the physical principles governing acquisition of spatially resolved images in the depth of live tissues were formulated [3], the first images were produced [4]. Biomedical applications of the laser optoacoustic imaging exploded in the 21st century, exponentially growing and involving non only physicists, but also biologists and medical practitioners. We will discuss the principles of operation, system design and methods of optoacoustic tomography, and its advantages and limitations for biomedical applications. Optoacoustic system provides optical contrast in tissue while mapping tissue structures with ultrasonic resolution. The main advantages of the optical contrast is the applicability of optical spectroscopy to high resolution imaging in order to (1) map distributions of blood concentration and its oxygen saturation (functional imaging) in the tissue being physiologically characterized and (2) map distribution of molecules of interest, such as cancer receptors or disease biomarkers (molecular imaging) using contrast agents either selectively accumulating or synthesized in the cells of medical interest. From the first *in vivo* images [5] to the first functional images of blood parameters [6] to the first molecular images using exogenous contrast agents [7], the optoacoustic imaging rapidly attracted attention of the biomedical research community. The total number of researchers who presently dedicate their careers to optoacoustic imaging is estimated at 450. These scientists and engineers published over 2200 papers total and 370 papers in 2014. At least twelve companies including small and very large presently commercialize optoacoustic imaging systems for biomedical applications today.

Spatial resolution of the optoacoustic imaging is scalable 1000x fold from submicron to submillimeter, simultaneously the depth of imaging in tissue proportionally scales from ~50 micron to ~50 mm. The most important parameters that define high resolution of the optoacoustic microscopy systems is the high frequency edge of the ultrasonic transducers (~40 MHz for acoustic resolution microscopes) and capability of the system to focus a short (1–5 ns) laser pulse into a submicron diameter spot through a layer of scattering biological tissue (for optical resolution microscopes). The most important parameter that provides clinical viability of any optoacoustic tomography system is its sensitivity (S_{input}) and noise equivalent pressure (NEP). The typical penetration depth from which clinically relevant information needs to be obtained is from 1 to 6 cm. To achieve maximum depth of imaging tissue structures, the system has to possess S_{input} of at least 20 μV/Pa and NEP of 1Pa. With such advanced technical specifications one may, for example, expect to use optical contrast of blood (specifically hypoxic blood) for visualization of the tumor angiogenesis, thereby providing functional information for differentiation of malignant and benign tumors in the breast.

The idea that drives developments in the field of clinical optoacoustic imaging in the past decade is that coregistration of optoacoustic and ultrasonic images would be a useful enhancement of almost every application of medical ultrasound [8]. Optoacoustic images can provide natural and clinically

useful enhancement of almost every application of medical ultrasound. Deep tissue imaging with high contrast and resolution is the most important niche for optoacoustic tomography, unattainable neither in pure optical imaging or pure ultrasonic imaging.

Since laser pulses are being employed to generate optoacoustic images, it is only natural to use laser pulses for generation of ultrasound images. Laser pulses can generate ultrawide-band nonreverberating ultrasonic pulses enabling higher resolution, higher contrast and deeper penetration for ultrasound tomography [9]. Recently, combined laser optoacoustic + laser ultrasonic images have been obtained contemporaneously [10], which reduces the time required for the clinical procedure (a very important feature for any doctor).

We will present the most important results of *in vivo* preclinical and clinical studies with three-dimensional optoacoustic imaging systems developed in the recent years, ranging from microscopy systems operating in real time to dual modality of optoacoustic and ultrasonic tomography systems that provide medical information, helping detect and differentiate breast cancer and potentially finding and characterizing other life threatening health conditions. When coregistered with tissue morphology, well depicted on ultrasound transmission or reflection images, optoacoustic tomography can find itself among the most comprehensive visualization technologies for diagnostic imaging in oncology, angiography and neurophysiology, for monitoring and guiding therapeutic and surgical procedures as well as in variety of preclinical research applications using small laboratory animals.

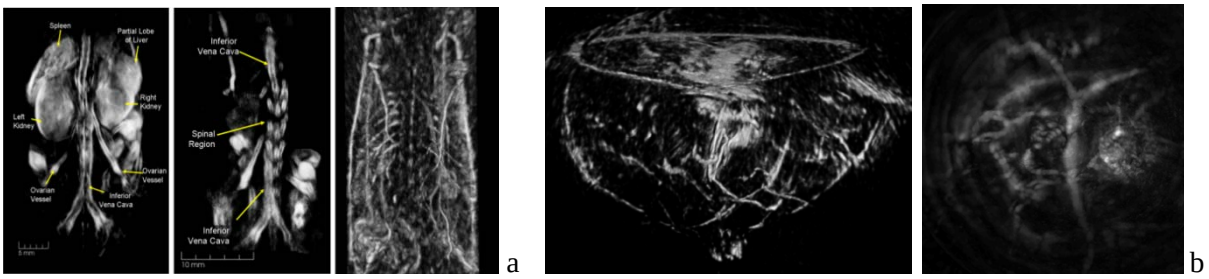

Fig. 1. Examples of 3-dimensional optoacoustic images obtained from a live mouse (a), and breast cancer patient (b).

Discoveries that made optoacoustic imaging the most rapidly developing biomedical imaging technology in the past 15 years are that (1) laser pulses may be effectively used to produce wide-band acoustic pressure (ultrasonic waves) in biological tissues, which carry its main energy in the lower frequency range and, thus, propagate in tissues with minimal attenuation, (2) 2D and 3D images of the absorbed optical energy can be reconstructed with high resolution under the illumination condition of pressure confinement in the course of the optical energy deposition in a voxel to be resolved. The technological developments that will transform optoacoustic imaging systems into compact and robust clinical modalities are the high power diode lasers and the supersensitive optical detectors transparent for the laser excitation [11].

Acknowledgements

Research described in this presentation was supported by various funding organizations in the USA and Europe. Author received funding for his research from The National Cancer Institute, The National Institute of Biomedical Imaging and Bioengineering and the Breast Cancer Research Program from the Department of Defense.

References

1. A.G. Bell, "On the Production and Reproduction of Sound by Light", *American Journal of Science, Series 3*, 1880, **20**(118), 305-324.
2. A. Rosencwaig and A. Gersho, "Theory of the photoacoustic effect with solids", *J. Appl. Phys.*, 1976, **47**, 64-75.
3. A.A. Oraevsky, S.L. Jacques, and F.K. Tittel, "Determination of tissue optical properties by time-resolved detection of laser-induced stress waves", *Proc. SPIE*, 1993, **1882**, 86-101.
4. R.A. Kruger, P. Liu, Y.R. Fang, and C.R. Appledorn, "Photoacoustic ultrasound (PAUS) reconstruction tomography", *Med. Phys.*, 1995, **22**(10), 1605-1609.

5. A.A. Oraevsky, "Optoacoustic Tomography: From Fundamentals to Diagnostic Imaging of Breast Cancer", in *Biomedical Photonics Handbook, Second Edition: Fundamentals, Devices, and Techniques*, ed. by T. Vo-Dinh, CRC Press, Boca Raton, Florida, 2014, **PM222**, Chapter 21, 715-757.
6. L.V. Wang and S. Hu, "Photoacoustic Tomography: *In vivo* Imaging from Organelles to Organs", *Science*, 2012, **335**(6075), 1458-1462.
7. D. Razansky, C. Vinegoni, and V. Ntziachristos, "Multispectral photoacoustic imaging of fluorochromes in small animals", *Opt Lett*., 2007, **32**(19), 2891-2893.
8. J.J. Niederhauser, M. Jaeger, R. Lemor, P. Weber, M. Frenz, "Combined ultrasound and optoacoustic system for real-time high-contrast vascular imaging *in vivo*", *IEEE Trans Med Imaging*. 2005, **24**(4), 436-40.
9. A. Conjusteau, S.A. Ermilov, R. Su, H-P. Brecht, M.P. Fronheiser, and A.A. Oraevsky, "Measurement of the spectral directivity of optoacoustic and ultrasonic transducers with a laser ultrasonic source", *Rev. Sci. Inst*., 2009, **80** (1-5), 093708.
10. S. Manohar, R.G. Willemink, F. van der Heijden, C.H. Slump, and T.G. van Leeuwen, "Concomitant speed-of-sound tomography in photoacoustic imaging", *Appl Phys Lett*., 2007, **91**, 131911.
11. P. Beard, "Biomedical photoacoustic imaging", *Interface Focus*, 2011, **1**, 602-631.

SINGLE MOLECULES AND SINGLE GOLD NANOPARTICLES: OPTICAL DETECTION AND SPECTROSCOPY

M. Orrit

[1] MoNOS, Leiden Institute of Physics, 2300 RA Leiden, Netherlands
orrit@physics.leidenuniv.nl

Abstract. I shall present several optical methods giving access to signals from single molecules and single gold nanoparticles. The latter objects are interesting because of their strong interaction with light mediated by their plasmon resonance, and because they are chemically and photochemically very stable. The experiments are based on fluorescence or photoluminescence, scattering, absorption detected by photothermal contrast, purely refractive effects leading to shifts of the plasmon resonance, or plasmon-enhanced fluorescence of weak emitters.

The optical isolation of single gold nanoparticles leads to their spectroscopic study on a single-particle basis and, through their plasmonic properties, to the study of their direct surroundings. I shall illustrate this general idea with some recent experiments from our laboratory.

1. Photothermal contrast and pump-probe spectroscopy give us knowledge of the mechanical properties of gold nanoparticles and of their environments. The sensitivity of photothermal contrast can be pushed to the detection of individual organic absorbers with negligible fluorescence yields [1]. By these methods, we have monitored the nanosecond dynamics of steam nanobubbles formed in a liquid around a nanoparticle upon plasmonic heating [2]. We show that steam nanobubbles are extremely nonlinear systems that present dynamics in the nanosecond time scale and are very sensitive to perturbations. For example, a nanobubble could probe changes in pressure and act as a fast acousto-optical transducer.

2. The surface plasmon resonance of gold nanorods is sensitive to refractive index changes in the environment, which allowed us to detect individual non-absorbing proteins. These biomolecules were bound to the functionalized metal surface with preferential attachment to the tips of the nanorod. The binding and unbinding of single protein molecules from the solution give rise to sudden absorption steps [3], and could be of use in micro-analytical applications and in-situ sensing.

3. The strong optical near field close to the tips of gold nanorods enhances coupling to optical waves, both for excitation and for emission. These two effects strongly resonate at the plasmon frequency of the rod and enable detecting single molecules of a weakly fluorescent dye, with quantum efficiency of 1% or less [4]. This method is a generalization of single-molecule spectroscopy to a broad class of bad fluorophores, with either low quantum yields or long fluorescence lifetimes. Comparison to finite-element calculations indicate that excitation and emission enhancements critically depend on the spectral overlap between the dye's absorption and fluorescence and the nanorod's surface plasmon resonance [5].

The strong light-matter interaction caused by plasmons opens many new experiments, such as the manipulation of position and orientation of anisotropic gold nanoparticles in complex media.

References

1. A. Gaiduk et al., *Science*, 2010, **330,** 353.
2. L. Hou et al., *New J. Phys.*, 2015, **17,** 013050.
3. P. Zijlstra et al. *Nat. Nanotech.*, 2012, **7**, 379.
4. H. Yuan et al., *Angew. Chem.*, 2013, **52,** 1217.
5. S. Khatua et al., *ACS Nano*, 2014, **8,** 4440.

QUANTITATIVE MOLECULAR IMAGING IN VIVO, WITH IMMUNOLOGIC BINDING ASSAYS & HIGH RESOLUTION CERENKOV MOLECULAR IMAGING

B.W. Pogue[1,2], R. Zhang[1], H. Lin[1], J. Gunn[1], A. Glaser[1], J. Andreozzi[1], S. Vinogradov[3], S. Jiang[1], D.J. Gladstone[1,2], and **L.A. Jarvis[1,2]**

[1] Thayer School of Engineering, Dartmouth College, Hanover NH USA 03755, brian.w.pogue@dartmouth.edu
[2] Geisel School of Medicine at Dartmouth, Hanover NH USA 03755
[2] Perelman School of Medicine at the University of Pennsylvania, Philadelphia PA USA 19104

Abstract. Molecular imaging using the Cerenkov as an internal tissue excitation system is shown, allowing high–resolution sensing of metabolites. Cherenkov light is stimulated by MeV beam irradiation from a radiation therapy device in a narrow beam, and raster scanned across the sample, with luminescence emission captured by a gated intensified detector. The dose delivered can be substantially lower than a CT scan, and yet the spatial resolution for imaging in rodents be near 0.2 mm. This is demonstrated in tissue phantoms as well as mouse studies, sensing molecular oxygen in lymph nodes *in vivo*. Diagnostic molecular guidance is feasible with this.

Introduction

Cerenkov light emission from MeV gamma-ray and electron beam delivery has recently been shown to be detectable and could be used in some applications for 3D dosimetry in radiation therapy in water tanks [1–3] or 2D surface dosimetry in humans [4, 5]. The major potential benefit of Cerenkov imaging is that it is a way to image beams in real time with several frames per second. As such, it is feasible to image treatment beams dynamically, and create composite visualizations of the treatment plans. This imaging can be used to verify new treatment plans prior to application to patients, or to quickly verify new machines, or testing in situations where access is limited. The strength of this optical imaging is that it is simple to implement, and provides immediate feedback. The drawbacks are related to minor differences between Cerenkov emission and dose, which make it not an exact measurement of dose.

In human imaging studies, clinical trials have been completed to image surface emissions in real time during therapy. Whole breast irradiation was followed for fractionated therapy in 12 patients. Positioning repeatability was within the 3mm distance to agreement criteria, and the Cerenkov images were able to be used to verify day-to-day patient alignment [4, 5].

This optical emission is broadband [6, 7] in origin, with a $1/\lambda^2$ dependence of intensity with wavelength, λ. Yet most of the UV-blue-green light is absorbed locally (within 100's of microns) by the blood in tissue, while the red-NIR wavelengths have longer path lengths (3–6 mm). As a result of this attenuation in vivo, ideal excitation reporters to be activated with this light have absorption in the red wavelengths with NIR emission [8, 9]. This is explored in this report.

Methods

Excitation from a 6 MV photon beam was used from a linear accelerator (LINAC, Clinac 2100CD, Varian Medical Systems) used for standard radiation therapy. The beam was collimated to be 5mm in diameter through positioning of the jaws and multileaf collimators (MLCs). A plan was created to raster scan the beam through movement of the MLCs, as appropriate for the beam size to cover the body of the phantom or animals studied.

Luminescence was detected from the specimens by a gated intensified CCD camera (ICCD PI-MAX4, Princeton Instruments) with triggering from the LINAC output, gating the intensifier amplify only during the 3 us bursts of radiation, delivered at 200 Hz. The camera was coupled to the phantom either directly for luminescence imaging or through a spectrometer for fluorescence imaging. The luminescence imaging is slow enough that spectral filtering was not needed, and temporal gating of the signal was sufficient for high S/N, whereas with fluorescence signals, they are emitted nearly instatntaneously with the 3us radiation and so needed to be separated from the background Cerenkov signal by spectral filtering through a spectrometer. Both approaches were outlined and evaluated in this study.

A range of reporters was tested for their efficiency in reporting signals from tissue phantoms. The main luminescent agent tested was PtG4 (platiunum-based oxyphor, S. Vinogradov, UPenn), which has a lifetime which is sensitive to the local oxygen concentration and a quantum yield of emission

near 20%. The fluorescent reporters tested were a range of IRDyes (LI-COR Biosciences) and red fluorescent proteins. The optimal luminescent and fluorescent reporters were then utilized for demonstration that high resolution oxygen sensing could be achieved in vivo in a rat model [9]. Additionally localization of red fluorescent protein expression in mice is demonstrated.

Results & Conclusions

The results show that luminescence imaging is readily achieved with temporal gating and with exceptionally strong S/N, because of the removal of the background Cherenkov signal from gating. The depth of sampling was better than 20 mm deep, and the ability to detect objects as small as 0.1 mm was demonstrated in tissue phantoms. There is a reciprocity between the amount of radiation dose needed for imaging and the concentration of fluorophore needed for detection. When typical in vivo concentrations of 1uM are used, then the imaging can be achieved with therapeutic fraction level doses (~1 Gy). Whereas when higher local concentrations were used, as might be seen in lymph nodes or pharmacologic doses (1 mM) then imaging can be achieved with radiation doses well below that of a radiologic imaging scan (<1 mGy). The signal also falls off with depth into the medium, but because it is only the exiting luminescence fluence which is attenuated, the signal simply falls off by about 1 order of magnitude per cm of tissue. This parameter space allows for high resolution imaging of rodents with reasonable biological concentrations of probes.

Acknowledgements

This work has been supported by NIH research grant R01CA109558.

References

1. A.K. Glaser, S.C. Davis, D.M. McClatchy, R. Zhang, B.W. Pogue, and D.J. Gladstone, "Projection imaging of photon beams by the Cerenkov effect", *Med Phys*, 2013, **40**(1), 012101.
2. A.K. Glaser, W.H. Voigt, S.C. Davis, R. Zhang, D.J. Gladstone, and B.W. Pogue, "Three-dimensional Cerenkov tomography of energy deposition from ionizing radiation beams", *Opt Lett*, 2013, **38**(5), 634-6.
3. A.K. Glaser, R. Zhang, D.J. Gladstone, and B.W. Pogue, "Optical dosimetry of radiotherapy beams using Cherenkov radiation: the relationship between light emission and dose", *Phys Med Biol*, 2014, **59**(14), 3789-811.
4. L.A. Jarvis, R. Zhang, D.J. Gladstone, S. Jiang, W. Hitchcock, O.D. Friedman, A.K. Glaser, M. Jermyn, and B.W. Pogue, "Cherenkov video imaging allows for the first visualization of radiation therapy in real time", *Int J Radiat Oncol Biol Phys*, 2014, **89**(3), 615-22.
5. R. Zhang, J.M. Andreozzi, D.J. Gladstone, W.L. Hitchcock, A.K. Glaser, S. Jiang, B.W. Pogue, and L.A. Jarvis, "Cherenkoscopy based patient positioning validation and movement tracking during post-lumpectomy whole breast radiation therapy", *Phys Med Biol*, 2015, **60**(1), L1-14.
6. G.S. Mitchell, R.K. Gill, D.L. Boucher, C. Li, and S.R. Cherry, "*In vivo* Cerenkov luminescence imaging: a new tool for molecular imaging", *Philos Trans A Math Phys Eng Sci*, 2011, **369**(1955), 4605-19.
7. R. Robertson, M.S. Germanos, C. Li, G.S. Mitchell, S.R. Cherry, and M.D. Silva, "Optical imaging of Cerenkov light generation from positron-emitting radiotracers", *Phys Med Biol*, 2009, **54**(16), N355-65.
8. R. Zhang, A. Glaser, T.V. Esipova, S.C. Kanick, S.C. Davis, S. Vinogradov, D. Gladstone, and B.W. Pogue, "Cerenkov radiation emission and excited luminescence (CREL) sensitivity during external beam radiation therapy: Monte Carlo and tissue oxygenation phantom studies", *Biomed Opt Express*, 2012, **3**(10), 2381-94.
9. R. Zhang, A.V. Dsouza, J.R. Gunn, T.V. Esipova, S.A. Vinogradov, A.K. Glaser, L.A. Jarvis, D.J. Gladstone, and B.W. Pogue, "Cherenkov-Excited Luminescence Scanned Imaging (CELSI)", *Opt. Lett.*, 2015 (in press).

CLINICAL RAMAN SPECTROSCOPY – A TOOL FOR UNMET MEDICAL CHALLENGES?

J. Popp[1,2]

[1] Leibniz Institute of Photonic Technology, Jena, Germany, juergen.popp@ipht-jena.de
[2] Institute of Physical Chemistry & Abbe-Center of Photonics, Friedrich-Schiller University Jena, Germany

Abstract. Here we report about the application of Raman approaches for the clinical diagnosis and therapy of infectious diseases and cancer representing unmet medical needs. We will present chip-based bacterial isolation strategies for a fast Raman spectroscopic identification of pathogens and the determination of their antibiotic resistances, which is crucial for patient's survival. Moreover, we report about Raman on-chip approaches for the identification of circulating tumor cells and therapeutic drug monitoring. Furthermore, we introduce linear and nonlinear Raman approaches for *ex-vivo* and *in-vivo* spectral histopathology for an early diagnosis of cancer.

A comprehensive analysis to determine diagnostic, prognostic and predictive factors in a few steps or ideally in one-step requires the development of new, fast and reliable approaches that support and supplement routine medical diagnostics and therapy. In the past years, medical photonics has witnessed the development of optical / photonic approaches that are potentially in a position to meet these aforementioned challenges. In this context, spectroscopic approaches like e.g. Raman spectroscopy are especially noteworthy. Raman spectroscopy is an especially efficient method since it probes molecular vibrations distinct for each type of molecule. A Raman spectrum can be seen as a characteristic "molecular fingerprint" of every sample. The ability to obtain specific chemical information labelfree makes Raman spectroscopy attractive for many clinical investigations of bodily fluids, pathogens, cells, and tissue biopsies [1]. In this contribution, we will summarize our recent results in implementing various Raman-approaches for infectious diseases and cancer, as these types of diseases harbor unmet needs regarding diagnosis and therapy.

We will start with highlighting the potential of Raman microspectroscopy for an early diagnosis and therapy of infectious diseases with special focus on sepsis. In the field of sepsis, the fast identification of pathogens, their resistances and the specific host is crucial for choosing the appropriate initial antibiotic therapy to save lives in intensive care units. It will be shown that Raman hold great promise as point-of-care approaches to address these challenging tasks [2–5]. In this context we will present innovative chip-based bacterial isolation strategies out of complex sample matrices (e.g. blood or urine) [6, 7].

The second part of this presentation focuses on Raman studies on eukaryotic cells for biomedical applications. Here, we will report about the great potential of Raman spectroscopy for a label-free discrimination between normal and (circulating) tumor cells and towards establishing a Raman spectroscopic hemogram [8–10]. In particular we will report about the recent progress we made towards Raman activated cell sorting (RACS) by coupling Raman spectroscopy with microfluidics and micromanipulation approaches [11, 12].

Besides single cells, whole tissue sections like biopsy specimens can be characterized by means of Raman-microspectroscopy enabling an objective evaluation of the tissue samples for an early diagnosis of cancer (= spectral histopathology) [13–15]. The potential to couple the Raman system via optical fibers to the point of measurements has enabled within the last years besides *ex-vivo* Raman studies on excised tissue also *in-vivo* Raman studies, i.e. Raman endospectroscopy. We will introduce novel Raman fiber probes for in-vivo tissue screening to reliably diagnose and screen cancer and other diseases like atherosclerosis in internal organs like e.g. colon, stomach or aorta [16].

While the advantage of Raman spectroscopy are its unprecedented high specificity it suffers from its poor sensitivity. This disadvantage can be overcome by utilizing non-linear Raman phenomena like CARS = coherent anti-Stokes Raman scattering. However, these methods as standalone techniques are typically highlighting a particular detail of e.g. pathological alterations in tissues and cells. In order to improve the diagnostic result a meaningful combination of different contrast mechanism in a multimodal approach in one microscopic setting has been proven to be extremely beneficial for biomedical imaging. Here we demonstrate how the combination of CARS, second harmonic generation (SHG) and two-photon excited autofluorescence (TPEF) to a multimodal imaging approach allows one to characterize the architecture and biochemical composition, i.e., the morphochemistry of frozen section biopsy specimens from a broad range of different tissues and pathologies [17–22]. We will demonstrate the detection of characteristic structures and the accompanying molecular changes of several

cancer entities. Increasing the spectral resolution and analyzing CARS images at multiple Raman resonances improves the chemical specificity [20]. To facilitate handling and interpretation of the image data characteristic properties can be automatically extracted by advanced image processing algorithms. Overall, the presented examples show the great potential of multimodal non-linear imaging to complement established clinical pathological diagnostic tools.

Acknowledgements

Financial support of the EU, the ”Thüringer Kultusministerium”, the ”Thüringer Aufbaubank”, the Federal Ministryof Education and Research, Germany (BMBF), the German Science Foundation, the Fonds der Chemischen Industrie and the Carl-Zeiss Foundation are greatly acknowledged.

References

1. C. Krafft and J. Popp, *Anal. Bioanal. Chem.*, 2015, **407**, 699-717.
2. S. Kloß, B. Kampe, S. Sachse, P. Rösch, E. Straube, W. Pfister, M. Kiehntopf, and J. Popp, *Anal. Chem.*, 2013, **85**, 697-708.
3. U.-Ch. Schröer, C. Beleites, C. Assmann, U. Glaser, U. Hübner, W. Pfister, W. Fritzsche, J. Popp, and U. Neugebauer, *Scientific Reports*, 2015, **5**, 8217-1-7.
4. C. Große, N. Bergner, J. Dellith, R. Heller, M. Bauer, A. Mellmann, J. Popp, and U. Neugebauer, *Anal. Chem.*, 2015, **87**, 2137-2142.
5. S. Kloß, P. Rösch, W. Pfister, M. Kiehntopf, and J. Popp, *Anal. Chem.*, 2015, **87**, 937-943.
6. S. Pahlow, S. Kloß, V. Blättel, K. Kirsch, U. Hübner, D. Cialla, P. Rösch, K. Weber, and J. Popp, *ChemPhysChem*, 2013, **14**, 3600-3605.
7. U.C. Schröder, A. Ramoji, U. Glaser, S. Sachse, C. Leiterer, A. Cszaki, U. Huebner, W. Fritsche, W. Pfister, M. Bauer, J. Popp, and U. Neugebauer, *Anal. Chem.*, 2013, **85**, 10717-10724.
8. U. Neugebauer, T. Bocklitz, J. H. Clement, C. Krafft, and J. Popp, *Analyst*, 2010, **135**, 3178-3182.
9. S. Dochow, C. Krafft, U. Neugebauer, T. Bocklitz, T. Henkel, G. Mayer, J. Albert, and J. Popp, *Lab Chip*, 2011, **11**, 1484-1490.
10. A. Ramoji, U. Neugebauer, T. Bocklitz, M. Foerster, M. Kiehntopf, M. Bauer, and J. Popp, *Anal. Chem.*, 2012, **84**, 5335-5342.
11. S. Dochow, M. Becker, R. Spittel, C. Beleites, S. Stanca, I. Latka, K. Schuster, J. Kobelke, S. Unger, T. Henkel, G. Mayer, J. Albert, M. Rothhardt, C. Krafft, and J. Popp, *Lab Chip*, 2013, **13**, 1109-1113.
12. S. Dochow, C. Beleites, T. Henkel, G. Mayer, J. Albert, J. Clement, C. Krafft, and J. Popp, *Anal. Bioanal. Chem.*, 2013, **405**, 2743-2746.
13. N. Bergner, B.F.M. Romeike, R. Reichart, R. Kalff, C. Krafft, and J. Popp, *Analyst*, 2013, **138**, 3983-3990.
14. N. Bergner, C. Krafft, K.D. Geiger, M. Kirsch, G. Schackert, and J. Popp, *Anal. Bioanal. Chem.*, 2012, **403**, 719-725.
15. N. Bergner, A. Medyukhina, K.D. Geiger, M. Kirsch, G. Schackert, C. Krafft, and J. Popp, *Anal. Bioanal. Chem.*, 2013, **405**, 8719-8728.
16. C. Matthäus, S. Dochow, G. Bergner, A. Lattermann, B.F. Romeike, E.T. Marple, C. Krafft, B. Dietzek, B.R. Brehm, and J. Popp, *Anal. Chem.*, 2012, **84**, 7845-7851.
17. C. Krafft, A.A. Ramoji, C. Bielecki, N. Vogler, T. Meyer, D. Akimov, P. Rösch, M. Schmitt, B. Dietzek, I. Petersen, A. Stallmach, and J. Popp, *J. Biophoton.*, 2009, **2**, 303-312.
18. T. Meyer, N. Bergner, C. Bielecki, C. Krafft, D. Akimov, B.F. M. Romeike, R. Reichart, R. Kalff, B. Dietzek, and J. Popp, *J. Biomed. Opt.*, 2011, **16**, 021113/1-021113/10.
19. T. Meyer, M. Baumgartl, T. Gottschall, T. Pascher, A. Wuttig, C. Matthaeus, B.F.M. Romeike, B.R. Brehm, J. Limpert, A. Tuennermann, O. Guntinas-Lichius, B. Dietzek, M. Schmitt, and J. Popp, *Analyst*, 2013, **138**, 4048-4057.
20. T. Meyer, M. Chemnitz, M. Baumgartl, T. Gottschall, T. Pascher, C. Matthaus, B.F.M. Romeike, B.R. Brehm, J. Limpert, A. Tünnermann, M. Schmitt, B. Dietzek, and J. Popp, *Anal. Chem.*, 2013, **85**, 6703-6715.
21. T. Meyer, O. Guntinas-Lichius, F. von Eggeling, G. Ernst, D. Akimov, M. Schmitt, B. Dietzek, and J. Popp, *HEAD & NECK*, 2013, E280-E287.
22. S. Heuke, N. Vogler, T. Meyer, D. Akimov, F. Kluschke, H.-J. Röwert-Huber, J. Lademann, B. Dietzek, and J. Popp, *British Journal of Deramatology*, 2013, **169**, 794-803.

UNIFIED MODEL OF PLASMA FORMATION, BUBBLE GENERATION, AND SHOCK WAVE EMISSION IN WATER FOR FEMTOSECOND TO NANOSECOND LASER PULSES

A. Vogel, X.-X. Liang, S. Freidank, and **N. Linz**

Institute of Biomedical Optics, University of Lübeck, Germany
vogel@bmo.uni-luebeck.de

Abstract. We established a self-consistent unified model that describes the dynamics of plasma formation and plasma-induced hydrodynamic effects over femtosecond to microsecond time scales. The model covers a large range of pulse durations, wavelengths, focusing angles and pulse energies, and it portrays the mechanisms of nonlinear material modifications from free-electron-induced chemical changes at low pulse energies to disruptive mechanical effects well above the breakdown threshold.

To date, optical breakdown modeling has mostly focused on tracking the evolution of free electron density and predicting breakdown thresholds defined by a critical free electron density. Such thresholds cannot easily be linked to experimental observations of breakdown events, which commonly rely on the detection of plasma luminescence, phase changes (leading to transient bubbles in water or permanent cavities in solids), or shock wave emission. We developed modeling tools for optical breakdown events in water, which span various phases reaching from breakdown initiation via solvated electron generation, through laser induced-plasma formation and temperature evolution in the focal spot to the later phases of cavitation bubble dynamics and shock wave emission.

The rate equation model considers the interplay of linear absorption, photoionization, avalanche ionization and recombination, traces thermalization and temperature evolution during the laser pulse, and portrays the role of thermal ionization that becomes relevant for $T > 3000$ K. Consideration of thermal ionization is crucial for the modeling of picosecond and nanosecond breakdown. Modeling of free-electron generation includes recent insights on breakdown initiation in water via solvated electron generation that were obtained by bubble threshold spectroscopy of IR nanosecond breakdown. The wavelength dependence of the breakdown threshold indicates that avalanche ionization is initiated via multiphoton excitation of valence band electrons into a solvated state at E = 6.6 eV followed by up-conversion into the conduction band level that is located at 9.5 eV.

The ability of tracing the temperature evolution in the focal volume allows for a comparison with experimental data on bubble thresholds and bubble size. The model of laser-induced plasma formation is linked to a hydrodynamic model of plasma-induced pressure evolution and phase transitions that enables to trace bubble generation and dynamics as well as shock wave emission. This way, the amount of nonlinear energy deposition in transparent dielectrics and the resulting material modifications can be assessed as a function of incident laser energy. The unified model of plasma formation and bubble dynamics yields an excellent agreement with experimental results over a large range of pulse durations and wavelengths, as shown in Fig. 1.

Future challenges are to include spatio-temporal aspects of optical breakdown associated with nonlinear light propagation and with the plasma growth during the laser pulse.

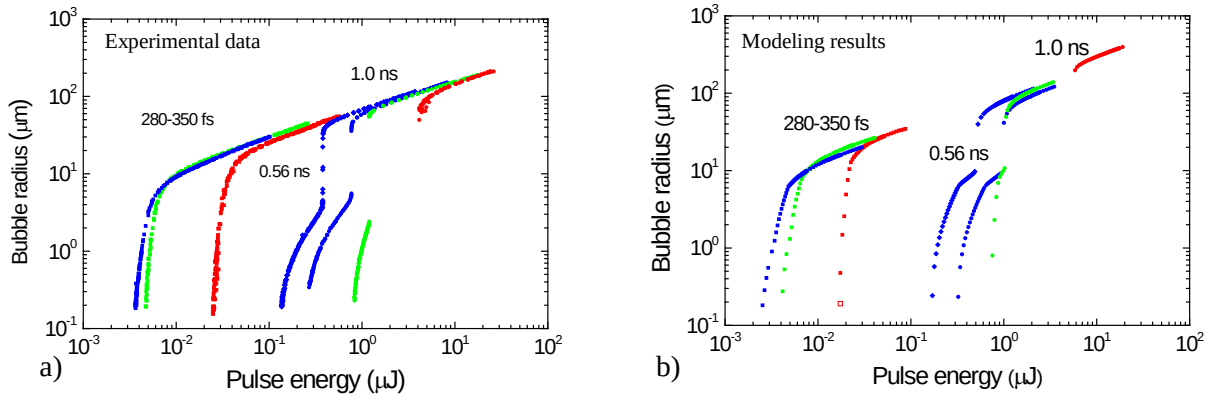

Fig. 1. Maximum cavitation bubble radius in water as a function of laser pulse energy for different pulse durations and wavelengths; NA = 0.8. Colors denote wavelengths: blue = 347 nm for fs pulses, and 355 nm for ns pulses; green = 520 nm and 532 nm, red = 1040 nm and 1064 nm. a) experimental data, b) modeling results

A COMPACT X-RAY FREE ELECTRON LASER (XFEL) FACILITY SACLA AND ITS SCIENTIFIC APPLICATIONS

M. Yabashi

RIKEN SPring-8 Center, Sayo, Hyogo, Japan, yabashi@spring8.or.jp

Abstract. SACLA has started user operation in March 2012, as the first compact XFEL facility. Over three years, SACLA has routinely generated XFEL light in a photon energy range from 4 to 15 keV. The facility supports experimental activities in broad fields by offering high-quality X-ray optics, diagnostics, and detectors with flexible experimental configurations. Key scientific results in diverse fields, as well as perspective on the facility upgrade, will be presented.

Introduction

In June 2011, SPring-8 Angstrom Compact free-electron LAser (SACLA) in SPring-8, Harima, Japan [1, 2] (Fig. 1) achieved the first lasing at 10 keV, after 5-year construction as a national project from FY2006 to FY2010. In March 2012, SACLA started user operation, as the second X-ray free-electron laser (XFEL) facility after the Linac Coherent Light Source (LCLS) in the United States, and the first compact XFEL facility in the world. By combining a low-emittance electron-beam injector, a high-gradient C-band linac, and short-period in-vacuum undulators, SACLA generates intense short-wavelength XFEL radiation below 1 Å with a moderate electron beam energy of 8 GeV and a relatively compact length of 700 m. To exploit full capability of SACLA, we have developed state-of-the-art X-ray optics, diagnostics [3], fast 2D detectors (MP-CCD [4]), and various types of experimental instruments [5].

Fig. 1. SACLA and SPring-8

Characteristics of XFEL light from SACLA

At a photon energy around 10 keV, SACLA generates a high pulse energy of ~0.5 mJ/pulse (~$3 \cdot 10^{11}$ photons/pulse) with a short pulse duration below 10 fs [6], which results in a high peak power of several tens gigawatts. To further increase an intensity, we have developed a 1-um focusing optics [7] and a 50-nm focusing optics based on a two-stage scheme [8], by using state-of-the-art reflective mirrors developed by a group of Prof. Yamauchi (Osaka Univ.). A significant intensity of 10^{20} W/cm^2 generated by the latter has enabled unique opportunities for conducting sciences in extreme conditions.

Another noticeable capability of SACLA is to generate two-color SASE XFEL light with a large wavelength separation over 30% by employing variable-gap, in-vacuum undulators [9].

A pump-probe scheme, which combines femtosecond optical laser for pump and XFEL for probe, is a powerful method to investigate ultrafast phenomena. Although a timing jitter between the optical pulse and XFEL pulse, typically ~150 fs rms, has limited a temporal resolution, we have recently developed an arrival timing tool [10], which improves the time resolution to a sub-100 fs range.

Scientific achievements of SACLA

Initial scientific results from SACLA appeared in the beginning of 2013. Since then, a number of papers in diverse fields, such as quantum X-ray optics, atom, molecular and optical (AMO) science, ultrafast chemistry, structural biology, coherent imaging, and even elementary particle physics, have been published. The latest publication list is found in ref. 11

One of the outstanding capabilities of SACLA is the ability to produce ultrahigh-intense X-ray pulses with the help of state-of-the-art X-ray focusing optics. Using the two-stage 50-nm focusing system to produce an ultrahigh intensity of 10^{20} W/cm^2, we observed an increase in the transmissivity of 7.1-keV X-rays by an order of magnitude for a 20-μm-thick iron foil [12]. This is the first observation of saturable absorption of hard X-rays, which originated from the depletion of atoms in the ground state after photoionization of the K-shell electrons.

Intense XFEL pulses can further reveal nonlinear interactions with vacuum. Quantum electrodynamics (QED) predicts the existence of photon-photon (γ-γ) scattering processes as a nonlinear effect of vacuum. An advantage of short-wavelength X-rays is a higher cross section of γ-γ scattering, which is proportional to the sixth power of the photon energy. Asai et al first attempted a direct search for γ-γ scattering in the X-ray region by developing a beam splitter optics based on an X-ray interferometric technique [13]. Even though no events were observed in the signal region (18.1–19.9 keV), further improvement of monochromaticity, as well as enhancement of the intensity, will enable us to improve the detection limit by several orders of magnitudes and to approach a prediction of QED.

For biological applications, intense femtosecond XFEL pulses are highly useful for analysing structures of small samples with a damage-free condition, based on a so-called "diffract-before-destruction" scheme. Shen et al. has revealed an intrinsic structure of photosystem II (PS-II) at an excellent resolution of 1.95 Å [14] by combining SACLA with a conventional crystallographic technique. As a next step, invetsigation of transient states after photo pumping will be expected. Also, SACLA's excellent transverse coherence with high brilliance is applied for coherent diffractive imaging (CDI) measurements for non-periodic, nano-sized particles. Nishino et al. reconstructed whole-cell images of M. lacticum in a living state, contained in a micro-liquid enclosure without any stains, with a full-period spatial resolution of ~37 nm. They observed a high electron-density region inside the cell, which possibly related to condensation of the DNA molecules.

Future perspective of SACLA

The limited availability of beamtime has been a common concern for world's XFEL activities. To address this issue, we started construction of a new beamline BL2 in 2013 as the second hard X-ray FEL beamline at SACLA. We have achieved the first lasing of BL2 in October, 2014, and started operation for users in April, 2015.

Combination of XFEL and high power lasers is a promising scheme for developing high energy density science. In tight collaboration with the HERMES (High Energy density Revolution of Matter in Extreme States) project commenced by Prof. Kodama (Osaka University), we have installed high-power laser systems, such as 40-TW and dual 500-TW lasers, and started commissioning.

References

1. T. Ishikawa et al., *Nature Photon.*, 2012, **6**, 540-544.
2. M. Yabashi et al., *J. Synchrotron Rad.*, 2015, **22**, 477-484.
3. K. Tono et al., *New J. Phys.*, 2013, **12**, 083035.
4. T. Kameshima et al., *Rev. Sci. Instrum.*, 2014, **85**, 033110.
5. K. Tono et al., *J. Synchrotron Rad.*, 2015, **22**, 532-537; C. Song et al., *J. Appl. Cryst.*, 2014, **47**. 188-197.
6. Y. Inubushi et al., *Phys. Rev. Lett.*, 2012, **109**, 144801.
7. K. Yumoto et al., *Nature Photon.*, 2013, **7**, 43-47.
8. H. Mimura et al., *Nature Commun.*, 2014, **5**, 3539.
9. T. Hara et al., *Nature Commun.*, 2013, **4**, 2919.
10. T. Sato et al., *Appl. Phys. Exp.*, 2015, **8**, 012702.
11. http://xfel.riken.jp/research/indexnn.html
12. H. Yoneda et al., *Nature Commun.*, 2014, **5**, 5080.
13. T. Inada et al., *Phys. Lett.* B, 2014, **732**, 356-359.
14. M. Suga et al., *Nature*, 2014, **517**, 99-103.
15. T. Kimura et al., *Nature Commun.*, 2014, **5**, 3052.

PHOTOLUMINESCENT NANOMATERIALS FOR VISUALISATION OF MOLECULAR TRAFFICKING IN CELLS TOWARDS DIAGNOSTICS AND THERAPY

A.V. Zvyagin

Laboratory of Optical Theranostics, N.I. Lobachevsky Nizhny Novgorod State University, Russia
Macquarie University, Sydney, Australia
andrei.zvyagin@mq.edu.au

Abstract. A productive confluence of Biophotonics with Nanotechnology have lead to emergance of new biofunctional nanomaterials. Reported here fluorescent nanodiamonds (FND), nanorubies and upconversion nanoparticles (UCNP) were applied to visualise and probe biomolecular processes in their comprehensive celluar context. The exceptional photophysical properties of these nanoparticle pushed the sensitivity limit to the single biomolecule detection, whereas the nanoparticles surface can host various surface moieties, enabling anchoring of targeting and/or therpeutic cargo molecules. These nanoparticle biocomplexes, e.g. FND-EGFP, nanoruby-DAMGO, (quantum dot)-somatostatin or UCNP-(mini-antibody) are pieced together to form hybrid nanocomplexes capable to enter cells or pathology lesions to enable diagnosis and therapy.

Development of new approaches for the diagnosis and therapy of tumours (taken together, termed Theranostics) – one of the most dynamic areas of Biomedicine, where new nanomaterials afford new opportunities. The nanomaterial merits include: programmability of their physical and chemical properties; abundance of reactive functional groups on the surface; large effective surface area; optimum size, which determines preferential accumulation of nanoparticles in tumour tissue due to the so-called enhanced permeability and retention effect, EPR [1]. This paper reports on multifunctional theranostic agents based on a new-generation biologically compliant photoluminescent nanoparticles with unique optical properties – fluorescent nanodiamonds [2], nanorubies and upconversion nanoparticles.

UCNPs in the form of hexagonal crystallites $NaYF_4$ doped with Yb^{3+} and Er^{3+} or Tm^{3+} were synthesised in the size range of 20–100 nm by a modified solvothermal method [3] [see Fig. 1 (a, b)]. Nanorubies mean-sized 30 nm were produced by a femtosecond laser ablation method and high-energy ball milling, allowing the gram-scale, low-cost production. Nanoruby water and buffers colloids

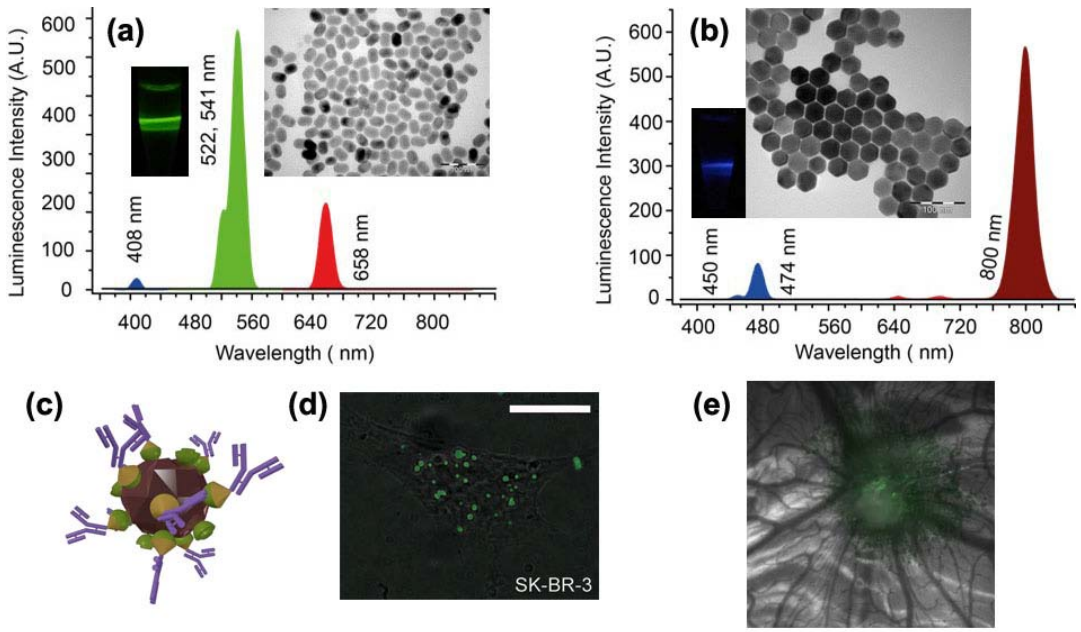

Fig. 1. Photoluminescence spectra at 975-nm laser excitation, TEM images and photographs of NaYF4:Yb:Er (a), (b) NaYF4:Yb:Tm nanomaterials. The laser path was visualised in green and blue, respectively. (c) 3D-rendering of UCNP-based nanocomplex (brown crystallite) with antibodies (double-strand purple structures) bound to its surface via molecular adaptors barnase (cones), barstar (hemispheres); (d) Epi-luminescence microscopy of the HER2/neu overexpressing SK-BR-3 cells (grey) with target-delivered UCNP complexes (green) analogous to these in (c). Scale bar, 20 μm. (d) A tumour grafted on the chicken embryo chorioallantoic membrane, showing accumulation of UCNPs via enhanced permeability and retention effect (EPR)

appeared to be remarkably stable, silane-based surface modification made the surface amenable for attachment of biomolecules, such as designed ankyrin repeat proteins (DARPin) and mini-antibodies. Initially hydrophobic UCNPs were hydrophilised and polymer-coated or impregnated into polymer beads. We demonstrated binding of functional proteins by flexible design using high-affinity protein adaptors Barnase:Barstar [4] [Fig. 1 (c)]. The attachment of therapeutic vectors for photodynamic therapy, miniSOG and others, were also developed and demonstrated.

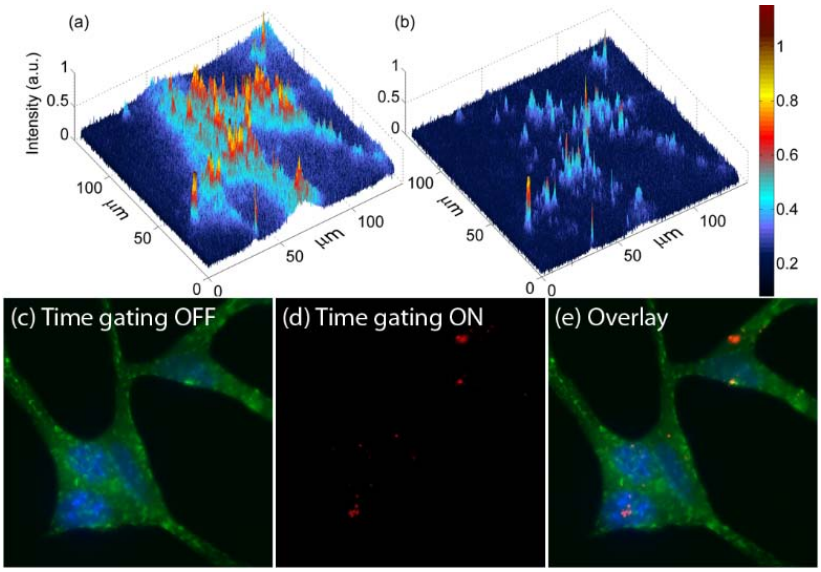

Fig. 2. Images of cells treated with nanoruby in (a) normal and (b) time-gating modes, where only nanorubies are visible. Nanoruby-treated cell membrane were immunostained (antibody-Alexa Fluor 594) and nuclei stained (Hoechst). Epiluminescence imaging display: (c) cell membrane and nuclei (green) (d) only nanorubies, using time-gated mode; (e) an overlay of (c) and (d)

Optical imaging of our photoluminescent nanoparticles in cells using a home-built epiluminescent microscope allowed visualisation of single nanorubies on the hefty background of cell autofluorescence and fluorescence dye-staining (Fig. 2). Target-delivered UCNPs rendered breast adenocarcinoma cells conspicuous among normal cells [Fig. 1 (d)]. The *in vivo* accumulation of UCNPs in a tumour grafted on the chicken embryo chorioallantoic membrane via EPR is shown in Fig. 1 (e), demonstrating target-delivery of drugs to cancer sites. The therapeutic potential of such drugs as photodynamic therapy active miniSOG-mini-antibody loaded onto UCNP was also successfully demonstrated in cells.

Acknowledgements

This work was supported by grant No. 14.Z50.31.0022.

References

1. H. Maeda, *Bioconjugate Chemistrym*, 2010, **21**, 797.
2. C. Bradac, T. Gaebel, N. Naidoo, M.J. Sellars, J. Twamley, L.J. Brown, A.S. Barnard, T. Plakhotnik, A.V. Zvyagin, and J.R. Rabeau, *Nature Nanotechnology*, 2010, **5**, 345.
3. A. Nadort, V.K.A. Sreenivasan, Z. Song, A.V. Nechaev, V.A. Semchishen, V.Y. Panchenko, and A.V. Zvyagin, *PLOS ONE*, 2013, **8**, e63292.
4. V.K.A. Sreenivasan, E.A. Ivukina, W. Deng, T.A. Kelf, T.A. Zdobnova, S.V. Lukash, B.V. Veryugin, O.A. Stremovskiy, A.V. Zvyagin, and S.M. Deyev, *J of Mater Chem*, 2011, **21**, 65.

Optical Bioimaging

Chairs

Karsten König
Saarland University, Germany
Ilya Turchin
Institute of Applied Physics RAS, Russia

Alex Vitkin
University of Toronto, Canada

Program Committee

Stefan Andersson-Engels
Lund University, Sweden
Johannes de Boer
VU University Amsterdam, The Netherlands

Valentin Gelikonov
Institute of Applied Physics RAS, Russia

Ivan Pelivanov
M.V.Lomonosov Moscow State University, Russia

Jorge Ripoll
The Charles III University of Madrid, Spain

Bruce Tromberg
Beckman Laser Institute and Medical Clinic, UC Irvine, USA

Valery Tuchin
Saratov State University, Institute of Precise Mechanics and Control RAS, Russia

Invited

NON-LINEAR PHOTOACOUSTICS USING GOLD COATED NANOEMULSIONS

B. Arnal[1], **C. Perez**[1], **C.-W. Wei**[1], **J. Xia**[1], **M. Lombardo**[1], **I. Pelivanov**[1,2], **D. Pozzo**[1], and **M. O'Donnell**[1]

[1] University of Washington, Dept. of Bioengineering and Chemical engineering, Seattle, WA, USA
bastien.arnal@gmail.com
[2] Moscow State University, International Laser Center, Moscow, Russia

Abstract. Targeted theranostic strategies can be achieved using phase-change contrast agents. Ultrasound can vaporize nanodroplets but often at high exposure parameters. We introduced light sensitive perfluorohexane nanodroplets, adding 12 nm gold nanospheres at their surface. Pulsed NIR light can vaporize these droplets, enhancing thermal expansion and allowing non-linear photoacoustic imaging to gain specificity for molecular imaging. Moreover, the vaporization thresholds can be reduced using combined ultrasound and laser emissions which enabled a real-time pulse sequence to image the droplets with very high contrast (30 dB) and specificity, even at low concentrations.

Gold-coated nanoemulsions synthesis

Colloidal gold nanospheres (GNS) with a mean diameter of 12 nm in an aqueous buffer were synthesized using a citrate reduction method. The particles were functionalized with two kinds of thiols, PEG-thiol which is hydrophilic and butane-thiol which is hydrophobic. As a results the GNS are stabilized at the oil-water interface [0] (cf. Fig. 1).

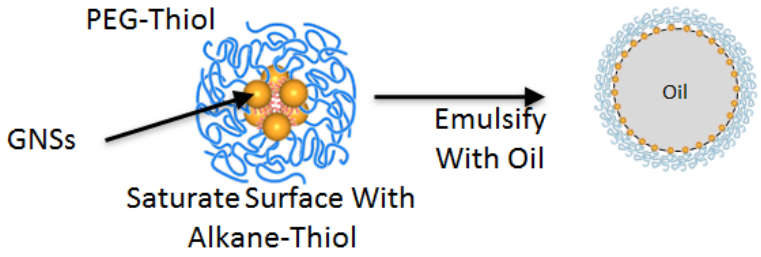

Fig. 1. Formulation of NEB-GNS

Non-linear photoacoustics

An OPO laser (Surrelite OPO plus, Continuum, Santa Clara, CA, USA) delivering 10-ns pulse at 750 nm was used in this study. From a few mJ/cm^2, the non-linear photoacoustic response of a NEB-GNS sample can be measured thanks to the increase in thermal expansion [1]. However, it may be difficult to achieve such fluencies with deep penetration into tissue. If light is emitted when an US pulse (here 1.2 MHz) reaches the target, there is a combined mechanical effect (from US) and heat (from light absorbed by the GNS) [3].

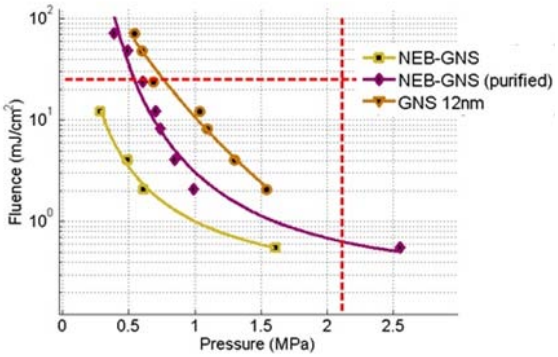

Fig. 2. Vaporization thresholds (cavitation probabilities = 50%) for different light and US exposures for the NEB-GNS sample, a purified one containing only nanodroplets and GNS as a reference

Given the high stability of nanodroplets due to high surface tension, one hypothesis was that the heat at the surface could decrease surface tension to facilitate vaporization. Indeed, as shown in Fig. 2,

the thresholds are shown to change dramatically [4]. In addition, the vaporization parameters are within the diagnostic exposure limits for both US and laser. Furthermore, when the droplet is vaporized, the US field is automatically scattered by the bubble, which enables a dramatic signal enhancement compared to pure photoacoustic measurements (more than 30 dB signal enhancement).

Sono-photoacoustic imaging

A linear array (L7-4, ATL, Bothell, WA, USA) was controlled by a Verasonics Vantage 128 US scanner (Redmond, WA, USA) operating with a custom interleaved PA – US sequence. The maximum voltage of 96 V was used to maximize the pressure amplitude. By focusing a broad beam further than the region of interest, the acoustic pressure was higher than in the case of a simple plane wave. For each SPA image, an US image was acquired with 6 plane waves (–5° to 5°). The SPA imaging sequence contains two reference US frames with N-cycle emissions (3 MHz) with positive and negative polarities (US^+ & US^-). Then, two subsequent laser+US (LUS) acquisitions are done with positive and negative polarities (LUS^+ & LUS^-) which have the vaporization SPA signal, US scattering and linear PA signals:

$$LUS^{+/-} = SPA^{+/-} + US^{+/-} + PA \tag{1}$$

To remove pure US scattering (Fig. 3 a), the subtraction ($LUS^{+/-} - US^{+/-}$) retreives the vaporization signals mixed with linear PA signals. Then the following subtraction cancels linear PA signals [5] (cf. Fig. 3 b):

$$SPA = \left(LUS^+ - US^+\right) - \left(LUS^- - US^-\right) \tag{2}$$

$$SPA = SPA^+ - SPA^- \tag{3}$$

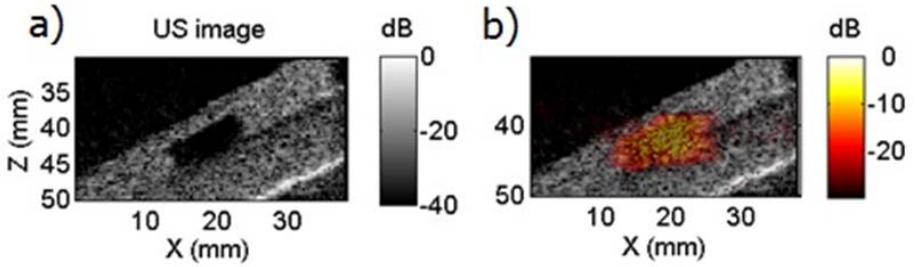

Fig. 3. a) US picture of a phantom: a PA acrylamide inclusion (dark) is filled with droplets at a 6.3 pM concentration. b) Sono-photoacoustic imaging (hot scale) superimposed on the US picture

Acknowledgements

This work was supported in part by NIH RO1-EB016034, R01- CA170734, RO1-HL121226, R01-HL125339, the Life Sciences Discovery Fund 3292512, NSF CBET-1236309, and the Department of Bioengineering at the University of Washington.

References

1. K. Larson-Smith et and D. C. Pozzo, *Soft Matter*, 2011, vol. 7 (nº 11), p. 5339, 2011.
2. C. Wei, M. Lombardo, K. Larson-Smith, I. Pelivanov, C. Perez, J. Xia, T. Matula, D. Pozzo, and M. O'Donnell, *Applied Physics Letters*, 2014, **vol. 104**, nº (3), p. 033701, jan. 2014.
3. C.-W. Wei, J. Xia, M. Lombardo, C. Perez, B. Arnal, K. Larson-Smith, I. Pelivanov, T. Matula, L. Pozzo, and M. O'Donnell, *Opt. Lett.*, 2014, **vol. 39**(nº 9), p. 2599-2602, may 2014.
4. B. Arnal, C. Perez, C.-W. Wei, J. Xia, M. Lombardo, I. Pelivanov, T. J. Matula, L. D. Pozzo, and M. O'Donnell, "Sono-photoacoustic imaging of gold nanoemulsions: Part I. Exposure thresholds", *Photoacoustics*, (2015.)
5. B. Arnal, C.-W. Wei, C. Perez, T.-M. Nguyen, M. Lombardo, I. Pelivanov, L. D. Pozzo, and M. O'Donnell, *Photoacoustics*, (2015).

Invited

NEW ADVANCED IMAGING APPROACHES APPLIED TO EXPERIMENTAL INFLAMMATORY BOWEL DISEASE

A. Arranz[1] and **J. Ripoll**[2,3]

[1] Dept. of Cell Biology and Immunology, Center for Molecular Biology "Severo Ochoa" (CBMSO), CSIC, Madrid, Spain, alicia.arranz@cbm.csic.es
[2] Dept. of Bioengineering, Universidad Carlos III of Madrid, Spain
[3] Hospital General Universitario Gregorio Marañón, Madrid, Spain

Abstract. A new technique termed Helical Optical Projection Tomography (hOPT) has been developed with the aim to overcome some of the limitations of current 3D optical imaging techniques [1, 2]. hOPT is based on Optical Projection Tomography (OPT) with the major difference that there is a translation of the sample in the vertical direction during the image acquisition process, requiring a new approach to image reconstruction. Contrary to OPT, hOPT makes possible to obtain 3D-optical images of intact long samples without imposing limits on the sample length. We here use hOPT to obtain 3D-reconstructed images of the colon of DSS-treated mice, a model for Inflammatory Bowel Disease, allowing the identification of the structural alterations.

Introduction

Long samples with high biological interest such as mouse spinal cord, long bones, colon or small intestine, amongst others, have to be segmented prior to imaging. Up to date, it has therefore been very difficult to image long samples in-toto with the existing techniques. Long samples such as the ones described above are of great significance in current biomedical research topics such as intestinal carcinogenesis, inflammatory bowel diseases, multiple sclerosis, and many others. Helical Optical Projection Tomography [1, 2] was developed with the purpose of imaging intact elongated samples. We here apply it to inflammatory bowel disease studies.

Methods

Sample Preparation: Animals were kept at standard housing conditions providing water and food ad libitum. The DSS model was established as described previously [3]. Briefly, age-matched mice received 3.5% weight/vol DSS (36–50 kDa, MP Biomedicals) in the drinking water for 5 days followed by 3 days of autoclaved water administration. Model development was followed up by measuring weight loss daily. Prior collection of tissue samples, animals were deeply anesthetized and euthanized. Tissues (colons, small intestines and spinal cords) were aseptically removed, washed with PBS (colons and small intestines were also flushed with PBS) and fixed in 4% PFA for at least 24h at 4 ºC. After fixation, samples were washed twice with PBS, incubated with 1% weight/vol Triton X-100 for 30 minutes and washed again with PBS prior staining. Single staining with propidium iodide (30 µg/ml in PBS; Sigma-Aldrich, St. Louis, MO) was performed at room temperature for 30 minutes in dark followed by three washes of 10 minutes each with PBS. Once the staining procedure was completed, samples were mounted in 1.3% low-melting agarose (SeaPlaque, Lonza Rockland Inc, Rockland, ME). Mounted samples were then dehydrated by successive washes through a graded series of methanol (25%, 50%, 75% and 1%; 1 hour per wash) and left in 100% methanol overnight. Mounted samples were then transferred to BABB (benzyl alcohol and benzyl benzoate in a 1:2 ratio; Sigma-Aldrich, St. Louis, MO) for at least 24 hours. Measurements were performed with the samples submerged in BABB.

Results

Making use of hOPT we imaged colons from both healthy and dextran sodium sulphate (DSS)-treated animals, as a model of Inflammatory Bowel Disease (see Methods). As shown in Fig. 1, not only macroscopic aspects such as colon length (note the reduced length of the DSS colon in Fig. 1a), but also alterations at a microscopic level (such as disruption of the villus structure) can be observed in the 3D volume rendered images in Fig. 1b and 1c.

Conclusions

We here show studies of inflammatory bowel disease of intact samples, which enable imaging of morphological changes with cellular resolution. It is important to note that these observations provide information on the development and severity of the disease by studying the intact 3D structure of the entire organ, which was previously only partly possible by histological analysis of successive micro-

tome slices of small portions of tissue or by imaging tissue segments [3, 4]. Here we demonstrate that the use of hOPT represents a potential fast alternative to such analysis allowing the visualization of the entire sample and therefore providing unique information not possible to obtain otherwise.

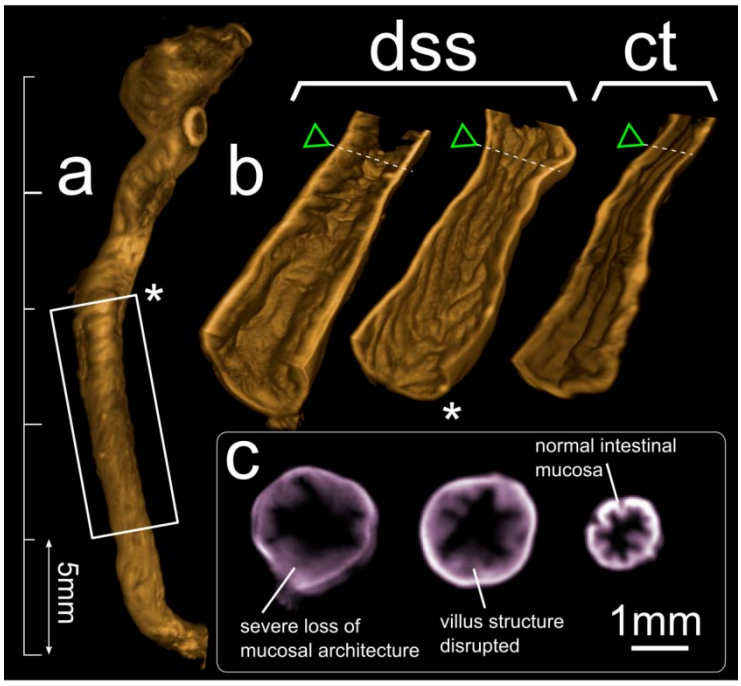

Fig. 1. Visualization of inflammation-derived alteration in mouse colons from DSS-treated animals. The DSS model of colitis was established in C57BL/6 mice. Colons were obtained from healthy and DSS-treated animals and samples were prepared and imaged as described in Methods. a) Volume render of a whole mouse colon from a DSS treated animal and (b) open volume renders of two DSS (asterisks indicate same colon sample) and one healthy (ct - control) mouse colon, including coronal slices of the area marked with the green arrowheads in (c). Tissue alteration in the inflamed mouse colon due to disruption of the villus structure can be observed in the 3D reconstructed data.

Acknowledgements

J.R. acknowledges support from the EC FP7 CIG grant HIGH-THROUGHPUT TOMO, and MINECO grant FIS2013-41802-R MESO-IMAGING. A. Arranz acknowledges support from the Marie Curie Intra-European Fellowship program (FP7-PEOPLE-2010-IEF).

References

1. A. Arranz, et al., "Helical optical projection tomography", *Opt. Express*, 2013, **21**, 25912–25.
2. A. Arranz, et al., "*In-vivo* Optical Tomography of Small Scattering Specimens: time-lapse 3D imaging of the head eversion process in Drosophila melanogaster", *Sci. Rep*., 2014, **4**, 7325.
3. S. Wirtz, C. Neufert, B. Weigmann, and M.F. Neurath, "Chemically induced mouse models of intestinal inflammation", *Nature protocols*, 2007, **2**, 541–6.
4. A. Ertürk, et al., "Three-dimensional imaging of the unsectioned adult spinal cord to assess axon regeneration and glial responses after injury", *Nature medicine*, 2012, **18**, 166–71.
5. Y.-Y. Fu, et al., "Microtome-free 3-dimensional confocal imaging method for visualization of mouse intestine with subcellular-level resolution", *Gastroenterology*, 2009, **137**, 453–65.

OPTICAL PROPERTIES OF TISSUES IN THE VISIBLE – NIR SPECTRAL REGION

A.N. Bashkatov[1,2], **E.A. Genina**[1,2], **V.V. Tuchin**[1,2]

[1]Research-Educational Institute of Optics and Biophotonics, Saratov State University, Saratov, Russia
a.n.bashkatov@mail.ru
[2]Interdisciplinary Laboratory of Biophotonics, Tomsk State University, Tomsk, Russia

Recent technological advancements in the photonics industry have real progress toward the development of clinical functional imaging, surgical and therapeutic systems. Development of the optical methods in modern medicine in the areas of diagnostics, surgery and therapy has stimulated the investigation of optical properties of human tissues, since the efficacy of optical probing of the tissues depends on the photon propagation and fluence rate distribution within irradiated tissues. Examples of diagnostic use are the following: the monitoring of blood oxygenation and tissue metabolism, detection of malignancies, and recently suggested various techniques for optical imaging. Therapeutic usage mostly includes applications in laser surgery and photodynamic therapy. For these applications, the knowledge of tissue optical properties is of great importance for interpretation and quantification of the diagnostic data, and for prediction of light distribution and absorbed energy for therapeutic and surgical use. Numerous investigations related to determination of tissue optical properties are available in literature however the optical properties of many tissues have not been studied in a wide wavelength range.

In this report the tissue optical properties (absorption coefficient, scattering coefficient, reduced scattering coefficient, and scattering anisotropy factor) are presented. We summarize the optical properties of human eye sclera, dura mater, bone, skin, subcutaneous adipose tissue, maxillary sinus, colon, muscle, parietal peritoneum, nails, lung, pancreas, nasal polyps, tonsils, and stomach mucous measured in the visible – NIR spectral region. Optical models, which describe wavelength dependence of the optical properties of the tissue, have been presented.

TIME-RESOLVED OPTICAL METABOLIC IMAGING OF PARKINSON'S DISEASE AT CELLULAR LEVEL

S. Chakraborty[1], F.-Sh. Nian[2], J.-W. Tsai[2], A. Karmenyan[3,4], and **A. Chiou[1,4]**

[1] Institute of Biophotonics, National Yang-Ming University, Taipei, Taiwan 11221, ROC
sandeep_nanotsk@yahoo.co.in
[2] Institute of Brain Science, National Yang-Ming University, Taipei, Taiwan 11221, ROC
[3] Department of Physics, National Dong Hwa University, Hualien, Taiwan 97401, ROC
[4] Biophotonics & Molecular Imaging Research Center, National Yang-Ming University, Taipei, Taiwan 11221, ROC

Abstract. Parkinson's disease is a progressive neurological disorder which can be associated with altered cellular metabolic state. We applied two-photon fluorescence lifetime imaging (TP-FLIM) of cellular coenzymes NADH and FAD to monitor the cellular metabolic state in PC12 cell based PD model. Our results show a significant decrease in the cellular metabolic rate and change in cellular microenvironment after the PC12 cells, were treated with NGF, and then with MPP^+ to induce PD like conditions at the cellular level. These findings may further pave the way for application of TP-FLIM in PD tissue and animal models.

Introduction

Fluorescence lifetime imaging microscopy (FLIM) of autofluorescent coenzymes reduced nicotinamide adenine dinucleotide (NADH) and flavin adenine dinucleotide (FAD) remains relatively unexplored as the optical metabolic imaging technique in neurodegenerative diseases. These metabolic coenzymes NADH (at complex I) and FAD (at complex II) are the primary electron donor and acceptor, respectively, in the electron transport chain of the oxidative phosphorylation process in mitochondria [1]. Moreover, mitochondrial dysfunction and metabolic state change are considered primary in the progressive neurodegenerative disorder in the development of Parkinson's disease (PD) [1]. In this work, two-photon fluorescence lifetime imaging microscopy (TP-FLIM) was applied to determine the fluorescence lifetime as well as the amounts of NADH and FAD in PC12 cells, treated with nerve growth factor (NGF) to differentiate into neuronal cells. The neuronal cells were further treated with MPP^+ (1-methyl-4-phenylpyridinium) to induce PD syndromes and the differences in fluorescence lifetime and the amounts of reduced NADH and oxidized FAD before and after the treatment were measured and compared. Our preliminary results show significant differences in the fluorescence lifetime of both free and bound NADH and FAD in the PD induced cells vs. the control cells. Moreover, the ratio of free to protein bound NADH as well protein-bound to free FAD ratios showed significant differences in PD induced cells vs. the control cells. Further studies will be required for a better understanding of the role of cellular metabolism in PD progression.

Materials and Methods

TP-FLIM, NADH and FAD Imaging, Data Analysis

A mode-locked Ti:sapphire laser (Tsunami, Spectra-Physics, USA), with 81 MHz picosecond laser pulses, was used as the two photon excitation source for imaging. In our study, 770 and 860 nm wavelengths were used for the excitation of NADH and FAD respectively. The fluorescence emission and the reference signals were combined with the time-correlated single-photon counting electronics board (TCSPC, PicoHarp300). Data acquisition and analysis was done by a commercial software package SymPho Time (PicoQuant GmbH, Germany). Fluorescence lifetime was determined from the decay function $I_c(t)$ of NADH (and FAD), derived from the convolution of an instrument response function (I_{instru}, ~ 188 ps in our case) with a double exponential function (Eq. 1), with offset correction for dark noise (I_0), as shown in Eq. 2.

$$F(t)=a_1 e^{-t/\tau_1}+a_2 e^{-t/\tau_2} \tag{1}$$

$$I_c(t)=\int_{-\alpha}^{\alpha} I_{instru}(t)\left[I_0+F(t)\right]dt \tag{2}$$

where $a_1 e^{-t/\tau_1}$ and $a_2 e^{-t/\tau_2}$ denote the contributed fuorescence decays from short and long lifetime components of free and bound NADH, respectively; τ_1 and τ_2 represent their corresponding lifetime constants; and a_1 and a_2 refer to their corresponding relative amounts. The interpretation of these is exactly the opposite for FAD contributions.

Results, Discussions, and Conclusions

In this study, we applied two photon fluorescence lifetime imaging technique to compare cellular metabolism between normal vs. PD induced neuronal cells. Fig. 1(A) shows the fluorescence lifetime images of NADH in the cells at several concentrations of MPP^+. Analysis of the fluorescence lifetime values in regions of interest (ROI) drawn around specific cells or group of cells reveals that the average lifetime of NADH and the short as well as long lifetime components decreased with increasing MPP+ concentrations [Fig. 1(B)], indicating a strong cellular microenvironment change. Moreover, ratio of the free to protein bound NADH components (a_1/a_2) increases statistically significantly [Fig. 1(C)] with increasing MPP+ concentrations, suggesting a lower metabolic rate in the PD induced cells.

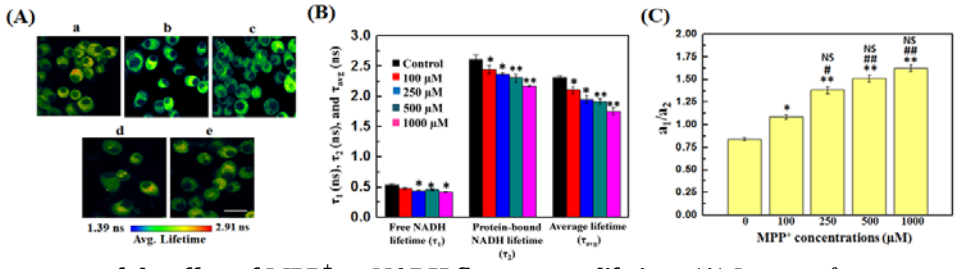

Fig. 1. Summary of the effect of MPP^+ on NADH fluorescence lifetime. (A) Images of average two-photon fluorescence lifetime (color coded) of NADH of (a) the control cells, and of cells treated with (b) 100, (c) 250, (d) 500, and (e) 1000 µM of MPP^+. Scale bar: 20 µm. (B) Summary of fluorescence lifetimes. (C) Dependence of free to bound NADH ratio (a_1/a_2) on MPP^+ concentrations. Statistical significance: *: $P < 0.05$, **: $P < 0.005$ for control vs. MPP+ treated cells; #: $P < 0.05$, ##: $P < 0.005$ for 100 µM vs. other MPP^+ treated cells; NS: $P > 0.05$ for insignificant difference among the cells treated with 250, 500, and 1000 µM of MPP^+

Likewise, Fig. 2(A) shows the fluorescence lifetime images of FAD. After analyzing the data, we observed that the two fluorescence lifetime components and the average lifetime decreased, compared with the control cells without MPP^+ treatment, further confirming the cellular microenvironment change [Fig. 2(B)]. In this case, the amount of change was relatively insensitive to the MPP^+ concentration. However, the ratio of free to protein bound FAD components (a_2/a_1) decreases significantly with increasing MPP^+ concentrations [Fig. 2(C)], suggesting a lower rate of metabolic activity in the PD induced cells.

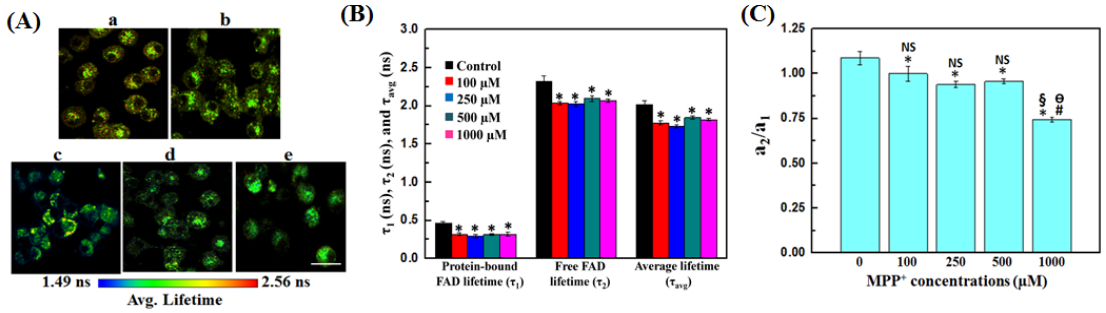

Fig. 2. Summary of the effect of MPP^+ on FAD fluorescence lifetime. (A) Images of average two-photon fluorescence lifetime (color coded) of FAD of (a) the control cells, and of cells treated with (b) 100, (c) 250, (d) 500, and (e) 1000 µM of MPP+. Scale bar: 20 µm. (B) Summary of fluorescence lifetimes. (C) Dependence of free to bound FAD ratio (a_2/a_1) on MPP+ concentrations. Statistical significance: *: $P < 0.05$ for control vs. other MPP+ treated cells; NS: $P > 0.05$ for insignificant difference among 100, 250, and 500 µM; #: $P < 0.05$ for 100 vs. 1000 µM; §: $p < 0.05$ for 250 vs. 1000 µM; ɵ: $p < 0.05$ for 500 vs. 1000 µM

In conclusions, TP-FLIM unravels the differences between normal vs. PD induced PC12 cells in the cellular metabolic level. Further studies may lead to a better understanding of the pathology of PD at the molecular level.

Acknowledgements. This work is supported by The Ministry of Science and Technology, Taiwan, ROC (Project No. NSC102-2218-E-010-003) and the Top University Project from Taiwan Ministry of Education.

References

1. K.F. Winklhofer and C. Hass, *Biochim. Biophys. Acta*., 2010, **1802**(1), 29-44.

Invited

ADVENTURES IN DIFFUSE OPTICAL IMAGING

H. Dehghani

University of Birmingham, United Kingdom
h.dehghani@cs.bham.ac.uk

Abstract. Diffuse optical imaging of tissue can be used to characterize molecular features of tissue for the detection, diagnosis, and/or management of cancer therapy. Current developments in technical and computational approaches for breast cancer imaging as well as functional imaging of the human brain as well as some preclinical applications will be presented.

Light is a powerful tool for in-vivo investigation of biological tissues [1]. In the 600–1100 nm range it is not harmful for biological media at low power densities (few mW/mm^2), permitting use of in vivo non-invasive diagnostics. The low tissue absorption in this wavelength range makes it possible to look into the body at few cm of depth (e.g. the brain cortex) or through more than 6–8 cm of tissue in transmittance (e.g. compressed breast). Furthermore, light carries multiple useful information from the visited tissues linked either to absorption (e.g. tissue composition, oxygenation), or to scattering (e.g. tissue microstructure) or even by exploiting selective fluorescent markers to specific biochemical targets. In the same spectral range most tissues are highly scattering. This is a most severe challenge, causing scattering to absorption coupling, strong attenuation of the remitted light with exponential dependence on the visited depth, blurring effects impairing spatial resolution.

Breast Imaging

Near-infrared spectroscopy (NIRS) of breast tissue can potentially provide quantification of absorbers, scattering and luminescent markers via the consideration measurement data and model-based parameter recovery which are based on realistic assumptions [2]. Such assumption, based on prior knowledge can be critical about things such as (i) the tissue shape and/or structure, (ii) spectral constituents, (iii) limits on parameters, (iv) demographic or biomarker data, and (v) biophysical models of the temporal signal shapes. Through the use of a framework based on NIRS imaging with prior information is shown that prior information datasets could be incorporated at any step in the NIRS process, with the general workflow being: (i) data acquisition, (ii) pre-processing, (iii) forward model, (iv) inversion/reconstruction, (v) post-processing, and (vi) interpretation/diagnosis.

One of the most exciting and promising applications of NIRS based imaging is through its use in prediction of breast tumor response to neoadjuvant chemotherapy [3, 4]. It has been shown that through quantitative imaging of total haemoglobin and oxygen saturation, of the same patient repeated over short period of time, it may be possible to identify responders from partial or non-responders to aid clinical prognosis.

Brain Imaging

Functional brain imaging has become an important neuroimaging technique for the study of brain organization and development. Compared to other imaging techniques Diffuse Optical Tomography (DOT) is a portable and low-cost technique that can be applied to infants and hospitalized patients. Studies have shown that brain activation tasks such as inhibiting reflexive saccades task and hierarchical language tasks are correlated across multiple brain regions. Some neurodevelopmental disorders such as Alzheimer's disease, schizophrenia and adolescent depression have also been shown to be related to the distributed brain networks. Functional connectivity brain imaging is focused on the correlation between diverse brain regions and mapping of the functional networks. Traditional task-based functional imaging may not be suitable for some subjects such as unconscious patients and infants. Resting-state functional connectivity imaging provides a task-less approach to analyse correlation between diverse brain regions during spontaneous activity and mapping the resting state networks [5]. Wide field imaging assesses brain activation from multiple functional regions simultaneously and can be used for both task-based functional connectivity and resting-state functional connectivity imaging. DOT is a NIR based imaging technique that has shown its ability to recover brain function of an adult, within 20mm depth of the cortex surface by monitoring changes in oxygenated haemoglobin and deoxygenated haemoglobin based on measures of transmitted/reflected NIR signal from the scalp [5].

Small Animal Luminescence Imaging

Bioluminescence imaging (BLI) is widely used for in vivo pre-clinical biomedical studies where the aim is to image distributed biological light sources, such as luciferase-tagged cancer cells, located inside a living animal. BLI images are often used to estimate the concentrations and spatial distributions of reporters and thus to infer biological activity from images of the measured surface radiance. However, the validity of quantification using BLI data is limited due to the unknown, highly attenuating and scattering properties of biological tissue. This leads to ambiguous data and inaccurate analyses derived directly from captured two-dimensional images, particularly for deep sources.

A novel multi-modal optical imaging system for quantitative 3D bioluminescence and functional imaging has been developed with key novelties of (1) the physical set-up and (2) it uses spectrally-constrained diffuse optical tomography to reconstruct concentrations of absorbing agents allowing the deduction of optical properties at wavelengths beyond those measured. This is a useful prior for bioluminescence tomography as well as a new window into small animal physiology [6].

Model-based image reconstruction

The development of diffuse optical tomography as a functional imaging modality has relied largely on the use of model-based image reconstruction. The recovery of optical parameters from boundary measurements of light propagation within tissue is inherently a difficult one, because the problem is nonlinear, ill-posed and ill-conditioned. Additionally, although the measured near-infrared signals of light transmission through tissue provide high imaging contrast, the reconstructed images suffer from poor spatial resolution due to the diffuse propagation of light in biological tissue. The application of model-based image reconstruction is reviewed in detail elsewhere [7], together with a numerical modeling approach to light propagation in tissue as well as generalized image reconstruction using boundary data.

There exists a set of open-source modeling and image reconstruction tools, NIRFAST (www.nirfast.org) that has provided a set of standardized tools for applications to DOT as well as small animal luminescence based imaging. Multimodal approaches that combine NIR and conventional imaging modalities have been shown to improve optical parameter estimation dramatically and representing a prevailing trend in NIR imaging. These approaches typically involve applying anatomical templates from magnetic resonance imaging/computed tomography/ultrasound images to guide the recovery of optical parameters. However, merging these data sets requires multiple software packages, substantial expertise, significant time-commitment, and often results in unacceptably poor mesh quality for optical image reconstruction. The open-source tools available via NIRFAST addresses these challenges directly by introducing automated digital imaging and communications in medicine image stack segmentation and a new one-click three-dimensional mesh generator optimized for multimodal NIR imaging, and combining these capabilities into a single software package (available for free download) with a streamlined workflow.

Acknowledgements

This work has been funded by the National Institutes of Health (NIH) Grant R01EB009233-2, RO1-CA132750 and EPSRC, UK.

References

1. V. Ntziachristos, et al., "Looking and listening to light: the evolution of whole-body photonic imaging", *Nat Biotechnol*, 2005 **23**(3), 313-20.
2. B.W. Pogue, et al., "Implicit and explicit priori information in near-infrared spectral imaging: accuracy, quantification and diagnostic value", *Phil. Trans. R. Soc. A*, 2011, **369**, 4531-4557.
3. S. Jiang, et al., "Predicting Breast Tumor Response to Neoadjuvant Chemotherapy with Diffuse Optical Spectroscopic Tomography prior to Treatment", *Clin Cancer Res*, 2014, **20**, 6006.
4. A.E. Cerussi, et al., "Diffuse optical spectroscopic imaging correlates with final pathological response in breast cancer neoadjuvant chemotherapy", *Phil. Trans. R. Soc. A*, 2011, **369**, 4512-4530.
5. A. Eggebrecht, et al., "Mapping distributed brain function and networks with diffuse optical tomography", *Nature photonics*, 2014, **8**(6), 448-454.
6. J.A. Guggenheim, et al., "Multi-modal molecular diffuse optical tomography system for small animal imaging", *Measurement Science and Technology*, 2013, **24**(10), 105405.
7. H. Dehghani, et al., "Numerical modelling and image reconstruction in diffuse optical tomography", *Phil. Trans. R. Soc. A*, 2009, **367**(1900), 3073-3093.

HOLOGRAPHIC AND FLUORESCENT TECHNIQUE FOR 3D OPTICAL MICROSCOPY

V.V. Dudenkova[1] and **Yu.N. Zakharov**[1,2]

[1] Lobachevsky State University of Nizhni Novgorod, Russia,
orannge@mail.ru
[2] Harvard University, Boston, USA

Abstract. The concept of extension and addition of holographic microscopy by advantages of a method of the fluorescence analysis of BaLM is provided. Ways of combination of techniques in the same optical scheme are described. The key parameters influencing achievement of maxsimum possible resolution are considered. As a result in case of visualization of the samples, which transparent in optical band, three-dimensional super resolution is received that significantly expands possibilities of the noninvasive analysis of biological samples.

At operation with the majority of biological objects researchers have some problems. The main problem is small distinctions in optical transparency of intracellular components. It gives low contrast of the image and integral distortions in case of study of non-uniform and optically translucent objects. Low contrast of the image complicates not only visual perception, but also hinders quantitative measurement of its characteristics. Applications of such approaches as a method of a dark field or a method of phase contrast [1] give only a qualitative result. Differential interference contrast (DIC) is acceptable for the quantitative estimates only for object areas with a high gradient of optical characteristics [2]. Lately, laser confocal scanning microscopes are used for laboratory researches of such objects. For example, this approach is actively used for research of biological samples structure and functional features. Such microscopes use z-scanning for obtaining the volume image, when the optical slices of the researching sample, which are received by means of a confocal diaphragm, are scanned sequentially with relocation along an optical axis between frames. Then the three-dimensional image is built by software processing operations. But use of such confocal microscopes only slightly improves transverse resolution, and longitudinal resolution, though considerably improves, remains limited by diffraction limit. Besides, in case of research of the fast-proceeding processes in live objects, the image thus received not absolutely correctly displays a real sample as scanning happens quite slowly and the object changes during such scanning. It doesn't allow to make quantitative measurements. For achievement of registration of dynamic changes in biological cultures with higher resolution the modern STED [3] methods or 4-π [4] microscopy are usually used. But any of the listed hi-end approaches doesn't yield the universal optimum results as it reaches improving separately of either longitudinal or transverse resolution. Simultaneous improvement of resolution in all spatial measurements is realized in technically difficult techniques of STED microscopy [5], STORM [6, 7], PALM [8] and others, but the long data collection is necessary, so they are suitable only for the fixed samples.

Application of holographic techniques for creation of the three-dimensional structure of biological samples is free of these limitations so it is the perspective direction in study of biological objects with achievement of ultrahigh three-dimensional and necessary time resolution.

Also, we show off-axis holography setup on the base of Carl Zeiss LSM 510 microscope, which allows to research dynamics of change of live biological objects. In this case, reference beam, which is coherent with the object beam, is introduced under the calculated optimum angle from the outside. The image of object is reconstructed numerically by double Fourier transformation algorithm with filtering in the frequency area.

As a result of application of the holographic recording method and further reconstructing of phase and amplitude information of object, there was an opportunity to carry out visualization of the dynamic changes in live biological samples. The developmental data on the example of research of neuronal plasticity were obtained. The perspective direction of development of this approach is a combination with methods enriching obtaining information at observation of neural cultures. For example holography united with calcium imaging is realized [9].

Application of holographic approach allows to receive ultrahigh sensitivity to longitudinal changes in optical length. But transversal resolution is the same as in diffraction limited microscopy. For resolve of this restriction it is possible to combine holographic method with one of approaches to improve transversal resolution, which meets certain requirements. Among them one of the main is speed of registration for achievement of high time resolution, and also compatibility with already applied

widely-distributed approaches to study biological objects, such as a calcium imaging or electrophysiology. Taking into account these restrictions, the best approach for overcoming of a diffraction limit in the transversal direction is the method of the fluorescence analysis of BaLM. (Bleaching/blinking assisted localization microscopy) [10]. It's fluorescence analysis, which basic approach consists in excitation of fluorescence and registration of fluorophore blinking. Then consecutive frames are subtracted the each other. This operation cleaning thereby a contribution from the molecules fluorescing on two subsequent frames. As a result there are images of separate molecules in the form of functions of a point spread function (PSF). All difference elements that is less, than the estimated PSF size, aren't considered. The remaining have a center of illumination that is given as localization of molecules of a fluorophor. Similar holographic scheme is suitable for use of BaLM method. However, for this purpose, to cut fluorescence of molecules from the exceeding exciting radiation it is necessary to set the filter before the registering matrix. Both for recording of holograms, and for fluorescence excitation, the coherent laser beam is used. For a holographic method the power of the used illumination influences only exposure time, but for the BaLM method the selection of the source of radiation and its parameters is absolutely important. Depending on a absorption spectrum of a specific fluorophore, it is necessary to select optimum wavelength of excitation. However it is most important to evaluate the power of exciting radiation correctly. Record of a series of frames with flicker is necessary for the accuracy of localization of separate molecules of a fluorophore, i.e. it is necessary to mark acts of ignition and blanking of separate molecules on all field of view in order to further definition of their centers. Therefore parameters of a fluorophore, lighting source, and also registering digital array shall be considered in calculation of optimum excitation power.

As a result of combination of holographic approach for improving of longitudinal resolution and a method of the fluorescent analysis of BaLM for overcoming of an Abbe diffraction limit in a transversal section, it was succeeded to work out approach for visualization of microscopic biological samples and dynamics of their changes with superresolution both in transversal plane and optical path difference.

Acknowledgements

The study was supported by RFBR (projects № 15-42-02658 and № 13-02-01420).

References

1. A. Bennett, H. Osterberg, H. Jupnik, and O. Richards, *Phase Microscopy*, 1951, p. 320.
2. M. Shribac, *Technical Digest. Optics in the Life Science*: Waikoloa Beach, Hawaii United States, 2013, NW4B.3.
3. S.W. Hell and J. Wichmann, *Optics Letters*, 1994, **19**, 780-782.
4. T.A. Klaк, S. Jakobs, M. Dyba, A. Egner, and S.W. Hell, *Proceedings of the National Academy of Sciences*, 2000, **97**, 8206-8210.
5. K.I. Willing, B. Harke, R. Medda, and S.W. Hell, *Nature methods*, 2007, **4**(11), 915-918.
6. M.J. Rust, M. Bates, and M. Zhuang, *Nature Methods*, 2006, **3**, 793-796.
7. M. Bates, B. Huang, G.T. Dempsey, and X. Zhuang, *Science*, 2007, **317**, 1749-1753.
8. E. Betzig, G.H. Patterson, R. Sougrat, O.W. Lindwasser, S. Olenych, J.S. Bonifacino, M.W. Davidson, J. Lippincott-Schwartz, and H.F. Hess, *Science*, 2006, **313**, 1642-1645.
9. M.S. Murav'eva, V.V. Dudenkova, A.I. Rybnikov, and Yu.N. Zakharov, *Radiophysics and Quantum Electronics*, 2015, **57**(8), 577-583.
10. D.T. Burnette, P. Sengupta, Y. Dai, J. Lippincott-Schwartz, and B. Kachar, *PNAS*, 2011, **108**(52), 21081-21086.

Invited

ADVANCING HIGH SPEED OPTICAL COHERENCE TOMOGRAPHY BY GOING PARALLEL

R.A. Leitgeb[1,2], D. Fechtig[1,2], L. Ginner[1,2], and **A. Kumar[1]**

[1] Center for Medical Physics and Biomedical Engineering, Medical University Vienna, Vienna, Austria
rainer.leitgeb@meduniwien.ac.at
[2] Christian Doppler Laboratory for Innovative Optical Imaging and its Translation to Medicine, Medical University Vienna, Vienna, Austria

Abstract. Point scanning OCT is ultimately limited in sensitivity and speed by shot noise and laser safety regulations. Higher speed is still possible by going parallel, either using full field or line field illumination. We demonstrate MHz A-scan rate with line field OCT for in-vivo retinal imaging, achieving over 94dB sensitivity in a single frame without averaging. The fast imaging rate is made possible by combining an off-axis approach for full range signal reconstruction with swept source based line field OCT (LPSI). Parallel OCT has the further advantage of intrinsic phase stability. We use this feature for digital refocusing employing a simple geometric optics based algorithm. With this algorithm we achieve an extended field of view over 3mm with maintained lateral resolution. Finally, fast tomogram sequences allow for lable-free retinal angiography as is shown for the parafoveal region *in-vivo*.

Summary

There are several inherent advantages of high speed imaging in OCT. For structural imaging high speed allows to record large field of view patches being only marginally affected by motion artifacts. Furthermore, an additional coordinate being time can be added to volumetric imaging, which is of gaining interest for studying dynamic sample properties as in elastography or in angiography. In particular Fourier Domain OCT enabled high speed imaging with high sensitivity: imaging speeds of up to 1 MHz were reported at a central wavelength of 840 nm, using spectrometer based FD OCT [1]. The development of frequency-domain mode-locked (FDML) swept source lasers set the stage for retinal imaging at acquisition speeds exceeding 1 MA-scans/s [2]. Point scanning devices are however ultimately limited in speed and sensitivity by shot noise and laser safety regulations. Klein et al. estimated a minimum required sensitivity of 95 dB for clinical imaging at 1060nm center wavelength with a corresponding maximum A-scan rate below 1 MHz [2]. Parallel OCT can further extend the speed capabilities of OCT, as line field (LF) or full field (FF) approaches are considered as extended illumination systems, that allow applying higher power to the sample. Retinal imaging with full field swept source OCT (FF SS OCT) was demonstrated at a maximum acquisition speed of equivalent 1.5 MA-scans/s [3]. FF OCT completely gives up the confocal gating, which results in loss of structural contrast due to scattered light. LF OCT on the other hand still keeps half of the confocal gate. With spectrometer based line field OCT an acquisition speed of 51 kHz for 3D imaging and a detection sensitivity of 89 dB has been achieved [4]. We present first results of *in vivo* three-dimensional (3D) retinal imaging with Line-field parallel swept source imaging (LPSI) and demonstrate 3D numerical refocusing to extend the effective depth of focus.

In LPSI a spectral interference pattern is obtained after illuminating a standard Michelson interferometer with a frequency swept source and detected by a fast linear pixel array sensor. The setup for *in vivo* retinal imaging is based on the one presented in our previous work and adapted for retinal imaging [5]. We employ a Superlum Broadsweeper 840M with a fiber output power of 20 mW. The sample power of 4.6 mW is well below the maximum permissible exposure (ANSI standards). A spectral bandwidth of approx. 30 nm full width at half maximum (FWHM) after applying a Gaussian window function yields an axial resolution of 12 µm in air. The optical path of the reference arm is aligned off-axis with respect to the sample arm, which is a well established method in holography to separate the complex conjugate (CC) artifact and the non-interferometric background (DC) from the interferometric cross correlation signal being the structure term. An angle between reference and sample field creates an intensity modulation of the cross correlation signal along the lateral parallel coordinate, which leads to a separation of the respective interference terms in spatial frequency space. Band-limiting the spatial frequency content of the imaged object structure to one half of the full frequency space via an adjustable slit allows removing the CC artifact and attenuating the DC term for full-range imaging. Hence, the number of spectral sampling points can be reduced by a factor of two to increase the imaging speed. We performed 3D retinal imaging at different lateral resolutions and acquisition speeds ranging from 600 to 1000 kA-scans/s and a detection sensitivity of 97 to 94 dB in a single frame without averaging, respectively. Furthermore we apply a scheme for mitigating the lateral Gaus-

sian signal decay through inverse Gaussian intensity weighting. Fig. 1 shows imaging results for in-vivo retinal imaging obtained at 600 kAscans/sec.

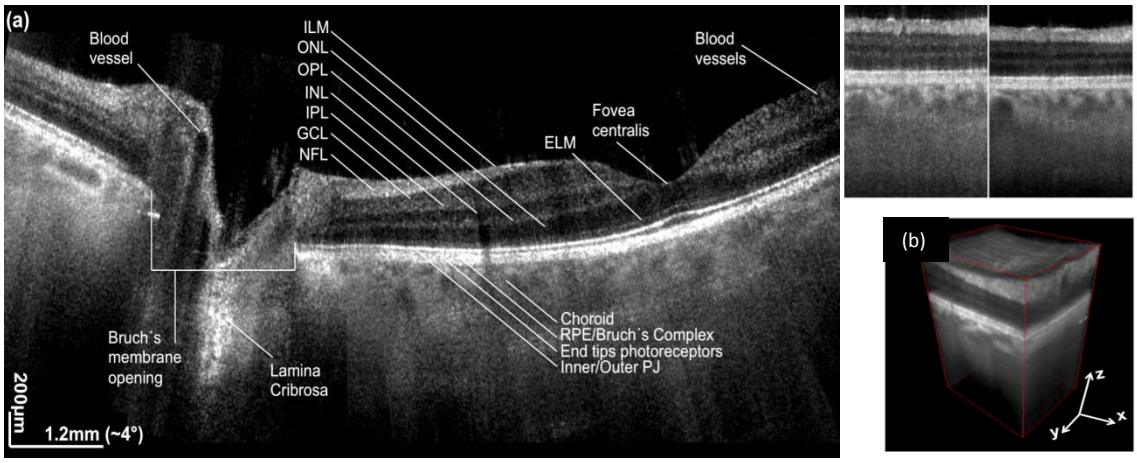

Fig. 1. (a) retinal scan across 30 deg at 600 kHz A-scan rate.(b) 3D rendered scan at optic nerve head region with orthogonal cross sections shown above

Figure 2 shows the performance for increasing A-scan rates, from 600 kHz to 1 MHz over a 6 deg lateral field of view. The spurious bright line is the rest of the DC term at the center of the axial full range. The tomograms are single frame images without any averaging applied.

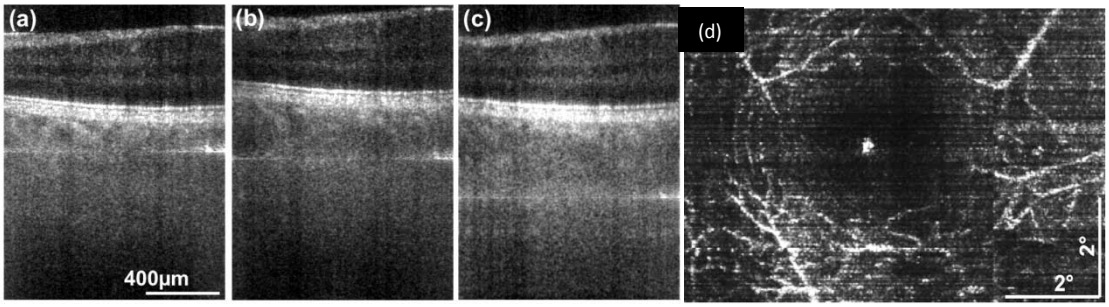

Fig. 2. Retinal imaging with (a) 600 kHz (b) 800 kHz (c) 1 MHz A-scan rate;(d) OCT microangiography

Fast tomogram sequences allow furthermore to perform OCT micro-angiography by calculating the average difference between successive logarithmically scaled tomograms [6]. The result is plotted in Fig. 2 (d) for the inner retinal vasculature in the parafoveal region. Parallel OCT has the advantage of being phase stable within full tomogram frames. In a recent work we were able to demonstrate the capability to perform digital refocusing over a field of view of 3 mm in depth [7]. In conclusion we demonstrate 3D *in vivo* retinal imaging of up to 1 MHz A-scan rate and more than 94 dB sensitivity with line-field parallel swept source interferometric imaging employing commercially available and cost-effective technology.

Acknowledgements. The financial support by the Austrian Federal Ministry of Economy, Family and Youth and the Austrian National Foundation of Research, Technology and Development and Carl Zeiss Meditec, Dublin is gratefully acknowledged.

References

1. O. Kocaoglu, T. Turner, Z. Liu, and D. Miller, *Biomed. Opt. Express*, 2014, **5**, 4186-4200.
2. T. Klein, W. Wieser, L. Reznicek, A. Neubauer, A. Kampik, and R. Huber, *Biomed. Opt. Express*, 2013, **4**, 1890-1908.
3. J.T. Bonin, G. Franke, M. Hagen-Eggert, P. Koch, and G. Hüttmann, *Opt. Lett.*, 2010, **35**, 3432-3434.
4. Y. Nakamura, S. Makita, M. Yamanari, M. Itoh, T. Yatagai, and Y. Yasuno, *Opt. Express*, 2007, **15**, 7103-7116.
5. D. Fechtig, T. Schmoll, B. Grajciar, W. Drexler, and R. Leitgeb, *Opt. Lett.*, 2014, **39**, 5333-5336.
6. C. Blatter, J. Weingast, A. Alex, B. Grajciar, W. Wieser, W. Drexler, R. Huber, and R. Leitgeb, *Biomed. Opt. Exp.*, 2012, **3**, 2636-2646.
7. D. Fechtig T. Schmoll, B. Grajciar, W. Drexler, and R. Leitgeb, *Proc. SPIE*, 2015, **9312**, 931203.

COMPARISON OF RECONSTRUCTION EFFICACY FOR DIFFERENT TRANSILLUMINATION FLUORESCENCE DIFFUSE TOMOGRAPHY METHODS

I. Fiks, M. Kleshnin, and **I. Turchin**

Institute of Applied Physics, Russian Academy of Sciences, 46 Ulyanov Street, 603950,
Nizhny Novgorod, Russia,
FiksII@yandex.ru

Abstract. We compared reconstruction efficacy for different transillumination fluorescence diffuse tomography (FDT) scanning methods: point source moving along object's boundary, and the detector is a stationary CCD camera (traditional FDT schema), spectral fluorescence diffuse tomography (SFDT) with a point excitation source and a point detector with spectral resolution move along the boundaries of the object, and different modifications of traditional FDT and SFDT schemes. It was found, that the one-sided scanning scheme is worse than the two-sided scheme with replacement of source and detector positions; for SFDT schemes it is preferable when source and detector move axially; the numerical characteristics of the 2-sided FDT and SFDT schemes are almost the same.

Introduction

The Reconstruction quality in Fluorescence Diffuse Tomography (FDT) depends essentially both on scanning method (optimal set of source and detector positions), and on the additional temporal and spectral information of the emission light. In this study we consider 6 transillumination schemes:

- FDT – a simple scheme: a point source with λ_{ex} wavelength moving along object's boundary, the detector is a stationary CCD camera with emission filter, thus detecting emission band λ_{em} integrally.
- FDT, 2 side – the scheme is similar to FDT, but the source and the detector are located on both sides (front and back) of the object.
- SFDT – spectral fluorescence diffuse tomography: a point excitation source λ_{ex} and a point detector with spectral resolution move axially along the boundaries of the object. The detector senses the whole emission spectrum λ_{em}.
- SFDT, 2 side – the scheme is similar to SFDT, but the source and detector are located on both sides of the object.
- SFDT-2 – spectral fluorescence diffuse tomography with point excitation source λ_{ex}. The point detector can move along object's boundary and sense the whole emission spectrum.
- SFDT-2, 2 side – the scheme is similar to SFDT-2, the source and detector are located on both sides of the object.

We compared the efficiency of these schemes in terms of reconstruction in the following numerical experiment.

Methods

If the initial volume is divided into N pairwise disjoint sets, then the spatial distribution of fluorophore concentration can be found as a solution of the system of linear equations with dimension $M \times N$:

$$Av = p,\ A \in R^{M \cdot N}, v \in R^N, p \in R^M$$
$$A = \left\{ a_{ij} \geq 0, i = \overline{1, M},\ j = \overline{1, N} \right\}, v = \left\{ v_j \geq 0,\ j = \overline{1, N} \right\}, \quad (1)$$

where M is the number of different positions of the source and detector pair for each $(\lambda_{ex}, \lambda_{em})$ pair, each element of matrix A corresponds to the point-spread function, v is a vector form fluorophore concentration, p is a vector of measurements.

Analysis of such a system is usually based on spectral decomposition of matrix A. The calculated singular values are sorted in descending order $s_{\max}(A) = s_1, s_2, s_3 \ldots s_N = s_{\min}(A)$, the $\frac{s_{\max}(A)}{s_{\min}(A)}$ ratio is called the condition number of matrix A and is denoted by *cond(A)*. It is supposed that, if $cond(A) \geq 10^{13}$, then system (1) is ill-conditioned and requires special, so-called regularizing methods

[1]. Another characteristic which can be used for solution of system (1) (with non-negative constraint of matrix elements and solution) is the number $m(A) = \min_k \sqrt{\sum_{i=1}^{M} a_{ik}^2}$. The meaning of the coefficient is described in more detail in [2].

Results and discussions

Numerical simulation was performed for the object with rectangular dimensions (W×H×D) 15×15×13 mm. The optical parameters were close to those of laboratory mice [3]. The anisotropy constant g = 0.7. Excitation and emission spectra corresponds to the far red fluorescent proteins and dyes: $\lambda_{ex} = 590$ nm, emission band is $\lambda_{em} = 600 \div 750$ nm. The number of experimental data points *M* was selected about the same ~ 28000 for all schemes. The reconstruction grid was 15×15×13 mm, i.e. *N* = 2925. The results of matrix analysis (singular values, condition number, and the number m) for different FDT methods are shown below.

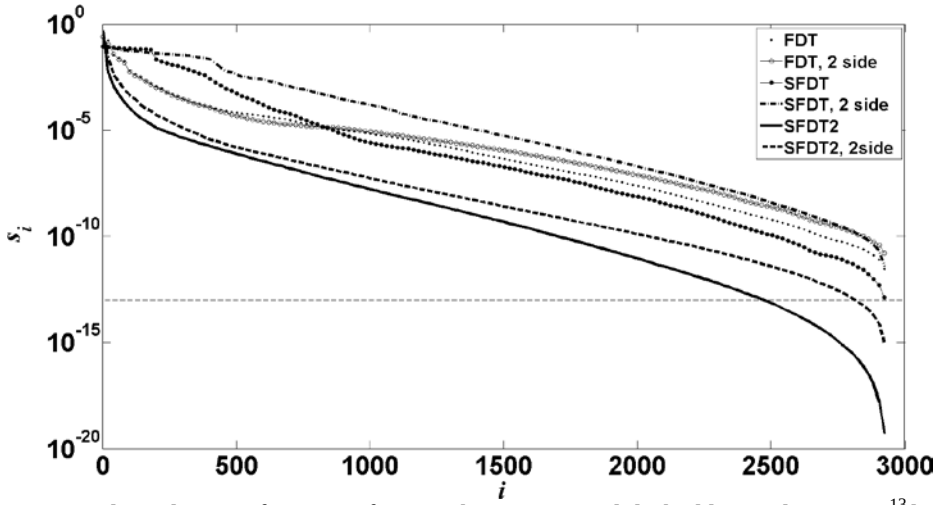

Fig. 1. Singular value as a function of its number. Horizontal dashed line indicates 10^{-13} level

	Scheme	FDT	SFDT	SFDT-2
Condition number	1 side	~10^{11}	~10^{12}	>10^{20}
	2 sides	~10^{10}	~10^{11}	>10^{15}
m(A)	1 side	~10^{-6}	~10^{-8}	~10^{-10}
	2 sides	~10^{-5}	~5×10^{-5}	~10^{-8}

The conclusions following from the table: 1) The one-sided scheme is worse than the two-sided scheme, 2) the SFDT-2 scheme is unviable, 3) the numerical characteristics of the 2-sided FDT and SFDT schemes are almost the same. But the singular values of SFDT are greater nearly everywhere than those of FDT (greater is better).

References

1. A.N. Tikhonov and V.I. Arsenin, *Solutions of Ill-posed Problems*, Winston, Halsted Press, Washington, New York, 1977, p. 258.
2. I.I. Fiks, *International Journal of Computational Methods*, 2014, **11**(5), 1350071, DOI: 0.1142/S0219876213500710.
3. A.D. Krainov, A.M. Mokeeva, E.A. Sergeeva, P.D. Agrba, and M.Yu. Kirillin, *Optics and Spectroscopy*, 2013, **115**(2), 193-200.

Invited

OPTOACOUSTIC MICROSCOPY FOR MALARIA DIAGNOSTICS IN THE BRAIN

F. Spadin[1], R. Nuster[1,2], M. De Niz[3], P. Subochev[4], V. Heussler[3], and **M. Frenz[1]**

[1] Institute of Applied Physics, University of Bern, 3012 Bern, Switzerland,
frenz@iap.unibe.ch
[2] Department of Physics, Karl-Franzens-University Graz, Austria
[3] Institute of Cell Biology, University of Bern, Switzerland
[4] Institute of Applied Physics, RAS, Nizhniy Novgorod, Russia

Abstract. An optoacoustic microscope was realized to image vasculature of rodent both with optical and acoustical resolution. Excitation is performed with a 100 Hz repetition OPO laser (680 – 900 nm) allowing a fast scan of a large field of view (9 × 9 mm). The acoustic pathway was optimized for high SNR. The microscope was used to image the vasculature in the brain of healthy and cerebral malaria infected mice with the goal to diagnose vessel dilatation and/or contraction, thickening of the vessel walls and vessel leakage. Preliminary results will be presented and discussed.

Introduction

Cerebral malaria is a complication of *Plasmodium* infections in humans that claims the lives of approximately 600,000 children in endemic areas. The pathology of cerebral malaria caused by the lethal strain Plasmodium falciparum is closely related to parasite sequestration in the brain vasculature, which results in vascular leakage, and microrrheological alterations that lead to severe restriction of the venous blood flow in the brain. This results in unarousable coma and death in humans. Surviving patients are at risk of neurological and cognitive defects, ad further disability. Although various hypotheses on the mechanisms of brain injury by P. falciparum have been developed, the exact mechanisms of damage and pathology, and ways to prevent such neurological complications, remain incompletely defined.

Experimental cerebral malaria (ECM) models are best reproduced by infection of C57B/6 mice with P. berghei ANKA. Within a window of 6–9 days post-infection, C57B/6 mice succumb to cerebral malaria, with symptoms including loss of coordination, weakness of muscles, loss of weight, and disorientation, among others. Following imaging of histology sections, intravital microscopy, micro-CT, and SPECT have shown that although parasite sequestration to brain venules is less pronounced in mice than in humans, significant recruitment of leukocytes to the brain contributed to important changes in hemodynamics and brain blood barrier disruption. Leukocytes include CD8+T cells, neutrophils, and macrophages, as well as upregulation of ICAM1 by vascular endothelia, which in humans is believed to enhance parasite sequestration. Both of the immunopathological effects of this recruitment and parasite sequestration result in an increase of intracranial pressure, leading to vasogenic oedema. Most studies so far have focused on single time analyses by intravital microscopy of host-parasite interactions in the brain at a cellular level. Macroscopic techniques so far used in the field, do not provide the necessary resolution to observe vascular leakage and changes over time.

The goal of this study therefore was to use optoacoustic imaging which has been proven to be capable of non-invasive, high-resolution, label-free imaging large field of view brain vasculature of rodent in-vivo with high resolution for detecting vascular changes in consequence of the development of cerebral malaria infection. Besides imaging structural changes optoacoustic imaging also is able to image oxygen metabolism due to the specific optical absorption spectra of oxy- and deoxyhemoglobin.

Materials and methods

An optoacoustic microscope was designed such that both optical resolution using a diffraction limited beam and acoustical resolution using either bright field or dark field illumination could be applied. For illumination a 100 Hz repetition rate OPO laser was used, coupled into an optical fiber and focused by a microscope objective onto the sample surface. Care was taken that the radiant exposure used was well below the laser safety limits. The generated optoacoustic signal is collected with an acoustic lens, reflected by a layer of silicone oil sandwiched between two prisms and finally detected by a 50 MHz center frequency ultrasonic transducer. This results in a measured acoustic resolution of 88 μm in lateral and of 43 μm in axial direction. Scanning (step size 30 μm) was performed by moving the whole microscope over the sample using a motorized x-y stage. For in-vivo optoacoustic scanning

a 9 × 9 mm region on the head of the mouse was imaged by raster scanning. The mouse was anesthetized and the body temperature of the animal was maintained using an IR-lamp. The experiments were performed with the approval of the Ethics Committee for Animal Experiments at the Canton of Bern, Switzerland.

Results and discussion

Figure 1 shows first results of the vasculature of a mouse before, 5 days and 7 days after cerebral malaria infection. The images were taken from three different animals which makes an interpretation of these preliminary results difficult. Nevertheless, repeated imaging of mice at different malaria infection stages showed similar results.

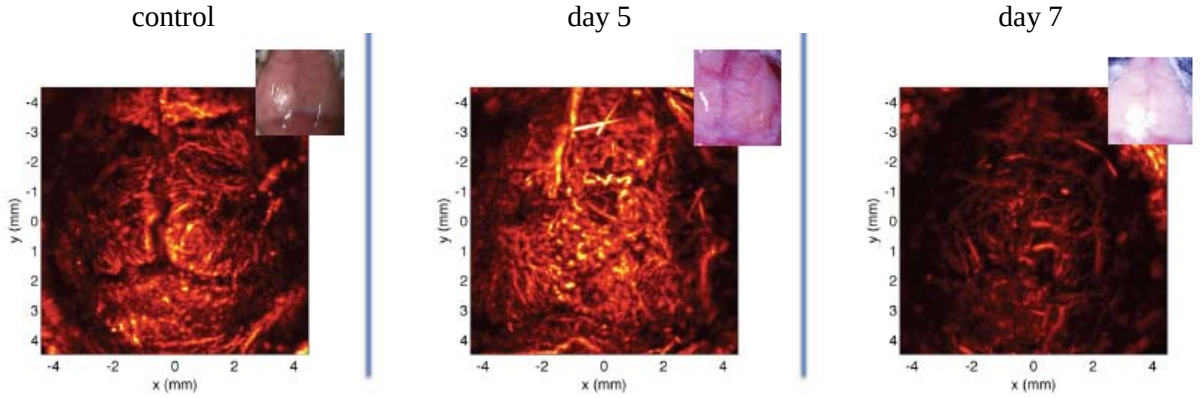

Fig. 1. Maximum intensity projection images of the brain vasculature of a mouse with the scalp removed. The comparison clearly shows a decrease in the symmetry of the vessel structure and an increase of vessels with continuation of the cerebral malaria infection

Future experiments will be performed on one animal and with different wavelengths to image not only the vessel distribution but also the blood oxygenation.

Currently, we are further reducing all the acoustic losses at the different interfaces to increase the SNR of our system. The goal is to image the vasculature of the brain with the scalp intact. This improving will render multispectral optoacoustic imaging possible.

Conclusion

Optoacoustic microscopy was used to image the brain vasculature of cerebral malaria infected mice. The comparison of images taken from different mice at various stages of infection showed changes in the number and orientation of the vessels, which has to be validated by experiments performed on one single animal but at different stages of disease.

Acknowledgements

This research was funded by the Swiss National Science Foundation (Nr: 205320_144443).

CROSS-POLARIZATION COMMON PATH ENDOSCOPIC SYSTEM WITH CIRCULAR POLARIZATION OF THE PROBE WAVE

G.V. Gelikonov[1,2,3], **S.Ju. Ksenofontov**[1], **A.A. Moiseev**[1,2], **D.V. Shabanov**[1], **P.A. Shilyagin**[1,2], **D.A. Terpelov**[1], and **V.M. Gelikonov**[1,2,3]

[1] Institute of Applied Physics RAS, 60390, Ulyanov St., 46, Nizhny Novgorod, Russia
grig@ufp.appl.sci-nnov.ru
[2] Nizhny Novgorod State Medical Academy, 603005, Minin and Pozharsky Sq., 10/1, Nizhniy Novgorod, Russia
[3] Nizhny Novgorod State University, 603950, Gagarina av., 23, Nizhny Novgorod, Russia

An endoscopic common-path OCT setup with circular polarization of a probe wave for cross-polarization (CP) measurements during pre-clinical and clinical studies and postoperative treatment is considered. This state provides similar efficiency of co- and cross-backscattering for the media containing randomly oriented anisotropic scatterers. Stable sensitivity of the cross-channel is of great importance for assessing the state of biotissue during treatment. Various optical fiber based methods have been developed for flexible assessment of polarizing properties of internal and external organs [1–6]. However, fiber based methods do not control the polarization state(s) incident onto the sample (the detailed review may be found in [7]). Therefore, these methods use at least two different incident polarization states for sample probing. Information on tissue polarizing properties is obtained from the data contained in 2 consecutively or simultaneously registered A-scans.

The present work is devoted to constructing a common-path endoscopic OCT setup which will allow eliminating the effects induced by birefringence in a single-mode fiber. This will also solve the problem of reproducibility of the optical properties of changeable flexible probes.

The developed optical setup of endoscopic common-path CP OCT-system is based on a single probe wave in circular polarization state and consecutive registration of co- and cross- backscattered waves. The main feature of the setup is the use of an automatic system that maintains circular polarization state at the end of an isotropic single-mode fiber based probe. The consecutive registration of co- and cross- backscattered parts of the OCT signal provides a rather low level of cross-talk and a high signal-to-noise ratio. In our paper “Active control of circular polarization of the probe wave in the common path endoscopic OCT” presented in these proceedings we described a 2-element phase modulator for automatic preserving the circular polarization state at the distal end of the flexible probe. The optical scheme of the cross-polarization common path endoscopic system with circularly polarized probe wave is shown in fig. 1.

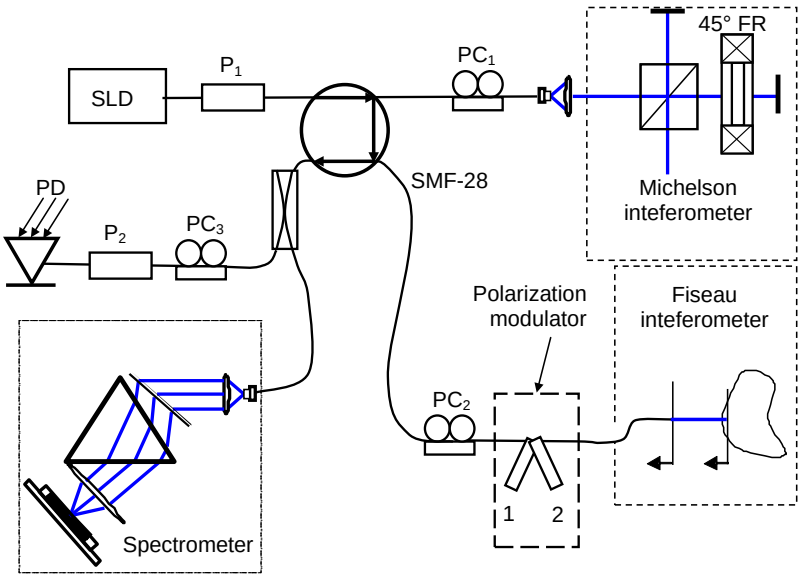

Fig. 1. Optical scheme of the CP OCT with circularly polarized probe wave

The setup consists of an SLD light source, leading Fiseau and tuning Michelson interferometers, a spectrometer registering the OCT signal and a number of optical elements for preserving the state of

polarization of the probe wave. The polarization-control system includes 2 active phase modulating anisotropic elements (1 and 2 in fig. 1). The linear (45º) polarization state at the entrance of the polarization-control system is aligned by the Lefeuvre polarization controller PC_2. The polarization state in the tuning Michelson interferometer is also linear and is aligned by the Lefeuvre polarization controller PC_1. For producing the error signal both elements of the polarization modulator are connected to the same AC voltage with relative phase difference $\pi/2$. The output signals from the synchronous detectors are used to obtain the minimum of the 1-st harmonic in both quadrature channels at the photoreceiver PD registering the light passing polarization controller PC_3 and polarizer P_2. The response time of the whole system preserving the polarization state is about tenths of a second, which is fast enough for relatively slow deformations of the flexible probe during object scanning. Switching between the co- and cross-channels in consecutive B-scans is attained by controlling the magnetic field in a 45° Faraday rotator FR in the "reference" arm of the tuning Michelson interferometer.

The experimentally investigated setup demonstrates the same sensitivity for co- and cross- backscattering in the media containing randomly oriented anisotropic scatterers. The cross-talk was observed at the level less than –20 dB level.

Acknowledgments

The project was supported by grant No NSh 2001.2014. of the Council in Support of Leading Scientific Schools at the President of the Russian Federation and by the grant of the Russian Federation Government No 14.B25.31.0015. GGV and GVM acknowledge partial support by the grant no. 02.B49.21.0003 of the Russian Ministry of Education.

References

1. V.M. Gelikonov and G.V. Gelikonov, *Laser Physics Letters*, 2006, **3**(9) 445-451.
2. Y. Gang and L.V. Wang, *Optics Letters*, 1999, **24**(8), 537-9.
3. J.E. Roth, J.A. Kozak, S. Yazdanfar, A.M. Rollins, and J.A. Izatt, *Optics Letters*, 2001, **26**(14), 1069-1071.
4. J. Zhang, W. Jung, J. Nelson, and Z. Chen, *Opt. express*, 2004, **12**(24), 6033-6039.
5. B. Park, M.C. Pierce, B. Cense, S.-H. Yun, M. Mujat, G. Tearney, B. Bouma, and J. de Boer, *Opt. express*, 2005, **13**(11), 3931-3944.
6. W.Y. Oh, S.H. Yun, B.J. Vakoc, M. Shishkov, A.E. Desjardins, B.H. Park, J.F. de Boer, G.J.Tearney, and B.E. Bouma, *Opt. Express*, 2008, **16**(2), 1096-1103.
7. K.H. Kim, B.H. Park, Y. Tu, T. Hasan, B. Lee, J. Li, and J.F. de Boer, *Opt. Express*, 2011, **19**(2), 552-561.

CONTROL OF CIRCULAR POLARIZATION OF THE PROBE WAVE IN COMMON PATH ENDOSCOPIC OCT

V.M. Gelikonov[1,2,3], **S.Ju. Ksenofontov**[1], **A.A. Moiseev**[1,2], **D.V. Shabanov**[1], **P.A. Shilyagin**[1,2], **D.A. Terpelov**[1], and **G.V. Gelikonov**[1,2,3]

[1] Institute of Applied Physics RAS, 60390, Ulyanov St., 46, Nizhny Novgorod, Russia
gelikon@ufp.appl.sci-nnov.ru
[2] Nizhny Novgorod State Medical Academy, 603005, Minin and Pozharsky Sq., 10/1, Nizhniy Novgorod, Russia
[3] Nizhny Novgorod State University, 603950, Gagarina av., 23, Nizhny Novgorod, Russia

The informativity of endoscopic cross-polarization optical coherence tomography (CP OCT) may be increased significantly using the information from both, cross-polarized backscattered light and co-polarized light [1]. The cross-polarization scattering is the main cause of formation of a visible signal in orthogonal polarization at relatively weak birefringence in mucosa [2]. In contrast to the case of co-scattering, the efficiency of cross-scattering is highly dependent on probe wave polarization [3]. In [3] it was shown that, at scattering by randomly oriented non-spherical particles, depolarization is less in the case of linearly polarized probe light compared to circularly polarized probe light. In biological tissues (and other media containing particles or inhomogeneities of comparable size) the difference in the cross-backscattered signal for both mentioned cases is about 4 dB. A similar effect is observed at Rayleigh scattering [4]. Thus, at random polarization of the probe light, the ambiguity of a cross-backscattered signal is about 4 dB. This value is close to diagnostically significant variations of the signal during CP OCT monitoring of the treatment of oncological and other diseases, which has a negative impact on quantitative assessment of the state of biotissue.

The only CP OCT setup free from this ambiguity is the one with circular polarization of the probe wave that demonstrates equal sensitivity in co- and cross-channels. Given stable circular polarization state at the ouput of a long flexible probe during CP OCT scanning, one can obtain reliable quantitative assessment of biotissue state.

An automatic system for maintaining circular polarization of the probe wave may be based on the well-known quarter-wave plates. If linearly polarized light is incident on the plate at an angle of 45° to its optical axes, then the light at the output will have circular polarization, and after backscattering it will be linear again, but the polarization plane will be orthogonal to the initial one [5, 6]. The OCT probe in the system with active polarization modulator at the input may be considered to be a quarter-wave plate under certain conditions. The instability of probe phase anisotropy can be corrected by controlling the birefringence generated by the polarization modulator. Fiber based 2-element phase polarization controllers were reported in [7–9]. In [9] the light polarization was controlled by the angle between the phase plates with arbitrary birefringence. In [7, 8] the polarization state of the transmitted light was controlled by the phase shift between the eigenwaves in the plates tilted by 45° relative to each other. However, unlike 3-element devices, 2-element polarization controllers require definite polarization of incident light. So, the necessary condition to obtain circularly polarized light at the probe output at arbitrary probe anisotropy is to maintain the linear polarization at an angle of 45° to the axes of the 1-st element of the controller. The transformation of light polarization on the Poincare sphere at direct (fig. 1, a) and reverse (fig. 1, b) passage through the probe is shown in fig. 1. Such a transformation is possible for any phase anisotropy of a single-mode fiber probe. In [10] it was demonstrated that the system controlling polarization state at the probe output window can work in automatic regime. For this, one should modulate the birefringence of both elements by a harmonic signal with small amplitude and relative phase difference of $\pi/2$.

We have implemented such a system in a CP OCT setup. It maintains circular polarization at the output of a long flexible fiber probe. This method was approved in a model experiment aimed at studying a possibility of using it in a multifunctional OCT system.

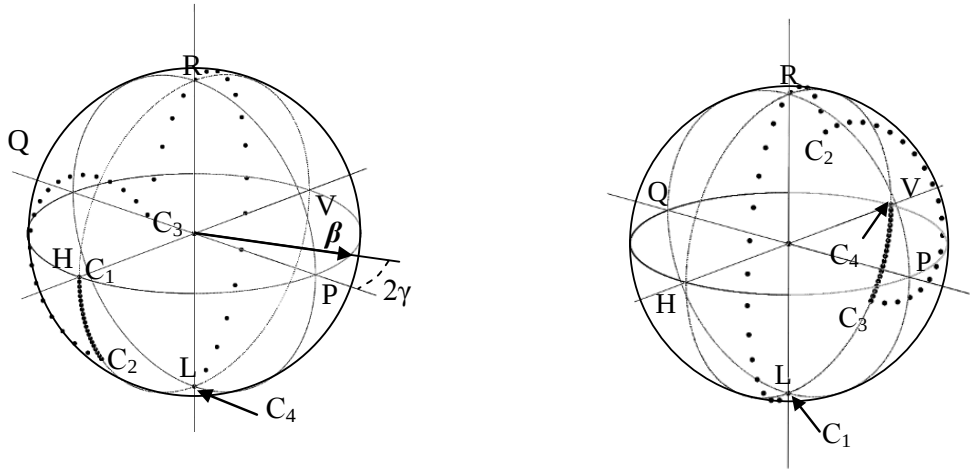

а) б)

Fig. 1. Transformation of light polarization by 2-element phase modulator at arbitrary fiber anisotropy: a – from linear state oriented at 45° to the 1-st element to circularly polarized state (light is transmitted from C_1 to C_4), b – the reverse transformation (light is transmitted from C_1 to C_4)

Acknowledgments

The project was supported by grant No NSh 2001.2014. of the Council in Support of Leading Scientific Schools at the President of the Russian Federation and by the grant of the Russian Federation Government No 14.B25.31.0015. GGV and GVM acknowledge partial support by the grant no. 02.B49.21.0003 of the Russian Ministry of Education.

References

1. N. Gladkova, E. Kiseleva, N. Robakidze, I. Balalaeva, M. Karabut, E. Gubarkova, and F. Feldchtein, *Journal of Biophotonics*, 2013, **6**(4), 321-329.
2. J.M. Schmitt and S.H. Xiang, *Optics Letters*, 1998, **23**(13), 1060-1062.
3. M.I. Mishchenko and J.W. Hovenier, 1995, **20**(12), 1356-1358.
4. V.P. Tishkovets and M.I. Mishchenko, 2009, **110**(1–2), 139-145.
5. K. Goto, T. Sueta, and T. Makimoto, *QE*, 1972, **8**(6), 486-493.
6. Yu.N. Kulchin, "Distributed Fiber-Optic Measuring Systems", *Fizmatlit*, Moscow, 2001, 272 p.
7. M. Johnson, *Applied Optics*, 1979, **18**(9), 1288-9.
8. Y. Kidon, Y. Suematsu, and K. Furuya, *IEEE Journal of Quantum Electronics*, 1981, **17**(6), 991-994.
9. I.V. Goltzer, M.I. Darsht, B.Ya. Zel'dovich, and N.D. Kundikova, *Quantum Electronics*, 1993, **20**(9), 916-918.
10. S. Ezekiel and H.J. Arditty, "Fiber-Optic Rotation Sensor and Related Technologies", ed. N.J. Heidelberg. Berlin: Springer-Verlag, 1982, 442 p.

EVALUATION OF ATHEROSCLEROTIC PLAQUES BY CROSS-POLARIZATION OCT

E.V. Gubarkova [1], V.V. Dudenkova [1, 2], M.Yu. Kirillin [1, 3], L.B. Timofeeva [1], L.N. Barbashova [1, 2], F.I. Feldchtein [1], and **N.D. Gladkova [1]**

[1] Nizhny Novgorod State Medical Academy, Nizhny Novgorod, Russia, kgybarkova@mail.ru
[2] N.I. Lobachevsky State University of Nizhny Novgorod, Nizhny Novgorod, Russia
[3] Institute of Applied Physics RAS, Nizhny Novgorod, Russia

Abstract. We performed a study combining cross-polarization optical coherence tomography (CP OCT) and a nonlinear microscopy based on second harmonic generation (SHG) and two-photon-excited fluorescence (2PEF) in order to assess condition of collagen fibers in the human *ex vivo* arterial blood vessels, including development of atherosclerotic plaques. We found that CP OCT provides visualization of collagen structure and coronary artery wall structure for different stages of atherosclerosis with high spatial resolution. The study shows potential of CP OCT for the assessment of collagen fibers condition in atherosclerotic arteries and proves that it can serve as a fast and nondestructive tool to assess plaque stability and predict the risk of plaque rupture.

Development of high spatial resolution imaging technologies opened new possibilities for studying spatial organization of cells and intercellular matrix in tissues in different pathologies [1]. Inflammation, typical for atherosclerosis, desorganises collagen fibers, which, in turn, affects evolution of polarization of probing radiation propagating through the tissue and can be used to characterize the atherosclerotic plaques [2]. In this study we demosntrate the possibilty of cross-polarization optical coherence tomography (CP OCT) to assess collagen fiber conditions in atherosclerotic plaques basing on the ratio of the CP OCT signal in the orthogonal and parallel channels .

Materials and methods

We used a common path Fourier-domain cross-polarization OCT system [3], with scanning rate of 20 000 A-scans per second. It employs a broadband light source with central wavelength of 1300 nm and optical power of 15 mW. The lateral and in-depth resolution are 25 μm and ~10 μm. The system is capable of cross-polarization OCT imaging [4]. The CP OCT images were compared with the data from non-linear microscopy using second harmonic generation (SHG) and two-photon-excited fluorescence (2PEF), which can selectively visualize structural changes in collagen and elastin fibers. Nonlinear microscopy signal detection was performed in two spectral channels using filters for 362–415 nm and 480–554 nm to register SHG and 2PEF respectively, which can be also shown together. We also used histopathology slides with Hematoxylin and Eosine, Van Gieson and Orcein staining. We used 40 *post mortem* specimen of the coronary arteries from the patients deceased from coronary diseases with arterial plaques at different stages of atherosclerosis. We studied a total of 60 regions of interest and found all stages of atherosclerotic plaque development, which were histologically confirmed.

Results

We found that the orthogonal component of the CP OCT image allows visualization of collagen fibers and arterial wall structure with different stages of the atherosclerotic plaque with good intrinsic contrast and high spatial resolution. In parallel polarization the stable plaque visualizes without pronounced contrast between lipid core and fibrose capsule. In orthogonal polarization the stable plaque appears as an inhomogeneous area allowing to distinguish the fibrose capsule and lipid core, so the capsule condition and thickness can be assessed. This conclusion is confirmed by a good correspondence between CP OCT images and histopathology slides. Comparison of CP OCT images with nonlinear microscopy images was performed evaluate the possibility of *in vivo* visualization and assessment of the arterial walls using CP OCT. A good correlation between the level of depolarization manifested as brightness of the CP OCT orthogonal channel and ability to generate second harmonic was found containing important information about stability of the thin fibrous capsule. In a thin fibrous capsule of a stable plaque the SHG reveals weekly disorganized (insignificant fibrinoid swelling of the fibers in histology), but densely packed collagen fibers, providing bright homogeneous OCT signal in orthogonal channel. The thin fibrous capsule of the unstable plaque produces a weak inho-

mogeneous signal in the SHG images (pronounced fibrinoid swelling with massive infiltration of giant foam cells of the smooth muscle origin in histology) corresponding to inhomogeneous orthogonal CP OCT signal. The latter clearly indicates the plaque vulnerability (propensity to rupture). Similar features were revealed for other plaque stages.

To conclude, the CP OCT imaging, is capable of visualizing condition of the collage fibers in the tissue without exogenous agents and has high potential as an effective tool to diagnose atherosclerotic plaque condition. We are planning to implement an automated image processing to objectively and quantitatively assess the main structural components of the atherosclerotic plaque development and rupture risk.

Acknowledgements

The study was supported by the Russian Science Foundation, grant 14-15-00538, the grant no.14.B25.31.0015 of the Russian Federation Government and RFBR (project 15-32-20250).

References

1. G.J. Tearney G.J., E. Regar E, T. Akasaka, T et al., *JACC,* 2012, **12**, 1058-72.
2. S.K. Nadkami S.K., B.E. Bouma B.E., and J. de Boer J., *Laser Med Sci*, 2009,; **24**(3),: 439-445.
3. V.M. Gelikonov V.M. and, G.V. Gelikonov, G.V. *Laser Physics Letters*, 2006, **3**(9), 445-451.
4. V.M. Gelikonov VM, G.V. Gelikonov GV, I.V. Kasatkina IV, et al., *Optics and Spectroscopy*, 2009, **106**(6), 895-900.

THE EFFECTS OF PHOTODYNAMIC THERAPY OF TUMOR MODELS IN EXPERIMENTAL ANIMALS: HOW TO EVALUATE THEM BY MULTIMODAL OCT?

N.D. Gladkova[1], M.A. Sirotkina[1], N.L. Buyanova[1], T.I. Kalganova[1], V.V. Elagin[1], L.A. Matveev[1,2], V.Yu. Zaitsev[1,2], G.V. Gelikonov[1,2], S.V. Gamayunov[1], N.M. Shakhova[1,2], S.S. Kuznetsov[1], L.B. Snopova[1], M.V. Shirmanova[1], F.I. Feldchtein[1], E.V. Zagaynova[1], and **A. Vitkin[1,3]**

[1] Nizhny Novgorod State Medical Academy, Nizhny Novgorod, Russia, natalia.gladkova@gmail.com
[2] Institute of Applied Physics Russian Academy of Science, Nizhny Novgorod, Russia
[3] University of Toronto, Toronto, Canada

Abstract. Our research was focused on the efficiency study of the photodynamic therapy (PDT) by multimodal OCT. The study was carried out on mice colon carcinoma CT-26 transplanted in the auricle. PDT was performed in three hours after intravenous injection of photoditazine. The tumors were irradiated by laser at the wavelength of 662 nm, 75 J/cm^2, 170 mW/cm^2 The efficiency of PDT was evaluated by microangiographic OCT (MA OCT) and confirmed by by histological analysis. It was demonstrated that multimodal OCT is promising method of *in vivo* visualization and estimation of anti-tumor impact of the PDT based on vascular damages.

Introduction

Individualization of anticancer therapy is an important trend of the modern medicine. Control of early response to the therapy is required to find some predictive factors to evaluate an efficiency of the therapy [1]. Disruption of tumor blood flow has been reported to be the main reason of tumor cells death after PDT [2]. The multimodal optical coherence tomography (OCT) is considered to be a promising approach for noninvasive monitoring of anticancer therapy [3].

The work was aimed to investigate the efficacy of the PDT by multimodal OCT.

Materials and Methods

Animals and tumor models. The study was carried out on BALB/C female mice aged 6–8 weeks bearing colon adenocarcinoma CT-26. Cancer cells were inoculated intradermally in auricle at the dose of 200 000 cells in 20 μl of PBS. When tumor size reached 3–3.5 mm^3 animals were randomly divided into two groups – treated by PDT (20 mice) and untreated control (3 mice).

Photodynamic therapy. Photosensitizer photoditazine (Veta-Grand, Russia) was applied intravenously at the dose of 5 mg per kg of body weight. PDT was performed in 3 hours after the injection of photoditazine in maximum of its accumulation in the tumor. The tumors were irradiated by the laser (Kreolka, Russia) at the wavelength of 662 nm, energy density 75 J/cm^2, power density 170 W/cm^2. The tumors were excised in 2 days after PDT for histological examination.

The efficienty of PDT was evaluated *in vivo* by multimodal OCT. The OCT device was developed at the Institute of Applied Physics (Nizhny Novgorod, Russia). The detailed technical specification of the device is available in [4–6]. The OCT device allows simultaneous imaging in initial polarization (co-polarized) and orthogonal polarization (cross-polarized) as well as visualizing the blood vessels network by microangiographic OCT imaging (MA OCT) [7]. OCT images were taken before PDT, immediately after PDT, 24 hours and 48 hours after PDT.

Results

The blood vessels network with abnormal shape and significant tortuosity was visualized by MA OCT on the 9 days after cancer cells inoculation. Immediately after PDT no changes in the vessels network were observed. But in 24 hours and 48 hours vessels network partly disappeared on the images. It was a reaction of blood vessels or microcirculation on PDT treatment. Histologycal analysis confirmed that the tumors had a good response on PDT. Pronounced blood vessels damagees, including thrombosis and stasis fenomena were found. Among cellular component there were about 75% of irreversibly damaged cancer cells. On the other hand no visible tumor damage (burn, hyperemia) was observed during or after treatment.

Unfortunately, we did not detect any visible changes in the OCT signal intensity or penetration depth on the initial and orthogonal polarization images after PDT. We suppose that quantitative analysis of cross-polarization OCT (CP-OCT) images can help to reveal the differences between treated and untreated tumors.

Conclusions

It was demonstrated that multimodal OCT is a promising method of *in vivo* visualization and assessment of anti-tumor impact of the PDT based on vascular damages. The MA OCT results are closely accordance with the histological data.

Acknowledgements

The design and manufacturing of multi-functional OCT scanner used in this study was supported by the grant no. 14.B25.31.0015 of the Russian Federation Government and the development of MA algorithm by RFBR grant 15-42-02513.

References

1. S.Y. Yoo, J.-S. Kim, K.W. Sung, T.Y. Jeon, J.Y. Choi, S.H. Moon, M.H. Son, S.H. Lee, K.H. Yoo, and H.H. Koo, *Cancer*, 2013, 656-664.
2. K. Chaundry, R.W. Keck, and S.H. Selma, *Photochemistry and Photobiology*, 1987, **46**(5), 823-827.
3. B. Davoudi, M. Morrison, K. Bizheva, V.X.D. Yang, R. Dinniwell, W. Levin, and I.A. Vitkin, *Journal of Biomedical Optics*, 2013, **18**(7), 076008.
4. V.M. Gelikonov, G.V. Gelikonov, I.V. Kasatkina, D.A. Terpelov, and P.A. Shilyagin, *Optics and Spectroscopy*, 2009, **106**(6), 895-900.
5. V.M. Gelikonov and G.V. Gelikonov, *Laser Physics Letters*, 2006, **3**(9), 445-451.
6. V.Y. Zaitsev, V.M. Gelikonov, L.A. Matveev, G.V Gelikonov, A.L. Matveyev, P.A. Shilyagin, and I.A. Vitkin, *Radiophysics and Quantum Eleectronics*, 2014, **57**, 52-66.
7. L.A. Matveev, V.Yu. Zaitsev, G.V. Gelikonov, A.L. Matveyev, A.A. Moiseev, S.Yu. Ksenofontov, V.M. Gelikonov, M.A. Sirotkina, N.D. Gladkova, V. Demidov, and A. Vitkin, *Optics Letters*, 2015, **40**(7), 1472-1475.

FLUORESCENCE MULTI-SCALE ENDOSCOPY AND ITS APPLICATIONS IN THE STUDY AND DIAGNOSIS OF GASTRO-INTESTINAL DISEASES: THE SYSTEM ASSEMBLY

P.A. Gómez-García[1,2], I. Martín[1,2], A. Arranz[3], M. Fresno[3], M. Desco[1,2], U. Mahmood[4], J.J. Vaquero[1,2], and **J. Ripoll[1,2]**

[1]Department of Bioengineering and Aerospace Engineering, Universidad Carlos III de Madrid
pablo.aero.upm@gmail.com
[2]Experimental Medicine and Surgery Unit, Instituto de Investigación Sanitaria, Hospital Gregorio Marañón
[3]Department of Cell Biology and Immunology, Center for Molecular Biology "Severo Ochoa", CSIC
[4]Athinoula A. Martinos Center, Massachusetts General Hospital, Charlestown, MA 02129, U.S.A.

Abstract. New endoscopy technologies, which are able to show microscopic changes in the mucosa structure, are necessary in order to address the lack of specificity and cell details of current commercial endoscopes. We present a multi-scale endoscope which combines confocal endomicroscopy for cellular level resolution and wide field fluorescence for fast and specific macroscopic information through the use of activatable probes. This multi-modal imaging module, compatible with commercial endoscopes, combines near-infrared fluorescence (NIRF) measurements (enabling specific imaging of markers of disease and prognosis) and confocal fluorescence endomicroscopy for several contrast agents. The system will be used in animal models exhibiting gastro-intestinal diseases in order to analyze the use of potential diagnostic markers in colorectal cancer.

Introduction

Endoscopy is used in the diagnosis of gastrointestinal conditions such as inflammatory bowel disease, Crohn's disease, ulcerative colitis or colorectal cancer, and there are a great number of different endoscopy systems with its corresponding applications [1–3]. It has great potential as a technique for early detection of alterations in the intestinal mucosa; however, such early lesions are not usually detected with conventional endoscopes. Confocal endomicroscopy allows cellular resolution imaging with contrast agents to provide a fluorescence signal for detection of tumors or structural alterations of the gastrointestinal mucosa like ulcerative colitis [4] or colorectal cancer [5]. In addition, the use of fluorescent probes that emits fluorescence in presence of a specific enzyme activity represents a powerful diagnostic tool. For that purpose, a new generation of endoscopes that incorporates NIRF imaging capabilities is needed.

Materials and methods

The multi-modal and multi-scale system is composed of two independent modules (Figure 1): a dual camera and dual excitation system for macroscopic imaging and a scanning endomicroscope, that work together in order to obtain both macroscopic and microscopic fluorescence images.

The wide field NIRF Module consist on a commercial endoscope (Hopkins II 0º 1.9mm Telescope, Karl Storz, Tuttlingen, Germany), which carries the image from the sample to the cameras. Two dichroic mirrors are used, one for combining the RGB and NIRF illumination and the other for splitting both images into the cameras (Edmund Optics, Barrington, NJ, USA). The images are projected onto the cameras through a lens (AC254-075, Thorlabs Inc, Delaware, USA) maximizing the coverage of the CMOS sensor (Thorlabs, Newton, NJ, USA) so that one camera is capturing the visible field and the other camera the fluorescence emitted by the contrast agent. The cameras (Manta G-145 Color and Manta G-145 NIR, Allied Vision technologies, Stadtroda, Germany) are working at 30 fps video rate so it is a real-time acquisition. The illumination consist on a broadband halogen lamp (OSL2, Thorlabs, Newton, NJ, USA) properly coupled to the endoscope and a laser for the excitation of the fluorophores. All the optical components were assembled and mounted on portable optical breadboards using conventional optomechanics (Thorlabs, Delaware, USA).

The Confocal module is based on the principles of confocal microscopy, but with the particularity that now the main element is a fiber bundle (FIGH-30-850N, Fujikura, Kōtō, TKY, Japan). A laser diode module (CPS520, Thorlabs Inc, Delaware, USA) is used to illuminate the sample, making use of 2D galvanometer mirrors (GVS012, Thorlabs Inc, Delaware, USA) to scan the fiber bundle (30.000 fibers), which carries the illumination to the sample and collects the fluorescence back to the photodiode (APD130A2, Thorlabs Inc, Delaware, USA). After the mirrors, a scan lens (LSM02, Thorlabs Inc, Delaware, USA), a relay lens (AC254-030, Thorlabs Inc, Delaware, USA) and an objective (Plan Apochromat 10X, Motic, Weztlar, Germany) are used. This lens system will focus the laser on each individual fiber so that the galvo scanning illuminates each fiber independently. A dichroic mirror and an emission filter (Edmund optics, Newport, NJ, USA) are also used in order to receive only fluorescence light on the photodiode. The fluorescence light is focused onto a pinhole (P25S, Thorlabs Inc,

Delaware, USA) which will block all the light that is not coming from the illuminated fiber, avoiding fluorescence signal coming from other points of the tissue and increasing the system resolution. The light exiting the pinhole is finally collected by the avalanche photodiode. All the optical components were assembled using a 30 mm cage assembly optomechanics (Thorlabs, Delaware, USA). The resolution of the system is limited by the core-to-core distance of the fiber bundle, which in this case is 4.5 µm, while the field of view is limited to the bundle diameter (1 mm). The endoscope examination sheath (STZ 61029D, Karl Storz, Tuttlingen, Germany) admits the Hopkins optic endoscope and also has a work channel of 1 mm ∅ for the fiber bundle, so both macroscopic and microscopic images can be acquired at the same time and the position of the fiber bundle can be monitored from the wide field image.

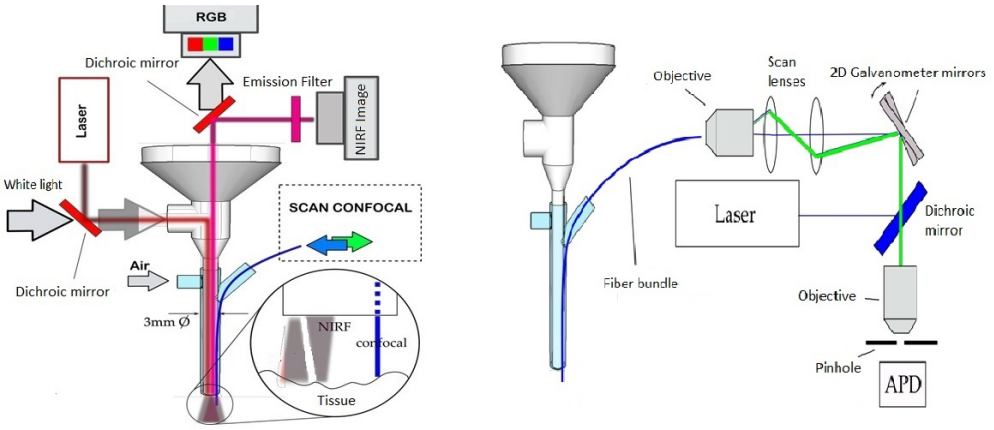

Fig. 1. Scheme of the system assembly. A) Wide field RGB/NIRF module. B) Confocal endomicroscopy module

Results

A 30fps video rate wide field image which combines RGB and NIRF is displayed by the software, allowing the detection and mapping of the desired regions of tissue. This is a fast and superficial exam that will inform about possible lesions for the subsequent detailed examination with the microscopic module for higher resolution -local imaging of the region of interest. For the microscopic module, several scanning methods have been studied in order to obtain a high-resolution image and a fast acquisition rate. It is worth mentioning that the acquisition rate is an extremely important parameter for in-vivo cellular resolution imaging, due to displacement due to breathing and inherent cell motility.

Conclusion and perspectives

A multi-scale high-resolution endoscopy system and its software have been developed, and its speed characterized in order to optimize the results for in-vivo imaging. Our system is currently capable of combining NIRF and RGB wide field images, together with high-resolution endomicroscopy images. The next step is to apply this set-up to in-vivo imaging of animal models, in particular, gastro intestinal diseases in murine models at both macroscopic and microscopic scales.

Acknowledgements

The authors acknowledge support from EC FP7 IMI project PREDICT-TB, the EC FP7 CIG grant HIGH-THROUGHPUT TOMO, the Spanish MINECO project grant FIS2013-41802-R MESO-IMAGING, and TOPUS S2013/MIT-3024 project from the regional government of Madrid.

References

1. B.A. Flusberg, E.D. Cocker, W. Piyawattanametha, J.C. Jung, E.L.M. Cheung, and M.J. Schnitzer, "Fiber-optic fluorescence imaging," *Nature Publishing Group*, 2005.
2. G.Oha and E.C.S.H. Yun, "Optical fibers for high-resolution *in vivo* microendoscopic fluorescence imaging," *Optical Fiber Technology*, 2013, **19**(6), Part B, 760–771.
3. M. Pierce and D.Y.R. Richards-Kortum, "High-resolution Fiber-optic Microendoscopy for *in situ* Cellular Imaging," *Journal of Visualized Experiments*, 2011.
4. R. Kiesslich, M. Goetz, K. Lammersdorf, C. Schneider, J. Burg, M. Stolte, M. Vieth, B. Nafe, P.R. Galle, and M.F. Neurath, "Chromoscopy-guided endomicroscopy increases the diagnostic yield of intraepithelial neoplasia in ulcerative colitis," *Gastroenterology*, 2007, **132**, 874-882.
5. A.L. Polglase, W.J. McLaren, S.A. Skinner, R. Kiesslich, M.F. Neurath, and P.M. Delaney, "A fluorescence confocal endomicroscope for *in vivo* microscopy of the upper- and the lower-GI tract," *Gastrointest Endosc*, 2005, **62**, 686-695.

THE STUDY OF EXPERIMENTAL TUMORS GROWTH USING THE MULTIMODAL OPTICAL COHERENCE TOMOGRAPHY

M. Karabut[1,2], M. Sirotkina[1], N. Buyanova[1], T. Kalganova[1], V. Elagin[1], S. Kuznetsov[1], L. Snopova[1], G. Gelikonov[1,3], L. Matveev[1,3], V. Zaitsev[1,2,3], F. Feldchtein[1], E. Zagayanova[1], A. Vitkin[1,4], and **N. Gladkova[1]**

[1] Nizhny Novgorod State Medical Academy, Nizhny Novgorod, Russia, maria.karabut@gmail.com
[2] Lobachevsky State University of Nizhni Novgorod, Nizhny Novgorod, Russia
[3] Institute of Applied Physics of the Russian Academy of Sciences
[4] University of Toronto, Toronto, Canada

Abstract. We report a feasibility study for the multi-modal optical coherence tomography for visualization of a CT-26 tumor growth into the surface of the mice auricle. The structural and microvascular peculiarities of CT-26 tumor growth were visualized using polarization and microvascular OCT images and confirmed by morphological study.

The main trend in modern experimental and clinical oncology is towards the individualization of a treatment. Optical coherence tomography (OCT) is a developing and promising method which can detect the dynamics of the structural and functional changes in tumor tissues in response to therapy [1]. The value of multimodal OCT requires the ability to detect changes of the tumor in response to treatment: of the cellular component (the tumor cells), of the tumor stromata (the connective tissue and extracellular matrix) and of the microvasculature [2]. For the feasibility assessment of the multimodal OCT, the experimental research on animal tumor models is a necessary step.

Materials and methods

The study was carried out on BALB/C mice with murine colon carcinoma CT-26 inoculated into auricle tissue ($2 \cdot 10^5$ cells in 0.2 ml of phosphate-buffered saline). An important advantage of this inoculation is the assured superficial growth of the nodule that is the main requirement for studies using OCT. Mice were followed up to 22 days. The research was performed on an experimental spectrometer-based OCT device developed by Institute of Applied Physics (Nizhny Novgorod, Russia) with the central optical wavelength $\lambda = 1.32$ μm and optical power ~15 mW. The axial and lateral resolutions are 10 and 20 μm. The probe has 4 mm external diameter, 10 cm length of rigid section. The system has a common-path optical layout and creates two OCT images simultaneously: one for scattered light that maintained initial polarization ("co-polarized"), and one that now exhibits orthogonal polarization ("cross-polarized") [3–5]. The software allows representing 3D rendering of OCT images and also has original means to visualize microvascular networks. The vascular network of CT-26 tumor was visualized in vivo by means of M-mode-like OCT [6]. At different time points the tumors were excised, and fixed in formalin for subsequent histological analysis.

Results

The CP OCT images of intact mice auricle was demonstrated a clear layered architecture. The cross-polarized OCT images had reduced brightness and contrast in comparison with co-polarized images. Histological image matched well the ear tissue layers visualized in OCT: epidermis, dermis with the skin appendages in its surface layers, muscle, cartilage thickness 27 μm. On the opposite side of cartilage, connective tissue coated epidermis and without adipose tissue was abutted on. The vessels in the dermis were located on the either side of the cartilage and had a diameter about 24–36 μm.

With the early stages of nodule formation (4–5th days after inoculation, volume 0.8–1 mm^3) the depth of CP OCT visualization made it possible to observe the whole tumor nodule both in the initial and orthogonal polarizations. Moreover, the OCT images clearly displayed the tissue layers including the epidermis, the cartilage with the perichondrium, the own vessels of the dermis (diameter 24–100 μm) confirmed by morphological study. It should be noted that the epidermis damaged in the late stages of tumor growth (19–22th day). So the tumor development is characterized by loss of a layered structure and fast OCT signal depth decay, especially in orthogonal polarization.

It is known, that tumor blood vessels have some features in comparison with normal vessels. In particular, the tumor vessels which number and volume density is significantly increased with tumor growth have an abnormal shape with significant tortuosity, random architecture and irregular lumen. On the 4th day after inoculation sinusoids diameter up to 20 μm were identified in the tumor. Micro-

vascular images on the 14th after inoculation was shown a sharp increase in the number of curved segments, which form a network.

Histological analysis revealed the structural and microvascular changes in the tumor growth. So the peak of mitotic activity of tumor cells and maximum of the vascular bed formation in the form of sinusoids diameter of 7–20 μm occurred on the 11th day after inoculation. The first appearance of spontaneous tumor regression observed on the 7th day. They were visualized as the formation of necrotic focus that primarily located in the deep parts of the tumor. The maximum degree of necrosis was achieved on day 21–22th days. Therefore, it was demonstrated that multimodal OCT can visualize *in vivo* the stages of tumor growth of CT-26 inoculated into auricle tissue. In the future, we are planning to apply automatically quantitative assessment of tumor microvasculature for more objective characterization of the tumor vessels growth**.**

Acknowledgements

The study was supported by the Russian Federation Government contract №14.B25.31.0015. The research to improve M-mode-like OCT method was partially supported by RFBR №15-42-02513 и the Russian Federation Government contract №02.B49.21.0003.

References

1. B. Davoudi, M. Morrison, K. Bizheva, et al., *Journal of Biomedical Optics,* 2013, **18**(7), 076008.
2. M.A. Sirotkina, N.L. Buyanova, T.I. Kalganova, et al., *Sovrem Tekhnol Med,* 2015, **7**(2), in press.
3. P.A. Shilyagin, G.V. Gelikonov, V.M. Gelikonov, et al., *Quantum Electronics,* 2014, **44**(7), 664 – 669.
4. A.A. Moiseev, G.V. Gelikonov, D.A. Terpelov, et al., *Quantum Electronics*, 2014, **44**(8), 732 – 739.
5. V. Y. Zaitsev, V. M. Gelikonov, L.A. Matveev, et al., *Radiophysics and Quantum Electronics*, 2014, **57**, 52–66.
6. L.A. Matveev, V.Yu. Zaitsev, G.V. Gelikonov, et al., *Optics Letters*, 2015, **40**(7), 1472 – 1475.

FLUORESCENCE LIFETIME IMAGING FOR FLUOROPHORES LOCATED IN SCATTERING AND ABSORBING MEDIUM

A.V. Khilov, I.I. Fiks, M.Yu. Kirillin, V.I. Plekhanov, and **I.V. Turchin**

Institute of Applied Physics, Russian Academy of Science, Nizhny Novgorod, Russia
alhil@inbox.ru

Abstract. For the correct identification of fluorophores in fluorescence lifetime imaging *in vivo* it is important to account for the distortion of fluorescence kinetics curve due to light scattering and absorption in a turbid medium. This distortion leads to changes in the shape of fluorescent response and to the difference between real and measured lifetimes of a fluorescent agent as well. In this paper we present study of the mentioned effect for media with different optical properties and lifetimes corresponding to those of real fluorophores using the Monte-Carlo simulation. We found that for the fluorophore depths up to 12 mm for reduced scattering coefficient varying from 0.15 to 4.8 mm^{-1} and absorption coefficient varying from 0.0025 to 0.08 mm^{-1} this difference is insignificant for long-lived fluorophores (typical fluorescent proteins), however, it should be taken into account for fluorophores with lifetimes of several hundred picoseconds.The results of numerical simulation are confirmed by the results of model experiment.

Fluorescence lifetime imaging is extremely important for a number of biological applications and allows differentiating fluorophores with similar spectral characteristics (excitation and emission spectra) which can be used, for example, for FRET microscopy [1]. In microscopy studies there is no need to account for widening of the fluorescence kinetics curve due to light scattering and absorption in tissues [2] originating from spreading of the excitation pulse and fluorescent response of the sample because its thickness usually does not exceed photon mean free path. However, this phenomenon is essential for in vivo studies. The above mentioned distortion leads to the difference between real and calculated lifetimes.

Light propagation in turbid medium is described by the radiative transfer equation (RTE). We assume that a dotted fluorophore is located on the axis of the excitation laser beam. The excitation pulse at the depth *z* at time moment *t* can be described by the following equation:

$$\phi_{ex}(z,t) = \int_0^t \phi_{ex}(z=0,t')\,\tilde{\phi}(z,t-t',\lambda_{ex})dt' \quad (1)$$

where $\phi_{ex}(z=0,t)$ is the initial excitation pulse and $\tilde{\phi}(z,t,\lambda_{ex})$ is Green's function of the medium corresponding to the excitation wavelength λ_{ex}. Similarly, fluorescent response at the fluorophore's depth is represented by the convolution of the excitation pulse and the exponential fluorescent response in free space, which is a single exponent function $exp\left(-\frac{t}{\tau_0}\right)$:

$$\phi_{em}(z,t) = \int_0^t \phi_{ex}(z,t')\,exp\left(-\frac{t-t'}{\tau_0}\right)dt' \quad (2)$$

The detected fluorescence is the convolution of fluorescent response and Green's function at the emission wavelength λ_{em}:

$$\phi_{em}(z=0,t) = \int_0^t \phi_{em}(z,t')\,\tilde{\phi}(z,t-t',\lambda_{em})dt' \quad (3)$$

This fluorescent response is approximated by an exponential decay function with time decay factor τ_m:

$$\phi_{em}(z=0,t) \propto e^{-\frac{t}{\tau_m}} \quad (4)$$

The difference between the calculated (τ_m) and the initial (τ_0) lifetimes will depend on optical parameters μ_s', μ_a of turbid medium, fluorophore embedding depth z, and real lifetime τ_0.

The result of approximation of the fluorescence kinetics obtained from a turbid medium will depend on the approximation interval chosen for calculation (Fig. 1a). The choice is determined by two factors. On the one hand, the fluorescent signal should exceed the noise level to ensure proper approximation by the exponential decay function; on the other hand, the beginning of the approximation interval should be far enough from the signal maximum to reduce its influence on the calculations. This optimal value depends on tissue properties, on fluorophore embedding depth and real lifetime, and on signal-to-noise ratio of the detecting system (Fig. 1b). Figure 1b was plotted for $\mu_a = 0.01\ mm^{-1}$, $\mu_s' = 0.6 mm^{-1}$, $\tau_0 = 2200$ ps and fluorophore embedding depth *z* = 5 mm.

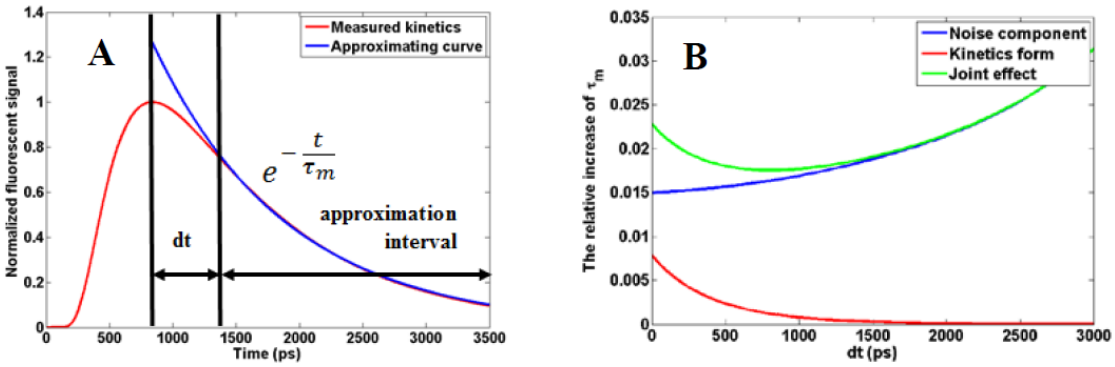

Fig. 1. (A) Approximation interval chosen for kinetics approximation with exponential decay. (B) The influence of noise component and kinetics shape on the choice of approximation interval

We performed a number of numerical simulations using the Monte-Carlo technique. The calculated lifetime versus fluorophore embedding depth is plotted in Fig. 2. The beginning of the approximation interval was chosen at 1000 ps from the kinetics maximum.

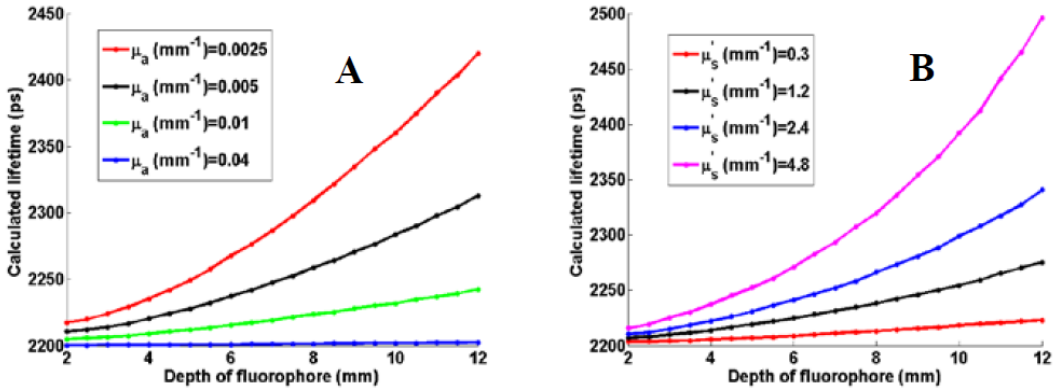

Fig. 2. Calculated lifetime versus fluorophore embedding depth for: (A) $\tau_0 = 2200$ ps, $\mu_s^{'} = 0.6$ mm^{-1} and different absorption; (B)$\tau_0 = 2200$ ps, $\mu_a = 0.01$ mm^{-1} and different reduced scattering

For verification of the results of our studies [3] we performed a model experiment. The scheme is shown in Fig. 3a. The model turbid medium in the 55×22×38 mm glass cuvette had the following optical parameters: $\mu_a = 0.005$ mm^{-1}, $\mu_s^{'} = 0.6$ mm^{-1}. The fluorescent agent (mKate fluorescent protein with lifetime of 2200 ps) was placed in a thin transparent glass ball with a diameter of 5 mm. The fluorophore embedding depth varied from 2 to 12 mm. The calculated lifetime vs fluorophore embedding depth obtained from numerical simulations and model experiment are plotted in Fig. 3b.

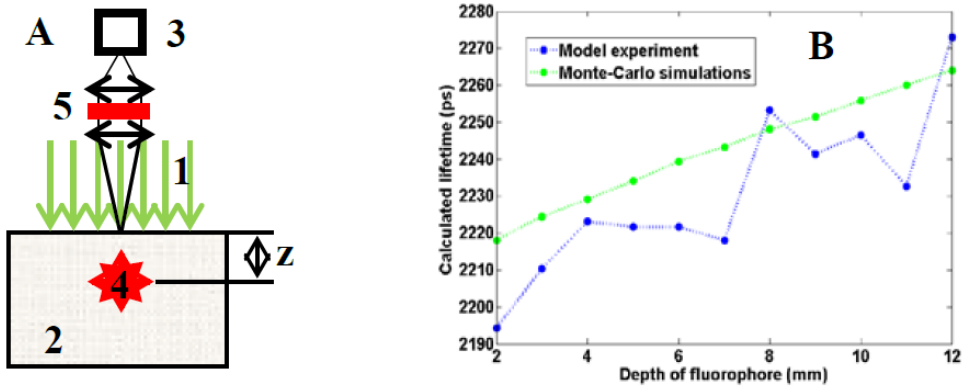

Fig. 3. (A) Scheme of numerical and model experiments. 1 – excitation pulse, 2 – turbid medium, 3 – photodetector, 4 – fluorescent agent, 5 – optical filter and lenses. (B) Calculated lifetime versus fluorophore embedding depth obtained from model experiment (dashed blue line) and in Monte-Carlo simulation (dashed green line)

Acknowledgements

This work was supported by the Russian Foundation for Basic Research grant No.13-04-40306.

References

1. V. Venugopal, J. Chen, M.Barroso, and X. Intes, “Quantitative tomographic imaging of intermolecular FRET in small animal s,” *Biomedical Optics Express*, 2012, **3**, 3161–3175.
2. M.A. O’Leary, D.A. Boas, X.D. Li, B. Chance, and A.G. Yodh, “Fluorescence lifetime imaging in turbid media,” *Optics Letters*, 1996, **21**(2), 158-160.
3. A.V. Khilov, I.I. Fiks, V.I. Plekhanov, M.Yu. Kirillin, and I.V. Turchin, “Fluorescence lifetime imaging for deep-seated fluorophore in turbid medium,” *Proceedings of SPIE*, 2015, **9448**, 94480F.

Invited

ENHANCING DIAGNOSTIC ACCURACY OF OPTICAL COHERENCE TOMOGRAPHY BY IMAGE QUANTIFICATION

M.Yu. Kirillin[1,2], N.M. Shakhova[1,3], O.G. Panteleeva[4], E.A. Sergeeva[1], P.D. Agrba[1,2], M.A. Pasukhin[1,2], E.S. Plankina[2], E.V. Gubarkova[3], E.B. Kiseleva[3], V.V. Dudenkova[2,3], N.D. Gladkova[3], and **I.A. Vitkin[5]**

[1] Institute of Applied Physics RAS, Nizhny Novgorod, Russia
mkirillin@yandex.ru
[2] N.I. Lobachevsky State University of Nizhny Novgorod, Nizhny Novgorod, Russia
[3] Nizhny Novgorod Medical Academy, Nizhny Novgorod, Russia
[4] Clinical Hospital of the Russian Railways, Nizhny Novgorod, Russia
[5] University of Toronto, Toronto, Canada

Abstract. Optical coherence tomography (OCT) can be employed for diagnostics of tissues of different localization. However, subjective evaluation of diagnostic OCT images may produce mistakes in diagnosing. Quantification of OCT images can provide a correct image interpretation and, thus, increase the diagnostic accuracy of the technique. In this paper we describe approaches to quantification of the diagnostic images of tissues of different localization, including skin, mucous tissues, and arterial walls obtained with both conventional and cross-polarization OCT modalities. The approaches are based on statistical and textural analysis of the images and analysis of probing radiation polarization state.

Optical coherence tomography (OCT) is currently becomes actively employed in diagnostics of tissues of different localization. However, interpretation of diagnostic OCT images often requires understanding the physical principles of OCT image formation which are usually unfamiliar to a physician. In such a situation quantification of OCT images appears a solution that can provide a correct image interpretation and, thus, increase the diagnostic accuracy of the technique. The most common approach to quantification of OCT images consist in approximation of OCT signal decay in logarithmic scale with linear function and measuring signal slope characterizing extinction coefficient of the tissue [1, 2]. However, this approach is appropriate for primarily homogeneous tissues, as presence of several layers or inclusions requires image segmentation which may appear a complex task, and only few papers employ this approach [3]. Alternative approach employs statistical analysis of OCT image speckle structure for local characterization of the tissue [4]. It consists in building a histogram of the entire OCT image or its fragment and its further fitting by multiparametric analytical function. Another approach to textural analysis includes processing of 2D Fourier transform of an OCT image which allows to characterize elongates structures in the image.

Employment of cross-polarization OCT (CP OCT) modality provides additional diagnostic data from characterization of evolution of probing radiation polarization state during its transport within studied tissue [5]. CP OCT is extremely sensitive to presence and state of collagen within tissues exhibiting strong birefrigent properties [6]. Traditional approach to quantitative analysis of polarization-sensitive OCT modality includes assessment of phase retardation map [7]. A closer approach based on calculation of an integral parameter, the integral depolarization factor (IDF) was proposed in our recent paper [6].

In present paper we report on application of OCT image quantification or enhancement of OCT diagnostic accuracy in gynecology, dermatology, and cardiology.

The considered gynecologic application of OCT included inspection of fallopian tubes in the course of laparoscopy procedure aiming for revealing the pathology causing infertility. Collected diagnostic data from 57 patients confirmed by subsequent histologic examination was separated into four groups: norm, edema, fibrosis, and transient state combining element of edema and fibrosis. In OCT images fibrosis is manifested by areas with increased OCT signal level while edema is manifested by large darker areas associated with presence of extracellular liquid. In this respect, analysis of image intensity distribution and search for pronounced structural boundaries should provide quantitative characterization of the images.

A histogram analysis was chosen for quantification of the diagnostic data. Different techniques of histogram analysis were compared. Noise equalization procedure was applied to the OCT images before building a histogram. Our previous studies employed trivial quantification of an image histogram consisting in calculation of linear combination of histogram counts for preliminary chosen intensity values [8]. Our new approach consisted in employment of neural network for classification of the his-

tograms of diagnostic OCT images. This approach allowed to separate fibrosis group with diagnostic accuracy exceeding 93% (exact value depend on neural network learning parameter).

In dermatology we applied quantification of OCT images for monitoring the state of human skin in course of treatment procedures. We employed similar approach with histogram analysis, however, in this application the histogram was fitted by an analytical function represented by a sum of two Gaussian functions. Noise contribution also represented by a Gaussian function has been subtracted from the total image histogram before analysis. We demonstrated that such parameters of the analytical function as width, maximum position and maximum value are sensitive to state of skin in course of treatment (medical treatment, mechanical compression and temperature action were considered).

A number of diagnostics tasks require evaluation of collagen state within biotissue. For example, in diagnostics of bladder cancer or evaluation of vulnerability of an atherosclerotic plaques knowledge of collagen state may significantly increase the accuracy of diagnosis. Collagen is known to reveal pronounced birefrigent properties depending on collagen type and organization. In this connection, CP OCT appears to be an efficient tool for non-invasive evaluation of collagen state. Ordered packed collagen fibers form birefrigent clusters systematically changing initial polarization of probing radiation. On the contrary, disordered or destroyed collagen fibers induced by various pathologies provide random changes of the polarization. This evolution of polarization can be traced by CP-OCT. For quantification of CP-OCT images we employ analysis of phase retardation map [7] and integral depolarization factor [5, 6]. Application of these approaches allowed to increase the accuracy of diagnostics of such hardly distinguishable, but clinically important cases as bladder cancer recurrence in post-operative scar and unstable atherosclerotic plaque.

Acknowledgements

The study was supported by RFBR (projects ## 15-32-20250, 15-42-02658 and 15-42-02503) and Ministry of Education and Science of the Russian Federation (grant 14.B25.31.0015).

References

1. Y. Yang, T. Wang, N. C. Biswal, X. Wang, M. Sanders, M. Brewer, and Q. Zhu, *J Biomed Opt.*, 2011, **16**(9), 090504.
2. I.V. Turchin, E.A. Sergeeva, L.S. Dolin, and V.A. Kamensky, *Laser Physics*, 2003, **13**(12), 1524-1529.
3. I.V. Turchin, E.A. Sergeeva, V.A. Kamensky, L.S. Dolin, N.M. Shakhova, and R. Richards-Kortum, *J Biomed Opt*, 2005, **10**(6), 064024.
4. V. Gelikonov, G. Gelikonov, M. Kirillin, N. Shakhova, A. Sergeev, N. Gladkova, and E. Zagaynova, Chapter 16 in *Handbook of Photonics for Biomedical Science* (ed. V.V. Tuchin), CRC Press, Boca Raton, London, New York, Washington, 2010, pp. 423-444.
5. E. Kiseleva, M. Kirillin, F. Feldchtein, A. Vitkin, E. Sergeeva, E. Zagaynova, O. Streltzova, B. Shakhov, E. Gubarkova, and N. Gladkova, *Biomedical Optics Express*, 2015, **6**(4), 1464-1476.
6. E.V. Gubarkova, M.Yu. Kirillin, E.A. Sergeeva, E.B. Kiseleva, L.B. Snopova, N.N. Prodanets, E.G. Sharabrin, E.B. Shakhov, S.V. Nemirova, and N.D. Gladkova, *Modern Technologies in Medicine*, 2013, **5**(4), 45-54.
7. W.-C. Kuo, Chapter 31 in *Advances in Lasers and Electro Optics* (ed. N. Costa and A. Cartaxo) ISBN 978-953-307-088-9, 2010.
8. M. Kirillin, O. Panteleeva, E. Yunusova, E. Donchenko, and N. Shakhova, *Journal of Biomedical Optics*, 2012, **17**, 081413.

ADVANCED MONTE CARLO SIMULATION OF BRAIN NIRS SENSING EMPLOYING INTEL MIC ARCHITECTURE

A.V. Gorskhov[1,2] and **M.Yu. Kirillin**[1,2]

[1] Institute of Applied Physics RAS, Nizhny Novgorod, Russia
mkirillin@yandex.ru
[2] N.I. Lobachevsky State University of Nizhny Novgorod, Nizhny Novgorod, Russia

Abstract. In the paper we discuss porting Monte Carlo (MC) technique for simulation of light transport in tissues to Intel Xeon Phi coprocessor. We show that employing the accelerator allows to significantly reduce computational time of MC simulation and obtain simulation speed-up comparable to GPU. Performance of the developed code for simulation of NIRS brain sensing and determination of the measurement volume is demonstrated.

Monte Carlo (MC) simulations are currently treated as a gold standard tool in biomedical optics applications since presentation of classical MCML code developed by Wang et al [1]. The numerical simulations can be employed in cases where application of various theoretical approaches is limited. However, this technique has a significant drawback – large computational requirements. Various efforts have been made to reduce simulation time, such as algorithm optimization and use of different hardware accelerators [2–6].

In this paper we present implementation of MC simulation code with Intel Many Integrated Core (MIC) architecture. Previously the code was tested with CPU and cluster systems [7]. The code allows simulating light propagation in media with complex geometry of layers whose boundaries are determined by triangulated surfaces. Intersection search algorithm employs bounding volume hierarchy (BVH) tree as accelerating structure.

Intel Many Integrated Core Architecture (or Intel MIC) is a multiprocessor computer architecture combining many Intel x86 CPU cores onto a single chip. Like a GPU, Intel Xeon Phi can be employed as a hardware accelerator for high-performance computations. The key advantage of this architecture is that accepts standard existing programming tools and methods, like OpenMP and MPI.

However, only the programs with high degree of parallelism and vectorization abilities can be efficiently accelerated with Intel Xeon Phi coprocessor, similar to GPU. MC simulation fits these requirements only partially: it features strong parallelism, however, the MC code is difficult to vectorize because of its stochastic nature.

In order to port a code to Intel MIC one needs to only recompile the source OpenMP/MPI based program using Intel Compiler for Xeon Phi. However, to obtain efficient performance of the code optimization is required. Since MC method is initially parallel, the main optimization aim is to reduce memory latency. We propose three following optimization steps. The first step consists in changing data structure for storing photon trajectories from a three-dimensional grid array to an array of grid coordinates for each thread. The second one is elimination of arrays copies which were previously used to avoid synchronization. These steps allow to reduce requirements to the memory size, and as a result, to improve performance, in spite of additional synchronization. The third step is directed to reduce memory access time in intersection search. BVH tree structure is updated to store vertex data as a single continuous memory region to more effectively employ hardware cache.

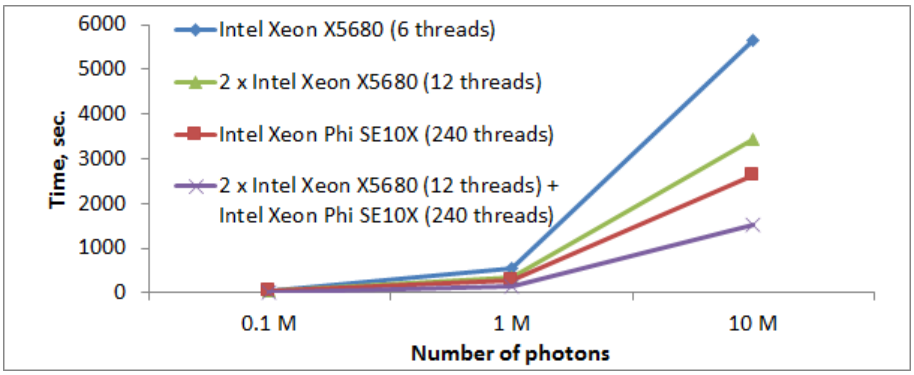

Fig. 1. Execution time of the MC simulation code at different hardware

As a result, we are obtained MIC program that is near 2 times faster than the program, which is executed on a 6-core Intel Xeon CPU (Fig. 1).

To demonstrate the code applicability for simulation of light transport in tissues we simulated performance of NIRS brain sensing [5, 7] that is one of the most computational-cost applications of MC technique in biomedical optics. In simulations we employed human head model consisting of 6 layers: scalp, fat, skull, cerebrospinal fluid (CSF), white matter and grey matter. The boundaries of these layers are adopted from real head geometry obtained from MRI data while optical properties of the layers are averaged from values available in literature.

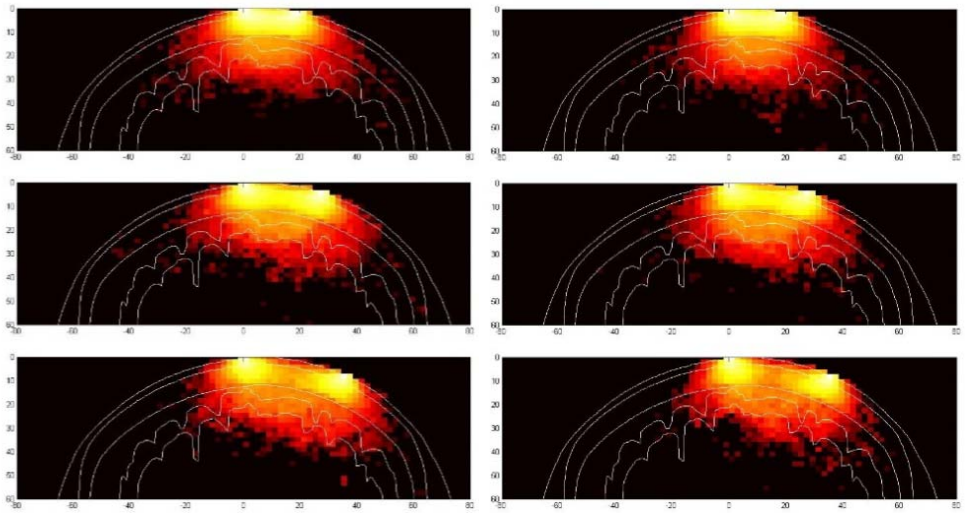

(a) (b)

Fig. 2. Two-dimensional photon trajectory maps for source-detector separations of 20 (top), 30 (middle), and 40 (bottom) mm for 830 (a) and 915 (b) nm

We built two-dimensional cross-sections of the photons trajectory map in the plane based on radiation incidence vector and source-detector vector for different source-detector separations and probing wavelengths (Fig. 2). Cross-sections of layers boundaries shown in the same figure allow evaluating the penetration depth of probing radiation thus determining the measurement volume of the simulated NIRS system. This figure shows that probing radiation reaches grey matter layer thus proving abilities of simulated NIRS system to monitor brain activity. On the other hand, one can see that for smaller source-detector separations the major number of trajectories does not reach grey matter thus increasing this distance leads to in-depth shift of measurement volume.

Thus, we demonstrated the abilities of the developed code in simulation of NIRS brain sensing for complex geometry based on diagnostic MRI data.

Acknowledgements

The study was supported by RFBR (projects ## 14-02-31549 and 15-02-04270).

References

1. L. Wang, S. Jacques, and L. Zheng, *Comput. Meth. Programs Biomed.*, 1995, **47**(2), 131-146.
2. N. Zolek, A. Liebert, and R. Maniewski, *Comput. Meth. Programs Biomed.*, 2006, **84**(1), 50-57.
3. L. Wang and S. Jacques, *Journal of Optical Society of America A.*, 1993, **10**(8), 1746-1752.
4. E. Alerstam, S. Anderson-Engels, and T. Svensson, *Journal of Biomedical Optics*, 2008, **13**(4), 041304.
5. N. Ren, J. Liang, X. Qu, J. Li, B. Lu, and J. Tian, *Optics Express*, 2010, **18**(7), 6811-6823.
6. A. Doronin and I. Meglinski, *Journal of Biomedical Optics*, 2012, **17**(9), 090504.
7. A. Gorshkov and M. Kirillin, *Journal of Computational Science*, 2012, **3**(6), 498-503.

SYSTEM FOR MONITORING PHOTODYNAMIC THERAPY PROCEDURE

M.S. Kleshnin[1], **I.I. Fiks**[1], **S.V. Gamayunov**[2,3], **V.I. Plekhanov**[1], and **I.V. Turchin**[1]

[1] Institute of Applied Physics RAS, Nizhny Novgorod, Russia, m.s.kleshnin@gmail.com
[2] Nizhny Novgorod State Medical Academy, Nizhny Novgorod, Russia
[3]Regional Oncological Hospital, Nizhny Novgorod, Russia

Abstract. The photodynamic therapy is one of the most promising methods for the treatment of oncological, inflammatory and degenerative diseases of the skin. The treatment efficacy is determined by proper assessment of drug concentration in the tissue lesion and sensitizer photobleaching during irradiation. We have developed a compact and low cost device for monitoring the photodynamic procedure. The created system based on a single CCD camera and two LEDs and is compatible with any therapeutic laser. In this paper we present the test results of the developed device in model experiments and clinical trials.

Introduction

Photodynamic therapy (PDT) is one of the rapidly developing methods of modern medicine, which is based on the interaction of light with a photosensitizer in the tissue [1–5]. The photosensitizer is injected into a patient prior to the PDT procedure and selectively accumulates in tumor or other target tissues, depending on the chemical nature of the drug and the tumor tissue [1].The irradiation of the affected area with a low intensity light in the absorption band of the sensitizer causes fluorescence of the accumulated drug and allows performing the fluorescence diagnosis of the patient's tissue [1, 2]. Irradiation of the tissue lesion with a high intensity light in the absorption band of the photosensitizer leads to death (necrosis and apoptosis) of the cancer cells due to highly toxic photochemical reactions [3]. Several weeks after the PDT, the tumor is destroyed and the affected tissues are partially or fully restored. The benefits of the PDT include: low pain level, good cosmetic results, wide range permit doses of a photosensitizer and light exposure, the possibility of multiple repetition of the procedure, as well as a combination with other treatments [3, 4]. The main drawbacks of PDT are empirical selection of light exposure and small depth of light penetration due to strong light attenuation in tissues. Moreover, the results of treatment depend on tumor oxygenation and blood flow [4]. However, objective information about sensitizer photobleaching during irradiation allows proving, optimizing and personalizing the therapeutic effect and permits eliminating some drawbacks of the procedure [5]. In this paper, we present a compact and low cost device for monitoring the PDT procedure and the test results of the developed device in model experiments and clinical trials.

Materials and methods

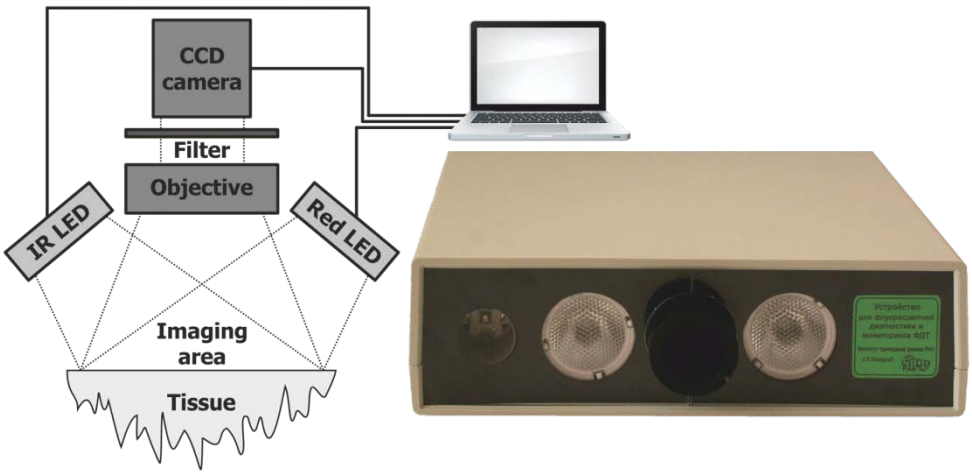

Fig. 1. Schematic diagram and photo of the system for monitoring photodynamic therapy

Figure 1 shows a schematic diagram and a photo of the created system for monitoring photodynamic procedure. This device is based on two LEDs emitting at different wavelengths, a CCD camera with emission filter (700–800 nm), and an objective lens. The light source in the excitation band (660 nm) of the photosensitizer produces fluorescent images and the light source in the emission band (740 nm) of the photosensitizer is intended for imaging in backscattered light. The LEDs are switched on sequentially, and each CCD frame is synchronized with the emission of the corresponding LED and

combined with subtracting of the dark field images to eliminate the influence of external light. This approach enables determining automatically the boundaries of the affected area and its location on the patient's body. In the case of low contrast, one can manually select the boundaries of the affected area in the obtained image. Moreover, the device tracks the position of the selected fluorescing area, which is essential for clinical trials due to patient involuntary movement.

For monitoring the sensitizer photobleaching during PDT procedure, the therapeutic laser must be switched off periodically. The created device tracks the disappearance of the strong laser signal from the CCD frames or the trigger pulse from the laser source and calculates the average fluorescent intensity in the area of interest.

The created device was successfully tested in model experiments on irradiation of cuvettes with various concentrations of «Photoditazin» drug in «Intralipid» solution. After that, the created system was tested on patients in clinic. All clinical trials have been approved by the IRB of the Regional Oncological Hospital.

Results and discussion

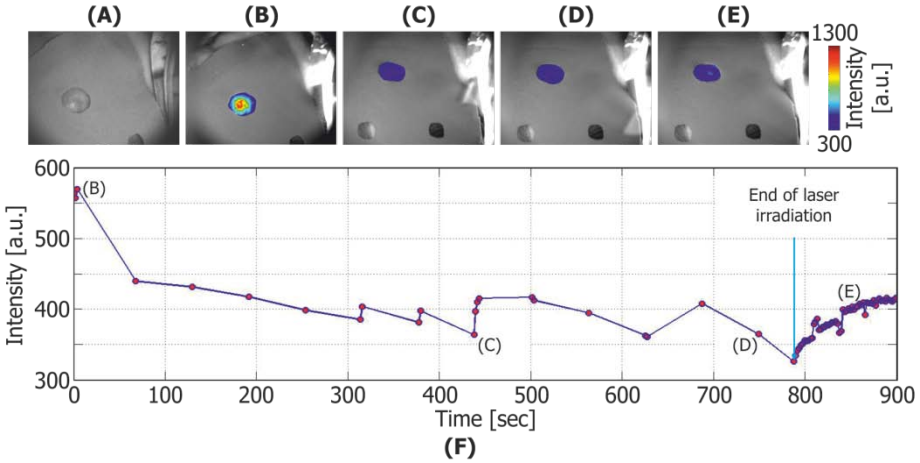

Fig. 2. (A) Image of tumor (recurrent multifocal basal carcinoma of the right parotid region, affected area 25 mm) obtained in backscattered light. (B), (C) (D) and (E) Fluorescent images of tumor obtained before, during and after PDT. (F) Diagram of sensitizer («Photoditazin» 1 mg/kg) photobleaching

Conducted experiments have shown that, the device provide sensitivity from 0.3 to 30 mg/kg of «Photoditazin» concentration for the 0.2 sec exposure of CCD camera. The results obtained in the experiments also clearly showed the efficacy of the developed system for monitoring sensitizer photobleaching during PDT. For example, figure 2 shows monitoring of «Photoditazin» (1 mg/kg) photobleaching during PDT of a female patient (65 years old, recurrent multifocal basal carcinoma of the right parotid region, affected area 25 mm). The device enabled localizing the tumor on the patient's body, estimating photosensitizer accumulation in the tumor and surrounding normal tissues and permitted monitoring the sensitizer photobleaching during laser irradiation. Therefore, the proposed system for monitoring the photodynamic therapy procedure is a promising tool for clinical application.

Acknowledgements

This work was supported by the Ministry of Education and Science of the Russian Federation (project No 14.604.21.0027, RFMEFI60414X0027). The authors are also grateful to V. Vorob'ev, V. Kozhevnikov, D. Moroskin and N. Shakhova for assistance in creating the device and conducting the clinical trials.

References

1. J. Celli, B. Spring, I. Rizvi, et al., *Chem. Rev.*, 2010, **110**, 2795-2838.
2. *Handbook of Biomedical Fluorescence*, A. Mycek, B. Pogue(Eds.), CRC Press, London, 2003, p. 688.
3. P. Agostinis, K. Berg, K. Cengel, et al., *CA: A Cancer Journal for Clinicians*, 2011, **61**(4), 250-281.
4. R. Allison, V. Bagnato, and C. Sibata, *Future Oncol.*, 2010, **6**(6), 929-940.
5. J. Tyrrell, S. Campbell, and A. Curnow, *Photodiag.Photodyn. Therapy*, 2011, **8**, 30-38.

MULTIPHOTON TOMOGRAPHY OF ASTRONAUTS TO EVALUATE SKIN AGEING PROCESSES

K. König[1,2]

[1] JenLab GmbH, Jena, Germany,
info@jenlab.de
[2] Saarland University, Dept. Biophotonics and Lser Technology Saarbrücken,
k.koenig@blt.uni-saarland.de

Abstract. Weightlessness over several months impairs the astronaut's health including skin modifications, bone loss (1% month-1), body fluidics shifts and eyesight damage. Skin impairments are one of the most frequent health problems. The ongoing European Space Agency Project *Skin B* hopes to answer the question how astronauts' skin regeneration is affected. For that purpose, high resolution MPT is employed to evaluate skin effects on a subcellular level in ISS astronauts.

A loss of elasticity, thinner skin and impaired healing effects have been reported based on a pilot study with the German astronaut *Thomas Reiter* in 2006 (1). Lack of gravity, reduced skin-material friction, and exposure to extraterrestrial radiation and to bioparticles from epidermal skin (terrestrial epidermis turnover: 1 month) may have an impact.

Pre-flight and post-flight label-free multiphoton skin biopsies were taken on the lower left arms. In particular, NAD(P)H in its free and bound form, keratin, melanin and elastin aswell as the collagen network was detected via two-photon autofluorescence excitation and SHG with 80 MHz femtosecond laser pulses at 780 nm using the mobile certified clinical multiphoton tomograph *MPTflex* with its optomechanical arm and the miniaturized 360° scan/detector head (2). The skin ageing index SAAID was determined based on the ratio of elastin to collagen at different depth in the upper dermis. Information on cell metabolism was obtained by fluorescence lifetime imaging (FLIM). The thickness of the *stratum corneum* and the viable epidermis as well as the architecture of the epidermal-dermal junction was determined by horizontal optical sectioning with 300 nm resolution in steps of 5 μm into a depth of 190 μm. One optical section (512x512 pixels @ 200x200 μm2) took 6.4 s. The preliminary results on Italian and German astronauts show a clear thinning of the living epidermis of about 15% after 6 months space flight. The SAAID values were significantly influenced. Currently, skin recovery effects are studied with MPT at the *European Astronaut Center* in Cologne (3).

Acknowledgements

The author acknowledges support from A. Pietruszka, R. Bückle (bothe JenLab) and N. Gerlach, U. Heinrich from DermaTronier GmbH.

References

1. H. Tronnier, M. Wiebusch, U. Heinrich, "Change in skin physiological parameters in space report on and results of the first study on man," Skin Pharmacol. Physiol., 2008, 21, 283-29.
2. K. König, "Hybrid multiphoton multimodal tomography of in vivo human skin," IntraVital, 2012, 1, 11-26.
3. K. König. Skin problems in outer space. The New Economy. Spring Edition 2015.

STUDY OF THE ACCURACY OF METHODS FOR DETERMINING OPTICAL PROPERTIES OF TURBID MEDIA

A.D. Krainov[1,2], **E. Sergeeva**[1], and **M. Kirillin**[1]

[1] Institute of Applied Physics RAS, Nizhny Novgorod, Russia
adkrainov@gmail.com
[2] N.I. Lobachevsky Nizhny Novgorod State University, Nizhny Novgorod, Russia

Abstract. We performed comparative analysis of the accuracy of different techniques for determining optical properties of turbid media basing on spectrophotometric measurement data. We compared 2-flux (Kubelka-Munk) and 3-flux models and an analytical model based on the least-scattering approximation of radiative transfer equation.

Light propagation in turbid media such as biological tissue is an important issue in many medical applications. Knowledge of precise values of tissue optical properties can significantly improve the quality of biomedical studies. The optical properties, i.e., the absorption coefficient μ_a, the scattering coefficient μ_s, and the anisotropy factor g, are often determined from measurement of the total diffuse reflectance R, the diffuse transmittance T and collimated transmittance C of a thin sample with an integrating sphere setup. Some methods allow determining the optical properties (μ_a, μ_s and g) of the tissue studied using analytical expressions [1]. However, the analytical solutions for $R(\mu_a, \mu_s, g)$, $T(\mu_a, \mu_s, g)$ and $C(\mu_a, \mu_s, g)$ have significant limitations; thus the majority of contemporary approaches are based on numerical methods, which provide higher accuracy, e.g., the inverse adding–doubling (IAD) method [2] or methods involving Monte Carlo simulations [3]. In these methods the optical properties values are determined by iterative numerical calculations procedure. This may prove to be to slow in some cases, e.g., applications involving real-time multiwavelength analysis. Availability of information on the accuracy of methods for determining optical properties of the medium allows to choose a more appropriate method for a specific task. The aim of this paper is to perform comparative analysis of several analytical methods for optical properties determination.

The Kubelka-Munk theory describes the propagation of a uniform, diffuse irradiance through a one-dimensional isotropic slab with no reflection at the boundaries. The simplicity of this model has made it a popular method for calculating the optical properties of tissue. The 2- and 3- flux models are based on expressions performed in [4]. The 2-flux model allows to determine μ_a, μ_s‘ as:

$$\mu_a = \frac{S_{KM}}{2},\ \mu_s' = \mu_a + \frac{4}{3}S_{KM}\,.$$

The 3-flux model allows to determine μ_a, μ_s, and g as:

$$\mu_a = \frac{S_{KM}}{2},\ \mu_s = \frac{1}{d}\ln C - \frac{K_{KM}}{2},\ g = 1 - \frac{K_{KM} + 8S_{KM}}{6\mu_s}.$$

Both models are not applicable in the case of strongly absorbing and highly scattering medium when $3\mu_s' < \mu_a$.

Another considered method is based on least-scattering approximation of radiative transfer equation [1] and uses following formulas:

$$\mu_a = \frac{1}{d}\ln\left(\frac{T_F^2}{R+T}\right),\ \mu_s = \frac{1}{d}\left[\ln\left(\frac{T+R}{C}\right)\right],\ g = 1 - R\left(T\ln\left[\frac{R+C}{C}\right]\right)^{-1},\ T_F = \frac{4n}{(n+1)^2},$$

where T_F is the Fresnel transmission coefficient for normal incidence of radiation on the boundary of the medium. Applicability of the model is limited by the condition $[\mu_s(1-g)+\mu_a]d \le 1$.

The accuracy of these methods was determined as follows. At the first step we calculated C, R and T using Monte Carlo technique. These calculations were performed for three and single layer media. The 3-layer sample geometry was a semi-infinite slab with thickness d = 0.5 cm placed between semi-infinite glass slides with thickness 0.1 cm and refractive index n_{slide} = 1.55 corresponding to standard quartz cuvette. The single layer geometry did not account for cuvette walls. In each simulation $1\cdot10^6$ photons were traced. The values of μ_a and μ_s were incremented in steps of 0.1 and 1 cm^{-1}, respectively, within the typical biological ranges: 0.1 cm^{-1} $\le \mu_a \le$ 5 cm^{-1} ,1 cm^{-1} $\le \mu_s \le$ 100 cm^{-1}, g = 0.7 and n = 1.33. Further, from the calculated values of C, R and T we determined μ_a, μ_s, μ_s‘ and g using the abovementioned methods. At the next step we calculated the relative error of the obtained values. The

results for 3-layer media are shown in Fig 1. Since the expression for the applicability range for the models depends on the thickness of the sample, the error estimates are given for dimensionless parameters $\mu_a d$ and $\mu_s d$. From obtained data we can conclude, that relative error of determination of μ_a for all studied models increases with increasing $\mu_a d$ and $\mu_s d$. The large relative error in determination of μ_a for $\mu_a d < 1.5$ is governed by the cuvette walls account. All models have a significant error in the determination of μ_s‘ for $\mu_s d > 20$. The method based on least-scattering approximation and the 3-flux Kubelka-Munk model are well suited for the determination of μ_s for $\mu_s d < 20$. It is worth mentioning that for large values of $\mu_a d$ and $\mu_s d$ the collimated transmittance C is extremely low which brings a significant error in determination of optical properties values.

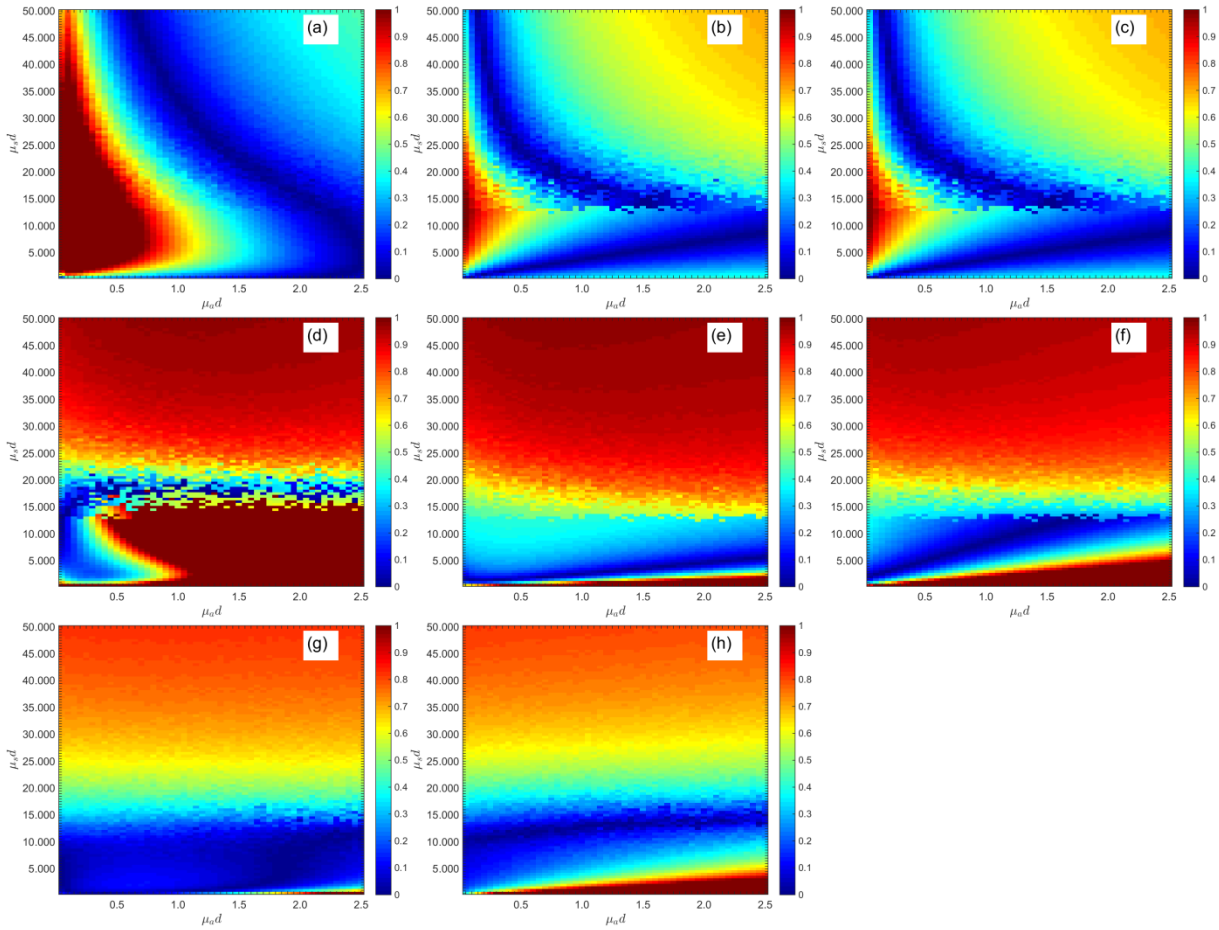

Fig. 1. Relative error of determination μ_a, (a, b, c), μ_s‘ (d, e, f) and μ_s (g, h) using method based on least-scattering approximation of radiative transfer equation (left column), 3-flux Kubelka-Munk model (central column) and 2-flux Kubelka-Munk model (right column). The charts are shown for dimensionless parameters $\mu_a d$ and $\mu_s d$

Acknowledgements

The work is financially supported by RFBR grants (## 14-02-31549 and 15-02-04270).

References

1. E.A. Sergeeva, D. Krainov, P.D. Agrba, and M.Yu. Kirillin, *Technique for experimental determination of nanoparticle solution optical properties from spectrophotometric data*, GSSSD ME 217 – 2014, 2014 (*in Russian*).
2. S.A. Prahl, M.J.C. van Gemert, and J. Welch, *Appl. Opt.*, 1993, **32**, 559-568.
3. C.R. Simpson, M. Kohl, M. Essenpreis, and M. Cope, *Phys. Med. Biol.*, 1998, **43**, 2465-2478.
4. M.J.C. van Gemert, A.J. Welch, and W.M. Star, *Las. Med. Sci.*, 1987, **2**, 295.

Invited

3D OPTICAL ELASTOGRAPHY IN REAL TIME

K.V. Larin

University of Houston, Houston, USA
klarin@uh.edu

Abstract. Here we evaluate the capability of a novel combined focused ultrasound/air-puff and phase-sensitive optical coherence elastography (OCE) system to assess biomechanical properties of ocular tissues (such as cornea and the lens) *in situ* and *in vivo* in 3D.

Optical elastography uses light to characterize cells and tissues based on their elastic and viscoelastic mechanical properties. In utilizing the high-resolution and high-contrast capability of optics, this rapidly emerging field builds on and complements the related USE and MRE techniques. Most recently, OCE has emerged as noninvasive biomechanical imaging technique that, beyond the structural 3D image, can provide additional qualitative and quantitative information about tissue elastic properties at the micro-scale level. Recently, we developed a new method for assessing tissue biomechanical properties by phase-sensitive analysis of the tissue surface response to a mechanical stimulation. In this method, an external stimulus (such as acoustic radiation force, focused air-puff, or a laser pulse) is used to remotely induce the deformation on tissue surface and a phase-sensitive optical coherence tomography (PhS-OCT) system, co-focused with the stimulus, utilized to monitor the localized temporal and spatial response of the deformations on the tissue surface with nanometer sensitivity. The dominant frequency from the amplitude spectra of the surface response and speed of the elastic wave propagation could be obtained and used as the indicator of the elasticity distribution in 3D.

Low-amplitude elastic deformations in soft tissues were measured by the OCE system consisting of a spectral-domain optical coherence tomography (OCT) combined with focused ultrasound or air-puff systems used to produce a transient force on the tissue surface. The amplitude, temporal profile, and the speed of the deformations were used to reconstruct tissue biomechanical properties using novel analytical models. Gold standard uniaxial compressional tests were used to validate the OCE data.

The OCE measurements in rabbit lens showed that the amplitude and the relaxation rate of the displacements (and, thus, Young's modulus and shear viscosity) of the young lenses were significantly larger than those of the mature lenses, indicating a gradual increase of the lens stiffness with age (2.5 kPa and 7.4 kPa, respectively). 3D visualization of the elastic wave propagating in rabbit corneas shows the obvious velocity difference in normal (0.79 ± 0.050 m/s) and CLX (2.00 ± 0.23 m/s) corneas. Then, the frequency analysis allowed depth-resolved analysis of cornea biomechanical properties clearly demonstrating the biomechanical differences of the corneal layers. Finally, the stress-strain measurements using uniaxial mechanical tests confirmed the results obtained by the OCE system. OCE measurements were also performed on cardiac muscle and kidney to assess progression of various diseases such as myocardium infarction and nephritis.

The results demonstrate that the OCE system can be used for noninvasive analysis and quantification of tissue biomechanical properties in 3D and as a function of age or therapy (e.g. CLX procedures). It can also provide a reliable marker for assessing severity of a disease.

MEASUREMENT OF OPTICAL PROPERTIES OF MICE TISSUES AND DESIGN OF THEIR OPTICAL PHANTOMS

D. Loginova[1,2], **A. Krainov**[1,2], **P. Agrba**[1,2], and **M. Kirillin**[1,2]

[1] Institute of Applied Physics RAS, Nizhny Novgorod, Russia, vekfy@inbox.ru
[2] Lobachevsky State University of Nizhny Novgorod, Nizhny Novgorod, Russia

Abstract. We measured the optical properties of mice tissues *ex vivo* in the range of 400–1100 nm by spectrophotometry technique. Measured values were employed for design of the optical phantoms that mimic optical properties of the studied mice tissues in the specified range. Designed phantoms are suitable in tomographic measurements for calibration of optical devices, approbation of novel techniques for biomedical diagnostics, and use as an immersion liquid.

Optical tomography is a widely used class of non-invasive techniques for imaging of biotissue *in vivo*. Phantoms that mimic optical characteristics of tissues are commonly employed in tomographic measurements for the calibration of optical devices, the approbation of new techniques for biomedical diagnostics before *in vivo* application. Furthermore, the optical phantoms are suitable for use as an immersion liquid, for example, to suppress the effect of complex boundaries in diffuse optical tomography.

In this work, we measured the optical properties of mice tissues *ex vivo* in the range of 400–1100 nm. Measured values were employed for design of the optical phantoms that mimic optical properties of the studied mice tissues in the specified range.

Ex vivo brain and hind limb muscle tissues of laboratory mice were extracted immediately after mice sacrifice. Each sample was homogenized and then placed in a 1-mm plane-parallel quartz cuvette. Using an AnalytikJena Specord 250 Plus spectrophotometer with an integral sphere we measured spectra of collimated and diffuse transmittance and diffuse reflection in the range of 400–1100 nm. In order to retrieve spectra of biotissue optical properties, namely, absorption coefficient μa (λ) and scattering coefficient μs (λ), from the measured data we apply the original technique [1], based on least-scattering approximation. Calculated spectra of absorption and scattering coefficients are shown in Figures 1a and 1b, respectively. Pronounced peaks of the absorption spectra correspond to those of hemoglobin, one of the main chromophores within tissue. These results are in good agreement with results of other studies [2, 3].

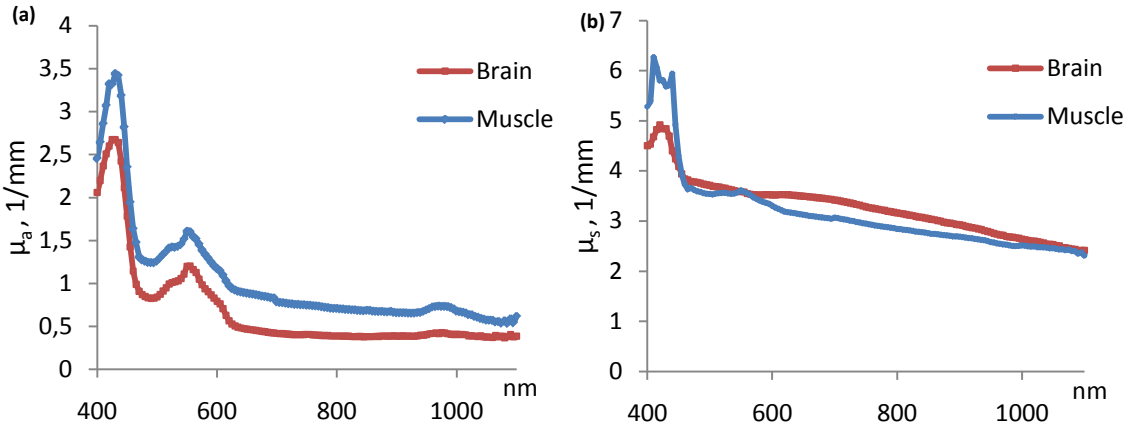

Fig. 1. Optical absorption (a) and scattering (b) coefficients for brain and muscle tissues

At the next step we designed the optical phantom with optical properties equivalent to those of brain tissue. Traditional components of phantoms are Intralipid and India ink [BOE 2014] mixed in a custom proportion, where Intralipid is mostly responsible for scattering properties, while India ink is responsible for absorption. In this study, instead of Intralipid we used Lipofundin as a scattering component of phantom and in addition to black India ink, which is an absorption component, red ink was used to more accurately mimic spectral dependencies of optical properties.

Unfortunately, significant qualitative difference between spectra of mice biotissues and phantom components does not allow to design a unified phantom mimicking their optical properties in the whole considered range (400–1100 nm). In this respect we developed two optical phantoms, mimick-

ing tissue optical properties in two intervals: 480–580 and 580–1080 nm. These phantoms have the same component composition (Lipofundin, black India ink, and red ink), however, mixed at different concentrations. Optical properties of these phantoms are shown in Fig. 2a and 2b for two selected intervals, respectively. The discrepancy between the values of tissue optical properties and those of the phantoms does not exceed 20 %.

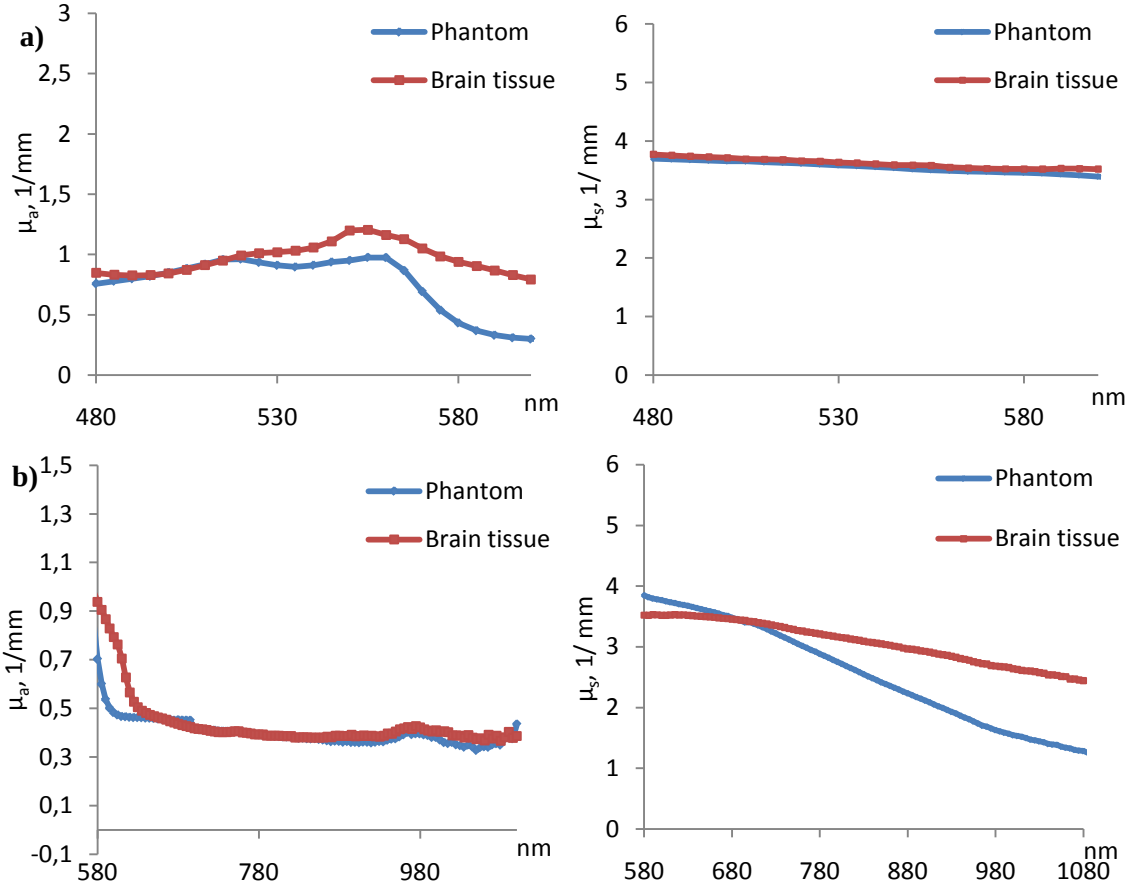

Fig. 2. Comparison of optical properties of brain tissue and a) the optical phantom for the range of 480–580 nm, b) the optical phantom for the range of 580–1080 nm

Acknowledgements

The work is supported by RFBR grants (## 14-02-31549 and 15-02-04270).

References

1. E.A. Sergeeva, D. Krainov, P.D. Agrba, and M.Yu. Kirillin, *Technique for experimental determination of nanoiparticle solution optical properties from spectrophotometric data GSSSD ME 217 – 2014*, 2014 (in Russian).
2. D. Krainov, A.M. Mokeeva, E.A. Sergeeva, P.D. Agrba, and M.Yu. Kirillin, *Optics and Spectroscopy*, 2013, **115**(2), 193-200.
3. M. Mesradi, A. Genoux, V. Cuplov, D.A. Haidar, S. Jan, I. Buvat, and F. Pain, *Journal of Biomedical Optics*, 2013, **18**(11), 117010.

Invited

MULTISPECTRAL FLUORESCENCE LIFETIME TECHNIQUES FOR CLINICAL APPLICATIONS

L. Marcu

University of California Davis, Davis, CA, USA
lmarcu@ucdavis.edu

Abstract. This presentation overviews time-resolved fluorescence spectroscopy (TRFS) and fluorescence lifetime imaging (FLIM) instrumentation and associated methodologies which allow label-free in-vivo evaluation of biological tissues. Emphasis is placed on recently developed techniques for real-time characterization and diagnosis of diseased tissues during clinical interventions. This includes intraoperative delineation of tumor margins (brain tumors and head and neck tumors) and intravascular diagnosis of atherosclerotic cardiovascular disease. Current studies in animal models and human patients demonstrate the ability of these techniques to provide rapid in-situ evaluation of tissue biochemistry and their potential to guide surgical and intravascular procedures.

Introduction

Most clinical diagnostic applications of autofluorescence have been based on steady-state technique that relies on measurement of emission intensity and/or spectra. These measurements are typically affected by numerous factors including irregular tissue surfaces, non-uniform sample illumination, and the presence of endogenous absorbers such as blood in the operative field. Time-resolved (lifetime) measurement of fluorescence emission have the potential to address such limitations and to improve the specificity of fluorescence measurements [1]. The full potential value of fluorescence lifetime techniques has been, however, only sparsely evaluated in clinical settings [2]. Their clinical translation has been hampered by the complexity of the instrumental setups, lengthy data acquisition and analysis, and high instrumentation costs associated with these techniques. In the following, we describe a fluorescence lifetime technique that has the potential to address such challenges and initial results obtained in pre-clinical settings using such technique.

Overview of the multispectral fluorescence lifetime technique

A recent multispectral time-resolved fluorescence spectroscopy (ms-TRFS) technique designed in our laboratory [3, 4] enables rapid and simultaneous recording of fluorescence decays in multiple spectral bands compatible with rapid in-vivo applications. In this configuration, the fluorescence emission is spectrally resolved using a set of dichroic and bandpass filters, allowing for selection of four channels or wavelength bands. Then, each channel is coupled to optical fibers of distinct lengths that act as optical delay lines. Thus, the spectrally resolved fluorescence decays arrive at the detector separated in time (~50 ns). The ms-TRFS device is based on pulse sampling and gated detection, where the detector a multi-channel plate photomultiplier remains on until the entire fluorescence transient pulse is recorded using a digitizer with high sampling frequency and analog bandwidth (8 Gsamples/s, 3 GHz).

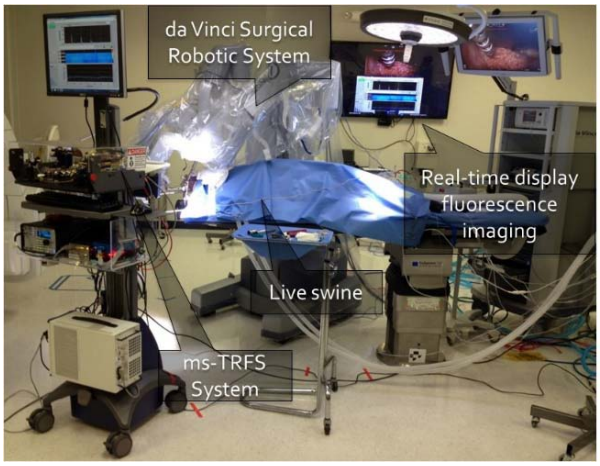

Fig. 1. Picture of the ms-TRFS experimental set-up adapted to work in conjunction with the da Vinci surgical robot. The fluorescence excitation is induced by a micro-Q-switched laser (355 nm, 600 ps, 700 nJ/pulse) that can operate with a variable repetition rate (20 Hz – 4 KHz). A MCP-PMT (rise time 50 ps) and a digitizer (3 GHz analog bandwidth, 12.5 Gs/s sampling speed) are used to detect and time-resolve the fluorescence detection)

If the tissue sample has high quantum efficiency, a single laser excitation pulse is enough to simultaneously record a complete transient fluorescent pulse for each channel (wavelength band). This method allows fast recording of fluorescence decays (e.g., <1 μs per data point) in multiple spectral bands generated in response to a single laser-pulse excitation. Figure 1 depicts a recent implementation of the ms-TRFS system as a diagnostic tool that works in conjunction with the da Vinci surgical robot. Notably, this versatile system enables acquisition and analysis of fluorescence data in several

operation modes. The same instrument can be used for point spectroscopy, linear scanning, and planar (xy) scanning as well as in pull-back motion-rotational modes. When used in planar or rotational pull-back it allows for recovery of spectroscopic or fluorescence lifetime imaging (FLIm) with high spatial resolution (<100 μm). The spectral channels can be adapted to resolve the autofluorescence emission of key biomolecules in tissue, including collagen, elastin, nicotinamide adenine dinucleotide (NADH), lipopigments, flavins, and porphyrins.

Validation of the ms-TRFS in tissue specimens (ex-vivo) and in animal models (in-vivo)

The performance of the ms-TRFS was tested on both tissue phantoms and biological tissue both ex-vivo and in-vivo. A few examples are presented in this section. Figure 2 depicts co-registered ms-TRFS data with conventional intravascular ultrasound (IVUS) acquired using a bimodal catheter from an ex-vivo human coronary artery. FLIm data corresponds to lifetime values from 390/40 nm wavelength band. Results from this study were recently reported [5]. Figure 3 show in-vivo ms-TRFS measurement on porcine animal model demonstrating the functionality of the lifetime overlay technique.

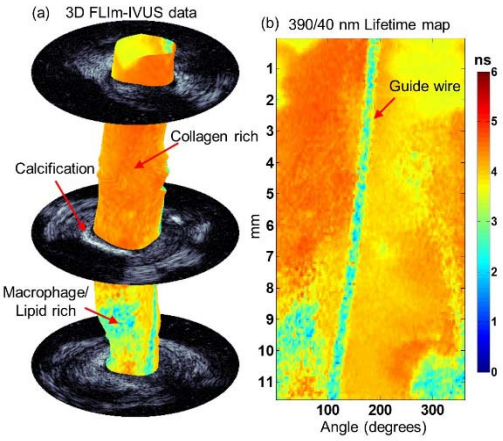

Fig. 2. a) ms-TRFS data in 3D co-registered with 3 selected IVUS frames. b) En-face lifetime map. Collagen-rich areas presents a higher lifetime relative to the macrophage-rich areas

Fig. 3. Left image shows the white-light image as acquired by the daVinci Surgical System integrated stereoscope (FireFly). Right image shows the same frame, but with lifetime values from one channel (wavelength band 542/50 nm) of the ms-TRFS system overlaid. The lifetime mask is dynamically updated during the scanning process and the user can switch between different channels in real-time. Experiment performed in the pig tongue in-vivo. Note the taste buds that have a shorter lifetime values (~3 ns) when compared with the lifetime of the surrounding epithelial tissue (~4.5 ns)

Conclusion

Current studies demonstrate the feasibility of ms-TRFS technique to operate in clinically relevant environments, to provide rapid in-situ evaluation of tissue biochemistry and show the potential of this technique to guide surgical and intravascular procedures.

Acknowledgements

The work presented here has been supported by the National Institutes of Health (Grants; R01HL067377, R01CA187427, R21CA178578), Comprehensive Cancer Center at UC Davis, Boston Scientific Corporation and Intuitive Surgical Inc. We also acknowledge the contribution of numerous other investigators at the University of California Davis including the members of the Biophotonics Laboratory (Julien Bec, MS, Diego Yankelevich, PhD, Dimitris Gorpas, PhD, Dinglong Ma, BS, Hussain Fatakdawala, BS, Brad Hartl, BS), clinical collaborators (Gregory Farwell, MD, Jeffrey Southard, MD, James Boggan, MD, Ruben Fragoso, MD, Fredric Gorin, MD) and industry collaborator Jonatan Sorger, PhD of Intuitive Surgical.

References

1. D.S. Elson, L. Marcu, and P.M.W. French, *Fluorescence lifetime spectroscopy and imaging: principles and applications in biomedical diagnostics*, CRC Press Taylor & Francis London UK, 2014, 3-21.
2. L. Marcu, *Ann. Biomed. Eng*., 2012, **40**(2), 304-31.
3. D. Yankelevich, D. Ma, J. Liu, Y. Sun, Y. Sun, J. Bec, D. S. Elson, and L. Marcu, *Rev. Sci. Instrum*., 2014, **85**,034303.
4. D. Ma, Bec, J. Bec, D. Gorpas, D. Yankelevich, and L. Marcu, *Biomed. Opt. Express*, 2015, **6**(3), 987-1002.
5. H. Fatakdawala, D. Gorpas, J.W. Bishop, J. Bec, D. Ma, J. A. Southard, K. Margulies, and L. Marcu, *J. of Cardiovasc. Trans. Res.* 2015, 1-11. Published on-line.

SIMULATIONS OF OCT SCAN FORMATION BASED ON A CLOSE-TO-REALITY MODEL IN THE CONTEXT OF ELASTOGRAPHIC AND ANGIOGRAPHIC IMAGING

L.A. Matveev[1,2*], **A.L. Matveev**[1,2], **G.V. Gelikonov**[1,2], **V.M. Gelikonov**[1,2,3], and **V.Yu. Zaitsev**[1,2,3]

[1] Institute of Applied Physics of the Russian Academy of Sciences, Nizhniy Novgorod, Russia
[2] Nizhniy Novgorod State Medical Academy, Nizhniy Novgorod, Russia
[3] Nizhniy Novgorod State University, Nizhniy Novgorod, Russia
*e-mail: lionnn52rus@mail.ru

Abstract. A robust model for simulating speckle pattern evolution in optical coherence tomography (OCT) depending on the OCT system parameters, tissue deformation and/or scatterer motions is reported. The model is based on application of close to reality procedures used in spectral-domain OCT scanners. It naturally generates images reproducing properties of real images in spectral-domain OCT, including the pixelized structure and finite depth of unambiguous imaging corresponding to the chosen distance between the spectral components and the optical spectrum shape, dependence on the optical wave frequency and coherence length, etc. Good agreement with generally accepted speckle features and properties of real OCT images is demonstrated.

The problem of modeling speckle patterns of OCT images attracts a significant attention because for many applications based on analysis of OCT images the speckle structure plays a key role. Since the first works (e.g. [1]) related to studies of speckle patterns in OCT, a number of methods that can be used for simulating speckle patterns and studying correlation properties have been discussed [2]. Recently we proposed a robust model for simulating speckle pattern evolution in OCT [3] based on application of close-to-reality procedures used in spectral-domain OCT scanners. The main advantages of this approach are that (i) it is not necessary to assume in advance the character of speckle decorrelation and properties of speckle-pattern evolution; (ii) for fixed parameters of the OCT-scanner, speckle structure changes only due to motion of the scatterers like for real OCT.

The development of the reported model was stimulated first of all by the necessity of studying the evolution of speckle patterns, including speckle decorrelation properties due to motion of scatterers for different parameters of the OCT system, which is a key issue in the context of development of new variants of elastographic and angiographic imaging in OCT [4, 5]. The same understanding is also indispensable for a wide range of problems related to the development of super-resolution methods for application to OCT image processing, perfection of speckle-suppression methods, etc. To study these problems, one needs a model for realistic description of speckle-pattern evolution caused by deformations/motions of the tissue and flows therein. Other important requirements to such a model include the possibility of studying the role of such characteristics as the coherence length of the optical field, the relation between the number of spectral harmonics used for image formation in spectral-domain OCT scanners and the number of discrete elements in real pixelized images, the density of scatterers distributed in the tissue, etc. Another desired requirement is the possibility to directly obtain pixelized images with the structure as close as possible to real OCT images, so that the images processing developed for simulated scans could be directly applied to real images. Although the reported model is based on the procedures close to those used in spectral-domain OCT, the obtained results can actually be applied to images obtained by time-domain OCT scanners (if the appropriate ratio between the optical wave length and the coherence length is used).

Each one-dimensional scan (A-scan) can be represented as a sum of contributions of all scatterers and all spectral components registered at the photodetector array:

$$A(q) = \sum_n \sum_j A_j S(k_n) \exp(i 2 k_n z_j) \exp(-i \frac{2\pi n}{H} z_q) \qquad (1)$$

where $A(q)$ is the complex amplitude of q-th pixel in the A-scan, z_q is the depth coordinate corresponding to the center of q-th pixel; n is the index of the discrete spectral components (n varies from -N/2 to N/2) where N is the total number of discrete spectral components registered by the receiving array and $k_n = k_0 + \pi n/H$ is the corresponding wave numbers; $k_0 = 2\pi f_0/c$ corresponding to the center frequency of the light source f_0; A_j is the amplitude of optical wave backscattered by j-th scatterer located at the depth z_j; factor $S(k_n)$ describes the spectral shape of the OCT system (for example, the spectral shape of the source); H is the maximum imaged depth corresponding to the step $|k_{n+1} - k_n|$ between the spec-

tral components (and $\sum_n ... \exp(-i2\pi n z_q / H)$ in (1) plays the role of inverse Fourier transform of the spectrum $S_n = \sum_j A_j S(k_n) \exp(i2k_n z_j)$).

Simulation of the sequence of the OCT images during the deformation of tissue consist of the following steps:

– For each scatterer, its current position in the deformed tissue is updated;

– As described above, the contribution of each scatterer to the spectrum is calculated independently and then contributions to the spectrum from all scatterers is summed to obtain the corresponding A-scan according to Eq. (1), taking into account the spectral shape of the OCT system.

It is important to note that the shift of each scatterer due sample deformation is rigorously determined. It can be also noted, that the proposed approach takes into account full complex OCT signal, from which either complex-valued scans or intensity only images can be formed.

The statistical parameters of the speckle patterns of real and simulated OCT images are in a good agreement. Fig. 1 (a) shows a histogram of distribution of speckle intensity for a real OCT image of silicone grease. Fig. 1 (b) shows a similar histogram corresponding to a simulated image. Fig. 1 (c) shows the dependences of the speckle decorrelation as a function of strain found using 7×7 px window for different values of the source spectral width $\Delta k/k_0$. In the case when the central wavelength and the coherence length are comparable ($k_0/\Delta k$ ~1) slow speckle blinking ensures weak decorrelation in the plotted range of stain. In the case when the wavelength is much less than the coherence length (the case ($k_0/\Delta k$ >>1) blinking is much stronger and causes almost complete decorrelation of the speckle structure for strains ~1.5–2% (see. [6]).

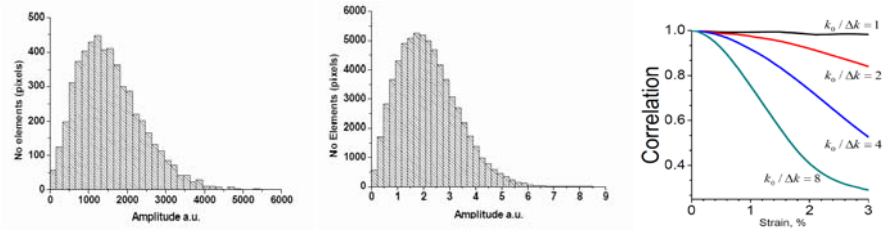

Fig. 1. Panel (a) shows a histogram of distribution of speckle intensity for a real OCT image of silicone grease; (b) shows a similar histogram corresponding to a simulated image; (c) shows the dependences of the speckle decorrelation as a function of strain found for 7×7 px correlation window for different values of the source spectral width

The proposed approach allows one to evaluate the influence of the main parameters of OCT systems (the coherence length, central wavelength, the number of spectral components and elements of the receiving array, etc.) on the evolution of OCT images during the tissue deformation and other scatterer motions (e.g. in the presence of flows). Therefore, the proposed approach can be used for numerical simulations/testing of a wide variety of algorithms for processing OCT signals in the problems of elastogaphic and angiographic imaging, as well as for mapping rheological properties of tissues.

Acknowledgements

This work is partially supported by the Russian Foundation for Basic Research (grant No. 15-42-02513 and 13-02-97131). The authors also acknowledge the OCT Lab of the Nizhny Novgorod State Medical Academy (under Russian Federation Government contract No. 14.B25.31.0015).

References

1. J.M. Schmitt, S.H. Xiang, and K.M. Yung, *Journal of biomedical optics*, 1999, **4**(1), 95-105.
2. D.D. Duncan and S.J. Kirkpatrick, *JOSA A*, 2008, **25**(1), 231-237.
3. V.Y. Zaitsev, L.A. Matveev, A.L. Matveyev, G.V. Gelikonov, and V.M. Gelikonov, *Laser Physics Letters*, 2014, **11**(10), 105601.
4. V.Y. Zaitsev, V.M. Gelikonov, L.A. Matveev, G.V. Gelikonov, A.L. Matveyev, P.A. Shilyagin, and I.A. Vitkin, *Radiophysics and Quantum Electronics*, 2014, **57**(1), 52-66.
5. V.Y. Zaitsev, I.A. Vitkin, L.A. Matveev, V.M. Gelikonov, A.L. Matveyev, and G.V. Gelikonov, *Radiophysics and Quantum Electronics*, 2014, **57**(3), 210-225.
6. V.Y. Zaitsev, L.A. Matveev, A.L. Matveyev, G.V. Gelikonov, and V.M. Gelikonov, *Journal of biomedical optics*, 2014, **19**(2), 021107.

TISSUE CHARACTERIZATION METHOD IN POLARIZATION SENSITIVE OPTICAL COHERENCE TOMOGRAPHY

A. Moiseev[1], **G. Gelikonov**[1], **V. Gelikonov**[1,3], **M. Sirotkina**[2], **N. Buyanova**[2], **L. Snopova**[2], and **N. Gladkova**[2]

[1] Institute of Applied Physics of the RAS, Nizhny Novgorod, Russia, aleksandr.moiseev@gmail.com
[2] Nizhny Novgorod State Medical Academy, Nizhny Novgorod, Russia
[3] Nizhny Novgorod State University, Nizhny Novgorod, Russia

Abstract. Method of automated characterization of tissue type of mouse ear is proposed. For classification purposes optical coherence tomography images obtained in two polarization channels were analyzed and probabilistic model was built based on these distributions using semi supervised learning method. Utilizing the model one can predict the probability of certain part of the OCT image to belong to one of the examined tissue types.

Optical Coherence Tomography (OCT) is a modern tool of visualization of inner structures of biological tissues. One of the emerging directions of OCT development is automated analysis of OCT images [1, 2]. In this work we develop method of automated segmentation of OCT images of mice ears. The method allows to automatically distinguish between normal and pathological tissues.

Method

To learn the algorithm we used several tomograms with manually marked morphologically different regions. Manual segmentation were based on histology specimens, taken in the same day as tomograms. The proposed algorithm is comprised of the following steps: first we represent each tomogram as a set of feature vectors. Then from big set of tomograms (labeled and unlabeled as well) we construct space of feature vectors. This space we reduce to small number (N~30) of vectors, using either of those methods: k-means clusterisation, Gaussian mixture approximation of the data set or principal component analysis (each of these methods leads to similar results). Such representation allows us to utilize not only small subset of labeled images, but the whole dataset of tomograms. Then every feature vector from labeled subset was decomposed with those obtained vectors. Decomposition coefficients were used to construct random forest tree classifier, which was eventually used to classify every new image.

As initial features (before clusterisation) we used simply intensity vale, intensity values of several neighboring values at the same A-scan and the values of the same pixels at the OCT image obtained in cross-polarization channel. It been shown previously that utilizing additional polarization channel may significantly improve sensitivity of OCT to cancer diseases.

Results

In figure 1 we show some examples of classified tomograms. In the left column of the first figure one can see tomogram in co- and cross-polarization channels, manually segmented regions (smooth regions right column, top) and corresponding classification result (right column, bottom). About 90% of manually segmented pixels are classified correctly with proposed method.

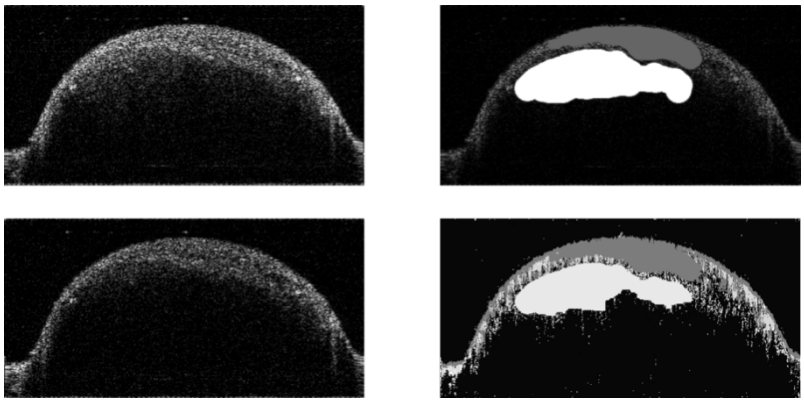

Fig. 1

In figure 2, from left to right: tomogram in co- and cross-polarization channels and classification result.

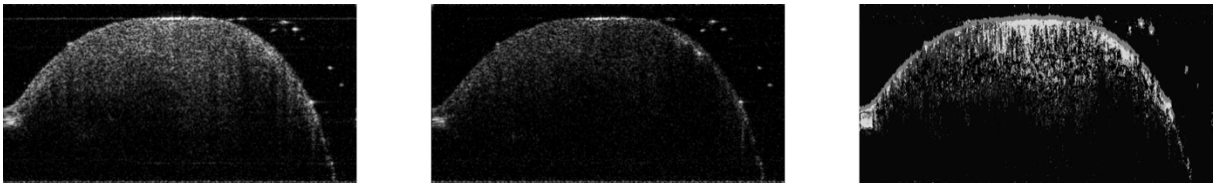

Fig. 2

Acknowledgements

The authors thank the researchers of the OCT Bio-imaging Laboratory at the Nizhny Novgorod State Medical Academy for help with the animal experiments. This work was supported by the grant of the Russian Federation Government No 14.B25.31.0015 and RFBR grant No 13-02-97131. VMG acknowledges partial support by the contract No 02.B49.21.0003 between the Russian Ministry of Education and Nizhny Novgorod State University.

References

1. K.A. Vermeer, J. Van der Schoot, H.G. Lemij, and J.F. De Boer, *Biomedical optics express*, 2011, **2**(6), 1743-1756.
2. D. Sheet, A. Chaudhary, S.P.K. Karri, D. Das, A. Katouzian, P. Banerjee, and A.K. Ray, *Journal of Biomedical Optics*, 2013, **18**(9), 090503-090503.

CONSTRUCTING STORM IMAGE FROM SPARSE SUBSET OF LOCALIZATIONS

A. Moiseev[1], **G. Gelikonov**[1], and **V. Gelikonov**[1,2]

[1] Institute of Applied Physics of the RAS, Nizhny Novgorod, Russia, aleksandr.moiseev@gmail.com
[2] Nizhny Novgorod State University, Nizhny Novgorod, Russia

Abstract. In this work we propose a method of constructing superresolution image of STochastical Reconstruction Microscopy (STORM) from a subset a localizations, insufficient for constructing image with conventional method. The approach may potentially decrease the time necessary for STORM data collection.

Localization microscopy such as STORM is an emerging tool for visualization biological structures stained with fluorescence dye with resolution up to several tens of nanometers [1]. The basic principle of constructing image in such microscopy is consecutive visualization and localization of sufficient number of fluorescent molecules. Since original approach requires nonoverlaping subsets of fluorophores at each frame, total time of data acquisition in STORM might be relatively large. Recent years several techniques were proposed which allow to localize molecules from overlapping subsets, thus reducing the time, required for data acquisition [2]. Here we propose a complementary method.

Method

The main idea of the proposed method is to guess, where the next molecules might appear, basing on the small subset of already localized fluorophores. To do so, we use an image of the same type of biological structure, visualized from the full subset of STORM data. Then we extract from this training image all possible patches, i.e. all mutual positions of localized molecules, presented in the training image. In first figure one can see an example of training image (left panel) and some of the extracted patches (right panel).

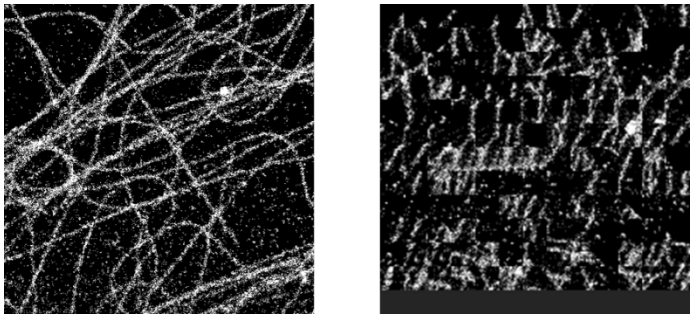

To reconstruct image of interest from sparse subset of data, we substitute each patch from this image with the closest one from the set of training patches (i.e. the patch with largest correlation coefficient with target patch). In the second figure STORM image reconstructed from full set of data (left panel), image, reconstructed from one sixth part of this data with conventional (center panel) and with proposed method (right panel). One can see, that proposed method makes visible most of the prominent image structures.

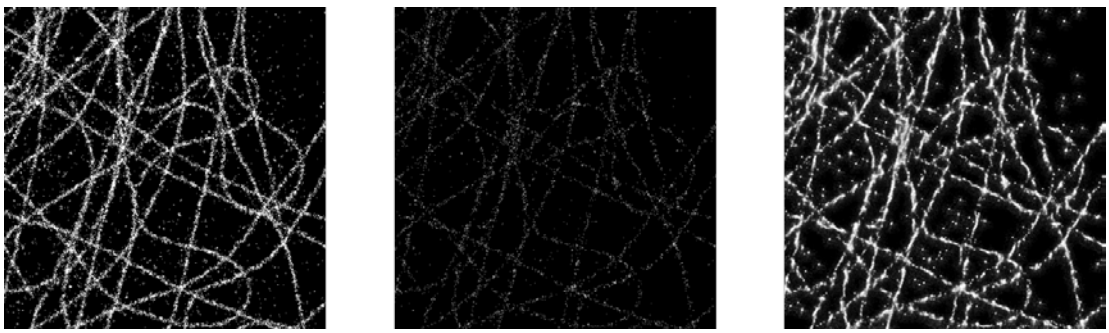

References

1. M.J. Rust, M. Bates, and X. Zhuang, *Nature methods*, 2006, **3**(10), 793-796.
2. L. Zhu, W. Zhang, D. Elnatan, and B. Huang, *Nature methods*, 2012, **9**(7), 721-723.

OPTICAL COHERENCE ELASTOGRAPHY FOR THE ASSESSMENT OF MECHANICAL PROPERTIES OF OCULAR TISSUE

T.M. Nguyen[1,2], **S. Song**[1,3], **B. Arnal**[1,2], **R.K. Wang**[1,4], and **M. O'Donnell**[1]

[1] University of Washington, Department of Bioengineering, Seattle (WA), USA
thu.mai.nguyen.tmn@gmail.com
[2] Institut Langevin Ondes et Images, ESPCI ParisTech, CNRS UMR 7587, Inserm ERL U979, Paris, France
[3]University of Dundee, School of Engineering, Physics and Mathematics, Dundee, United Kingdom
[4]University of Washington, Departement of Ophthalmology, Seattle (WA), USA

Abstract. Optical coherence elastography (OCE) aims at mapping mechanical properties of tissue to complement morphologic images obtained by optical coherence tomography (OCT). Tissue stiffness can be determined from the speed of propagating shear waves launched in tissue. We propose a method using phase-sensitive OCT to track ultrasound-induced shear waves. Ultrasound bursts of hundreds of microseconds are commonly used to remotely generate displacements in tissue. Here, we investigate the use of amplitude-modulated ultrasound emissions to enhance the shear wave signal-to-noise ratio and obtain high-quality elastic maps of tissue mimicking phantoms at low ultrasound pressures.

Introduction

Optical coherence tomography (OCT) is routinely used in ophthalmology for morphologic imaging of the cornea and retinal layers with a micron scale resolution. Assessing the mechanical properties of these tissue could help the diagnosis and/or the management of ophthalmic pathologies (e.g. post-refractive surgery complications, glaucoma, etc…). A number of groups have worked on developing optical coherence elastography (OCE) which aims at assessing the elastic properties of biological tissue using OCT. For instance, tissue stiffness can be determined from the speed of a shear wave propagating in the tissue. Ophthalmic applications require a shear source that is non-invasive and can potentially reach different parts of the eye: cornea, lens, and retina. We have previously introduced a method that combines ultrasound for remote shear wave generation and phase-sensitive OCT for shear wave tracking [1]. Here, we propose the use of amplitude-modulated ultrasound emission combined with a pulse compression algorithm to improve the shear wave signal-to-noise ratio (SNR) at low pressure levels to comply with safety regulations on ultrasound exposure in ophthalmology.

Material and methods

We performed experiments on gelatin phantoms containing latex microbeads for optical scattering. The phase-sensitive OCT system is a fiber-based spectral-domain OCT setup with a broadband light source (central wavelength 1310 nm, bandwidth 56 nm) and an ultrafast spectrometer (1024 pixels) operating at a 47-kHz acquisition rate. The sample is illuminated from the top. Displacements occurring in the sample are detected by acquiring a set of 256 A-lines at one given location at 47 kHz (M-scan). The phase difference between consecutive A-lines yields depth-resolved axial displacements. M-scans are acquired at 128 adjacent lateral locations to sweep the entire sample. A complete acquisition (256 A-lines x 128 locations) lasts ~ 1 sec. A single-element, spherically focused transducer (central frequency 7.5 MHz, focal distance 3.5 cm, diameter 2.3 cm) is placed at the bottom of the sample. An ultrasound beam is emitted at the beginning of each M-scan to generate a shear wave by acoustic radiation force. Different types of emissions were investigated: 1) a 200-µs burst and 2) a 3-ms long, amplitude-modulated emission. For both cases, ultrasound pressures between 1.5 and 3 MPa were tested, corresponding to a mechanical index (MI) of respectively 0.55 and 1.10. The amplitude modulation is illustrated in Fig. 1a. The resulting displacements are numerically compressed using a pulse compression approach described in [2]. The post-compression displacement field is used to reconstruct shear wave speed maps of the sample using a time-of-flight algorithm based on cross-correlation of neighboring signals. Normalized correlation coefficients smaller than 0.9 were rejected.

Results

Fig. 1b shows the temporal profile of the displacements induced in a gelatin phantom by the amplitude-modulated ultrasound emission at MI = 1.10. The displacements are a linear-swept frequency signal with a spectral content matching that of the amplitude-modulation. Fig. 1c shows the displacements obtained after applying the numerical pulse compression algorithm. In other words,

Fig. 1b and Fig. 1c are respectively the raw version and post-compression version of the same data. The pulse compression gives a SNR gain of more than 27 dB.

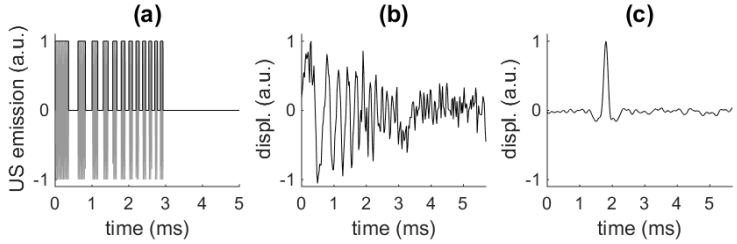

Fig. 1. (a) Amplitude-modulated ultrasound (US) emission: the 7.5-MHz driving sine wave (gray) is gated by a linear-swept frequency square wave (black). (b) Resulting axial displacements obtained in a 10%-gelatin phantom, SNR = 11.9 dB. (c) Displacements obtained after applying pulse compression, SNR = 39.7 dB

We compared the quality of elastic maps reconstructed using either a burst or an amplitude-modulated ultrasound emission for shear wave generation. The heterogeneous phantom is shown in Fig. 2a. Fig. 2b to 2d are elastic maps where the shear wave speed is color-coded and black pixels correspond to rejected speed estimates (normalized correlation coefficient smaller than 0.9). At MI = 1.10, the burst gives a sufficient displacement SNR to estimate the shear wave speed at each pixel of the imaging area (see Fig. 2b). The speeds in the left and right parts of the phantom are respectively 2.2 ± 0.3 m/s and 3.1 ± 0.6 m/s, which is close to the expected value extracted from the literature [3]. At a lower MI, the burst yields a low-quality reconstruction because of a poor displacements SNR (Fig. 2c). In contrary, the amplitude-modulated emission at low MI (Fig. 2d) enables to recover a similar elastic map to that obtained with a burst at higher MI.

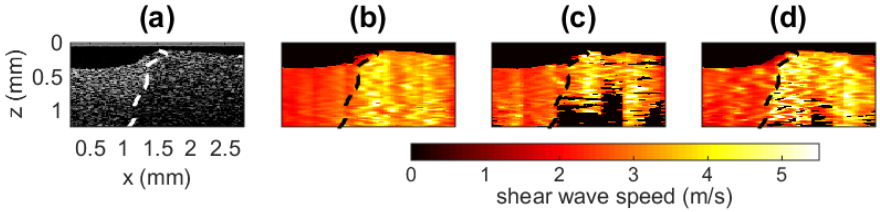

Fig. 2. (a) B-mode image of a heterogeneous phantom made of 5%-gelatin on the left side and 10%-gelatin on the right side. The dash line delineates the interface between both parts. (b – d) Shear wave speed maps reconstructed from either a 200-µs burst at MI = 1.10 (b), a 200-µs burst at MI = 0.55 (c) or a 3-ms amplitude-modulated emission at MI = 0.55 (d)

Conclusion

We have implemented a non-contact shear wave elastography method based on acoustic radiation force as a shear source and phase-sensitive OCT for detection. We have demonstrated on tissue-mimicking phantoms that amplitude-modulated ultrasound emission provide high-SNR, broadband shear waves at low pressures. Further work will focus on testing ocular tissue such as the cornea.

Acknowledgements

This work was supported in part by NIH R01EB016034, R01CA170734, R01EB009682, R01HL093140, R01DC010201, Life Sciences Discovery Fund 3292512, the Coulter Translational Research Partnership Program, and the Department of Bioengineering at the University of Washington.

References

1. T.-M. Nguyen, S. Song, B. Arnal, Z. Huang, M. O'Donnell, and R. K. Wang, "Visualizing ultrasonically induced shear wave propagation using phase-sensitive optical coherence tomography for dynamic elastography," *Opt. Lett.*, 2014, **39**(5), 838–841.
2. T. Nguyen, B. Arnal, S. Song, Z. Huang, R. K. Wang, and M. O'Donnell, "Shear wave elastography using amplitude-modulated acoustic radiation force and phase-sensitive optical coherence tomography," *J. Biomed. Opt.*, 2015, **20**(1), 016001.
3. T.J. Hall, M. Bilgen, M.F. Insana, and T.A. Krouskop, "Phantom materials for elastography," *IEEE Trans. Ultrason. Ferroelectr. Freq. Control*, 1997, **44**(6), 1355–1365.

Invited

SIMULTANEOUS PHOTOACOUSTIC AND LASER-ULTRASOUND TOMOGRAPHY

G. Paltauf, G. Wurzinger, and **R. Nuster**

Department of Physics, University of Graz, Austria, guenther.paltauf@uni-graz.at

Abstract. Photoacoustic tomography provides images with optical contrast of strongly light-scattering biological tissue. In order to extend the contrast to variations in mechanical properties, laser ultrasound techniques are proposed that are based on acoustic back scattering and transmission. With an external absorber, parts of the same laser pulses are used to generate co-registered optical absorption and acoustic back scattering images. Adding a laser ultrasound target for generation of temporally encoded sound waves extends this method to the acquisition of speed of sound images. Examples are shown on phantoms and biological tissue, using an optical sensor for recording the sound waves.

Photoacoustic imaging (PAI) combines optical and ultrasound techniques for the visualization of optically absorbing structures in biological tissue. It provides images mainly of vasculature in regions where the incoming light pulses are strongly scattered. Although the contrast and resolution of blood vessels makes this imaging method very attractive for the diagnostics of vascular abnormalities, it lacks contrast for structures that do not absorb light. Therefore, there have been various attempts to combine PAI with other imaging modalities, such as pulse-echo ultrasound (US) [1], or optical coherence tomography (OCT) [2]. Both of these techniques provide contrast for structures such as tissue boundaries, which reflect and scatter ultrasound and light, respectively.

For the combination of PAI and US it is possible to use the same laser pulse for both, the excitation of sound waves in the imaged object (PAI) and on an external target (US) [3–5]. Moreover, the externally generated sound wave can be launched in different ways, enabling either pulse echo images or ultrasound transmission images. The former gives rise to images depicting structures with acoustic scattering contrast, the latter can be used to visualize speed of sound (SOS) distributions and also acoustic attenuation [6].

In the presented work several tomographic methods are shown, which use the combination of PAI and LUS. Both, the pulse echo and transmission mode are used to obtain complete information about the optical and mechanical contrast in biological objects. In particular, a planar absorber combined with an acoustic line detector are combined to achieve three-dimensional tomographic images of the distribution of absorbed optical energy density (from direct illumination of the object) and of acoustic scattering contrast (from illumination of the external target). Reconstruction methods are very similar, using back projection of recorded pressure signals to possible source positions of optical absorption and acoustic scattering. Since the procedure for acquiring data for a three-dimensional image with a single detector is very time consuming, we also have developed a two-dimensional section imaging device, which uses focused detection from a planar section within an object, combined with focused emission of externally generated LUS.

A further development extends this combined imaging technique with ultrasound transmission tomography (Fig. 1). An arrangement of cascaded external absorbers creates a set of distinct ultrasound waves, where the arrival time at the line detector and the location where the waves pass the object are correlated. From measurements of the temporal shift in the presence of the object relative to a reference signal without object it is possible to obtain a linear projection image of the speed of sound in the observed slice. By rotating the object, a set of such projection images is recorded, followed by an inverse Radon transform that finally yields the two-dimensional SOS map. With the same setup, photoacoustic signals can be recorded after illuminating the object directly with laser pulses and LUS signals by irradiating a linear external target.

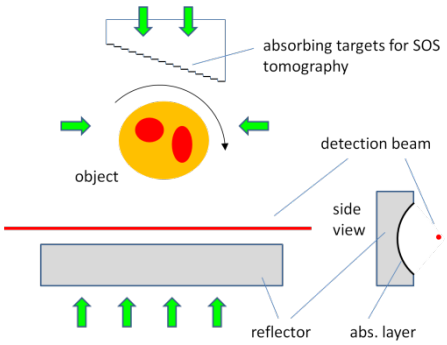

Fig. 1. Experimental setup for simultaneous photoacoustic, speed-of-sound and laser-ultrasound imaging. The green arrows indicate the direction of the incoming laser pulses. The acoustic reflector is made of glass and is coated with a black layer for generation of ultrasound. Sound waves are recorded with an optical detection beam, which is part of an interferometer

With this combined setup we recorded an image of a phantom containing optical absorption, speed of sound and density heterogeneities. The resulting image is shown in Fig. 2. Apart from the complete information available in such a set of images about the optical and mechanical properties, the speed of sound data can also be used to improve the PA and LUS images. Normally, in PA and LUS reconstruction a constant, average speed of sound is assumed. However, with the knowledge of the SOS distribution the reconstruction, which uses the time of flight information of the recorded sound waves, can be corrected.

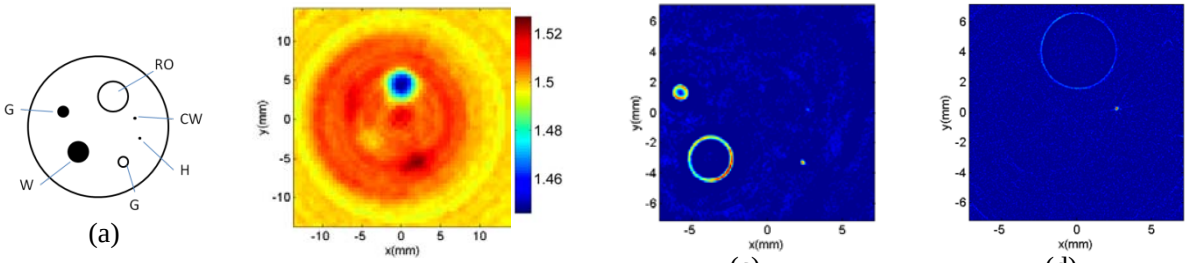

Fig. 2. (a) Layout of the scattering agar phantom. G: gelatin, RO: rape seed oil, CW: copper wire, H: hair, W: water. (b) SOS image, (c) photoacoustic image, (d) laser ultrasound image

Acknowledgement

This work has been supported by the Austrian Science Fund (FWF), Project Nos. S10502-N20, S10508-N20 and S10509-N20.

References

1. J.J. Niederhauser, M. Jaeger, R. Lemor, P. Weber, and M. Frenz, "Combined Ultrasound and Optoacoustic System for Real-Time High-Contrast Vascular Imaging *in vivo*," *IEEE Trans.Med.Imag*. 2005, **24**(4), 436-440.
2. E.Z. Zhang, B. Povazay, J. Laufer, A. Alex, B. Hofer, B. Pedley, C. Glittenberg, B. Treeby, B. Cox, P. Beard, and W. Drexler, "Multimodal photoacoustic and optical coherence tomography scanner using an all optical detection scheme for 3D morphological skin imaging," *Biomedical Optics Express*, 2011, **2**(8), 2202.
3. R. Nuster, N. Schmitner, G. Wurzinger, S. Gratt, W. Salvenmoser, D. Meyer, and G. Paltauf, "Hybrid photoacoustic and ultrasound section imaging with optical ultrasound detection," *Journal of Biophotonics*, 2013, **6**(6-7), 549-559.
4. P. Subochev, A. Orlova, M. Shirmanova, A. Postnikova, and I. Turchin, "Simultaneous photoacoustic and optically mediated ultrasound microscopy: an *in vivo* study," *Biomed.Opt.Express*, 2015, **6**(2), 631-638.
5. G. Wurzinger, R. Nuster, N. Schmitner, S. Gratt, D. Meyer, and G. Paltauf, "Simultaneous three-dimensional photoacoustic and laser-ultrasound tomography," *Biomed.Opt.Express*, 2013, **4**(8), 1380-1389.
6. J. Jose, R.G.H. Willemink, W. Steenbergen, C.H. Slump, T.G. van Leeuwen, and S. Manohar, "Speed-of-sound compensated photoacoustic tomography for accurate imaging," *Med. Phys*., 2012, **39**, 7262.

SENSITIVITY OF OPTOACOUSTIC MICROSCOPE FOR ESTIMATIONS OF BLOOD OXYGEN SATURATION: PHANTOM STUDY

V.V. Perekatova[1,2], P.V. Subochev[1], I.I. Fiks[1], M.S. Kleshnin[1] and **I.V. Turchin[1]**

[1]Institute of Applied Physics, Nizhny Novgorod, Russia,
Valeriya1000@yandex.ru
[2]Lobachevsky State University of Nizhny Novgorod, Russia

Abstract. We carried out model experiments to investigate the sensitivity of earlier developed bimodal optoacoustic (OA) microscope using two antennas with different resonance frequencies (14 MHz and 20 MHz) and the equal bandwidth at the level of –6 dB (10 MHz). We used the phantom imitating the optical properties of biological tissue containing blood vessels. We work towards theoretical and experimental evaluation of maximum sensitivity of multi-spectral OA microscope to local changes in tissue oxygenation at various depths of optoacoustic imaging.

Optoacoustic (OA) diagnostics is a novel method of biomedical imaging, based on the detection of ultrasonic waves excited by the optical inhomogeneities absorbing optical laser pulses in the investigated medium. Since a hemoglobin is a strong absorber of optical radiation, OA imaging is widely used for visualization of blood vessels. Multi-spectral OA measurements allow calculating the relative concentrations of oxy-(HbO_2) and deoxyhemoglobin (Hb), and therefore blood oxygen saturation (StO_2). In this work, we will demonstrate theoretical and experimental evaluation of sensitivity of the developed OA methods to local changes in concentrations of HbO_2 и Hb at various depths of photoacoustic sensing using earlier developed bimodal OA microscope [1]. Similar numerical experiments were performed in [2] for the estimation of maximum sensitivity in defining of StO_2.

As far as local concentrations of HbO_2 и Hb are known, the blood oxygen saturation is given by the formula:

$$StO_2 = \frac{C_{HbO_2}}{C_{HbO_2}+C_{Hb}} \cdot 100\%, \quad (1)$$

where C_{HbO_2} и C_{Hb} are relative concentrations of oxy- and deoxyhemoglobin.

Let us define the accuracy of OA measurements of oxygen saturation as δStO_2. The following formula provides with the analytical connection between δStO_2 at various depths Z and parameters of the medium or OA measurement system.

$$\delta StO_2(Z) = \frac{(\mu_2-\delta\mu_2\cdot StO_2)^2}{\delta\mu_2\cdot\mu_1-\delta\mu_1\cdot\mu_2}\cdot\left[\frac{1}{SNR_a}\cdot\left(\frac{H_2}{H_1}+\frac{\mu_1-\delta\mu_1\cdot StO_2}{\mu_2-\delta\mu_2\cdot StO_2}\right)+\frac{1}{SNR_o}\cdot\left(\frac{H_2}{H_1}+1\right)\cdot\frac{\mu_1-\delta\mu_1\cdot StO_2}{\mu_2-\delta\mu_2\cdot StO_2}\right]\cdot 100\%, \quad (2)$$

where $SNR_a(Z)$ is the acoustic signal-to-noise ratio measured at wavelength λ_2 at given depth Z; $SNR_o(Z)$ is the optical signal-to-noise measured at wavelength λ_2 at given depth Z; $\mu_{1,2}$ is the optical absorption of Hb at wavelength $\lambda_{1,2}$; $\delta\mu_{1,2}$ is the difference between the optical absorption of HbO_2 and Hb at wavelength $\lambda_{1,2}$; $H_{1,2}$ is the optical fluence distribution at wavelengths $\lambda_{1,2}$ at different depths.

According to Eq.2 it is possible to minimize δStO_2 by choosing optimal wavelengths for OA sensing, however the parameters of acoustic and optical signal-to-noise ratios and the optical fluence distribution should be known.

In order to estimate SNR_a we conducted the experiment to investigate the sensitivity of earlier developed bimodal optoacoustic (OA) microscope using two antennas with different resonance frequencies (14 MHz and 20 MHz) and the equal bandwidth at the level of –6 dB (10 MHz). To estimate $SNR_a(Z)$ the original model of biological tissue with seven blood vessels oriented along the *Y*-axis and located at different depths *Z* ranging from 1 to 6 mm (Fig. 1a, d) was developed. We used 1.5% water dilution of intralipid as the model of biological tissue, cylindrical tubes of polyimide with an inner diameter of 400 mm and a wall thickness of 50 μm as the model of blood vessels and 4% water dilution of black ink as a model of blood.

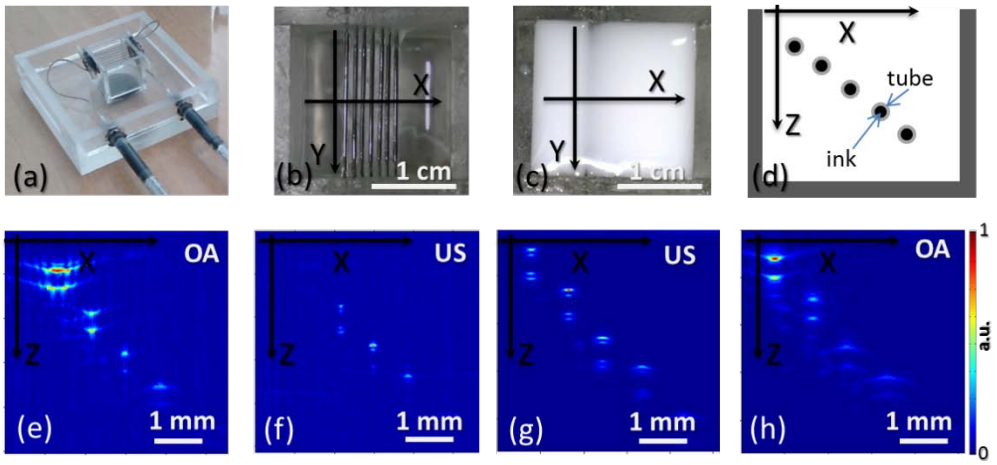

Fig. 1. (a, b) – the developed phantom in the air (c) – the phantom filled with the 4% water dilution of intralipid (d) – the scheme of location of blood vessels in the plane of visualization (e, f) ¬ OA and US B-scans obtained using the detector with 20 MHz (g, h) ¬ OA and US B-scans obtained using the detector with 14 MHz

The spectral dependency (Fig. 2) of the optical properties of intralipid and black ink in selected concentrations was obtained in the experiment using the spectrophotometer Specord 250 plus.

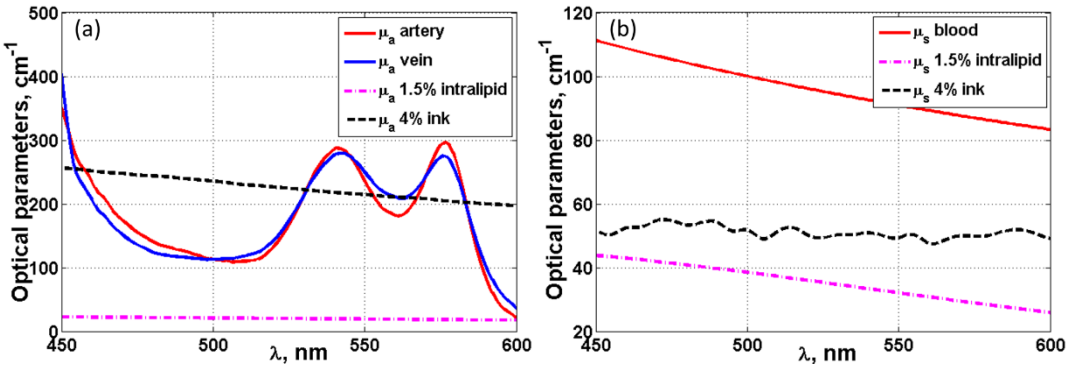

Fig. 2. Optical properties of biological and biosimilar tissues:
(a) – the optical absorption coefficients (b) – the optical scattering coefficients

Mechanical scanning of OA microscope was carried out along the *X*-axis with a 60 μm step. In Fig. 1, e–h OA and ultrasound (US) B-scans in the plane *XZ* consisted of 1000 A-scans. The total scanning time was 100 seconds due to the limited repetition frequency of laser pulses (10 Hz). Based on OA images (Fig. 1, e, g) it was possible to calculate $SNR_a(Z)$.

As the optical fluence distribution is also included into Eq.2, the next step is determination of the optical fluence H and SNR_o. At this moment we are preparing the in vivo experiments on transillumination optical spectroscopy of little animals. Combining experimentally obtained H, SNR_o and SNR_a we are going to find wavelengths minimizing δStO_2 parameter at Eq.2. The results will be presented at the conference.

Acknowledgements

This work was supported by Russian Foundation for Basic Research (projects № 14-02-00836 A, 13-02-01289 A). Authors are thankful to M.Yu. Kirillin and A.D. Krainov for helpful discussions.

References

1. P. Subochev, A. Orlova, M. Shirmanova, A. Postnikova, and I. Turchin, *Biomedical Optics Express*, 2015, **6**(2), 631-638.
2. R. Hochuli, P.C. Beard, B. Cox, *Proc. SPIE* 9323, Photons Plus Ultrasound: Imaging and Sensing 2015, 93231V (March 11, 2015).

NOVEL ADVANCES IN MULTISPECTRAL IN-VIVO FLUORESCENCE TOMOGRAPHY

J. Ripoll[1,2*], **A. Arranz**[3,4(+)], and **M. Rudin**[3,4]

[1] Dept. of Bioengineering, Universidad Carlos III of Madrid, Spain
[2] Hospital General Universitario Gregorio Marañón, Madrid, Spain
[3] Institute for Pharmacology and Toxicology, University Zurich, Switzerland
[4] Institute for Biomedical Engineering, University and ETH Zurich, Zurich, Switzerland
[(+)] Current address: Dept. of Cell Biology and Immunology, Center for Molecular Biology "Severo Ochoa" (CBMSO), CSIC, Madrid, Spain

Abstract. Fluorescence molecular tomography (FMT) offers great advantages such as high sensitivity and specificity, together with the quantitative information that optical tomography approaches offer for *in-vivo* imaging. One of the drawbacks of fluorescence in-vivo imaging methods, however is the presence of autofluorescence, which lowers the signal to background ratio of the measurements. One of the most robust approaches to effectively remove the contribution of autofluorescence is by making use of multispectral unmixing approaches. In order to be implemented in an optical tomography setup, however, several steps, unique to FMT, are important in order to obtain quantitative information.

Introduction

Tumor growth, angiogenesis, invasiveness and metastasis are main hallmarks that determine the malignancy of cancer. For all of them, remodeling of the extracellular matrix and the vascular or epithelial basal membranes is required and is orchestrated by several proteases [1], such as Cathepsin B. The main aim of this work is to develop a brain-specific fluorescence molecular tomography (FMT) setup that enables in vivo imaging of tumor growth during the progression of a glioma model. In order for this approach to present high sensitivity, it is important that the contribution of autofluorescence is removed. Autofluorescence is non-specific fluorescence originating from several tissue components, with the relevant and significant feature that its emission spectrum varies from subject to subject, and is different at different tissue regions. Several approaches make use of unmixing methods, however all these approaches make use of the raw data [2], a fact which is incompatible with tomographical approaches.

Methods

Animal Preparation: 2x105 Gl261-iRFP [3] expressing cells were implanted in the right striatum. The activatable probe Cathepsin B 750 (Perkin Elmer) was used to assess cathepsin B activity in vivo [4]. Measurements were performed over time using a FMT setup adapted specifically for multispectral brain imaging developed in-house at the ETH.

FMT multispectral setup: In order to cover a large spectrum of NIR emission the customized FMT setup included 10 filters spanning the range from 680 nm to 800 nm, with spectral widths of 10 nm. 598 nm, 635 nm, 670 nm and 750 nm lasers where used for excitation, in order to recover the multispectral matrix.

Multispectral Inversion: Each tomographic measurement comprised a scan of a point source over the surface of the head of the mouse, recovering an excitation image and the whole multispectral set of emission images. Once these images where acquired, spectral unmixing was applied to the reconstructed image, in order to properly account for the effect of tissue scattering and absorption in the spectrum. In order to properly recover the concentration of known fluorophores and fluorescent proteins the spectrum of these was used as prior knowledge.

Results

The multispectral FMT reconstruction approach consisted on two main steps: 1) an FMT reconstruction using excitation and a single emission wavelength, routine which was repeated for all possible excitation/emission combinations; and 2) an inversion of the multispectral reconstruction matrix in order to recover the specific concentration of the expected fluorophores and fluorescent proteins. This approach was implemented in the the novel brain-FMT imaged developed at the ETH and was applied to evaluate tumor growth and cathepsin B activity levels in vivo during the development of the orthotopic Gl261 glioma tumors.

Conclusions

3D reconstructed images multispectral images allowed accurate quantification of fluorescent probes and fluorescent proteins in-vivo, significantly increasing our signal to background ration and our sensitivity.

The brain-FMT multispectral imager developed at the ETH enables to follow-up tumor progression and thus has great potential in the evaluation of the effect of experimental therapeutic treatments.

Acknowledgements

J.R. acknowledges support from the EC FP7 CIG grant HIGH-THROUGHPUT TOMO, and MINECO grant FIS2013-41802-R MESO-IMAGING. A. Arranz acknowledges support from the Marie Curie Intra-European Fellowship program (FP7-PEOPLE-2010-IEF).

References

1. K.M. Bell-McGuinn, A.L. Garfall, et al., "Inhibition of cysteine cathepsin protease activity enhances chemotherapy regimens by decreasing tumor growth and invasiveness in a mouse model of multistage cancer", *Cancer Res*, 2007, **67**(15), 7378-85.
2. H. Xu and B.W. Rice, "*In-vivo* fluorescence imaging with a multivariate curve resolution spectral unmixing technique", *J. Biomed. Opt*., 2009, **14**, 064011; doi:10.1117/1.3258838.
3. G.S. Filonov, K.D. Piatkevich, L.M. Ting, J. Zhang, K. Kim, and V.V. Verkhusha, “Bright and stable near-infrared fluorescent protein for *in vivo* imaging”, *Nat Biotechnol*., 2011, **29**(8), 757-61.
4. V. Ntziachristos, C.H. Tung, et al., "Fluorescence molecular tomography resolves protease activity *in vivo*", *Nat Med*, 2002, **8**(7), 757-60; D. Four and E. Five, *Proc. 6th Intern. Conf. Nonlinear Waves: ICNW VI*, F. Six (Ed.), Moscow, 1999, 555-560.

Invited

PARAMETRIC OPTICAL COHERENCE TOMOGRAPHY IMAGING OF ATTENUATION, BIREFRINGENCE, SPECKLE DECORRELATION, AND STIFFNESS, THROUGH FREE SPACE AND IN NEEDLES

D.D. Sampson[1,2], **P. Gong**[2], **L. Chin**[2], **P. Wijesinghe**[2], **S. Es'haghian**[2], **W.M. Allen**[2], **B.R. Klyen**[2], **A. Curatolo**[2], **R.A. McLaughlin**[2] and **B.F. Kennedy**[2]

[1] Centre for Microscopy, Characterisation & Analysis, The University of Western Australia, Perth, Western Australia
[2] Optical+Biomedical Engineering Laboratory, School of Electrical, Electronic & Computer Engineering, The University of Western Australia, Perth, Western Australia
David.Sampson@uwa.edu.au

Abstract. Two "grand challenges" in optical bioimaging are how to penetrate the superficial layers of biological tissue to provide cellular-resolution optical microscopy centimeters deep in tissue, and how to provide sufficient contrast, in living tissue, to differentiate the tissue constituents of interest. In our group, we have been developing advanced forms of optical coherence tomography to address these challenges. Microscope-in-a-Needle technology enables delivery of the imaging beam deep in tissue, and parametric imaging of attenuation, birefringence, speckle decorrelation or stiffness adds contrast beyond that provided by native scattering. This talk will describe our latest developments in these areas.

Motivation

If optical coherence tomography (OCT) is to maximise its potential for application in solid biological tissues beyond where it sits today, advances must be made in depth penetration and the ability to differentiate tissue constituents (contrast), whilst maintaining, or improving, resolution. We have been focussing on pragmatic approaches to address these issues: the Microscope-in-a-Needle platform [1], to enable deep penetration, and parametric OCT [2], which is a promising approach to extracting additional information from three-dimensional OCT scans of tissue, beyond simple imaging by backscatter contrast. Our focus has been on the parameters of attenuation, birefringence, speckle decorrelation, and stiffness.

OCT Microscope-in-a-Needle

Our OCT imaging needle probes have now advanced sufficiently to be able to compete with conventional OCT systems in terms of sensitivity (>100 dB) [3], with slightly lower resolution (10–20 μm), and slower scan speeds (0.5 frames per second). Lately, we have begun to address the scan-speed issue with promising results from a prototype high-speed push-pull scanner at 80 frames per second. We are adding functions to the basic OCT needle platform, for example, by combining fluid delivery – an optofluidic needle [4], and by combining with fluorescence: multi-modal molecular imaging [5]. These advances will help move this platform forwards in our main application areas of intraoperative surgical and biopsy guidance, with a focus on breast cancer [6].

Parametric Imaging

The parametric approach uses models parameterised with the property, or properties, of interest, and signal processing to fit these models to the acquired data. Such properties are generally (but not necessarily) optical, for example, axial attenuation (extinction) [7–9], birefringence [10–12], or speckle decorrelation [13]. We have also been exploring parametric imaging of mechanical contrast, including the parameters of strain [14], surface stress [15, 16], and stiffness.

In all cases we have explored to date, the parameter of interest is determined in the axial direction only and, in order to do so, some sacrifice is made in axial resolution, that is, compared to the native OCT axial resolution (although this loss of resolution is not intrinsic to the concept). The natural mode of display of such images is in the *en face* dimension, as maps of the parameter. A key element of our parametric imaging in vascular tissue has been masking out the highly scattering vessels in order to properly measure the parameter of interest in the residual tissue. In this way, we have developed effective means of separately characterising microvasculature and collagenous tissue, the key components of scars, but also of many tumours. Our work to date has demonstrated enhanced contrast between different soft tissue constituents in tissues across applications in muscular dystrophy [9], burn scars [8, 12] and breast cancer [17].

Conclusion

The platform of tools we developed for characterizing tissue lends itself to many applications beyond our current focus on breast cancer, burn scars and muscular dystrophy. This includes cancer in the brain, head and neck, lung, and prostate. In particular, the combination of microvasculature imaging with parametric imaging of attenuation, birefringence, and stiffness would provide a comprehensive characterization of many tissues, and we are well placed to advance this.

Acknowledgements

We acknowledge the many colleagues and collaborators who have contributed to this research and funding support from, amongst others, the Australian Research Council, National Breast Cancer Foundation (Australia), the National Health & Medical Research Council (Australia), and Cancer Council Western Australia.

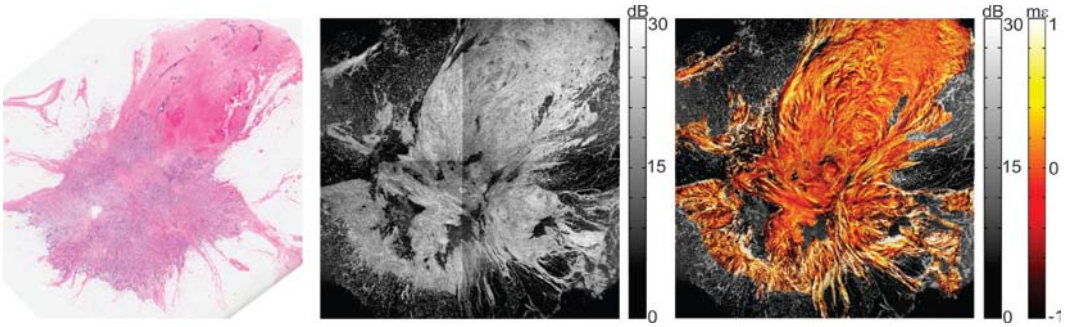

Fig. 1. Example of parametric OCT of stiffness (strain) in ductal cell carcinoma. (a) Haematoxylin and eosin histology; (b) En face OCT, and (c) strain overlaid on the OCT. Images are 19 × 19 mm [17]

References

1. D. Lorenser, R.A. Mclaughlin, and D.D. Sampson, "Needle Probes For Optical Coherence Tomography," in *Optical Coherence Tomography Technology and Applications*, W. Drexler and J.G. Fujimoto, Eds., Second ed: Springer, 2015.
2. R.A. McLaughlin, L. Scolaro, P. Robbins, C. Saunders, S.L. Jacques, and D.D. Sampson, "Pa-rametric imaging of cancer with optical coherence tomography," *Journal of Biomedical Optics*, vol. 15, no. 4, art. 046029, 2010.
3. L. Scolaro, D. Lorenser, R.A. McLaughlin, B.C. Quirk, R.W. Kirk, and D.D. Sampson, "High-sensitivity anastigmatic imaging needle for optical coherence tomography," *Optics Letters*, v. 37, no. 24, pp. 5247-5249, 2012.
4. B.C. Quirk, R.A. McLaughlin, A.M. Pagnozzi, B.F. Kennedy, P.B. Noble, and D.D. Sampson, "Optofluidic needle probe integrating targeted delivery of fluid with optical coherence tomography imaging," *Optics Letters*, vol. 39, no. 10, pp. 2888-2891, 2014.
5. L. Scolaro, D. Lorenser, W.-J. Madore, R.W. Kirk, A. Kramer, G.C. Yeoh, N. Godbout, D.D. Sampson, C. Boudoux, and R.A. McLaughlin, "Molecular imaging needles: dual-modality optical coherence tomography and fluorescence imaging of labeled antibodies deep in tissue," *Biomedical Optics Express*, vol. 6, no. 5, pp. 1767-1781, 2015.
6. R.A. McLaughlin, B.C. Quirk, A. Curatolo, R.W. Kirk, L. Scolaro, D. Lorenser, P.D. Robbins, B.A. Wood, C.M. Saunders, and D.D. Sampson, "Imaging of breast cancer with optical coherence tomography needle probes: Feasibility and initial results," *IEEE Journal of Selected Topics in Quantum Electronics*, vol. 18, no. 3, pp. 1184-1191, 2012.
7. L. Scolaro, R.A. McLaughlin, B.R. Klyen, B.A. Wood, P.D. Robbins, C.M. Saunders, S.L. Jacques, and D.D. Sampson, "Parametric imaging of the local attenuation coefficient in human axillary lymph nodes assessed using optical coherence tomography," *Biomedical Optics Express*, vol. 3, no. 2, pp. 366-379, 2012.
8. P.J. Gong, R.A. McLaughlin, Y.M. Liew, P.R.T. Munro, F.M. Wood, and D.D. Sampson, "Assessment of human burn scars with optical coherence tomography by imaging the attenuation coefficient of tissue after vascular masking," *Journal of Biomedical Optics*, vol. 19, no. 2, art. 021111, 2014.
9. B.R. Klyen, L. Scolaro, T. Shavlakadze, M.D. Grounds, and D.D. Sampson, "Optical coherence tomography can assess skeletal muscle tissue from mouse models of muscular dystrophy by parametric imaging of the attenuation coefficient," *Biomedical Optics Express*, vol. 5, no. 4, pp. 1217-1232, 2014.

10. L.X. Chin, X.J. Yang, R.A. McLaughlin, P.B. Noble, and D.D. Sampson, "En face parametric imaging of tissue birefringence using polarization-sensitive optical coherence tomography," *Journal of Biomedical Optics*, vol. 18, no. 6, art. 066005, 2013.
11. X.J. Yang, L.X. Chin, B.R. Klyen, T. Shavlakadze, R.A. McLaughlin, M.D. Grounds, and D.D. Sampson, "Quantitative assessment of muscle damage in the mdx mouse model of Duchenne muscular dystrophy using polarization-sensitive optical coherence tomography," *Journal of Applied Physiology*, vol. 115, no. 9, pp. 1393-1401, 2013.
12. P. Gong, L.X. Chin, S. Es'haghian, Y.M. Liew, F.M. Wood, D.D. Sampson, and R.A. McLaughlin, "Imaging of skin birefringence for human scar assessment using polarization-sensitive optical coherence tomography aided by vascular masking," *Journal of Biomedical Optics*, vol. 19, no. 12, art. 126014, 2014.
13. Y.M. Liew, R.A. McLaughlin, P.J. Gong, F.M. Wood, and D.D. Sampson, "In vivo assessment of human burn scars through automated quantification of vascularity using optical coherence tomography," *Journal of Biomedical Optics*, vol. 18, no. 6, art. 061213, 2013.
14. B.F. Kennedy, R.A. McLaughlin, K.M. Kennedy, L.X. Chin, A. Curatolo, A. Tien, B. Latham, C.M. Saunders, and D.D. Sampson, "Optical coherence micro-elastography: mechanical-contrast imaging of tissue microstructure," *Biomedical Optics Express*, vol. 5, no. 7, pp. 2113-2124, 2014.
15. K.M. Kennedy, S. Es'haghian, L.X. Chin, R.A. McLaughlin, D.D. Sampson, and B.F. Kennedy, "Optical palpation: optical coherence tomography-based tactile imaging using a compliant sensor," *Optics Letters*, vol. 39, no. 10, pp. 3014-3017, 2014.
16. S. Es'haghian, K.M. Kennedy, P. Gong, D.D. Sampson, R.A. McLaughlin, and B.F. Kennedy, "Optical palpation in vivo: imaging human skin lesions using mechanical contrast," *Journal of Biomedical Optics*, vol. 20, no. 1, art. 016013, 2015.
17. B.F. Kennedy, R.A. McLaughlin, K.M. Kennedy, L. Chin, P. Wijesinghe, A. Curatolo, A. Tien, M. Ronald, B. Latham, C.M. Saunders, and D.D. Sampson, "Investigation of optical coherence micro-elastography as a method to visualize cancers in human breast tissue," *Cancer Research*, in press, 2015.

3-PORT COUPLER BASED SD OCT SETUP

P.A. Shilyagin, A.A. Sharogradskaya, I.V. Kasatkina, G.V. Gelikonov, and **V.M. Gelikonov**

Institute of Applied Physics RAS, Nizhny Novgorod, Russia
paulo-s@mail.ru

Abstract. A 3-port coupler setup is proposed to eliminate mirror artifacts in spectrometer based OCT.

Fourier domain optical coherence tomography (FD OCT) is based on measuring optical spectrum of a sum of two interfering waves: the reference one and the wave backscattered from the object [1, 2]. The information about object's inner structure is reconstructed by inverse Fourier transform of the optical spectrum. The obtained spectrum corresponds to the intensity of analyzed optical radiation, so it is the real function of optical frequency. The reconstructed by Fourier transformation image has mirror-symmetrical structure relative to zero of path-difference between interferometer arms. Some methods of eliminating of the mirror artifacts, obtained for SD-OCT [1–4], are based on consecutive obtaining of spectral components with different phase shift between reference and object waves. The simultaneous obtaining of full complex spectrum makes possible eliminating the influence of Doppler phase shifts of moving scatterers in the object [5–6]. The simultaneous obtaining of quadrature interference components in spectrometer-based OCT by using dual linear CCD array was proposed in [7] and investigated in detail in [8]. The setup described in [8] requires very precise tuning of all elements of bulk optical interferometer, which is unavailable in common-path devices.

The work is devoted to examine the possibility of the use of 3-port coupler in spectrometer-based OCT for reconstructing the complex amplitude of the interference signal.

The interference comb after passing of a multiple-arms coupler has an evenly distributed phase component due to the energy conservation law. So it the number of coupler arms is 3, the interference pattern registered in different arms should have a phase difference of $2\pi/3$ between each two arms. Due to commutability of Fourier transformation this property is applicable for both spectral and lateral presentations of registered SD OCT signal.

Using Fourier transformation for spectrum obtained in every arm of the coupler (fig. 1) one can find the following equations for SD OCT signal in axial presentation

$$\Delta_A = r(D(z) + D(-z))$$

$$\Delta_B = \frac{rD(z')}{2}\left(i\sqrt{3} - 1\right) - \frac{rD(-z')}{2}(i\sqrt{3} + 1)$$

$$\Delta_C = -\frac{r}{2}D(z)\left(1 + i\sqrt{3}\right) + \frac{r}{2}D(-z)(i\sqrt{3} - 1)$$

where r is the field scattering coefficient for the reference arm of the interferometer, $D(z)$ denotes the amplitude of the field backscattered in the object from depth z and reached the coupler. $D(-z)$ is the mirror artifact. Any autocorrelation artifacts (such as coherent noises, DC component) are supposed to be eliminated.

Combining theses equations one can eliminate $D(-z)$ component from the image:

$$\alpha \cdot \Delta_A + \beta \cdot \Delta_B + \gamma \cdot \Delta_C = rD(z)$$

where

$$\alpha = 1; \quad \beta = \frac{1 - i/\sqrt{3}}{2}; \quad \gamma = \frac{1 + i/\sqrt{3}}{2}.$$

Figure 2 represents the effectiveness of the reconstruction for eliminating of the mirror artifacts.

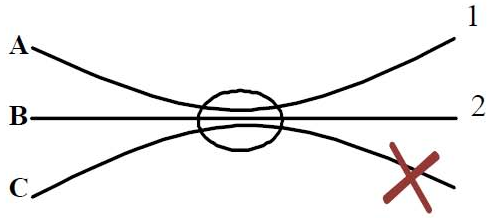

Fig. 1. A schematic setup of 3-port coupler SD OCT. 1 – reference arm; 2 – probe arm

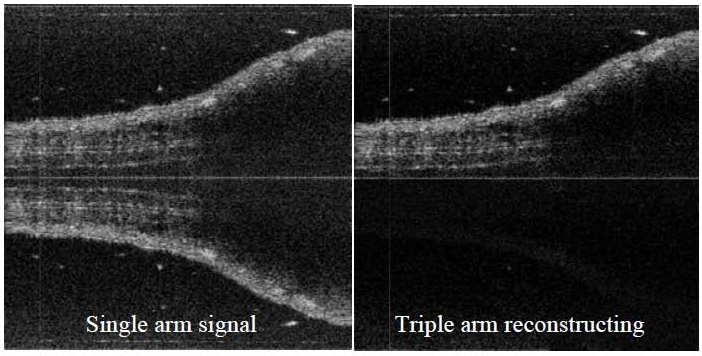

Fig. 2. An illustration of mirror artifacts elimination using 3-port coupler SD OCT

Acknowledgements

This research was supported in part by Contract of the Russian Federation grant No 11.G34.31.0066 and the Council in Support of Leading Scientific Schools at the President of the Russian Federation (grant no. NSh 5430.2012.2).

References

1. A.F. Fercher, R.A. Leitgeb, C.K. Hitzenberger, et al., *SPIE Proc*., 1999, **3564**, 173.
2. M. Wojtkowski, A. Kowalczyk, R. Leitgeb, et al., *Optics Letters*, 2002, **27**(16), 1415.
3. R.A. Leitgeb, C.K. Hitzenberger, A.F. Fercher, et al., *Optics Letters*, 2003, **28**(22), 2201.
4. P. Targowski, M. Wojtkowski, A. Kowalczyk, et al., *Optics Communications*, 2004, **229**(1-6), 79.
5. M.A. Choma, C.H. Yang, J.A. Izatt, *Optics Letters*, 2003, **28**(22), 2162.
6. Y.H. Zhao, Z.P. Chen, Z.H. Ding, et al., *Optics Letters*, 2002, **27**(2), 98.
7. G.V. Gelikonov, V.M. Gelikonov, P.A. Shilyagin, *SPIE Proc*., 2011, **7889**, 788925.
8. P.A. Shilyagin, G.V. Gelikonov, V.M. Gelikonov, et al., *Quantum Electronics*, 2014, **44**(7), 664.

Invited

DEPTH-RESOLVED INCOHERENT AND COHERENT WIDE-FIELD HIGH-CONTENT IMAGING

P.T.C. So[1,2,3,4], **D. Wadduwage**[4], **H. Choi**[1], **Y. Choi**[3], **V. Singh**[4], **Y. Kim**[1], and **Z. Yaqoob**[3]

[1] Department of Mechanical Engineering, MIT, Cambridge, MA,USA, ptso@mit.edu
[2] Department of Biological Engineering, MIT, Cambridge, MA,USA
[3] Laser Biomedical Research Center, MIT, Cambridge, MA, USA
[4] Singapore-MIT Alliance for Science & Technology Center, Singapore

Abstract. Recent advances in depth-resolved wide-field imaging technique has enabled many high throughput applications in biology and medicine. Depth resolved imaging of incoherent signals can be readily accomplished with structured light illumination. This approach is demonstrated by a study where we measure cellular radiation damage by quantifying number of nucleic DNA double strand breaks. The integration of this high throughput system with novel spectroscopic resolving elements further enable high-content information extraction. The extension of incoherent depth-resolved wide-field imaging to coherent modality is non-trivial. Here, we will cover recent advances in novel phase and transient absorption imaging systems.

Structured light 3D tissue cytometer

A high throughput 3D image cytometer have been developed that improves imaging speed by an order of magnitude over current technologies. This imaging speed improvement was realized by combining several key components. First, a depth-resolved image can be rapidly generated using a structured light reconstruction algorithm that requires only two wide field images, one with uniform illumination and the other with structured illumination. Second, depth scanning is implemented using the high speed remote depth scanning. Finally, the large field of view, high NA objective lens and the high pixelation, high frame rate sCMOS camera enable high resolution, high sensitivity imaging of a large cell population. This system can image at 800 cell/sec in 3D at submicron resolution corresponding to imaging 1 million cells in 20 min. The statistical accuracy of this instrument is verified by quantitatively measuring rare cell populations with ratio ranging from 1:1 to 1:10^5.

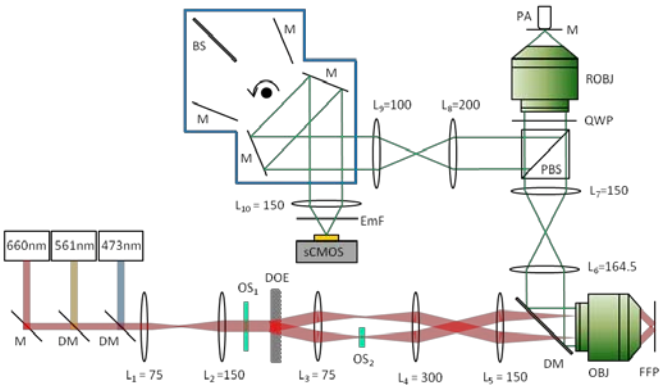

Fig. 1. Structured light cytometer

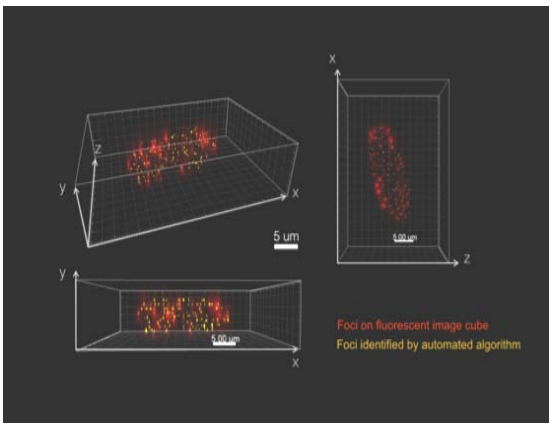

Fig. 2. 3D resolved counting of DNA double strand break in an nucleus

Speckle-based reflection-mode phase microscope

We demonstrate a quantitative reflection-phase microscope based on time-varying speckle-field illumination. Due to the short spatial coherence length of the speckle field, the proposed imaging system features superior lateral resolution, 520 nm, as well as high-depth selectivity, 1.03 μm. Off-axis interferometric detection enables wide-field and single-shot imaging appropriate for high-speed measurements. In addition, the measured phase sensitivity of this method, which is the smallest measurable axial motion, is more than 40 times higher than that available using a transmission system. We demonstrate the utility of our method by successfully distinguishing the motion of the top surface from that of the bottom in red blood cells. The proposed method will be useful for studying membrane dynamics in complex eukaryotic cells.

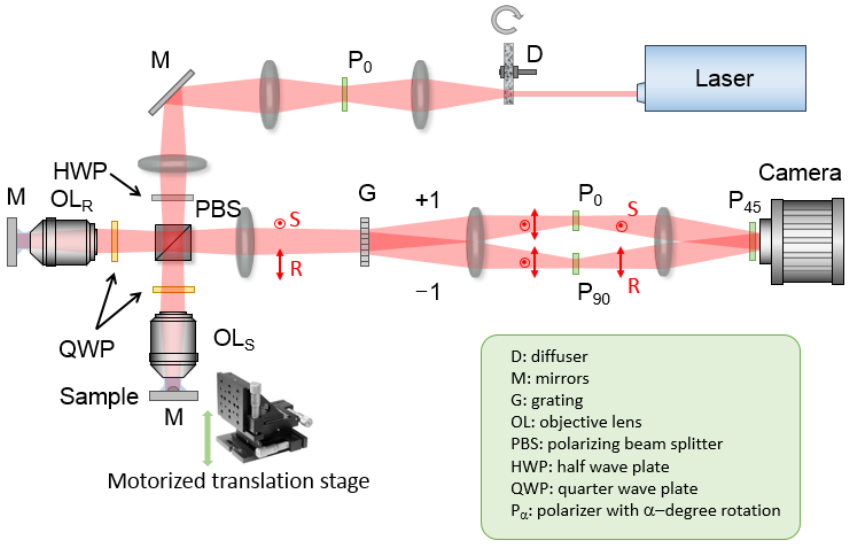

Fig. 3. Speckle-based reflection phase microscope

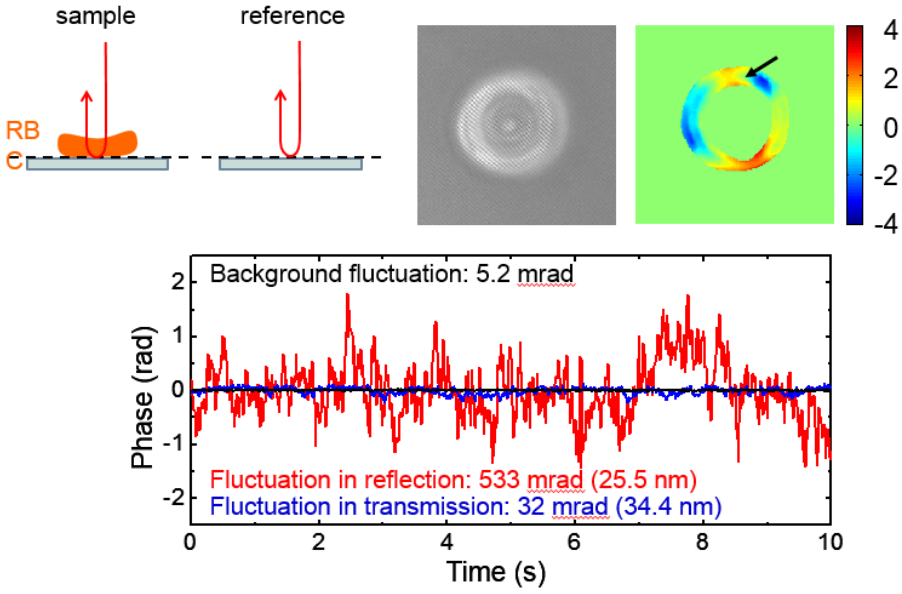

Fig. 4. Resolving nanometer scale fluctuation from epical and basal RBC surfaces

Acknowledgements

This work was supported by NIH 9P41EB015871-26A1, 1R01HL121386-01A1, 2R01EY017656-06A1, 1U01NS090438-01, 1R21NS091982-01, 5R01NS051320, DP3DK101024-01, 4R44EB012415-02, NSF CBET-0939511, the Singapore-MIT Alliance for Science and Technology Center (BioSym IRG), the MIT SkolTech initiative, the Hamamatsu Corp. and the Koch Institute for Integrative Cancer Research Bridge Project Initiative.

ACOUSTIC DIFFUSE OPTICAL REFLECTOMETRY (ADOR): TOWARDS TRIPLE-MODALITY OPTO-ACOUSTIC IMAGING

P.V. Subochev[1], I.I. Fiks[1], M. Frenz[2], and **I.V. Turchin[1]**

[1]Institute of Applied Physics, N. Novgorod, 46 Ulyanov Str, Russia, Pavel.Subochev@gmail.com
[2]Institute of Applied Physics, University of Bern, Bern, 5 Sidlerstrasse, CH-3012, Switzerland

Abstract. The wide clinical applicability of optoacoustic methods is currently limited by the difficulties of spatial reconstruction of the concentrations of tissue chromophores. A major challenge for quantitative optoacoustic imaging is the unknown optical fluence within the tissue being studied as fluence cannot be independently measured using the traditional methods of optoacoustic sensing. The incorporation of diffuse optical measurements into a traditional optoacoustic system eases optoacoustic quantification by using the theoretical relationships between the optical fluence and the diffuse reflectance. In this work we propose to measure the diffuse reflectance by using a new ADOR technique that relies on the thermoelastic signal generated at the surface of the optoacoustic detector by the backscattered photons. We have performed the phantom experiments using the ADOR technique and demonstrate, that the sensitivity of ADOR allows investigation of biotissues. The results of the experiments reveal the similarities of the ADOR technique to the traditional method of diffuse optical reflectometry. In this study we implemented the ADOR technique as a third optical modality for a previously developed dual-modality optoacoustic/ultrasonic microscope. In general, the ADOR technique could also be realized as a "free" upgrade to other optoacoustic systems.

Optoacoustic (OA) (or photoacoustic) imaging is a modern method of biomedical visualization based on the remote detection of ultrasonic (US) pulses generated in the tissue under investigation due to the absorption of nanosecond laser pulses by optical heterogeneities. Hybrid methods of OA imaging combine the advantages of both the optical and US modalities. The large differences in the optical absorption by the target endogenous or exogenous chromophores ensure that the OA images have a high contrast-to-noise ratio, while the minimal US scattering and frequency-dependent US attenuation of biotissues determine the scalable diagnostic depth and spatial resolution.

Modern clinical facilities demand multi-spectral OA imaging systems that are capable of 3D reconstruction of tissue chromophore concentrations. However, leading optoacoustic groups have highlighted the multiple challenges facing quantitative optoacoustic imaging (QOI). One of the most significant aspects of QOI is the unknown spatial distribution of the optical fluence inside the biotissue that impacts on the amplitudes of the OA pressure signals that are generated.

One of the ways to compensate for inhomogeneous fluence distribution in multi-spectral OA images is to use model-based algorithms. To avoid computational difficulties it is also possible to measure the optical fluence directly. Different authors proposed utilizing the methods of diffuse optical tomography alongside the traditional OA systems. However, due to the limited space above the imaging object the incorporation of independent diffuse optical equipment into the OA imaging head can be challenging (especially in the case of reflection-mode geometries).

In this work we propose the concept of acoustical diffuse optical reflectometry (ADOR) that allows measuring the diffuse reflectance, since the absorption of backscattered light by the OA detector causes a signal. Necessary relations between diffuse reflectance, fluence and absorption can be further specified by the theoretical models. However, the application of ADOR technique to quantitative optoacoustic methods are not be addressed in this work.

In Figure 1a we present our implementation of the ADOR technique, based on our previously developed dual-modality OA/US microscope [1, 2]. A solid-state laser, LT-2214-PC (LOTIS TII, Belorussia), provides 18 ns optical pulses across a tunable 400–2100 nm wavelength range. The output laser beam is collimated into a fiber bundle (Ceram Optec, Germany). The custom-made 10:90 beam splitter with a calibrated pyroelectric sensor ES111C (Thorlabs, USA) is used to determine the energy for each single laser pulse at the distal fiber tips needed to calculate the effective radiant exposure at the surface of the object. The radiant exposure was kept below 10 mJ/cm^2 to satisfy the 20 mJ/cm^2 standard for laser safety).

Fourteen output arms of the fiber bundle (each arm of 2.5 mm diameter and with a 0.17 numerical aperture in water) are homogeneously distributed along a conical surface at an angle of 40 degrees [3] to the Z axis providing illumination of the object. A polyvinylidene difluoride (PVDF) OA detector PI-35-2 (Olympus-NDT, USA) with NA = 0.25, f = 32 MHz central frequency, Δf = 34 MHz frequency band and F = 12.7 mm focal distance is directed into the center of the optical illumination. The ana-

log signals from the OA detector are sent through a custom-made AD4817-based low-noise amplifier and custom-made high-pass filter with a 5 MHz cut-off frequency to an analog-to-digital converter (ADC) based on an NI5761 14-bit 250-MS/s adapter with an NI FlexRIO FPGA PXI-7952R (National Instruments, USA). The digitized signals are then subjected to a Hilbert transform. To estimate the diffuse reflectance the ADOR technique measures the signals generated by the backscattered photons at the metalized surface of the PVDF detector (Fig. 1b).

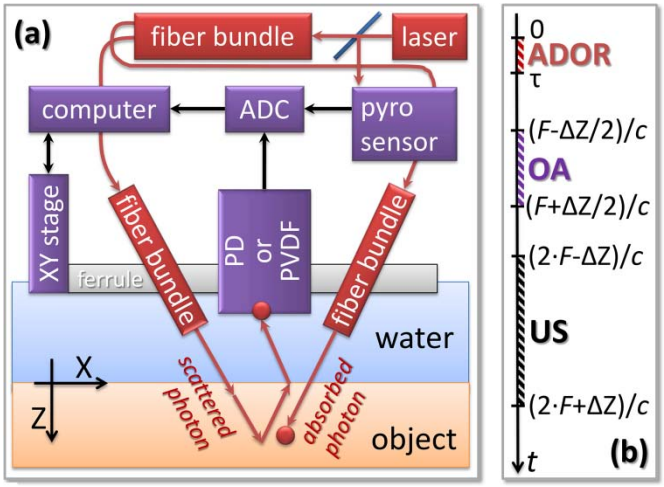

Fig. 1. The experimental setup for OA/US/ADOR or DOR imaging. (a) Schematic of the experimental setup. (b) Sketch of the information contained in an A-scan with the sequence of the ADOR, OA, and US signals

To carry out ADOR imaging, the scanning head with the PVDF detector was mounted on two linear positioning slides with a maximum travel range of 6.25 mm (Automation Gages, USA), driven by AM-23-239-3 step motors (Advance Microsystems, USA), inside an immersion chamber filled with distilled water (Fig. 1a). The movement of the translation stage was matched to the 10 Hz repetition rate of the laser pulses. Polyethylene film of thickness 60 μm covered the bottom of the immersion chamber providing necessary acoustic coupling to the object under investigation.

To realize the ADOR technique as a third modality for the OA/US system the automation algorithm inquired the definition of the scanning range $\Delta X=\Delta Z$, the scanning step size δx, the focal length F, the average speed of sound c, and the average duration of the laser pulse τ. Figure 1b schematically represents the sequence of signals to be registered by the PVDF detector at each of the $\Delta X/\delta x$ scanning positions of the opto-acoustic head. The ADOR signal is detected during the time period from $t = 0$ (corresponding to the trigger signal from the photodetector) to $t = \tau$. The OA A-scan is detected during the time period from $t = (F-\Delta Z/2)/c$ to $t = (F+\Delta Z/2)/c$, and this is then normalized in relation to the energy of the laser pulse (while OA amplitudes are proportional to laser pulse energy, the laser pulse energy of Q-switch laser demonstrates some deviations). The US A-scan is detected during the time period from $t = (2\cdot F-\Delta Z)/c$ to $t = (2\cdot F+\Delta Z)/c$, and this is then normalized by ADOR signal (while optically-mediated US amplitudes are proportional to the diffuse reflectance, optical heterogeneities inside the medium deviate the amount of backscattered photons).

At TPB-2015 conference we will present the results of ADOR imaging of tissue-like phantoms. We will compare the imaging capabilities of ADOR compare with traditional DOR measurements based on the detection of backscattered photons using a photodetector. We will also demonstrate the opportunities of triple-modality imaging, since the ADOR technique can be added as a third modality to our previously developed dual-modality OA/US microscope.

Acknowledgements

This work was supported financially by the Russian Science Foundation (project No14-15-00709). The authors are grateful to Roman Belyaev, to Vladimir Vorobyev, and to Sergey Pozhidaev for their engineering contributions to this work and to Dr. Mikhail Kirillin for his valuable discussions.

References

1. P. Subochev et al., *Optics letters*, 2012, **37**, 4606-4608.
2. P. Subochev et al., *Biomedical Optics Express*, 2015, **6**, 631-638.

Invited

ADVANCES IN MULTI-MODAL OCT: OVERVIEW OF NIZHNYI NOVGOROD + TORONTO COLLABORATION DEVELOPMENTS

A. Vitkin[1,2]

[1] University of Toronto, Toronto, Canada
[2] Nizhny Novgorod State Medical Academy, Nizhny Novgorod, Russia

Despite considerable progress in, and im pressive effectiveness of various non-invasive cancer treatments such as radiotherapy (RT) and chemotherapy (ChT), the clinical outcomes are somewhat variable because of the variation in individual patient responses. If some convenient measurements from specific patients undergoing specific treatments could be made that report on treatment progress and response, these could be used to select responders from non-responders, alter 'the doses' for the remaining treatment, and in general optimize the therapies based on individual treatment feedback.

In this Nizhnyi Novgorod + Toronto collaboration, we are developing the enabling optical coherence tomography (OCT) imaging technologies and conducting preclinical and selected clinical studies to come up with quantifiable metrics of tumour and normal tissue responses to a variety of minimally invasive therapies. Specifically, the OCT imaging platform is being expended / refined to enable multiple modes of operation, including direct structural, polarization-sensitive, angiographic, and elastographic regimes. These yields unique high-resolution imaging information on tissue cellular organization, connective tissue compartment, blood microcirculation, and tissue hardness / stiffness, respectively. The ability of these multiple important and complimentary information channels to detect treatment-induced changes is investigated preclinically in a series of normal and tumour-bearing small animals (mice, hamsters) undergoing ChT, RT, and also photodynamic therapy (PDT). A series of treatment-specific multi-modal OCT response metrics are derived, and then tested in a series of further clinical pilot studies of PDT, RT and ChT in the pathologies of oral cavity and skin. Representative project results will be highlighted in this presentation. It is hoped that the multimodal OCT technologies and treatment response metrics thus developed will help usher in the era of "personalized cancer medicine" of the 21stcentury.

NON-CONTACT IN VIVO TIME-DOMAIN DIFFUSE OPTICAL IMAGING

H. Wabnitz[1], **M. Mazurenka**[1], **L. Di Sieno**[2], **G. Boso**[3], **W. Becker**[4], **K. Fuchs**[1], **D. Contini**[2], **A. Dalla Mora**[2], **A. Tosi**[3], **Y. Hoshi**[5], **R. Macdonald**[1], and **A. Pifferi**[2]

[1] Physikalisch-Technische Bundesanstalt (PTB), Berlin, Germany, heidrun.wabnitz@ptb.de
[2] Dipartimento di Fisica, Politecnico di Milano, Milano, Italy
[3] Dipartimento di Elettronica, Informazione e Bioingegneria, Politecnico di Milano, Milano, Italy
[4] Becker&Hickl GmbH, Berlin, Germany
[5]Tokyo Metropolitan Institute of Medical Science, Tokyo, Japan

Abstract. Our novel non-contact system for time-domain functional near-infrared spectroscopy performs scans of the tissue with a fixed, small (few mm) separation between the illumination and detection spots and a frame rate of ~1/s. A fast-gated single-photon avalanche diode is utilized to eliminate the intense early part of the diffusely remitted signal and to detect late photons only that carry information on absorption changes deeply within the tissue. The system was characterized by a set of phantom measurements. First in vivo tests included the imaging of haemodynamic changes in the brain during cognitive and motor activation tasks.

Introduction

During twenty years of development of functional near-infrared spectroscopy (fNIRS) of the brain, numerous approaches and technical solutions have been reported, among them continuous wave (CW) optical topography and tomography employing multiple sources and detectors or time-domain fNIRS imaging [1]. While these techniques usually rely on direct contact between fibre-based optodes and the tissue surface, there is a trend towards non-contact approaches. They allow problems to be avoided that arise from pressure and unstable coupling between the optodes and the skin. Another advantage of non-contact approaches is the opportunity to obtain images that contain a much larger number and more densely spaced measurement positions compared to arrays of multiple optodes.

A specific development for time-resolved diffuse reflectance measurements for the characterization of deep tissue compartments is the null source-detector separation approach [2] in conjunction with a single-photon avalanche diode (SPAD) operated in fast-gated mode [3]. By gating off early photons, late photons that visited deep tissue regions can be recorded with increased signal-to-noise ratio.

The novel non-contact scanning approach described in this contribution combines the following features, i) non-contact imaging, ii) a dense and flexible grid of measurement positions, iii) depth-selective detection for depths up to ~2 cm by time-resolved recording. Proof-of-principle tests of our non-contact method on phantoms were reported in [4]. The implementation of a scanning setup and first *in vivo* tests were described in [5].

Here we present an upgraded and optimized scanning setup, its comprehensive characterization and results of various in-vivo tests.

System architecture

Trains of picosecond pulses (< 100 ps, repetition rate 40.5 MHz) were provided by a supercontinuum (SC) laser (Fianium Ltd, UK) equipped with an 8-channel acousto-optical tunable filter (AOTF). The output beam of the AOTF was directed to the tissue by the mirrors of a 2-axis galvanometer scanner. Light diffusely reemitted from the tissue passed the scanner again and was imaged onto a multimode fibre that guided it to the detector. The optical system was designed such that reflections from the tissue surface as well as from optical components were suppressed as far as possible.

A second generation compact fast-gated SPAD module (Politecnico di Milano, Italy) with embedded gating and signal conditioning circuitry [6] was employed for selective detection of late photons. The gate delay was adjusted by a home-built transmission-line based delay generator with 25 ps steps. A second parallel detection channel was equipped with a non-gated detector, to additionally record superficial absorption changes.

Distributions of times of flight of photons (DTOFs) of the gated and non-gated detectors were recorded in each pixel by an imaging TCSPC module (SPC-150, Becker&Hickl, Germany). A GVD-120 scan controller card (Becker&Hickl, Germany) was employed to control the scan as well as the image acquisition. The parameters were adjusted to cover a scan area of e.g. 4×4 cm^2 on the tissue with a 32×32 pixel frame size. The frame time was chosen to be 1 s, resulting in a pixel time of ~1 ms. The wavelength was switched between two wavelength bands, centred at 760 nm and 860 nm, from line to line.

Phantom characterization

The system was characterized by a set of phantom measurements according to the protocols developed in the "nEUROPt" project [7, 8]. In particular, the responsivity of the detection system [7] was measured to evaluate and optimize the optical system. To assess the spatial resolution performance, measurements were carried out on two types of inhomogeneous phantoms [8]. Lateral spatial resolution and penetration depth were obtained from scans of a liquid turbid phantom based on intralipid and ink [9] with black cylinders of various sizes immersed [10]. For the assessment of depth selectivity, a two-layer liquid phantom was employed in which the absorption coefficient was changed in the upper and lower layer separately.

In-vivo results

We performed several *in vivo* experiments on healthy adult subjects executing specific exercises to activate regions in the brain, inducing local changes in oxy- and deoxyhaemoglobin concentrations. The data processing was based on a time-window analysis within the late-photon part of the DTOF that was selected by the fast-gated detector. The concentration changes of oxygenated and deoxygenated haemoglobin in each pixel were estimated on the basis of the time-resolved (or microscopic) Beer-Lambert law.

In particular, the haemodynamic response to brain activation by various cognitive and motor stimulation paradigms was recorded. For the motor stimulation paradigm (20 trials of 32 s of finger tapping followed by 32 s of rest), a clearly localized cerebral response, with an increase of oxy- and decrease of deoxyhaemoglobin concentrations, was found in the block-averaged signals.

These tests demonstrated the successful non-contact imaging of haemoglobin concentration changes in deep tissues. Although its applicability is restricted to hairless parts of the body, the non-contact scanning approach may be advantageous for a number of applications where high density functional optical mapping of deep tissues is required or helpful. Examples are the localization of functional activation in the prefrontal cortex, the study of peripheral vascular pathologies or intraoperative monitoring.

Acknowledgements

The research leading to these results has received funding from the European Community's Seventh Framework Programme [FP7/2007-2013] under grant agreement n° FP7-HEALTH-F5-2008-201076.

References

1. A. Torricelli, D. Contini, A. Pifferi, M. Caffini, R. Re, L. Zucchelli, and L. Spinelli, *NeuroImage*, 2014, **85 Pt 1**, 28–50.
2. A. Pifferi, A. Torricelli, L. Spinelli, D. Contini, R. Cubeddu, F. Martelli, G. Zaccanti, A. Tosi, A. Dalla Mora, F. Zappa, and S. Cova, *Phys. Rev. Lett.*, 2008, **100**, 138101.
3. A. Dalla Mora, A. Tosi, F. Zappa, S. Cova, D. Contini, A. Pifferi, L. Spinelli, A. Torricelli, and R. Cubeddu, *J. Select. Topics Quantum Electron.*, 2010, **16**, 1023–1030.
4. M. Mazurenka, A. Jelzow, H. Wabnitz, D. Contini, L. Spinelli, A. Pifferi, R. Cubeddu, A. Dalla Mora, A. Tosi, F. Zappa, and R. Macdonald, *Opt. Express*, 2012, **20**(1), 283–290.
5. M. Mazurenka, L. Di Sieno, G. Boso, D. Contini, A. Pifferi, A. Dalla Mora, A. Tosi, H. Wabnitz, and R. Macdonald, *Biomed. Opt. Express*, 2013, **4**(10), 2257–2268.
6. G. Boso, A. Dalla Mora, A. Della Frera, and A. Tosi, *Sensors and Actuators A: Physical*, 2013, **191**, 61–67.
7. H. Wabnitz, D.R. Taubert, M. Mazurenka, et al., *J. Biomed. Opt*., 2014, **19**(8), 086010.
8. H. Wabnitz, A. Jelzow, M. Mazurenka, et al., *J. Biomed. Opt*., 2014, **19**(8), 086012.
9. L. Spinelli, M. Botwicz, N. Zolek, et al., *Biomed. Opt. Express*, 2014, **5**(7), 2037–2053.
10. F. Martelli, P. Di Ninni, G. Zaccanti, et al., *J. Biomed. Opt*., 2014, **19**(7), 076011.

M-MODE-LIKE IN VIVO OCT ANGIOGRAPHIC IMAGING USING REFERENCE-FREE PROCESSING OF COMPLEX-VALUED B-SCANS

V.Y. Zaitsev[1,2], **L.A. Matveev**[1,2], **G.V. Gelikonov**[1,2], **A.L. Matveyev**[1,2], **A.A. Moiseev**[1], **S.Y. Ksenofontov**[1], **V.M. Gelikonov**[1,2], **M.A. Sirotkina**[2], **N.D. Gladkova**[2], **V. Demidov**[3], and **A. Vitkin**[2,3]

[1] Institute of Applied Physics RAS, 60390, Ulyanov St., 46, Nizhny Novgorod, Russia
[2]Nizhny Novgorod State Medical Academy, 603005, Minin and Pozharsky Sq., 10/1, Nizhniy Novgorod, Russia
[3] University of Toronto and University Health Network, M5G 2M9, Toronto, Ontario, Canada

Abstract. We propose a novel OCT-based method for visualizing microvasculature in 3D using reference-free processing of individual complex-valued B-scans with highly overlapped A-scans. In the lateral direction of such a B-scan, the amplitude and phase of speckles corresponding to vessel regions exhibit faster variability, and thus can be detected without comparison with other B-scans recorded in the same plane. This method combines elements of several existing OCT angiographic approaches, and exhibits: (i) enhanced robustness with respect to bulk tissue motion with frequencies up to tens of Hz; (ii) resolution of microcirculation images equal to that of structural images and (iii) possibility of quantifying the vessels in terms of their decorrelation rates.

The need for increased information content in optical coherence tomography (OCT) of biological tissues has been exemplified by recent efforts to complement conventional structural images with additional contrast mechanisms [1, 2]. One of them is contrast-agent free microangiographic imaging in OCT, in which the own motion of scattering particles in the blood is used as a contrast mechanism to discriminate the blood in the vessels and surrounding "rigid" tissue [3–17]. The known approaches can roughly be divided into two main groups. One group uses the Doppler frequency shift of the OCT signal scattered by moving blood particles in the vessels (e.g. [3, 5, 10]). Usually comparison of phases of consequently obtained one-dimensional A-scans is used to estimate the Doppler shift. The main advantage of this approach is the possibility to quantitatively assess the axial component of the blood-flow velocity. Another popular group of methods is usually called speckle-variance (Sv) approach and is based on the estimate of speckle variance for several (usually 4–8) two-dimensional B-scans consequently obtained at the same position. The main advantage of this method is its sensitivity to motion of scatterers in the direction orthogonal to the optical beam, because this motion also causes speckle variations.

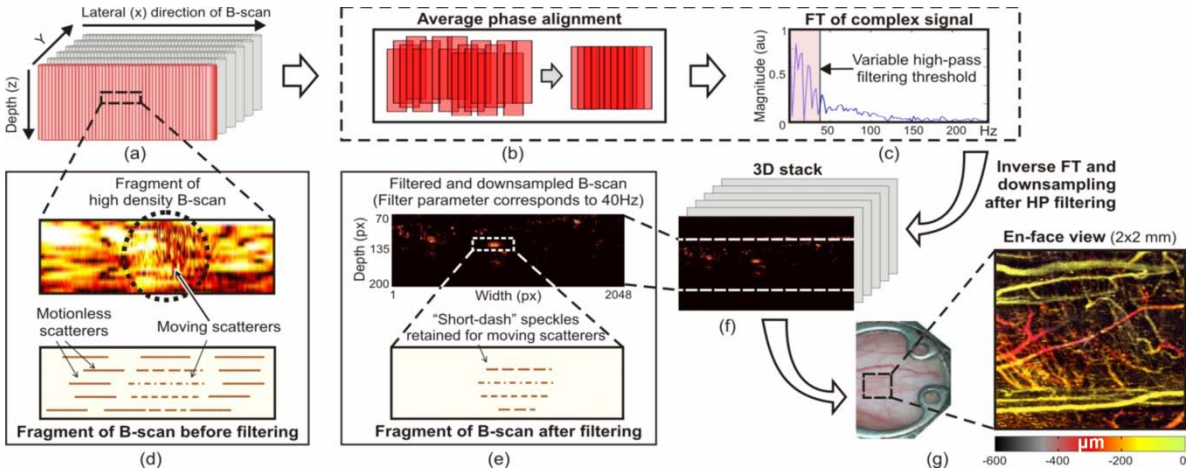

Fig. 1. Principle of operation of the MMLSV approach: (a) – A stack of dense B-scans with strongly overlapped A-scans; (b) – a single B-scan before and after equalization of average phases of neighboring A-scans; (c) – spatial spectrum of a single horizontal array of pixels in a dense B-scan, where low-frequency components correspond to slowly varying motionless scatterers. (d) – experimental B-scan fragment with encircled region of rapidly varying speckles corresponding to a vessel cross-section (top) and a schematic B-scan with speckles slowly and rapidly varying in the horizontal direction (bottom); (e) – same as (d), but after high-pass filtering (only vessels cross-sections are now visible); (f) shows an photo of a mouse dorsal window chamber and an example of *en-face* depth-encoded view of a 2mm x 2mm (lateral) 0–0.6 mm (depth) region of the detected mouse microvasculature

Since both approaches use motion of scatterers as a contrast mechanism, natural bulk motions (clutter) of living tissues may significantly degrade the flow-reconstruction quality. We propose an approach that can be considered as a hybrid one, based of reference-free processing of individual B-scans with densely overlapped A-scans (i.e., M-mode like). The use of full complex-valued signal combines some features of phase-resolved Doppler methods and Sv-approach (although here the speckle variability is assessed within a group of A-scans in individual B-scans). Aligning of average phases of A-scans is helpful for suppression of clutter motion as is schematically shown in Fig. 1. Singling out the moving scatterers in vessels is then made by applying high-pass filtering of the so-obtained B-scans in the lateral direction. After obtaining a stack of such B-scans with retained vessel cross-sections, en-face projection of the micro-vessels in the inspected volume can be made as illustrated in Fig. 2.

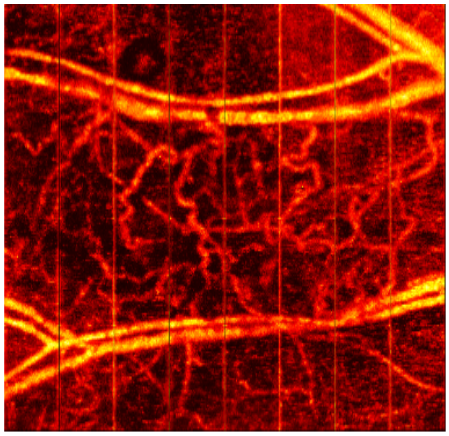

Fig. 2. An example of *en-face* maximum-intensity projection microangiographic image 2x2mm in size obtained using the proposed method in the region of tumor inoculated at an ear of a Bulb-C mouse

Although the tradeoff for the better tolerance to clutter motions is noticeable increase in total scanning time compared with inter-B-scan Sv/Cm methods [11, 12]), in many cases robustness to bulk motion artefacts may be more important, and thus longer total imaging time quite acceptable. Besides, quantification of blood vessels in terms of faster/slower decorrelations is also naturally enabled through the user-selected cut-off frequency of the high-pass filtering, and may be linked to physiologically important dynamic variables such as flow velocity and perfusion. In more detail the features of the proposed method are discussed in [18].

The study was supported by the RFBR grant No 15-42-02513. The experiments with the animals were performed in the OCT Lab of the Nizhny Novgorod State Medical Academy (under Russian Federation Government contract No. 14.B25.31.0015).

References

1. V.Y. Zaitsev, V.M. Gelikonov, L.A. Matveev, G.V. Gelikonov, A.L. Matveyev, P.A. Shilyagin, and I.A. Vitkin, *Radiophys. Quant. Electron*., 2014, **57**, 52.
2. V.Y. Zaitsev, I.A. Vitkin, L.A. Matveev, V.M. Gelikonov, A.L. Matveyev, and G.V. Gelikonov, *Radiophys. Quant. Electron*., 2014, **57**, 210.
3. R. Leitgeb, L. Schmetterer, W. Drexler, A. Fercher, R. Zawadzki, and T. Bajraszewski, *Opt. Express*, 2003, **11**, 3116.
4. V.X.D. Yang, M.L. Gordon, B. Qi, J. Pekar, S. Lo, E. Seng-Yue, A. Mok, B.C. Wilson, and I.A. Vitkin, *Opt. Express*, 2003, **11**, 794.
5. R.K. Wang, S.L. Jacques, Z. Ma, S. Hurst, S.R. Hanson, and A. Gruber, *Optics Express*, 2007, **15**, 4083.
6. M. Szkulmowski, A. Szkulmowska, T. Bajraszewski, A. Kowalczyk, and M. Wojtkowski, *Opt. Express*, 2008, **16**, 6008.
7. R.K. Wang and L. An, *Opt. Express*, 2009, **17**, 8926.
8. R.K. Wang, *IEEE J. Select. Topics Quant. Electron*., 2010, **16**, 545.
9. E. Jonathan, J. Enfield, and M.J. Leahy, *J. Biophotonics*, 2011 **4**, 583.
10. K. Kurokawa, K. Sasaki, S. Makita, Y.J. Hong, and Y. Yasuno, *Opt. Express*, 2012, **20**, 22796.
11. A. Mariampillai, B.A. Standish, E.H. Moriyama, M. Khurana, N.R. Munce, M.K.K. Leung, J. Jiang, A. Cable, B.C. Wilson, I.A. Vitkin, and V.X.D. Yang, *Opt. Lett*., 2008, **33**, 1530.

12. A. Mariampillai, M.K.K. Leung, M. Jarvi, B. A. Standish, K. Lee, B.C. Wilson, A. Vitkin, and V.X.D. Yang, *Opt. Lett.*, 2010, **35**, 1257.
13. Y.K. Tao, A.M. Davis, and J.A. Izatt, *Opt. Express*, 2008, **16**, 12350.
14. S. Yousefi, J. Qin, and R.K. Wang, *Biomed. Opt. Express*, 2013, **4**, 1625.
15. Y. Jia, O. Tan, J. Tokayer, B. Potsaid, Y. Wang, J.J. Liu, M.F. Kraus, H. Subhash, J.G. Fujimoto, J. Hornegger, and D. Huang, *Opt. Express*, 2012, **20**, 4710.
16. V. Srinivasan, J. Jiang, M. Yaseen, H. Radhakrishnan, W. Wu, S. Barry, A.E. Cable, and D.A. Boas, *Opt. Lett*., 2010, **35**, 43.
17. J. Lee, V. Srinivasan, H. Radhakrishnan, and D.A. Boas, *Opt. Express*, 2011, **19**, 21258.
18. L.A. Matveev, V.Y. Zaitsev, G.V. Gelikonov, A.L. Matveyev, A.A. Moiseev, S.Y. Ksenofontov, V.M. Gelikonov, M.A. Sirotkina, N.D. Gladkova, V. Demidov, and A. Vitkin, Opt. Lett., 2015, **40**, 1472.

Nanobiophotonics

Chairs

Juergen Popp, Friedrich Schiller University of Jena;
Institute for Photonic Technology, Germany

Elena Zagaynova, Nizhny Novgorod Medical Academy, Russia

Program Committee

Martin Leahy
National University of Ireland, Galway, Ireland

Sergey Lukyanov
Shemyakin and Ovchinnikov Institute of Bioorganic Chemistry, Moscow,
Nizhny Novgorod State Medical Academy, Russia

Alexander Savitsky
Institute of Biochemistry RAS, Russia

Michael Schmitt
Institute of Physical Chemistry, Friedrich-Schiller University Jena, Germany

Vladislav Shcheslavskiy
Becker&Hickl GmbH, Germany

Irina Larina
Baylor College of Medicine, USA.

Boris Chichkov
Laser Centre Hannover e.V., Germany

Andrei Zvyagin
Macquarie University, Australia; Lobachevsky State University of Nizhny Novgorod

SYNTHESIS AND OPTICAL PROPERTIES OF NANOSTRUCTURES «PLASMON CORE-SEMICONDUCTOR SHELL»

D.A. Afanasyev, **N.Kh. Ibrayev, T.M. Serikov,** and **A.A. Epp**

Academician E.A. Buketov Karaganda State University, Karaganda, Kazakhstan
a_d_afanasyev@mail.ru

Abstract. The results of the synthesis of nanostructures «Ag-TiO_2» are presented. Optical properties and stability of silver nanoparticles were studied in various solvents. The dimensions and shape of the nanostructures «Ag-TiO_2» was determined. Absorption and fluorescence spectra were measured. The weight ratio between the core and shell were evaluated from absorption spectra. Practical yield was defined for the synthesis of the core-shell nanoparticles.

At present, the availability of the use of metal nanoparticles having localized plasmon resonance (PR) in photovoltaics, biophotonics and biomedicine is not doubt. There are many works in this scientific direction. However, the use of plasmonic nanoparticles with semiconductor or dielectric shell is more promising in practical application [1]. Using of shell helps to protect plasmon core from the negative impact of the external environment. As well the change of the frequency and intensity of PR could be done by changing of geometric dimensions of the shell.

The results of the synthesis of nanoparticles (NPs) with the semiconductors shell of titanium dioxide (TiO_2) are presented in this paper. Microstructure of NPs and their optical properties was investigated.

Initially, the synthesis of silver NPs was made. Silver NPs were used as plasmonic core. $AgNO_3$ salt was used for the synthesis of stable nanoparticles. Ethylene glycol was used as solvent. Poly-N-vinylpyrrolidone with different molecular weights was added to the solution to prevent coagulation of the silver NPs. The absorption band of silver NPs observed in the absorption spectra of solutions was associated with PR. Formation of silver NPs of various sizes depends on the molecular weight of the polymer. Repeatability of results was observed if all conditions of synthesis were maintained. Additionally, the stability of polymer-sealing silver NPs was investigated.

Silver NPs were transferred from ethylene glycol to ethanol before the synthesis of semiconductor membranes. Titanium tetraisopropoxide ($Ti\{OCH\ (CH_3)_2\}_4$ in alcoholic solution was added in Ag NPs solution to obtain semiconductor shell of titanium dioxide. The size and shape of the obtained core-shell nanoparticles (C-S) were measured by laser dynamic light scattering and electron microscopy. It was shown that the weight of the synthesized shell increases with increasing of concentration of titania precursor. Absorption and fluorescence spectra of ethanol solutions of C-S nanoparticles were measured. The weight ratio of the silver core and the shell of the titanium dioxide were found from the absorption spectra. Chemical composition of particles C-S was determined by energy dispersive methods. Practical yield that was determined for the synthesized C-S nanoparticles was equal to 72% of the original mass of the reactants used.

Nanoparticles «titanium semiconductors core-silver shell» have been synthesized in order to control the spectral characteristics of PR in nanostructures based on silver and titanium dioxide. We measured the absorption spectra of nanoparticles. For these NPs low-frequency shift of the maximum of PR band was observed in comparison with silver NPs.

References

1. S.A. Maier, *Plasmonics: Fundamentals and Applications*. Springer, NY, 2007, p. 224.

Invited

UPCONVERTING NANOPARTICLES FOR DEEP TISSUE IMAGING

S. Andersson-Engels, M. Mousavi, H. Söderlund, and **H. Liu**

Department of Physics, Lund University, Lund, Sweden
stefan.andersson-engels@fysik.lth.se

Abstract. Upconverting nanoparticles (UCNPs) is a novel class of contrast agent for bioimagng. These nanoparticles can emit anti-Stokes shifted light, which tremendously improves the contrast of the signal by enabling autofluorescence free detection. In addition, owing to the quadratic power dependence of the UCNPs, we have also shown that the reconstructions are more sharply defined compared with the reconstructions of a linear fluorophore. In this presentation we will present how we can reach deeper into tissue by employing pulsed light excitation, by codoping the UCNPs to shift the excitation wavelength from the water absorption region and by efficiently suppressing scattered excitation light.

Introduction

During the last decade upconverting nanoparticles (UCNPs) have gained an increasing interest in the field of bioimaging in diverse applications, such as e.g. photodynamic therapy (PDT) [1, 2], multimodality imaging [3], diffuse optical imaging [4–8], and microscopy [9–12]. Upcoverting nanoparticles are usually rare-earth-metal-based luminescent contrast agents. They provide an anti-Stokes shifted light emission upon near infrared excitation. They are generally composed of a crystal host material doped with two types of rare-earth ions, one serving as sensitizer to absorb excitation energy and the other as activator to accept energy from the sensitizer and generate emission. The higher energy upconverted emission is achieved by summing up the excitation energy through step-wise energy transfer between the sensitizer and activator. The upconvertion process thereby provides a signal at shorter wavelength than the excitation light. This feature makes it possible to fully suppress any superimposed tissue autofluorescence in the detection of the signal, as the signal and autofluorescence are completely spectrally separated [8]. This is a very important advantage for deep tissue imaging, as the signals from UCNP-labeled tissue then are highly attenuated by the tissue. Such weak signals would with imaging of conventional fluorophores quickly be dominated even by relatively weak autofluorescence from superficial tissue regions, experiencing much lower attenuation being so much closer to the detection at the surface. Tissue autofluorescence is in this way limiting the usefulness of deep tissue fluorescence imaging with conventional chromophores. Instead many whole-body imaging protocols are today based on bioluminescence imaging, providing a much weaker signal, but totally background-free [13]. Bioluminescence may, for this reason, provide more robust interpretation of the signals, and is thereby in many applications beneficial, even though the image acquisition requires long exposure times and genetically modifies cell lines to work.

Results

Pulsed light provides a more efficient excitation. This is because the non-linear behavior when several photons are required for the stepwise excitation. As the excitation is stepwise, one photon at a time, one has to consider the lifetimes of the various involved energy levels. We have conducted studies to clarify what pulse length is optimal and how much can be gained by pulsing the excitation [14, 15].

The most efficient UCNPs for tissue imaging has been $NaYF_4$:Yb,Tm. They can be excited at 975 nm with an emission wavelength of 800 nm. Both these wavelengths fall into the optical window for tissue, allowing deep tissue imaging. However, 975 nm is not ideal from a tissue perspective, as water has a relatively high absorption at this wavelength. Thus co-doping the UCNPs with Nd-ions can be used, providing a possibility to excite the particles slightly above 800 nm. In this case Tm is replaced by Er, yielding an emission at 650 nm. This improves the possibilities for deep tissue imaging as is illustrated in Fig. 1 from a tissue phantom study.

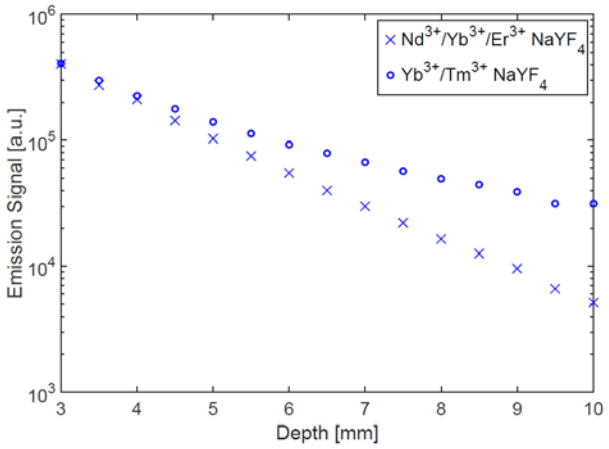

Fig. 1. Two recordings of light emitted from a thin rod with UCNPs located at various depths inside an 18 mm thick flat tissue phantom. Measurements were conducted in transmission geometry. It can be clearly seen that the Nd-codoped UCNPs provide a stronger signal deeper inside the tissue phantom. This is an effect of the lower absorption of the excitation light at 808 nm as compared to at 975 nm

Acknowledgements

Support by Swedish Research Council is greatly acknowledged.

References

1. D.K. Chatterjee, Z. Yong, *Nanomedicine*, 2008, **3**(1), 73-82.
2. A. Punjabi, X. Wu, A. Tokatli-Apollon, M. El-Rifai, H. Lee, Y. Zhang, et al., *ACS Nano*, 2014, **8**(10), 10621-30.
3. C.J. Carling, J.C. Boyer, and N.R. Branda, *Org Biomol Chem*., 2012, **10**(30), 6159-68.
4. H. Liu, C.T. Xu, and S. Andersson-Engels, *Optics Letters*, 2010, **35**(5), 718-20.
5. P. Svenmarker, C.T. Xu, and S. Andersson-Engels, *Optics Letters*, 2010, **35**(16), 2789-91.
6. C.T. Xu, J. Axelsson, and S. Andersson-Engels, *Applied Physics Letters*, 2009, **94**(25).
7. C.T. Xu, P. Svenmarker, H. Liu, X. Wu, M.E. Messing, L.R. Wallenberg, et al., *ACS Nano*, 2012, **6**(6), 4788-95.
8. C.T. Xu, N. Svensson, J. Axelsson, P. Svenmarker, G. Somesfalean, G. Chen, et al., *Applied Physics Letters*, 2008, **93**(17).
9. Y.I. Park, K.T. Lee, Y.D. Suh, and T. Hyeon, *Chem Soc Rev*., 2015, **44**(6), 1302-17.
10. T.V. Esipova, X. Ye, J.E. Collins, S. Sakadzic, E.T. Mandeville, C.B. Murray, et al., *Proc Natl Acad Sci. USA*, 2012, **109**(51), 20826-31.
11. C.F. Gainer, U. Utzinger, and M. Romanowski, *J. Biomed Opt*., 2012, **17**(7), 076003.
12. J.D. Bhawalkar, J. Swiatkiewicz, S.J. Pan, J.K. Samarabandu, W.S. Liou, G.S. He, et al., *Scanning*, 1996, **18**(8), 562-6.
13. C. Darne, Y. Lu, and E.M.Sevick-Muraca, *Phys. Med. Biol*., 2014, **59**(1), R1-64.
14. H. Liu, C.T. Xu, D. Lindgren, H. Xie, D. Thomas, C. Gundlach, et al., *Nanoscale*, 2013, **5**(11), 4770-5.
15. H.C. Liu, C.T. Xu, G. Dumlupinar, O.B. Jensen, P.E. Andersen, and S. Andersson-Engels, *Nanoscale*, 2013, **5**(20), 10034-40.

Invited

FLUORESCENCE LIFETIME IMAGING BY MULTI-DIMENSIONAL TCSPC: TECHNIQUE AND APPLICATIONS

W. Becker

Becker & Hickl GmbH, Nahmitzer Damm 30, 12277 Berlin, Germany
E-mail: becker@becker-hickl.com

Abstract. TCSPC FLIM is based on scanning a sample with a focused laser beam, detecting single fluorescence photons, and building up a photon distribution over the times of the photons after the excitation pulse and the coordinates of the scan. Main applications are measurements of molecular environment parameters, FRET experiments, and metabolic imaging via the autofluorescence of endogenous fluorophores. TCSPC FLIM can be extended by including additional parameters of the photons in the photon distributions. These techniques record multi-wavelength FLIM, Z-stack FLIM, combined FLIM/PLIM, and FLIM data showing fast transient effects in the fluorescence behaviour of a sample.

Requirements to FLIM in Biology

A fluorescence lifetime imaging (FLIM) technique for application in biology has to combine near-ideal photon efficiency, recording of the full fluorescence decay profiles in the pixels, and suppression of laterally and longitudinally scattered and out-of-focus excited fluorescence light. Moreover, it should be possible to record physiological effects induced in the sample by external stimulation. In any case, artefacts in the recorded decay profiles by physiological changes during the acquisition time should be avoided.

FLIM Technique

We will show that the combination of multi-dimensional time-correlated single photon counting (TCSPC) with confocal or two-photon laser scanning meets these requirements almost ideally. Multi-dimensional TCSPC differs from classic TCSPC in that the photon density is not only recorded over the time in the fluorescence decay but also over additional parameters. For FLIM, the sample is repetitively scanned by a high-repetition rate pulsed laser beam, single photons of the fluorescence signal are detected, and each photon is characterised by its time in the laser pulse period and the coordinates of the laser spot in the scanning area in the moment its detection. The recording process builds up a photon distribution over these parameters, see **Fig. 1**. The photon distribution can be interpreted as an array of pixels, each containing a full fluorescence decay curve in a large number of time channels [1, 2]. The result is independent of the scan rate. The signal-to-noise ratio depends only on the total acquisition time and the available photon rate.

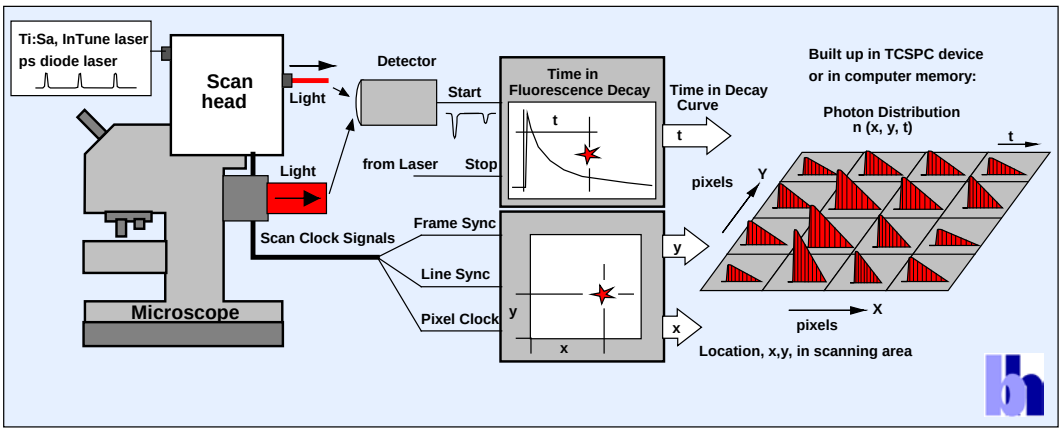

Fig. 1. Principle of TCSPC FLIM

Applications

The main applications of TCSPC FLIM in biological and biomedical imaging are measurements of molecular environment parameters, protein-interaction experiments by FRET, and imaging of the metabolic state of cells and tissue via the autofluorescence of endogenous fluorophores. These applica-

tions make use of the fact that the fluorescence lifetime is (within reasonable limits) independent of the fluorophore concentration. Absolute values of ion concentrations, ph, viscosity, or other local environment parameters can therefore be obtained without the need of special ratiometric dyes [1]. In FRET experiments, FRET efficiencies are obtained from a single lifetime image of the donor, and interacting and non-interacting donor fractions can be distinguished. Autofluorescence FLIM not only distinguishes different tissue constituents but also yields information on the bound/unbound ration of NADH. Examples are shown in **Fig. 2** and **Fig. 3**.

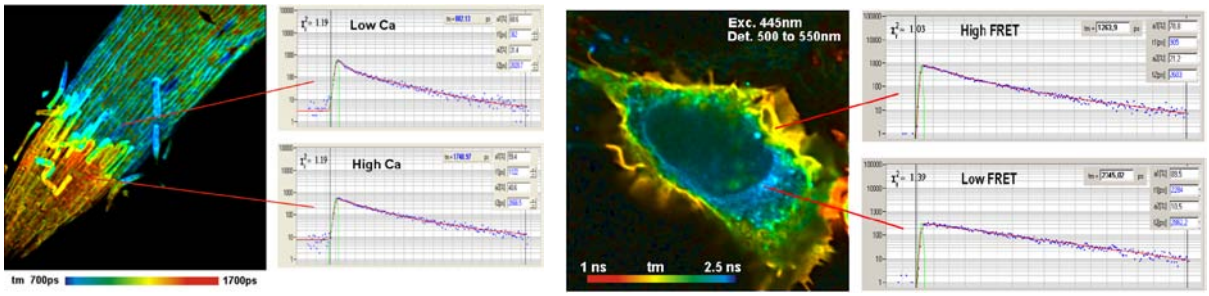

Fig. 2. *Left*: Ca++ concentration in a barley root (left) recorded via the lifetime of Oregon Green.
Right: FRET measurement, interacting proteins in cell membrane

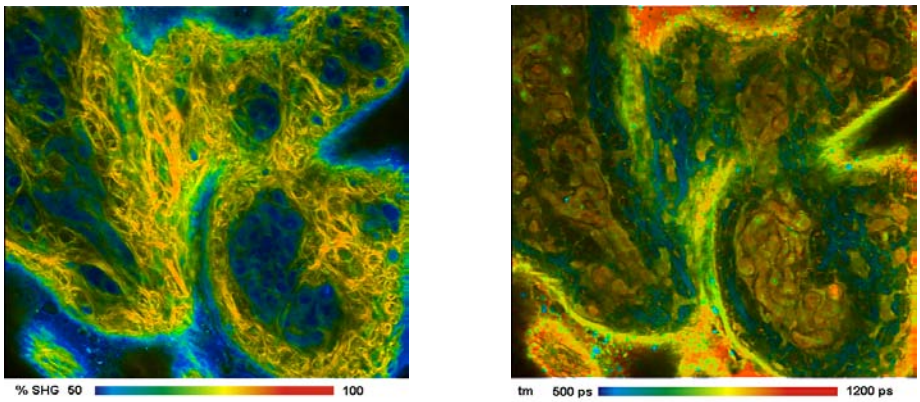

Fig. 3. Autofluorescence FLIM of PIG skin, 2p excitation.
Left: Emission < 460 nm, colour shows fraction of SHG from collagen.
Right: Emission > 480 nm, colour shows fluorescence lifetime

Advanced Techniques

The recording process can be extended by including additional dimensions in the photon distribution. These can be the depth of the focus in the sample, the wavelength of the photons, the time after a stimulation of the sample, or the time within the period of an additional modulation of the laser. These advanced techniques can be used to record Z stacks or lateral mosaics of FLIM images [3], multi-wavelength FLIM images [2], images of physiological effects occurring in the sample [1, 2], or to simultaneously record fluorescence and phosphorescence lifetime images [2, 5].

References

1. W. Becker (ed.), "Advanced time-correlated single-photon counting applications", Springer, 2015.
2. W. Becker, "The bh TCSPC Handbook, 6th edition", Becker & Hickl GmbH, 2015.
3. H. Studier and W. Becker, "Megapixel FLIM", *Proc. SPIE*, 2014, 8948.
4. W. Becker, V. Shcheslavkiy, S. Frere, and I. Slutsky, "Spatially Resolved Recording of Transient Fluorescence-Lifetime Effects by Line-Scanning TCSPC", *Microsc. Res. Techn.*, 2014, **77**, 216-224.
5. W. Becker, B. Su, A. Bergmann, K. Weisshart, and O. Holub, "Simultaneous Fluorescence and Phosphorescence Lifetime Imaging", *Proc. SPIE*, 2011, **7903**, 790320.

Invited

NANODIAMOND FOR THERANOSTIC APPLICATIONS: TOXICITY EVALUATION AND MODELS IN SMALL ANIMAL AND MICROORGANISMS

Y.-C. Lin[1], K.-T. Wu[1], E. Perevedentseva[1,2], L.-W. Tsai[1], and **C.-L. Cheng[1]**

[1] Department of Physics, National Dong Hwa University, Hualien, Taiwan; clcheng@mail.ndhu.edu.tw
[2] P.N. Lebedev Physics Institute, Russian Academy of science, 119991 Moscow, Russia

Abstract The physical-chemical properties of nanodiamond (ND) and low toxicity suitable for theranostic applications are discussed with models of microorganism and zebra fish embryo. A rapid, sensitive and reproducible zebra fish embryo model developed for safety evaluation of ND-based nano-carrier or nano-label, including anti-cancer drug delivery systems is discussed.

Nanodiamond (ND) has been demonstrated to be very promising for bio-imaging, drug delivery, and other bio/medical applications, owing to its superb properties such as biocompatibility, fluorescence and Raman signals for spectroscopic detection and for drug delivery [1]. Much of the cellular models have been successfully developed. Here we take and microorganisms and small-sized animal (zebra fish) as our focus to discuss the possible theranostic applications of nanodiamond.

The biocompatibility and bio labeling of ND are demonstrated via the interaction with microorganisms, protists microorganisms Paramecium caudatum and Tetrahymena thermophile, in vitro and in vivo. The processes of ND engulfment by P. caudatum and T. thermophile with localization in food vacuoles and followed excretion are observed using ND spectroscopic properties opens further facilities for controlled engulfment and extraction via varying ND size, surface properties and surface coating, as well as integration with unicellular organisms; and correspondingly, opens new opportunities for the ND bio applications.

Establishing a relatively simple, reliant and cost-effective animal test will greatly facilitate the research for nano-drug- delivery development. A rapid, sensitive and reproducible zebra fish embryo model for in vivo toxicity test was designed. We optimize the conditions for the animal model and analyze the zebrafish embryo development in the presence of ND. ND is observed in the embryo in vivo using laser confocal fluorescence microscopy. Using the zebrafish model for a safety evaluation of ND-based nano-carrier or nano-label is discussed. This model is expected to be applicable for other nanoparticle systems. As an example, anti-cancer drug (doxorubicin, DOX) was conjugated to ND via human serum albumin (HAS). The ND-HSA-DOX complex was tested in for the drug delivery functionality.

Acknowledgements

The research was supported by Ministry of Science and Technology of Taiwan with grant No. 103-2112-M-259-001-MY3.

References

1. E. Perevedentseva, Y.-C. Lin, Mona Jani, and C.-L. Cheng, *Future Medicine. Nanomedicine*, 2013, **8**(12), 2041-2060.

Invited

FLUORESCENCE AND SURFACE-ENHANCED RAMAN AS COMPLEMENTARY TECHNIQUES IN NANOMEDICINE RESEARCH

I. Chourpa[1], A. Carrouée[1,2], E. Allard-Vannier[1], L. Douziech-Eyrolles[1], M. Soucé[1], E. Munnier[1], S. Même[2], and **J.-C. Beloeil[2]**

[1] EA 6295 Nanomédicaments et Nanosondes, Université François Rabelais de Tours, Tours, France, igor.chourpa@univ-tours.fr

[2] CNRS-UPR 4301 - Centre de Biophysique Moléculaire - Equipe «IRM, signaux, images et expression des gènes», Orléans, France

Abstract. Nanomedicine is a pluridisciplinary research domain highly stimulating progress in technology, methodology and fundamental science. Indeed, multiple challenges of nanomedicine development can be more efficiently taken up with help of optical spectroscopy and microscopy approaches since they allow for direct non-invasive analysis of biological systems. Fluorescence emission-based approaches are widely used in biomedical research. More recent, but very promising techniques like surface-enhanced Raman scattering (SERS) are currently winning a place of merit in bio-analytical and diagnostic protocols. Although fluorescence emission is often seen as a process concurrent to conventional Raman scattering, SERS and in particular SERRS (SERS with resonant excitation) can be advantageously used in combination with fluorescence. We will present here several examples of complementary use of fluorescence and of surface-enhanced Raman spectrosocopy in the research activity of our team focused on development of nanosystems for anticancer drug delivery and for cancer cell detection/imaging.

Novel biocompatible nanosystems rationally designed for theranosis (therapy and diagnosis) of cancers [1, 2] are developed and studied in our laboratory. Fluorescence- and SERS-based appoaches are strongly present in our research. This is due to the potential of these techniques able to selectively provide molecularly specific information in complex media. In the present talk, we will illustrate several applications of fluorescence and SERS and SERRS: physico-chemical characterization of nanomedicines [3, 4], study of drug loading/release in/from nanomedicines in suspension [4-6], nanomedicines internalization and drug delivery in live cancer cells [7, 8]. On the other hand, we will discuss about a coupling of these techniques in frame of multimodal biomedical imaging as a part of cancer theranosis [9].

Acknowledgements

We acknowledge financial support from Région Centre, ARC and from Ligue Nationale contre le Cancer.

References

1. J. Gautier, E. Allard-Vannier, E. Munnier, M. Soucé, and I. Chourpa, "Recent advances in theranostic nanocarriers of doxorubicin based on iron oxide and gold nanoparticles", *J. Control Release*, 2013, **169**(1-2), 48-61.
2. J. Gautier, E. Allard-Vannier, et al., "Efficacy and Hemotoxicity of Stealth Doxorubicin-Loaded Magnetic Nanovectors on Breast Cancer Xenografts", *J. Biomed. Nanotechnol*, 2015, **11**, 177-189.
3. K. Kaaki, K. Hervé-Aubert, M. Chiper, A. Shkilnyy, M. Soucé, R. Benoit, A. Paillard, P. Dubois, M.L. Saboungi, and I. Chourpa, "Magnetic nanocarriers of doxorubicin coated with poly(ethylene glycol) and folic acid: relation between coating structure, surface properties, colloidal stability, and cancer cell targeting", *Langmuir*, 2012, **28**(2), 1496-505.
4. M. Chiper, K. Hervé Aubert, A. Augé, J.F. Fouquenet, M. Soucé, and I. Chourpa, "Colloidal stability and thermo-responsive properties of iron oxide nanoparticles coated with polymers: advantages of Pluronic® F68-PEG mixture", *Nanotechnology*, 2013, **24**(39), 395605.
5. J. Gautier, E. Munnier, L. Douziech-Eyrolles, A. Paillard, P. Dubois, and I. Chourpa, "SERS spectroscopic approach to study doxorubicin complexes with Fe(2+) ions and drug release from SPION-based nanocarriers", *Analyst*, 2013, **138**(24), 7354-61.
6. P. Šimáková, J. Gautier, M. Procházka, K. Hervé-Aubert, and I. Chourpa, "Polyethylene-glycol-Stabilized Ag Nanoparticles for Surface-Enhanced Raman Scattering Spectroscopy: Ag Surface Accessibility Studied Using Metalation of Free-Base Porphyrins", *J. Phys. Chem. C*, 2014, **118**, 7690–7697.
7. I. Chourpa, F.H. Lei, P. Dubois, M. Manfait, and G.D. Sockalingum, "Intracellular applications of analytical SERS spectroscopy and multispectral imaging", *Chem. Soc. Rev*., 2008, **37**, 993-1000.
8. J. Gautier, E. Munnier, M. Soucé, I. Chourpa, and L. Douziech Eyrolles, "Analysis of doxorubicin distribution in MCF-7 cells treated with drug-loaded nanoparticles by combination of two fluorescence-based techniques, confocal spectral imaging and capillary electrophoresis", *Anal Bioanal Chem*, 2015, DOI:10.1007/s00216-015-8566-9.
9. A. Louie, "Multimodality imaging probes: design and challenges", *Chem. Rev.*, 2010, **110**, 3146-95.

THE EFFECTS OF GOLD NANORODS AND LASER IRRADIATION ON CANCER CELLS

V.V. Elagin[1], E.A. Sergeeva[2], M.L. Bugrova[1], and **E.V. Zagaynova[1]**

[1] Nizhny Novgorod State Medical Academy, Nizhny Novgorod, Russia, elagin.vadim@gmail.com
[2] Institute of Applied Physics of Russian Academy of Sciences, Nizhny Novgorod, Russia

Abstract. Gold nanoparticles are widely used in different biomedical areas. This presentation is focused on the challenge associated with applying nanoparticles for laser treatment of cancer cells. The first section of the study is devoted to penetration gold nanorods into cells. The influence of the stabilizing agents on the internalization efficiency is considered. The effect of laser irradiation of cells with gold nanorods is examined in the second part. Comparison of cells viability after treatment by continuous wave laser is investigated.

Using gold nanoparticles for laser treatment of cancer cells is a perspective and actual area. Among a huge set of the nanoparticles synthesized nowadays, the rod-shaped gold nanoparticles are of great interest. Nanorods have plasmon resonant peak in “tissue optical window”. Moreover they are proved to convert electromagnetic energy of incident light into thermal energy much better compared to nanospheres [1]. On the other hand, nanorods are known to penetrate into cells 3-5 times worse than spherical nanoparticles of the same size [2].

The performed research is devoted to study the interaction of the gold nanorods stabilized by biocompatible agents with cancer cells. Another goal is assessment of the laser irradiation effects of cancer cells with nanoparticles.

The work was carried out on human ovarian adenocarcinoma SKOV-3 cells. The gold nanorods (Sigma Aldrich, USA) used in this work have a plasmon resonance peak at 808 nm. The nanoparticles were stabilized by Pluronic F127, chitosan or polyethylene glycol with 6 kDa and 40 kDa molecular weight. Gold nanoparticles penetration was investigated by the transmission electron microscopy (TEM) and two-photon luminescence microscopy (TPL) techniques. To study cell viability after laser irradiation a continuous wave laser with 810 nm wavelength was used. The cells viability was estimated by MTT.

TPL microscopy showed that the nanoparticles stabilized by chitosan penetrated into cells the most efficiently (fig. 1). There were more luminescent objects in cells compared to the nanoparticles stabilized by other agents. The nanoparticles stabilized by PEG 40 kDa penetrated into cells less efficiently than chitosan stabilized particles. The nanoparticles stabilized by PEG 6 kDa and Pluronic F127 penetrated worse than those stabilized by other agents. The least amount of luminescent objects in cells was recorded in these nanoparticles. All nanorods solutions under study appear to have some common features. The amount of luminescent objects in cells grew with the increase of the incubation time. Based on the microphotographs obtained by TEM, the nanoparticles found in cells were divided into three types: single nanoparticles, large clusters and aggregates. Large clusters of nanoparticles represent groups of a large number of single nanorods located closely to each other. Aggregates are groups of closely packed nanoparticles, inside which single nanoparticles are impossible to separate. It is significant that single nanoparticles were found in cells less frequently than large clusters of nanoparticles or aggregates. Nanoparticles in cells were registered either free, or surrounded by membrane structures. The presence of a membrane was typical for aggregates and large clusters of nanoparticles. After one-hour incubation the amount of the nanoparticles stabilized by PEG 6 kDa and 40 kDa, in cells was higher compared to those stabilized by other agents. The increase of the incubation time was accompanied with the growing number of single nanorods. The number of aggregates in cells also increased. The nanoparticles stabilized by chitosan after one-hour incubation were presented in cells generally as aggregates. After 3 h the quantity of single nanoparticles and large clusters did not change, and the number of aggregates doubled. The time increase up to 6 h led to further growth of a number of aggregates. The nanoparticles stabilized by Pluronic F127 penetrated into cells less efficiently. Single nanorods and large clusters of nanoparticles were found even after 6 h incubation. To confirm that endocytosis promotes the penetration of nanoparticles into cells, the cells with nanoparticles were incubated for 3 h at low temperature (+4°C). The TPL microscopy analysis revealed no luminescent objects in cells. This regularity similar behavior was observed for the nanoparticles stabilized by all studied agents. However, the TEM found single aggregates and large clusters of the nanoparticles stabilized by Pluronic F127 and chitosan. PEG-stabilized nanoparticles showed the greatest

efficiency of penetration into cells at low temperature. It is significant that all aggregates and large clusters of nanoparticles found in cells had no surrounding membrane structures.

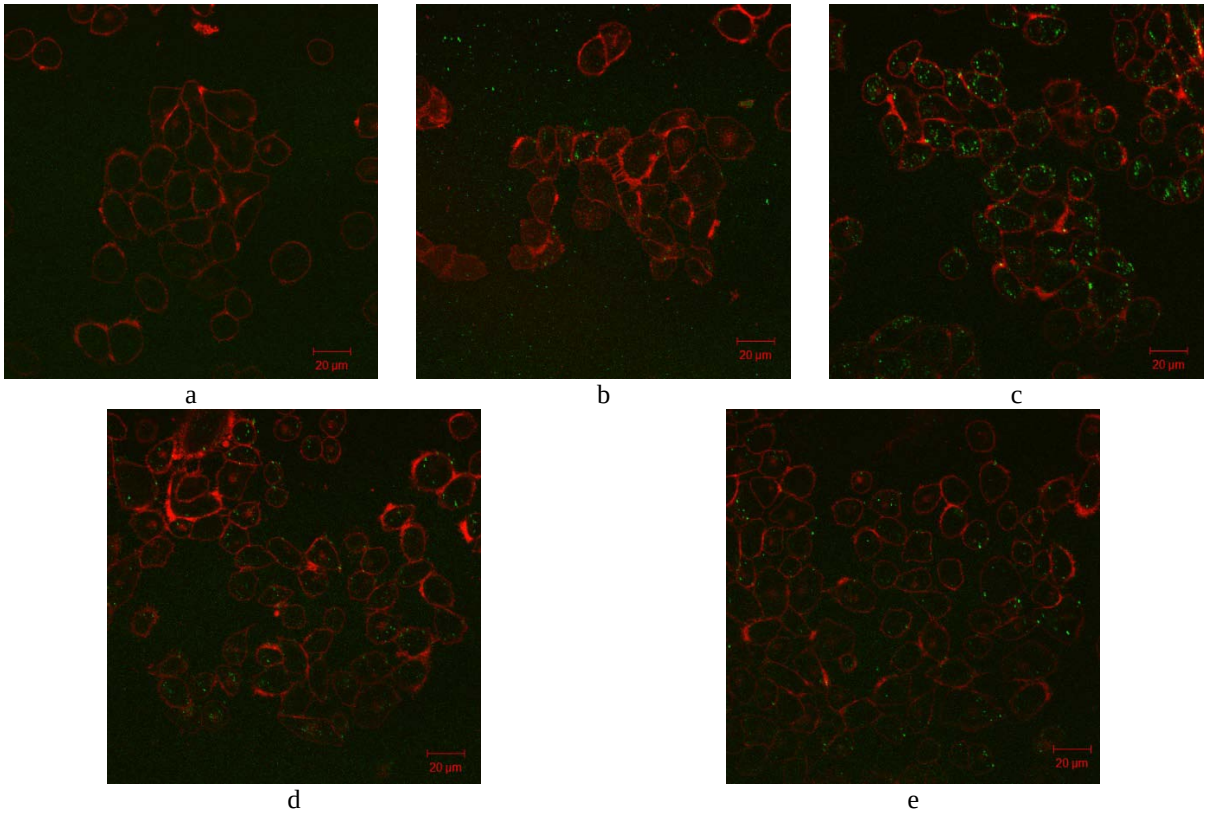

Fig. 1. Two-photon luminescent microscopy of the control cells (a) and cells incubated 3 h with the nanoparticles stabilized by Pluronic F127 (b), chitosan (c), PEG 6 kDa (d), PEG 40 kDa (e)

We also studied viability of cells with the nanoparticles after laser irradiation. MTT-assay showed that the continuous wave laser irradiation of cells without nanoparticles changed their viability insignificantly. Treatment of cells after 6 h incubation with nanorods led to decrease of amount of alive cells depending on stabilizing agents. It should be noted that viability of cells incubated with chitosan-stabilized nanorods decreased by 15% after irradiation at 10 W/cm^2. In contrast treatment of cells after incubation with PEG 6 kDa had stimulating effect. In the case of Pluronic and PEG 40 kDa stabilized nanorods laser irradiation provided no effect on cells viability.

In summary, we have shown that chitosan-stabilized nanoparticles penetrate efficiently at long-term period of incubation. Penetration of these nanoparticles is associated with endocytosis. PEG-stabilized nanoparticles penetrate well at early periods of incubation (up to 3 h) including low-temperature conditions. Laser irradiation of cells after incubation with nanorods does not lead to significant decrease of cells viability. Therefore, the next stage of our research will be focused on implementation of pulsed laser for cell irradiation.

Acknowledgements

This work was supported by the Ministry of education and science of the Russian Federation (project# 14.B25.31.0015).

References

1. N. Rozanova and J.Zhang, *Sci China Ser B: Chem*., 2009, **52**(10), 1559–1575.
2. B.D. Chithrani, A.A. Ghazani, and W.C. Chan, *Nano Lett*., 2006, **6**(4), 662–668.

Invited

INTERACTIONS OF NUCLEOSOMES WITH PROTEINS: SINGLE-PARTICLE FRET ANALYSIS

A.V. Feofanov[1,2], K.S. Kudryashova[1,2], A.V. Lyubitelev[1], O.V. Chertkov[1,2], D.V. Nikitin[1], M.P. Kirpichnikov[1,2], and **V.M. Studitsky[1,3]**

[1] Biological Faculty, M.V.Lomonosov Moscow State University, Moscow, Russia
avfeofanov@yandex.ru
[2]Shemyakin-Ovchinnikov Institute of Bioorganic Chemistry, Russian Academy of Sciences, Moscow, Russia
[3]Cancer Epigenetics Program, Fox Chase Cancer Center, Philadelphia, USA, Vasily.Studitsky@fccc.edu

Abstract. Results of development of single particle Forster resonance energy transfer (spFRET) microscopy approach to study structural reorganization of DNA in nucleosomes is presented. Design of mononucleosomal particles that are assembled from core histones and short DNA labeled with Cy3 and Cy5 fluorophores is discussed. Experimental setup for the measurements and analysis of freely diffusing single particles is described. Mononucleosomal particles are shown to be very useful to study various aspects of nucleosome interactions with different proteins including histone H1, chromatin remodelers and RNA polymerase (RNAP).

Mononucleosomal particles that are assembled from core histones and short DNA are simple but very useful experimental system to study many aspects of nucleosome interactions with different proteins including histone H1, chromatin remodelers and RNA polymerase (RNAP). Last achievements in fluorescent microscopy allows one to complement biochemical and molecular biology approaches with analysis of single nucleosomes and their complexes on the basis of Forster resonance energy transfer (FRET) effect, the technique known as single particle FRET (spFRET) microscopy. FRET efficiency is sensitive to a distance between two responsive fluorophores, donor and acceptor, in the range of 3–9 nm that is well consistent with a nucleosome size (*ca.* 10 nm). Single particle analysis facilitates the study of complex heterogeneous systems allowing recognition and separate characterization of structurally different subpopulations of nucleosomes and their complexes. Large sampling of measured particles provides statistically proved conclusions.

To measure fluorescence from a single molecular emitter, microscopes with high light transmission and sensitivity are required which are equipped with advanced low noise detectors such as avalanche photodiodes or EM CCD camera. In order to use an optical microscopy having spatial resolution of ca. 200 nm for investigation of single nucleosomes, these particles should be isolated in space or in time. In solution, it can be achieved by manifold dilution of nucleosomes and application of a confocal scheme of spatial signal filtration. Nucleosomes diffuse in solution and pass accidentally through the focus of the laser beam. During each given time interval only one nucleosome is in the focus. Fluorescence of Cy3 and Cy5 coming from a focal volume (*ca.* 1 femtoliter) is measured, and FRET efficiency is calculated. Up to 10^4 nucleosomes can be analyzed in this way during 10 minutes of a measurement.

For spFRET microscopy studies of nucleosome complexes with histone H1, mononucleosomes were constructed from core histones and DNA containing a strong 603 nucleosome-positioning sequence with solution-exposed 30-bp DNA linkers. These linkers were labeled with Cy3 and Cy5 fluorophores (one on each linker) (Fig. 1 A). Three variants of labeling were realized with different expected distances between Cy3 and Cy5. The labeled nucleosomes are characterized with low or very low FRET efficiency depending on relative positions of Cy3 and Cy5 in the linkers. A considerable increase in FRET efficiency manifests formation of complexes with histone H1 and helps to characterize equilibrium between two subpopulations, free nucleosomes and complexes with H1. This experimental system is demonstrated to be very convenient for comparative studies of nucleosome interactions with different variants of histone H1 and can be applicable for investigation of remodelers affecting interactions of H1 or conformation of linkers.

For investigation of a nucleosome structure during transcription with RNAP, nucleosomes were assembled from core histones and short DNA (603 sequence template) containing the T7A1 promoter. Cy3 and Cy5 were introduced in the non-transcribing DNA chain in order to provide contiguity of labeles in the neighboring coils of nucleosome DNA (Fig. 1 B). Three variants of labeling were realized: (i) close to the promoter-proximal boundary of a nucleosome; (ii) in the median part of a nucleosome; (iii) close to the promoter-distal boundary of a nucleosome. Up to 80-90% of the labeled nucleosomes (any variant of labeling) adopt a native conformation with high FRET between Cy3 and Cy5. Such labeling allows DNA structure reorganization to be monitored as changes in FRET efficiency in three

regions of a nucleosome. Labeled nucleosomes were shown to support transcription with RNAP. We present the results of comparison of structural organization of DNA in nucleosomes before and after transcription as well as in some elongation complexes obtained by stalling RNAP in distinct positions on the nucleosomal DNA during transcription (Fig. 1 B). Apart from the analysis of elongation complexes, these variants of labeled nucleosomes can be used to study effects of different remodelers on a nucleosome structure and transcription with RNAP.

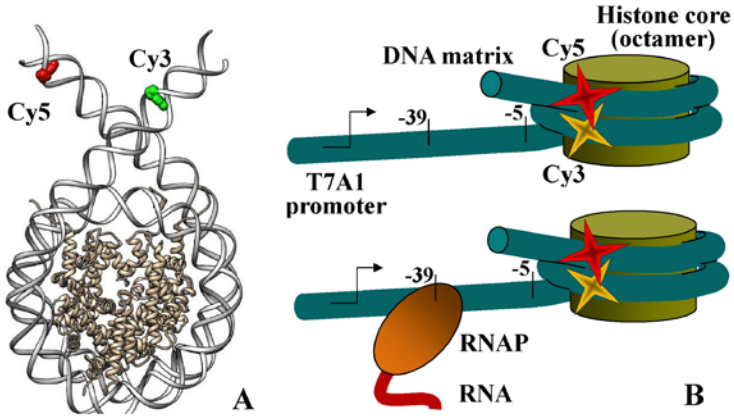

Fig. 1. Structures of labeled mononucleosomes that are used for investigation of complexes with histone H1 (A) and elongation complexes with RNAP (B) by spFRET microscopy

Acknowledgements

This work was funded by the Russian Science Foundation (grant 14-24-00031).

References

1. D.A. Gaykalova, O.I. Kulaeva, N.A. Pestov, F.K. Hsieh, and V.M. Studitsky, *Methods Enzymol.*, 2012, **512**, 293-314.
2. D.A. Gaykalova, O.I. Kulaeva, V.A. Bondarenko, and V.M. Studitsky, *Methods Mol. Biol.*, 2009, **523**, 109-123.
3. K.S. Kudryashova, O.V. Chertkov, D.V. Nikitin, N.A. Pestov, O.I. Kulaeva, A.V. Efremenko, A.S. Solonin, M.P. Kirpichnikov, V.M. Studitsky, and A.V. Feofanov, *Methods Mol. Biol.*, 2015, in press.
4. A.V. Feofanov, K.S. Kudryashova, O.V. Chertkov, D.V. Nikitin, N.A. Pestov, O.I. Kulaeva, V.M. Studitsky, and M.P. Kirpichnikov, *Proceedings of the 2nd International Multidisciplinary Microscopy and Microanalysis Congress*, E.K. Polychroniadis, A.Y. Oral, M. Ozer (Eds.), *The Springer Proceedings in Physics*, 2015, in press.

Invited

OPTICAL MONITORING OF TRANSCUTANEOUS PARTICLE DELIVERY USING FRACTIONAL LASER MICROABLATION

E.A. Genina[1,2]*, **A.N. Bashkatov**[1,2], **E.V. Volkova**[1], **I.Yu. Yanina**[1], **N.A. Navolokin**[3], **L.E. Dolotov**[1], **P.A. Timoshina**[1], **V.D. Genin**[1], **G.S. Terentyuk**[1], **Yu.I. Svenskaya**[1], **A.B. Bucharskaya**[3], **V.V. Kochubey**[1], **A.P. Popov**[4], **D.A. Gorin**[1], **G.B. Sukhorukov**[1,5], **and V.V. Tuchin**[1,2,6]

[1] Remote Controlled Theranostic System Lab, Saratov State University, Saratov, Russia,
*eagenina@yandex.ru
[2] Tomsk State University, Tomsk, Russia
[3] Saratov State Medical University, Saratov, Russia
[4] University of Oulu, Finland
[5] The Queen Mary University of London, London, UK
[6] Institute of Precise Mechanics and Control of RAS, Saratov, Russia

Abstract. We are presenting the results of transcutaneous delivery of upconversion particles (UPs) and $CaCO_3$-particles doped with the different contrast agents. Fractional laser microablation of skin was provided for effective delivery of the particles to the depth about 300 μm. For monitoring of particle localization during two weeks, optical coherence tomography, reflectance spectroscopy, fluorescence spectroscopy of skin *in vivo*, luminescence of UPs in skin, and light microscopy of histological specimens were used. For enhancement of the particle visualization, tissue optical clearing method was applied. Results have shown that the particles may be monitored in the dermis with different optical techniques during 8 days.

Introduction

Fractional laser microablation (FLMA) is one of the relatively safe and effective method used to administer micro- and nanoparticles into the skin at sufficiently large depth in comparison with surface ablation and mechanical treatments because of the low area of skin damage and, therefore, reduced risk of infection [1, 2]. We are presenting results on transcutaneous delivery of composite microparticles (Y_2O_3:Yb, Er, $CaCO_3$-Fe_2O_3 and $CaCO_3$-ZnCdS) *in vivo* using the FLMA of the skin surface with the view of developing a reliable and reproducible method of particle delivery in the tissue.

Methods and materials

For transcutaneous delivery we used upconversion particles (UPs) Y_2O_3:Yb, Er [3] and $CaCO_3$-particles doped with nanoparticles Fe_2O_3 or ZnCdS. The UP average size was about 1.6 μm. The $CaCO_3$ particle average size was about 2 μm. The suspensions of powder in water with concentration 0.5 g/mL were used.

Fractional laser microablation of skin was provided by a system based on a pulsed Er:YAG laser with the following parameters: the wavelength 2940 nm, the pulse energy 3.0 J, the pulse duration 15ms. 64 vertical micro-channels were created in the skin in the area with the dimensions of 8×8 mm^2. For delivery of the particles mechanical massage or sonophoresis with a low-frequency therapeutical ultrasound during 2 min was used. *In vivo* rat skin was studied.

For monitoring of the treated skin sites during two weeks, the following optical methods were used: optical coherence tomography (OCT) (~930 nm), reflectance spectroscopy (400-2000 nm), fluorescent spectroscopy of skin *in vivo* (under excitation at 405 nm for visualization of $CaCO_3$-ZnCdS), luminescence of UPs in the range 640-690 nm under excitation at 980 nm, and light microscopy of histological specimens stained with hematoxylin and eosine. Skin optical clearing with Omnipaque during 30 min was used for enhanced visualization of UP luminescence.

Results and Conclusion

Images of histological sections of the studied skin sites are presented in Figure 1. Areas of particle localization are marked with arrows. Staining has allowed enhancing the image contrast of skin with $CaCO_3$-Fe_2O_3 particles (c).

Figure 2 show OCT images of rat skin *in vivo* just after FLMA (a) and particle delivery (b–d). All studied particles filling the channels were visualized with a good contrast. $CaCO_3$-Fe_2O_3 (c), and $CaCO_3$-ZnCdS (d) microparticles created the reflecting screen on the skin surface and in the channel. Sonophoresis allowed increasing the depth of the particle penetration and better filling of the channels. Contrast of OCT-visualization of the particles inside skin was saved during 3–4 days.

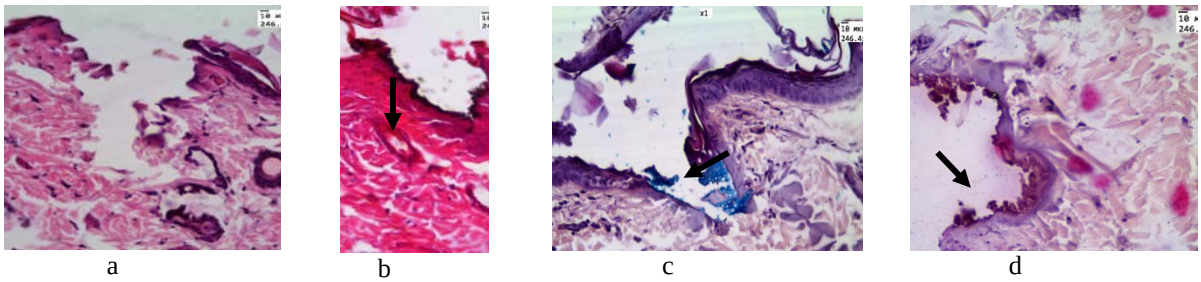

a b c d

Fig. 1. Histological sections of rat skin *in vivo* after FLMA (a) and particle delivery: (b) UPs with sonophoresis, (c) $CaCO_3$-Fe_2O_3, and (d) $CaCO_3$-ZnCdS with massage (×246.4)

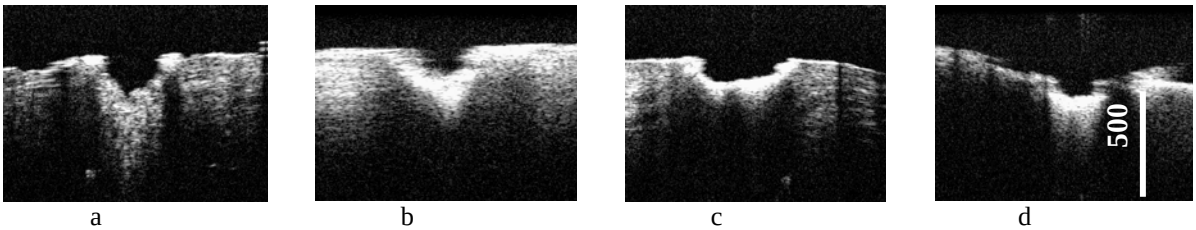

a b c d

Fig. 2. OCT images of rat skin *in vivo* after FLMA (a) and particle delivery: (b) UPs with sonophoresis, (c) $CaCO_3$-Fe_2O_3, and (d) $CaCO_3$-ZnCdS with massage

UP luminescence peaks was observed for 8 days with a gradual decrease in the intensity. Optical clearing allowed for increasing the level of the signal up to 1.3 folds. A fluorescence peak of $CaCO_3$-ZnCdS particles on the background of skin autofluorescence was observed for 5 days with a gradual decrease in the intensity.

Reflectance spectroscopy was used for monitoring of skin physiological reaction on FLMA and delivered particles. The intensity of reflectance spectrum in the range 400-650 nm is related to skin erythema development. For longer wavelengths (900–2000 nm), reflectance is sensitive to water content in skin tissues, i.e. characterizes skin edema. Analysis of the spectra has shown decreasing of skin erythema and edema in two days after FLMA for control group (FLMA alone) and for treated groups (FLMA+particles) as well. Thus, the studied particles at used concentrations do not have noticeable additional inflammatory effect on the skin.

Fractional laser microablation was used for enhancement of transcutaneous delivery of different composite particles. For monitoring of the particle delivery and localization inside rat skin *in vivo* during two weeks, optical coherence tomography, luminescent/fluorescent spectroscopy, and light microscopy of histological specimens were used. Results have shown that the particles may be seen in dermis during 5–8 days. Reflectance spectroscopy can be used for evaluation of skin physiological reaction on FLMA injury and particle presence.

Acknowledgements

The work was carried out under the partial support byRussian Federation Governmental No. 11.G.34.31.0030 designed to support scientific research projects implemented under the supervision of leading scientists at Russian institutions of higher education.

References

1. B.D. Zelickson, S.E. Walgrave, M.Y.H. Al-Arashi, G.B. Altshuler, I.V. Yaroslavsky, J.J. Childs, R.H. Cohen, A.V. Erofeev, E.F. Depina, M.Z. Smirnov, D.A. Kist, and D.R. Tabatadze, *Lasers Surg. Med*., 2009, **41**, 634-642.
2. E.A. Genina, A.N. Bashkatov, L.E. Dolotov, G.N. Maslyakova, V.I. Kochubey, I.V. Yaroslavsky, G.B. Altshuler, and V.V. Tuchin, *J. Biomed. Opt.*, 2013, **18**(11), 111406.
3. A.P. Popov, A.V. Karmenyan, A.V. Bykov, E.V. Khaydukov, A.V. Nechaev, O.A. Bibikova, V.Ya. Panchenko, V.A. Semchishen, V.N. Seminogov, A.S. Akhmanov, V.I. Sokolov, M.T. Kinnunen, V.V. Tuchin, and A.V. Zvyagin, *Proc. of OSA-SPIE*, 2013, **8801**, 88010C.

Invited

IMAGING OF INTRACELLULAR ION CONCENTRATION BY FLUORESCENCE LIFETIME IMAGING (FLIM) IN LIVING CELLS

T. Gensch

Institute of Complex Systems 4 (ICS-4; Cellular Biophysics) Forschungszentrum Juelich, Leo-Brandt-Str., 52428 Juelich, Germany, t.gensch@fz-juelich.de

Abstract. The use of fluorescence microscopy for the determination of the intracellular concentration of physiologically relevant ions is a valuable and well-established tool in cell biology. Commonly, it is based on the read out of fluorescence intensity, which, however, does not allow to obtain absolute concentration values, but specially designed ratiometric sensors are required. Alternatively, fluorescent sensors with a fluorescence lifetime contrast can be used. In this contribution the principles of fluorescence lifetime imaging will be presented together with examples of organic dyes or genetically encoded fluorescent sensors of pH, Ca^{2+} and Cl^- and their applications in living cells and tissue.

Introduction

The concentration of ions in compartments, organelles, and the cytosol of mammalian cells is a fundamental parameter for cell physiology setting affecting most biochemical reactions of life and many other vital processes like intra- and intercellular signal transduction or enzyme reactivity. In the past decades a multitude of analytical and microscopical fluorescence techniques have been developed allowing – in conjunction with the in-parallel designed fluorescent sensors – the non-invasive determination of ion concentrations in living cells, tissue and even organisms (bacteria, plants, animals). One method especially well-suited for quantitative measurements is fluorescence lifetime imaging, since the fluorescence lifetime does not depend on the concentration of the fluorescent sensor or the excitation intensity. This contribution contains the basics of the method, characterization of fluorescent ion sensors and their application in studies on living cells and tissues

Fluorescence Lifetime Imaging

The fluorescence lifetime of fluorescent molecule can be determined in three different ways – 1. by direct, fast time-gated detection, 2. by intensity modulation of a cw laser and comparison of the frequency of excitation and fluorescence signal and 3. by time correlated single photon counting (TCSPC) [1]. The latter method gives the most precise lifetime results – especially for non-monoexponential fluorescence decays, which is almost exclusively found for fluorophores in cellular environment – and TCSPC is also applied in my lab [2]. The excitation source is a pulsed laser (fs-ps) with high repetition rate (MHz) – here a Ti:Sapphire laser emitting near-infrared light used for two-photon excitation. The detector (photomultiplier, Avalanche photodiode or a hybrid detector) works in single photon counting mode and registers at most one photon per excitation pulse. In practice the detection rates are 20 to 1000 times lower than the excitation rates. Special electronics allows the precise determination of the temporal distance between the excitation pulse and the photon registration event. Repeated excitation and registration allows to build up the photon arrival histogram which can be analyzed – most commonly by a sum of exponential functions. Such fluorescence intensity decay is measured at every pixel of the fluorescence image of the sample realized by scanning the focused excitation laser across the sample. Two-photon excitation has the advantage of an intrinsic three-dimensional imaging capability, a lower phototoxicity and the possibility to image deep into biological tissue (200 μm and more).

Fluorescent biosensors

Fluorescent organic molecules often show a pH-dependence of their fluorescence properties including the fluorescence lifetime, but other ions, like Na^+, K^+, Ca^{2+} or Cl^-, do not. Instead, specially developed and synthesized derivatives of fluorophores (e.g. addition ion-binding groups that change the fluorescence properties upon binding or molecular extensions making the organic molecules cell membrane permeable) are used. A second class of fluorescent ion sensors based on fluorescent proteins (FPs, Green Fluorescent Protein (GFP) and such) is extremely powerful because of the simple ways to express and target them in biological cells and tissue. Also FPs often show pH-dependent fluorescence properties, but they are mostly indifferent to other ions. Fusing ion-sensitive protein domains to special conformational sensitive fluorescent proteins or design sensor based on Förster Re-

sonance Energy Transfer enables the creation of FP-based sensors for other ions. Development, modification and photophysical characterization of both types of fluorescent sensors in solution and cellular environment is a crucial task in ion imaging [3-6].

Intracellular ion concentration imaging with FLIM in living cells and tissue

Intracellular ion imaging by fluorescence microscopy has been successfully performed by the author's lab for pH [7], Ca^{2+} [7–9] and Cl^- [2, 10–12]. An overview of the different results in primary cells, cell-culture cells as well as in neuronal tissue will be given in this contribution. An example – the FLIM-image of an acute mouse retina slice stained with the Cl^--sensitive dye MQAE [13] is shown in Figure 1. The boxed area shows a zoom into the INL layer of the retina where neighboring bipolar cells with different intracellular Cl^- concentrations are depicted (red: short fluorescence lifetime; blue: long fluorescence lifetime) [14].

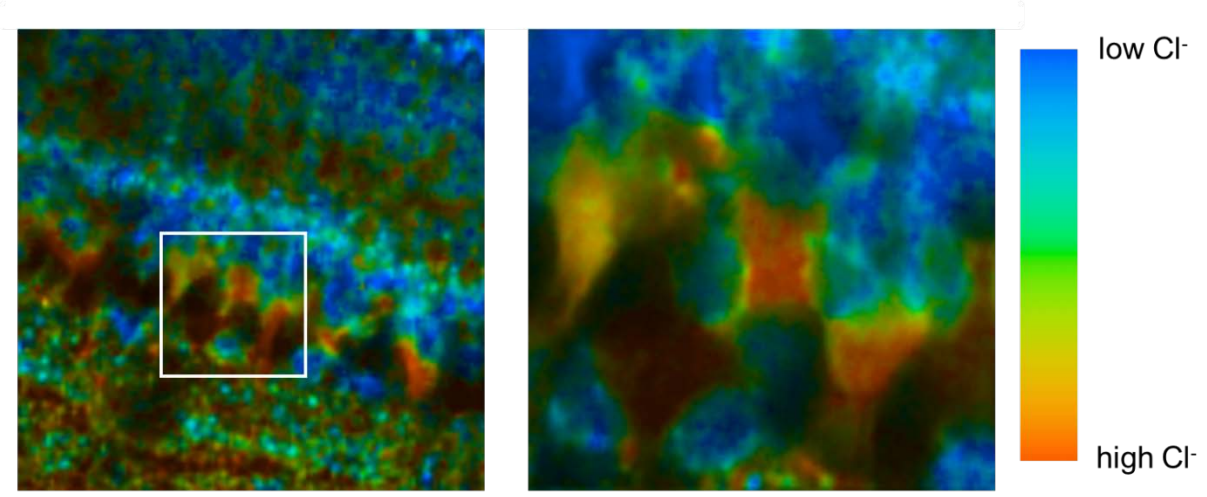

Fig. 1

References

1. W. Becker, *Advanced Time Correlated Single Photon Counting Techniques. Springer Series in Chemical Physics 81*, W. Becker ed. Springer, Berlin, 2005.
2. T. Gensch, V. Untiet, A. Franzen, P. Kovermann, and C. Fahlke, *Advanced Time-Correlated Single Photon Counting. Springer Series in Chemical Physics 111*, W. Becker ed. ,Springer, Berlin, 2015 chapter 4.
3. M. Cotlet, J. Hofkens, M. Maus, T. Gensch, J. Michiels, G. Dirix, M. van Guyse, J. Vanderleyden, A.J.W.G. Visser, and F.C. De Schryver, *J. Phys.Chem. B*, 2001, **105**, 4999-5006.
4. J. Potzkei, M. Kunze, T. Drepper, T. Gensch, K.-E. Jaeger, and J. Büchs, *BMC Biol*., 2012, **10**, 28.
5. A. Geiger, L. Russo, T. Gensch, T. Thestrup, S. Becker, K.-P. Hopfner, C. Griesinger, G. Witte, and O. Griesbeck, *Biophys. J*., 2012, **102**, 2401-2410.
6. M. Wingen, J. Potzkei, S. Endres, G. Casini, C. Rupprecht, C. Fahlke, U. Krauss, K.-E. Jaeger, T. Drepper, and T. Gensch, *Photochem. Photobiol. Sci*., 2014, **13**, 875-883.
7. C. Biskup and T. Gensch, *Fluorescence Lifetime Spectroscopy and Imaging. Principles and Applications in Biomedical Diagnostics*, D. Elson, P.W.M. French and L. Marcu, eds. Taylor & Francis, 2014, pp. 555-566.
8. S. Dangwal, B.H. Rauch, T. Gensch, L. Dai, E. Bretschneider, T. Vogelaar, K. Schrör, and A.C. Rosenkranz, *Arterioscler. Thromb. Vasc. Biol*., 2011, **31**, 624-633.
9. M. Hoff, S. Balfanz, P. Ehling, T. Gensch, and A. Baumann, *FASEB J*., 2011, **25**, 2482-2491.
10. H. Kaneko, I. Putzier, S. Frings, U.B. Kaupp, and T. Gensch, *J. Neurosci*., 2004, **24**, 7931-7938.
11. D. Gilbert, C. Franjic-Wuertz, K. Funk, T. Gensch, S. Frings, and F. Moehrlen, *Int. J. Dev. Neurosci*., 2007, **25**, 479-489.
12. K. Funk, A. Woitecki, C. Franjic-Wuertz, T. Gensch, F. Moehrlen, and S. Frings., *Mol. Pain*, 2008, **4**, 32-43.
13. H. Kaneko, I. Putzier, S. Frings, and T. Gensch, *PCalcium-activated chloride channels. Series Current Topics in Membranes*, 2002, **53**, 163-185.
14. D. Kaschuba, C. Aretzweiler, F. Müller, and T. Gensch, *unpublished* 2006.

DISSOLUTION OF BIOCOMPATIBLE SILICON NANOPARTICLES IN AQUEOUS SUSPENSIONS DEFINED BY THEIR PHOTOLUMINESCENCE

M.B. Gongalsky, Yu.I. Bezsudnova, L.A. Osminkina, and **V.Yu. Timoshenko**

M.V. Lomonosov Moscow State University, Faculty of Physics, Moscow, Russia
mgongalsky@gmail.com

Abstract. Silicon nanoparticles are known to be promising biocompatible and biodegradable agents for both diagnostics and therapy of cancer. Efficient photoluminescence allows to achieve optical bioimaging, while generation of singlet oxygen by nanoparticles opens framework for cancer photodynamic therapy. The biodegradability of nanoparticles is demonstrated to be related to their dissolution in aqueous suspensions, but physicochemical processes are still unclear. This work is devoted to qualitative characterization of the process and estimation of key parameters, i.e. dissolution rate, photoluminescent quantum yield, size of nanoparticles, surface composition, etc. during storage in aqueous mediums by means of photoluminescent spectroscopy.

Introduction

Silicon nanoparticles (SiNPs) attract attention of physicists and biomedical scientists due to their high biocompatibility and biodegradibility [1]. They possess efficient photoluminescence (PL) in red and near infrared region of spectrum with typical quantum yield about 5–10%. SiNPs were demonstrated to be useful contrast agents for bioimaging both *in vitro* [2] and *in vivo* [3]. Very low PL lifetime of SiNPs by comparison with biological autofluorescence opens pathways to lifetime selective imaging, which provides really high contrast unlike conventional techniques [4]. Another advantage of SiNPs is their ability to kill cancer cells via singlet oxygen generation [5]. Thus, SiNPs potentially can provide theranostic approach to cancer treatment combining photodynamic therapy and optical bioimaging *in vivo*.

Important aspect for biomedical applications of SiNPs is their biodegradability, which is provided by dissolution of SiNPs in aqueous medium. Unlike silica (amorpous SiO_2) nanoparticles SiNPs can dissolve into water forming silicic acid due to the breakage of relatively weak Si-Si bonds inside the nanoparticle. This process depends on various factors, i.e. diameter of SiNPs, their local concentration, flow velocity of external liquid, pH level, surface composition and essentially biological factors. The aim of this work is to analyze influence of some factors to the dissolution process in modelling systems by means of photoluminescent spectroscopy.

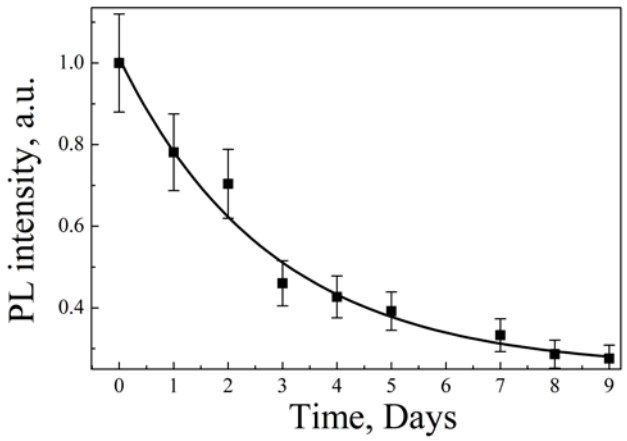

Fig. 1. PL intensity of SiNPs as a measure of their concentration versus time of storage in aqueous suspension

Experimental

Aqueous suspensions of SiNPs were made by wet grinding of microporous silicon layers in the planetary mill. Porous silicon was fabricated by electrochemical etching of monocrystalline silicon wafers with specific resistivity 1...10 Ohm*cm in hydrofluoric acid mixed with ethanol. Then a set of aqueous suspension was made by application of centrifugation and ultrasonic treatment. In order to investigate influence of the factors separately we made some subsets characterized by variation of the

single parameter, i.e. diameter of SiNPs, concentration of SiNPs, speed of the suspension stirring and different coating (uncoated SiNPs and dextran-coated). Then modification of photoluminescence, optical absorption, hydrodynamic diameter of SiNPs was investigated during the storage in aqueous medium.

First of all, concentration of SiNPs in suspensions did not influence a lot to the time of dissolution up to value of 10 g/l which exceeds biocompatible limit and dangerous for some cells. This means that factor of SiNPs concentration can be important only in huge agglomerates of SiNPs inside the human body, which can be presumably formed in filtering organs, i.e. kidneys, spleen and liver. Opposite tendency takes place for diameter of SiNPs, since smaller SiNPs (diameter is about 50 nm) dissolve 2 times faster than 200-nm ones. It allows to control biodegradability of SiNPs by alteration of their size. Please note, that every SiNP is highly porous and it consists of 3-5 nm silicon nanocrystals disjointed by nanometer-scale pores. Another important factor is the flow speed of aqueous suspension, since it was found to be able to reduce time of dissolution tenfold or even more. This observation is accordant with fast dissolution of SiNPs in blood flow by comparison with intracellular space found in the experiments *in vivo* [6]. Dextran coating essential for high blood compatibility of SiNPs was found to slow down dissolution of SiNPs only in suspensions with low stirring speed. This can be explained by weakness of the binding between dextran molecules and SiNPs surface and low part of the coated surface. It means that dextran significantly increase blood biocompatibility of the SiNPs, but almost has no affect dissolution properties of SiNPs. Situation can be different in agglomerated of SiNPs in the places with limited diffusion of liquids.

Modelling

Dissolution process of SiNPs was numerically simulated by a set of kinetic equations including non-linear diffusion equation with the sources of dissolved matter inside the SiNPs. Each SiNP represents as a porous sphere in the liquid flow, porosity of the SiNPs is introduced as a spherically uniform function of radius increasing during the dissolution process. This leads to the increase of effective diffusion coefficient, which eventually (after complete dissolution of the SiNP) turns to be equal to regular diffusion coefficient of silicic acid in water. Numerical results confirmed experimental results and conclusions made in the literature.

Acknowledgements

M.B. Gongalsky is grateful to Russia President Grant Council for support by means of scholarship for young researches.

References

1. A. Durnev, A. Solomina, E. Shreder, E. Nemova, O. Shreder, N. Daugel'-Dauge, A. Zhanataev, V. Veligura, L.A. Osminkina, M.B. Gongalsky, and V.Yu. Timoshenko, *Int. J. Biomed. Nanosci. Nanotech.*, 2010, **1**, 70-86.
2. L.A. Osminkina, K.P. Tamarov, A.P. Sviridov, R.A. Galkin, M.B. Gongalsky, V.V. Solovyev, A.A. Kudryavtsev, and V.Yu. Timoshenko, *J. Biophot.*, 2012, **5**(7), 529-535.
3. J.H. Park, L. Gu, G. von Maltzahn, E. Ruoslahti, S.N. Bhatia, and M.J. Sailor, *Nat. Mater.*, 2009, **8**, 331-336.
4. L. Gu, D.J. Hall, Z. Qin, E. Anglin, J. Joo, D.J. Mooney, S.B. Howell, and M.J. Sailor, *Nat. Commun.*, 2013, **4**, 2326.
5. L.A. Osminkina, M.B. Gongalsky, A.V. Motuzuk, V.Yu. Timoshenko, and A.A. Kudryavtsev, *Appl. Phys. B*, 2011, **105**, 665-668.
6. H.A. Sanders, *Porous silicon for biomedical applications*, Woodhead Pub., Cambridge, 2014, p. 129.

THERANOSTIC SYSTEMS COMBINED SERS BASED SENSING AND DRUG DELIVERY

I.Y. Stetciura[1], D.N. Bratashov[1], A.M. Yashchenok[1], G.B. Sukhorukov[2], and **D.A. Gorin[1]**

[1] Saratov State University, Saratov, Russia, gorinda@mail.ru
[2] School of Engineering and Materials Science, Queen Mary University of London, United Kingdom

Abstract. The current problems connected with application of Surface Enhancement Raman Scattering (SERS)-sensors for biomedicine were discussed. It was shown, that Layer by Layer (LbL) method allows fabrication of SERS platforms with high reproducibility of enhancement factor to increase signal/noice ratio. LbL approach opens an avenue to implement a novel type of theranostic systems combining SERS based sensing and drug delivery in one entity. The area of encapsulation development towards smart multifunctional theranostic systems could bring benefits for personalized medicine and should minimize costs and resources at preclinical and clinical study in pharmacology while testing new bioactive compounds.

Detection of pharmaceutically important molecules in tiny amounts is one of actual task of bioanalytical science. Current methods of detection of important analytes are based on chromatographic or spectrophotometric approaches and have limits in sensitivity, time and in vivo detections. Alternative approach for detection of biologically important substances is Raman spectroscopy, which has been used for biomedical applications [1, 2] due to noncontact measurements and direct identification of substances using nonlabeled detection what is achieved by comparison with calculated or premeasured spectra.

The effect of Raman scattering is a change in wavelength of light, scattered by some material, due to interaction of electromagnetic waves and mechanical vibrations of chemical bonds in analyzed sample via the sample electrical polarization. The effect is very weak, so it requires high power of incident light that can damage the analyzed sample or long spectra acquisition times, making impractical molecular microscopy with acquisition of Raman spectra in each point of sample or not allowing to investigate rapid chemical processes [3, 4]. These difficulties can be overcome achieved by "so-called" Surface Enhancement Raman Scattering (SERS) [5, 6]. SERS can be achieved by interaction of light with analyzed sample near a special active surface. There are two main mechanisms of enhancement discussed so far in literature. First one is so called "physical" effect due to large increase of electromagnetic field amplitude in the closed proximity of a structured conducting surface. This effect appears due to synchronous confined motion of electron cloud and electromagnetic field called as the plasmon resonance. Between electrons and electron-free parts of conducting surface appears new field with much larger amplitude in a close proximity that rapidly decreases with the distance from surface ("near-field"). The second mechanism is so called "chemical" type of SERS. It requires formation of rather strong chemical bond and charge transfer path along that bond between surface and analyzed molecule. This kind of SERS process include excitation of electrons by incident light in active surface, charge transfer to analyzed molecule, change of electronic state due to vibrations in molecule, charge transfer back to surface and relaxation there to initial state with the generation of new scattered photon, i.e. new electromagnetic wave with changed wavelength. Or it can be simplified with semiconducting surface by simultaneous transfer of electron and vacant electron state (hole) forming the exciton to analyzed molecule and electron relaxation on molecule itself, that makes this process much more probable. So the good enhancement of this type is usually achieved at semiconductor surface, either in form of bulk material or in form of nanoparticles [7]. The best performance require stable nanoparticle, either in ultrasmall fullerene-like form without dangling bonds, or oxide semiconductor in highest oxidation state [8], and also with self-cleaning effects in materials like TiO2.

SERS sensors allow us go to in vivo detection because energy dose, that is a product of laser power and integration time, do not effect on the cell and tissue [9, 10]. The structure, shape and size of SERS platforms are defined by applications. Nanostructured surface can be obtained by layer-by-layer (LbL) assembly method [10]. The LbL technique allows us to control nanoarchitecture of SERS platform and has high potential for expansion of SERS platform functionality [9, 11–15], for example, use of carbon structures as one of structure layers of core-shell structure allows application of such platforms in hyperthermia due to high thermal conductivity of graphene-like substances [11]. The additional benefit of ordered carbon structures is the existence of easily recognizable peak in Raman spectrum that can be used as a nonbleached label in high scattering environments such as cells, biological liquids and tissues. Microstructures described above are attractive objects of research on the following rea-

sons: they are easily obtained in a large scale; there are many “hot spots” on a surface of such platforms. Therefore, good reproducibility for SERS measurements can be expected. Such particles are usually placed on to glass or other substrate for measurement and after that are used as platforms, that leads to decreasing of contact between these particles and target analyte and can limit analyte concentration on a platform. This problem can be solved, for example, by coupling of SERS spectroscopy and optical tweezers. Using of optical tweezers for platform delivery in a required place of a cell or tissue can be used [16].

Development of such new remote control sensors for implementation of biological processes monitoring in living cells is important for main pathophysiological processes understanding and, therefore, for improvement of modern medicine and pharmacology techniques. Biocompatibility of sensors can be reached by means of use of nontoxical materials for SERS platforms. So popular biocompatible basis of the platforms obtained by a layer-by-layer method is the calcium carbonate [11, 12]. Use of a calcium carbonate allows to carry out capsulation and delivery of medicinal substances into pores of such platform. Plasmon hollow shells that were made by layer-by-layer assembly [13], can have several functions: delivery of medicinal substances and platform for SERS imaging for research of processes inside cells and control of intracellular drug delivery. The spherical platforms obtained by layer-by-layer technology were used for investigation of scaffold materials which used for cell growing [11]. This technology can be used for highly sensitive monitoring of cell in situ [9].

SERS-sensors based on microparticles are hard and inflexible for in vivo applications, but suitable for remote control and drug delivery. Nanosized encapsulated SERS-sensors are more mobile, but have low capacity for drug delivery and must be used at high concentrations for remote controle. At the best of our knowledge there is no one commercial available SERS-sensors modified by capsulation approaches that slow down progress in real-world application the SERS-sensors.

Encapsulated SERS platform demonstrates a good potential for selective detection of compounds. LbL approach enables to construct core-shell structures where “hot-spots” are placed on outer layer and provide detection of analytes and allows fabrication of encapsulated SERS platforms with high reproducibility of enhancement factor to increase signal/noice ratio. The major advantage over most of conventional detection methods based on fluorescence signaling is related with possibility to use multifunctionality while assembling SERS platform for multiple detection of different components. These sensitive platforms encapsulated in one entity, or in other words in one core/shell structure includes carbon-based ordered structures, magnetite nanoparticles, gold and silver nanoparticles. As shown above SERS sensors are used for hyperthermia treatment of cancer. Promising approach is sought when using of inorganic microparticles as template for SERS surface preparation that increases effectiveness of SERS sensors. Surface functionalization of SERS sensors can improve selectivity in detection, biocompatibility and also could contribute in facilitation of cell uptake process. A porous core or shell used as substrate for SERS platform fabrication could be exploited for drug capsulation while surface functionalization promotes intracellular delivery.

LbL encapsulation approach opens an avenue to implement a novel type of theranostic systems combining SERS based sensing and drug delivery in one entity. SERS platform produced by LbL method would be perspective for applications in medicine for carrying out preclinical and clinical study and while medical treatment is on agenda these structure could contribute in curing by releasing drugs which could be of importance, for example for treatment of diabetes or cancer. For example, the SERS platforme can be used to determine the glucose level and response by injecting encapsulated insulin at needed concentrations. Identification of the tumor cells coupled with release photodynamic dyes in close proximity of should facilitate treatment of cancerous cells reducing side effects.

We suggest that combination of SERS based sensing and smart drug delivery could be realized via encapsulation in one construct [15]. It can be obtain the systems enabling measurement of signal and dose controlled release at designated site. Smart multifunctional theranostic systems could bring benefits for personalized medicine and should minimize costs and resources at preclinical and clinical study in biomedicine while testing new bioactive compounds.

Acknowledgements

The reported study was partly supported by RFBR № 15-29-01172 and Government of the Russian Federation (grant №14.Z50.31.0004 to support scientific research projects implemented under the supervision of leading scientists at Russian institutions and Russian institutions of higher education).

References

1. J. Popp, C. Kraft, and T. Mayerhoefer, *Optik&Photonik*, 2011, **6**, 24-28.
2. C. Mallidis, V. Sanchez, J. Wistuba, et al, *Hum Reprod Update*, 2014, **20**, 403-414.
3. A.M. Yashchenok, D.N. Bratashov, D.A. Gorin, et al, *Adv Funct Mater*, 2010, **18**, 3136-3142.
4. D.N. Bratashov, A. Masic, A.M. Yashchenok, et al, *J Raman Spectrosc*, 2011, **42**, 1901-1907.
5. S. Schluecker, *Angew Chem Int Ed*, 2014, **53**, 4756-4795.
6. B. Sharma, M.R. Ma, K. Glucksberg, and R.P. Van Duyne, *J Am Chem Soc*, 2013, **135**, 17290-17293.
7. X. Wang, W. Shi, G. She, and L. Mu, *Phys Chem Chem Phys*, 2012, **14**, 5891-5901.
8. I. Alessandri and L.E. Depero, *Small*, 2014, 1294-1298.
9. A. Yashchenok, A. Masic, D. Gorin, et al, *Small*, 2013, **9**, 351-356.
10. G. Decher, *Science*, 1997, **277**, 1232-1237.
11. I.Y. Stetciura, A.V. Markin, A.N. Ponomarev, et al, *Langmuir*, 2013, **29**, 4140-4147.
12. B.V. Parakhonskiy, Yu.I. Svenskaya, A.M. Yashchenok, et al, *Colloids Surf B*, 2014, **118**, 243-248.
13. W.F. Dong, G.B. Sukhorukov, and H. Moehwald, *Phys Chem Chem Phys*, 2003, **5**, 3003-3012.
14. A. Yashchenok, A. Masic, D. Gorin, et al, *Small*, 2015, **11**, 1320–1327.
15. I.Y. Stetciura, A.V. Markin, D.N. Bratashov, et al, *Cur Opinion in Pharmacology*, 2014, **18**, 149–158.
16. I. Stetciura, A. Yashchenok, A. Masic, et al, *Analyst*, 2015, under revision.

TWO-COLOR FLUORESCENT PROTEIN-BASED REPORTER FOR NONSENSE-MEDIATED mRNA DECAY

N.G. Gurskaya[1,2], **A.P. Pereverzev**[1], and **K.A. Lukyanov**[1,2]

[1] Institute of Bioorganic Chemistry, Miklukho-Maklaya 16/10, 117997 Moscow, Russia; ngurskaya@mail.ru
[2] Nizhny Novgorod State Medical Academy, Minin Sq. 10/1, 603005 Nizhny Novgorod, Russia

Abstract. Nonsense-mediated mRNA decay (NMD) is an evolutionarily conserved mechanism that eliminates transcripts with premature termination codons. We developed a new fluorescent proteins-based two-color NMD reporter that enables quantification of NMD activity at the level of single live cells. Using this reporter we detected considerable difference in NMD activity in different cell lines. Moreover, a strong heterogeneity was revealed in some cell lines that include clearly distinct subpopulations of cells with high and low NMD activity. We believe that the new reporter is a useful tool to study NMD regulation in various biological models, as well as for small molecule screening.

Nonsense-mediated mRNA decay (NMD) is a ubiquitous mechanism of degradation of transcripts with a premature termination codon (PTC). mRNAs with PTC result from various events – gene mutations, alternative splicing, programmed DNA rearrangements in immune cells and others [1]. The main function of NMD is clearance of C-terminally truncated proteins. Further, many normal transcripts carry stop codons which are recognized as PTCs and thus undergo NMD [2, 3]. Recent data suggest that NMD is an important mechanism of global regulation of gene expression [4, 5].

It is generally accepted that NMD is triggered by abnormal composition of the mRNA-associated proteins downstream of the terminating ribosome. When newly synthesized mRNAs began to translate, the translation complex pauses at a premature termination codon (PTC) upstream of an exon junction complex, the RNA helicase UPF1/Rent1, an essential component of the NMD process, is recruited and then targets the transcript for degradation [4].

Here, we describe new method to quantify NMD activity at single cell level using fluorescent proteins of two colors, green TagGFP2 and far-red Katushka. TagGFP2 was encoded by mRNA targeted to splicing-dependent NMD pathway. Katushka was used as a control of expression level. Comparison of fluorescence intensities of cells expressing this vector (pNMD+) and cells expressing TagGFP2 and Katushka from corresponding control NMD-independent vector pNMD– allowed NMD activity to be assessed at single cell level using fluorescence microscopy and flow cytometry (Fig. 1). This is especially important for complex models with potentially heterogeneous spatio-temporal patterns of NMD activity [6].

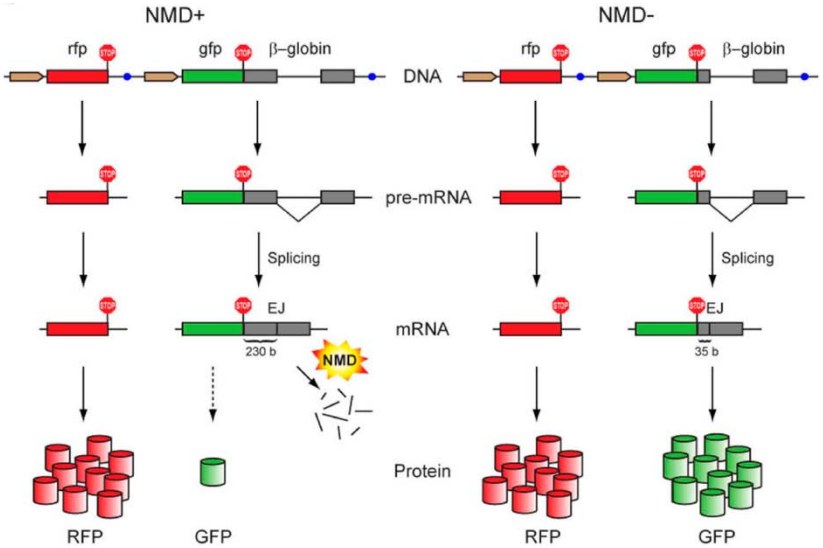

Fig. 1. Schematic outline of the reporter functioning. Vector pNMD+ (left) carries two fluorescent proteins, one of which (GFP) is encoded by NMD-targeted transcript and the other (RFP) serves as a control of expression efficiency. Control vector pNMD– (right) encodes both RFP and GFP by NMD-independent transcripts. Comparison of green-to-red fluorescence ratio in pNMD+ and pNMD– samples allows calculation of NMD activity. Brown arrows – promoters. Red, green and grey rectangles – coding regions for RFP, GFP and β-globin, respectively. Blue circles – transcription terminators. Red "STOP" signs – stop codons. Red and green cylinders – translated GFP and RFP proteins

The proposed reporter system was thoroughly tested in HEK293T cell line. NMD activity in these cells was found to be approximately 15-fold (i.e. 15-fold decrease of level of NMD-targeted transcript was observed) (Fig. 2a). To check the ability of our reporter system to assess NMD regulation, we tested for the known effects of NMD inhibition by some chemicals and specific RNAi. In all cases, fluorescence reporter detected the expected decrease of NMD activity similar to that measured by control quantitative PCR.

In order to test NMD efficiency in different models the following cell lines were analyzed: HeLa, mouse embryonic fibroblasts (MEF), mouse embryonic stem (ES) cells, mouse colon carcinoma CT26, mouse Lewis lung carcinoma LLC, human T-cell leukemia Jurkat, and spontaneously immortalized human keratinocytes HaCaT. These cell lines demonstrated very different NMD activities. In CT26, NMD activity was low, whereas in LLC it was high (8.5-fold higher than in CT26). Jurkat and HaCaT as well as overgrown HEK293T cells possessed strong heterogeneity and consisted of two cell subpopulations with high and low NMD activities (Fig. 2b) – phenomenon that cannot be discovered by classical methods.

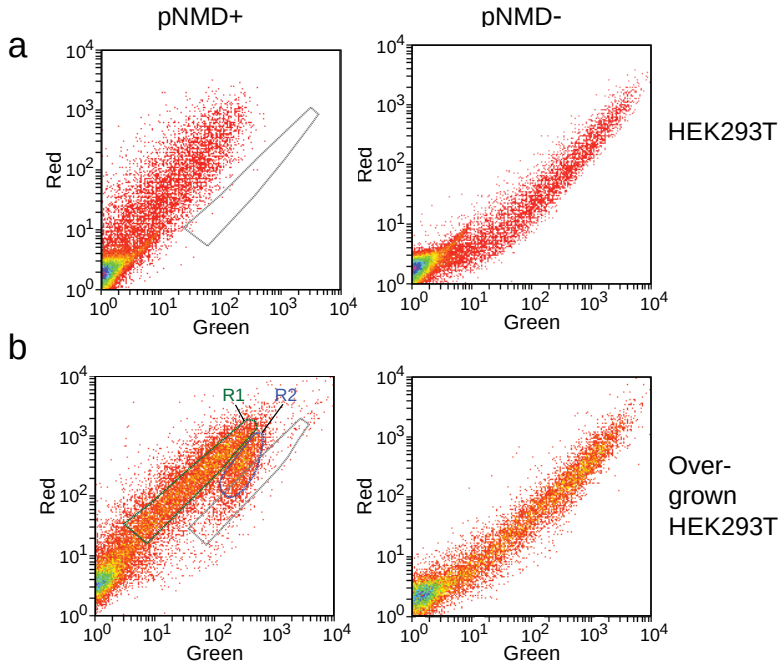

Fig. 2. Flow cytometry analysis of the cells transiently transfected with pNMD+ (left plots) or pNMD– (right plots). Corresponding pairs of cell samples HEK293T were analyzed using the same settings of the flow cytometer. Area of corresponding NMD– cells is outlined by a gray dashed line on each NMD+ plot. a. HEK293T cells grown in normal conditions. b. Overgrown HEK293T cells. Green and blue dashed lines show cell populations R1 and R2 with high and low NMD activity

Acknowledgements

This work was supported by Russian Science Foundation (14-25-00129).

References

1. L. Huang and M. Wilkinson, *RNA*, 2012, Wiley Interdiscip. Rev, **3**, 807-828.
2. J. Mendell, N. Sharifi, J. Meyers, F. Martinez-Murillo, and H. Dietz, *Nat. Genet.*, 2004, **36**, 1073-1078.
3. J. Rehwinkel, I. Letunic, J. Raes, P. Bork, and E. Izaurralde, *RNA*, 2005, **11**, 1530-1544.
4. L. Gardner, *Mol. Cancer Res.*, 2010, **8**, 295-308.
5. I. Bruno, R. Karam, L. Huang, A. Bhardwaj, C. Lou, E. Shum, H. Song, M. Corbett, W. Gifford, J. Gecz, S. Pfaff, and M. Wilkinson, *Mol. Cell*, 2011, **42**, 500-510.
6. A. Pereverzev, N. Gurskaya, G. Ermakova, E. Kudryavtseva, N. Markina, A. Kotlobay, S. Lukyanov, A. Zaraisky, and K. Lukyanov, *Sci Rep.*, 2015, **5**, 7729.

PLASMON RESONANCE EFFECT OF SILVER NANOPARTICLES ON PHOTONICS OF CHROMENE DYE

N.Kh. Ibrayev and **E.V. Seliverstova**

Institute of Molecular Nanophotonics, Y.A. Buketov Karaganda State University, Karaganda, Kazakhstan
niazibrayev@mail.ru

Abstract. Effect of silver nanoparticles on spontaneous and stimulated emission of chromene-3 in ethanol solution is studied. It is established, that upon laser photoexcitation of solution the spontaneous fluorescence is observed, which with increasing of pumping energy transforms in stimulated emission. The increasing of fluorescence, stimulated emission and lasing threshold was observed upon addition of silver nanoparticles. The dependence of intensity of lasing of silver concentration correlates with data of fluorescence.

Creating of new active laser media in the visible spectral range is relevant with the solution of a number of biomedical problems, since the laser light of these wavelengths can penetrate deeply into biological tissue. Radiation in red spectral range commonly used in photodynamic therapy of cancer.

This paper presents the results of a study on the plasmon effect of chromen-3 dye (3–(diethylamino)-7-oxo-7 H –benzo [4,5]-imidazo [1,2-a]chromeno [3,2-c]pyridine-6- carbonitrile).

Spectral and luminescent properties of dye were studied in ethanol solution. Concentration of ye molecules was equal to 10^{-4} mol/l. Silver nanoparticles (NPs) was prepared by laser ablation of metallic Ag in ethanol. The size of Ag nanoparticles in colloidal solutions was determined by dynamic light scattering analyzer of the sizes of submicron particles Zetasizer Nano ZS (Malvern).

Fluorescence spectra were registered with Cary Eclipse spectrofluorometer. The fluorescence decay kinetics of dye was measured using a pulsed spectrofluorometer with picosecond resolution and registration of the time-correlated photon counting mode. Fluorescence excitation of samples was performed using a pulsed laser with λgen = 488 nm and a pulse width at half-maximum τ = 40 ps (Becker & Hickl). Absolute quantum yield of dye was measured in reflectometric sphere AvaSphere-50-REFL (Avantes BV) and was equal to 0.99. Measurements of the spectral and energy characteristics of induced emission of solutions of chromene-3 were performed upon excitation of samples by second harmonic of Nd:YAG laser (SOLAR LQ 215, λ_{gen} = 532 nm, E_{imp} = 90 mJ, τ = 10 ns) in the cross-version. Pump power density was varied with the help of neutral density filter and was 0.005–0.2 MW/cm^2. Stimulated emission with the help of converging lens focused on the input of optical fiber spectrometer AvaSpec-2048.

The results of the studying of absorption, fluorescence and stimulated emission od dye in ethanol solution upon change of silver NPs concentration are shown in the Table. It is evidence that absorbance of dye molecules increases with the growth of concentration of Ag NPs. Maxima of absorption coefficient is observed for $C_{Ag}=10^{-5}$ mol/l. Optical density decreases with further increase in the concentration of NPs. Fluorescence intensity behaves similarly. The fluorescence lifetime is not changed.

C_{Ag}, mol/l	λ_{abs}, nm	$\Delta\lambda^{ab}_{1/2}$, nm	D	λ_{fl}, nm	I_{fl}, a.u.	τ_{fl}, ns	λ_{las}, nm	$\Delta\lambda^{las}_{1/2}$, nm (P=0.05 MW/cm^2)	I_{las}, a.u.
0	550	68	0.45	580	7.7	4.1	580	27	12
$6\cdot10^{-6}$	550	68	0.48	580	7.6	4.1	580	26	13.1
10^{-5}	550	68	0.54	580	8.6	4.1	580	16	24.8
$3\cdot10^{-5}$	550	68	0.52	580	8.5	4.1	580	23	16.5
$6\cdot10^{-5}$	550	68	0.50	580	8.0	4.1	580	27	12.5

Properties of stimulated emission of dye are also dependent on the concentration of silver NPs. The emission intensity increases in 2 times when $C_{Ag}=10^{-5}$ mol/l. At this concentration, there is a minimum of half-width of the spectrum of stimulated emission is observed. Dependence of lasing intensity on concentration of Ag nanoparticles correlate with the data on spontaneous fluorescence. Measurements of the intensity and half-width of band of stimulated emission on the pumping power have shown that the lasing threshold under the influence of the plasmon effect decreases.

Invited

ULTRAPURE LASER-SYNTHESIZED NANOMATERIALS FOR BIOMEDICAL APPLICATIONS

A.V. Kabashin

Aix-Marseille University (AMU), LP3 UMR 7341 CNRS, Campus de Luminy, Case 917,
13288 Marseille Cedex 09, France
kabashin@lp3.univ-mrs.fr

Abstract. This presentation overviews our results on laser-ablative synthesis of ultrapure nanomaterials for biomedical applications. Running experiments in vitro and in vivo, we conclude on "zero" toxicity of such nanomaterials. We then describe a novel method for cancer therapy, in which Si nanoparticles are used as sensitizers of RF-induced hyperthermia

Inorganic nanomaterials demonstrate extremely promising characteristics for tasks of cancer diagnostics and therapy (theranostics), but biomedical prospects of such nanomaterials are complicated by toxicity issues arising as a result of relatively dirty pathways for their fabrication. As an example, Si nanoparticles are biocompatible and even biodegradable in pure state, but conventional chemical and electrochemical routes for their synthesis inevitably lead to a surface contamination by toxic products. As a solution of the toxicity problem, we recently introduced a series of physical methods based on ultrashort laser ablation and fragmentation in aqueous biocompatible solutions in order to synthesize novel classes of ultrapure nanomaterials for biomedical tasks [1].

This presentation will overview our results on the laser synthesis of some important inorganic nanomaterials (Si, Au etc) and their tests in biological systems. First, our tests in vitro using cancer and normal cell lines demonstrate the innocuousness and safety nanoparticles (zero toxicity), while protein covering after the incubation of nanoparticles in real biological environment suggests potential successful transport of nanoparticles in vivo and minimal immune response effects [2, 3]. In vivo tests in small animal model using systemic administration of nanoparticles also do not reveal any sign of toxicity effects. We then examine optical, photochemical and photo-thermal characteristics of laser-synthesised nanomaterials in the view of their potential cancer theranostic applications [3–5]. Finally, we describe a novel method for mild cancer therapy, in which Si nanoparticles are used as sensitizers of radio-frequency induced hyperthermia. The efficiency of this method is confirmed by successful tests in vitro and in vivo [3].

References

1. A.V. Kabashin, Ph. Delaporte, A. Perreira, D. Grojo, R. Torres, Th. Sarnet, and M. Sentis, *Nanoscale Res. Lett*., 2010, **5**, 454–463.
2. F. Correard, K. Maximova, M.-A. Estève, C. Villard, A. Al-Kattan, M. Sentis, M. Roy, M. Gingras, A.V. Kabashin, and D. Braguer, *Int. J. Nanomedicine*, 2014, **9**, 5415–5430.
3. K.P. Tamarov, L.A. Osminkina, S.V. Zinovyev, K.A. Maximova, J.V. Kargina, A.P. Sviridov, M. Sentis, A.V. Ivanov, V.N. Nikiforov, A. Kabashin, and V.Yu. Timoshenko, *Scientific Reports*, 2014, **4**, 7034, DOI: 10.1038/srep07034.
4. D. Rioux, M. Laferriere, A. Douplik, D. Shah, L. Lilge, A.V. Kabashin, and M. Meunier, *J. Biomed. Optics*, 2009, **14**, 021010.
5. P. Blandin, K.A. Maximova, M. Gongalsky, J.F. Sanchez-Royo, V.S. Chirvony, M. Sentis, V.Yu. Timoshenko, and A.V. Kabashin, *J. Mater. Chem. B*, 2013, **1**, 2489-2495.

Invited

NIR PHOTODYNAMIC TREATMENT OF HUMAN CANCER WITH VITAMIN B2 PHOTOSENSITISED BY UPCONVERSION NANOPARTICLES

E.V. Khaydukov[1], **K.E. Mironova**[2], **V.A. Semchishen**[1], **A.N. Generalova**[1,2], **A.V. Nechaev**[1,3], **D.A. Khochenkov**[1,4], **E.V. Stepanova**[4], **A.V. Zvyagin**[1,5], **S.M. Deev**[2], and **V.Ya. Panchenko**[1]

[1] Institute on Laser and Information Technologies of the Russian Academy of Sciences, 1 Svyatoozerskaya, Shatura 140700, Russia; khaydukov@mail.ru

[2] Shemyakin-Ovchinnikov Institute of Bioorganic Chemistry of the Russian Academy of Sciences, 16/10 Miklukho-Maklaya, Moscow 117997, Russia

[3] Lomonosov Moscow University of Fine Chemical Technology, 86 Prospect Vernadskogo, 119571 Moscow, Russia

[4] Federal State Scientific Institution Russian Cancer Research Center them. Blokhin, 23 Kashirskoye, Moscow, 115478, Russia

[5] Macquarie University, MQ Biofocus Research Centre, NSW 2109, Australia

Riboflavin, also known as vitamin B2, is involved in various biological processes as such required for a variety of flavoprotein enzyme reactions including activation of other vitamins. Its dysregulation, as in the case of human breast adenocarcinoma cells, results in its abnormally large accumulations in cancer cells. Herein, we report a facile strategy for riboflavin-mediated specific photodynamic treatment of breast adenocarcinoma cells SK-BR-3 based on its effective singlet oxygen generating properties (~50%). However, the efficacy of riboflavin PDT is limited by penetration depth of exciting radiation in biological tissues at the level 500 μm. We demonstrate a solution to this problem by the rational photoluminescent nanotechnology design. Specifically, upconversion nanoparticles (UCNPs) offer a lucrative possibility to kindle UV or visible light at the sub-centimetre depth in tissue, owing to their property to convert infrared radiation at the wavelength in the biological tissue transparency window 975 nm. We designed upconversion nanoparticles (UCNP) of the composition NaYF4:Yb3+:Tm3+ that yielded UV/blue emission bands critical for the photosensitising of riboflavin. We achieved a high Förster resonance energy transfer (FRET) efficiency from UCNPs to vitamin B2, which facilitates a large production of cytotoxic singlet oxygen and thus an enhanced PDT efficacy. We demonstrate the NIR triggered PDT agent for specific inhibition of SK-BR 3 tumor cell growth in vitro and in vivo, thereby revealing the considerable potential of the UCNPs based PDT system as NIR triggered deep PDT agents for cancer therapy.

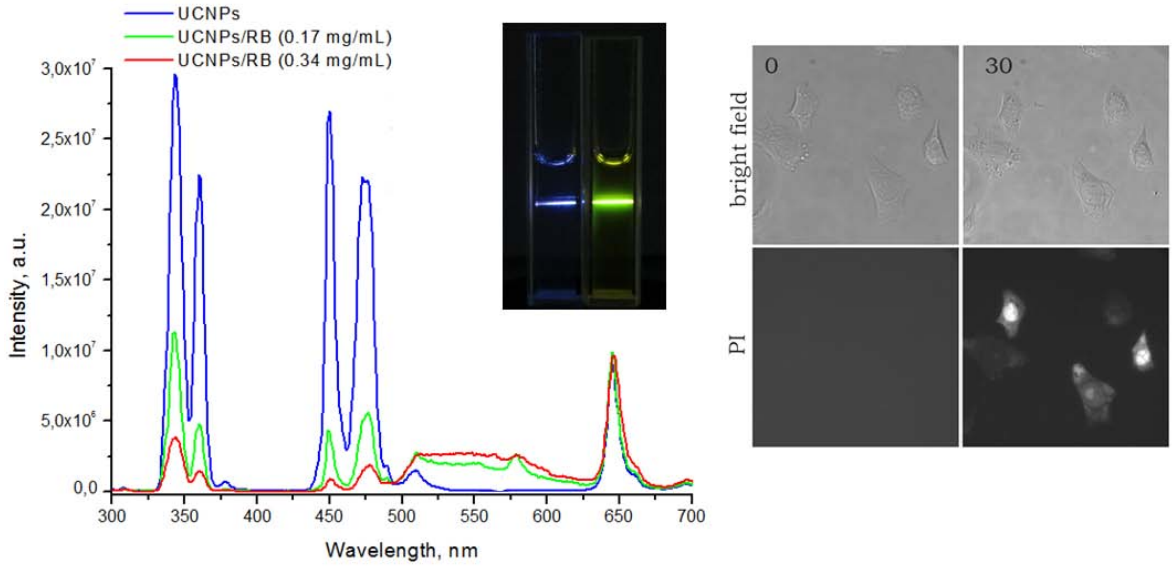

Fig. 1. Upconversion emission spectra of core/shell $NaYF_4$: $Yb^{3+}Tm^{3+}$/ $NaYF_4$ under excitation on 975 nm without (blue curve) and with (green and red curve) presence of vitamin B2. On insert: photo of UCNPs water solution and UCNPs mixture with vitamin B2 under 975 nm illumination. Green luminescence demonstrates effective FRET from UCNPs to vitamin B2. Optical image of SK-BR-3 cells incubated with nanocomplex UCNPs-riboflavin and PI. PI luminescence after cell irradiation on 975 nm demonstrates photodynamic treatment of breast adenocarcinoma cells SK-BR-3

Invited

AU NANOCLUSTERS: EVERY ATOM IS IMPORTANT FOR BIOPHOTONICS

B.N. Khlebtsov[1,2], **E.S. Tuchina**[2], **V.V. Tuchin**[2], and **N.G. Khlebtsov**[1,2]

[1] Institute of Biochemistry and Physiology of Plants and Microorganisms,
13 pr. Entuziastov, Saratov 410049, Russia,
bkhl@ibppm.sgu.ru
[2] Saratov State University, 83 Astrakhanskaya, Saratov 410012, Russia

Gold nanoclusters (AuNCs) are a new type of luminescent nanomaterials, usually comprising nanoparticles (AuNPs) smaller than 2 nm and typically composed of a few to about 100 gold atoms [1]. AuNCs are distinguished from other Au nanomaterials with strong photoluminescence, large Stokes shift and high emission rates. The luminescent AuNCs provide the bridge between atomic and NP behavior in noble metals and exhibit molecule-like photophysical properties, large surface area-to-volume ratios, easy surface manipulation and color tenability [2]. Compared with other types of luminescent materials, such as small-molecular dyes, fluorescent proteins, semiconductor quantum dots, dye-doped NPs, up-converting lanthanide-doped NPs and carbon nanodots, AuNCs have many advantages, including being relatively simple to prepare, high quantum yield in NIR range, good water solubility, low toxicity, biocompatibility and surface fictionalization, so they have shown great potential in theoretical studies and practical applications.

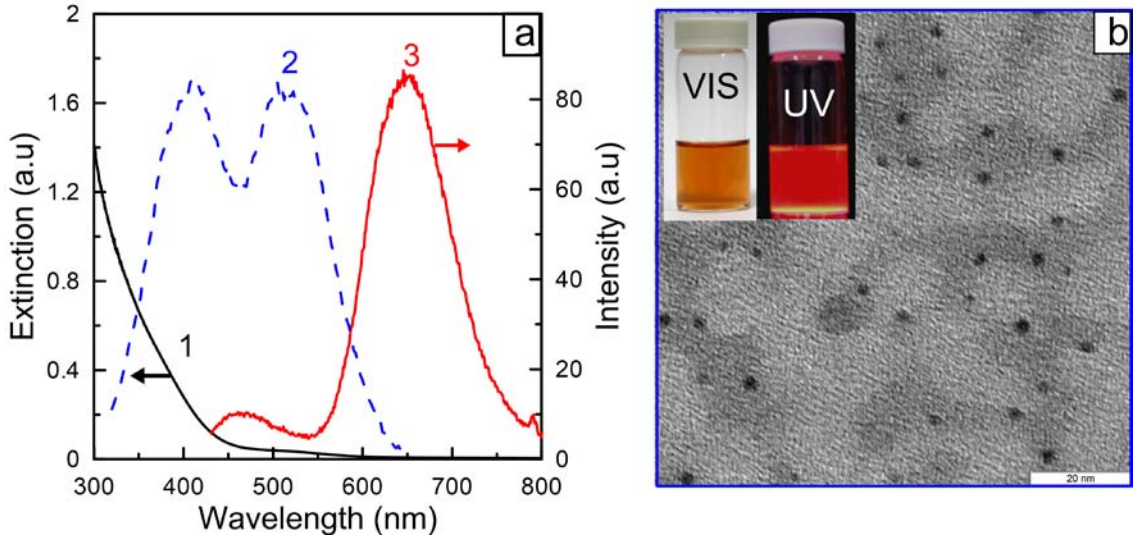

Fig. 1. (a) Extinction spectra (1) and fluorescence excitation (2) and emission (3) spectra of Au25 nanoclusters. (b) TEM images of Au25 nanoclusters. The insets show the digital photos of the nanoclusters solution under white light (left) UV light (right), respectively

As an example Fig. 1 shows extinction, emission and excitation spectra of Au nanoclusters composed with 25 gold atoms in bovine serum albumin matrix. TEM image is also shown at panel (b).

In this talk, we focus our discussions on the synthesis strategies, and the size-dependent fluorescence of AuNCs. We cover their applications in biophotonics for cancer cell and tissue imaging, chemical analysis, and environmental monitoring.

We take special care our recent advances in detection of pathogen bacteria and AuNCs guided photodynamic treatment. For such experiment Au25 nanoclusters (with high QY in red and near IR spectral range) were functionalized with human antistaphylococcus immunoglobulin as a targeted agent and with aluminum phtalocyanine (Photosens) as a photodynamic drug. We use these multifunctional conjugates for simultaneous fluorescent detection (under 514 nm excitation) and photodynamic treatment of Staphylococcus aureus bacteria.

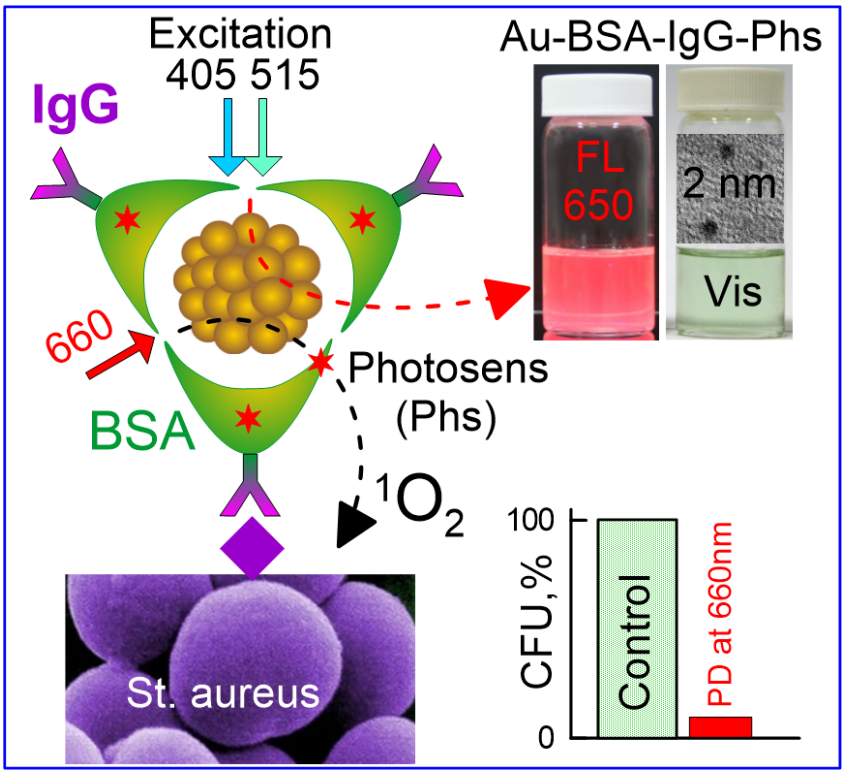

Fig. 2. TOC scheme of using Au nanoclusters as platform for multifunctional fluorescent imaging and photodynamic suppression of bacteria

Acknowledgements

This research was supported by grants from the Program of the Presidium of the Russian Academy of Sciences “Nanostructures: Physics, chemistry, biology and basic technologies”, grant from Russian scientific foundation №14-13-01167 and the Government of the Russian Federation (grant 14.Z50.31.0004).

References

1. M. Cui, Y. Zhao, and Q, Song, *Trends in Analytical Chemistry*, 2014, **57**, 73-82.
2. J. Zheng, P.R. Nicovich, and R.M. Dickson, *Annu Rev Phys Chem*., 2007, **58**, 409-31.

EX VIVO SUPER-RESOLUTION FLUORESCENCE IMAGING OF ACTIN CYTOSKELETON IN TUMORS

N.V. Klementieva[1], **O.E. Furman**[2], **E.V. Zagaynova**[1], **K.A. Lukyanov**[1,3], and **A.S. Mishin**[1,3]

[1] Nizhny Novgorod State Medical Academy, Nizhny Novgorod, Russia,
nvklementieva@gmail.com
[2] N.I. Lobachevsky State University of Nizhny Novgorod, Nizhny Novgorod, Russia
[3] M.M. Shemyakin and Yu.A. Ovchinnikov Institute of Bioorganic Chemistry
of the Russian Academy of Sciences, Moscow, Russia

Abstract. Actin cytoskeleton remodeling has been described as a marker of metastasis activity and drug sensitivity of cancer cells. Super-resolution microscopy techniques enable to study microfilament networks at the molecular level. Here, we visualized actin ultrastructure at high-resolution in ex vivo tumor model. Subcutaneous tumors were formed in BALB/c and C57BL/6 mice by injection of CT26 and LLC1 cancer cells, correspondingly. We applied novel fluorogenic probe SiR-actin for staining of beta-actin in tumor cryoslices and further TIRF imaging. To process raw data 3B analysis was used. As a result, we could obtain super-resolved images of beta-actin structure in tumor tissue.

The actin cytoskeleton has a key role in cell survival and growth, responsible for variety of normal cellular functions. Actin is a highly conserved essential protein that cells use to move, polarize, divide and maintain organization within tissues [1–3]. Such processes as cell adhesion, migration, invasion into surrounding tissue, which is driven by actin cytoskeleton dynamics, are typical for cancer cells. Consequently, the rearrangement of microfilaments leading to changes in cell shape and plasticity is considered as an important regulatory mechanism of metastasis [4–7]. In this light, actin cytoskeleton can be regarded as a target for anticancer chemotherapy [8, 9]. Meanwhile, the ultrastructure of actin network, the molecular basis of its changes might be understood only using super-resolution microscopy methods overcoming diffraction limit [10]. Single-molecule localization microscopy (PALM, STORM, GSDIM, etc) are becoming more widespread in cell biology [11–13]. However, there are some practical challenges for *in vivo* application of these techniques [14]. In our research we have applied TIRF microscopy for *ex vivo* cryotissue samples and imaged actin cytoskeleton structure at high-resolution in tumors.

To generate primary tumor models we used CT26 (mouse colon carcinoma) and LLC1 (mouse Lewis lung carcinoma) cell lines. Subcutaneous tumors were formed in BALB/c and C57BL/6 mice by injection of 500,000 CT26 or LLC1 cancer cells into the flanks, correspondingly. On day 14 after inoculation the mice were sacrificed and the tumors were obtained and immediately frozen. Using Leica CM 1100 cryostat 10 μm-thick slices were cut and placed on 0,17 mm coverslips suitable for inverted microscope. The cryosections were fixed in 4% paraformaldehyde and then labelled with novel fluorogenic probe SiR-actin for beta-actin filaments. This tool has been recently reported as an extremely photostable and bright dye for endogenous cytoskeletal structures imaging in live and fixed cells [15]. In addition, Hoechst 33342 was used for nuclei staining. The cryosections were also examined by standard histological analysis (H&E staining) to verify tumor tissue morphology.

The actin ultrastructure of tumor tissue was visualized with Eclipse Ti inverted microscope (Nikon) equipped with EM-CCD camera. The cryoslices were imaged in TIRF mode allowing to reduce background signal that might be high in thick sample. For SiR-actin-based imaging of fixed tissue samples we tested a range of microscope settings. Eventually, 2% laser power (647 nm) and exposure time of 16 ms proved to be efficient. We established that the fluctuation rate of SiR-actin averaged fluorescence intensity at selected conditions was sufficient for applying 3B (Bayesian analysis of blinking and bleaching) algorithm. This modern localization microscopy analysis allows for many overlapping fluorophores in each frame as well as the use of information from bleaching events [16]. A series of 2000 sequential images was acquired for further processing. As a result, we could obtain super-resolved images of actin cytoskeleton structure of CT26 (fig. 1) and LLC1 tumors.

In summary, we for the first time demonstrated single-molecule localization microscopy of actin organization in *ex vivo* tumor model.

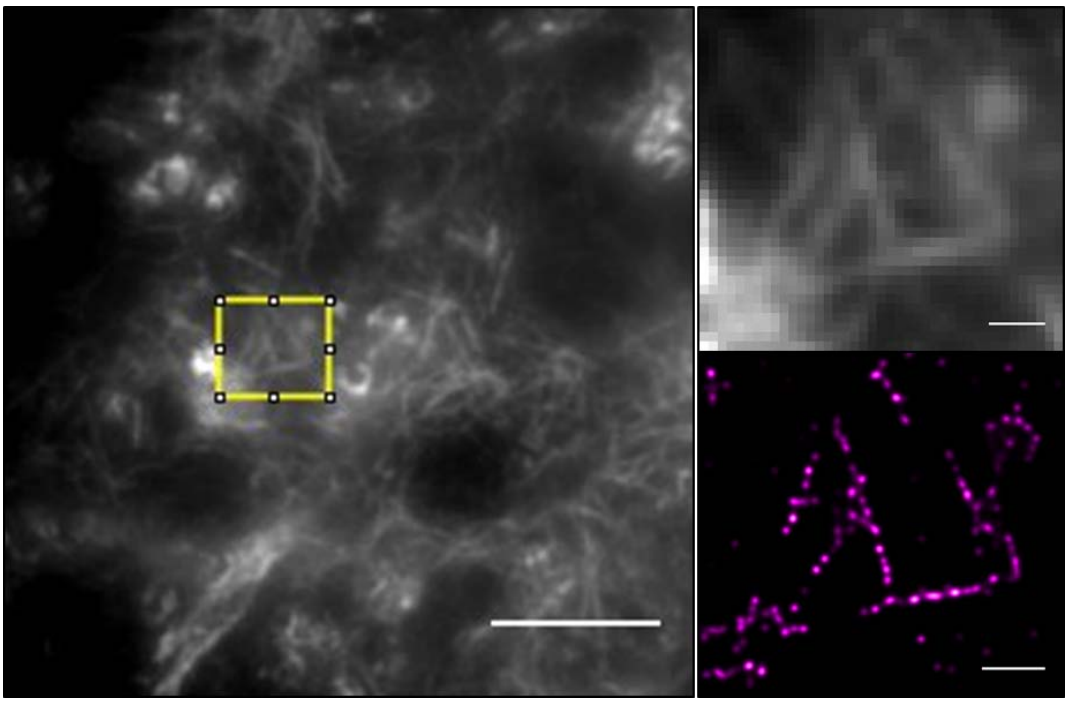

Fig. 1. SiR-actin labeling of CT26 tumor cryotissue. Left: Wide-field image (averaging of 500 frames) of sample region. The yellow square indicates the analyzed area in right panel. Scale bar, 10 μm. Right: Magnifications of the analyzed area. Averaged wide-field (upper) and corresponding super-resolved image (lower) obtained by means of 3B algorithm. Scale bar, 1 μm

Acknowledgements

This work was supported by the Ministry of Education and Science of the Russian Federation (projects No. 14-25-00129) and the Russian Foundation for Basic Research (No. 13-04-40304-H comfi). We thank Dr. N.N. Prodanets and Dr. L.B. Snopova for their assistance with the histological techniques.

References

1. R.P. Stevenson, D. Veltman, L.M. Machesky, *J Cell Sci*., 2012, **125**(Pt 5), 1073-1079.
2. P. Gaspar and N. Tapon, *Curr Opin Cell Biol*., 2014, **31**, 74-83.
3. R. Dominguez, K.C. Holmes, *Annu Rev Biophys*., 2011, **40**, 169-186.
4. X. Yuan, L. Yu, J. Li, et al., *Cancer Res*., 2013, **73**(12), 3625-3637.
5. M.F. Olson and E. Sahai, *Clin Exp Metastasis*, 2009, **26**(4), 273-287.
6. B.N. Brandhagen, C.R. Tieszen, T.M. Ulmer, et al., *BMC Cancer*, 2013, **13**, 35.
7. M. Desouza, P.W. Gunning, and J.R. Stehn, *Bioarchitecture*, 2012, **2**(3), 75-87.
8. T.T. Bonello, J.R. Stehn, and P.W. Gunning, *Future Med Chem*., 2009, **1**(7), 1311-1331.
9. H. Vindin, L. Bischof, P. Gunning, et al., *J Biomol Screen*, 2014, **19**(3), 354-368.
10. S. Sharma, C. Santiskulvong, L.A. Bentolila, et al., *Nanomedicine*, 2012, **8**(5), 757-766.
11. J. Rossy, S.V. Pageon, D.M. Davis, et al., *Curr Opin Immunol*., 2013, **25**(3), 307-312.
12. T. Tabarin, S.V. Pageon, C.T. Bach, et al., *Chemphyschem*., 2014, **15**(4), 606-618.
13. T. Klein, S. Proppert, and M. Sauer, *Histochem Cell Biol*., 2014, **141**(6), 561-575.
14. D. Baddeley, D. Crossman, S. Rossberger, et al., *PLoS One*, 2011, **6**(5), e20645.
15. G. Lukinavičius, L. Reymond, E. D'Este, et al., *Nat Methods*, 2014, **11**(7), 731-733.
16. S. Cox, E. Rosten, J. Monypenny, et al., *Nat Methods*, 2011, **9**(2), 195-200.

IMPACT OF NANOPARTICLES ON THE IN VITRO DEVELOPMENT OF EARLY MAMMALIAN EMBRYOS

M. Kormacheva[1,2], E. Perevedentseva[2], A. Krivokharchenko[3], A. Karmenyan[2], P.-H. Chung[2], A.-I. Ahmed[2], and **C.-L. Cheng[2]**

[1] Lomonosov Moscow State University, Moscow, Russia
[2] National Dong Hwa University, Hualien, Taiwan, kormacheva.marie@gmail.com
[3] N.N. Semenov Institute of Chemical Physics, RAS, Moscow, Russia

Abstract. Nowadays nanotecnologies are widely developed for use in different fields, including biology and medicine. As the result, development of nanotecnologies at whole, on the one hand, and development of reproductive technologies (for human and animals), on the other hand, including *in-vitro* operations with early embryos, can lead to increase the interaction probability between nanoparticles and the embryo. In present work we test the impact of nanoparticles on mammalian (mice) embryo to estimate their potential for researches and theranostic applications and analyze their toxicity for embryo.

In vitro fertilization (IVF) is rapidly growth with the advantage of opportunity to diagnose some disease on the stage of preimplantation embryo such as genetic abnormalities and genetic predisposition to some heavy disease. There is number of methods to return the potential for proper development, increasing the chance of pregnancy. The unique physicochemical properties of nanoparticles could help to implement drug delivery into this micro system, mammalian embryo, and expand the scopes of IVF.

Over the past years nanoparticles have attracted attention due to their unique physicochemical properties, which are promising for biomedical application [1] as a drug carriers, biosensors, coating for medical implants and more. Today industry invents various surface functionalizations to customize nanomaterials for different application.

Despite of all advantages of nanoparticles the biological impact is still not properly studied. Our work aims to test the toxicity and the probable penetration inside the mammalian embryo of different nanoparticles.

For that purpose we used embryos from mice. The 2-cell stage embryos have been recovered from female mice of C57bl/6 strain. Nanoparticles have been added into culture medium and development of the in vitro cultivated embryos was evaluated during 72 h. The developmental rate has been compared with control embryos. All embryos were cultivated in 4-well plates with culture medium in incubator at 37°C with 5% of carbon dioxide.

Some nanoparticles were examined, such as different kinds of ND, titanium dioxide particles of different structure, etc., with various concentrations and times of interaction. These kinds of nanoparticles have been selected due to previously demonstrated non-toxicity for cellular models and their optical-spectroscopic properties promising for imaging applications and some bio-optical treatments [2, 3]. NP was added into the medium with 2-cell embryos in concentrations, the highest equaled 200 μg/ml.

The interaction of the nanoparticles with the embryos was analyzed via the confocal fluorescence microscopy (with confocal scanning microscope TCS SP5, Leica, Germany). Due to spectroscopic properties of the used nanoparticles their localization on/in the embryo could be analyzed via their fluorescence. The images of embryos with and without NP are compared on the Fig. 1. No disturbing effect of these nanoparticles in applied concentrations neither well-observable penetration of the nanoparticles into the embryos has been detected. It opens more wide opportunities for nanobioapplications.

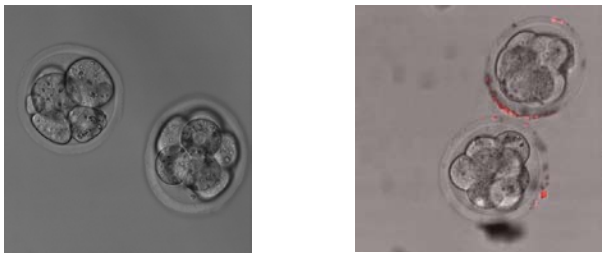

(a) (b)

Fig. 1. Mice embryos development in presence of nanoparticles
a) control (without ND), b) 100 nm nanodiamond

Difference in the interaction of embryos with on embryos by different nanoparticles is showed on the Fig. 2. The reason why some particle barely lay over the zona pellucida, and some completely cover it, remains to be studied.

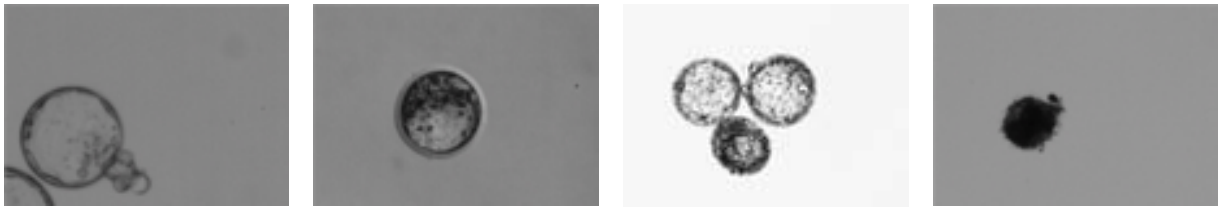

a) b) c) d)

Fig. 2. Mouse blastocysts developed from 2-cell stage embryos in a) control culture medium and culture medium containing various types of NP: b) 40 nm fluorescent ND, c) TiO_2, d) ND obtained with method of laser ablation [3] with aminated surface

Acknowledgements

The research was supported by Ministry of Science and Technology of Taiwan with grant No. 103-2112-M-259-001-MY3. Authors thanks also Dr. O. Levinson, Ray Technology Ltd. (Israel) for the samples of laser-ablated NDs.

References

1. K. Riehemann, S.W. Schneider, T.A. Luger, B. Godin, M. Ferrari, and H. Fuchs, *Angew. Chem. Int. Ed.*, 2009, **48**, 872-897.
2. E. Perevedentseva, Y.-C. Lin, Mona Jani, and C.-L. Cheng, *Future Medicine. Nanomedicine*, 2013, **8**(12), 2041-2060.
3. E. Perevedentseva, D. Peer, V. Uvarov, B. Zousman, and O. Levinson, *J. Nanoscience & Nanotechnology*, 2015, **15**(2), 1045-1052.

Invited

PLASMONIC LIPOSOME-NANOPARTICLE HYBRIDS FOR BIOMEDICAL APPLICATIONS

A.B. Kotlyar and **M. Fattal**

Department of Biochemistry and Molecular Biology, The George S. Wise Faculty of Life Sciences,
Tel Aviv University, Ramat Aviv, Tel Aviv, 69978 Israel
s2shak@post.tau.ac.i l; http://www.sashakot.com/

Abstract. Liposome-nanoparticle hybrids are stable under physiological conditions in contrast to plasmonic noble metal nanoparticles that irreversibly aggregate at physiological salt concentrations. High stability of the hybrids together with absorption of light in a near-infrared region of the spectrum makes the structures useful for a variety of theranostic applications.

Noble metal nanoparticles (NPs) strongly absorb light in the visible range of spectrum. Absorption of light in so called biological (or therapeutic) window, where tissues are relatively "transparent" to near-infrared photons (wavelengths from 650 to 900 nm), makes the particles useful for photothermal therapy. Illumination of the particles attached to a target tumor cell by near-infrared light leads to liberation of heat and as results in killing the cell and those in a close proximity to the target one. The main disadvantage of the noble NPs in general and gold NPs (AuNPs) in particular that strongly limits their application in the field of biomedicine is low stability of the nanoparticles under physiological conditions. At a physiological ionic strength (roughly 150 mM NaCl) AuNPs aggregate and lose their unique plasmonic properties. Different capping ligands have been employed to prevent aggregation of the particles under physiological conditions. However, despite considerable progress achieved in the field in the last decade, the problem of plasmonic nanoparticles delivery into target cells is not solved so far.

Liposomes, spherical vesicles consisting of an aqueous core surrounded by a lipid bilayer, is an ideal system for drug delivery into the cells. They can carry hydrophobic drugs well as hydrophilic compounds to the cells. The latter ones are encapsulated in the aqueous phase of the liposome, while the hydrophobic drugs are located in a non-polar core of the bilayer. Several liposome-drug complexes have received approval from FDA and many others are in clinical trials now.

The liposome-nanoparticle hybrids (see images below) overcome the limitations associated with low stability of the NPs at physiological ionic strengths. At physiological salt concentrations common ligand-coated charged NPs collide with one another during their motion due to the lack of repulsion. This leads to irreversible binding of the particles and to their aggregation. Liposome-encapsulated nanoparticles are separated from each other by the phospholipid membranes and can't interact. The nanoparticle-loaded liposomes thus overcome the instability problem and provide a methodology to deliver plasmonic nanostructures to target cells.

Those are some issues I am going to address in the lecture: plasmonic nanoparticles instability under physiological conditions; synthesis and properties of nanoparticle-loaded liposomes and potential theranostic applications of liposome-nanoparticle hybrid constructs.

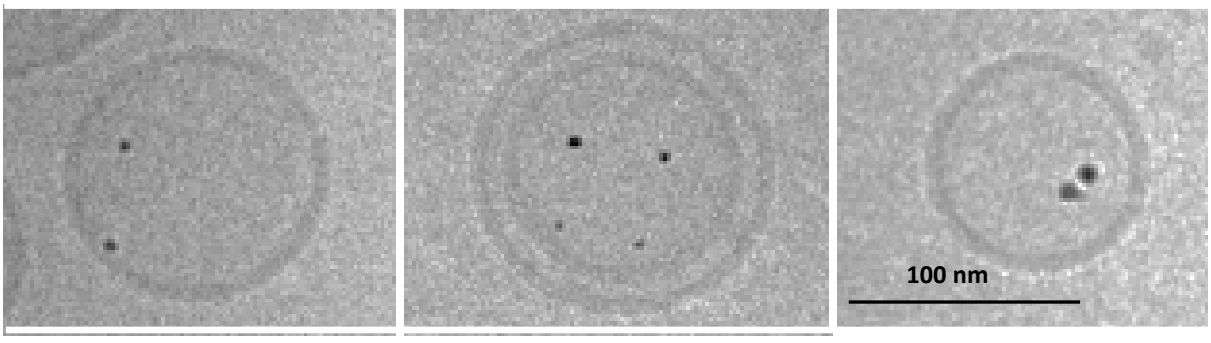

Cryo-TEM images of nanoparticle loaded liposomes. The particles are clearly visible as dark spots

Acknowledgements

This research is supported by supported by the Israel Science Foundation, grant 1589/14.

Invited

THREE-DIMENSIONAL SUPER-RESOLUTION OPTICAL FLUCTUATION MICROSCOPY

M. Leutenegger[1,2], **S. Geissbuehler**[1], **A. Sharipov**[1], and **Th. Lasser**[1]

[1] École Polytechnique Fédérale de Lausanne, Laboratoire d'Optique Biomédicale, Lausanne, Switzerland
marcel.leutenegger@a3.epfl.ch
[2] Max-Planck-Institut für biophysikalische Chemie, Abteilung NanoBiophotonik, Göttingen, Germany

Abstract. Super-resolution optical fluctuation imaging (SOFI) overcomes the diffraction limit in all three spatial dimensions by analyzing an image sequence of blinking fluorophores with higher-order cumulants. In order to benefit of a three-dimensional data analysis, we introduce a multiplane wide field microscope for simultaneously imaging several object planes for increasing the depth sampling and reducing the acquisition time. We show super-resolved images of the three-dimensional structure of organelles in fixed and live cells. We discuss issues when imaging living specimen and attempt to improve the quality of the super-resolved images by estimating and modeling the imaging performance.

Since the invention of stimulated emission depletion (STED) fluorescence microscopy in the early 1990s, diffraction-unlimited optical microscopy of living cells has become an important research field for further the understanding of life [1, 2]. Prominent methods achieve super-resolution by a targeted read-out of ensembles in strongly confined regions, e.g. STED, or by precise localization of individual blinking emitters in thousands of images, e.g. stochastic optical reconstruction microscopy (STORM). Recently, super-resolution optical fluctuation imaging (SOFI) was introduced as an elegant way to overcome the diffraction limit in all spatial dimensions [3, 4]. SOFI analyzes the intensity traces of blinking emitters over time for correlated signals. Because emitters blink independently, correlated intensity fluctuations in a point-spread function sized region originate from individual emitters, which allows to distinguish the emitters in more detail. Balanced SOFI linearizes the image contrast and was shown to yield an about four-fold resolution improvement in fixed cells [5].

We present super-resolved three-dimensional (3D) cell structures imaged with a multi-plane wide-field microscope [6] and address issues when imaging living specimen that express photo-switchable fluorescent proteins. For further optimizing the imaging process, the quality of the super-resolved images can be assessed by estimating their signal-to-noise ratio (SNR) and the modulation transfer function (MTF) of the microscope.

Three-dimensional imaging

Multi-plane 3D SOFI is a wide field imaging method that analyzes image sequences of stochastically blinking fluorophores by spatio-temporal cumulants of several orders [6]. The simultaneous acquisition of several object planes enables a 3D data analysis to refine the acquired images in all spatial dimensions. Compared to a sequential plane-by-plane imaging, the 3D imaging significantly reduces the acquisition time and helps limiting the photo-bleaching of the fluorophores. We imaged Tom20, an abundant protein of the mitochondria outer membrane, labeled with Alexa 647 in fixed C2C12 cells. We further imaged the vimentin network in living HeLa cells using the reversibly photo-switchable fluorescent protein Dreiklang [7] as exemplified in the figure.

SOFI image quality

The SNR can be estimated on a per-pixel basis by calculating the variance of SOFI images derived from different blinking subsequences. The jackknife statistics can also be useful to quantify the MTF via the spatial frequency content of these SOFI images. The estimated SNR and the MTF help choosing the appropriate image sequence length and cumulant order for tuning the resolution and contrast of the super-resolved images. We present a SNR model taking into account the important experimental parameters and we compare the results of our model with Monte-Carlo simulations and measurements.

Conclusions

Whereas SOFI is conceptually simple its application bears a number of pitfalls common to super-resolution microscopy. In particular, the potential instability of the opto-mechanical components and the mobility of living specimen need close attention because SOFI is fairly sensitive to motion artifacts and because image co-registration is of limited applicability. Therefore, shortening the acquired image sequences is tempting if the resulting image quality can be kept at an acceptable level. An au-

tomatic quantification of the SOFI image SNR and the MTF supports appropriate choices of imaging parameters.

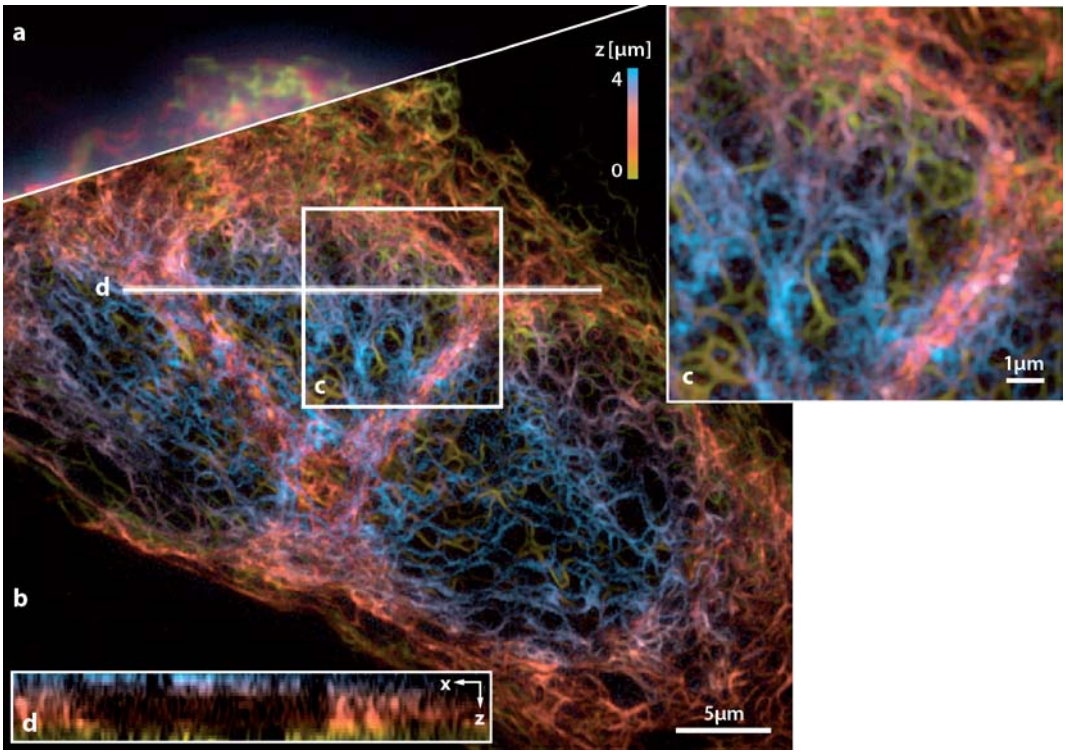

Live-cell multiplane SOFI of HeLa cells expressing vimentin-Dreiklang [6]. (a) Maximum intensity projection of wide field images. (b) Maximum intensity projection of second-order balanced SOFI. (c) Zoomed region highlighted in b. (d) *x*–*z* section highlighted in (b)

Acknowledgements

Prof. Johan Auwerx kindly provided the C2C12 cells. We acknowledge Aurélien Godinat, Noelia L. Bocchio, Patrick A. Sandoz, Anja Huss, Nickels A. Jensen and Gennady Nikitin for help with the sample preparation and cell labelling. We thank Wim Vandenberg and Peter Dedecker for sharing ideas on the image quality in SOFI.

This research was supported by the Swiss National Science Foundation (SNSF) under grants CRSII3-125463/1 and 205321-138305/1. Prof. Elena A. Dubikovskaya and A.G. acknowledge the grants of the Neva Foundation. Prof. Stefan Jakobs and Prof. Jörg Enderlein acknowledge financial support by the Deutsche Forschungsgemeinschaft through SFB 755 (projects A5 and B10) and by the Cluster of Excellence Nanoscale Microscopy and Molecular Physiology of the Brain (S.J.). A.H. thanks the German Bundesministerium für Bildung und Forschung (BMBF) for funding via the Bernstein Center for Computational Neuroscience (BCCN, project A2, FKZ 01GQ1005A), Göttingen.

References

1. S.W. Hell, *Science*, 2007, **316**, 1153–1158.
2. S. Van De Linde, M. Heilemann, and M. Sauer, *Ann. Rev. Phys. Chem.*, 2012, **63**, 519–540.
3. T. Dertinger, R. Colyera, G. Iyer, S. Weiss, and J. Enderlein, *Proc. Natl. Acad. Sci. USA*, 2009, **106**(52), 22287–22292.
4. T. Dertinger, R. Colyer, R. Vogel, J. Enderlein, and S. Weiss, *Opt. Express*, 2010, **18**(18), 18875–18885.
5. S. Geissbuehler, N.L. Bocchio, C. Dellagiacoma, C. Berclaz, M. Leutenegger, and T. Lasser, *Opt. Nanoscopy*, 2012, **1**, 4.
6. S. Geissbuehler, A. Sharipov, A. Godinat, N.L. Bocchio, P.A. Sandoz, A. Huss, N.A. Jensen, S. Jakobs, J. Enderlein, F.G. van der Goot, E.A. Dubikovskaya, T. Lasser, and M. Leutenegger, *Nature Commun.*, 2014, **5**, 5830.
7. T. Brakemann, A.C. Stiel, G. Weber, M. Andresen, I. Testa, T. Grotjohann, M. Leutenegger, U. Plessmann, H. Urlaub, C. Eggeling, M.C. Wahl, S.W. Hell, and S. Jakobs, *Nature Biotechnol.*, 2011, **29**, 942–947.

THERANOSTIC APPLICATIONS OF LOW-TOXIC SILICON NANOPARTICLES: BIOIMAGING & SONOSENSITISING

L.A. Osminkina[1], V.A. Sivakov[2], E. Tolstik[2,3], U.A. Natashina[1], K.E. Tsurikov[1], M.B. Gongalsky[1], A.A. Kudryavtsev[4], and **V.Yu. Timoshenko[1]**

[1] Lomonosov Moscow State University, Physics Department, Moscow, Russia, osminkina@vega.phys.msu.ru
[2] Leibniz Institute of Photonic Technology, Jena, Germany
[3] Institute of Physical Chemistry &, Abbe Center of Photonics, Friedrich-Schiller-University, Jena 07743, Germany
[4] Institute of Theoretical and Experimental Biophysics, RAS, Pushino, Russia

Abstract. Evaluation of photoluminescence, bio-imaging, cytotoxicity and sono-sensitizing properties of silicon nanoparticles (SiNPs) have been investigated. The prepared SiNPs exhibit efficient room temperature photoluminescence (PL) in the spectral region of 600–1000 nm. On the one hand in-vitro studies have demonstrated low cytotoxicity of SiNPs and possibilities of their bio-imaging applications. On the other hand, it has been found that SiNPs can act as efficient sensitizers of ultrasound induced suppression of the viability of Hep2 cancer cells. Listed modalities open new possibility of SiNP theranostic (therapy and diagnostic) applications.

Introduction

Currently a lot of works are devoted to bioapplications of different silicon nanostructures, e.g. porous silicon (PSi), which consists of a network of intersecting silicon nanocrystals (nc-Si) separated by nanometer-sized pores [1]. Usually PSi films are formed by electrochemical etching of bulk crystalline silicon (c-Si) in highly concentrated hydrofluoric acid (HF) solutions. In 1995 L. Canham [2] discovered biocompatibility of PSi and suggested its applications in biomedicine.

Besides the electrochemical treatment of c-Si there is another simple and cheap method to obtain PSi-like nanostructures, i.e. silicon nanowires (SiNWs), based on metal-assisted wet chemical etching (MACE) approach [3]. This is a simple method of wet chemical processing under the near ambient conditions, which allows us to treat a large area of c-Si without creation of back electrical contacts. The formed arrays of SiNWs consist of an almost non-intersecting nanowires and pores with diameters from several to hundreds nm [4].

Experimental results

We use SiNWs grown by the MACE method [5] on c-Si substrates of heavily boron-doped (0.001 Ω·cm) (100)-oriented wafers to produce of SiNWs. Figure 1 (a) shows typical cross-sectional scanning electron microscopy (SEM) micrographs of SiNW arrays on c-Si. As can see from SEM (inset in Fig.(1a)), SiNWs have a highly porous structure, which is also confirmed by the TEM image of single SiNW as presented in Figure 1(b). Inset in Fig. 1(b) shows the corresponding electron diffraction pattern obtained in the "transmission" geometry for SiNWs. A TEM image of SiNPs, fabricated by ultrasound grinding of SiNWs in water, is presented in Figure 1(c). Insets in Figs 1(b) and 1 (c) show the electron diffraction pattern for SiNWs and SiNPs, respectively, and indicate the preservation of misoriented nanocrystals in SiNWs and SiNPs. Fig. 1(d) shows a size distribution function of SiNPs, obtained by DLS, which was characterized by a maximum at 135 nm. ZP of SiNPs in the initially obtained aqueous suspensions was –20±2 mV.

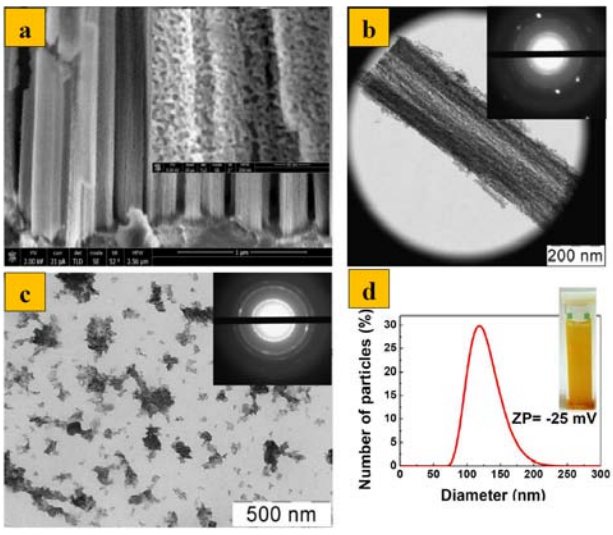

Fig. 1. (a) Cross-sectional SEM image of SiNW arrays on c-Si (the inset shows porous structure of SiNW); **(b)** TEM image of single SiNW (the inset shows the electron diffraction pattern of the SiNW); **(c)** TEM image of SiNPs (the inset shows the electron diffraction pattern of the SiNPs); **(d)** size distribution function of SiNPs, obtained by DLS (the inset shows digital photo of the SiNPs aqueous suspension with the concentration of 1 mg/ml)

The PL spectra of SiNWs and SiNPs consist of a broad band in the visible range with the maximum in the photon energy at 850 nm (1.7 eV) (see Fig. 2 (a)). The PL spectra of the samples are well explained by the radiative recombination of excitons confined in small silicon nanocrystals with average size about 2–6 nm [1]. Such nanocrystals were found by electron microscopy in porous volume of SiNWs and SiNPs as shown in Figure 1 (a) and (c). Produced SiNPs were relatively non-toxic to Hep2 cells in the concentration range of 2–125 μg/ml (see Fig. 2 (b)). The spatial distribution of SiNPs inside the cytoplasm of MCF-7 cells 24 h after their incubation was confirmed by a 3D high-resolution structured-illumination microscopy (HR-SIM) projection with a lateral resolution of 100 nm (see Fig. 2 (c)). Fig. 2 (d) represents the living Hep2 cell viability dependence on USI (0.88 MHz, 1 W/cm^2) duration. Set-up of in-vitro experiments is given in inset. It was found out that USI essentially no affect on the cell viability within the time interval from 0 to 10 min. At the same time, the combined action of ultrasound and SiNPs led to 50 % drop in the number of living cells as compared to the control. The effect of ultrasound and SiNPs on the cell viability can be explained by appearance of local increasing of temperature near SiNPs, so-called hyperthermia, caused by absorption of the ultrasound energy [6]. Also, the possibility of appearance of cavitation near the nanoparticles under ultrasound irradiation cannot be excluding.

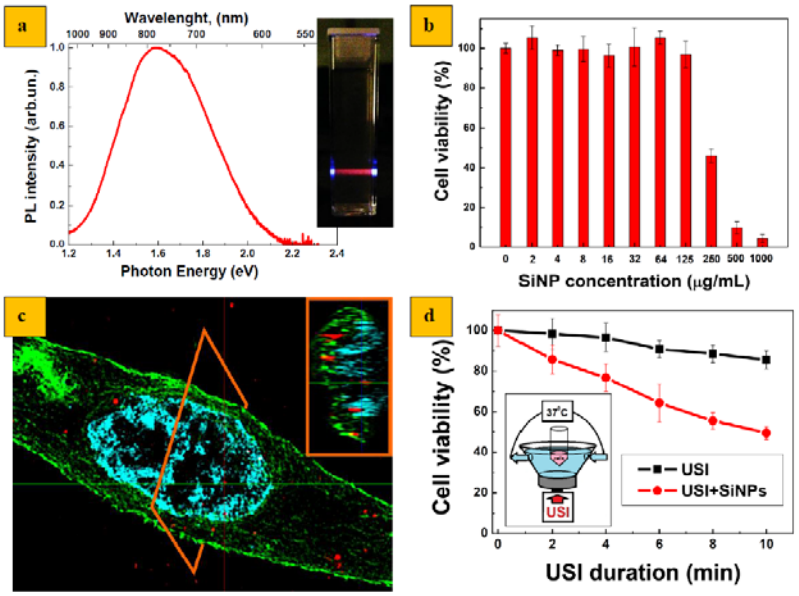

Fig. 2. (a) PL spectra of aqueous suspensions of SiNPs prepared from SiNWs (inset: typical appearance of the SiNP suspension under the UV line of argon-laser radiation); **(b)** In-vitro cytotoxicity of SiNPs towards living Hep2 cells; **(c)** Fluorescent HR-SIM images of MCF-7 cells 24h incubated with SiNPs; **(d)** The dependence of in-vitro cell viability on USI duration. The cells have been exposed to USI (black curve) or to the combined action of USI and SiNPs (red curve) (inset: schematic representation of the set-up for in vitro USI experiments)

In summary, low toxicity, photoluminescent and sonosensitizing properties of SiNPs, prepared by ultrasound milling of porous SiNW arrays, open new possibility of their theranostic (therapy and diagnostic) applications.

Acknowledgements

The work was partially supported by RFBR (Grant No. 15-52-15041). LAO greatly acknowledge the financial support by the joint program of MSU-DAAD “Vladimir Vernadsky” (A1479120).

References

1. A.G. Cullis, L.T. Canham, and P.D. Calcott, *J. Appl. Phys.*, 1997, **82**, 909.
2. L.T. Canham, *Adv. Mater.*, 1995, **7**(12), 1033.
3. Z. Huang, N. Geyer, P. Werner, J. de Boor, and U. Gösele, *Adv. Mater.*, 2011, **23**, 285.
4. Sivakov, G. Brönstrup, B. Pecz, A. Berger, G.Z. Radnoczi, M. Krause, and S.H. Christiansen, *J. Phys. Chem. C*, 2010, **114**, 3798.
5. K.A. Gonchar, L.A. Osminkina, R.A. Galkin, V.S. Marshov, D.V. Petrov, V.V. Solovyev, A.A. Kudryavtsev, V.A. Sivakov, and V.Yu.Timoshenko, *JNO*, 2012, **7**, 602.
6. A.P. Sviridov, V.G. Andreev, E.M. Ivanova, L.A. Osminkina, K.P. Tamarov, and V.Yu. Timoshenko, *Appl. Phys. Lett.*, 2013, **103**, 193110.

Invited

LARGE AREA MORPHO-FUNCTIONAL IMAGING OF EXCITABLE TISSUES

A.L. Allegra Mascaro[1,2], L. Silvestri[1,2], I. Costantini[1], L. Sacconi[1,2], B. Maco[3], G.W. Knott[3], and **F.S. Pavone[1,4,5]**

[1]LENS, Univ. of Florence, Sesto Fiorentino, Italy;
[2]National Institute of Optics, National Research Council, Florence, Italy,
[3]Ctr. Interdisciplinaire de Microscopie Electronique, Ecole Polytechnique Federale de Lausanne, Lausanne, Switzerland;
[4]Dept. of Physics, Univ. of Florence, Sesto Fiorentino, Italy;
[5]International Center of Computational Neurophotonics (ICON), Florence, Italy, pavone@lens.unifi.it

Abstract. Information processing inside the central nervous system takes place on multiple scales in both space and time. To obtain an integrated view, complementary approaches combining different imaging techniques should be combined. Two-photon fluorescence microscopy, combined with multi-photon laser nanosurgery, allow following the dynamics of damaged neurons in the cerebral cortex of living mice. We dissected the ultrastructural features of the same neuron previously imaged in vivo by means of correlative light and electron microscopy. The behavior of single cells depends on the network they are integrated, which needs to be investigated with large area optical techniques. We show how the apical dendritic arbor of a single cortical pyramidal neuron imaged in living mice was found in the large-scale brain reconstruction obtained with light sheet microscopy. With the correlative approach presented here, and the implementations we propose, researchers will be able to integrate the information obtained in a multi-level framework.

Brain activity involves many levels of organization that spans several orders of magnitude in space and time [1, 2]. Correlative microscopy strategies conveys multiple levels of complementary information from the same sample in an integrated dimension. For example, two-photon fluorescence microscopy (TPFM) can be used to monitor the activity and the plasticity of selected neurons in living mice, with resolution of single spines or varicosities [2, 3]. In combination with fluorescent protein expression techniques, two-photon microscopy has become an indispensable tool to image cortical plasticity in living mice [4]. In parallel to its application in imaging, multiphoton absorption has also been used as a tool for the selective disruption of intracellular structures *in vivo* [5, 6]. The resolution of TPFM is not enough to achieve subcellular details at the nanometer scale. A fruitful example of correlative approach is the combination of scanning electron and two-photon microscopy, which allows visualizing the ultrastructure of neurons after observing neuronal dynamics *in vivo* [7, 8]. The mating between light and electron microscopy, by bridging the gap between the micro- and the nanoscale, attracted the interest of many neuroscientist. An interesting example of this fruitful combination has been provided by imaging with focused ion beam milling and scanning electron microscopy (FIB-SEM) [8] the ultrastructural details of a regenerated axonal branch previously laser dissected and imaged with TPFM [6]. This combination, that exploit fiducial marks burned around the area of interest to retrieve the same region in the sample embedded for electron microscopy [9], allowed to dissect how regenerated axon interacts with possible postsynaptic targets. EM 3D reconstructions shows the close proximity of this newly formed branch with a spiny branch of a Purkinje cell, the postsynaptic neuronal target. The EM serial images allows visualizing both the distribution of mitochondria and synaptic vesicles inside the axon, and the structural interplay between the axon and the dendrite [6].

TPFM though able to investigate the long-term dynamics of events that last over months, is limited in the space it can access. It might be hard to perform a neuroanatomical classification of the neuron imaged with TPFM from superficial anatomical details. On the other hand, large-scale neuroanatomical data can be obtained, with cellular resolution, by a number of techniques like ultramicroscopy [10] and confocal light sheet microscopy (CLSM) [11]. Notably, these methods based on light sheet illumination are currently the only in which the sample is preserved without slicing, allowing multiple imaging rounds and therefore a greater flexibility. Anyhow, these approaches can only be applied to fixed samples, making it impossible to get any information about the temporal evolution of brain structure.

Here we show that by combining in vivo TPF microscopy with ex vivo confocal light-sheet and electron microscopy we can place high-resolution time-lapse images of selected neurites in a wider or more detailed anatomical framework, respectively. We could image the apical portion of a neuron in living mice using TPF microscopy, and afterwards we could find the same neuronal process after tissue fixation, dehydration and clearing. By acquiring many adjacent image stacks with two-photon microscopy, it was possible to observe a relatively large field of view with high resolution, high enough

to detect single dendritic spines. By using major blood vessels as landmark points, the same neuronal process observed in vivo was retrieved in the cleared tissue. Starting from this portion, the dendritic arbor can be reconstructed down to the cellular soma [12]. With the correlative approach presented here, researchers can now place in a three-dimensional anatomic context the neurons whose dynamics have been observed with high detail *in vivo*.

Finally, we will show the development of a new set of tools for improving the performances of CLSM and TPFM and their combination, and a new versatile clearing method for two photon and light sheet microscopy.

Acknowledgements

This research has received funding from LASERLAB-EUROPE (grant agreements no. 284464, EC's Seventh Framework Programme) and has been supported by the Italian Ministry for Education, University and Research in the framework of the Flagship Project NANOMAX. Regione Toscana supported this work in the framework of POR-CreO 2007-2013 action (SMAG project). This work has been supported by "Ente Cassa di Risparmio di Firenze." This work is part of the activities of the European Flagship Human Brain Project (grant agreement no. 604102). Part of this work was performed in the frame of the Proof of Concept Studies for the ESFRI research infrastructure project Euro-BioImaging at the PCS facility LENS.

References

1. A. Holtmaat, & K. Svoboda, "Experience-dependent structural synaptic plasticity in the mammalian brain", *Nat Rev Neurosci*, 2009, **10**, 647-658.
2. G.W. Knott, A. Holtmaat, L. Wilbrecht, E. Welker, & K. Svoboda, "Spine growth precedes synapse formation in the adult neocortex *in vivo*", *Nature neuroscience*, 2006, **9**, 1117-1124.
3. V. De Paola, *et al.*, "Cell type-specific structural plasticity of axonal branches and boutons in the adult neocortex" *Neuron*, 2006, **49**, 861-875.
4. F. Helmchen, & W. Denk, "Deep tissue two-photon microscopy", *Nat Methods*, 2005, **2**, 932-940.
5. A.L. Allegra Mascaro, L. Sacconi, & F.S. Pavone, "Multi-photon nanosurgery in live brain", *Frontiers in neuroenergetics*, 2010, **2**.
6. A.L. Allegra Mascaro, *et al.*, "*In vivo* single branch axotomy induces GAP-43-dependent sprouting and synaptic remodeling in cerebellar cortex", *Proceedings of the National Academy of Sciences of the United States of America*, 2013, **110**, 10824-10829.
7. B. Maco, *et al.*, "Correlative *in vivo* 2 photon and focused ion beam scanning electron microscopy of cortical neurons", *PloS one*, 2013, **8**, e57405.
8. G. Knott, H. Marchman, D. Wall, & B. Lich, "Serial section scanning electron microscopy of adult brain tissue using focused ion beam milling", *The Journal of neuroscience : the official journal of the Society for Neuroscience*, 2008, **28**, 2959-2964.
9. D. Bishop, *et al.*, "Near-infrared branding efficiently correlates light and electron microscopy", *Nature methods*, 2011, **8**, 568-570.
10. H.U. Dodt, *et al.*, "Ultramicroscopy: three-dimensional visualization of neuronal networks in the whole mouse brain", *Nat Methods*, 2007, **4**, 331-336.
11. L. Silvestri, A. Bria, L. Sacconi, G. Iannello, & F.S. Pavone, "Confocal light sheet microscopy: micron-scale neuroanatomy of the entire mouse brain", *Opt Express*, 2012, **20**, 20582-20598.
12. L. Silvestri, A.L. Allegra Mascaro, I. Costantini, L. Sacconi, & F.S. Pavone, "Correlative two-photon and light sheet microscopy", *Methods*, 2014, **66**, 268-272.

Invited

NANOPARTICLES FOR TWO-PHOTON AND LIFETIME BIO-IMAGING

E. Perevedentseva[1,2], A. Karmenyan[1], C.Y. Lin[1], A.S. Krivokharchenko[3], A.-I. Ahmed[1], M. Kormacheva[1], and C.L. Cheng[1]

[1] National Dong Hwa University, Hualien, Taiwan,
elena@mail.ndhu.edu.tw
[2] P.N. Lebedev Physics Institute of Russian Academy of Sciences, Moscow, Russia
[3] N.N. Semenov Institute of Chemical Physics of Russian Academy of Sciences, Moscow, Russia

Abstract. Nanoparticles-based systems are developed and realized for bio-imaging as an alternative to fluorescent dyes. Particularly, nanodiamonds' (ND) photoluminescence properties make them promising for number of imaging and probing bio-applications. In this work we discuss detection of the ND biodistribution in the zebrafish embryo model using different optical-spectroscopic methods of observation (confocal fluorescence microscopy, two-photon microscopy and life-time imaging) with the purpose to develop and optimize the methods for imaging and drug delivery tracing using ND, and compare with other nanoparticles (NP).

Nanoparticles applications in biology and medicine are nowadays widely developed [1]. In presented work we focus mostly on nanodiamonds (ND) bio-imaging and bio-labeling applications, based on their luminescence (fluorescence) properties. The main origins of the ND's fluorescence are defects and admixtures embedded in the diamond lattice (color centers). They reveal well-detectable, stable luminescence in different ranges of spectra, which can be excited with various excitations. The ND fluorescence strongly depends on ND structure. That allows development of various methods to optimize ND fluorescence properties modification In the combination with ND surface properties which allow the particles modification with bio-active molecules for interaction with target biosystem and treatment, these properties do ND promising nanomaterial for further development of ND theranostics applications, as imaging and delivery tracing, bio-sensing, photothermal treatment, etc. [2].

Development of ND use for bio-imaging and drug delivery tracing utilizes one-photon fluorescence of different color centers of ND, ability to excite two-photon fluorescence of some centers and analysis of fluorescence lifetimes. The methods to increase the ND fluorescence allow improving their properties both for fluorescence imaging and for fluorescence lifetime imaging (FLIM). Particularly, fluorescent ND (FND) emits the fluorescence with lifetime longer than lifetimes of dyes for the biological samples staining or of cellular autofluorescence sources, allowing separation of FND emission from the fluorescence background [3].

In this study lifetime imaging has supplemented the fluorescence confocal microscopy and two-photon imaging to observe and analyze the nanoparticles interaction with such biological living object as early-stage embryos focusing on the well-reproducible zebrafish embryo model. The nanoparticles biodistribution in the embryo *in vivo* during its growth and development was observed. NDs of size 100 nm have been injected in early-stage fish embryo in concentration 1 mg/ml, 4.6 nl per embryo, in yolk; the development of embryo and NDs' distribution were watched up to 72 hs. Additionally, embryo development and morphology have been analyzed in the presence of nanoparticles inside the embryos (zebrafish embryo) or in growth medium (mammalian – mice – embryo), effects from particles with different structure, optical and surface properties have been compared.

The two-photon images were obtained and fluorescence lifetimes of the embryo structures and nanodiamonds have been measured using Ti-sapphire laser with excitation 800 nm; 150 fs; 80 MHz connected with two-dimensional scanner. The registration was done with single photon counting cooled PMT. The time delay curves and histograms of distribution on the lifetimes for studied NDs and fish embryos are shown in Figure 1. In the Figure 2 the confocal image (obtained with confocal scanning microscope TCS SP5, Leica, Germany, using excitation 488 nm), two-photon image and lifetime image of the fish embryo with ND after 4 h past the injection are presented. Further observation allows detection of ND in/relatively the embryo during development, as well as demonstrating low toxicity of ND for the embryo. The zebrafish model for a safety evaluation of the ND biodistribution and interaction with different organs of developing larvae, for using ND-based nano-carrier or nano-label is discussed. Additionally to NDs of various properties, other kinds of nanoparticles are tested and compared with NDs.

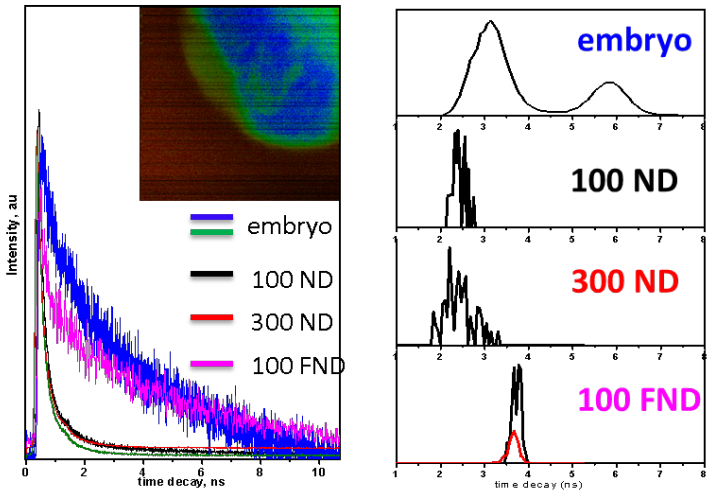

(a) **(b)**

Fig. 1. Interaction of different kinds of nanodiamonds with zebrafish embryos. (a) Time decay curves; inset is FLIM of the embryo without ND; (b) corresponding to (a) histograms of distribution on the life-times for the embryo structures and different kinds of NDs

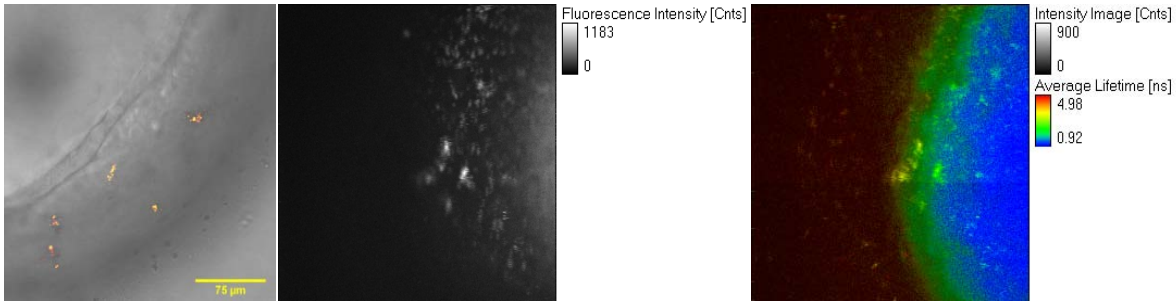

(a) **(b)** **(c)**

Fig. 2. Images of embryo with FND of size 40 nm: (a) confocal fluorescence image, excitation 532 nm, detection in range 600–670 nm; (b) two-photon image and (c) FLIM measured at excitation 800 nm and detected in range 450–640 nm

Acknowledgements

The research was supported by Ministry of Science and Technology of Taiwan with grant No. 103-2112-M-259-001-MY3

References

1. K. Riehemann, S.W. Schneider, T.A. Luger, B. Godin, M. Ferrari, and H. Fuchs, *Angew. Chem. Int. Ed.*, 2009, **48**, 872 – 897.
2. E. Perevedentseva, Y.-C. Lin, Mona Jani, and C.-L. Cheng, *Future Medicine. Nanomedicine,* 2013, **8**(12), 2041-2060.
3. Y. Kuo, T.-Y. Hsu, Y.-C. Wu, and H.-C. Chang, *Biomaterials*, 2013, **34**, 8352-8360.

Invited

IMAGING PROTEIN-PROTEIN INTERACTIONS IN LIVING SPECIMENS: FLIM AND FRET MICROSCOPY

A. Periasamy

The W.M. Keck Center for Cellular Imaging, Physical and Life Sciences Building (PLSB), Departments of Biology and Biomedical Engineering, University of Virginia, Charlottesville, VA 22904, USA
ap3t@virginia.edu

Key words: FRET, FLIM, Protein-protein Interactions, Visible Fluorescent Proteins, NADH. Tryptophan (TRP), Prostate Cancer Cells.

Förster resonance energy transfer (FRET) technique is increasingly employed to access the molecular mechanisms governing diverse cellular processes such as vesicular transport, signal transduction and the regulation of gene expression. FRET to occur, the protein molecules should be close together within 10 nm, the dipole moment of the fluorophore targeted to the proteins should have an appropriate orientation, and the spectral overlap of the donor emission to the acceptor absorption should be >30% for FRET to occur [1–2]. FRET can be used to estimate the distance between interacting protein molecules in vivo or in vitro using light microscopy systems. Visible fluorescent proteins (VFPs) have been widely used as a FRET pair in addition to organic dyes. Light microscopy techniques including wide-field, confocal and multiphoton microscopy systems provide spatial information of the interacting proteins with nanometer resolution [3]. The microscopy technique provides contamination in the FRET signal due to spectral overlap of donor emission to the acceptor absorption. These contaminations have to be removed to make a reasonable interpretation of the FRET data [3–6]. Number of algorithms has been developed to remove the contaminations in the FRET signal. On the other hand, fluorescence lifetime imaging microscopy (FLIM) approach provides quantitative information with spatial and temporal details of protein-protein interactions. In FLIM-FRET technique one follows the change in lifetime value of the donor without and with the acceptor molecules [7–8]. FLIM is sensitive to the local microenvironment of the molecule but insensitive to the change in fluorophore concentration or excitation intensity. No algorithm is required to remove the contamination. In FLIM-FRET techniques one should follow the change in donor molecule lifetime in the presence and the absence of acceptor. All the above mentioned techniques require the protein molecules should be labeled or expressed with organic dyes or VFPs. As an example, we describe the usage of FRET methodologies using Cerulean-Venus as a FRET pair to investigate the C/EBPα dimerization in the living GHFT1 live cell nucleus (2- and 3-color FRET).

On the other hand FRET can also be measured using the natural fluorescence of the molecules such as interaction between NADH and tryptophan. Changes in energy metabolism, mitochondrial function and levels of reactive oxygen species have been shown to induce alterations in cellular activities which are different in cancer vs. normal cells. Investigation of the metabolic activity at the molecular level potentially provides a method of detection of cancer at the early stages [9]. Three-photon excitation microscopy in combination with fluorescence lifetime imaging microscopy (FLIM) and FRET allows us to investigate the molecular behavior over time and space at different environmental conditions. In our earlier investigation of tryptophan (TRP) as a metabolic marker, we have shown statistically significant differences in the TRP fluorescence lifetimes in non-tumorigenic versus tumorigenic cells by 3P-FLIM-FRET imaging [10]. Our investigations suggest that the TRP fluorescence lifetimes in the cytosol-mitochondria are quenched by NADH at higher bound/free ratios.

In this investigation we used LNCaPs- Caucasian prostate cancer cell line [11]. We used 3p-FLIM-FRET microscopy to investigate the metabolic response of LNCaPs cells at various conditions using the drug taxol. We observed the metabolic mechanism/profile of mitochondria differently in normal versus LNCaP cell lines due to taxol treatment.

References

1. T. Förster, "Energy migration and fluorescence," *J. Biomed. Opt*., **17**(1), 011002.
2. J.R. Lakowicz, "*Principles of Fluorescence Spectroscopy*," 3rd Ed., Springer.
3. A. Periasamy and R.N. Day, "*Molecular Imaging: FRET Microscopy and Spectroscopy*, " Oxford, NY, 2005.

4. Y. Chen, M. Elangovan, and A. Periasamy, "*FRET data analysis: The algorithm*," in Molecular Imaging: FRET Microscopy and Spectroscopy, A. Periasamy and R.N. Day, Eds. New York: Oxford, 2005, pp.126-145.
5. Y. Sun, C. Rombola, V. Jyothikumar, and A. Periasamy, "Förster resonance energy transfer microscopy and spectroscopy to localize protein-protein interactions in live cells, " *Cytometry A*, 2013, **83A**(9), 780-793.
6. Y. Sun, H. Wallrabe, C. Booker, R.N. Day, and A. Periasamy, "Three-color spectral FRET microscopy localizes three interacting proteins in living cells," *Biophy. J.*, 2010, **99**, 1274-1283.
7. A. Periasamy and R.M. Clegg, *FLIM Microscopy in Biology and Medicine*. CRC Press (Taylor & Francis Group), NY, 2010.
8. Y. Sun, R.N. Day, and A. Periasamy, "Investigating protein-protein interactions in living cells using fluorescence lifetime imaging microscopy," *Nature Protocols*, 2011, **6**, 1324-1340.
9. Q. Yu, & A.A. Heikal, "Two-photon autofluorescence dynamics imaging reveals sensitivity of intracellular NADH concentration and conformation to cell physiology at the single-cell level," *J. Photochem Photobiol B*, 2009, **95**(1), 46-57.
10. V. Jyothikumar, Y. Sun, and A. Periasamy, "Investigation of tyrptopahn-NADH in live human cells using 3-photon fluorescence lifetime imaging," *J. Biomed. Opt*., 2013, **18**(6), 060501.
11. S. Koochekpour, T. Marlowe, K.K. Singh, K. Attwood, and D. Chandra, "Reduced mitochondrial DNA content associates with poor prognosis of prostate cancer in african american men," *PLoS ONE*, 2013, **8**(9), e74688.

Invited

IN VIVO AND EX VIVO MULTIPHOTON IMAGING OF NANOPARTICLE AND DRUG INTERACTIONS WITH LIVING SYSTEMS

M.S. Roberts[1,2], X. Liu[2], A. Holmes[1], C. Thompson[1,2], M. Pastore[1], Y. Mohammed[2], J.E. Grice[2], H.Wang[2], X. Laing[2], W. Sanchez[2], H. Studier[1]

[1] The University of South Australia, School of Pharmacy and Medical Science, Adelaide, SA, 5001,
[2] The University of Queensland, School of Medicine, Princess Alexandra Hospital, Brisbane, QLD, 4102, Australia

KEY WORDS: multiphoton tomography (MPT), fluorescence lifetime imaging (FLIM), nanoparticle, disposition, viability, skin, liver, melanoma.

One of our key goals is to visualize the *in vivo* targeted delivery of diagnostic and therapeutic agents in animals and humans at a cellular level. In this paper, we directly observe and quantify solute and nanoparticle localization, metabolism, and tissue responses in various organs in space over time using high resolution, non-invasive biophotonic imaging. Studies were undertaken *in vivo* and *ex vivo* after parenteral and topical administration using state-of-the multiphoton tomography with fluorescence lifetime imaging.

This work was supported by the National Health & Medical Research Council (NHMRC) of Australia, the Australian Research Council (ARC) and the Cancer Councils of Queensland and South Australia. We acknowledge advice and support given by Victoria Cogger, David Le Couteur, Darrell Crawford, Robert Hoffman, Karsten Konig, Tarl Prow and Wolfgang Becker in the undertaking of this work

Invited

TRAPPING FAST TRANSIENT EFFECTS IN FLUORESCENCE LIFETIME IMAGING

V. Shcheslavskiy[1], W. Becker[1], S. Frere[2], and **I. Slutsky[2]**

[1]Becker&Hickl GmbH, Berlin, Germany, e-mail:vis@becker-hickl.de
[2]Tel Aviv University, Sackler Faculty of Medicine, Sagol School of Neuroscience, Tel Aviv, Israel

Abstract. We present a technique that records transient changes in the fluorescence lifetime of a sample with spatial resolution along a one-dimensional scan. The technique is based on scanning the sample with a high-frequency pulsed laser beam, detecting single photons of the fluorescence light, and building up a photon distribution over the distance along the scan, the arrival times of the photons after the excitation pulses and the time after a stimulation of the sample. The maximum resolution at which lifetime changes can be recorded is given by the line scan period. Transient lifetime effects can thus be resolved at a resolution of about one millisecond. We demonstrate the technique for recording photochemical and nonphotochemical chlorophyll transients in plants and transient changes in free Ca^{2+} in cultured neurons.

Introduction

Fluorescence lifetime imaging (FLIM) by multidimensional TCSPC is based on raster-scanning a sample, detecting single photons of the fluorescence light emitted, and building up a photon istribution over the coordinates of the scan area, x and y, and the arrival times, t, of the photons after the laser pulses. For multi-wavelength FLIM the wavelength of the photons is added as an additional imension. The results can be interpreted as an array of pixels, each containing a large number of time channels for consecutive times after the excitation pulses [1]. Transient effects in the fluorescence lifetime can be recorded by time-series FLIM. Subsequent FLIM recordings are performed, and the data saved into consecutive data files. Time-series of FLIM images can be recorded at surprisingly high rate, especially if readout times are avoided by dual-memory recording. Nevertheless, each step of a time series requires at least one complete x-y scan of the sample. With the typical frame rates of fast galvanometer scanners lifetime changes can be recorded at a maximum resolution on the order of 100 ms to 1 second. Lifetime changes faster than that can be recorded by single-point measurements, as has already been demonstrated in [1]. However, single-point measurements do not deliver information about the spatial distribution of the effects observed.

Technical Solution

A solution to spatially-resolved transient recording is, again, provided by multi-dimensional TCSPC. The approach is illustrated in Fig. 1. Figure 1, left, shows the photon distribution built up by normal TCSPC FLIM. It is a distribution of photon numbers over x, y, and t. In Fig. 1, right, one spatial coordinate (y) has been replaced with an 'experiment time', T. The experiment time, T, is the time after a stimulation of the sample, or after any other event that is expected to be temporally correlated to a lifetime change in the sample. X is the distance along a spatially one-dimensional scan.

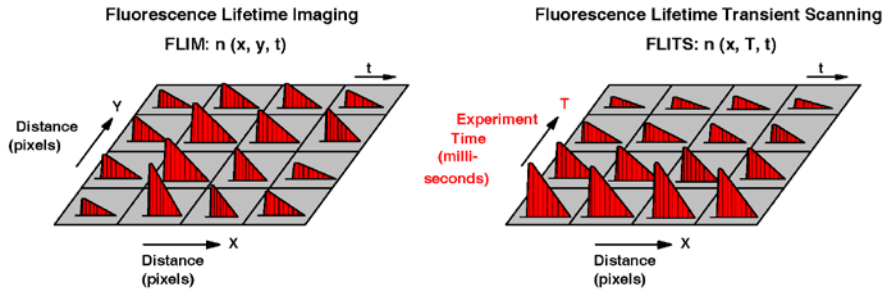

Fig. 1. Left: Photon distribution built up by standard FLIM.
Right: Photon distribution built up by fluorescence lifetimetransient scanning

As long as the stimulation occurs only once the recording process appears simple: The sequencer of the TCSPC module starts to run with the stimulation, and puts the photons in consecutive time channels along the T axis. The result is a time-series of line scans. Obviously, the resolution in T is limited by the period of the line scan only, which is about 1 ms for the commonly used scanners.

Results

To demonstrate fluorescence lifetime-transient scanning we used the 'chlorophyll transients' that occur when a live plant is exposed to light. Upon illumination, the fluorescence lifetime (and intensity) first increases. The increase happens within a few milliseconds or tens of milliseconds. It is attributed to the progressive saturation of photosynthesis channels, and a corresponding decrease in fluorescence quenching. The increase in the fluorescence quantum efficiency is therefore called 'photochemical transient'. Recording the photochemical transient requires periodical stimulation and acquisition of the data over a long period of time. Both the laser on-off signal and the frame clock were therefore generated by a bh DDG-210 pulse generator card. The on-off period was 1 second, the 'on' time within the period was 200 ms. Each turn-on of the laser initiates a photochemical transient, i.e. a increase of the fluorescence lifetime. In the laser-off period the leaf partially recovers, so that the next laser-on initiates a new transient. The total acquisition time was 40 seconds, i.e. 40 on-off periods were accumulated. The result is shown in Fig. 2.

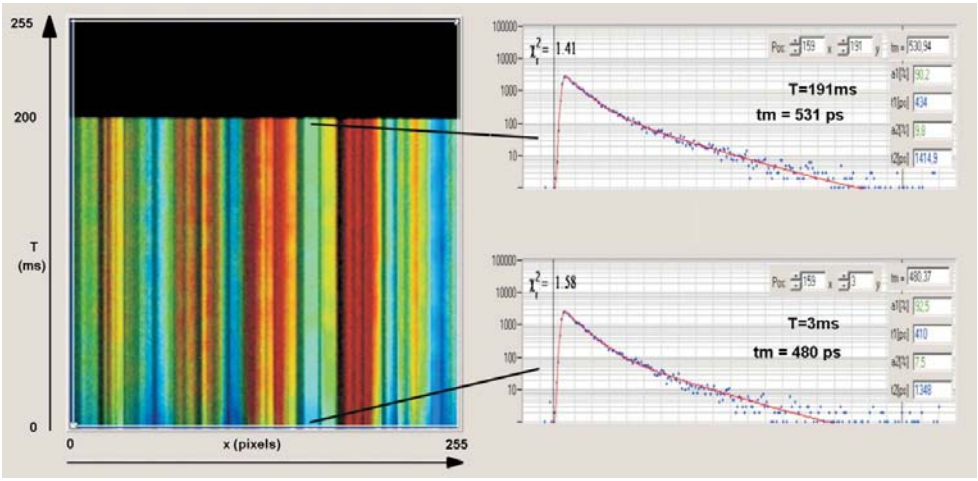

Fig. 2. FLITS image of photochemical chlorophyll transient. Horizontal: Distance along the line scanned. Vertical, bottom to top: Time, T, after the start of illumination. Line time 1 ms, 256 lines, total time interval recorded 256 ms. Laser turned on at T=0, laser-on time 200 ms. Left: Lifetime image. Right: Amplitude-weighted lifetime of double-exponential decay, blue to red corresponds to 450 ps to 650 ps. Decay curves for a selected pixel (x5159) within the line for T53 ms and T5191 ms into the laser-on phases. The amplitude-weighted lifetime increases from 480 ps to 531 ps

Summary

FLITS records fluorescence-lifetime transients at a time scale down to about one millisecond with spatially one-dimensional resolution. Technically, FLITS is obtained by line scanning and replacing the 'frame clock' of a TCSPC FLIM system with a trigger pulse that is synchronous with the event that stimulates the lifetime change in the sample. The technique can thus easily be implemented in confocal or multiphoton laser scanning microscopes, provided these are able to run a fast line scan. The technique works both with single-shot stimulation, or with periodic stimulation. For a given photon detection rate, the lifetime accuracy for single-shot stimulation decreases with decreasing time-channel width along the transient-time axis. This is not the case for periodic stimulation: Here the accuracy depends on the total acquisition time. Periodic stimulation is thus the key to high fluorescence-transient resolution. Potential applications of FLITS are experiments of plant physiology, electrophysiology, and Ca^{+} imaging of neuronal tissue.

References

1. W. Becker, *Advanced time-correlated single-photon counting techniques*, Springer, Berlin, 2005.

BIOCOMPATIBLE POLYMERIC NANOPARTICLES DOPED WITH CYANOPORPHYRAZINE CHROMOPHORS AS POTENTIAL PHOTOSENSITIZER FOR FLUORESCENCE DIAGNOSTICS AND PHOTODYNAMIC THERAPY

N.Y. Shilyagina[1], N.N. Peskova[1], S.A. Lermontova[2], M.V. Shirmanova[3], A.V. Yakimansky[4], S.V. Gamayunov[1,5], L.G. Klapshina[1,3], and **I.V. Balalaeva[1]**

[1] N.I. Lobachevsky State University of Nizhny Novgorod, Nizhny Novgorod, Russia, nat-lekanova@yandex.ru
[2] Institute of Organometallic Chemistry of RAS, Nizhny Novgorod, Russia
[3]Nizhny Novgorod State Medical Academy, Nizhny Novgorod, Russia
[4]Institute of Macromolecular Compounds of RAS, St.Petersburg, Russia
[5]Regional Oncological Hospital, Nizhny Novgorod, Russia

Abstract. The comparative investigation of the photobiological properties of potential photosensitizing agents based on tetra(4-fluorophenyl)tetracyanoporphyrazine incorporated into different water-soluble polymer nanoparticles was carried out. Nanoparticles based on polymer brushes (polyimide-*graft*-polymethacrylic acid) was shown to be the most perspective in terms of achievement the maximal accumulation selectivity in tumor tissues, high cellular uptake and photoinduced cell toxicity.

Novel class of tetratetracyanoporphyrazine chromophores combining properties of photosensitizers and molecular rotors was synthesized recently [1]. For biocompatibility enhancement and improvement of pharmacokinetic properties we incorporated one of the chromophores (namely, tetra(4-fluorophenyl)tetracyanoporphyrazine, Pz) into different water-soluble polymer nanoparticles based on polyethylene glycol (PEG), methylcellulose (MC), sodium alginate (AlgNa) and novel polymer compound "polymer brushes" (PB, polyimide-*graft*-polymethacrylic acid [2]) (hereinafter, Pz-doped nanoparticles). Photobiological properties of Pz-doped nanoparticles were tested both *in vitro* and *in vivo*.

Optical properties of all biocompatible forms prepared were investigated. The excitation maximum at 590 nm and fluorescence in red spectral region (maximum at 635 nm) were observed for all types of Pz-doped nanoparticles independently from polymer used. The intensity of fluorescence strongly depended on local environment parameters such as viscosity and protein presence. The fluorescence quantum yield for Pz-doped nanoparticles in presence of albumin was significantly higher than in distilled water solution – up to 100-fold in case of PB nanoparticles.

All Pz-doped nanoparticles were shown to lead to Pz accumulation in living tumor cells during the first 30 minutes after injecting into the cell growth medium (Fig. 1). The accumulation was shown for several human and murine tumor cells lines – A431, T24, HeLa, CT-26. The uptake was not associated with clathrin-mediated pathway of endocytosis as it was shown in experiments with inhibition of this pathway by chlorpromazine. The presence of proteins in cell grow medium was shown to have significant impact on Pz uptake into cells – the Pz accumulation decreases with adding of serum proteins in the medium.

In cell culture experiments the Pz-doped nanoparticles were shown to be localized in intracellular membranes (presumably endoplasmic reticulum and Golgi apparatus) and nuclear membranes. The accumulation of Pz in nuclear and perinuclear regions has a very significant value in PDT, because nuclear membranes assumed to be the most vulnerable to photodamage.

Photoinduced and dark toxicity of Pz-doped PB-nanoparticles were investigated *in vitro*, the half maximal inhibitory concentration (IC50) was determined. The IC50 for this type of nanoparticles was shown to be 20 μM for 10 J/cm^2 illumination by 625 nm light, and much higher than 60 μM when incubated in dark. It confirms the efficacy of Pz-doped PB-nanoparticles as a potential agent for photodynamic therapy. PB-nanoparticles *per se* demonstrated no cell toxicity.

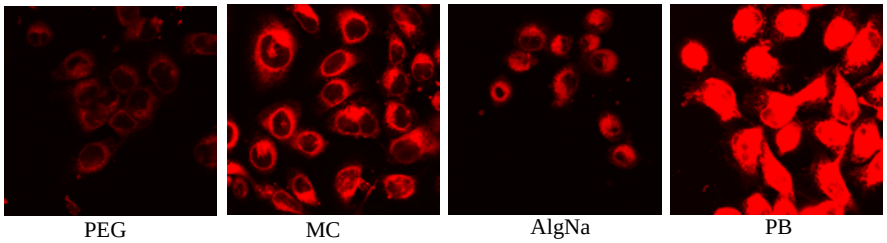

Fig. 1. Cellular uptake of the Pz-doped nanoparticles based on different biocompatible polymers

Experiments on mice bearing subcutaneously grafted metastatic colorectal carcinoma CT-26 demonstrated strong dependence of Pz pharmacokinetics on nanoparticles (Fig. 2). Pz-doped PB-nanoparticles demonstrated the most selective accumulation of Pz in tumor relative to normal tissues. The maximal contrast of accumulation (4-fold) was reached 24 hours after injection. High selectivity of Pz-accumulation in tumor was confirmed by confocal microscopy *ex vivo*.

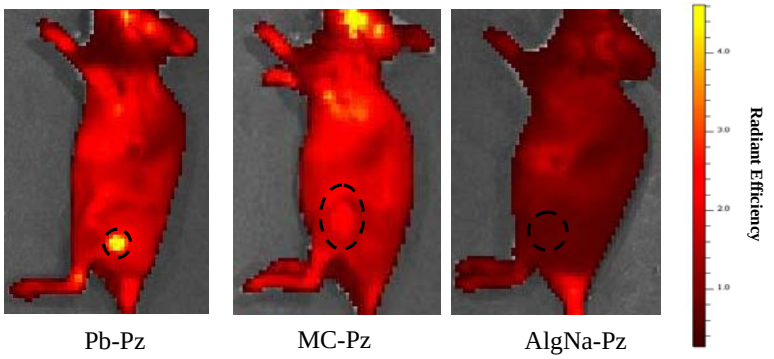

Pb-Pz MC-Pz AlgNa-Pz

Fig. 2. Fluorescent images of mice with CT-26 tumors 3 hours after injection of Pz-doped nanoparticles. Tumor region is outlined by dashed line

Conclusions

Among Pz-doped nanoparticles, PB-nanoparticles proved to be promising for fluorescence diagnostics and photodynamic therapy due to the highest selectivity of accumulation in tumor, high cellular uptake and photoinduced cell toxicity. Localization of Pz in perinuclear region is very beneficial for an efficient photodinamic therapy. Furthermore, belonging Pz to the group of fluorescent molecular rotors make it possible to monitor the physiological effects of PDT-treatment by estimation its photophysical parameters.

Acknowledgements

This work was partly supported by Ministry of Education and Science of Russian Federation grant (contract №14.Z50.31.0022)**,** the Russian Foundation for Basic Research (projects №14-02-00753).

References

1. M.A. Izquierdo, A. Vysniauskas, S.A. Lermontova, et al., *Journal of Materials Chemistry B,* 2014, **3**(6), 1089.
2. A.V. Yakimansky, T.K. Meleshko, D.M. Ilgach, et al., *Journal of Polymer Science Part A: Polymer Chemistry*, 2013, **51**(20), 4267.

Invited

BIOMEDICAL APPLICATIONS OF MAGNETO-PLASMONIC NANOCLUSTERS

K. Sokolov[1,2*], C.-H. Wu[1], J. Cook[1], T. Zal[3], and **S. Emelianov[1,2]**

[1]Department of Biomedical Engineering, University of Texas at Austin, Austin, Texas 78712, USA
[2] Department of Imaging Physics, University of Texas M.D. Anderson Cancer Center, Houston, Texas 77030, USA,
ksokolov@mdanderson.org
[3]Department of Immunology, University of Texas M.D. Anderson Cancer Center, Houston, Texas 77030, USA

Abstract. Multimodal nanoparticles can offer unique solutions to many challenging biomedical problems. Specifically, magneto-plasmonic nanoparticles with a strong red-NIR absorbance, superparamagnetic properties and a high magnetic moment can be used for multimodal imaging and magnetic manipulations. This combination of properties is highly advantageous in detection of circulating tumor cells (CTCs) in whole blood without intermediate purification steps. Furthermore, magneto-plasmonic nanoparticles can provide novel solutions to enhancement and monitoring of cell based therapies.

Current and emerging technologies for CTC assays include the CellSearch™ system (Veridex, FDA approved for prognosis in breast, prostate, and colorectal cancer) that utilizes ferrofluids consisting of magnetic nanoparticles coated with antibodies against epithelial cell adhesion molecules (EpCAM) [1]. Micro-fluidic technology has also been applied for CTC detection, capable of separating of CTCs from whole blood samples [2, 3]. Like CellSearch, cells are visualized by fluorescent staining. Isolation of CTCs by size aims at direct enrichment of epithelial cells using filtration-based approaches [4]. Microscopic approaches, such as fiber-optic array–scanning technologies, are based on scanning of nucleated cells deposited on a glass slide. The putative CTCs are subsequently stained with a Wright-Giemsa stain or Papanicolau stain and compared to the primary and metastatic tumors [5].

These methods often fail to detect CTCs in patients with metastatic cancers, possibly, due to down-regulation of EpCAM in metastases initiating cells (MIC) [6]. Furthermore, most of them require multiple enrichment, purification, extensive washing, and staining steps to minimize background from normal cells. These excessive handling can result in a loss of CTCs. Therefore, new approaches that minimize processing steps and are not dependent on EpCAM are required for a highly sensitive and specific detection of CTCs.

Here we address this challenging problem by developing nanoparticle probes with multiple functionalities. Integration of multiple components in a single nanostructure is a challenging task. Most of the existing approaches to synthesis of hybrid nanoparticles require cumbersome multi-step protocols and result in nanostructures with limited tunability of physical and optical properties. Here, we developed a new type of nanoparticles which consist of primary 6 nm iron oxide core-gold shell nanoparticles that form highly uniform spherical assemblies with sizes that can be varied from *ca.* 70 to 180 nm [7, 8]. The magneto-plasmonic nanoclusters exhibit strong red-NIR absorbance and superparamagnetic properties with a high magnetic moment in an external magnetic field. We conjugated the nanoclusters with monoclonal antibodies specific for tumor biomarkers of breast, colon and skin cancers and demonstrated molecular specific optical and photoacoustic (PA) imaging with high sensitivity. We carried out experiments in whole blood from a normal volunteer spiked with various amounts of cancer cells. It was shown that cell capture efficiency exhibits a linear behavior from 5 to 500 cells per 2.5 mL of the whole blood. Furthermore, we showed that molecular targeted nanoclusters can be used for simultaneous magnetic capture and PA detection of cancer cells in whole blood with greater than 90% capturing efficiency with no laborious processing steps that are commonly used in other cancer cell capture and enumeration assays [9]. The magneto-plasmonic nanoparticle platform is being tested in blood samples of cancer patients with metastatic disease with a very good capture efficiency as compared to FDA approved CellSearch system.

Our immunotargeted nanoparticles can be easily adapted to a variety of biomarkers, targeting both surface receptor molecules and intracellular biomarkers of epithelial-derived cancer cells. In this presentation we will explore the opportunities afforded by the hybrid magneto-plasmonic nanoparticles and PA imaging for the development of a low cost simple and nearly real-time assays for capture, separation and enumeration of rare cells.

Acknowledgements

We gratefully acknowledge support from National Health Institute grants R01 EB008101 and R01 CA103830.

References

1. S. Riethdorf, H. Fritsche, V. Müller, T. Rau, C. Schindlbeck, B. Rack, W. Janni, C. Coith, K. Beck, F. Jänicke, S. Jackson, T. Gornet, M. Cristofanilli, and K. Pantel, *Clin. Cancer Res.*, 2007, **13**, 920.
2. S. Nagrath, L.V. Sequist, S. Maheswaran, D.W. Bell, D. Irimia, L. Ulkus, M.R. Smith, E.L. Kwak, S. Digumarthy, A. Muzikansky, P. Ryan, U.J. Balis, R.G. Tompkins, D.A. Haber, M. Toner, *Nature*, 2007, **450**, 1235.
3. E. Ozkumur, A.M. Shah, J.C. Ciciliano, B.L. Emmink, D.T. Miyamoto, E. Brachtel, M. Yu, P.I. Chen, B. Morgan, J. Trautwein, A. Kimura, S. Sengupta, S.L. Stott, N.M. Karabacak, T.A. Barber, J.R. Walsh, K. Smith, P.S. Spuhler, J.P. Sullivan, R.J. Lee, D.T. Ting, X. Luo, A.T. Shaw, A. Bardia, L.V. Sequist, D.N. Louis, S. Maheswaran, R. Kapur, D.A. Haber, and M. Toner, *Science Translational Medicine*, 2013, **5**, 179ra47.
4. G. Vona, A. Sabile, M. Louha, V. Sitruk, S. Romana, K. Schutze, F. Capron, D. Franco, M. Pazzagli, M. Vekemans, B. Lacour, C. Brechot, and P. Paterlini-Brechot, *Am J Pathol*, 2000, **156**, 57.
5. D. Marrinucci, K. Bethel, R.H. Bruce, D.N. Curry, B. Hsieh, M. Humphrey, R.T. Krivacic, J. Kroener, L. Kroener, A. Ladanyi, N.H. Lazarus, J. Nieva, and P. Kuhn, *Hum Pathol*, 2007, **38**, 514.
6. S.A. Joosse and K. Pantel, *Cancer Research*, 2013, **73**, 8.
7. C.H. Wu, J. Cook, S. Emelianov, and K. Sokolov, *Advanced Functional Materials*, 2014, **24**, 6862.
8. C.H. Wu and K. Sokolov, *J. Vis. Exp.*, 2014, **90**, e52090.
9. C.-H. Wu, Y.-Y. Huang, P. Chen, K. Hoshino, H. Liu, E.P. Frenkel, J.X.J. Zhang, and K.V. Sokolov, *ACS Nano*, 2013, **7**, 8816.

Invited

MICROENCAPSULATED DELIVERY SYSTEMS FOR CELL MANIPULATION AND INTRACELLULAR INTERROGATION

G.B. Sukhorukov[1,2]

[1] Queen Mary University of London, London, United Kingdom, g.sukhorukov@qmul.ac.uk
[2] Saratov State University, Saratov, Russia

One of the challenges in the bionanotechnology field is development of nano-sized delivery systems comprising different functionalities. These systems should enable to ship and to carry bioactive substances to pre-defined site and unload it in designed time and place. Layer-by-layer assembled capsules are have been intensively studied in last few years owing to their ability to encapsulate a wide range of chemicals, for their permeability to be modified and their responsiveness to different factors and functionalities to be tailored in one capsule entity. Current research leads to the fabrication of carriers with remote guiding and activation by optical, magnetic and ultrasound addressing, what envisages unique applications as multifunctional biomaterials *in-vivo*. Microcapsules display a broad spectrum of qualities over other existing microdelivery systems such as high stability, longevity, versatile construction and a variety of methods to encapsulate and release substances. Release and encapsulation of materials by light and ultrasound and their navigation with magnetic field is a particularly interesting topic. Microcapsules can be made sensitive to light by incorporation of light sensitive polymers, functional dyes and metal nanoparticles. Optically active substances can be inserted into the shell during their assembly as a polymer complex or following the shell preparation. Visible- and infrared- addressable microcapsules offer a large array of release strategies for capsules, from destructive to highly sensitive reversible approaches. The paper demonstrates application for intracellular delivery of compounds and cellular response as well as in vivo perspectives.

Submicron sized capsules are good model to mimicking bio-chemical processes in a confined geometry imitating cell organelles, whilst delivered inside cell (including neurons) and tissues the capsules could serve as intracellular reporter or enzymatic reactor. Biophotonic approaches are envisaged to enhance the possibilities for multifunctional use of capsules. The talk discusses possible solutions and promising applications as combined delivery and sensing inside biological cells.

References

1. G. Sukhorukov, "A smart pill", *Materials World*, 2011, 19(2), 23-24.

AG ON CARBON NANOWALLS SERS SUBSTRATES: AFFINITY TO AROMATICS

M.Yu. Tsvetkov[1], **S.A. Evlashin**[2], **K.V. Mironovich**[2], **N.V. Suetin**[2], and **V.N. Bagratashvili**[1]

[1] Institute on Laser and Information Technologies RAS, Moscow, Troitsk, Russia,
mtsvet52@mail.ru
[2] D.V. Skobeltsyn Institute of Nuclear Physics, M.V. Lomonosov Moscow State University,
Moscow, Russia

Abstract. We have elaborated substrates for surface enhanced Raman scattering (SERS) based on carbon nanowalls (CNW) with thin Ag films deposited on them. The morphology of nanowalls coated with solid silver film promotes strong inhomogeneous localization of optical radiation incident on the substrate, and the formation of numerous hot spots, which provide a huge enhancement of the Raman signal. It was found that the developed substrates possess high affinity for aromatic compounds, which allowed to reach the detection limit up to 10^{-7} M.

Among the various analytical methods developed at the present time in order to solve problems of early and very early diagnosis of various diseases, one of the most sensitive method is the Surface Enhanced Raman Scattering (SERS) [1]. It provides the plasmonic enhancement up to ~10^8 when registering integrated Raman scattering signals and to ~10^{12} during the registration of so-called "hot spots". However, in order to introduce SERS spectroscopy in biomedical practice it is necessary to solve the problem of providing direct contact of the test-analyte with plasmon environment (which is usually gold and silver nanoparticles and nanostructures). Only in this case it is possible to achieve high SERS enhancement factor needed to ultrasensitive diagnostics. Usually, this problem is solved by a variety of physical, chemical or biological approaches for surface modification and functionalization of nanostructured materials. However, these problems often have to be solved every time for each particular analyte. Therefore, SERS substrate attract substantial interest in which an affinity for the analyte is incorporated into their structure.

This report considers the SERS substrate formed by depositing of silver on carbon nanofilms (CarbonNanowalls – CNW) [2, 3]. CNWs are materials consisting of densely packed arrays of layered graphite-like micron-sized petals with a predominant vertical orientation and chaotic transverse to the average distance between the petals of hundred nanometers. The thickness of each petal can be varied from a few layers of graphene to tens nanometers. Silver film with a thickness of 100–300 nm are deposited on the surface of CNW by magnetron sputtering at direct current. Morphology of carbon nanowalls which are coated with solid silver film, contributes to strong inhomogeneous localization of optical radiation incident on the substrate, and the formation of numerous hot spots, which led to analytical SERS enhancement factor up to 5×10^4 for the dye Rhodamine 6G [4].

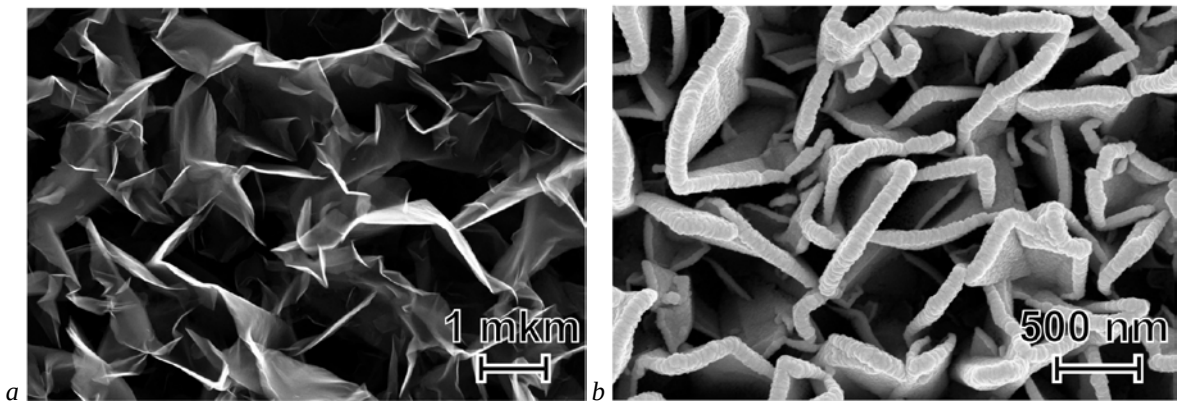

a *b*

Fig. 1. SEM image CNW (*a*) and a silver film deposited on CNW (*b*)

It is found that SERS substrate have a strong affinity for aromatic compounds which is explained by π-π stacking interaction of aromatics with the surface of CNW [5, 6]. During the study of this effect aromatic compound 4-aminothiophenol (4ATP) was used as the analyte. Detection limit has been reached up to 10^{-7} M, which significantly exceeds the limit of detection for Rhodamine 6G.

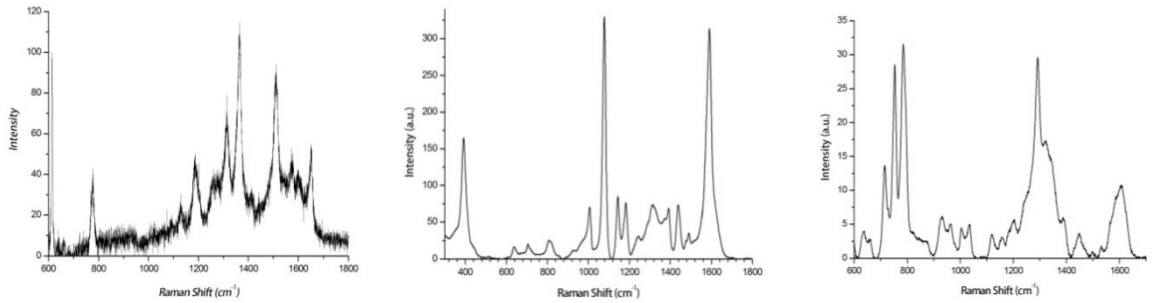

a *b* *c*

Fig. 2. SERS spectra of Rhodamine 6G (*a*), 4-aminothiophenol (*b*) and dopamine (*c*)

A comparative test of SERS substrates developed using sodium glutamate and dopamine as test analytes was carried out. These neurotransmitters are essentially characterized by the fact that dopamine composition has an aromatic ring. It has a crucial impact on the SERS enhancement.

Acknowledgements

The work on CNW synthesis, Ag nanofilms sputtering was supported by the Government of the Russian Federation (Grant of the Government of the Russian Federation for the Support of Scientific Investigations under the Supervision of Leading Scientists, Contract No. 14.B25.31.0019). We would like to thank the Russian Science Foundation (Grant 14-13-01422) for support of SERS analysis. MT and SE are grateful the Russian Foundation for Basic Research (Grants 13-02-01075 and 14-02-31575) for the financial support.

References

1. E.C. Le Ru and P.G. Etchegoin, *Principles of Surface Enhanced Raman Spectroscopy*, Elsevier, 2009.
2. M. Hiramatsu and M. Hori, *Carbon Nanowalls. Synthesis and Emerging Applications*, Springer-Verlag, 2010.
3. V.A. Krivchenko, S.A. Evlashin, *et al.*, *Scientific Reports*, 2013, **3**, doi:10.1038/srep03328.
4. M.Yu. Tsvetkov, S. A. Evlashin, *et al.*, *Proceedings SPIE*, 2015, **9450**, 94501V.
5. Z. Liu, J.T. Robinson, *et al.*, *Materials Today*, 2011, **14**(7-8), 316-323.
6. X. Liu, L. Cao, *et al.*, *Appl. Mater. & Interf.*, 2011, **3**, 2944-2952.

Invited

NANO-OPTICAL PROBES FOR ENHANCED IMAGING, SENSING AND THERAPY

V.V. Tuchin[1,2,3]

[1] Research-Educational Institute of Optics and Biophotonics, Saratov State University, Saratov, Russia;
[2] Institute of Precision Mechanics and Control of RAS, Saratov, Russia;
[3] Optoelectronics and Measurement Techniques Laboratory, *University of Oulu, Finland*
tuchinvv@mail.ru

Abstract. Nanoparticle/laser diagnosis and therapy of diseases is a novel modality realizing principles of theranostics which were recently formulated. To protect skin from UV, to provide cancer and inflammatory diseases treatment, and cell optoporation/transfection, technologies based on gold nanoparticles (nanoshells, nanorods, nanocages, and nanostars), gold/carbon nanotubes, TiO_2 nanoparticles and nanowires, and nanoparticle/PDT dye composites will be discussed. Nanoparticle delivery in tissues and applications of gypsum-titania nanocomposites for indoor antimicrobial coatings, gold nanoagents for optical imaging and therapy, and upconversion nanoluminophores for deep-tissue imaging will be analyzed.

Introduction

Nanoparticle/laser diagnosis and therapy of diseases is a novel modality realizing principles of theranostics, which were formulated and overviewed recently [1, 2]. For many years, TiO_2-nanoparticles used successfully to protect skin from UV light. Gold nanoparticle technologies are intensively developing to provide efficient cancer and inflammatory diseases treatments. Problems of tissue engineering and some specific diseases treatments can be solved on the basis of robust cell optoporation/transfection techniques by using appropriate nanoparticles and laser irradiation protocols. The goal of this study is to summarize recent achievements in the field of interaction of laser radiation with nanoparticles embedded into a tissue or cell in order to design nano-optical probes for enhanced imaging, sensing and therapy.

Methods and materials

To enhance diagnostic and therapeutic abilities of photothermal/PDT/photocatalytic technologies in treatment of cancer and inflammatory diseases and to provide controllable tissue and cell optoporation, different types of nanoparticles designed in many collaborating groups were used in this study [3-9]. Gold nanoparticles (GNPs) in the form of bulk spheres (GNSps), nanoshells (GNShs), nanorods (GNRs), nanocages (GNCs), and nanostars (GNSts) (IBPPM RAS; IFAC, Italy; Aix-Marseille University, France; Duke University, USA), photocatalytic TiO_2-nanospheres, -nanowires, and nanoparticle enriched gypsum (University of Oulu, Finland), nanocomposites – nanoparticle/photodynamic dye conjugates (IBPPM RAS), and upconversion luminescence nanoparticles (University of Oulu) were utilized in *in vitro*, *ex vivo* and *in vivo* measurements with animals.

Results and Conclusion

The distributions of differential and integral absorbing power of a gold nanoparticle, temperature increment, and Arrhenius damage integral were used to quantify biological action of CW laser heated nanoparticle [10, 11]. The effectiveness of biological response was presented in the two-dimensional coordinate space "laser wavelength (λ) × radius of nanoparticle (R)." It was found that the area in the space ($\lambda \times R$) with a minimal criticality to alterations of the local hyperthermia may be significantly displaced from the position of the plasmonic resonance. The generalization of the proposed methodology to the analysis of local hyperthermia produced by nanoparticles of different shapes (nanoshells, nanorods, nanostars) at pulse laser irradiation is possible.

Nanocomposites (NCs) consisting of a gold nanorod core and a mesoporous silica shell doped with hematoporphyrin (HP) was used to improve the efficiency of cancer treatment by combining photothermal and photodynamic therapies (PDT + PTT) at application to a xenografted tumor rat model *in vivo*. NCs directly injected into a solid tumor, generated singlet oxygen under 633-nm excitation and produced heat under 808-nm NIR laser irradiation. The efficiency of the combined therapy was evaluated by optical coherence tomography, histological analysis, and by measurements of the tumor volume. This treatment resulted in the large-area tumor necrosis and dramatic decrease in the tumor volume.

The effect of NIR laser radiation (808 nm) and gold nanorods on the cells of methicillin-sensitive *Staphylococcus aureus* (MSSA) and methicillin-resistant (MRSA) was studied. Nanorods having the dimensions 10×44 nm with the absorption maximum in the NIR, functionalized with human immunoglobulins IgA and IgG were used [5]. The killing efficiency up to 97 % of the population of microorganisms was demonstrated for both strains at the laser fluence of 180 J/cm^2.

The developments of antibacterial coatings based on photocatalytic nanomaterials is a promising route towards potential environmentally friendly applications in public buildings and health care facilities. Various types of TiO_2 nanofiber-based photocatalytic materials (nitrogen-doped and/or palladium nanoparticle decorated) and their composites with gypsum were demonstrated excellent antimicrobial properties by killing both MSSA and MRSA strains under blue LED light (405 nm) [7, 8]. In the case of MSSA cells, the palladium nanoparticle-decorated and nitrogen-doped TiO_2 composites demonstrated the highest antimicrobial activity.

There were also demonstrated that gold nanocomposite designing is a promising platform for optical imaging and treatment at cellular and tissue levels, usage of upconversion nanoluminophores is an attractive tool for deep-tissue imaging at tissue optical clearing, and nanosized extracellular vesicles generated by adipocytes at laser heating and photodynamic action is a new field for theranostics.

Acknowledgements

The study was supported by grant No. 14-15-00186 of the Russian Science Foundation.

References

1. V.V. Tuchin, R. Drezek, S. Nie, and V.P. Zharov (Guest Editors), "Nanophotonics for Diagnostics, Protection and Treatment of Cancer and Inflammatory Diseases", *J. Biomed. Opt.*, 2009, **14**(2).
2. N. Khlebtsov, V. Bogatyrev, L. Dykman, et al., *Theranostics*, 2013, **3**, 167-180.
3. G. Terentyuk, E. Panfilova, V. Khanadeev, et al., *Nano Res.*, 2014, **7**(3), 325-337.
4. B.N. Khlebtsov, E.S. Tuchina, V.A. Khanadeev, et al., *J. Biophotonics*, 2013, **6** (4), 338-351.
5. E.S. Tuchina, P.O. Petrov, K.V. Kozina, et al., *Quant. Electr.*, 2014, **44** (7), 683-688.
6. N.A. Trunina, M.E. Darvin, K. Kordas, et al., *IEEE J. Select. Tops. Quant. Electr.*, 2014, **20**(3), 7300108.
7. A. Sarkar, A. Shchukarev, A.-R. Leino, et al., *Nanotechnology*, 2012, **23**, 475711-1-8.
8. M. Mohl, A. Dombovari, A.-R. Rautio, et al., *J. Materials Chem. B.*, 2014, **2**, 1307-1316.
9. A.P. Popov, A.V. Karmenyan, A.V. Bykov, et al., *Proc. of OSA-SPIE*, 2013, **8801**, 88010C.
10. Yu.A. Avetisyan, A.N. Yakunin, and V.V. Tuchin, *J. Biophotonics*, 2012, **5**, 734-744.
11. A.N. Yakunin, Yu.A. Avetisyan, and V.V. Tuchin, *J. Biomed. Opt.*, 2015, **20**(5), 051030.

THE STUDY OF BIODISTRIBUTION OF CHLORIN E6 WITH AMINOALKYLAMIDE LINKER AND ITS BORON-COMPRISING NANOCONJUGATE FOR BORON-NEUTRON CAPTURE THERAPY

A.B. Voloveckiy[1], **N.Y. Shilyagina**[1], **I.V. Balalayeva**[1], **A.V. Maslennikova**[1,2], **M.A. Grin**[3], **A.F. Mironov**[3], and **A.V. Feofanov**[4,5]

[1] N.I. Lobachevsky State University of Nizhny Novgorod, Russia, voloveckiy91@gmail.com
[2] Nizhny Novgorod State Medical Academy
[3] Lomonosov Moscow State University of Fine Chemical Technologies
[4] M.M. Shemyakin and Yu.A. Ovchinnikov Institute of bioorganic chemistry of the Russian Academy of Sciences, Moscow
[5] Faculty of Biology of Lomonosov Moscow State University

Abstract. The work objective was comparing the biodistribution of chlorin e6 with aminoalkylamide linker and its boron-comprising nanoconjugate. The study was performed on 18 tumor-bearing Balb/c mice. Mice colon carcinoma CT-26 was used as a tumor model. The solutions of preparations were injected into a tail vein in a dose of 10 mg/kg of body weight. Animals were euthanized in 3 hours after injection. *Ex vivo* imaging of tumor, liver, lung, spleen, heart, skin, colon, muscle and kidney was performed by AxioObserver Z1 LSM 710 DUO RP NLO (Carl Zeiss, Germany). Excitation was implemented at a wavelength of 633 nm, registration was performed at two wavelengths: 583-653 nm and 653-730 nm. In 3 hours after injection, a high level of chlorine fluorescence was observed in liver, spleen and lung. Chlorine e6 with aminoalkylamide linker demonstrated a high uneven accumulation in tumor tissue. A boron-comprising nanoconjugate accumulated in the tumor significantly less.

Boron neutron capture therapy is a form of radiation therapy using the high propensity of the non-radioactive nuclide boron-10 to capture thermal neutrons resulting in the prompt nuclear reaction $^{10}B(n, \alpha)^{7}Li$. The products of this reaction have high linear energy transfer characteristics. Therefore, it is possible to selectively irradiate those tumor cells that have taken up a sufficient amount of ^{10}B (10^{9}/per one cell) [1]. For successful clinical use, the synthesis of boron compounds that allow achieving this concentration in tumor tissue is necessary. One of the prospective trends here is the use of boron-comprising porphyrin nanoconjugates [2]. In this case porphyrins are used as boron "transporters" to the target (tumor) due to their ability to accumulate and stay in tumor tissue (enhanced permeability and retention effect, EPR) [3].

The work objective was comparing the biodistribution of chlorin e6 with aminoalkylamide linker (n=6) and its boron-comprising nanoconjugate (fig. 1).

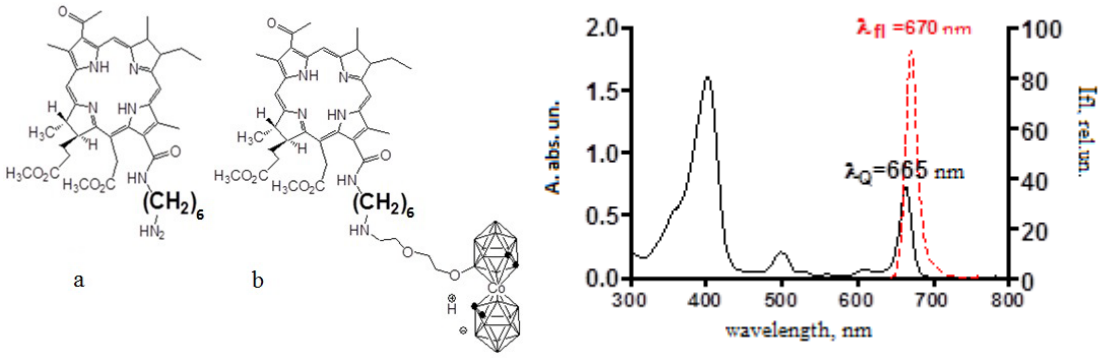

Fig. 1. Structures of chlorin e6 with aminoalkylamide linker (n=6) (a) and its boron-comprising nanoconjugate (b). The plot to the right shows absorption and fluorescence spectra of chlorin e6 with aminoalkylamide linker (n=6)

The study was carried out on male Balb/c tumor-bearing mice (18 animals total). Mice colon carcinoma CT-26 was used as a tumor model. Experiments were performed on the 9^{th} – 10^{th} day after tumor transplantation when a tumor size was 5–7 mm. The solutions of chlorin e6 derivate and its boron-comprising nanoconjugate were injected into a tail vein in a dose of 10 mg/kg of body weight. In three hours after injection, animals were euthanized by cervical dislocation. After preparation, the imaging of tumor, liver, lung, spleen, heart, skin, colon, muscle and kidney was carried out by AxioObserver

Z1 LSM 710 DUO RP NLO system (Carl Zeiss, Germany). For microscopic imaging, we used excitation at 633 nm and registration of a reflected signal at 583-653-nm range (white channel). The emission of chlorin e6 derivate was registered at 653–730 nm (red channel) under identical conditions for all images.

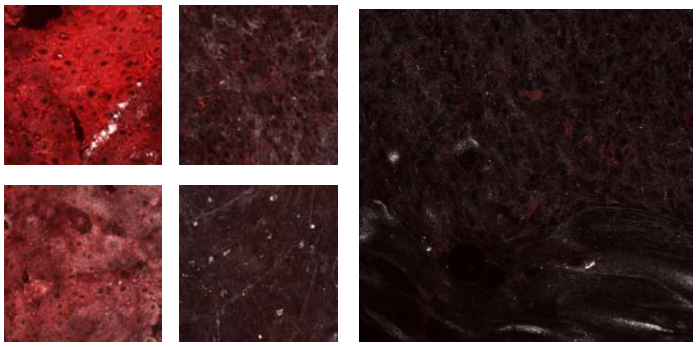

a b

Fig. 2. Biodistribution of chlorin e6 with aminoalkylamide linker (n=6) (a) and its boron-comprising nanoconjugate (b) in tumor tissue. Confocal microscopy, image size 225x225 μm. Wavelength 670 nm

In all organs, we observed a fluorescence signal at 670 nm, corresponding to chlorin e6 fluorescense. After injection of chlorin e6 with aminoalkylamide linker (n=6) a high uneven level of fluorescence was observed in tumor tissue (Fig. 2a). A boron-comprising chlorin e6 nanoconjugate demonstrated an essentially lower accumulation in tumor tissue (Fig. 2b). High accumulation of both compounds was registered in liver, kidney and spleen (Fig. 3). A characteristic peak at 670 nm was almost not observed in muscle, skin and smooth muscle (Fig. 3).

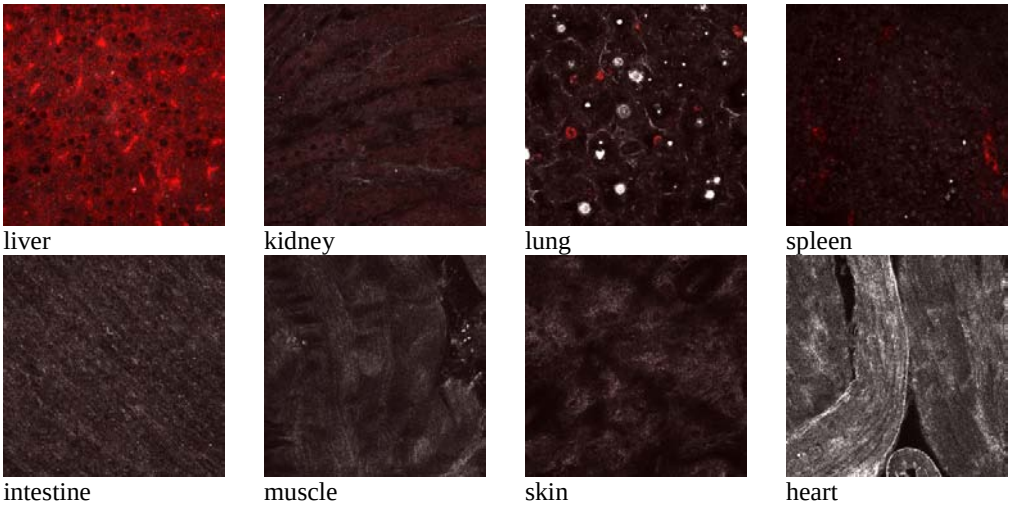

Fig. 2. Biodistribution of boron-comprising nanoconjugate of chlorin e6 in organs and tissures. Confocal microscopy, image size 225x225 μm. Wavelength 670 nm

Acknowledgements

This work was supported by RFBR (project № 14-02-00715).

References

1. A.K. Azab, H. Abu Ali, and M. Srebnik, Chapter 5: Boron Neutron Capture Therapy, *Studies in Inorganic Chemistry*, 2006, **22**, 337-366.
2. M.A. Grin, R.A. Titeev, D.I. Brittal, A.V. Chestnova, A.V. Feofanov, I.A. Lobanova, I.B. Sivaev, V.I. Bregadze, and A. F. Mironov, "Synthesis of cobalt bis(dicarbollide) conjugates with natural chlorins by the Sonogashira reaction", *Russ. Chem. Bull*., 2010, **59**, 219-224.
3. H. Maeda, "Macromolecular therapeutics in cancer treatment: The EPR effect and beyond", *J Control Release*, 2012, **164**(2), 138-44 1.

PORPHYRIN DIMER – FLUORESCENT DUAL-MODE VISCOSITY AND TEMPERATURE SENSOR

A. Vyšniauskas[1] and **M.K. Kuimova**[2]

[1] Imperial College London, London, United Kingdom,
a.vysniauskas12@imperial.ac.uk
[2] Imperial College London, London, United Kingdom,
m.kuimova@imperial.ac.uk

Abstract. Viscosity and temperature variations in the microscopic world are of paramount importance for the rates of diffusion and reactions. Both parameters can show complex non-homogeneous distribution on the microscopic scale and are challenging to measure with precision. Here we report a deep red emitting dual viscosity sensor **1**, which allows both the ratiometric and the lifetime imaging of viscosity. We also examine the unique effect of temperature on the photophysical behavior of **1.** This allowed us to measure both viscosity and temperature concurrently.

Viscosity is an important characteristic of a microenvironment, since it determines the micro- and macroscopic properties of materials and controls the rates of processes and reactions on the microscopic scale. Among several methods that allow the detection of viscosity on such scale, detection of molecular rotors' fluorescence has secured its place as a versatile technique that allows non-destructive *imaging* of viscosity in heterogeneous samples and on-line detection of *changing* viscosity [1]. The viscosity sensitivity of such fluorophores is typically brought about by the interplay between 'bright' and 'dark' excited states, which is controlled by the rate of intramolecular rotation. We have investigated a porphyrin dimer **1**, which is a red emitting molecular rotor. We have discovered that viscosity can be measured with **1** ratiometrically by using its fluorescence spectra (Figure 1a, c) as well as by its fluorescence lifetime (Figure 1b, c) [2]. Only a few dual-mode molecular rotors have been published to date, combining the capabilities of both these approaches. We have used the dual imaging approach to detect viscosity in model lipid systems (monolayers and bilayers) and in live biological cells [2]. We also measured dynamically changing viscosity during photodynamic therapy in these systems [2].

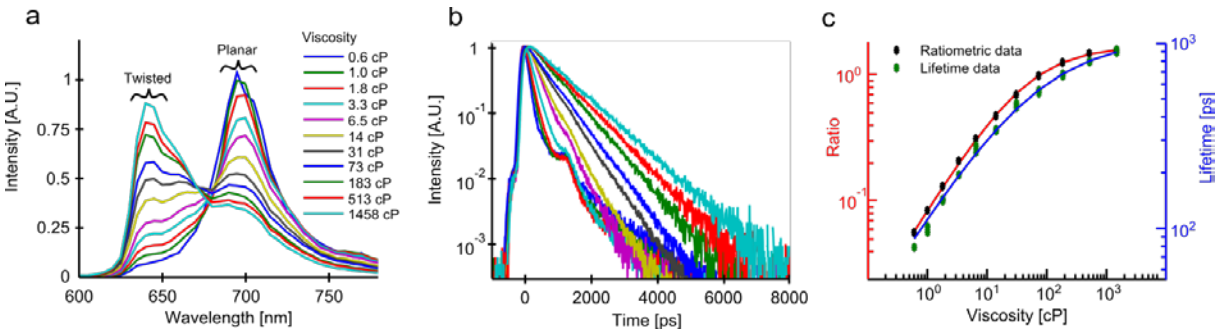

Fig. 1. Calibration of **1** in methanol/glycerol mixtures, λ_{exc} = 453 nm. a) Fluorescence spectra showing viscosity-dependent ratio of two peaks. b) Fluorescence decays recorded at 640±5 nm. c) Ratiometric (red) and lifetime (blue) calibration curves

Temperature can affect the balance in the relative population of the bright and dark excited states of fluorophores by enabling or precluding the bright-to-dark state transitions, *e.g.* by changing the Boltzmann distribution in the excited state(s). We have examined the effect of temperature on the photophysical behavior of **1** between 10 and 90 ˚C temperatures in methanol/glycerol mixtures (0–100% glycerol). It is clear from Figure 2a that all 640/700 nm ratios recorded in various mixtures at different temperatures overlap perfectly. This close overlap indicates that the ratios depend on viscosity alone. However, no such overlap was seen for fluorescence lifetimes (Figure 2b), which indicates that fluorescence lifetime of **1** depends on both viscosity and temperature.

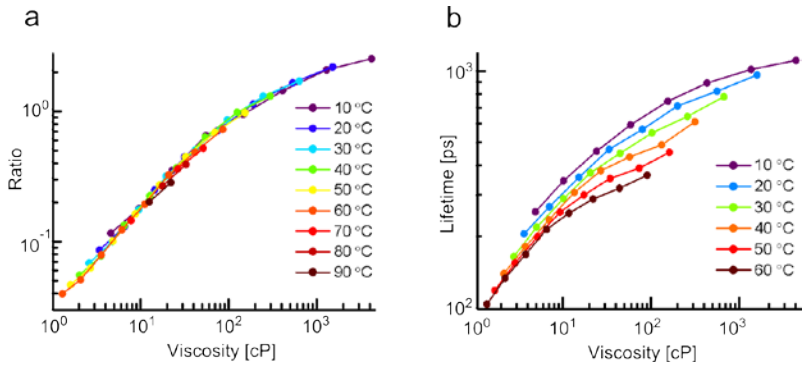

Fig. 2. (a) Ratios of fluorescence intensity at 639 nm vs 706 nm in these mixtures recorded in methanol/glycerol mixtures (30-100% glycerol) at different temperatures. (d) Fluorescence lifetimes of 1 recorded in these mixtures at different temperatures

This unexpected result in principle allows us to measure viscosity at unknown temperature by ratiometric method and then extract the temperature from fluorescence lifetime of **1** using already measured viscosity. We have experimentally verified that dual imaging of **1** does indeed allow simultaneous determination of viscosity and temperature in a model viscous solution heated by a copper wire under the microscope. We have measured series of ratiometric (Figure 3a) and fluorescence lifetime (FLIM) images (Figure 3b) and then used them for constructing viscosity and temperature maps (Figure 3 c,d) [3]. To the best of our knowledge, this is the only example of a fluorophore with such dual functionality.

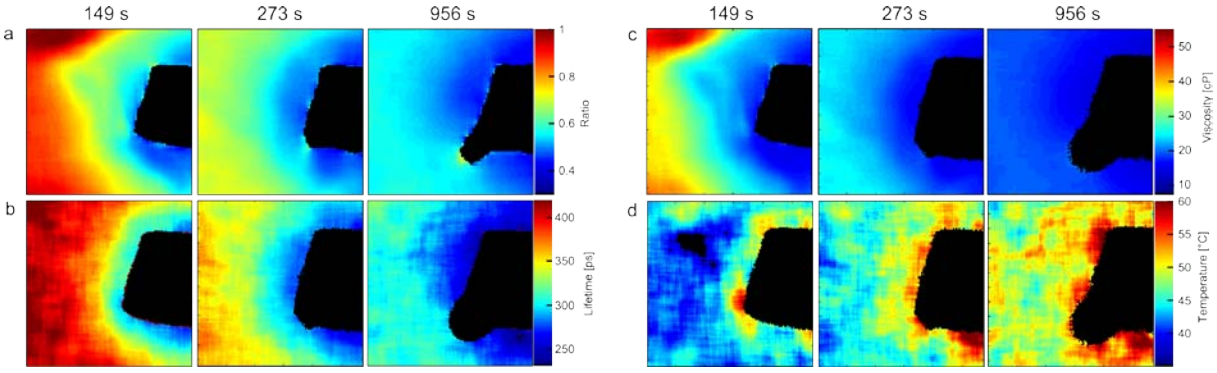

Fig. 3. Ratiometric (a) and FLIM images (b) of **1** together with calculated viscosity (c) and temperature (d) maps of 3:7 methanol/glycerol mixture during the course of heating with hot copper wire (black object in each image). The heating times are shown above each column. A black round structure appearing at later heating times (column three) is a gas bubble

Acknowledgements

AV thanks the EPSRC for the Prize Studentship. MKK is thankful to the EPSRC for the Career Acceleration Fellowship.

References

1. M.K. Kuimova, *Phys. Chem. Chem. Phys.*, 2012, **14**, 12671-12686.
2. A. Vysniauskas, M. Balaz, H.L. Anderson, and M.K. Kuimova, *Phys. Chem. Chem. Phys.*, 2015, **17**, 7548-7554.
3. A. Vysniauskas, M. Qurashi, N. Gallop, M. Balaz, H.L. Anderson, and M.K. Kuimova, *submitted*.

LIFE-TIME IMAGING OF THE DISCRETE DISTRIBUTIONS OF UPCONVERSION NANOPARTICLES IN BIOLOGICAL TISSUE

A.V. Yudintsev[1], **E.V. Khaydukov**[2], **V.V. Rocheva**[2], **V.A. Vodeneev**[1], **S.M. Deev**[1,3], and **A.V. Zvyagin**[1,4]

[1] Lobachevsky State University of Nizhny Novgorod, Nizhny Novgorod, Russian Federation, ayudintsev@mail.ru

[2] Institute on laser and information technologies of the Russian Academy of Sciences, Shatura, Russian Federation

[3] Shemyakin-Ovchinnikov Institute of Bioorganic Chemistry of the Russian Academy of Sciences, Moscow, Russian Federation

[4] Macquarie University, Sydney, Australia

Abstract. We propose and demonstrate a novel image acquisition modality, where a specimen labelled will photoluminescent nanomaterials is rapidly raster-scanned, while its persistent photoluminescence signal is acquired from the entire scan area. The resultant blurred image is post-processed using a developed deconvolution algorithm to reconstruct the diffraction-limited image. This deconvolution procedure allows precise localisation and determination of the lifetime of photoluminescent nanomaterials, specifically, upconversion nanoparticles, which were used to label biological pathways in an experimental animal model.

Photoluminescent nanomaterials, such as upconversion nanoparticles (UCNP), have shown a considerable promise in various biomedical applications. The key advantage of UCNPs is their unique photochemical structure that enables "upconversion" of near-infrared excitation light (975 nm) of the modest intensity (100 W/cm^2) to the shorter-wavelength visible/near-infrared emission (450–850 nm). Since no known biological molecule is capable of such conversion, the intrinsic tissue fluorescence, termed autofluorescence, can be eliminated in the detection path by conventional optical short-pass filtering. The exceptionally long (sub-ms) photoluminescence lifetimes of UCNPs allow realisation of time-gated detection schemes, which can completely suppress the residual back-scattered laser excitation bleeding through the (interference) spectral filters.

The maximum efficiency of UCNP photoluminescence (up to 2%) can be achieved using a confocal imaging modality. An excitation laser beam is focused and raster-scanned across the specimen, and an image is acquired pixel-by-pixel mode, i.e. serially. Due to the sub-ms long lifetime of UCNP photoluminescence, such serial image acquisition results in a considerable increase of the scanning time (~30 min to acquire a 512×512 pixels image, 10 ms pixel dwell time). In the alternative wide-field imaging mode, the requirement of the high excitation intensity for UCNPs is met by the use of high-power lasers, exceeding the maximum laser permissible exposure.

We propose a hybrid image acquisition modality by employing the non-descanned detection mode implemented in a commercial multiphoton laser-scanning microscope. An UCNP-labelled specimen is rapidly raster-scanned, while its persistent photoluminescent signal is continuously acquired from the entire scan area. If the sample contains a set of discrete nanoparticles randomly buried in biological tissue, the recorded image represents a set of comet-like photoluminescent signals superimposed on the autofluorescence background of the biological object, such as a mouse liver tissue shown in Figure 1(a).

The resultant blurred image can be reconstructed by performing an image deconvolution procedure with a temporal point-spread function of individual UCNPs. The key parameter of this function is the lifetime of UCNPs photoluminescence. The deconvolution procedure allows determining the lifetime of various purpose-designed UCNPs. This leads to lucrative opportunity for labelling various biomolecules/tissues with UCNPs encoded with different lifetimes.

We demonstrated the power of this proposed approach by imaging of a thin slice of the liver tissue extracted from a mouse after several hours post injection [Figure 1(a), (b)] and a mixture of two types of UCNPs with different lifetimes ($NaYF_4$:Yb:Er and $NaYF_4$:Yb:Tm). During the rapid image acquisition, blurred signals from single or clustered UCNPs were recorded, and after applying the developed image deconvolution procedure converted into a set of intense narrow discrete peaks [Figure 1(c)]. The UCNP PL lifetime was determined to be in the range of sub-milliseconds, which was in a good agreement with the expected value.

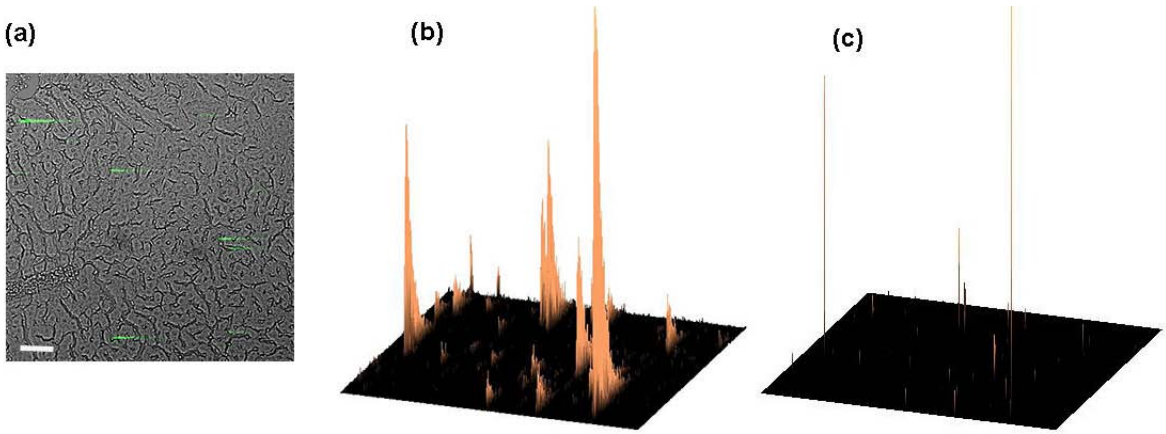

Fig. 1. **(a)** An overlay of the bright field image of a mouse liver tissue (grey) and photoluminescent (PL) signal of UCNPs (green) deposited in the liver post-intravenous injection. Scale bar, 50 μm. **(b)** Surface plots of (b) originally acquired and **(c)** deconvolved PL images of UCNPs in the liver, as in (a)

Acknowledgements

This work was supported by the Ministry of Education and Science of the Russian Federation (the project № 14.Z50.31.0022).

Novel Laser Applications in Biomedicine

Chairs

Jean-Claude Kieffer
Institut National de la Recherche Scientifique, Université du Québec, Canada

Alexander Sergeev
Institute of Applied Physics RAS, Russia

Alfred Vogel
University of Luebeck, Germany

FEMTOSECOND LASER MATERIAL PROCESSING AND OPTOPORATION OF CELL MEMEBRANE WITH DIELECTRIC MICROSPHERES AND OPTICAL TWEEZERS

A.A. Astafiev[1], **V.A. Nadtochenko**[2,3], **A.A. Osychenko**[2], and **A.M. Shakhov**[2,3]

[1]Institute of Chemical Physics RAS, Moscow, Russia, astafiev.artyom@gmail.com
[2] Institute of Chemical Physics RAS, Moscow, Russia
[3] Moscow Institute of Physics and Technology (State University), Dolgoprudniy, Russia

Abstract. We report a method of femtosecond laser material processing which is based on radiation focusing in the near field of a dielectric microsphere held and manipulated by optical tweezers. Results on subwavelength structuring of various materials are presented and compared with Lorentz Mie theory based simulations. We demonstrated application of the method for optoporation of cell membrane, insertion and manipulation of a single microsphere inside the mouse oocyte which can be used for controlled delivery of external genes into cells.

Micro- and nanostructuring of materials in intensive light field of tightly focused femtosecond near-IR laser radiation is of much interest for technical and biomedical applications. These applications rely on the use of nonlinear absorption of intensive radiation produced by tightly focused ultrashort laser pulses which enables processing of materials transparent in visible wavelength range [1].

The common problem of optical methods is the diffraction limit which does not allow to focus radiation into an area smaller than approximately half a wavelength of light or several hundreds of nanometers in visible and near-IR range. Nevertheless the diffraction limit can be circumvented using electromagnetic near-field modes produced by nano- and microparticles [2]. In this work we present a novel approach to laser material structuring using fetosecond laser pulses focused by spherical microlense probes held and manipulated by an optical trap [3]. Owing to near-field effects this approach allows to overcome the diffraction limit of light focusing that exists for conventional optical elements [4–6].

To optically trap microparticles we used either femtosecond laser pulses train at 80 MHz repetition rate, 780 nm wavelength, up to 10 nJ pulse energy and 55 fs duration or CW laser radiation at 830 nm, to process material – either the same femtosecond pulses train or single pulses with energy amplified up to 1 μJ. Focusing of the trapping radiation by a microscope objective lens produced optical tweezers trapping a polysterene or silica microsphere from a water solution. Processing radiation was focused in the near-field zone adjacent to the micropshere surface. The probe was placed in contact with the sample surface and processing radiation was absorbed through nonlinear process in the contact zone. Depending on energy and number of laser pulses absorption led to a range of modification of material surface that included holes formed through laser ablation, convex bumps formed through laser swelling and mechanical damage due to laser cavitation and shock-wave generation following a laser-induced breakdown in water. The optically trapped probe was precisely moved relative to the sample using a piezo stage to enable complex patterns writing.

In this work we demonstrate application of the method described above for processing methacrylate polymers, borosilicate glass and biological materials. We show formation of surface structures as small as 100 nm or 1/8 of light wavelength. Writing of arbitrary 1D and 2D patterns on material surface was performed with a tweezers-manipulated probe. We studied effects of the microsphere size, laser pulse energy and light polarization, spacing between objective focal plane and sample surface on the pattern size experimentally and theoretically. Generalized Lorentz-Mie theory was used for simulation of light field distribution near the uniform dielectric sphere illuminated by a focused laser beam which reasonably matches experimental results. Stability conditions for effective manipulation of the particle by the pulsed beam were considered and a Klein-Kramers and Brownian motion models were used to analyze the positional accuracy of femtosecond tweezers.

The microsphere probe technique was applied to puncture the cell membrane of mouse oocyte cells through laser-induced breakdown in the vicinity of the probe. Subsequently the trapped probe was inserted into the optoporated cell through the punctured hole using optical tweezers. A possibility of manipulating the probe inside the cell was demonstrated. Thus our technique can be potentially used for controlled delivery of external genes through specific point of the cell membrane and into specific area of the cell using optically trapped probes as micro-containers [7].

Aknoledgements

The work was supported by the Russian Academy of Science Presidium's programme No.1 (II-1) of 2015. A.A. Astafiev and A.M. Shakhov had financial support from the Russian President's grant MK-5486.2014.2.

References

1. F. Korte, J. Serbin, J. Koch, A. Egbert, C. Fallinich, A. Ostendorf, and B.N. Chichkov, *Appl. Phys. A*, 2003, **77**, 229-235
2. A. Plech, P. Leiderer, and J. Boneberg, *Laser&Photonics Rev*., 2009, **3**(5), 435-451.
3. A.A. Astafiev, A.M. Shakhov, O.M. Sarkisov, and V.A. Nadtochenko, *Quantum Electronics*, 2013, **43**(4), 361-364.
4. L. Novonty and B. Hecht, *Principles of Nano-Optics*, Cambridge University Press, 2006, p. 47.
5. B.S. Luk'yanchuk, M.Mosbacher, Y.W. Zheng, and H.-L. Münzer, *Laser Cleaning*, B.Luk'yanchuk (Ed.), World Scientific, New Jersey, 2002, 103-178.
6. R. Fardel, E. McLeod, C. Tsai, and C.B. Arnold, *Appl. Phys. A*, 2010, **101**, 41-46.
7. M. Walled, S.-U. Hwang, J,-D. Kim, I. Shabbir, S.-M. Shin, and Y.-G. Lee, *Biomedical Optics Express*, 2013, **4**(9), 1533-1547.

Invited

LASER PRINTING OF NANOPARTICLES AND LIVING CELLS

B. Chichkov

Laser Zentrum Hannover e.V., Hollerithallee , 30419 Hannover, Germany
b.chichkov@lzh.de

I will report on our recent progress in the development of laser printing technologies. Laser printing of nanoparticles and living cells for the fabrication of complex nanoparticle structures [1, 2] and tissue substitutes [3] will be discussed. Laser functionalization of biomedical implants will be demonstrated.

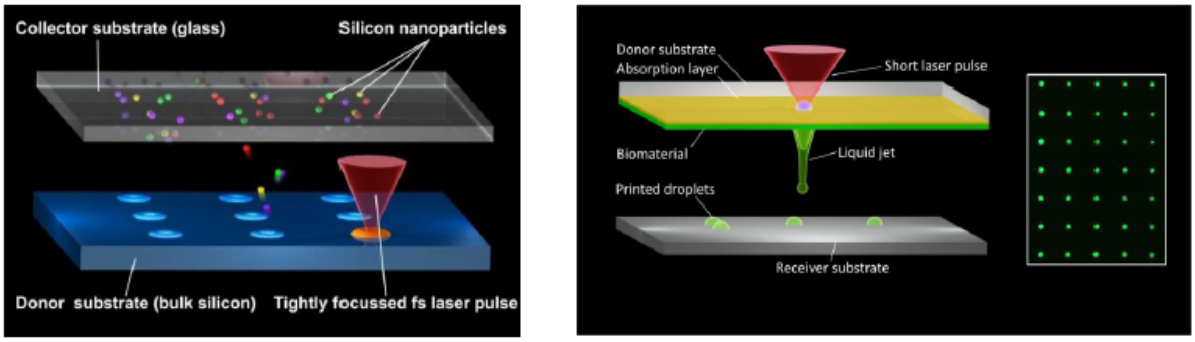

Fig. 1. Experimental setup applied for laser printing of nanoparticles and living cells

References

1. U. Zywietz et. al., *Appl Phys A*, 2014, **114**, 45.
2. U. Zywietz et. al., *Nature Commun*., 2014, **5**, 3402.
3. L. Koch et.al., *Biotechnol Bioeng*., 2012, **109**,1855.

Invited

IN VIVO LASER-ASSISTED VESSEL SOLDERING USING AN ELECTROSPUN PATCH

A. Schönfeld[1], Z. Mbaïdjol[2], M.A. Constantinescu[2], and **M. Frenz[1]**

[1] Institute of Applied Physics, University of Bern, 3012 Bern, Switzerland, frenz@iap.unibe.ch
[2] Clinic of Plastic and Hand Surgery, University Hospital, 3010 Bern, Switzerland

Abstract. Laser assisted vessel soldering has various advantages compared to conventional suture ligation, such as reduced needle trauma, decreased foreign body reactions and watertight closures [1]. However, laser soldering is not yet clinically applied, mainly due to a lack of reproducibility. This study investigates the feasibility of using electrospinning to quantitatively bind the light absorbing chromophore. The produced patch is tested ex vivo and in an acute in vivo pig study using an intraluminal light source.

Introduction

Laser tissue soldering enables secure, rapid and easy fusion of tissue through the denaturation and coagulation of proteins by thermal effect. The use of a polycaprolactone (PCL) scaffold that is being soaked in the protein albumin (bovine serum, BSA) and the chromophore indocyanine green (ICG) has been shown to improve tissue fusion [2, 3]. However, the control of the maximum temperature reached during soldering is still insufficient. Previous studies showed that the flow-off and thus the dilution of the chromophore during the surgery causes inhomogeneous and irreproducible soldering strengths [4].

In this study we face that problem by incorporating the chromophore into electrospun fibers. A blend of polycaprolactone and indocyanine green enables the fixation of the chromophore in polymer fibers and thus its quantitative binding.

This feasibility of this patch is tested ex vivo with rabbit aortas. The patch is soaked in liquid albumin and wrapped around the vessel. An intraluminal balloon catheter that holds the laser light source ensures homogenous irradiation of the vessel and an easy alignment of the vessel stumps [4]. The vessel is irradiated with an 800 nm diffusor fiber. During the procedure the surface temperature is measured with an infrared camera. The quality of the soldered vessel is determined by measuring the tensile strength.

Finally we demonstrate the clinical relevance of this technique in an acute pig study.

Materials and methods

Electrospinning setup and parameters

For electrospinning, a solution made of 9 % wt. PCL in chloroform/methanol (75/25 v/v) with 10 % wt. ICG based on PCL is pumped into a 21 G syringe needle. A flow rate of 30 µl/min, a gap distance of 15 cm between the needle tip and the grounded collector plate and a positive potential of 15 kV are employed. Humidity and temperature are controlled at 21 °C and 30 % RH.

Ex vivo anastomosis

Rabbit aortic arteries are cut transversal and placed onto a water filled balloon catheter (Armada 35 PTA catheter, Abbott). The electrospun patch is soaked in 40 % wt. BSA in water and wrapped around the vessel. A diffusor laser fiber (Laser und Medizintechnologie Berlin, Germany) is inserted into the catheter and attached to an 810 nm diode laser (Intros, Germany). The vessels are irradiated using 4 W, continuous wave. The temperature is controlled with a thermal camera. The vessel is irradiated for 30 seconds at a temperature range between 75 and 85 °C. A test stand with a fixed force gauge is used to measure the tensile strength.

In vivo anastomosis

The animals are anesthetized for laser-assisted anastomosis. The latissimus dorsi flap is separated and its artery is isolated. The balloon catheter is inserted via the artery saphena into the artery femoralis and both, the flap's artery and the arteria femoralis, are positioned on the catheter. The electrospun patch, which is soaked before in liquid BSA solution, is *wrapped* around the two vessel stumps. The diffusor fiber is inserted and the vessels are soldered together. After the surgery, the vessels are visually evaluated, dissected and undergo tensile strength measurement. Figure 1 shows the principle of the setup for laser-assisted vascular anastomosis.

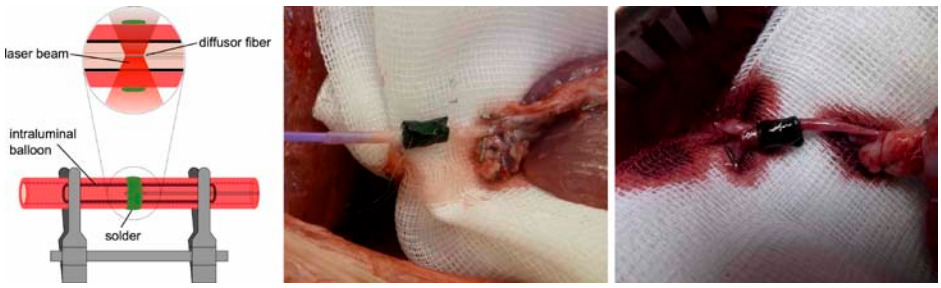

Fig. 1. Schematic of laser-assisted vessel soldering using a balloon catheter and a radially emitting laser fiber (left). Intraoperative images before (middle) and after (right) soldering showing the two vessel stumps of the artery femoralis and of the attached flap

Results

The patches for laser tissue soldering are prepared using electrospinning. After a spinning duration of 75 min we obtain a patch with a diameter of 10 cm and a thickness of 287 ± 59 µm. The amount of albumin per patch is 47 ± 5 mg.

A typical temperature curve of anastomoses is shown in figure 2. The tensile strength of ex vivo experiments is 1571 ± 538 mN (n=10).

8 pigs underwent laser-assisted vascular anastomosis with the latissimus dorsi flap being attached to the artery femoralis. Six pigs had a successful anastomosis, without any leakage and with a blood flow through the venous end of the flap. Two experiments failed in our preliminary trail due to insufficient wrapping of the patch and due to defective approximation of the vessel stumps and the laser fiber. Bonding was obtained after a mean time of laser irradiation for 79 ± 11 s. The tensile strength of the patent anastomoses was 1058 ± 306 mN. Therefore we did observe a lower tensile strength in vivo, which might be due to more difficult handling and due to the usage of pig arteries instead of rabbit aortas.

In both, the ex vivo and the in vivo experiments, we did observe no leakage of the chromophore, which confirms its stabilization in electrospun fibers.

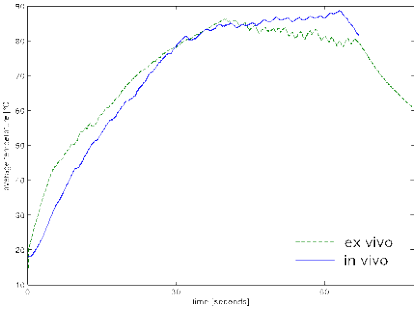

Fig. 2. Solder-surface temperature of a typical ex vivo experiment using rabbit aorta and of an in vivo experiment with a flap model in pig. The graph shows the average temperature of the irradiated vessels during soldering

Conclusion

Electrospinning allows producing a scaffold that is pliable, tear-proof and easy-to-use. More importantly, it ensures a constant concentration of the chromophore during the surgery. Patent and strong anastomoses could be obtained ex vivo and in vivo. This study serves as a first preclinical step that can facilitate the clinical application of laser-assisted vessel soldering.

Acknowledgements.

This research was funded by the Swiss National Science Foundation (Nr: 32003B_133083).

References

1. L.S. Bass and M.R. Treat, *Lasers Surg Med.*, 1995, **17**(4), 315-349.
2. D.S. Schöni, S. Bogni, A. Bregy, A. Wirth, A. Raabe, I. Vajtai, U. Pieles, M. Reinert, and M. Frenz, *Lasers Surg Med.*, 2011, **43**(10), 975-983.
3. A. Bregy, S. Bogni, V.J.P. Bernau, I. Vajtai, F. Vollbach, A. Petri-Fink, M. Constantinescu, H. Hofmann, M. Frenz, and M. Reinert, *Lasers Surg Med.*, 2008, **40**(10), 716-725.
4. S. Bogni, O. Stump, M. Reinert, and M. Frenz, *J. Biophoton.*, 2010, **3**(5-6), 284-295.
5. B. Ott, M. A. Constantinescu, D. Erni, A. Banic, T. Schaffner, and M. Frenz, *Lasers Surg Med.*, 2004, **35**(4), 312-316.

Invited

REVIEW OF LASER ACCELERATED IONS AND APPLICATIONS

J. Fuchs

Ecole Polytechnique, France

I will review the mechanisms, illustrated by results, allowing laser-acceleration of MeV-tens of MeV ions, using intense, short-pulse lasers. This has been the subject of intense research within the community for the last fiteen years due to the interesting characteristics displayed by these beams that are complementary to the ones provided by beams accelerated using conventional methods. I will also review some recent results obtained in transiting from the common surfacic process of laser-acceleration of ions from solid foils to a volumetric one from low-density plasmas, which not only relaxes constraints on the laser and target parameters, but also allows moving toward high-repetition rate targetry better adapted to the next generation of high-power lasers. I will present as well some ways to control the beam, i.e. focus it as well as on energy-selecting it, and assess the respective interest, merit and shortcomings of the techniques that are used for this purpose. I will finally review some recent use of those techniques in the frame of bio applications.

Invited

RECENT ADVANCES IN PHASE CONTRAST X-RAY IMAGING

R. Gupta, MD, PhD and Yo. Sung, PhD

Department of Radiology,
Massachusetts General Hospital and Harvard Medical School
Boston, MA, USA

Clinical X-ray imaging systems use photon attenuation as their primary source of tissue contrast. The X-ray attenuation difference is small among different soft tissues leading to poor low-contrast detectability of these structures. For example, various components of atherosclerotic plaque such as the fibrous cap and atheroma are essentially indistinguishable at percutaneous trans-luminal catheter angiography (PCTA) or X-ray computed tomography (CT). Similarly, in the absence of edema, calcification, or architectural distortion, it may be hard to distinguish cancer from surrounding healthy tissue in a non-contrast CT scan.

X-ray phase contrast imaging (PCI) improves soft-tissue contrast of traditional attenuation-based X-ray imaging (1). For example, we recently demonstrated that X-ray PCI can characterize atherosclerotic plaque and discriminate benign from cancerous tissue (2) (Figure 1). Unlike attenuation, which is modulated by atomic number differences, X-ray phase is altered by the electron density of imaged object (1). Electron density differences between different tissue types manifest themselves as small angular deviations (~10^{-4} to 10^{-5} degrees) in the incident X-ray beam as it travels through the body. These small angular deviations are hard to measure with a conventional X-ray imaging system and require special instrumentation.

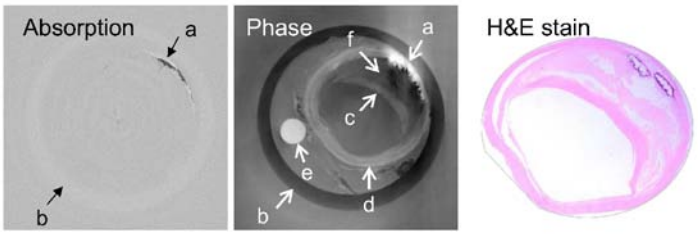

Fig. 1. An example of improved soft-tissue contrast afforded by X-ray PCI (1). An iliac artery with extensive atherosclerotic disease demonstrating different plaque components in the phase but not attenuation image (a: calcification; b: plastic container; c: fibrous cap; d: tri-laminar arterial wall; e: fiducial marker; f: soft plaque or atheroma).

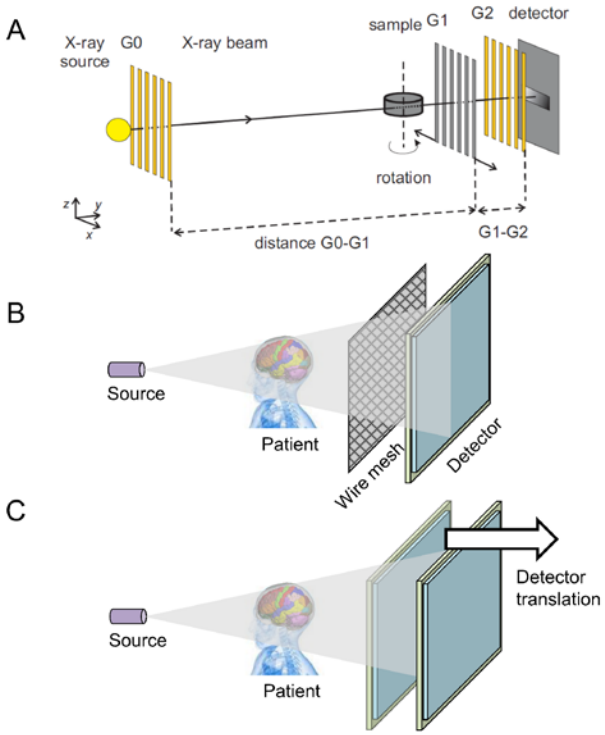

Fig. 2. Schematic diagrams of three X-ray PCI setups that will be modeled using the proposed framework: (a) Grating-based method (8), (b) scatter imaging using grid optics (10), and (c) propagation-based phase imaging (5).

Because X-ray phase-contrast imaging (PCI) holds great promise in improving soft-tissue contrast of traditional X-ray imaging, a variety of X-ray PCI methods such as crystal interferometry, analyser-based imaging, propagation-based methods, and grating-based systems have been demonstrated in bench-top experiments. A variety of experimental X-ray PCI setups have been reported. While most use coherent X-ray radiation from a synchrotron (3–7), traditional non-coherent X-ray sources (8–12) have also been demonstrated. Published X-ray PCI techniques include: crystal interferometry (3, 4), analyser-based imaging using crystals in the Bragg mode (6) or transmission Laue mode (7), propagation-based methods (5), Talbot interferometry using gratings (13), and grid-based systems (10, 12). Our group has pioneered a new technique called X-ray dark field imaging (XDFI) (2) that can achieve both high angular sensitivity and high spatial resolution using the Takagi-Taupin equation (14–16).

Despite this flurry of research activity, the future of X-ray PCI as a clinical modality remains uncertain. In fact, serious objections have been raised about the scalability of the grating-based X-ray PCI, a popular methodology for extracting phase signatures, due to its unfavourable noise power spectrum (17). At the present time, there is no direct way of comparing the performance of the various X-ray PCI techniques for a human-scale object. It is also unknown how the phase noise changes with the size of the anatomy.

Three factors contribute to this knowledge gap: (i) lack of a generally accepted numerical phase phantom of the human body; (ii) unavailability of a wave-propagation engine to advance X-ray waves through a numerical tissue phantom, and (iii) lack of a framework for simulating various X-ray PCI techniques and assessing their performance on an equal basis.

The goal of this talk is to describe the fundamental concepts of phase contrast imaging. We will also describe three popular PCI paradigms: (i) X-ray PCI using a sequence of three gratings; (ii) frequency-domain measurement of coherent and incoherent scattering using X-ray optics; and (iii) propagation-based in-line holography. Because each system is built using a unique combination of various optical components, their performance and noise characteristics are quite distinct. Each system also poses different challenges in scaling up the size for clinical imaging.

References

1. Paganin DM. Coherent X-ray optics: Oxford University Press, USA; 2006.
2. Ando M, Sunaguchi N, Wu Y, Do S, Sung Y, Louissaint A, et al. Crystal analyser-based X-ray phase contrast imaging in the dark field: implementation and evaluation using excised tissue specimens. European Radiology. 2013:1-11.
3. Bonse U, Hart M. An X-ray interferometer. Appl Phys Lett. 1965;6(8):155-6.
4. Momose A. Demonstration of phase-contrast X-ray computed tomography using an X-ray interferometer. Nuclear Instruments and Methods in Physics Research Section A: Accelerators, Spectrometers, Detectors and Associated Equipment. 1995;352(3):622-8.
5. Wilkins S, Gureyev T, Gao D, Pogany A, Stevenson A. Phase-contrast imaging using polychromatic hard X-rays. Nature. 1996;384(6607):335-8.
6. Chapman D, Thomlinson W, Johnston R, Washburn D, Pisano E, Gmür N, et al. Diffraction enhanced x-ray imaging. Physics in medicine and biology. 1997;42(11):2015.
7. Ando M, Maksimenko A, Sugiyama H, Pattanasiriwisawa W, Hyodo K, Uyama C. Simple X-ray dark- and bright-field imaging using achromatic Laue optics. Jpn J Appl Phys. 2002;41(9A/B; ISSU 374):1016-8
8. Pfeiffer F, Weitkamp T, Bunk O, David C. Phase retrieval and differential phase-contrast imaging with low-brilliance X-ray sources. Nature Physics. 2006;2(4):258-61.
9. Kashyap YS, Yadav P, Roy T, Sarkar P, Shukla M, Sinha A. Laboratory-based X-ray phase-contrast imaging technique for material and medical science applications. Applied radiation and isotopes. 2008;66(8):1083-90.
10. Wen H, Bennett EE, Hegedus MM, Carroll SC. Spatial harmonic imaging of x-ray scattering—initial results. Medical Imaging, IEEE Transactions on. 2008;27(8):997-1002.
11. Morgan KS, Paganin DM, Siu KK. Quantitative single-exposure x-ray phase contrast imaging using a single attenuation grid. Optics express. 2011;19(20):19781-9.

12. Olivo A, Arfelli F, Cantatore G, Longo R, Menk R, Pani S, et al. An innovative digital imaging set-up allowing a low-dose approach to phase contrast applications in the medical field. Medical physics. 2001;28:1610.
13. David C, Nohammer B, Solak HH, Ziegler E. Differential x-ray phase contrast imaging using a shearing interferometer. Applied Physics Letters. 2002;81(17):3287-9.
14. Taupin D. Dynamic theory of x-ray diffraction in crystals. Bull Soc Fr Mineral Crystallogr 1964;87.
15. Takagi S. A dynamical theory of diffraction for a distorted crystal. J Phys Soc Japan. 1969;26(5):1239-53.
16. Takagi S. Dynamical theory of diffraction applicable to crystals with any kind of small distortion. Acta Crystallographica. 1962;15(12):1311-2.
17. Raupach R, Flohr TG. Analytical evaluation of the signal and noise propagation in x-ray differential phase-contrast computed tomography. Physics in medicine and biology. 2011;56(7):2219.
18. Segars W, Sturgeon G, Mendonca S, Grimes J, Tsui B. 4D XCAT phantom for multimodality imaging research. Medical physics. 2010;37:4902.

FUTURE DIRECTION IN X-RAY COMPUTED TOMOGRAPHY

R. Gupta, MD, Dept of Radiology

Massachusetts General Hospital and Harvard Medical School

Boston, MA, USA

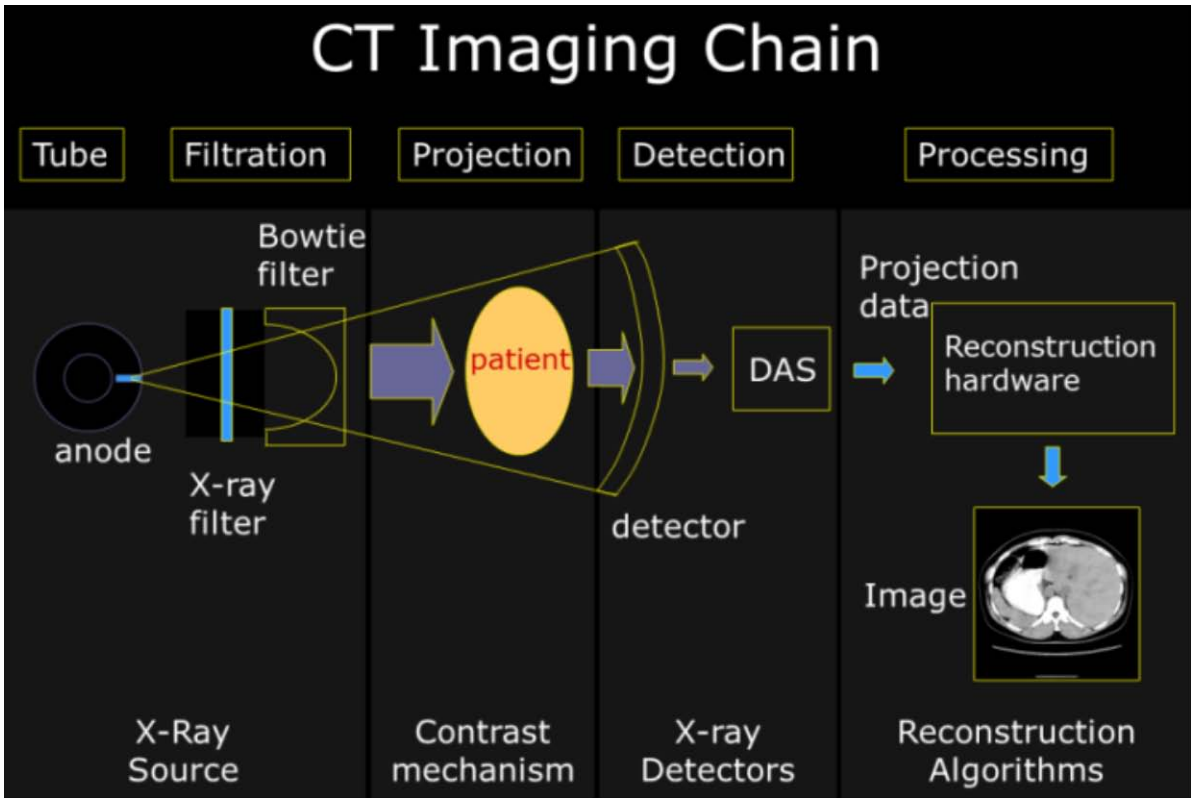

Multi-detector computed tomography (MDCT) technology has been greatly refined and serves as an immensely valuable imaging modality for the diagnosis of diseases throughout the body. While both the 1st and 2nd generation CT scanners have become obsolete, and despite the fact that 4th and 5th generation scanners have been build and tested, 3rd generation scanners represent the most prevalent technology currently in use. These scanners are characterized by an X-ray souce and a detector in a fixed configuration with each other, mounted on a rotating gantry capable of 3-4 rotations per second. This presentation will describe the imaging chain of a modern 3rd CT scanner, starting with the X-ray source, propogation through the patient, detection, and reconstruction. At each stage within the imaging chain, limitations of the current technology will be illustrated with the help of clinical examples.

In recent years, there have been many technical advances in MDCT that have helped to increase accessibility to the modality, increased the speed of acquisition, spatial resolution, decreased radiation dose, and provide additional diagnostic information. Notable advances include dual energy CT, iterative reconstruction, and portable CT. These techniques and their corresponding imaging features and potential limitations will be reviewed. Alternate ways of generating X-ray photons and different ways of imparting anatomic contrast in the transmitted beam will be discussed. The presentation will also discuss the advantages and key challenges in implementing spectral and photon counting detectors. New advances in CT reconstruction algorithms will be briefly described.

Invited

MECHANISMS AND APPLICATIONS OF GOLD NANOPARTICLE MEDIATED LASER MANIPULATION OF CELLS

A. Heisterkamp[1,3], S. Kalies[2,3], D. Heinemann[2,3], M.L. Torres[1,3], J. Krawinkel[4], M. Schomaker[2], T. Ripken[2], H. Meyer[2,3]

[1]Leibniz Universitaet Hannover, Welfengarten 1, D-30167 Hannover, Germany

[2]Laser Zentrum Hannover, Biomedical Optics Department, Hollerithallee 8, D-30419 Hannover, Germany

[3]Cluster of Excellence REBIRTH, D-30625 Hannover, Germany

[4]Friedrich-Schiller-University Jena, Institute of Applied Optics, Froebelstieg 1, D-07743 *Jena, Germany*

Abstract. By illuminating gold nanoparticles, gold coated or structured surfaces, near field enhancement is employed to selectively open the cell membrane using ultrashort laser pulses. This plasmon resonance based method for introducing foreign material into living cells is studied with special respect to the fundamental mechanisms and dependencies such as cell type, molecule type and illumination parameters.

Introduction

In the field of molecular biology the targeting of the cell membrane with short or ultrashort laser pulses allows the delivery of extracellular compounds to the target cell, as for example needed in gene therapy or high-throughput screening. Tightly focused laser pulses allow the precise and minimal invasive manipulation of cells and cell compartments with subcellular resolution. Several works have shown successful delivery with high cell viabilities in different model system over the past two decades [1–3]. However, due to their focusing conditions, these techniques are very limited with respect to cell throughput. To overcome these limitations, several approaches are possible, for example microfluidics [4] or special beam shapes [5] to mitigate this specific drawback. In contrast, other approaches employ micro- or nanoparticles [6–8], Wu et al. immobilized these particles on a surface [9]. Moreover, gold structures (among other noble metals) can confine the energy of a loosely focused laser beam into the near, due to the creation of localized surface plasmons [10, 11]. Here, we show an overview of these different approaches, especially gold-nanoparticles and nanostructured surfaces and presenting our work with different laser systems at 532 nm and 800 nm with pulse durations in the ps- and fs-regime.

Methods

Before experimental use, the different shapes of nanostructures on surfaces and sizes nanoparticles were modeled within COMSOL Physics (Multiphysics 4.2a) using a Finite Element Method (FEM) and the software DDSCAT. Different sizes of gold nanoparticles were simulated (between 20 nm and 200 nm) and different surface structures, as for example nanoparticles attached to a surface or other structures. The irradiation wavelength was varied between 400 nm – 1100 nm and the near-field enhancement was calculated ($\eta=|E|/|E0|$). To study different wavelengths, an ultrashort tunable oscillator (COHERENT, Ultra II) was used, delivering 140 fs pulses at 80 MHz with a maximum output power of 4 W and a wavelength range between 680–1080 nm. Additionally, a microchip laser (HORUS LASER) at 532 nm and 850 ps pulse duration at 20 kHz with an output power of 100 mW and a fs-Laser system (Spitfire Pro, Newport Corp., USA) at 120 fs and 796 nm with an output power of 2.1 W at 5 kHz were used to excite at the plasmon resonance of gold. The structures and particles were incubated with different standard cell lines and seeded 24 h before manipulation. As a standard molecule, lucifer yellow, a membrane impermeable dye was used to monitor the uptake of extracellular molecules upon laser irradiation.

Results

Using different substrates and shapes, successful cell manipulation (uptake of membrane impermeable extracellular molecules) could be demonstrated. Based on the mechanistic investigations, we assume that an enhancement of the near field occurs at AuNP clusters. This leads to the generation of a low density plasma with multiphoton ionization of the surrounding liquid, which in turn perforates the cell membrane. The found effects correlated well with the findings from the simulations.

Discussion

The plasmon-based cell perforation using different shapes and structures heavily depends on size, geometry and illumination parameters (pulse duration and wavelength), see fig. 1. Especially the charge of DNA apparently plays a role in nanoparticles based delivery approaches. Different mechanisms can play a role in permeabilizing the membrane, leading for example to a thermal fragmentation of the particles after exposition at 532 nm in the ps regime, whereas nearly no thermal melting of structures or particles was found at NIR wavelengths in the fs regime [13]. Furthermore, the relation between plasmon resonance and illuminating wavelength plays an important role as well. This has consequences for possible applications, as thermally denatured particles might act toxic in vivo applications, whereas they might prove useful for screening applications [14].

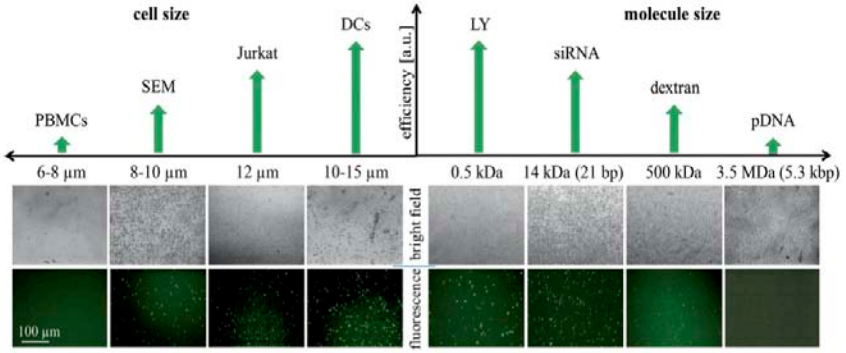

Fig. 1. (*Left*) Influence of cell size on delivery efficiency. Different cell types were used in combination with Lucifer Yellow as marker. (*Right*) Influence of molecule size on delivery efficiency, increasing molecule size leads to less efficient delivery [12]

Conclusion

Using gold-coated nanostructures and nanoparticles, the transient perforation of cell membranes by laser irradiation could be shown. Due to the moderate focusing conditions, high throughput using multi-well plates is enabled, allowing applications in siRNA-screening or gene knockdown. Depending on laser wavelength and pulse duration, different fundamental mechanisms for creating the membrane opening are found.

References

1. M. Tsukakoshi, S. Kurata, Y. Nomiya, Y. Ikawa, and T. Kasuya. Applied. Physics B. 35, 3, 135–140. (1984).
2. U.K. Tirlapur and K. Koenig. Nature 418, 6895, 290–291, (2002).
3. D. Stevenson, B. Agate, X. Tsampoula, P. Fischer, CTA Brown, W. Sibbett, A. Riches, F. Gunn-Moore, K. Dholakia. Opt Express 14, 16, 7125–7133, (2006).
4. R.F. Marchington, Y. Arita, X. Tsampoula, F.J. Gunn-Moore, and K. Dholakia. Biomed. Opt. Express 1(2) (2010), 527–536.
5. H.A. Rendall, R.F. Marchington, B.B. Praveen, G. Bergmann, Y. Arita, A. Heisterkamp, F.J. Gunn-Moore , K. Dholakia. Lab on a Chip, 12, 22, 4816–4820, (2012).
6. C.M. Pitsillides, E.K. Joe, X. Wei, R.R. Anderson, and C.P. Lin. Biophys J 84, 6, 4023–4032, (2003).
7. C. Yao, R. Rahmanzadeh, E. Endl, Z. Zhang, J. Gerdes, G. Huettmann. J. Biomed Opt 10(6) (2005), p. 064012.
8. E.Y. Lukianova-Hleb, A.P. Samaniego, J. Wen, L.S. Metelitsa, C.-C. Chang, D.O. Lapotko. J. Control Release 152(2) (2011).
9. T.-H. Wu, S. Kalim, C. Callahan, M.A. Teitell, and P.-Y. Chiou. Opt Express 18(2) (2010), p. 938–946.
10. S. Courvoisier, N. Saklayen, M. Huber, J. Chen, E.D. Diebold, L. Bonacina, J.P. Wolf, E. Mazur. Nano Letters, (2015) DOI: 10.1021/acs.nanolett.5b01697
11. Y.C. Wu, T.H. Wu, D.L. Clemens, B.Y. Lee, X. Wen, M.A. Horwitz, M.A Teitel, P.Y. Chiou, Nature Methods, (2015); DOI:10.1038/NMETH.3357
12. M. Schomaker, D. Killian, S. Willenbrock, D. Heinemann, S. Kalies, A. Ngezahayo, I. Nolte, T. Ripken, C. Junghanss, H. Meyer, H. Murua Escobar, A. Heisterkamp. J. Biophotonics 1–13 (2014) / DOI 10.1002/jbio.201400065
13. M. Schomaker, D. Heinemann, S. Kalies, S. Willenbrock, S. Wagner, I. Nolte, T. Ripken, H. Murua Escobar, H. Meyer, A. Heisterkamp. Journal of Nanobiotechnology (2015) 13:10 DOI 10.1186/s12951-014-0057-1
14. D. Heinemann, M. Schomaker, S. Kalies, M. Schieck, R. Carlson, H. Murua Escobar, T. Ripken, H. Meyer, A. Heisterkamp. Plos One, 8, 3, e58604, (2013)

Invited

LASER EMBRYOLOGY – PERSPECTIVE OF LASER METHODS FOR INVESTIGATION OF PREIMPLANTATION EMBRYO STATE AND DEVELOPMENT

A.V. Karmenyan[1], **A.S. Krivokharchenko**[2], **E.V. Perevedentseva**[1], and **C.-L. Cheng**[1]

[1] Department of Physics, National Dong Hwa University, Hualien, Taiwan,
artashes@mail.ndhu.edu.tw
[2] Semenov Institute of Chemical Physics, RAS, Moscow, Russia

Abstract. A number of modern optical methods were tested to find the optimal way for monitoring the status of mammalian ovary during preimplantation development without losing the gametes and embryos quality. We demonstrate the possibility to use Raman microspectroscopy, 2-photon excited fluorescence spectroscopy and lifetime imaging and have selected appropriate and safety parameters of laser exposure. The measured spectra and images allow analyzing the embryo state without destructive effects on further development.

In this era of rapid development of artificial reproductive technologies, an increasing number of pre-implantation embryos are manipulated and treated *in vitro*. Accordingly, it becomes a paramount importance in developing more readily reproducible robust non-destructive and low invasive fast and precise test of the quality of the material in use for appropriate purpose.

This problem is very significant in reproductive medicine in increasing the efficiency of applied in-vitro methods, and to reduce the risk of the necessity of repeated procedures, etc. Moreover, this is also a topical problem in Artificial Reproductive Technologies applied in agricultural animal industry, and can be met at using laboratory animals in research procedures as well.

Hence, finding the correct methods to determine the quality of the gametes and embryos and to estimate the degree of active development has great fundamental significance for understanding the mechanisms of development including investigation of Embryonic Stem Cells (ESC) origin.

Today, two kinds of methods in wide use, in this area, are (1) embryo destruction and (2) live object metabolomics [1] which allows to study biochemical process; and time lapse study of morphological dynamics. Here, we propose that laser methods facilitate the investigation of the mentioned parameters in one step.

The laser based methods possesses several advantages as it provides a platform for nondestructive, noninvasive way of extracting maximum reliable information concerning state, or condition of early mammalian embryos (EME).

In the present work, different optical-spectral methods, as indicated below, are used and their applicability is compared and discussed for diagnostics and control of conditions of gametes and embryos:

– Raman spectroscopy, including Raman imaging, was used; the spectra in different localizations inside the EME and in different stages of development were measured and analyzed.

– Fluorescence lifetime imaging (FLIM) with 2-photon excitation was used to analyze autofluorescence from metabolic cofactors reduced nicotinamide adenine dinucleotide (NADH) and flavin adenine dinucleotide (FAD). The lifetimes all through the embryo were measured and distribution of lifetimes and intensity of 2-photon excited autofluorescence in different areas were analyzed to understand a relation between metabolic processes, their dynamics in various stages of development of gametes and embryos.

– Multispectral imaging of embryos in transmission mode of light was obtained for estimation of embryos state.

– Estimation of in vitro development of EME was done via 2-photon excitation of stained nuclei to count cells.

The main criterion, for all investigation methods applied to living embryos in this study, was to find the optimal parameters of laser treatment which doesn't affect the further embryo development with high precision. The laser wavelength, exposure powers and times were selected as the parameters and optimized to provide nondestructive effect on the embryonic development which proceeded as close as possibly to the control samples.

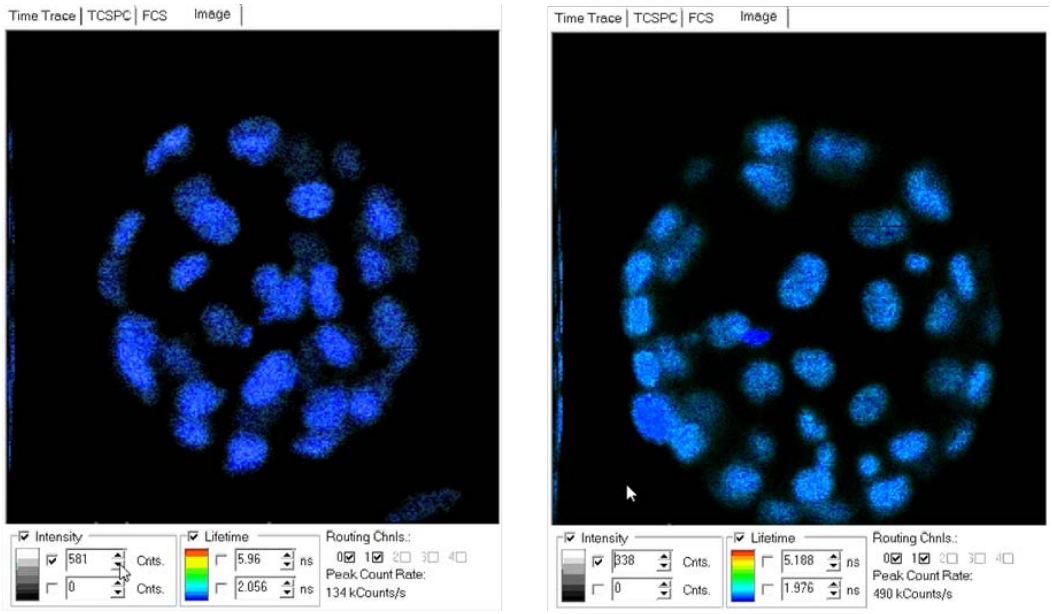

(a) (b)

Estimation of *in vitro* cultered embryo quality after Raman investigation by nuclear number counting. 2-photon fluorescence images of the embryo cell's nuclei were stained with Hoechst33342 in (a) sample (embryo cells after 72h Raman studies); (b) control. For 2-p excitation with 740 nm fs laser was used

Acknowledgements

The research was supported by Ministry of Science and Technology of Taiwan with grant No. 103-2112-M-259-001-MY3

References

1. R. Singh and K.D. Sinclair, *Theriogenology*, 2007, **68S**, S56–S62.

Invited

HIGH RESOLUTON BIO-IMAGING WITH ELECTRON BEAM EXCITATION MICRSOCOPY

Yo. Kawata[1,2], **Ya. Nawa**[1], and **W. Inami**[1,2]

[1] Research Institute of Electronics, Shizuoka University, Hamamatsu, Japan, kawata@eng.shizuoka.ac.jp
[2] CREST, Japan Science and Technology Agency, Chiyoda-ku, Tokyo, Japan

Abstract. We present optical nanoimaging system and demonstrate the observation of biological specimens without any stained process. The electron-beam excited assisted (EXA) optical microscope has a few tens nanometer spatial resolution laterally and is possible to observe dynamic behaviors of specimens in various surroundings such as air or liquids. In the EXA-microscope, a nano-light source in a few nanometers size is excited by focused electron beam in an emission layer. We have successfully observed fine structures of the cells without any stain process.

1. Introduction

Nanoimaging of specimens in liquid conditions are highly required in various applications such as analysis of colloidal solutions, observation of microcrystal growth and self-assembly process, etc. Especially, imaging of biological specimens with high resolution is crucial for a deeper understanding of cell functions. Fluorescence microscopy has been widely used to analyze the dynamic behavior of cellular components in living cells, because stained molecules of interest in the specimens can be imaged with high contrast [1, 2].

In this paper, we present the evaluation of spatial resolution of EXA microscope and application to observation of cultured biological cells. We have successfully observed the fine structure of intercellular granules in HeLa cells without any stain process.

2. Development of EXA microscope

Figure 1(a) shows schematic diagram of the proposed EXA microscope and Fig. 1(b) shows the principle of optical scanning imaging with electron beam excitation. As shown in Fig. 1(b), an electron beam is focused on a luminescent film and excited the point light source. Since the electron beam is focused in a few nanometer size, it is possible to excite nanometric point light source. A specimen is put on the luminescent film directly. The light source illuminates the specimen, and the scattered or transmitted light is detected with an optical microscope system as shown in Fig. 1(a). A photomultiplier tube (PMT) is used for detection of the light. By scanning the electron beam, the light source can be scanned for forming of observation image.

In the developed EXA microscope, the focused electron beam limits the size of optical light source. The nanometric light source is main factor to achieve superresolution imaging. A few tens nanometer size optical spot is produced easily, by electron beam focused in a few nanometers area. This is very similar to conventional near-field optical microscopes, although they confine optical spot size with small apertures.

The EXA microscope is possible to observe dynamic activities of living biological specimens with video frame or faster frame rate, because electron beam can be scanned with modulation of magnetic or electric field without any mechanical moving parts. Higher signal-to-noise ratio is possible, by using highly efficient luminescent film for electron beam irradiation. We have successfully observed intercellular granules without staining process.

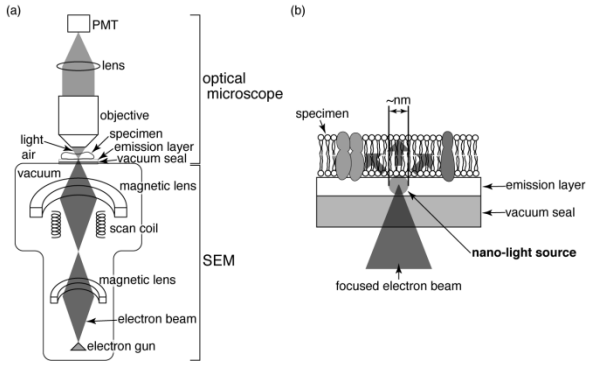

Fig. 1. (a) Schematic diagram of EXA microscope. (b) Point light source with electron beam excitation. The electron beam is focused into a luminescent film and excites the nanometric light source

To verify feasibility of the high resolution EXA microscope, we used silicon nitride (SiN) film of 50 nm thickness as a luminescent material and all optical components were inserted in vacuum chamber of scanning electron microscope (SEM) (JEOL, JSM-6390). SiN film emits blue to ultra-violet (UV) light by irradiation of electron beam. We confirmed in a preliminary experiment that SiN film of 50 nm thickness had enough strength to separate 1 atm air pressure from vacuum.

In the experiment, electrons were accelerated with 10 kV voltage and focused to a 8nm diameter spot on the SiN film to excite nanometric light source. Scattered or transmitted light from the specimen was collected by a lens with numerical aperture 0.65 and detected with a photomultiplier tube (PMT) (Hamamatsu Photonics, R7400-U20). Images were reconstructed from the signal detected with raster scanning of electron beam using a computer. We used polystyrene latex spheres dispersed on the SiN film directly as specimens for resolution veri- fication. The latex spheres were dispersed in monolayer, which was confirmed with an atomic force microscope (Seiko, SPI-3800).

Figure 2(a) and 2(b) show observation images acquired with the SEM and EXA microscopes, respectively. The two images were acquired successively. The scale bars in the images represent 100 nm length. The acquisition time of EXA image was 16 minutes at 512 by 512 pixels. The resolution and signal-to-noise ratio of the SEM image in Fig 2(a) is poor because the SEM image was acquired through the SiN membrane. Each latex sphere of 100 nm diameter was observed clearly and its position in the EXA image was identified with that in the SEM image. This allows us to conclude that EXA microscope has resolution higher than the diffraction limit.

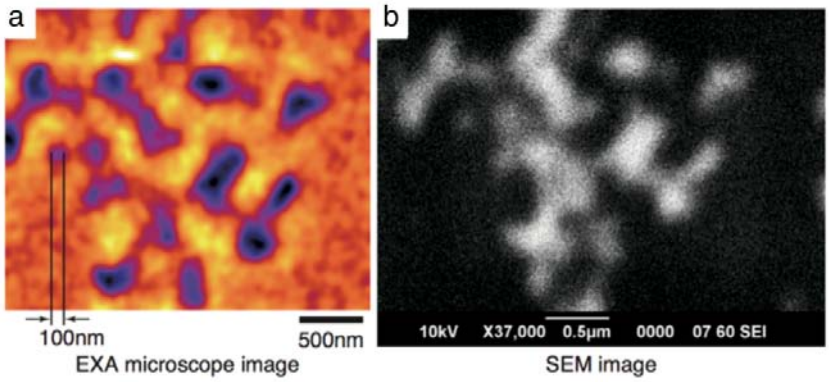

Fig. 2. (a) EXA microscope image of 100 nm latex spheres, (b) SEM image of the same area as in (a)

Figure 3(a) shows a luminescence image of the cells acquired with the EXA microscope, and Fig. 3(b) shows a phase contrast microscope image. Cells were observed in culture solution without any treatments, such as fixation and drying. The shape of each cell was clearly recognized and some bright spots were observed in cells.

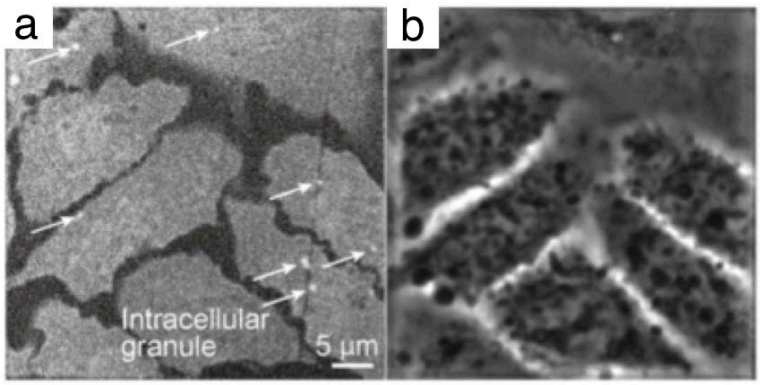

Fig. 3. Observation results of of living MARCO-expressing CHO cells with (a) EXA microscope and (b) phase contrast microscope

References

1. W. Inami, K. Nakajima, et.al., *Opt. Exp*., 2010, **18**, 12897.
2. Y. Nawa, W. Inami, A. Ono, et. al., *Opt. Exp.*, 2012, **20**, 5629.

OPTIMIZATION OF TARGET NORMAL SHEATH PROTON ACCELERATION IN TARGETS WITH SUBWAVELENGTH SURFACE GRATING

A.V. Korzhimanov[1,2] and **M. Marklund**[3]

[1] Institute of Applied Physics RAS, Nizhny Novgorod, Russia,
kav@ufp.appl.sci-nnov.ru
[2] University of Nizhny Novgorod, Nizhny Novgorod, Russia
[3] Chalmers University of Technology, Goteborg, Sweden

Abstract. A proton acceleration in thin gold foils irradiated by powerful femtosecond laser pulses is investigated by means of 2D3V and fully 3D numerical simulations. In the regime of Target Normal Sheath Acceleration (TNSA) we study the efficiency increase in the presence of a subwavelength grating deposited on an irradiated side of the target. The optimal parameters for the highest proton maximal and total energies are found and theoretically explained.

The laser proton and light-ion acceleration is a perspective source for a hadron cancer therapy [1]. Recent progress in developing Ti:sapphire laser sources producing pulses from several terawatts to several hundreds terawatts make them wide-spread among laboratories across the whole world [2]. A terawatt-level pulse focusing on a thin metal foil or plastic film is known to produce bunch of ions with energies of the order of several MeVs [3]. A regime of the acceleration for such pulses has been named Target Normal Sheath Acceleration (TNSA). It is based on laser heating of electrons to relativistic temperatures and subsequent expansion of a hot electron cloud beyond the target forming a sheath accelerating protons and light-ions from the rare target side by electrostatic forces.

The TNSA scheme though being quite simple has however quite low efficiency. For simple flat targets only up to several percents of laser energy may be transferred to accelerated protons. Recently it has been shown that the efficiency may be enhanced by using targets with non-flat front surfaces [4]. The irregularities increase laser-target coupling leading to higher electron temperatures and/or higher number of heated electrons. So the energies of accelerated protons are increasing as well.

Here we report on an extensive numerical study performed by us on the efficiency of proton acceleration process in targets with rectangular surface grating. We vary parameters of the grating (period, width and height of a ledge) seeking for a range in which the total energy and maximal energy of protons are maximal for a given laser pulse.

By means of 2D3V simulations performed with PICADOR code [5, 6] we found that optimal parameters for maximal energy and total energy are significantly different. The total energy is maximized in the region where laser efficiently heats high number of electrons to a relatively low temperature. Whereas the maximal energy is maximized in the region where the number of hot electrons is not very high but they have much higher temperature.

By means of fully 3D simulations we investigated the difference between three type of rectangular gratings: brush, holes and rods. We found that the results for brush and holes are close to each other and to the 2D3V simulations. The case of rods differs significantly. It has different optimal parameters and the overall efficiency is somewhat lower at least in the investigated parameters range.

In the work we investigated a joule-level 40-fs laser pulse and found that even though the grating increase acceleration efficiency up to several times comparing to flat targets, the energy of protons and their number is still insufficient for such a demanding application as the proton therapy. So laser systems with higher pulse energies and at the same time high repetition rate and good repeatability are badly needed. Structured targets, however, may somewhat ease those requirements bringing a day when the laser based proton therapy will cure first patient closer.

Acknowledgements

The 2D3V simulations were performed on resources provided by the Swedish National Infrastructure for Computing (SNIC) at High Performance Computing Center North (HPC2N). The fully 3D simulations were performed on the MVS-10P supercomputer provided by the Joint Supercomputer Center of the Russian Academy of Sciences and on the Lobachevsky supercomputer provided by the University of Nizhny Novgorod.

References

1. K.W.D. Ledingham, P.R. Bolton, N. Shikazono,and C.-M.C. Ma, *Appl. Sci*., 2014, **4**, 402-443.
2. A.V. Korzhimanov, A.A. Gonoskov, E.A. Khazanov, and A.M. Sergeev, *Physics-Uspekhi*, 2011, **54**, 9-28.
3. A. Macchi, M. Borghesi, and M. Passoni, *Rev. Mod. Phys.*, 2013, **85**, 751.
4. Y. Nodera, S. Kawata, N. Onuma, J. Limpouch, O. Klimo, and T. Kikuchi, *Phys. Rev. E*, 2008, **78**, 046401.
5. S. Bastrakov, R. Donchenko, A. Gonoskov, E. Efimenko, A. Malyshev, I. Meyerov, and I. Surmin, *J. Comp. Sci.*, 2012, **13**, 474-479.
6. I.A. Surmin, S.I. Bastrakov, A.A. Gonoskov, E.S. Efimenko, and I.B. Meyerov, *Vych. Met. Programmirovanie*, 2014, **15**, 530-536.

WAVELENGTH DEPENDENCE OF OPTICAL BREAKDOWN IN WATER: CONCLUSIONS FOR THE BAND STRUCTURE OF WATER AND THE INTERPLAY OF MULTIPHOTON AND AVALANCHE IONIZATION

X.-X. Liang, N. Linz, S. Freidank and **A. Vogel**

Institute of Biomedical Optics, University of Lübeck, Lübeck, Germany, liang@bmo.uni-luebeck.de

Abstract. Investigation of the wavelength dependence (725 – 1025 nm) of the threshold for nanosecond optical breakdown in water revealed steps consistent with breakdown initiation by multiphoton ionization, with an initiation energy of about 6.6 eV. This value is considerably smaller than the autoionization threshold of about 9.5 eV, which can be regarded as band gap relevant for avalanche ionization. Breakdown initiation is likely to occur via excitation of a valence band electron into a solvated state, followed by rapid excitation into the conduction band. Theoretical analysis based on these assumptions suggests a pronounced wavelength dependence of the seed electron density required for initiating avalanche ionization.

IR laser-induced breakdown in water and aqueous media is utilized for microsurgery in transparent tissues and cells as well as for producing spherical bubbles in basic investigations of cavitation bubble dynamics. Theoretical modeling of the breakdown process requires a clear picture on the fundamental mechanisms providing seed electrons for avalanche ionization, as well as a profound knowledge of the band structure of liquid water and the possible excitation pathways. We present a novel technique of optical breakdown threshold spectroscopy that addresses both issues by investigating the wavelength dependence of the breakdown threshold in water for nanosecond (ns) IR laser pulses.

Avalanche ionization is the most powerful mechanism driving IR ns laser-induced dielectric breakdown. It depends on the availability of seed electrons in the conduction band that can gain energy through inverse Bremsstrahlung absorption and multiply by impact ionization. For ns breakdown, it is still a matter of debate whether such seed electrons are available as background electrons, formed at impurities, or whether they are generated by multiphoton ionization (MPI) of the water itself. If breakdown initiation depends on MPI, the wavelength dependence of the breakdown threshold, $I_{th}(\lambda)$, should exhibit a sharp rise whenever one photon more is needed to overcome the initiation energy E_{ini}. By contrast, if it relies on background electrons or thermal ionization of impurities, the $I_{th}(\lambda)$ curve should vary monotonously.

To date, optical breakdown models treat water as amorphous semiconductor and identify E_{ini} with the band gap energy. However, spectroscopic evidence collected in the past two decades suggests that this approach oversimplifies the band structure and that direct ionization occurs only at considerably higher excitation energies of $\geq$ 9.5 eV. The previously assumed "ionization energy" of 6.5 eV turned out to be the minimum energy needed for excitation of a valence band electron into a solvated state.

We investigated the optical breakdown threshold in water at 21 wavelengths between 725 nm and 1025 nm using bubble formation as threshold criterion [1]. Measurements were performed using 2-ns IR single-longitudinal mode laser pulses providing a smooth, reproducible temporal pulse shape that is essential for a precise threshold determination. Figure 1 shows the existence of steps in the $I_{th}(\lambda)$

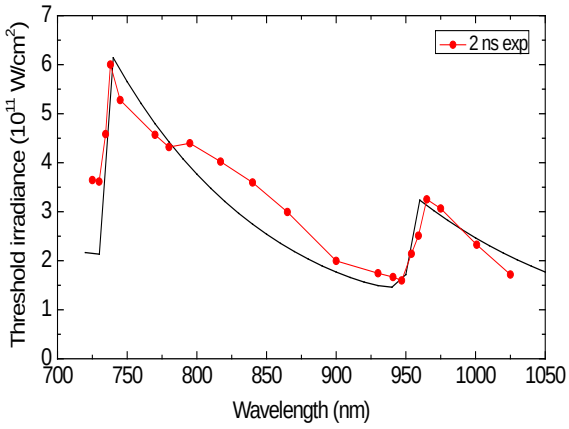

Fig. 1. Wavelength dependence of the irradiance threshold for optical breakdown in water produced by 2-ns laser pulses, compared with model predictions (black line). The steps in the $I_{th}(\lambda)$ spectrum indicate multiphoton initiation of breakdown spectrum verifying multiphoton-initiation of nanosecond IR breakdown. The steps in the $I_{th}(\lambda)$ spectrum are consistent with an initiation energy of $\approx$ 6.6 eV which is considerably smaller than the band gap energy of $\approx$ 9.5 eV.

We conclude that breakdown initiation likely occurs via excitation of a valence band electron into a solvated state, followed by rapid excitation into the conduction band. Therefore, an additional "initiation channel" involving an intermediate energy level must be introduced into breakdown models for water. Theoretical analysis of the measurement results corroborated our hypothesis on breakdown initiation.

Fitting of model predictions to $I_{th}(\lambda)$ as shown in Fig. 1 revealed that the seed electron density required to initiate avalanche ionization drops from above 10^{15} cm^{-3} at 725 nm to below 10^{12} cm^{-3} at 1025 nm. Similar seed electron densities as in water will probably be needed also for plasma formation in transparent cells and tissues. However, in those media bio-molecules can provide additional sources for free-electron generation, and the breakdown threshold may be lowered.

References

1. N. Linz, S. Freidank, X.-X. Liang, H. Vogelmann, T. Trickl, and A. Vogel, accepted by *Phys. Rev. B.*, 2015.

Invited

ADVANCED CONCEPTS FOR CORNEAL DISSECTION BY FEMTOSECOND AND PICOSECOND LASER PULSES: FOCUS SHAPING AND WAVELENGTH TUNING

N. Linz[1], **S. Freidank**[1], and **A. Vogel**[1]

[1] Institute of Biomedical Optics, University of Lübeck, Lübeck, Germany, linz@bmo.uni-luebeck.de

Abstract. Refractive surgeries like LASIK and SMILE are based on corneal dissection by focusing laser pulses in a raster pattern into the corneal stroma. Improvements of the cutting quality can be achieved by employing a vortex beam that has a ring-shape focus, with the same length in axial direction as for a Gaussian beam but a two-fold larger diameter. This facilitates cleavage along the corneal lamellae and allows cutting with lower plasma energy density, higher precision and less mechanical side effects. Further improvements can be achieved by use of shorter wavelengths than the commonly used IR wavelength.

1. Introduction

Two strategies are presently used for corneal refractive surgery: In LASIK, an incision parallel to the corneal surface creates a thin 'flap', and excimer laser ablation of stromal material corrects the refractive error. In SMILE, two intrastromal incisions produce a lenticule that is removed with forceps through small side cuts. This allows for a one-step refractive correction without flap lifting. For dissection, laser pulses are in both procedures focused in a raster pattern into the corneal stroma, and plasma-induced microexplosions generate cavitation bubbles that cleave the lamellae.

Cutting precision is compromised by the elongated shape of the laser plasma, which is oriented along the optical axis, i.e. perpendicular to the desired cutting direction. Substantial improvements of the cutting quality can be achieved by converting the linear polarized Gaussian beam into a helically phased "vortex" beam by means of a spiral phase plate. The laser focus then has a ring-shape, with the same length in axial direction as for a Gaussian beam but a larger diameter (Fig. 1). This facilitates cleavage along the corneal lamellae, enabling to cut with lower plasma energy density, higher precision and less mechanical side effects. Further improvements can be achieved by using a laser wavelength considerably shorter than the commonly used IR wavelengths around 1040 nm.

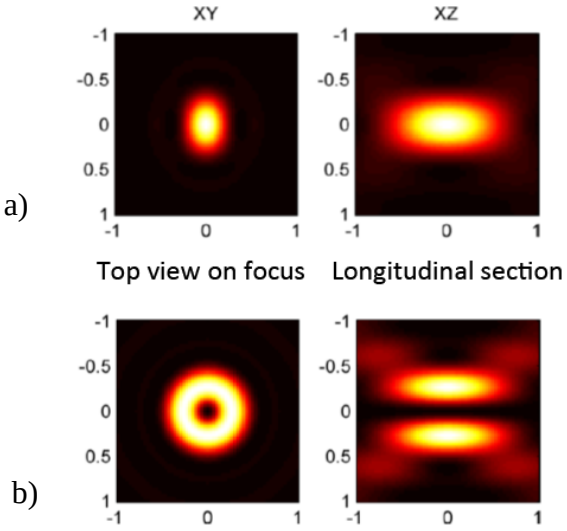

Fig. 1. Calculated focus shapes of Gaussian beam (a) and vortex beam (b) for the same focusing angle [1]. The focus shapes are shown in top and side view

2. Methods

Laser-induced bubble formation in corneal stroma is investigated by high-speed photography at 1–50 million frames/s. Incident and absorbed laser energy needed for easy removal of flaps created in porcine corneas are determined for Gaussian and vortex beams with pulse durations from 200 fs to 9 ps for IR wavelengths and 1 ps to 850 ps for UVA wavelengths. For each laser parameter, cutting dynamics and amount of bubble production are documented by video and macro-photography. The cutting quality is investigated by scanning electron microscopy.

3. Results

Time-resolved photography demonstrates that laser-induced cavitation bubbles exhibit a lobular shape and extend over a depth of several lamellae (Fig. 2a). This makes it difficult to achieve homogenous, smooth cuts. Cutting quality can be improved and tissue bridges reduced by strategies which provide short plasma and facilitate cleavage along the corneal lamellae. This can be achieved by use of short wavelengths, large NAs, and vortex beams. The excellent cutting precision achievable with UVA picosecond lasers is shown in Fig. 2(b). The short, donut-shaped focus produced by vortex beams

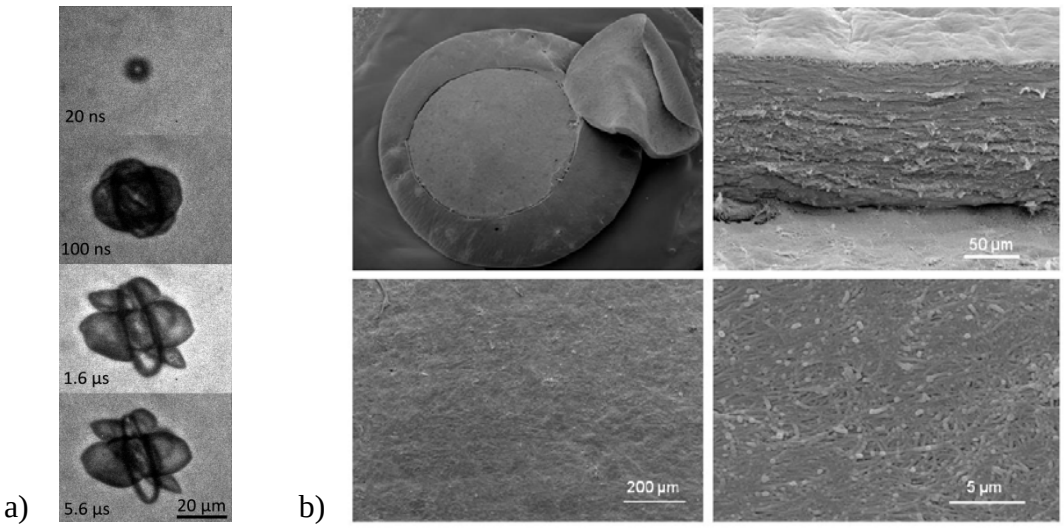

Fig. 2. (a) High-speed photography of cavitation bubble dynamics in porcine cornea, (b) scanning electron microscopic images of a flap cut produced with an UVA laser (355 nm, 550 ps) at NA = 0.38

allows for efficient and precise dissection along the corneal lamellae. For all pulse durations and wavelengths investigated, the incident laser pulse energy required for flap cutting was higher for vortex than for Gaussian beams (Fig. 3 a), but the efficient cutting mechanism resulted in a dramatic reduction of the absorbed energy needed for cutting and thus of mechanical side effects, especially for UVA pulses (Fig. 3b). Furthermore, we found that the use of a vortex beam strongly diminishes bubble formation in the cutting plane, and leads to a smoother dissection.

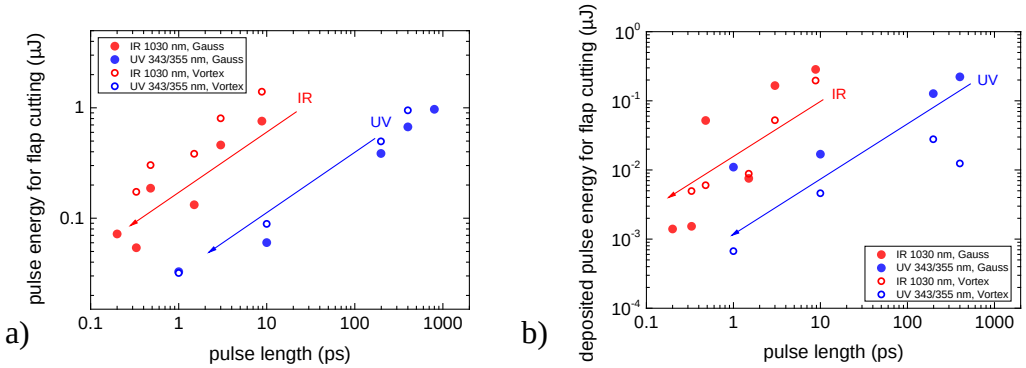

Fig. 3. (a) Incident and (b) absorbed pulse energy required for flap cutting with UVA and IR laser pulses in dependence on pulse duration. Flap cutting was performed with 6 µm x 6 µm spot separation at NA = 0.38

4. Conclusions

Focus shaping and use of shorter wavelengths open new avenues in refractive surgery. A combination of UVA laser pulses with vortex beams for corneal dissection may provide the option to replace femtosecond lasers by compact UVA laser technology. Ring foci from vortex beams generally improve precision and efficiency of cuts, regardless of wavelength and pulse duration.

The reduced bubble formation in the cutting plane is of interest both for LASIK and SMILE. In LASIK, it facilitates pupil tracking in subsequent excimer laser surgery, and the reduction of mechanical side effects may decrease the incidence of diffuse lamellar keratitis (DLK). In SMILE, the refractive outcome largely relies on the precision of lenticule dissection which can be increased by minimizing the amount of bubble formation.

References

1. X. Hao, C. Kuang, T. Wang, and X. Liu, *Journal of Optics*, 2010, **12** (11), 115707.

Invited

LASER-WAKEFIELD ACCELERATION AS A BETATRON RADIATION SOURCE FOR BIOLOGICAL IMAGING

N.C. Lopes[1,2], **J.M. Cole**[1], **K. Poder**[1], **J. Wood**[1], **P. Abel**[3], **R. Abel**[6], **S. Alatabi**[1], **J. Bryant**[1], **D. Dangor**[1], **A. Jin**[6], **S. Kneip**[1], **S.P.D. Mangles**[1], **K. Mecseki**[1], **N. Ngo**[3], **Q.D. Nguyen**[3], **M. Sroya**[4], **D.R. Symes**[5], **M. Winkler**[3], and **Z. Najmudin**[1]

[1] The John Adams Institute for Accelerator Science, Imperial College London, SW7 2AZ, UK
[2] GoLP/IPFN, Instituto Superior Técnico, UL, Lisboa, Portugal
[3]Imperial College, Faculty of Medicine, Dep. of Surgery & Cancer, Imperial College London, W6 8RF, UK
[4]Imperial College Healthcare Tissue Bank, Imperial College London, W6 8RF, UK
[5]Laser Facility, STFC, Rutherford Appleton Laboratory, Didcot, OX11 0QX, Uk
[6] MSK Laboratory, Charing Cross Hospital, Imperial College London, W6 8RF, UK

Abstract. A lensless x-ray microscope was used for biological imaging. The light source was a laser-plasma wakefield accelerator driven by 10 J, 45 fs laser pulses producing 0.5–1 GeV electron bunches. The betatron motion of the electrons in the plasma structure generates a synchrotron like x-ray beam with 30 keV critical energy, 10^9 photons per shot with a micron scale source size. The x-ray beam was used in phase-contrast and absorption-contrast configurations to image soft (prostate) and hard (bone) tissue samples with a few-micron resolution.

Laser-plasma wakefield accelerators [1, 2] using Ti:Sapphire laser pulses with energies of 10 J and durations of 50 fs can produce electron bunches with charges of a few tens of pC and energies of 1 GeV. The plasma accelerator parameters (mainly laser spot size, and pulse energy and duration as well as gas-target density, length and position) can be optimized to reduce the amplitude of the betatron motion of the electron bunch in the plasma accelerating structure. The radiation generated by the electron betatron motion in the plasma accelerating structure [3–5] possesses favourable characteristics for imaging, namely a high brilliance, small source-size and short pulse duration. The resolution obtained with lenseless imaging is limited by the radiation source size. Therefore the reduction of the x-ray betatron source size (to a few microns) allows features of similar size to be resolved. This is especially important for x-ray energies where optics are not practical or inexistent. Moreover, the small source size allows for phase-contrast imaging due to the consequent high spatial coherence of the beam. The disadvantage of the source size reduction is a significant reduction in the x-ray yield. However, the high energy of the electron bunch (1 GeV) compensates the betatron radius reduction and the final number of photons on the detectors is still adequate for high imaging quality over both the 5–9 keV and 5-50 keV windows.

An experiment dedicated to study the application of betatron radiation towards high-resolution biological imaging was carried out on the Astra-Gemini Laser facility, UK. We used a standard setup for relativistic electron acceleration, focusing the 15 J, 45 fs, 800 nm laser beam into a 20 micron spot, coincident with a variable length helium filled gas cell with sub-mm apertures on the laser axis for the propagation of the beams. For these laser parameters the gas pressure and length producing the highest resolution images were 60 mbar and 10 mm respectively. This resulted in electron beams with energies in the range 0.7–1.1 GeV and charges < 100 pC. Both the laser and the electron beams were removed from the accelerator axis by a reflective foil and a magnetic field respectively, allowing the placement of samples as close as 0.4 meters from the x-ray source and resulting in geometric magnifications of up to 8.7. Phase-contrast images of millimeter thick fixed and paraffin embedded prostate slices were obtained in this configuration using a direct detection x-ray CCD (sensitive to the x-rays in the range 5–9 keV). The field of view in the sample plane, limited by the detector size, necessitated a raster scan with images taken by displacing the sample by 2mm in both vertical and horizontal directions. The resulting images were processed by removing noise, correcting for the beam profile and stitched together to form a composite phase-contrast image of the whole sample. In figure 1 (left) we present the composite image for a millimeter thick sample.

This resolution of this image is close to what can be obtained with histology techniques. In contrast with these techniques, we are able to resolve the interior structure of the tissue inside the sample slice along with the surface detail.

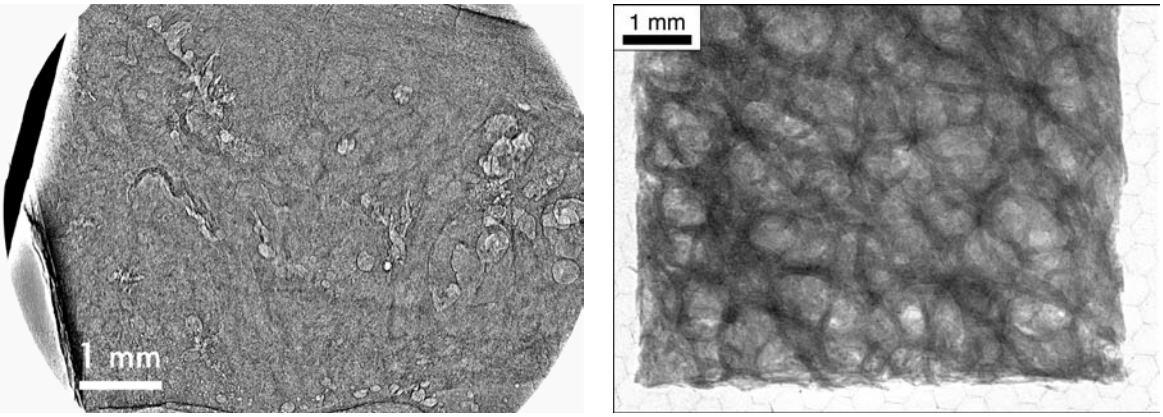

Fig. 1. Raster scan image of a millimeter thick prostate sample obtained in phase-contrast using betatron x-rays in the range 5–9 keV (*left*). Single-shot x-ray image of a cylindrical femoral sample of trabecular bone obtained using betatron x-rays in the range 20-50 keV (*right*)

By changing the x-ray detector to a scintillator based x-ray CCD and using filters it was possible to move the detection window to the 20-50 keV range. This setup provided adequate absorption contrast for imaging of a 7 mm thick sample of femoral trabecular bone. An image of this sample obtained in a single shot is presented in figure 1 (right). Similar images were obtained for 180 different exposure angles and were used to produce a tomographic reconstruction of the sample to a resolution of approximately 50 microns.

In conclusion, we report on the development of a compact x-ray light source based on laser-plasma wakefield acceleration as well as its application in biological imaging. The source presents an adequate combination of characteristics to be used in micron-resolution biological and medical imaging from thin and soft tissue samples in propagation based phase-contrast to hard samples in absorption contrast.

Acknowledgements

This work was supported by STFC grant ST/J002062/1. We acknowledge the help of the staff of the CLF, Rutherford-Appleton Laboratory for assistance during the experiment.

References

1. T. Tajima and J. M. Dawson, "Laser electron accelerator", *Phys. Rev. Lett*., 1979, **43**, 267.
2. S.P.D. Mangles, *et al.,* "Monoenergetic beams of relativistic electrons from intense laser-plasma interactions", *Nature,* 2004, **431,** 535–538.
3. S. Kneip, C. McGuffey, J.L. Martins, et al., "Bright spatially coherent synchrotron x-rays from a table-top source", *Nat. Phys*., 2010, **6**, 980-983.
4. E. Esarey, B.A. Shadwick, P. Catravas, and W.P. Leemans, "Synchrotron radiation from electron beams in plasma-focusing channels", *Phys. Rev. E,* 2002, **65,** 056505.
5. J.M. Cole, et al., "Laser-wakefield accelerators as hard x-ray sources for 3D medical imaging of human bone, submitted for publication", 2015.

Invited

FRONTIERS OF FEMTOSECOND LASER APPLICATIONS IN OPHTHALMOLOGY

H. Lubatschowski

ROWIAK GmbH, Hannover, Germany,
h.lubatschowski@rowak.de

Abstract. Femtosecond lasers for refractive corneal surgery (fs-LASIK) have increased their market share from 0 percent in 2001 to over 55 percent in 2010. Now, in cataract surgery a similar revolution may take place. What makes this technology so special and which new areas of surgery will furthermore be entered in the future? This review elucidates the most important technical features of the fs lasers and interaction processes with the tissue in Ophthalmology. It is intended to provide an overview of the current clinical situation on the one hand. In addition, it can be estimated what kind of short- and long-term development this technology could take in the future.

Invited

TOWARDS LASER-DRIVEN ION SOURCES FOR RADIOTHERAPY

J. Metzkes[1,5], M. Baumann[2,3,4], E. Beyreuther[2], M. Bussmann[2], T.E. Cowan[2,5], W. Enghardt[2,3,4], L. Karsch[3], T. Kluge[2], S.D. Kraft[2], F. Kroll[2,5], L. Laschinsky[3], U. Masood[2,3], M. Oppelt[2,3], J. Pawelke[2,3], C. Richter[3], R. Sauerbrey[2,5], U. Schramm[2,5], M. Schürer[3], M. Siebold[2], and **K. Zeil[2]**

[1] Helmholtz-Zentrum Dresden – Rossendorf, Dresden, Germany, j.metzkes@hzdr.de
[2] Helmholtz-Zentrum Dresden – Rossendorf, Dresden, Germany
[3] OncoRay – National Center for Radiation Research in Oncology, Dresden, Germany
[4] Klinik für Strahlentherapie und Radioonkologie, Universitätsklinikum Carl Gustav Carus der TU Dresden, Dresden, Germany
[5] Technische Universität Dresden, Dresden, Germany

Abstract. The talk gives an overview over the multi-disciplinary research program in Dresden, which aims at the development of laser-driven ion sources for radiotherapy, including the translation of the technology into clinical application. The progress of the program will be discussed by presenting experimental results from the last years and discussing the laser facility at the Helmholtz-Zentrum Dresden – Rossendorf.

Laser-driven ion sources (LDIS) exploit the extremely high electric fields (TV/m) that can be supported in laser-produced plasmas. These extreme fields, exceeding the capabilities of conventional accelerators by six orders of magnitude, considerably reduce the necessary accelerator length and render possible compact LDIS-based particle accelerators.

The most matured physical mechanism underlying LDIS is target normal sheath acceleration (TNSA) [1–3]. In TNSA, an ultra-intense ($I \sim 10^{18}$–10^{21} W/cm^2) laser pulse ($\tau \sim 10$–100 fs) irradiates the surface of a µm thick solid target, rapidly ionizing the material and creating a plasma. Electrons, oscillating in the electric component of the laser field, gain relativistic energies and set-up quasi-static electric space-charge fields at the target surfaces, which serve the acceleration of ions. LDIS can produce ~10 MeV/nucleon protons and ions on ~µm spatial scales. In combination with the favorable properties of laser-accelerated ions, such as their high flux, the ps pulse duration at the source and the high laminarity, LDIS are potentially advantageous for numerous applications [4, 5]. LDIS-based particles sources for radiation therapy of cancer are one of the currently pursued fields of application [4, 5].

In this talk, the according effort in Dresden (Germany) will be presented, which is a multi-disciplinary project aiming at the translation of the LDIS technology into clinically applicable machines for radiation therapy. As a cooperation of clinical-based institutions (OncoRay – National Center for Radiation Research in Oncology, Technische Universität Dresden) as well as groups focused on laser-plasma research (Helmholtz-Zentrum Dresden – Rossendorf, HZDR), the project encompasses the entire task area from developing the laser-driven accelerator, designing pulsed magnet beam delivery systems [6-8], developing dosimetry for pulsed sources [9] and studying the *in vitro* and *in vivo* radiobiological effectiveness of laser-accelerated protons [10, 11].

For the accelerator research, the HZDR operates the 150 TW, high repetition rate (10 Hz), ultra-short pulse (τ=30 fs) laser system Draco, which is based on the chirped pulse amplification (CPA) technique. By achieving maximum proton energies of up to 20 MeV at the Draco system, it was proven that CPA-based ultra-short pulse lasers – capable of ~Hz repetition rates in contrast to high energy, long pulse laser systems – can serve as efficient drivers for LDIS [12]. The development of LDIS is further strongly advanced by rapid progress in laser technology, which leads to an increasing availability of CPA ultra-short pulse PW laser sources with Hz repetition rate [13]. Laser power scalings for TNSA predict that particularly protons with kinetic energies exceeding 100 MeV will be achievable with this class of laser systems [14].

At the HZDR, a dual approach is taken regarding PW class laser system development. On the one hand, the 150 TW Draco laser system is currently upgraded to a dual beam facility, delivering in its final setup two simultaneously usable laser pulses at 150 TW and 1 PW which can be synchronized at the interaction point. Moreover, the diode-pumped PW laser system PEnELOPE (Petawatt, Energy-Efficient Laser for Optical Plasma Experiments) is developed in-house [15].

Sufficient particle energies of ~200 MeV are a precondition for LDIS to be used for the treatment of deep-lying tumors. Besides laser development, an increase of the available proton energies from laser-driven sources is approached by optimization of the acceleration process itself, e.g. by using specific target designs. At the HZDR and in a cooperation at the LULI laser facility, the effect of reduced mass targets, i.e. targets with a finite transverse size, was investigated experimentally [16, 17]. Both experiments

showed approximately a doubling of the maximum proton energy and an increase in particle yield when comparing large foils and the optimal RMT size [16, 17]. This is attributed to a refluxing of the laser-accelerated electrons within the target volume, which leads to an increased electron density, temperature, homogeneity and particle source size in the accelerating Debye sheath [16, 17].

In the last years, the available high repetition rate ~100 TW laser systems have been used for radiobiological studies with laser-accelerated protons by a number of groups [4, 5]. These studies mark a necessary step towards medically applied laser-based accelerator since the properties of laser-accelerated proton pulses differ significantly from the radiation delivered by conventional proton sources (e.g. cyclotrons) regarding the pulse structure, peak current and spectrum. Hence, an experimental comparison of the biological effectiveness of both radiation qualities is mandatory. The studies performed at the 150 TW Draco laser system indicated no significant difference in the biological effectiveness [11]. Regarding the performance of the laser-based accelerator, the key result is however the achieved dose uncertainty $\Delta D/D$ below 10% averaged over all individual cell samples irradiated, comparable to conventional irradiation data [11]. Basis for this achievement is firstly, a dedicated dosimetry system combining absolute and online relative dose measurements, both adapted to the properties of laser-accelerated proton pulses [9], and secondly, a high stability of the laser system and the laser-target interaction conditions [10, 11]. The next step are *in vivo* irradiations using the Draco PW laser system and a pulsed magnet based beam delivery [11].

Acknowledgements

The work has been supported by the German Federal Ministry of Education and Research (BMBF) under contract number 03ZIK445.

References

1. S.P. Hatchett *et al.*, *PoP*, 2000, **7**(5), 2076.
2. R.A. Snavely *et al.*, *Phys.Rev. Lett.*, 2000, **85**(14), 2945.
3. S.C. Wilks *et al.*, *PoP*, 2001, **8**(2), 542.
4. H. Daido *et al.*, *Rep. Prog. Phys.*, 2012, **75**(5), 056401.
5. A. Macchi *et al.*, *Rev. Mod. Phys.*, 2013, **85**(2), 751.
6. T. Burris-Mog *et al.*, *Phys. Rev. STAB*, 2011, **14**, 121301.
7. S. Busold *et al.*, *Phys. Rev. STAB*, 2013, **16**(10), 101302.
8. U. Masood *et al.*, *Appl. Phys. B*, 2014, **117**(1), 41.
9. C. Richter *et al.*, *Phys. Med. Biol.*, 2011, **56**(6), 1529.
10. S.D. Kraft *et al*, *New. J. Phys.*, 2010, **12**(8), 85003.
11. K. Zeil *et al.*, *Appl. Phys. B*, 2012, **110**(4), 437.
12. K. Zeil *et al. Nat. Com.*, 2012, **3**, 874.
13. T.M. Jeong *et al.*, *Ann. Phys.*, 2014, **526**(3), 157.
14. T. Kluge *et al.*, *Phys. Rev. Lett.*, 2011, **107**(20), 205003.
15. M. Siebold *et al.*, *Proc. SPIE*, 2013, **8708**, 870805.
16. S. Buffechoux *et al.*, *Phys. Rev. Lett.*, 2010, **105**(1), 15005.
17. K. Zeil *et al.*, *Plasma Phys. Control. Fusion*, 2014, **56**(8), 084004.

Invited

NANOPLASMONICS ENHANCED ULTRAFAST LASER NANOSURGERY

M. Meunier

Polytechnique Montréal, Montréal, Canada
Michel.meunier@polymtl.ca

Abstract. In this invited talk, I will review recent developments of the fundamentals and applications of nanoplasmonics enhanced ultrafast laser nanosurgery of living cells. Modeling and experiments were developed to understand the basic phenomena occurring during ultrafast laser irradiation of plasmonics nanostructures. Applications in laser optoporation and transfection of cells will be discussed.

Irradiating metallic nanostructures by a femtosecond laser beam produces highly localised processes on the nanoscale in the surrounding medium. This particular process is mainly attributed to the surface plasmon resonance of the nanostructures. When these nanomaterials are imbedded in a biological media, their irradiation by a femtosecond laser could results in a highly localized plasma, heat production and mechanical effects yielding to the nanosurgery of cells [1–12].

Fundamentals

A complete partial differential equation based model has been developed to describe the interaction of an ultrafast laser with a plasmonic nanostructure in water [2-3]. Apart from heating the structure itself, it is shown that this interaction also leads to the generation of a plasma in the water medium and to the production of a strong pressure wave and a nanobubble in the vicinity of the structure. Plasma collision and relaxation are shown to be the main source of mechanical stress in the medium and the dominant factor for the pressure wave and bubble creation.

An all-optical technique able to detect plasmonic enhanced bubble formation and pressure wave generation is also presented [2, 6–7]. Results show that for longer pulses, bubbles are independent of the polarization, in agreement with a linear thermally induced formation mechanism. In opposition, for shorter femtosecond pulses, bubble sizes are shown to depend on the polarization, a characteristic signature of nonlinear energy absorption in the near-field of the particle. This result thus offers a simple and intuitive demonstration that strongly supports plasma-mediated mechanism for off-resonance ultrafast laser nanocavitation.

We also demonstrated with a single-particle monitoring that 100 nm AuNPs irradiated by off-resonance femtosecond (fs) laser in the tissue therapeutic optical window (λ = 800 nm), can act as a durable nanolenses in liquid and provoke nanocavitation while remaining intact [9, 11]. We observed an effective laser processing window, ranging from 145 mJ/cm^2 to 240 mJ/cm^2, in which, the plasmonic AuNPs act as durable nanolenses, resulting in successive generation of multiple nanobubbles (radius: 550 nm – 700 nm, life time: 34 ns – 44 ns). The latter is of significant importance for future development of *in-vivo* AuNP-assisted laser nanosurgery and theranostic applications, where AuNP fragmentation should be avoided to prevent side effects, such as cytotoxicity and immune system's response.

Applications in nanomedecine

These nanoparticles could be functionalized to target specific biological entities, thus performing multiple targeted surgeries on the nanoscale (10). As an example, the laser nanosurgery technique was employed to perform gene transfection in living cell with an optoporation efficiency as high as 80% [1]. For human cancer melanoma cells, the treatment leads to a very high perforation rate of 70%, transfection efficiency three times higher than for conventional lipofection, and very low toxicity (< 1%) [1]. Off-resonance laser excitation inhibited the fracture of the nanoparticles into possibly toxic DNA intercalating particles. This efficient and low toxicity method is a promising alternative to viral transfection for skin cancer treatment. Our laser technique shows promises as an innovative tool for fundamental research in biology and medicine as well as an efficient alternative nanosurgery technology that could be adapted to therapeutic tools in the clinic. It is now being developed in close collaboration with researchers in hospital for applications in cancer treatment, ophthalmology and neurology. Recent developments in these fields will also be presented.

References

1. J. Baumgart, L. Humbert, E. Boulais, R. Lachaine, J.J. Lebrun, and M. Meunier, "Off-resonance plasmonic enhanced femtosecond laser optoporation and transfection of cancer cells", *Biomaterials*, 2012, **33**, 2345-2350.

2. E. Boulais, R. Lachaine ,and M. Meunier, "Plasma mediated off-resonance plasmonic enhanced ultrafast laser induced nanocavitation", *Nanoletters*, 2012, **12**, 4763-4769.
3. E. Boulais, R. Lachaine, A. Hatef, and M. Meunier, "Plasmonics for pulsed-laser cell nanosurgery: fundamentals and applications", *Journal of Photochemistry and Photobiology C*, 2013, **17**, 26-49.
4. E. Boulais, R. Lachaine, and M. Meunier, "Plasma-Mediated Nanocavitation and Photothermal Effects in Ultrafast Laser Irradiation of Gold Nanorods in Water", *J. Physical Chemistry C*, 2013, **117**, 9386-9396.
5. B. St-Louis Lalonde, É. Boulais, J.J. Lebrun, and M. Meunier, "Visible and Near infrared resonance plasmonic enhanced nanosecond laser optoporation of cancer cells", *Biomedical Optics Express*, 2013, **4**, 490-499.
6. R. Lachaine, E. Boulais, E. Bourbeau, and M. Meunier, "Effect of pulse duration on plasmonic enhanced ultrafast laser-induced bubble generation in water", *Applied Physics A*, 2013, **112**(1), 119-122.
7. R. Lachaine, E. Boulais, and M. Meunier, "From Thermo- to Plasma-Mediated Ultrafast Laser Induced Plasmonic Nanobubbles", *ACS Photonics*, 2014, **1**, 331-336.
8. A. Hatef and M. Meunier, "Plasma-mediated photothermal effects in ultrafast laser irradiation of gold nanoparticle dimers in water", *Optics express*, 2015, **23**(3), 1967-1980.
9. C. Boutopoulos, E. Bergeron, and M. Meunier, "Cell perforation mediated by plasmonic bubbles generated by a single near infrared femtosecond laser pulse", accepted in *J. of Biophotonics*, 2015.
10. E. Bergeron, C. Boutopoulos, R. Martel, A. Torres, C. Rodriguez, J. Niskanen, J.-J. Lebrun, F.M. Winnik, P. Sapieha, and M. Meunier, "Cell-specific optoporation with near-infrared ultrafast laser and functionalized gold nanoparticles", submitted to *Biomaterials*, 2015.
11. C. Boutopoulos, A. Hatef, M. Fortin-Deschênes, and M. Meunier, "Dynamic imaging of single gold nanoparticle in liquid irradiated by off-resonance femtosecond laser", submitted to *Nanoscale*, 2015.

Invited

DEVELOPMENT OF HIGHLY FUNCTIONAL ULTRASHORT PULSE FIBER LASER SOURCES FOR ULTRAHIGH RESOLUTION OPTICAL COHERENCE TOMOGRAPHY

N. Nishizawa, **H. Kawagoe**, **M. Yamanaka**, and **S. Ishida**

Nagoya University, Furo-cho, Chikusa-ku, Nagoya 464-8603, Japan, nishizawa@nuee.nagoya-u.ac.jp

Abstract. We have been investigating highly functional ultrashort pulse fiber laser sources for ultrahigh resolution optical coherence tomography (UHR-OCT). The coherent, low noise, and Gaussian like wideband supercontinuum (SC) sources were developed at five different wavelength regions between 0.8 and 1.7 μm in order to investigate the wavelength dependence of the OCT imaging. Especially, a SC source at 1.7 μm wavelength region was developed using a carbon nanotube fiber laser. A fiber laser based, rapid, widely wavelength tunable narrow linewidth source was also developed using nonlinear fiber phenomena. The UHR-OCT imaging of biological samples were demonstrated using the developed SC sources.

Optical coherence tomography (OCT) is an non-demolition, cross-sectional imaging technique using wideband light source and optical interferometer. The axial resolution of OCT is determined by the wavelength and bandwidth of the light source, and theoretically, the wider the bandwidth of the light source is, the higher the axial resolution is.

Supercontinuum (SC) is wideband light source broadened by nonlinear optical effect. Using the ultrashort pulse and adequate optical fibers, we can generate coherent, low-noise SC. The spectral shape can be optimized by the control of pump pulse and nonlinear fibers.

We have been investigating highly functional ultrashort pulse fiber laser sources for ultrahigh resolution (UHR) OCT [1]. Coherent, wideband SC sources were developed at five different wavelength regions in order to investigate the wavelength dependence of the OCT imaging. A novel, widely, and rapid wavelength tunable narrow linewidth source was also demonstrated.

Figure 1 shows the SC generated at 0.8 μm wavelength region. A Kerr-lens mode-locked ultrashort pulse Ti:Sapphire laser and polarization maintaining fiber were used for SC generation. A clean, high power, Gaussian-like shaped SC was generated. The average power was up to 300 mW. We confirmed the coherence and low noise properties for this generated SC [1, 2].

Figure 2 shows the observed UHR-OCT images using the generated high power SC in Fig. 1. The observed axial resolution was 2 μm in tissue and 3 μm in air. The high sensitivity of about 100 dB was achieved. The precise cross-sectional structures of the biological samples were clearly observed and highly sensitive UHR-OCT imaging was achieved [1, 2].

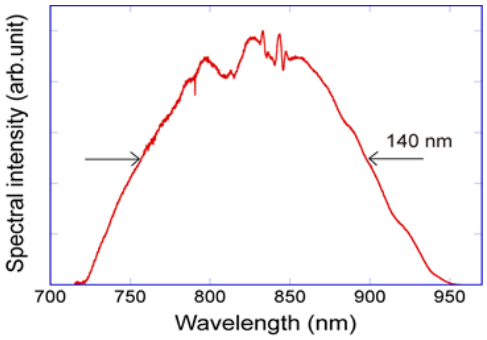

Fig. 1. Optical spectrum of generated supercontinuum at 0.8 μm wavelength

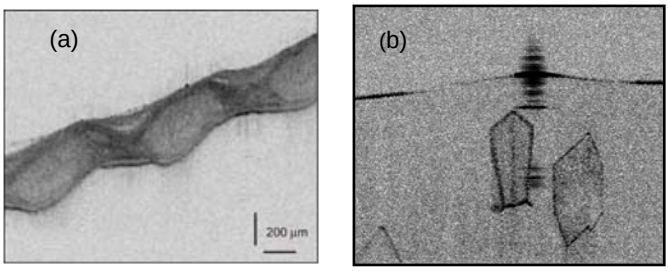

Fig. 2. Observed cross-sectional images by UHR-OCT with SC at 0.8 μm wavelength, (a) rat trachea, and (b) protein crystals

Figure 3 shows the ultrashort pulse fiber laser based SC source at wavelength of 1.7 μm region [3]. A high repetition rate, ultrashort pulse fiber laser using single wall carbon nanotube was developed and used as the seed pulse source. The output pulses were amplified in Er-doped fiber amplifier, and high power ultrashort pulses were generated. Then the generated pulses were introduced into polarization maintaining fiber, and Raman shifted soliton pulses were generated. The generated soliton pulses were picked off with the long pass filter, and they were coupled into highly nonlinear fibers. Thanks to the ideal shape of soliton pulse and adequate characteristics of highly nonlinear fiber, a Gaussian-like shaped, low noise, coherent SC was generated. The bandwidth was 242 nm, and the average power was 60 mW.

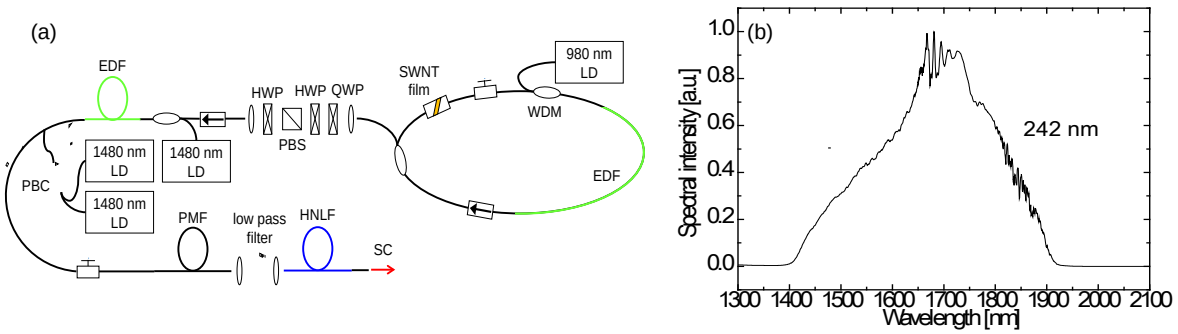

Fig. 3. (a) Configuration of 1.7 μm high power SC generation system with Er-doped SWNT fiber laser. (b) Optical spectra of generated SC at 1.7 μm

Generally speaking, the OCT imaging of biological samples is affected by the absorption and scattering, which depend on the wavelength. In order to investigate the wavelength dependence of UHR-OCT imaging, we developed five SCs and corresponding OCT systems at different wavelength region between 0.8 and 1.7 μm [2]. Figure 4 shows the optical spectra of developed SC sources at five wavelength regions.

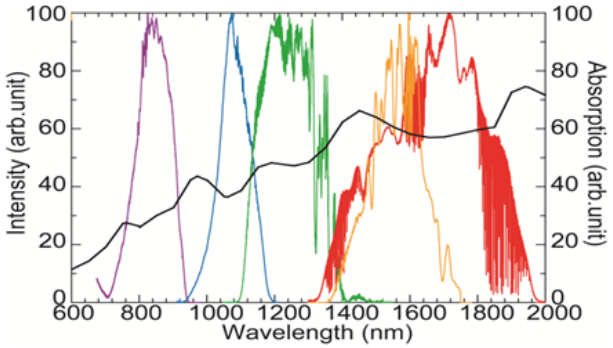

Fig. 4. Optical spectra of developed SC sources at 0.8~1.7 μm wavelength regions

Figure 5 shows the observed UHR-OCT images of pig trachea and human baby tooth at 0.8 and 1.7 μm wavelengths. We can see the difference of UHR-OCT images for wavelengths. For 0.8 μm wavelength, the precise structures were observed owing to the highest axial resolution. For 1.7 μm wavelength region, since the effect of scattering is decreased, the deeper penetration depth was achieved especially in low water absorption samples. Now we have been investigating the wavelength dependence of UHR-OCT imaging of several different samples.

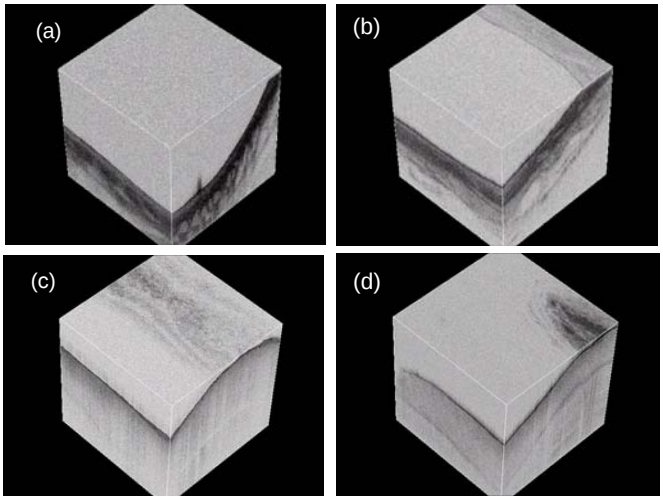

Fig. 5. Observed UHR-OCT images at (a, c) 0.8 and (b, d) 1.7 μm wavelengths, (a, b) pig trachea, and (c, d) human baby tooth

Recently, the high speed and highly sensitive OCT imaging using swept sources has been investigating by many groups. Generally, the bandwidth of swept source for OCT is limited by the bandwidth of the gain devices, and the realization of wideband swept source has been desired to improve the axial resolution.

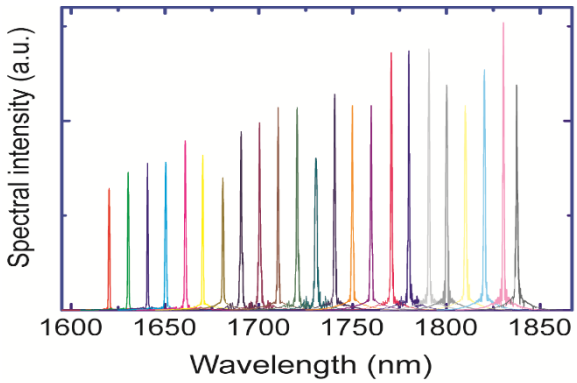

Fig. 6. Optical spectra of widely wavelength tunable narrow linewidth source by comb profiled fiber

We have been investigating widely wavelength tunable soliton pulse sources using fiber nonlinear effect [4]. Recently, we demonstrated spectral compression of the soliton pulses, and we demonstrated wideband, narrow-linewidth, rapid wavelength tunable pulse sources. Figure 6 shows the optical spectra of wideband wavelength tunable narrow linewidth source. Using the intensity modulator, we can tune the wavelength of the pulse shot by shot.

References

1. N. Nishizawa, *Opt. Fiber Technol.*, 2012, **18**, 394; *Jpn. J. Appl. Phys.*, 2014, **53**, 090101.
2. S. Ishida and N. Nishizawa, *Biomed. Opt. Express*, 2012, **3**, 282; *Biomed. Opt. Express*, 2012, **3**, 735.
3. H. Kawagoe, S. Ishida, N. Nishizawa, et al., *Biomed. Opt. Express*, 2014, **5**, 932.
4. N. Nishizawa, K. Takahashi, Y. Ozeki, and K. Itoh, *Opt. Express*, 2010, **18**, 11700.

EFFECTS OF LOW POWER LASER RADIATION ON PROTEINS, MITOCHONDRIA AND TISSUES

A.N. Osipov[1], E.A. Buravlev[1], T.V. Machneva[1], and **Yu.A. Vladimirov[1,2]**

[1] NI Pirogov Russian National Research Medical University, Moscow, Russia,
anosipov@yahoo.com
[2] MV Lomonosov Moscow State University, Moscow, Russia

Abstract. This study is based on the experimental approach that one of the major mechanisms of laser light physiological activity is due to the photolysis of NO-containing compounds and subsequent free NO release. In organism, the most common compounds that can release nitric oxide upon laser irradiation are nitrosyl hemoproteins and non-heme complexes. We present the experimental data that demonstrates that enzymatic activity of some proteins or mitochondrial respiration can be inhibited by nitric oxide and restored by low power laser irradiation. These effects of laser radiation can affect tissue microcirculation.

Effects on proteins

Hemoglobin and cytochrome c can effectively react with nitric oxide to produce corresponding nitrosyl complexes. These complexes are photosensitive and can undergo decomposition upon laser irradiation to release free nitric oxide. Nitrosyl complex production results in the inhibition of hemoglobin oxygen transport and cytochrome c electron transport. Decomposition of these complexes restores the protein function.

Effects on mitochondria

When liver mitochondria are subjected to nitric oxide or NO synthesis in tissues is activated by lipopolysaccharide injection, nitrosyl complexes of mitochondria electron transport proteins are produced. Formation of nitrosyl complexes inhibits mitochondria respiration in a concentration-dependent manner. Low power laser radiation can destroy nitrosyl complexes and restore mitochondrial respiration.

Effects on microcirculation

Decomposition of hemoglobin nitrosyl complexes upon radiation can be used to deliver nitric oxide to the tissues. We demonstrated that if erythrocytes, containing nitrosylated hemoglobin, are injected into the blood vessel and these vessels are subjected to irradiation than the enhancement of microcirculation is observed. This effect can facilitate skin flap engraftment upon transplantation.

Acknowledgements

These studies were supported by the Russian Foundation for Basic Research grants # 03-04-48891; 06-04-49296 and 11-04-01455

References

1. Yu. Vladimirov, G. Borisenko, N. Boriskina, K. Kazarinov, and A. Osipov, *J Photochem Photobiol B*, 2000, **59**(1-3), 115-122.
2. E.A. Buravlev, T.V. Zhidkova, Yu.A.Vladimirov, and A.N. Osipov, *Lasers Med Sci.*, 2013, **28**(3), 785-790.
3. E.A. Buravlev, T.V. Zhidkova, Yu.A.Vladimirov, and A.N. Osipov, *Lasers Med Sci.*, 2014, **29**(6), 1861-1866.
4. E.A. Buravlev, T.V. Zhidkova, A.N. Osipov, and Yu.A.Vladimirov, *Lasers Med Sci.*, 2015, **30**(1), 173-180.
5. R. Mittermayr, A. Osipov, C. Piskernik, S. Haindl, P. Dungel, C. Weber, Yu. Vladimirov, H. Redl, and A. Kozlov, *Mol Med.*, 2007, **13**(1-2), 22-29.

MICE EMBRYOS VIABILITY AND DEVELOPMENT RESEARCH AFTER LASER FEMTOSECOND TREATMENT

A.A. Osychenko[1], A.A. Zalesskij[1,5], A.A. Astafiev[1], A.M. Shakhov[1], A.S. Krivokharchenko, A.K. Shakhbazyan [1], A.V. Ryabova[3], and **V.A. Nadtochenko[1,2,4]**

[1] Semenov Institute of Chemical Physics, RAS, Russia, 119991, Moscow, Kosygin str., 4; alina.chemphys@gmail.com
[2] Institute of Problems of Chemical Physics, RAS, Russia, Chernogolovka, Moscow region,142432., Akademican Semenov, 1
[3] Prokhorov General Physics Institute, RAS, 119991, Moscow, Vavilov Str., 38
[4] MSU, Faculty of Chemistry, Russia,119991,Moscow,, 1-3 Leninskiye Gory
[5] Moscow Institute of Physics and Technology (State University), 141700, Dolgoprudny, 9 Institutskiy per., Moscow Region

Abstract. Effects of mice preimplantation embryo viability and development after laser femtosecond treatment with various pulse energies and pulse duration have been studied. It was shown that femtosecond laser treatment of 2 cell embryo does not sufficiently affect development to the blastocyst stage at low energies. Investigation of blastocyst cell number of treated and untreated embryos have shown that treated embryos has sufficiently lower cell number, even if they were not fused after exposure to laser beam. Also comparison of nucleus area in diploid and tetraploid blastocysts has demonstrated that tetraploid nucleuses are two time bigger then diploid ones.

Femtosecond (fs) laser nanosurgery is a novel method for manipulations with cellular organelles [1] [2] , individual cells [3], embryos [4, 5] and tissues [6]. Due to high light intensity of the focused fs pulse a nonlinear optical absorption is a dominant mechanism of interaction with a cell. Because cells contain at least 90% H_2O, water is commonly used for physical modelling of fs laser pulse and cell interaction. The goal of this research was to determine mechanism of fs laser interaction with living cells: embryos and oocytes.

After exposure of two cell embryos to laser beam, focused in a cellular contact field, 4 possible outcomes released:

1) No morphological changes occurs;
2) Blastomeres fused into a single cell;
3) One of two blastomeres destroyed;
4) Two blastomeres destroyed.

In experiments with germinal vesicle oocytes nucleolinus exposed to fs laser beam. In this case 2 possible outcomes released: oocyte did not undergo morphological changes or oocyte destroyed. After cultivation oocytes ejected 1-st polar body.

Biological features, such as polar body ejection, development dynamics and blastocyst cell number, are suggested for estimation of fs laser pulse effect on embryo or oocyte. We determined that no significant difference occurs between development of untreated and treated at low energies embryos to the blastocyst stage. But laser treatment affects blastocyst cell number and hatching ratio in treated groups. Polar body ejection ratio in treated and control oocytes does not significantly differ, but this result is discussible.

Variations of absorption coefficient in cellular material after exposure of cell to fs laser beam have been detected. This absorption is stipulated by nonlinear optical femtosecond laser exposure, resulting in photochemical reactions. This fact urges to revise existing conceptions concerning about laser nanosurgery mechanism using consequence of femtosecond laser pulses.

Acknowledgements

This work is supported by Russian Science Foundation grant 14-14-00856.

References

1. C. Tängemo, J. Colombelli, U. Haselmann, J.C. Simpson, C. Antony, E.H. Stelzer, R. Pepperkok, and E.G. Reynaud, "A novel laser nanosurgery approach supports de novo Golgi biogenesis in mammalian cells", *J Cell Sci*., 2011, **124**, 978-987.

2. N. Shen, Ch.B. Schaffer, Ph. LeDuc, E.M. Donald, and E. Ingber, "Ablation of cytoskeletal filaments and mitochondria in cells using a femtosecond laser nanoscissor", *Mech Chem Biosyst*, 2005, **2**(1), 17-25.
3. Ю.В. Барбашов, М.А. Березуцкая, Г.В. Максимов, А.Б. Рубин, О.М. Саркисов, В.А. Надточенко, "Нелинейно-оптическое воздействие фемтосекундного лазерного излучения ближнего ИК-диапазона на морфологию и структуру нервной клетки в поле оптической “ловушки”", *Химическая Физика*, 2012, **31**(6), 9-15.
4. А.К. Шахбазян, А.В. Карменян, А.С. Кривохарченко, Л.М. Чайлахян, "Использование лазера для получения реципиентных цитопластов при пересадке ядер у млекопитающих", *Доклады академии наук*, 2009, **428**(3), 1-4.
5. A. Krivokharchenko, O. Sarkisov, M. Bader, A. Chiou, and A. Shakhbazyan, "Laser Fusion of Mouse Embryonic Cells and Intra-Embryonic Fusion of Blastomeres without Affecting the Embryo Integrity", *PLOS One*, 2012, **7**(12), e50029.
6. N. Suhm, et al., "Ablation of neural tissue by short-pulsed lasers - A technical report", *Acta Neurochirurgica*, 1996, **138**(3), 346-349.

Invited

TWO-COLOR PICOSECOND LASER SOURCES FOR STIMULATED RAMAN SCATTERING MICROSCOPY

Ya. Ozeki

Department of Electrical Engineering and Information Systems, The University of Tokyo, Tokyo, Japan
ozeki@ee.t.u-tokyo.ac.jp

Abstract. Stimulated Raman scattering (SRS) microscopy is emerging as a powerful technique for fast, label-free biomedical imaging. In order to promote widespread use of this technique, it is important to develop functional and practical laser sources that can generate synchronized two-color picosecond pulses. This paper explains the principle of SRS microscopy, and introduces our recent development of fast wavelength-tunable picosecond lasers for high-speed SRS spectral imaging, fiber lasers with intensity noise cancelling capability, and novel laser sources.

Introduction

Raman imaging is recently attracting much attention because Raman scattering gives rich spectroscopic information of transparent molecules, and therefore enables label-free biomedical imaging based on chemical contrast. Previously, Raman imaging suffered from slow imaging speed, which is typically on the order of 1 pixel/s. Recent developments on coherent Raman imaging techniques [1] including coherent anti-Stokes Raman scattering (CARS) and stimulated Raman scattering (SRS) microscopies allow for label-free imaging at a much faster speed up to video rates (i.e. 30 frames/s), which correspond to a pixel rate of ~10 Mpixels/s. Nevertheless, CARS microscopy suffered from unwanted nonresonant background, which distorts the vibrational spectrum and complicates the image analysis. In contrast, SRS microscopy is advantageous because SRS is almost free from nonresonant background, and allows for quantitative visualization of molecules of interest. Furthermore, various kinds of multivariate analysis techniques can be straightforwardly applied to SRS spectral images, enhancing the chemical specificity in label-free imaging.

In order to promote widespread use of SRS microscopy, it is important to develop practical and functional laser sources suited for SRS microscopy. There are several requirements for laser pulse sources of SRS microscopy such as (i) two-color pulses typically at wavelengths of ~800 nm and ~1000 nm, (ii) picosecond pulse duration, (iii) low intensity noise for sensitive detection of SRS signal, (iv) fast wavelength tunability within milliseconds for high-speed spectral imaging, and (v) compactness and long-term stability from a practical point of view.

This paper introduces our recent development of fast wavelength-tunable picosecond lasers for high-speed SRS spectral imaging, fiber lasers with intensity noise cancelling capability for practical implementation of SRS microscopy, and novel laser sources.

SRS microscopy

Figure 1 schematically illustrates the principle of SRS microscopy. We use synchronized two-color laser pulses, which are called pump and Stokes. The Stokes laser beam is intensity-modulated beforehand. Then these pulses are focused on a sample. When the optical frequency difference matches the molecular vibrational resonance of molecules in the focal volume, SRS occurs. Through SRS, pump pulses are attenuated and Stokes pulses are amplified. As a result, the intensity modulation is transferred to the other beam. The transferred modulation is measured by the photodetection followed by the lock-in detection. SRS imaging is accomplished by scanning the laser beam with a beam scanner (not shown). The wavelength of Stokes pulses or pump pulses is also scanned to conduct spectral imaging.

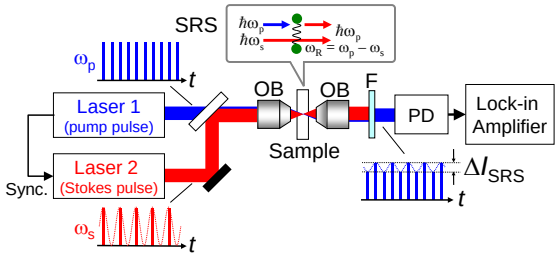

Fig. 1. Schematic of stimulated Raman scattering (SRS) microscopy. OB: objective lens. F: filter

Two-color, wavelength-tunable picosecond laser sources for SRS imaging

In order to fully utilize the fast imaging capability of SRS microscopy, we have recently developed high-speed SRS spectral microscopy [2] using a picosecond Ti:sapphire laser as a pump pulse source and a wavelength-tunable Stokes pulse source. The Stokes pulse source is based on the spectral filtering of broadband optical pulses generated by a passively mode-locked Yb fiber laser, followed by post amplification with Yb-fiber amplifiers [3]. The SRS spectral microscope allows video-rate SRS imaging with frame-by-frame wavenumber tunability of ~300 cm^{-1}, which can cover the entire CH-stretching region. After the image acquisition, spectral images can be processed by multivariate analysis based on principal component analysis and independent component analysis to produce multi-color images of tissue in a short period of time. We have succeeded in label-free imaging of several types of tissue samples [2, 4]. Furthermore, we recently developed real-time imaging and visualization system based on high-speed data acquisition hardware [5]. This system will be useful for rapid observation of unstained tissues in a wide field of view.

Fiber laser sources with intensity noise cancellation

Fiber lasers have several practical features such as compactness, long-term stability, and low cost. When fiber lasers are applied to SRS microscopy, however, intensity noise of fiber lasers should be mitigated. This is because the output power of typical fiber lasers is low, and therefore optical amplification is necessary. This leads to the onset of amplified spontaneous emission noise, which contributes to excess noise in lock-in detection of SRS signal. In optical measurement, balanced detection (BD) can be used to cancel the effect of the excess noise. In optical imaging, however, laser beams are raster-scanned, and therefore the beam intensity is not kept constant due to the scattering by samples. This makes it difficult to apply BD to SRS microscopy.

In order to cope with this, we demonstrated the collinear balanced detection (CBD) technique [6, 7]. In CBD, a pulse train is split into two, and they are combined with a delay difference in a delay-add-line. When the combined pulse train is photo-detected, the photocurrents of the pulse trains interfere with each other. As a result, the intensity noise is canceled at a specific frequency, which is determined by the delay difference. By using CBD, we have demonstrated SRS imaging with shot-noise-limited sensitivity based on synchronized Er- and Yb-fiber lasers.

Novel laser sources for SRS microscopy

Although we have developed practical fiber laser sources, further simplification of laser sources is under way. I'd like to introduce recent development of wavelength-tunable mode-locked fiber laser oscillator [8] and semiconductor-based laser source [9].

Acknowledgements

I'd like to acknowledge Prof. K. Itoh of Osaka University, Prof. N. Nishizawa of Nagoya University, Dr. Y. Otsuka, Dr. S. Satoh, and Dr. H. Hashimoto of Canon Inc., Prof. M. Sakamoto of Keio University, and Prof. H. Yokoyama of Tohoku University. This work was supported by JSPS KAKENHI Grant Numbers 25702026 and 25600116, Advanced Photon Science Alliance, and Inamori Foundation.

References

1. J.-X. Cheng and X.S. Xie, 'Coherent Raman scattering microscopy,' *CRC Press*, 2013.
2. Y. Ozeki, W. Umemura, Y. Otsuka, S. Satoh, H. Hashimoto, K. Sumimura, N. Nishizawa, K. Fukui, and K. Itoh, *Nature Photon*., 2012, **6**, 845-851.
3. Y. Ozeki, W. Umemura, K. Sumimura, N. Nishizawa, K. Fukui, and K. Itoh, *Opt. Lett*., 2012, **37**, 431-433.
4. S. Satoh, Y. Otsuka, Y. Ozeki, K. Itoh, A. Hashiguchi, K. Yamazaki, H. Hashimoto, and M. Sakamoto, *Pathology Int*., 2014, **64**, 518-526.
5. Y. Otsuka, K. Makara, S. Satoh, H. Hashimoto, and Y. Ozeki, *Analyst*, 2015, **140**, 2984-2987.
6. K. Nose, Y. Ozeki, T. Kishi, K. Sumimura, N. Nishizawa, K. Fukui, Y. Kanematsu, and K. Itoh, *Opt. Express*, 2012, **20**, 13958-13965.
7. K. Nose, T. Kishi, Y. Ozeki, Y. Kanematsu, H. Takata, K. Fukui, Y. Takai, and K. Itoh, *Jpn. J. Appl. Phys*., 2014, **53**, 052401.
8. Y. Ozeki and D. Tashiro, *CLEO*, 2015, paper STh1L.3.
9. K. Tokunaga, Y. -C. Fang, Y. Kusama, H. Yokoyama, and Y. Ozeki, *CLEO-PR* 2015 (accepted).

Invited

INTERACTION OF RED BLOOD CELLS IN VARIOUS ENVIRONMENTS ASSESSED WITH LASER TWEEZERS

A.V. Priezzhev[1,2], Kisung Lee[1], A.V. Danilina[1], and **A.V. Potkin[1]**

[1] Physics Department and [2] International Laser Center of Lomonosov Moscow State University
Moscow, Russia, avp2@mail.ru

Abstract. The potentialities of laser tweezers (LT) to measure the parameters of interaction of red blood cells (RBCs) related to one of their intrinsic microrheologic properties, spontaneous and reversible aggregation, in various environments and in conditions of norm and pathologic alterations are explored. Our measurements clearly show that the mechanics of RBC interaction in blood plasma and plasma proteins solutions are more likely consistent with the moving cross-bridge model. We also demonstrate that the spontaneous aggregation rate, aggregation force and disaggregation force measurable with LT are informative parameters that can be used as optical bio-markers of socially important diseases.

Introduction and motivation

Aggregation of RBC is one of important factors affecting hemorheology and microcirculation. During the last few decades it was studied intensively as a promising indicator of the hemorheological status of the organism. In the majority of cases, the mechanics of RBC interaction were studied in model solutions of neutral macromolecules, e.g. dextrans. In the plasma or plasma protein environments, they had not been studied sufficiently. Therefore, we focused our work on elucidating the mechanisms of RBC interaction using the LT technique. We measured the interaction forces between pairs of RBCs *in vitro* in solutions of fibrinogen, fibrinogen and albumin, globulins, and autologous plasma. The interaction force was determined as the minimum force required to fully disaggregate a pair of interacting RBCs (disaggregation force – DF).

Materials and methods

Blood was drawn from human individuals (healthy ones and ones suffering various diseases) and/or laboratory animals - white rats (healthy controls and those with experimentally induces diabetes). The measurements were performed using a home made set-up comprising two independent laser tweezers based on single-mode infrared Nd:YAG laser (1064 nm, 200 mW), water-immersion objective (100x, NA=1.00) [1]. Heating of the trapped cells was negligibly small due to the fact that the lasers wavelength was in the transparency window of blood and water, and there is an efficient heat dissipation due to the suspending medium. The average time of contact of the laser beam with the power not exceeding 30 mW with a cell in our experiments usually did not last longer than 3–5 minutes.

Sample preparation and measurement protocols

All measurements were conducted *in vitro* at room temperature with EDTA-stabilized blood samples freshly blood within two to four hours after drawing. Special disposable couvettes holding 50 μl of highly diluted suspension of RBC were used in each experiment.

Our experimental procedure consisted of two steps. First, two single RBCs were captured by two independent optical traps and attached to each other with carefully controlled interaction area. After a certain time one of the cells was slowly pulled from the other with the known (increasing step-by-step) pulling force until disaggregation. In this way, we measured the DF dependence on the interaction time and area.

The experiments were carried out with the doublets of RBCs. We measured several parameters characterizing the interaction of individual cells forming a doublet. The first group of measured parameters relates to spontaneous aggregation, as a process of spontaneous of the individual cells onto each other after forming a local contact. The second group includes the parameters of RBC disaggregation, as a process of LT-forced separation of RBCs in a doublet.

The measurement of each parameter was conducted with 10 to 20 pairs of RBCs for each blood sample. The experimental results were averaged over the RBCs of several donors, and hence, over several tens of pairs of cells. The main contribution to the statistical scatter in the results was made by the differences in the properties of individual cells.

Results

Using the LT technique, a number of parameters characterizing the interaction of RBC at their aggregation in model solutions of proteins and of neutral macromolecules, as well as in plasma and serum, was measured. It was shown for the first time that in the presence of solely fibrinogen the RBC aggregation does not occur spontaneously. However, the strength and the rate of spontaneous aggregation in plasma is significantly higher than in serum. This is due to the absence of fibrinogen in serum, this fact showing the importance of fibrinogen during spontaneous aggregation. It was also shown that in protein solutions, even in the absence of spontaneous aggregation, the RBCs can interact strongly with one another. By measuring the forces disaggregating the RBC doublets, we show the differences in the dynamics of RBC disaggregation in solutions of neutral macromolecules in comparison to those in plasma proteins solutions, blood plasma and serum. To describe the interaction of RBC in protein solutions, plasma and serum we proposed to use the model of "moving bridges" previously proposed by other authors to describe the interaction of white blood cells.

Conclusion

Though the LT technique that we used is adequate for studying the microrheologic properties of RBCs from basic science to clinical application perspectives, its further development may raise the efficiency of the measurements and information content of the obtained data. We propose the directions of further research in this relation.

Acknowledgements

The research was partially supported by the Russian Science Foundation grant № 14-15-00602.

References

1. K. Lee, M. Kinnunen, A.E. Lugovtsov, A.V. Priezzhev, and A.B. Karmenyan, *Optoelectronics, Instrumentation and Data Processing*, 2014, **50**(5), 1–6.

APPLICATIONS OF FEMTOSECOND LASER ABLATION IN NEUROSURGERY

C.B. Schaffer

Department of Biomedical Engineering, Cornell University, Ithaca, NY, USA, cs385@cornell.edu

Abstract. When tightly focused into tissue, short pulse lasers have the unique capability to cause micrometer-scale disruption that is located beneath the surface of the tissue, with minimal collateral damage to surrounding structures. Here we describe the use of this technique to cut neural connections in targeted cortical layers as a means to inhibit the propagation of focally-initiated epileptic seizures in rats. Current therapies for focal epilepsy involve highly-invasive resection of the seizure focus and cause significant side effects. By comparison, the approach proposed here would preserve more cortical function while still inhibiting seizures.

We use tightly-focused, femtosecond duration, infrared wavelength laser pulses as a laser scalpel to sever neural connections beneath the surface of the brain around an epileptic focus to prevent seizure propagation in animal models of focal epilepsy. Near infrared light is not normally strongly absorbed by tissue. However, when a femtosecond duration, near infrared laser pulse is tightly focused inside a tissue the laser intensity becomes so high that the material in the focus is literally ripped apart due to energy deposition by highly nonlinear optical absorption. Because this interaction is highly nonlinear, its effects can be confined to the micrometer-sized focal region that is located in the bulk of the tissue. Essentially, the laser provides a very precise scalpel that can ablate material and cut inside a tissue without affecting the surface. In previous work, we showed that 800-nm, 50-fs pulses focused at a numerical aperture of 1.0 could produce cuts with a size of ~10 μm more than 1 mm beneath the surface of rat cortical tissue [1]. With longer wavelength sources, where tissue scattering is reduced, even greater penetration should be possible; 1.3 μm light should enable cuts as deep as ~4 mm into tissue.

Focal neocortical epilepsy is a largely intractable medical problem, with most cases responding poorly to anti-convulsive medications and current surgical treatment options limited because of the likelihood of neurological deficits. Because much information processing is vertically organized in cortex, while seizure propagation occurs primarily through lateral connections, a series of incisions could prevent the spread of seizures but largely preserve function [2]. Such cuts could also reduce seizure incidence by separating aberrant activity in different areas of cortex and thus preventing coalescence of microseizures. The incisions must not cut the blood vessels on the brain surface and should sever connections in as few cortical layers as possible to achieve seizure control with minimal neurological impact. Current implementations of this idea utilize a hook-shaped mechanical tool that causes significant collateral damage. Tightly-focused femtosecond laser pulses may provide a unique tool to produce incisions that could block seizure propagation while minimally damaging cortical tissue.

To test this concept, we produced a “box” cut in the cortex of anesthetized rats that was 750 μm in extent laterally and extended from 150 μm to 800 μm beneath the cortical surface. This cut essentially extends through Layer II/III of the cortex, which previous data suggested was critical for seizure propagation [3]. We then injected the potassium channel blocker, 4-aminopyridine (15 mM, 0.5 μl) inside the box using a micropipette and recorded local field potential (LFP) inside and outside the box. We found that a single box cut reduced the incidence of seizures by about 50% as compared to animals with sham cuts. Furthermore, the cuts blocked the propagation of seizures that did initiate in about 40% of cases. Those seizures which did successfully propagate outside of the box were reduced in amplitude by ~30% and their propagation was delayed by several seconds. The cuts did not inhibit the ability of the tissue inside the box to respond to a peripheral stimulus, although the amplitude of the LFP response was attenuated by ~30%.

Overall, these data suggest that femtosecond laser cuts targeted to cortical layers important for seizure propagation can inhibit initiation and propagation of seizures while minimally affecting normal function. Future work will explore additional geometries of cuts to increase seizure inhibition and test the efficacy of this approach in chronic animal models of epilepsy.

This work was supported by the National Institute of Neurological Disorders and Stroke (NS078644).

References

1. Nguyen, J., et al., *Sub-surface, micrometer-scale incisions produced in rodent cortex using tightly-focused femtosecond laser pulses*. Lasers in Surgery and Medicine, 2011. **43**: p. 382-391.
2. Morrell, F., *Mutliple subpial transections for the surgical treatment of focal epilepsy*. Electroencephalogr. Clin. Neurophysiol., 1973. **34**: p. 714.
3. Telfian, A.E. and B.W. Connors, *Layer-specific pathways for the horizontal propagation of epileptiorm discharges in neocortex*. Epilepsia, 1998. **39**(7): p. 700-708.

NOVEL LASER APPLICATIONS IN OPHTHALMOLOGY FOR NON-ABLATIVE CORRECTION OF EYE REFRACTION AND NORMALIZATION OF INTRAOCULAR PRESSURE

E. Sobol[1], **O. Baum**[1], **A. Bolshunov**[2], **V. Siplivy**[2], **O. Chomchik**[2], **A. Omelchenko**[1], and **S. Avetisov**[2]

[1]Institute on laser and information technologies, Russian Academy of Sciences, Troitsk, Russia
esobol@rambler.ru
[2]Institute on eye diseases, Russian academy of medical sciences, Moscow, Russia

Abstract. We present a novel approach for innovating applications of biophotonics in ophthalmology, based on thermo-mechanical effect of laser radiation, for normalization of the intraocular pressure in glaucomatous eyes and correction of the eye refraction due to non-destructive cornea reshaping. The advantages of novel technologies are provided by safety and efficacy of laser treatment of the eye tissues and structures.

Cornea is a rigid tissue with high internal mechanical stress. It is shown that cornea deformation followed by laser-induced stress relaxation allows changing cornea shape without its destruction [1]. Experiments on cornea reshaping were performed in vitro in the eyes of pigs, rabbits, cadavers, and in-vivo in rabbit eyes using an Erbuim glass fiber laser of 1.56 microns in wavelength. Thermo-mechanical properties of sclera and cornea during laser heating were studied with an indenter test and using thermo mechanical analyzer. The alterations in eye refraction were measured with various optical techniques including optical coherent tomography, confocal microscopy and shlieren visualization [2]. Histological technique was used to study possible alterations in tissues structure. Optimal laser settings were established allowing obtain refraction correction without visible damage and denaturation of the eye tissues. The maximal change of eye refraction obtained was of 6 diopters [2, 3]. The stability of the rabbit eye refraction was established during at least 6 months. Histological analysis did not revile any alterations in cornea structure [3]. Measurements of optical properties of cornea before and after laser treatment did not show any changes in cornea transparency [4].

A novel and innovative technique for intraocular pressure (IOP) normalization is based on enhancing role of sclera outflow. The technique creates permeable pathways for water transport as a result of formation of nano- and micro-pores under nondestructive thermo-mechanical effect of pulsed laser irradiation [5]. The results of in-vivo experiments in rabbit eye sclera have shown that laser irradiation leads to substantial increase of water permeability trough sclera. Pre-clinical trials performed for 49 eyes of 49 patients with open angle glaucoma have demonstrated stable normalization of the IOP with one year follow-up observations [6]. The advantages and prospects of novel technique for glaucoma treatment have been demonstrated.

Acknowledgements

The work is supported by the Russian Foundation for Basic Research.

References

1. E. Sobol, A. Bolshunov, N. Vorobieva, et al., *Quantum Electronics*, 2002, **32**(10), 909-912.
2. E. Sobol, O. Baum, A. Bolshunov, et al., *Laser Physics*, 2006, **16**(5), 735-740.
3. A. Bolshunov, E. Sobol, S. Avetisov, et al., *Acta Ophthalmologica*, 2011, s.**89**: 0. doi: 10.1111/j.1755-3768.2011.2172.
4. A. Yuzhakov, A. Sviridov, O. Baum, et al., *Journal of Biomedical Optics*, 2013, **18**(5), 1-6.
5. O. Baum, E. Sobol, A. Bolshunov, et al., *Lasers in Surgery & Medicine*, 2014, **46** (1), 46-53.
6. S. Avetisov, A. Bolshunov, O. Chomchik, et al., *Glaucoma*, 2015, **14**(3).

PILOT EXPERIMENTS ON LASER DRIVEN PROTON TREATMENT OF CANCER CELLS AT PEARL

A. Soloviev

Institute of Applied Physics Russian Academy of Sciences, Nizhny Novgorod, Russia

Pilot experiments on biological objects treatment by laser-driven protons have been conducted at the laser-plasma facility PEARL (IAP RAS, Nizhny Novgorod). The main goals of the experiments are to test the hardware module transferring laser-driven protons to a biological tissue and to study the biological effectiveness of the laser-driven proton beams for cancer treatment. It is shown that a laser-driven proton source based on the TNSA mechanism of particle acceleration, using 5 J / 70 fs laser pulse focused on a 10 μm aluminum target, can be used to significantly affect biological cells. The object of investigation is human cervical carcinoma cell culture (Hela). The vitality of cells has been estimated by a standard MTT-test. Indeed, destruction of 50% of cancer cells has been observed with 0.5 Gy of the absorbed radiation dose. Possible ways of improvement of the laser-based proton source from the point of view of proton energy separation and proton beam focusing are discussed. The results are expected to be utilized for applications connected with laser-driven hadron therapy of cancer.

NOVEL BIODEGRADABLE POLYMERS FOR LASER STEREOLITHOGRAPHY TECHNIQUE

P.S. Timashev, A.V. Koroleva, B.N. Chichkov, and **V.N. Bagratashvili**

Institute of Laser and Information Technologies, 142191, Troitsk, Moscow, Russia
timashev.peter@gmail.com

Abstract. It is known that the main problem of laser additive technologies introduction to clinical practice and utilization of 3D structures for the certain injuries treatment (restoration of functional activity of nerves, regeneration of bone, urethroplasty) is the lack of commercially available biodegradable polymers. This work is focused on novel biodegradable materials synthesis followed by 3D structuring with laser stereolithography and microstereolithography and in vivo and in vitro scaffolds testing.

Laser stereolithography is an effective method 3D structures creation a with sizes ranging from hundreds of nanometers to tens of centimeters. The method consists in the initiation of local spatial cross-linking between the reactive units of macromolecules by UV laser radiation. Like most of additive technologies, laser stereolithography allows to create the structure of a given architectonics based on a computer model that can be developed using special computer software, and data obtained by the analysis of the spatial structure of the object in vivo (for example by MRI tissue defects when creating a suitable polymeric implants) [1]. Ability to use data on the structure of the defect obtained directly from the patient, allow the utilize laser additive manufacturing methods to solve some cases in the field of biomedical engineering, for example for the manufacture of custom matrices for cranioplasty [2] or support scaffolds for complex abdominal operations [3]. Recently, cells support matrix (scaffolds) for tissue engineering with novel biocompatible materials has produsedby laser microstereolithography [4]. In particular, it has been shown that one of the most promising polymers for scaffolds structuring are modified natural polysaccharides [5] and aliphatic polyethers [6]. With all the obvious advantages of additive manufacturing approach, there are only few papers focused on novel biodegradable polymer synthesis. The aim of the present work is to develop new photopolymerizable materials based on natural polysaccharides and aliphatic polyesters with a wide variability of properties (mechanical, hydrophilic, and others.) As the initial material we used natural polysaccharide – chitosan modified under shear conditions grafted unsaturated low molecular weight compounds. The resulting material had 10–15 percent degree of substitution and could be structured in the presence of water-soluble photoinitiators with laser stereolithography technique. As another photopolymerizable matrix starlike oligomers were synthesized based on polylactide and e-caprolactone. The strategy of synthesis allowed to change characteristics molecular weight rays allowing controlled changes in the mechanical properties of matrices as well as their rate of biodegradation. Applied oligomers with masses of 200 to 1500 D were synthesised, structuring was performed in presence of 2% by weight Michler's ketone as a photoinitiator. All the resulting structures were tested for cytotoxicity.

Acknowledgements

This work was supported by the Russian Foundation for Basic Research Grant no. 14-29-07234-ofi_m and Russian Science Foundation Grant no. 14-13-01422.

References

1. N.J. Mankovich, D. Samson, W. Pratt, D. Lew, and J. Beumer, *Otolaryngol. Clin. North Am.*, 1994, **27**(5), 875-882.
2. P.S. D'Urso, W.J. Earwaker, T.M. Barker, M.J. Redmond, R.G. Thompson, and D.J. Effeney, *Br. J. Plast. Surg.*, 2000, **53**(3), 200-206.
3. D.P. Sarment, P. Sukovic, and N. Clinthorne, *Int. J. Oral Maxillofac. Implants*, 2003, **18**(4), 571-574.
4. A. Koroleva, A. Deiwick, A. Nguyen, S. Schlie-Wolter, R. Narayan, P. Timashev, V. Popov, V. Bagratashvili, and B. Chichkov, *Plos One*, 2015 in press.
5. A. Koroleva, O. Kufelt, S. Schlie-Wolter, U. Hinze, and B. Chichkov, *Biomed. Tech.*, 2013, **5**(58), 399-410.
6. A. Koroleva, A.A. Gill, I. Ortega, J.W. Haycock, S. Schlie, S.D. Gittard, B.N. Chichkov, and F. Claeyssens, *Biofabrication*, 2012, **4**, 025005.

Invited

LASERS AND BIOSCIENCE IN JAPAN

Ken-ichi Ueda

Institute for Laser Science, University of Electro-Communications, Japan

Biomedical applications of laser technology have been known for quite a time already. Some of them have been developed well and commercialized in this field, but many of them are not developed sufficiently even today. I will try to discuss what is the baseline to find the new channel of bio and medial application of laser technology.

MULTIFREQUENCY LASER SPECTROSCOPY OF BIOLOGICAL TISSUES ODORS

V.L. Vaks[1,2], **M.B. Chernyaeva**[1,2], **E.G. Domracheva**[1,2], and **S.I. Pripolzin**[1,2]

[1] Institute for Physics of Microstructures RAS, Nizhny Novgorod, Russia, vax@ipmras.ru
[2] Lobachevsky State University, Nizhny Novgorod, Russia

Abstract. Our paper is devoted to the combined MIR-THz spectrometer that increases the number of gases to be identified and the reliability of the detection by confirming the signature in both THz and MIR ranges. The radiation sources based on harmonics generator and quantum cascade lasers and unique receiver block have been developed. The fresh meat and fish odor composition under study includes organic compounds and amino acids, which vanish during natural decay, that is characterized by appearance of sulfur and nitrogen compounds. The advantages of the combined MIR-THz spectrometer for analysis of the biological tissues odors have been demonstrated.

Introduction

The important concern of the growing food industry involves control and monitoring of the product's quality that stimulates development and optimization of instrumental methods. One of the promising techniques for rapid, non-destructive analysis involves examination of the food's smell that is e-nose technology. This examination is considerably complicated by a need to analyze a multicomponent gas mixture that requires reliable detection, discrimination and quantification of many volatile compounds.

The combined IR-THz gas analyzer

Development of a combined IR-THz gas analyzer increases the number of gases that can be identified and the reliability of the detection by confirming the signature in both THz and MIR ranges. The subTHz, THz and MIR radiation sources of the spectrometer based on solid state harmonics generator and quantum cascade lasers (QCL) have been developed. The subTHz radiation source has been developed on the solid state harmonics generator. It has a number of advantages comparing with other well-known microwave generators. For THz and MIR ranges the QCLs are used. They have a high output power and can generate radiation in pulse and continuous modes together with fast tuning of frequency. Detection of the radiation in all three frequency ranges (subTHz, THz and MIR) are realized by the unique receiver block based on quantum semiconductor superlattices.

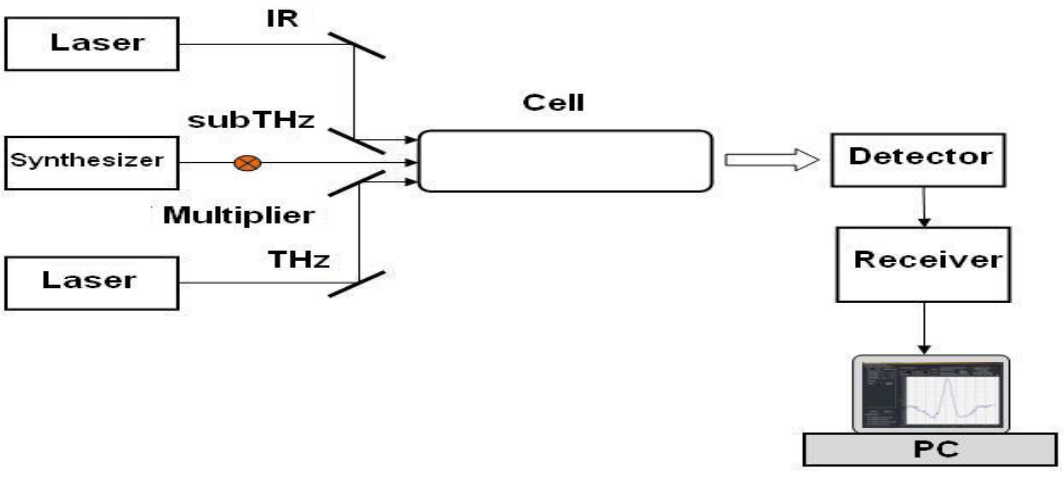

Fig. 1. The scheme of subTHz-THz_MIR spectrometer

Experimental results

We have studied odors composition of fresh meat (veal, chicken), fish (salmon, trout) and their vapors during natural decay. The sample preparation was the same for meat and fish. Before measurements the tissue sample was cut to pieces and dried in a vacuum cell to remove the water. The spectroscopic analysis was done with the sample at room temperature and heated up to 100 - 150°C. The

studies started on the day of meat (fish) purchase and continued the following days up to appearance of the new volatile compounds, signaling of the sample natural decay. Between measurements the tissues were kept in a refrigerator at +4°C. The results demonstrate that the fresh meat odor composition includes ethyl formate, diethyl ether, alanine and glycine (fig. 2, 3), which vanish during natural decay. The later is characterized, first of all, by appearance of sulfur-containing substances (H_2S, SO_2) (fig. 4). Then decay is followed by emission of ammonia (fig. 5) and organic molecules (phormamid, ethylamine). The vapor composition of the spoiled fish contains propylene glycol, urethane, hydrogen sulphide, sulfur dioxide and nitriles.

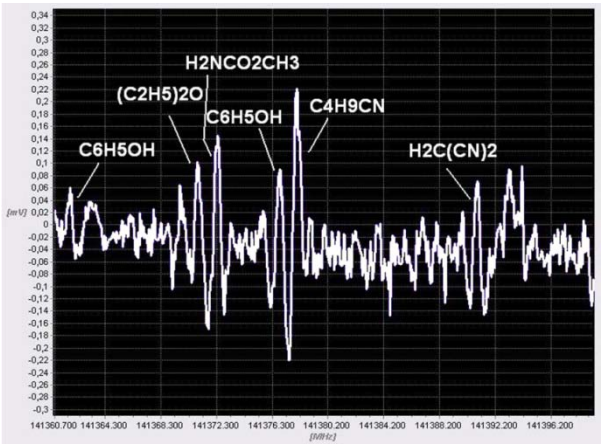

Fig. 2. The record of absorption spectrum near 141 GHz of the veal sample odor

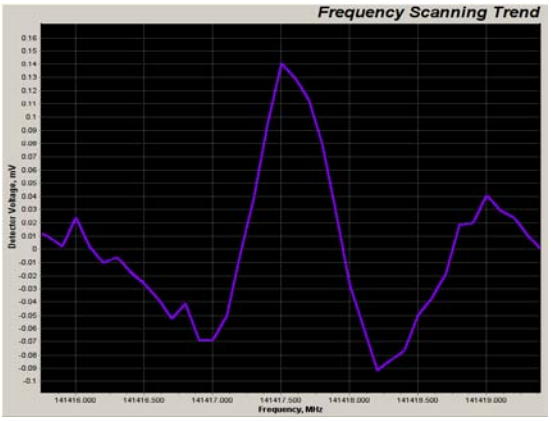

Fig. 3. The record of absorption line of alanine at the frequency of 141.417 GHz in the odor of sample of fish

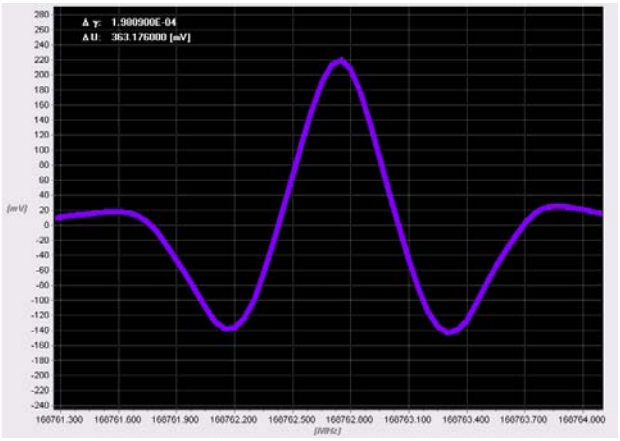

Fig. 4. The record of absorption line of H_2S at the frequency of 168.762 GHz in the odor of sample of veal during natural decay

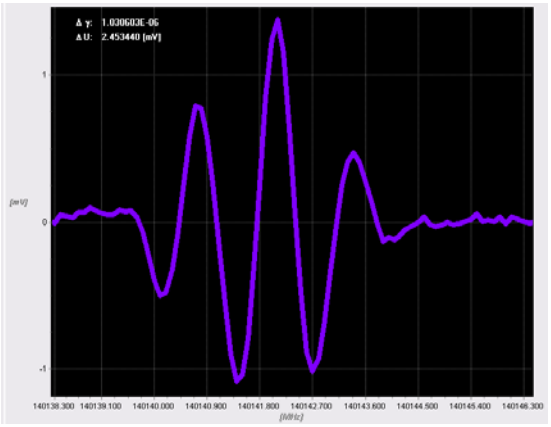

Fig. 5. The record of absorption line of NH3 at the frequency of 140,142 GHz in the odor of sample of veal during natural decay

Conclusion

The preliminary investigations of biomarkers in three frequency ranges have demonstrated the advantages of the combined MIR-THz spectrometer for analysis of the composition for multicomponent gas mixtures, including biological tissues odors.

Acknowledgements

The authors acknowledge support from The grant of the Government of the Russian Federation № 11.G34.31.0066, Program of Presidium RAS "Modern problems of radiophysics", TeraDec 047.018.005, NATO.EAP.SFPP 9840.

Invited

ALL-OPTICAL, LOW DIVERGENCE THOMSON RADIATION SOURCE VIA LASER PLASMA ACCELERATOR

P.A. Walker[1,2] and **F. Grüner** [1,2]

[1] Center for Free-Electron Laser Science, Hamburg, Germany, andreas.walker@desy.de
[2] Department of Experimental Physics, University of Hamburg, Germany

Abstract. The field of medical X-ray imaging uses to date conventional X-ray tubes and, in some places, experimental studies performed at large-scale synchrotron radiation facilities. The latter provide X-ray beams with unprecedented quality such as monochromaticity and ultra-low beam divergence. In order to miniaturize such brilliant X-ray sources, a new approach is undertaken for utilizing so-called laser-plasma accelerators and Thomson backscattering. The physics of laser plasma acceleration will be discussed along site an overview of experimental results within the field with a detailed description of a low divergence, brilliant, and compact X-ray source based on these plasma accelerators.

Accelerators have found applications within the fields of physics right after their discovery. For example the Large Hadron Collider (LHC) situated on the border of Switzerland and France provides an extraordinary tool with which to discover new science. While the LHC might have been the most visible accelerator in recent years, other accelerators that are smaller and more numerously available, provide a diverse community of medical, biological, chemical and physical scientists with the tools to probe materials, study life, and treat patients. Such accelerators allow scientists to advance knowledge, probe theories and engineer new devices. Synchrotrons in which electrons are accelerated, stored in large circular rings, and their radiation harnessed to irradiate matter are one example of such accelerators. Free-electron lasers, a more recent invention, are another example in which radiation is generated via undulating electrons at the end of linear accelerators.

All currently available accelerators within user facilities are based on conventional radio- frequency acceleration, meaning that charged particles are accelerated in the electric fields established between conducting electrodes or excited in an electromagnetic cavity. Conventional accelerators are built of materials which can sustain fields of order 50 MV/m before electrical break down occurs and, therefore, conventional accelerators have to be long to create high energy particle beams. In contrast, plasma accelerators use fields within a plasma to accelerate particles. Since in a plasma the atoms or molecules are already ionised, these accelerators are not subject to electrical breakdown limits that affect conventional accelerators. Hence the accelerating field developed in a plasma accelerator can be three orders of magnitude larger than in a radio-frequency accelerator, and as a consequence, kilometre scale machines can, in principle, be reduced to the metre scale. Therefore, plasma based accelerators present a great step forward in creating new, cheaper and much shorter accelerators for science. Figure 1 shows both a conventional and plasma accelerator.

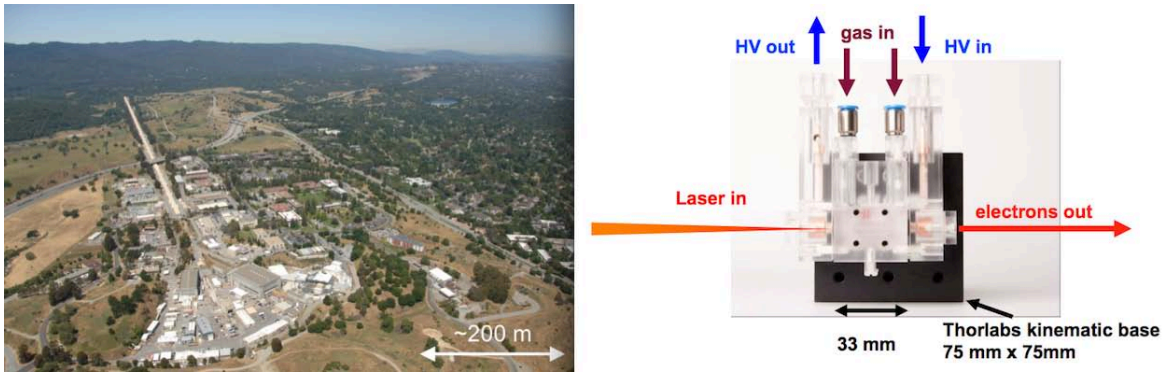

Fig. 1. (*Left*) Photograph of the SLAC National Accelerator Laboratory which operates a two-mile linear conventional accelerator, the housing of which can be identified by its linear, white roof. Photo courtesy of SLAC Linear Accelerator Laboratory. (*Right*) A photograph of a capillary discharge waveguide, a plasma accelerator of 33 mm length

The potential of plasma waves for particle acceleration was first recognized by Tajima and Dawson in 1979 [1]. The longitudinal plasma waves excited by intense laser pulses are well suited for accelerating charged particles to relativistic energies, because they also propagate with speed near the speed

of light and can stay in phase with such high-energy particles. In early work on laser-driven plasma accelerators performed in the 1990s, the generated electron beams had a very broad energy spectrum, but in 2004 several groups reported the generation of beams with quasi-monoenergetic energy spectra in the 100–200 MeV range [2–4]. In 2006 the energy of laser-accelerated electron beams was increased to 1 GeV by channelling the driving laser pulse in the plasma channel formed in a capillary discharge waveguide [5].

Further progess was made over the last ten years to increase the energy and decrease the divergence and emittance of the electron beams to create radiation from the plasma accelerated beams. For example, soft X-rays were produced from a plasma source in 2008 and 2009 [6, 7]. More recently several authors have presented Thomson scattering radiation with up to 18 MeV photon energies [8–12].

In this talk the physics of laser plasma acceleration will be discussed and an overview of experimental results up to now will be given. Special attention is given to radiation sources from plasma accelerators. A new design for creating low divergence, brilliant, and compact X-ray sources based on these plasma accelerators is presented.

Acknowledgements

These efforts are being undertaken within the LAOLA collaboration between the University of Hamburg and DESY.

References

1. T. Tajima *et al.,* "Laser electron-accelerator", *Phys. Rev. Lett.*, 1979, **43**(4), 267– 270; ISSN 0031-9007.
2. S.P.D. Mangles *et al.,* "Monoenergetic beams of relativistic electrons from intense laser–plasma interactions", *Nature,* 2004, **431**, 535-8.
3. J. Faure *et al.,* "A laser–plasma accelerator producing monoenergetic electron beams", *Nature,* 2004, **431**, 541-4.
4. C.G.R. Geddes *et al.,* "High-quality electron beams from a laser wakefield accelerator using plasma-channel guiding", *Nature,* 2004, **431**, 538-41.
5. W.P. Leemans *et al.,"* GeV electron beams from a centimetre-scale accelerator", *Nature Phys.,* 2006, **2**, 696-9.
6. H.P. Schlenvoigt *et al.,* "A compact synchrotron radiation source driven by a laser- plasma wakefield accelerator", *Nat. Phys.,* 2008, **4**, 130-133.
7. M. Fuchs, *et al.,* "Laser-driven soft-X-ray undulator source", *Nat. Phys.,* 2009, **5**, 826-829.
8. K.Ta Phuoc *et al.,* "All-optical Compton gamma-ray source", *Nature Photonics,* 2012, **6**, 308-311.
9. S. Chen *et al.,* "MeV-Energy X Rays from Inverse Compton Scattering with Laser-Wakefield Accelerated Electrons", *Phys. Rev. Lett.*, 2013, **110**, 155003.
10. N. D. Powers *et al.,* "Quasi-monoenergetic and tunable X-rays from a laser-driven Compton light source", *Nature Photonics*, 2014, **8**, 28-31.
11. C. Liu *et al.,* "Generation of 9 MeV x-rays by all-laser-driven Compton scattering with second-harmonic laser light", *Optics letters*, 2014, **39**, 14.
12. G. Sarri *et al.,* "Ultrahigh Brilliance Multi-MeV x-Ray Beams from Nonlinear Relativistic Thomson Scattering", *Phys. Rev. Lett.*, 2014, **113**, 224801.

Invited

ACCELERATING LIGHT SHEET MICROSCOPY

Z. Yang[1], **M. Prokopas**[1], **J. Nylk**[1,2], **C. Coll-Lladó**, **F.J. Gunn-Moore**[2], **D.E.K. Ferrier**[3], **T. Vettenburg**[1], and **K. Dholakia**[1]

[1] SUPA, School of Physics and Astronomy, University of St Andrews, St Andrews, UK, zy6@st-andrews.ac.uk
[2] Medical and Biological Sciences Building, School of Biology, University of St Andrews, St Andrews, UK
[3] The Scottish Oceans Institute, School of Biology, University of St Andrews, St Andrews, UK

Abstract. Light sheet fluorescent microscopy has gained its popularity in the biomedical applications in the recent years. The thickness of illumination light sheet in the microscope affects the axial resolution. However there is a strong compromise between this and the usable field of view for conventional Gaussian illumination. Here we demonstrate a low cost modification on conventional light sheet system to achieve propagation-invariant Airy beam illumination to largely extend the field of view. This brings wide field light sheet imaging to a boarder range of applications.

The development in laser and computer technology in the last decades enabled the re-invention of light sheet fluorescent microscopy (LSFM). LSFM uses a thin sheet of light to illuminate the sample, whilst the fluorescent signal is taken perpendicular to the illuminated plane. This simple configuration brings several advantages compared to conventional microscopies. Firstly, only illuminated plane in the sample produces fluorescent signal. This eliminates the out-of-focus signal, and hence improves the contrast of the image. Secondly, illumination and detection in LSFM are independent. A low magnification detection axis can be used to achieve large field of view (FOV), whilst still obtain good axial resolution due to the optical sectioning ability from the light sheet illumination. Thirdly, the photon efficiency in this configuration is much higher than other conventional microscopy, for example in epi-fluorescent microscopy or confocal fluorescent microscopy. This minimum the photo-blenching and photo-damaging brought to the specimens. In addition, as the whole plane to be imaged is illuminated simultaneously, the imaging speed is dramatically enhanced compare to laser scanning microscopies.

The axial resolution in LSFM is determined by the thickness of the illumination light sheet and the numerical aperture (NA) of detection objective. When using a low NA detection objective, i.e. with long depth of focus, the axial resolution is totally determined by the former. However, when the illumination beam is tightly focused to achieve thin light sheet, here is a trade-off on the shortened useable field of view, in which the thickness of the light sheet remains relatively constant.

Recently, there is literature demonstrating the use of propagation-invariant Bessel beam [1] or Airy beam [2] to largely extend the field of view in LSFM compared to conventional Gaussian beam. Compared to Gaussian beams, propagation-invariant beams maintain the beam profile in a much larger distance, hence creating a longer usable FOV. In addition, Bessel and Airy beams hold so called “self-healing” property, which means they are not sensitive to the obstacle on the illumination path. In particular, it has been demonstrated the advantage of using Airy light sheet over either Gaussian or Bessel beams in light sheet imaging, in terms of both FOV and axial resolution under same NA [2]. In addition, the generation of Bessel beam illumination creates transverse ring structures in the beam which degrade the quality of the image, whilst the side lobes in Airy beam illumination contribute positively to the imaging process.

An Airy beam can be generated through the Fourier transformation of a cubic phase imposed upon an incident Gaussian beam [3]. This phase modulation can be achieved with devices such as liquid crystal spatial light modulator (LC-SLM), or customized cubic phase mask. Both of them are expensive and not readily available. We have demonstrated using a tilted optical lens to intentionally introduce optical coma aberration to create Airy light sheet [4]. Simulation in Zemax showed that tilting the cylindrical lens allowed a controllable amount of cubic phase modulation in order to generate the Airy light sheet, whilst the additional tilt and defocus are readily compensated for by appropriate use of relay optics. Based on an open-access platform openSPIM, this experimental implementation of Airy light- sheet system is able to demonstrate the advantages of beam-shaping techniques for advanced light sheet microscopy.

Acknowledgements

We thank the UK Engineering and Physical Sciences Research Council (EPSRC) (EP/J01771X/1) and the 'BRAINS' 600th Anniversary appeal for funding.

References

1. T.A. Planchon, L. Gao, D.E. Milkie, M.W. Davidson, J.A. Galbraith, C.G. Galbraith, and E. Betzig, *Nat. Methods*, 2011, **8**(5), 417–423.
2. T. Vettenburg, H.I.C. Dalgarno, J. Nylk, C. Coll-Lladó, D.E.K. Ferrier, T. Cižmár, F.J. Gunn-Moore, and K. Dholakia, *Nat. Methods*, 2014, **11**(5), 541–544.
3. G. a Siviloglou and D.N. Christodoulides, *Opt. Lett.*, 2007, **32**(8), 979–981.
4. Z. Yang, M. Prokopas, J. Nylk, C. Coll-Lladó, F.J. Gunn-Moore, D.E.K. Ferrier, T. Vettenburg, and K. Dholakia, *Biomed. Opt. Express*, 2014, **5**(10), 3434.
5. D.G. Papazoglou, S. Suntsov, D. Abdollahpour, and S. Tzortzakis, *Phys. Rev. A*, 2010, **81**(6), 061807.

LASER TWEEZERS – NONINVASIVE TOOL FOR DEMORABILITY STUDIES OF SOFT BIOMATERIALS

A.D. Zalessky[1,4], **A.A. Osychenko**[1], and **A.V. Nadtochenko**[1,2,3]

[1] Semenov Institute of Chemical Physics, RAS, Russia, 119991, Moscow, Kosygin str. 4;
e-mail: nadtochenko@gmail.com
[2] Institute of Problems of Chemical Physics, RAS, Russia, 142432Chernogolovka, Akademican Semenov str. 1, Moscow region,
[3] MSU, Faculty of Chemistry, Russia,11999, Moscow, 1-3 Leninskiye Gory
[4] Moscow Institute of Physics and Technology (State University), 141700, Dolgoprudny, Institutskiy per. 9, Moscow Region

Abstract. Optical manipulation of mice germinal vesicle oocyte nucleolus by means of laser tweezers was studied. It was shown that nucleolus can be elastically deformed and displaced using tightly focused laser beam. Oocyte viability and development after laser treatment were studied. Fluorescent studies of nucleolus adjacent were carried out. Change of elastic properties of nucleolus bounding was shown after fluorescent light (with wavelength of 385 nm) illumination. Mean value of force constant of oocyte nucleolus elasticity was determined.

Optical manipulation is a promising research technique with wide range of applications in such area as physics, chemistry and biology. In this work we performed laser manipulations of mice germinal vesicle oocyte nucleolus by means of laser tweezers. Laser tweezers were realized with tightly focused laser from Ti:sapphire oscillator (wavelength 780 nm, mean power at the sample plane 260 mWt). Laser was focused in the oocyte nucleolus with microscope objective (magnification 60x, N.A. 0,7). It was shown that native oocyte nucleolus exhibit elastic bounding to the initial position. Fluorescent staining of oocytes with Hoehst 33342 was performed. It was revealed that after fluorescent light illumination (wavelength 385 nm) initial elastic bounding of nucleolus was broken. Mean trapping force of laser tweezers acting on nucleolus was determined as 7 pN and elastic deformation of nucleolus was investigated. Characteristic deformation can be seen on figure 1.

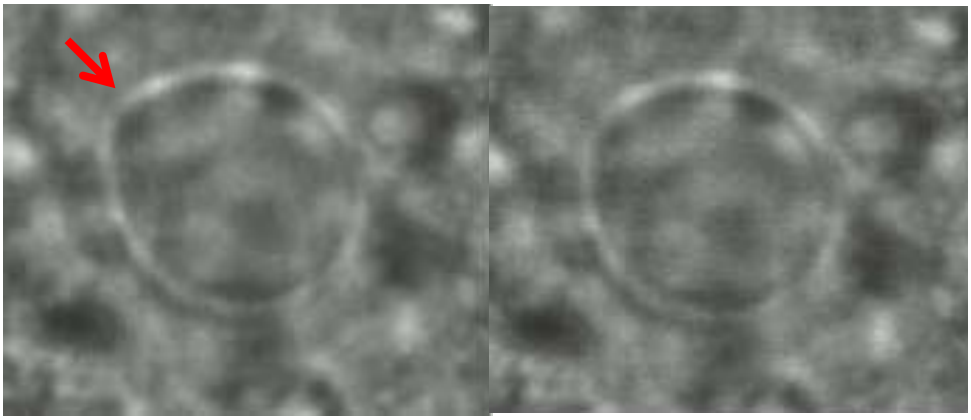

Fig. 1. Oocyte nucleolus under laser tweezers treatment, point of laser focusing is depicted with arrow (*left*). Oocyte nucleolus after treatment is ceased (*right*)

Mean value of deformation was estimated as length change of laser illuminated area of nucleolus. Deformation was shown to be elastic – after laser illumination ceased it was vanished. Mean value of stiffness coefficient was determined.

Biological features, such as polar body ejection and development dynamics were suggested for estimation of laser effect on oocyte viability.

Acknowledgements

This work is supported by Russian Science Foundation grant 14-14-00856.

WORKSHOPS

Clinical Biophotonics

Chairs

Natalia Shakhova
Institute of Applied Physics RAS, Nizhny Novgorod State Medical Academy, Russia

Herbert Stepp
Laser Research laboratory, LIFE Center, University Clinic, Munich, Germany

NUMERICAL ANALYSIS OF OCT-IMAGES FOR FAST ASSESSMENT OF HUMAN SKIN

P.D. Agrba[1,2], **M.A. Pasukhin**[1], and **M.Yu. Kirillin**[2,1]

[1] Lobachevsky State University of Nizhny Novgorod, Nizhny Novgorod, Russia
agrbapd@gmail.com
[2] Institute of Applied Physics RAS, Nizhny Novgorod, Russia

Abstract. Optical coherence tomography is a modern technique for visualization of internal structure of biotissues up to several mm in depth with resolution down to several μm. However, results based on qualitative analysis of OCT-images depend on clinician subjectivism which worsens diagnostic value of the technique. We show that numerical analysis of OCT-image histogram can serve as additional instrument for independent assessment of biotissue state.

Introduction

Optical coherence tomography (OCT) is a modern technique of visualization of internal structure of biotissue at the depth up to several mm with resolution down to several μm [1-3]. This technique based on low coherence interferometry that employs information from photons backscattered from inhomogeneities of refractive index within biotissue. However, evaluation of tissue condition based on qualitative analysis of OCT-images depends on clinician subjectivism, which worsens diagnostic value of OCT. In order to enhance this value it is preferable to use impersonal method for OCT-image assessment. Such methods allow to obtain additional information about biotissue that could be taken into account in a line with qualitative information.

Intensity of OCT-signal depends on distribution of optical properties within biotissue. Different biotissue conditions, caused by external factors, such as compression or abnormal temperature regime, or pathologic processes as well, correspond to different distribution of optical properties. Alterations in distribution of optical properties induce alterations in backscattering from biotissue and, respectively, in numerical parameters that can be extracted from an OCT-image. In this work we used the histogram of an OCT-image for quantitative assessment of biotissue condition.

The aim of this work was to compare histograms of OCT-images of normal human skin with those of skin under external action (mechanical compression, extreme temperature regimes) or with pathology (psoriasis, scleroderma).

Materials and methods

The study was performed *in vivo* on human volunteers. At the first stage of work we studied alterations of histogram of skin OCT-image under long-term pressure (several minutes) and after preliminary temperature action (heating or cooling). The pressure to the inspected skin area was kept constant and equal to 0.21 N/mm^2 during the whole time of observation. OCT images of skin were obtained each 5 seconds after measurement start during 7 minutes.

At the second stage we performed pilot study of histogram assessment in OCT skin monitoring in course of therapy of such skin pathologies as psoriasis and scleroderma. For each patient the OCT-images were obtained before therapy start, in the middle of therapy period and at the end of therapy period. Each time three OCT-images with constant pressure were obtained: immediately after measurement start, in 30 second and in 1 minute. This approach allowed to compare histograms without and with compression effect.

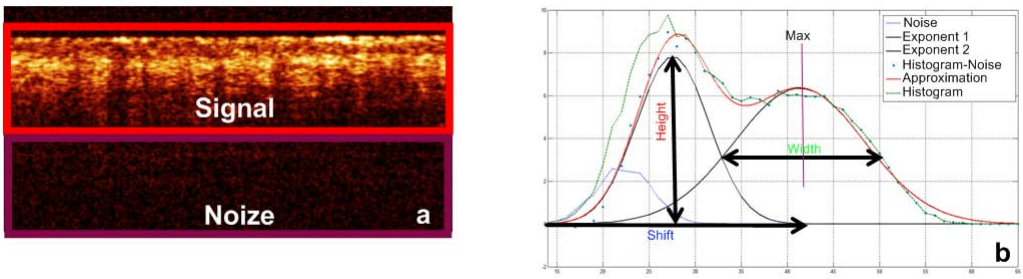

Fig. 1. OCT-image separated into fragments containing only noise signal and the one combining useful signal with noise (a) and process of histogram calculation (b)

In the frames of OCT-image analysis was separated into fragments containing only noise signal and the one combining useful signal with noise (Fig 1a). For each fragment the histogram was calculated. The histogram of the noise fragment was further used to separate noise component from the histogram of fragment containing useful image (Fig 1b). The resultant histogram was approximated by an analytical function represented by a sum of two exponentials with three parameters (width, height, shift) for each of them:

$$S = a_1 \cdot e^{-\left(\frac{b_1 - x}{c_1}\right)^2} + a_2 \cdot e^{-\left(\frac{b_2 - x}{c_2}\right)^2}$$

Alterations of these parameters were treated as impersonal criteria of alterations of biotissue condition.

Results and discussion

The algorithm of OCT-image histogram analysis was firstly approbated in OCT monitoring of effects of compression, cooling or heating on human skin in vivo. We demonstrated that all the considered parameters are sensitive to changes in OCT images induced by these external actions. In particular, parameter a_1 increased under mechanical compression and during skin relaxation after preliminary heating and weakly decreased after preliminary cooling. Parameter a_2 increased after preliminary heating and decreased for other considered actions cases. Parameter b_1 was not affected by compression and grew weakly after thermal action. Parameters b_2 and c_2 demonstrated similar increase in all cases. Parameter c_1 increased after preliminary heating and slightly alternated for other cases.

The second stage of the study included OCT image analysis in course of OCT monitoring of psoriasis and scleroderma treatment. Temporal dependence of all considered parameters (before therapy, in middle of therapy period, and at the end of therapy) are shown in figure 2 in relation to corresponding values for norm. It should be noted that at the end of treatment parameters may differ from those for norm, because healing can last after the end of treatment. From these results one can conclude that employment of histogram analysis can potentially serve for quantification of changes in pathologic skin induced by therapy, however, further studies are required to statistically prove our assumptions and choose proper parameters mostly affected by corresponding changes in inspected skin.

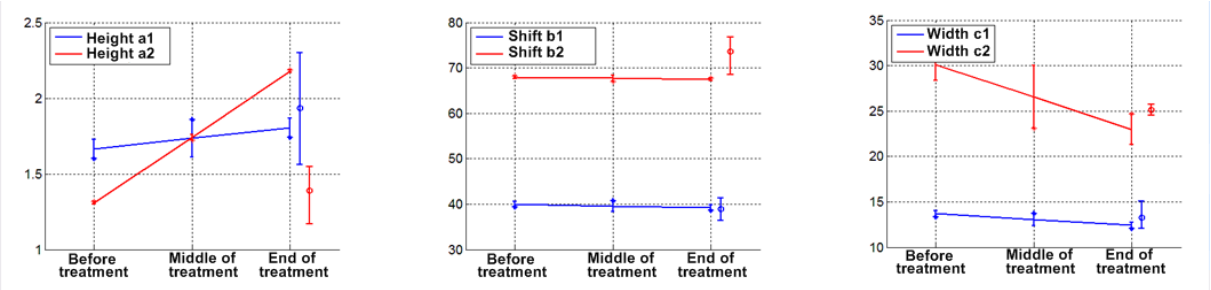

Fig. 2. Temporal dependences of the exponential fitting parameters in course of therapy. Separate points to the left correspond to respective values for norm

In future these parameters can be used as additional information about skin condition and potentially can increase diagnostic value of the OCT technique.

Acknowledgements

The work was supported by grants from the Russian Foundation for Basic Research (Nos. 15-32-20250 and 15-42-02503).

References

1. *Handbook of Optical Coherence Tomography*, Edited by B.E. Bouma, G.J. Tearney, New York: Marcel Dekker, 2002, 741 p.
2. V.M. Gelikonov, G.V. Gelikonov, L.S. Dolin, V.A. Kamensky, A.M. Sergeev, N.M. Shakhova, N.D. Gladkova, and E.V. Zagaynova, *Laser Physics*, 2003, **13**(5), 692-702.
3. A.M. Sergeev, L.S. Dolin, and D.N. Reitze, *Optics & Photonics News*, 2001, 28-35.

Invited

PHOTODYNAMIC THERAPY AND FLUORESCENCE IMAGING OF LUNG CANCER

A. Akopov, G. Papayan, A. Rusanov, N. Kazakov, I. Chistiakov, A. Gerasin, and **A. Karlson**

Pavlov First State Medial University, Saint-Petersburg, Russia
akopovand@mail.ru

Abstract. We present our experience of lung cancer treatment with new laser methods for endoscopic and surgical photodynamic therapy and high energy laser ablation as well as a new technology for intraoperative diagnosis of lymph node involvement in lung cancer with the use of near-infrared laser fluorescence imaging system.

Background

Bronchoscopic photodynamic therapy (PDT) and laser resection are well known methods to treat or relieve the symptoms of non-small cell lung cancer (NSCLC). We discuss possibility to extend indications for endobronchial laser treatment as a component of multidisciplinary treatment of locally advanced and metastatic lung cancer. We also evaluated the feasibility, safety and accuracy of intraoperative near-infrared (NIR) fluorescence imaging for sentinel lymph nodes (SLN) mapping in patients with NSCLC.

Methods

From Jan 2008 to Dec 2014, 350 patients with locally advanced and metastatic NSCLC underwent endobronchial laser resection and/or PDT. New approaches used were: PDT "through the endobronchial/endotracheal stent" (48 patients), PDT for peripheral lung cancer (14 patients), laser ablation (LA) of endobronchial tumor in an argon atmosphere (59 patients). Indications for PDT and LA were obstructing central disease as well as local recurrence after surgical treatment (29 patients) and critical airway obstruction (33 patients). In 55 patients preoperative PDT and LR were done to facilitate surgical resection for initially borderline or irresectable (inoperable) NSCLC. Most of patients (329, 94%) underwent endobronchial treatment in combination with chemo- and targeted therapy. PDT involved intravenous administration of chlorine E6 (Radachlorin) in the dose of 1 mg.kg-1 followed by irradiation with 662 nm laser light up to a total dose of 100 J/cm^2. LA was done with a wavelength of 1060 nm, an argon flow rate – 1.6–2.6 liters/min, and a power density of 75–100 W/cm^2.

Additionally twelve patients (6 – after neoadjuvant chemotherapy) who underwent pulmonary resection were investigated for visualization of lymphatic migration and SLN. Immediately after thoracotomy indocyanin green (ICG) was injected around the tumor and fluorescence real-time identification was applied by an infrared light device. SLN were identified intraoperatively, dissected and histologically evaluated.

Results

Cranial part of endobronchial tumor was localized in the right main bronchus in 42 (12%) patients, left main bronchus – in 29 (8%), tracheal bifurcation – in 62 (18%) and trachea – in 217 (62%) patients. The average duration of PDT session to reach the desired radiation dose was 11,5 min, LA session – 8,0 min. No patients had major complications. Of the 295 patients treated without resection, 41 achieved complete response (14%), 203 – partial response (69%), 51 – no response (17%). The one year survival rate for patients with stage III was 70%, stage IV – 56%, median survival was 19 months. After neoadjuvant endobronchial PDT and LA 51 patients of 55 operated (93%) underwent complete resection. 5-year survival rate for surgical patients was 71%.

Intraoperative fluorescence real-time identification of pulmonary lymphatic flow was successful in 8 of 12 cases (75%). 21 sentinel lymph nodes were identified in 10 patients (total identification rate 83%), 13 nodes in hilum, 8 nodes in mediastinum. Both SLN failure patients received neoadjuvant chemotherapy resulted complete remission. 7 lymph nodes (4 patients) had metastases on histological analysis. Metastatic nodal disease was never identified in patients with a histologically negative SLN (overall accuracy rate 100%). No adverse reactions were noted.

Conclusion

Endobronchial PDT and LA in combination with drug therapy are safe and effective option for advanced obstructing endobronchial lesions. Endobronchial approaches may also be used to convert to surgery candidates in stage III central NSCLC patients. ICG fluorescence is feasible for SLN biopsy. Absence of metastatic disease in the SLN directly correlates with final nodal status of the lymphadenectomy specimen.

Invited

STEADY-STATE FLUORESCENCE TECHNIQUES FOR SKIN NEOPLASIA DETECTION

E. Borisova[1], **A. Zhelyazkova**[1], **T. Genova**[1], **M. Keremedchiev**[2], **N. Penkov**[2], **E. Pavlova**[2], **P. Troyanova**[2], and **L. Avramov**[1]

[1] Institute of Electronics, Bulgarian Academy of Sciences, Sofia, Bulgaria, e-mail: borisova@ie.bas.bg
[2] University Hospital "Tsaritsa Yoanna- ISUL"

Abstract. We will present our recent investigations of the fluorescence properties of cutaneous neoplasia using excitation-emission matrices (EEMs) and synchronous fluorescence spectroscopy (SFS) measurement modalities. The spectral peculiarities observed will be discussed and the endogenous sources of the fluorescence signal – addressed. Measurements are made, using FluoroLog 3 spectrofluorimeter, on freshly surgically excised skin neoplasia and safety area normal skin after tumor resection. EEMs are obtained in the region of 280–440 nm – excitation and 300–800- emission, and SFS data are obtained in the same excitation-emission spectral range using constant wavelength interval $\Delta\lambda$ in the region of 10–100 nm, with step of 10 nm.

1. Introduction

Optical spectroscopy techniques have found a wide range of applications because they are non-destructive and deliver morphological and biochemical information about the investigated tissues [1]. Steady – state autofluorescence, where information about specific emission spectra of different endogenous fluorophores – its spectral range and relative intensity for each wavelength is applied in the recent clinical investigations as a very sensitive and accurate method for detection of early changes in many cancer types [2]. It has been widely used to study a number of skin conditions including psoriasis, melanoma and non-melanoma skin cancers. Fluorescence detection is a non-invasive and fast approach has gained increasing interest for its application in diagnosis and demarcation of various cancers [3]. We will describe two approaches of steady–state autofluorescence detection of tissue endogenous fluorophores – so called – excitation-emission matrices (EEMs) detection and synchronous fluorescence spectroscopy (SFS). In the first case EEM is graphically represented with excitation wavelength on one axis, emission wavelength on the second, and fluorescence intensity forms the third axis. This method for three-dimensional fluorescence spectroscopy provides enough information about the fluorescence spectra of biological tissue samples for determining excitation wavelengths that gave emission fluorescence spectra containing the most diagnostic meaning for clinical diagnostic analysis. EEMs allow to reveal real fluorescent properties of the samples investigated.

Second approach for the fluorescence signal detection – SFS appears to provide more information, in comparison with EEMs, based on its greater selectivity. Investigating autofluorescence through the method of SFS is performed by maintaining constant wavelength interval between excitation wavelength and emission wavelength through the spectrum. This allows optimal excitation of the emission maxima, which result in narrower emission peaks. That is the main reason for the greater sensitivity of SFS in comparison with EEMs. However, the SFS approach narrow the real spectral shape of the compounds detected and the results are in a form of "effective" fluorescence signals.

2. Materials and methods

In our study we measured excitation–emission matrices (EEM) and synchronous fluorescence spectroscopy data (SFS) from normal and diseased human skin samples, namely basal cell, squamous cell carcinoma, and malignant melanoma tumours, received after surgical excision during procedures for removal of skin neoplasia lesions. Ethical approval for our investigations is received from Ethical Committee of University Hospital "Queen Jiovanna-ISUL" – Sofia, where from the samples are obtained as well.

The fluorescence excitation emission matrix spectra were acquired using a commercial spectrofluorometer (FluoroLog3, Horiba Jobin Yvon). Additional fiber-optic module – F-3000 with fiber optic probe – 1950-1M allows to measure tissue samples. *Ex vivo* point-by-point measurements were taken from the excised tumour lesions and outwards from surrounding skin. Excitation applied is in 280–440 nm region. Fluorescence emission were measured between 300 nm and 800 nm. SFS measurements were performed with excitation wavelength in the spectral range of 280–440 nm with wavelength interval in the range of $\Delta\lambda$ = 0–200 nm increment of 10 nm.

3. Results and discussion

EEM data and SFS for different excitation wavelengths of normal skin are presented in Fig. 1a) and b). On the next two figures are presented our results when lesion was investigated – Malignant Melanoma (MM) (fig. 1a) and b)). In the spectra detected we observed signals from amino acids – tyrosine and tryptophan, structural proteins such as collagen and elastin, their cross-links, as well as keratin.

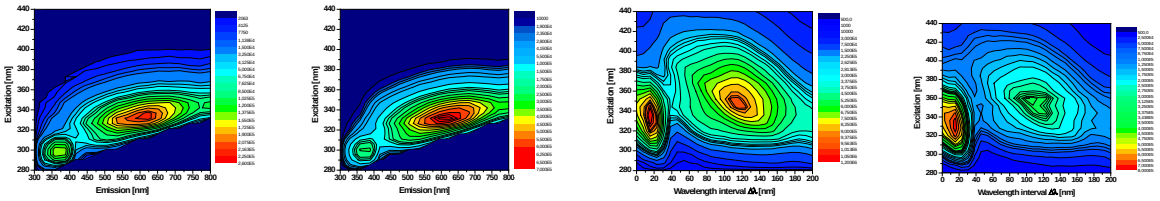

(a) (b) (c) (d)

Fig. 1. a) and b) EEM map, c) and d) SFS map of normal skin tissue and MM respectively

The fluorescence spectra with excitation in the deep UV range (260-280 nm) is dominated by the aromatic amino acids tyrosine, phenylalanine and tryptophan – with maxima at 300–350 nm. The NADH metabolic co-factor has excitation maximum at 340 nm and emission at 450–470 nm. Respectively, the flavins have excitation at the 420–460 nm and fluorescence maximum at 500–520 nm. Collagen type I has been excited at the region of 320–390 nm and emit fluorescence at 390–420 nm. Elastin has two excitation maxima – around 280 and 360 nm, and emission maxima are centered around 350 and 410 nm. The protein cross-links excitation maximum is around 380–420 nm and the emission maxima are around 390–440 nm and 460–500 nm for collagen and elastin respectively. The decrease in the fluorescence intensity of the malignant tissues is due to cancer induced destruction of collagen and elastin cross-links surrounding the tumor cells.

The main differences observed between the fluorescence spectra of healthy skin and cancerous tissue are in the intensity of the fluorescence from the amino acids – tyrosine and tryptophan, the enzymes and coenzymes NADH and FAD, and from the structural proteins elastin and collagen. In the SFS spectra of cancerous tissue, additional difference, in comparison with the SFS spectra of normal tissue is the spectral shift of the NADH and FAD maxima in the range of the FAD fluorescence, which can be interpreted like increasing of FAD contained in the cancerous tissue or it's a result of the lower NADH fluorescence in combination with the superior sensitivity of the SFS to EEMs.

We foresee to increase our database of EEM and SFS data, including other skin pathologies, benign and malignant lesions. Data received will be applied for improvement of optical fluorescence diagnostic system prototype, which we intend to introduce into clinical practice for initial detection of skin neoplasia. This technique has potential to provide real-time diagnosis of malignant and premalignant skin tissue, eliminating the invasive of biopsy and the histopathology procedures.

Acknowledgements

This work is supported partially by the National Science Fund of Bulgaria under grant #DFNI-B02/9, COST Action BM1205, and under personal fellowship of E. Borisova from Foundation UNESCO/L'Oreal "For young women in life sciences", Bulgaria – 2014.

References

1. J.R. Lakowicz, *Principles of Fluorescence Spectroscopy*. 2nd. Ed., Plenum Press, New York, 1999, p. 11-39.
2. J. Zhao, S. Zandi, F. Feng, H. Zeng, D. McLean, and H. Lui, *Proc. of SPIE - Photonic Therapeutics and Diagnostics VII*, N. Kollias (ed.)., 2011, **7883**, 7883-0I.
3. A. Zhelyazkova, E. Borisova, L. Angelova, E. Pavlova, and M. Keremedchiev, *Proc. SPIE*, 2013, **9032**, 9032-0A.

Invited

PDT FOR BILE DUCT AND PANCREATIC CANCER – A REVIEW

S.G. Bown and **S.P. Pereira**

National Medical Laser Centre and Institute for Liver and Digestive Health,
University College London, UK
s.bown@ucl.ac.uk

Abstract. Bile duct and pancreatic cancers threaten life; few are amenable to definitive surgery. Photodynamic Therapy (PDT) is under assessment as adjunctive therapy to slow tumour growth. Most studies suggest PDT increases survival for bile duct cancers, but randomized studies are contradictory. More randomised trials are needed (stenting with and without PDT), ensuring all other factors, particularly chemotherapy, are identical in each group. PDT produces necrosis in pancreatic cancers which heals safely. New imaging options improve prediction of necrosis extent. New trials will deliver light using an echoendoscope rather than percutaneously, combine PDT with chemotherapy and treat pre-cancerous pancreatic cysts.

Background

Pancreatic and biliary cancers have a poor prognosis apart from the few suitable for surgical resection. For inoperable bile duct cancer, tumour growth blocks the flow of bile from the liver to the intestine so the main aims of palliation are to maintain the flow of bile and to slow tumour progression. Metal or plastic stents can be inserted endoscopically to hold the duct open, but these can get blocked by tumour growth. Radiotherapy and chemotherapy can slow down overall tumour progression a little. PDT is being assessed as a means of suppressing tumour growth in and around the bile duct.

Pancreatic cancer is one of the worst cancers. Less than 1 in 10 survive for more than a year after diagnosis. 90% are inoperable and the response to chemotherapy and radiotherapy is poor, only increasing survival by a few weeks. PDT has been shown to produce local areas of necrosis in these cancers without serious complications. Techniques are now being explored to refine this approach and combine it with chemotherapy.

Methods

Bile duct. Over the last 10 years, several groups around the world have tried adding PDT to conventional stenting for bile duct cancer, and this has appeared to show some improvement in survival [1]. A Korean study compared stenting with and without PDT and no other treatment (no radiotherapy or chemotherapy). This showed a 2.5 month increase in survival, but the trial was not randomized [2]. A UK trial (not yet published in full) was randomized between stenting with and without PDT, but was not controlled with regard to chemotherapy.

Pancreas. PDT for pancreatic cancer was first described using the photosensitizer mTHPC in 2002 [3] and shown to be safe with percutaneous, image guided light delivery. The current study used verteporfin with a similar protocol and described refinements in correlating the extent of necrosis with the treatment parameters (drug and light dose) using contrast enhanced CT imaging [4]. This has led to the development of a major ongoing programme which is just getting under way.

Results and Future Plans

Bile duct cancer. The results of the randomized UK study of stenting with and without PDT were unexpected and disappointing. The patients receiving PDT had a shorter survival than those who did not. However, detailed analysis revealed unanticipated confounding factors. The patients had not been randomized with regard to adjuvant chemotherapy. Those in the control group received more chemotherapy and at an earlier stage than those in the PDT group (unlike the Korean study, where the patients received neither radiotherapy nor chemotherapy). Thus the true value of PDT in bile duct cancer is still unclear. A new randomized study is required, comparing stenting with and without adjuvant PDT, but in which every patient receives exactly the same chemotherapy regime.

Pancreas cancer. The recent study using verteporfin (shorter period of photosensitivity than mTHPC) showed that the extent of necrosis correlated better with the vascularity of tissue around the tumour, as documented on contrast enhanced CT, than with the drug and light dose. In one case, an inoperable cancer became operable after PDT (the first such case documented). Our anticipated new developments are a) to deliver light to the pancreas with the optical fibre passed through an echoen-

doscope, to avoid the need to pass needles through the skin and across the stomach, b) to combine PDT with chemotherapy, and c) to treat pre-cancerous cysts in the pancreas.

Verteporfin PDT. *Left:* contrast CT, low attenuation mass in head of pancreas. Centre: needle in tumour. *Right*: day 5 post PDT contrast CT with zone of necrosis in pancreatic head [5]

Conclusions

PDT shows promise for increasing survival in inoperable bile duct cancer, but the evidence is not yet strong enough to recommend it as a routine treatment. PDT can produce necrosis in localized pancreatic cancer, but many further studies are required to establish the best way to use it and whether it can be combined with chemotherapy

References

1. W.R. Matull, D.K. Dhar, L. Ayaru, N.S. Sandanayake, M.H. Chapman, A. Dias, J. Bridgewater, G.J. Webster, J.J. Bong, B.R. Davidson, and S.P.Pereira, "R0 but not R1/R2 resection is associated with better survival than palliative photodynamic therapy in biliary tract cancer", *Liver Int.*, 2011, **31**(1), 99-107.
2. Y.K. Cheon, T.Y. Lee, S.M. Lee, J.Y. Yoon, and C.S. Shim, "Long term outcome of photodynamic therapy compared with biliary stenting alone in patients with advanced hilar cholangiocarcinoma", *HPB (Oxford)*, 2012, **14**(3), 185-93.
3. S.G. Bown, A.Z. Rogowska, D.E. Whitelaw, W.R. Lees, L.B. Lovat, P. Ripley, L. Jones, P. Wyld, A. Gillams, and A.W. Hatfield, "Photodynamic therapy for cancer of the pancreas", *Gut.*, 2002, **50**(4), 549-57.
4. M. Jermyn, S.C. Davis, H. Dehghani, M.T. Huggett, T. Hasan, S.P. Pereira, S.G. Bown, and B.W. Pogue, "CT contrast predicts pancreatic cancer treatment response to verteporfin-based photodynamic therapy", *Phys Med Biol.*, 2014, **59**(8), 1911-21.
5. M.T. Huggett, M. Jermyn, A. Gillams, R. Illing, S. Mosse, M. Novelli, E. Kent, S.G. Bown, T. Hasan, B.W. Pogue, and S.P. Pereira, "Phase I/II study of verteporfin photodynamic therapy in locally advanced pancreatic cancer", *Br J Cancer*, 2014, **110**(7), 1698-704.

Invited

ADVANCED NONINVASIVE REAL-TIME MONITORING FOR PDT REGIME OPTIMIZATION

S.V. Gamayunov[1,2,4], E.V. Grebenkina[1], K.S. Korachgina[5], I.V. Turchin[3], S.S. Kuznetsov[2], E.V. Gubarkova[2], R.R. Skrebtsova[1], V.A. Karov[1], I.G. Terentiev[2], and **N.M. Shakhova[3,2,4]**

[1] Nihzny Novgorod Regional Oncologic Clinic, Nizhny Novgorod, Russia, gamajnovs@mail.ru
[2] Nizhny Novgorod State Medical Academy, Nizhny Novgorod, Russia
[3] Institute of Applied Physics RAS, Nizhny Novgorod, Russia
[4] N.I. Lobachevsky State University of Nizhny Novgorod, Nizhny Novgorod, Russia
[5] A.I. Evdokimov Moscow State Medical Stomatology University, Moscow, Russia

Abstract. Advisability and efficacy of different imaging techniques in PDT monitoring are demonstrated and compared. None of considered techniques demonstrated sensitivity to all PDT components proving that multimodal approach in PDT monitoring is reasonable. Ways for further improvement of the techniques are proposed.

Photodynamic therapy (PDT) is a modern minimally invasive treatment technique, which provides selective multi-factorial damage of tumor tissue [1]. The dependence of the procedure efficiency on the parameters of blood flow, tumor oxygenation, individual interstitial photosensitizer biodistribution, and kinetics of light-drug and light-tissue interaction necessitates transition from regimes developed on the basis of empirical exposure selection to application of personalized treatment approaches on the basis of objective monitoring of the various PDT components [1].

In this connection, development and introduction to clinical practice of different noninvasive optical imaging techniques, including fluorescence imaging [2, 3], optical coherence tomography (OCT) [4], laser Doppler fluorimetry (LDF) [5], spectroscopic techniques for assessing oxygenation and concentration of photosensitizer [6] are the most promising.

The aim of this work is to compare advisability and efficacy of different imaging techniques in PDT monitoring.

Materials and methods

The work is performed at the Nizhny Novgorod Oncologic Clinic. A total of 950 patients were enrolled in the study underwent PDT of skin, cervical, and vulvar tumors. Fluorescence imaging, laser spectroscopy, OCT, LDF were treated as the monitoring techniques. Fluorescence parameters were evaluated using fluorescence imaging system (LLC "Atkus" .S. Petersburg), spectroscopy was performed using a laser spectroscopy system LESA (JSC "Biospec", Moscow), OCT inspection was performed using OCT-1300U (IAP, LLC "BioMedTeh", Nizhny Novgorod), and laser analyzer of capillary blood flow LAK-2 (LLC ”Lazma”, Moscow) was employed for LDF. Comparative analysis of the obtained monitoring data was performed.

Results

Analysis of the collected data showed that fluorescence diagnostics and spectroscopy allow estimating the accumulation of a photosensitizer (PS) and its photobleaching level, which can be used to predict the immediate and long-term results: in patients with high accumulation of PS recurrence rate of 4.1% was observed against 9.5% for cases of low accumulation and no accumulation of the drug ($p = 0.044$). A tendency towards increase in recurrence rate is noted in the absence of PS photobleaching reaching 10.4% versus 4.4% for the full and partial photobleaching ($p = 0.051$), a combination of high accumulation and complete photobleaching resulted in percentage of full tumor responses of 94% with a 3% recurrence rate (follow-up period lasted up to 25 months). OCT allows for real time assessment of changes in tissue structure in course of PDT process which may be used for early monitoring of the selected regime efficiency. LDF data provide information on changes in the vascular component of photodynamic treatment.

It is worth mentioning that none of these techniques demonstrated sensitivity to all PDT components, as a result, the drawbacks of the techniques were outlines and ways for further improvement of the techniques were proposed.

In order to improve the efficiency of fluorescent imaging, we improved the hardware and software base of diagnostic equipment. The technique for quantitative evaluation of the fluorescence integral level from the entire tumor area was developed, allowing accounting for the heterogeneity of the tumor tissue (Fig. 1a). The technique for real time photobleaching monitoring directly in the course of PDT process was also developed, which will further allow personalization of the laser radiation parameters basing on thresholds photosensitizer concentrations (Figure 1b).

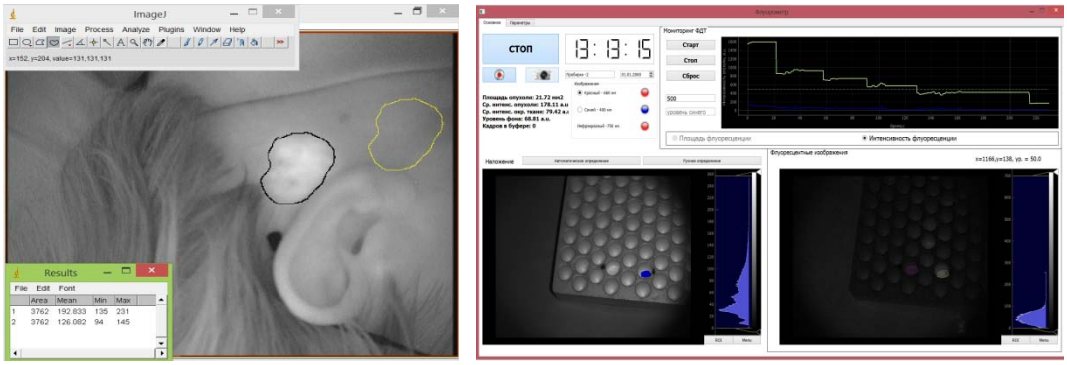

Fig. 1. Monitoring of PDT process with fluorescent imaging: a) quantitative evaluation of integral fluorescence level from the entire tumor area compared to corresponding fluorescence from the healthy skin site (male patient, 67 years old, primary basal cell skin cancer behind the left ear N2N0M0, stage II, 30×25 mm) b) real-time photobleaching monitoring directly in the course of model PDT procedure with chlorine E6 photosensitizer (Photoditazin, Vetagrand, Russia) diluted at concentration of 1 μg/ml in 1% Lipofundin solution, the object is irradiated with 662-nm laser with intensity of 0.3 W/cm^2, dose density of 400 J/cm^2

Improved OCT setup was also employed for monitoring. We revealed that cross-polarization OCT (CP OCT) is able to detect key morphological changes in the course of PDT treatment of skin and cervical cancer (edema, necrosis, structure recovery). The higher efficiency in OCT employment can be reached for long-term monitoring (30–35 days after PDT procedure) for evaluation of the completeness of tissue stromal component recovery. OCT monitoring of tumor blood flow also has high potential as an early indicator of biologic response to PDT treatment.

Employment of the novel class of PS allowing to perform theranostics are perspective for PDT optimization. Wide classes of markers known as molecular rotors being excited by light induce singlet oxygen production and demonstrate string dependence of fluorescence parameters on medium viscosity. This ability determines the possibility of their employment as photosensitizers for PDT which allow to observe photodynamic reaction by variation of intracellular viscosity [7].

Currently, our studies show that multimodal approach in PDT monitoring is reasonable. Comparative analysis revealed complementary instead of competitiveness of the considered techniques, and confirmed the possibility of their combined use to monitor various aspects of PDT. Improvement of monitoring techniques and further studies on their applications are required for development of the protocol for clinical use and optimization of PDT treatment parameters.

Acknowledgements

The study is performed in the frames of complex program of PDT development and introduction into practice with additional financial support by RFBR (projects 14-02-00753 and 15-35-20250) and the Ministry of Education and Science of Russian Federation (projects RFMEFI60414X0027 and 14.B25.31.0015). The authors are grateful to the management and staff of Nizhny Novgorod Oncologic Clinic for the possibility to conduct clinical studies.

References

1. P. Agostinis, K. Berg, K.A. Cengel, T.H. Foster, A.W. Girotti, S.O. Gollnick, et al., *CA Cancer J Clin*., 2011, **61**(4), 250-281.
2. J.P. Celli, B.Q. Spring, I. Rizvi, C.L. Evans, K.S. Samkoe, S. Verma, et al., *Chem Rev*, 2010, **110**(5), 2795-2838.
3. S.V. Gamayunov, V.A. Karov, R.R. Kalugina, E.V.Grebenkina, O.V. Onoprienko, M.V. Pavlov, and N.M. Shakhova, *Proc. of the IV International Symposium TOPICAL PROBLEMS OF BIOPHOTONICS*, 2013, 297-298.
4. B.A. Standish, V.X. Yang, N.R. Munce, L.M. Wong Kee Song, G. Gardiner, A., Lin, et al., *Gastrointest Endosc*., 2007, **66**(2), 326-33.
5. A.M.K.Enejder, C. af Klinteberg, I. Wang, S. Andersson-Engels, N. Bendsoe, S. Svanberg, et al., *Acta Dermato-Venereologica*, 2000, **80**(1), 19-23.
6. A. Douplik, A.A. Stratonnikov, V.B. Loshchenov, V.S. Lebedeva, V.M. Derkacheva, A. Vitkin, et al., *J Biomed Opt*., 2000, **5**(3), 338-49.
7. M.K. Kuimova, S.W. Botchway, A.W. Parker, M. Balaz, H.A. Collins, H.L. Anderson, K. Suhling, and P.R. Ogilby, *Nature Chemistry*, 2009, **1**, 69-73.

PERSONIFICATION OF CERVICAL AND VULVAR PATHOLOGY TREATMENT WITH OPTICAL METHODS

E.V. Grebenkina[1], **D.D. Eliseeva**[2], **S.V. Gamayunov**[1,2], **N.A. Illarionova**[1], **O.V. Kachalina**[2], **S.S. Kuznetsov**[2], **O.V. Onoprienko**[1], and **N.M. Shakhova**[2,3]

[1] Regional Oncological Hospital, Nizhny Novgorod, Russia, gelena1980@mail.ru
[2] State Medical Academy, Nizhny Novgorod, Russia,
[3] Institute of Applied Physics RAS, Nizhny Novgorod, Russia

Abstract. Existing methods for treatment of early forms of cervical and vulvar neoplasia are not sufficiently effective and excessively aggressive. The alternative method used is photodynamic therapy (PDT). The paper discusses the application of optical bioimaging techniques for monitoring of PDT of the lower genital tract pathology. A total of 215 female patients undergone PDT treatment. Planning and monitoring of PDT was performed using optical methods: fluorescence imaging and optical coherence tomography (OCT). It was shown that applied optical bioimaging techniques have high potential not only for controlling, but also for individualization of treatment of cervical and vulva pathologies.

Cervical and vulvar pathology remains one of the most important problems in gynecology as they have a significant impact on the basic functions of the female body (sexual and reproductive) and predispose to the development of genital cancers [1, 2]. Existing methods for treatment of early forms of cervical and vulvar cancer and precancer are either not sufficiently effective, or excessively aggressive [1, 3]. The alternative method used is photodynamic therapy (PDT) [4, 5]. For efficient use of PDT for treatment of cervical and vulvar pathologies it is important to properly choose the PDT modality and regime. The paper discusses the use of optical imaging techniques for optimization and personalization of PDT of the pathology of the lower genital tract.

The study was performed at the Oncogynecological department of Regional Oncological Hospital. A total of 215 patients with the pathology of the lower genital tract undergone PDT treatment, including 86 with cervical intraepithelial neoplasia (CIN) and cervical cancer in situ (CIS), and 129 with vulva pathology, including 28 cases of vulvar cancer and high grade vulvar intraepithelial neoplasia (VIN) and 101 cases of cancer precursors: lichen sclerosus (LS), squamous cell hyperplasia (SCH). In this study we used the chlorine photosensitizers (PS) in a dose of 1 mg per kilo of weight; the drug was injected intravenously with 200 ml of saline solution during 30 minutes. Laser irradiation was done at the wavelength of 662 nm. In CIN and cervical cancer laser irradiation was performed in 1.5–2 hours after PS injection. Light dose was 100–200 J/cm^2, intensity was 250–400 mW/cm^2. In vulva pathology the laser irradiation was conducted under general anesthesia (narcosis, spinal or epidural anesthesia) in 2–3 hours after drug injection. The total light dose was 100–200 J/cm^2 for areas with benign vulva pathology and VIN, 200–300 J/cm^2 for areas with cancer in situ, and 300–400 J/cm^2 for areas with local vulvar cancer recurrence. The light intensity amounted 0.7–0.9 W/cm^2, 1–2 W/cm^2, and 1.5–2 W/cm^2 respectively. Follow up period varied from 2 to 72 months, with median value of 35 months. Assessment of the immediate and long-term results was based on a comprehensive diagnosis including clinical data (visual inspection, survey), instrumental (colposcopy, OCT) and laboratory (cytology, histology, polymerase chain reaction (PCR)) techniques. Planning and monitoring of PDT was performed using fluorescence imaging and OCT. Fluorescence imaging was performed with the system based on the laser radiation source at wavelength of 622 nm and photodetection unit with central wavelength of 755nm. OCT imaging was performed using “OCT-1300U” device (probing wavelength is 1280 nm, in-depth resolution is 15 μm, lateral resolution is 30 μm, imaging rate is 8–10 frames per second, probing depth is up to 2 mm, replaceable endoscopic probe with 2.4 mm in diameter).

No complications or side effects were observed in follow-up of PDT procedure. In cervical pathology (CIN3 and CIS) visual inspection, colposcopy and OCT in the early stages (1.5–2 months) revealed signs of cervicitis. The long-term results did not demonstrate sings of malignancy by colposcopy and OCT. Cytological studies did not revealed atypia in 46 cases, in 28 cases CIN 1 was founded , and in 12 cases CIN 2 was diagnosed. PCR study prior to PDT procedure revealed HPV in all 86 cases, after PDT HPV was not identified in 75 cases. In course of 12 months follow-up period no CIN progression or recurrences were diagnosed. Optical diagnostics allowed to optimize and personalize the PDT treatment. Thus, fluorescence imaging allowed determining the optimal time of laser irradiation. OCT was used in the group of patients where PDT was used as an additional treatment technique.

In this situation, OCT data were decisive for determining the indications for PDT and choice of treatment protocol.

In case of prevalence of malignant types of OCT images excision of the cervix was chosen as the primary treatment technique. PDT was performed either as neoadjuvant treatment a month before the excision in order to reduce the amount of tissue removed, or after excision as adjuvant therapy in the morphological verification of positive tumor margins. In case of CIN 1,2 and benign OCT images either treatment was not performed and the patient was a subject for monitoring, or PDT was performed as anti-inflammatory therapy. In case of vulvar cancer in most cases PDT was followed by a complete or partial tumor response; stabilization and progression were detected only in 2 and 1 case, respectively. In benign vulva pathology two-thirds of the total patients reported relief of symptoms while the other demonstrated a significant reduction of the disease manifestation.

It is worth mentioning that all PDT failures were received in case of recurrence tumors. In these cases weak accumulation of PS was expected associated with scar changes on the periphery of the tumor, developed as a consequence of previous treatment. However, fluorescence imaging did not reveal such a correlation. In our opinion, I this respect the fluorescence imaging system employed in the study requires modification. Further studies are needed to reveal the potential of the fluorescence imaging as a technique for monitoring of PDT aiming for individualization of treatment and predicting outcomes.

Obtained results correspond to the data reported by other authors on the effectiveness of PDT and the possibility of using it as an alternative treatment of noninvasive carcinoma and cancer precursors of low genital tract [6, 7]. In our opinion, PDT is the method of choice in recurrent vulva carcinoma. Failures are associated with inadequate light dose and insufficient PS accumulation in tumor. These effects can be minimized by employing adequate techniques for treatment planning and monitoring. Application of such methods as fluorescent imaging and OCT has high potential not only for controlling, but also for individualization of treatment of cervical and vulva pathologies.

Acknowledgement

The authors are grateful to the personnel of Nizhny Novgorod Regional Oncology Clinic. The work is financially supported by the Ministry of Education and Science of Russian Federation (projects RFMEFI60414X0027 and № 14.B25.31.0015).

References

1. L.S. Massad, M.H. Einstein, W.K. Huh, et al., *Journal of Lower Genital Tract Disease,* 2013, **17**(5), S1-S27.
2. C.C. Chi, G. Kirtschig, M. Baldo, et al., *J Am Acad Dermatol.*, 2012, **67**(2), 305-12.
3. G.W. Kim, H.J. Park, H.S. Kim, et al., *J Dermatol.*, 2012, **39**(2), 145-50.
4. A. Olejek, K. Steplewska, A. Gabriel, et al., *Int J Gynecol Cancer.*, 2010, **20**(5), 879-87.
5. P. Soergel, X. Wang, H. Stepp, H. Hertel, and P. Hillemanns, *Lasers Surg Med.*, 2008, **40**(9), 611-5.
6. X.H. Tao, Y. Guan, D. Shao, et al., *Photodiagnosis Photodyn Ther.*, 2014, **11**(2), 104-12.
7. P. Soergel and P. Hillemanns, *Photodiagnosis Photodyn Ther.*, 2010, **7**(1), 10-4.

Invited

NON-INVASIVE DETECTION OF IRON DEFICIENCY

H. Stepp[1], G. Hennig[1], Ch. Homann[1], R. Sroka[1], I. Teksan[2], U. Hasbargen[2], S. Hasmüller[2], N. Khaled[3], Th. Stauch[4], L.M. Holdt,[5] M. Vogeser[5], and **G. Brittenham[6]**

[1] LIFE-Center, University Hospital of Munich, Munich, Germany, herbert.stepp@med.lmu.de
[2] Dept of Gynecology and Obstetrics, University Hospital of Munich, Munich, Germany
[3] Nestlé Research Center, Nestec Ltd., Lausanne, Switzerland
[4] MVZ Labor PD Dr. Volkmann und Kollegen, Karlsruhe, Germany
[5] Institute of Laboratory Medicine, University Hospital of Munich, Munich, Germany
[6] Dept of Pediatrics, Columbia University, New York, USA

Abstract. Iron deficiency can be detected by measuring the fluorescence of zinc protoporphyrin IX (ZnPP) in red blood cells. We have developed a non-invasive optical fiber-based method that does not require a blood sample to measure ZnPP-fluorescence in the microcirculation of the lower lip. The autofluorescence background is greatly reduced by excitation with two wavelengths (407 nm and 425 nm) and subtraction of the corresponding emission spectra. A spectral decomposition of the resulting difference spectrum yields quantitative values for the ratio of ZnPP/heme, which is the relevant measure to assess iron deficiency.

Introduction

Iron deficiency affects up to 2 billion people worldwide, predominantly infants, children and women of childbearing age, especially during pregnancy. Iron deficiency causes anemia, compromises immune function, decreases physical performance, leads to lower birth weight and preterm delivery, and is responsible for irreversible detrimental effects on cognitive development in early childhood [1]. Populations in developing countries are at the greatest risk for these adverse effects of iron deficiency.

With iron deficiency, the supply of iron to the developing red blood cell becomes insufficient, making divalent iron unavailable for insertion into protoporphyrin IX (PpIX) to form heme. Instead of divalent iron, zinc ions are then inserted into PpIX, forming ZnPP. Unlike heme, ZnPP (in hemoglobin) is fluorescent when excited at 425 nm. Iron-deficient erythrocytes are red fluorescent (peak at 590 nm). This fluorescence can be measured by conventional hematofluorometers on blood samples obtained by veni- or finger-puncture, yielding values calibrated in µmol ZnPP/mol heme. This ratio is generally independent of the concentration of erythrocytes in the sample. No non-invasive method to measure erythrocyte ZnPP has been available.

Tissue autofluorescence intensity is two orders of magnitude greater than the signal from erythrocyte ZnPP, even in iron-deficient individuals. To quantify ZnPP, this autofluorescence background must be eliminated.

Results

We have previously shown that ZnPP fluorescence can be detected from whole blood *in vitro* with sequential excitation at 407 nm and 425 nm followed by calculation of difference fluorescence spectra to eliminate the background fluorescence of plasma proteins (Fig. 1 left and Fig. 2) [2]. With a fiber-based (1 mm quartz fiber) device, fluorescence spectra were recorded from the lower lip *in vivo* (Fig. 1 right) and calculated in a similar manner, resulting in difference spectra in which the contribution of ZnPP fluorescence was comparable to its contribution in whole blood despite the much lower concentration of erythrocytes in the tissue (Fig. 3).

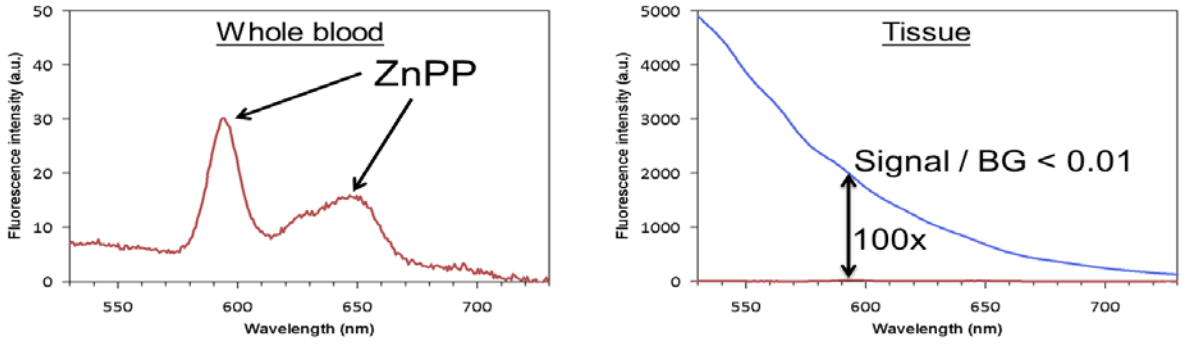

Fig. 1. Fluorescence spectra of whole blood and tissue (lower lip) of an iron-deficient individual

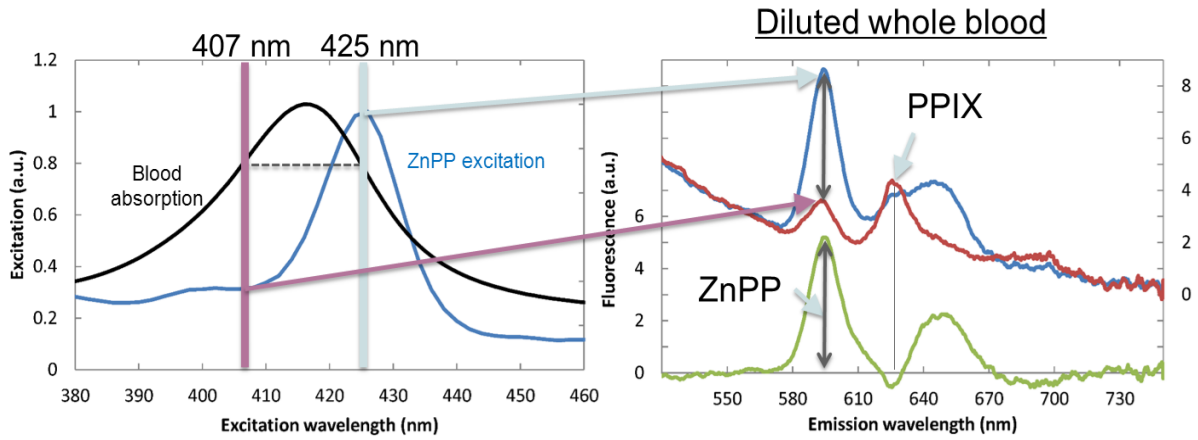

Fig. 2. Blood absorption and ZnPP excitation spectra of whole blood (*left*) and fluorescence spectra (*right*), including difference spectrum

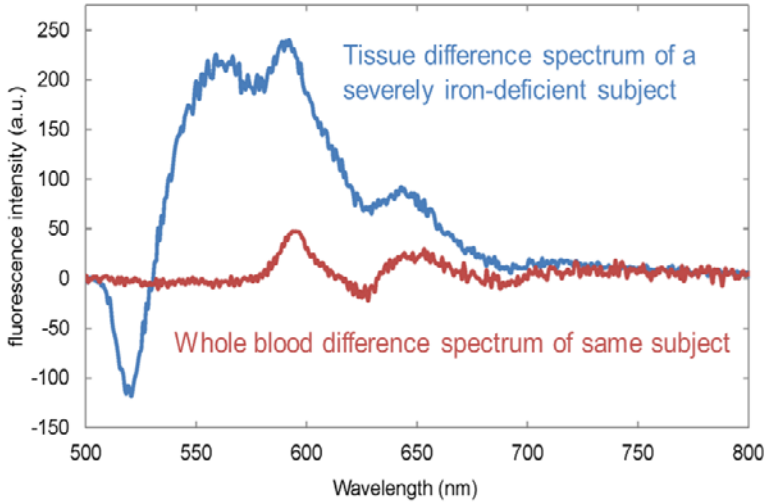

Fig. 3. Difference spectra of tissue and whole blood

With spectral decomposition, the contributions of ZnPP, PpIX, background and blood absorption to the fluorescence spectra can be quantitatively disentangled. The amplitudes for the ZnPP contribution correlate with the ratio µmol ZnPP/mol heme.We have further improved the device by implementing an algorithm for assesment of the tissue blood volume and are currently evaluating its performance in a larger clinical study.

Acknowledgements

The study was substantially supported by Nestec Ltd., Vevey, Switzerland.

References

1. C. Algarin, C.A. Nelson, P. Peirano, A. Westerlund, S. Reyes, and B. Lozoff, *Dev Med Child Neurol.*, 2013, **55**(5), 453-8.
2. G. Hennig, C. Gruber, M. Vogeser, H. Stepp, S. Dittmar, R. Sroka, et al., *J Biophotonics*, 2014, **7**(7), 514-24.

Invited

PHOTODYNAMIC INACTIVATION FOR THE TREAMENT OF INFECTIOUS DISEASES

C. Kurachi[1], **A.P. Silva**[1], **L. Pires**[1], **S.M.G. Bosco**[2], **V.S. Bagnato**[1], and **N.M. Inada**[1]

[1] São Carlos Institute of Physics, University of São Carlos, Brazil, cristina@ifsc.usp.br
[2] School of Veterinary Medicine and Animal Science, Universidade Estadual Paulista, Brazil

Abstract. Photodynamic therapy induces cell death mainly through the production of the highly reactive singlet oxygen after the photoactivation of a sensitizer compound. Until the present, most of the clinical protocols are for the treatment of cancer lesions. Several studies have showed efficacy of the photodynamic inactivation (PDI) of bacteria, fungi, and protozoa species. Clinical protocols and optical instrumentation were developed based on the infected host tissue and microorganism characteristics. The results of the experimental and clinical studies for onychomycosis and pythiosis showed the efficacy and safety of the PDI.

Introduction

Photodynamic therapy (PDT) is a treatment modality that was initially developed for the cancer lesions, especially for carcinoma at skin or mucosa at fiberoptically accessible organs, as oral cavity, esophagus and bladder. Its main action mechanism is based on the production of singlet oxygen and other reactive species after the photoactivation of a sensitizer compound. The photosensitizer must be previously delivered to the target tissue, and the photodynamic reaction only starts to take place with the illumination of a specific wavelength. Nowadays, PDT has been also approved for the treatment of potentially malignant lesions, as actinic keratosis and Barrett's esophagus, and for facial cosmetics. The photodynamic inactivation (PDI) for the treatment of several species of microorganisms has also been presented [1–4]. The main advantage of the PDI is the local response with low side effects. PDI application is especially relevant for infectious diseases, where there is no effective treatment option or with poor response to the available antibiotic drugs.

Onychomicosis

Onychomycosis is a fungal disease that affects the nails, mainly of the feet. The conventional treatment is based on the topical application and oral administration of an antifungal drug [5]. Unfortunately, the drug distribution in the infected tissue is not adequate, so the treatment may usually takes at least 6 months. The antifungal compounds are toxic for the kidney and liver, so the prolonged treatment can result in a relevant side effect, as well as it shows a high patient drop out.

***In vitro* assays.** Inactivation fungi experiments were performed on *Candida albicans*, *Trichophyton rubrum* and *Trichophyton.mentagrophytes* evaluating a a haematoporphyrin derivative (Photogem®, Russia) and a curcumin (PDTPharma®, Brazil) under different irradiation protocols. The best results were achieved with curcumin and 35 mW/cm^2 at 450nm LED illumination.

Clinical trial. A customized device for the onychomycosis treatment was developed [6]. The 450nm LED-based device was specially designed to deliver a uniform illumination and addressing a comfortable wearable unit. The present protocol starts with a polishing nail session and the application of urea cream. The PDT session is performed using a curcumin gel incubated for 30 minutes and 120 J/cm^2 irradiation. The number of PDT sessions varies depending on the case, but the average complete response is achieved after 6–8 sessions.

Pythiosis

Pythiosis is an infection caused by a fungus-like microorganism called *Pythium insidiosum*, but due to the lack of ergosterol, the main target of the antifungal drugs, at its cell wall, no treatment response is observed. The most used treatment is the surgical resection, even with a high recurrence rate, since it is difficult to delimitate the infected tissue with the fast hyphal growth. Horses and dogs are the animals most affected by pythiosis, but it has been already identify in humans, goats, calves, cattle, and recently in birds [7–9].

***In vitro* assays.** The oomycete isolate was obtained from a horse attended at the School of Veterinary Medicine and Animal Science at Universidade Estadual Paulista (Botucatu, SP, Brazil). It was evaluated 3 different photosensitizers: a haematoporphyrin derivative (Photogem®, Russia), glucosamine salt of chlorine (e6) (Photodithazine®, Russia) and MB (Sigma Aldrich®) in different concentrations, incubation times and irradiation parameters. PDT was evaluated on both, zoospores and hyphae

form of the microorganism. The best PDT response was obtained for the Photodithazine reaching 100% of hyphae inhibition and zoospores inactivation. This result agrees with the dye distribution observed on the kinetics study due to its homogeneous distribution inside the cell [10, 11].

***In vivo* assays.** Ten thousand zoospores were injected subcutaneously on New Zealand rabbits and the PDT treatment started when the lesions reached 1 cm in diameter. The Photodithazine was administered intravenously and its presence on the lesion was monitored by laser induced fluorescence spectroscopy. After the dye detection, the PDT treatment started. Histology analysis revealed that the infection was cured in 19 animals. In one animal, the disease affected the bone and, for this reason, the PDT was not effective.

Veterinary clinical case. PDT was evaluated in a horse attended at Veterinary Medicine School from São Paulo State (Universidade Estadual Paulista-UNESP) with pythiosis lesion in fetlock region in right hind limb with 20 centimeter in diameter. The animal also showed compromised of motor function due to lesion size and pain. Surgery resection was performed and twenty-four hours later the photodynamic therapy treatment started. Chlorin e6 diluted in DMSO was injected in different sites of the lesion and the irradiation was carried out using a 660nm diode laser. Immediately after the first PDT session it was observed that the exudate was interrupted and lesion dried. Five days after the procedure it was observed discrete granulation tissue. Fifteen days later, the lesion recurred and a new PDT session was performed. Five days after the second PDT session it was observed healing tissue, recovery of motor function and absence of kunkers. No recurrence was observed within 30 days.

A LED-based device at 660nm was later designed to reduce the PDT illumination time [12].

Conclusions

Photodynamic therapy is an attractive treatment option for the local treatment of infectious diseases, especially for the ones that show low or none response to the available therapies. PDI protocols must be safe for the host tissues and show high microorganism inactivation rates. Effective photodynamic response was observed for onychomycosis and pyhtiosis for the developed instrumentation and PDT parameters.

Acknowledgements

The authors acknowledge the support provided by the Brazilian agencies Capes, CNPq (INOF - INCT: 573587 / 2008-6) and FAPESP (CEPOF-CEPID Program: 2013 / 07276-1).

References

1. B. Zeina, J. Greenamn, W.M. Purcell, and B. Das, *Brit. J. Dermatol*., 2001, **144**, 274-278.
2. T. Maisch, S. Hackbarth, J. Regensburger, et al., *J. German Soc Dermatol*, 2005, **9**, 360-366.
3. P.G. Calzavara-Pinton, M. Venturini, and R. Sala, *J. Photochem. Photobiol*., 2005, **78**, 1-6.
4. Y. Yang, Y. Hu, J. Zhang, et al., *Med. Mycol*., 2012, 1-5.
5. A.K. Gupta, J.E. Ryder, and A.M. Johnson, *Brit. J. Dermatol.*, 2004, **150**(3), 537-544.
6. A.P. Silva, C. Kurachi, V.S. Bagnato, and N.M. Inada, *Photodiag. Photod. Ther*., 2013, **10**, 328-330.
7. L. Mendoza, L. Ajello, and M.R. McGinnis, *J. Mycol. Med*., 1996, **6**, 151-154.
8. M.J. Dykstra, N.J. Sharp, T. Olivry, et al., *Med. Mycol*., 1999, **37**, 427-433.
9. S.M.G. Bosco, E. Bagagli, J.P. Araujo, et al., *Emerg. Infect. Diseases*, **11**, 715-718.
10. L. Pires, S.M.G. Bosco, N.F. Silva, and C. Kurachi, *Veter. Dermatol.*, 2013, **24**, 130-e30.
11. L. Pires, S.M.G. Bosco, M.S. Baptista, and C. Kurachi, *PLOS One*, 2014, **9**(1), e85431.
12. C. Kurachi, V.S. Bagnato, L. Pires, et al., Patent number BR102012008710-A2, 2014.

APPROACHES TO MORPHOLOGIC DIAGNOSTICS OF TUMORS EMPLOYING LASER SCANNING MICROSCOPY

S.S. Kuznetsov[1], V.V. Dudenkova[1,2,3], and **N.M. Shakhova[3]**

[1] State Medical Academy, Nizhny Novgorod, Russia,
zunek@mail.ru
[2]Lobachevsky State University of Nizhny Novgorod, Nizhny Novgorod, Russia
[3]Institute of Applied Physics RAS, Nizhny Novgorod, Russia

Abstract. The paper presents the results of study of native tumor samples of different locations using nonlinear laser scanning microscopy (LSM) in second-harmonic generation (SHG) and two-photon excitation fluorescence (2PEF) modes. The differences in the structure of normal tissues, tumors and metastatic lymph nodes were revealed, with attention paid to the state of collagen and elastin containing structures and, stromal-parenchymal relationship. The potential of LSM in intraoperative rapid diagnosis of tumors and their metastases was evaluated. Employment of two-photon excitation following by spectral selection of fluorescence and backscattering SHG combines high spatial resolution, minimal time requirements, and no need of pre-histological staining of samples, which allows to detect alterations that are not visible with the routine microscopy.

Development of organ-preserving treatment techniques in oncology requires development of novel diagnostic techniques. Intraoperative rapid diagnosis is of key importance as it should provide under time constraints the data, which determine the amount of surgical intervention: diagnosis of the tumor, the differential diagnosis of malignant and benign tumors, the presence of cancer cells at the resection line [1]. Additionally, the information on specific molecular features of tumors is of importance. In the study of surgical specimens it is important to obtain such information from the native tissue without special preparation and staining of samples. In recent years the potential of 2PEF microscopy for such studies has been investigated [2, 3]. The studies mainly focus on such objects as the skin; the technique was also applied for the diagnosis of gliomas [4, 5]. Thus, development of a technique that can be applied to a wide range of tumors is a topical problem. The aim of present paper is to study the potential of 2PEF microscopy for detection of endogenous fluorophores and spectral features of *ex vivo* native tumor tissue (biopsy and postoperative samples) from different localizations.

The study employed laser scanning confocal microscope CarlZeiss LSM 510META. Femtosecond laser MAITAIHP (SpectraPhysics) with a pulse repetition rate of 80 MHz and a duration of about 100 femtoseconds was used as a source of exciting radiation. Samples of breast and colon tumors were studied. Elastin and collagen were studied as endogenous fluorescent markers of unaltered and tumor tissues. It is known that collagen and elastin have very similar absorption and emission spectra, therefore the excitation wavelength of 800 nm (the upper limit of elastin two-photon absorption spectrum [6]) was used. In this case, elastin can be imaged due to its multiphoton fluorescence, while collagen, which is an anisotropic medium, generates the second harmonic of probing laser radiation. The use of two-photon excitation provides high image quality and imaging depth compared to the single-photon confocal mode because scattering and absorption of NIR radiation in tissues are smaller compared to those of UV or visible range. This nonlinear mechanism of excitation provides better localization of excitation in the bulk sample. Detection was performed simultaneously in the two channels using filters in the range of 362-415nm and 480-554nm. At the excitation power of 5 mW this approach allowed to visualize the structure of elastin and collagen fibers in unstained samples. As a result of the selective detection of the signal from collagen and elastin the obtained images were composed of two channels: signal from collagen (backscattering SHG), multiphoton fluorescence from elastin; an overlap of these two images provides the structure of the samples.

Our study revealed differences in structure of normal tissues and tumors. For example, in adenocarcinoma of the colon, in addition to general disorders of tissue anatomical structure blurring of cell and basal membranes contours accompanied by their thinning were observed. At the same time we detected reduction of elastin content in basal membrane of tumor glandular-like complexes. Simultaneously we found decrease of mucus production by tumor cells, which is typical for normal epithelial cells of the colon, and appears in the images as intracellular dark round inclusions. Moreover, the intensity of mucus production was higher in well-differentiated tumors compared to poorly differentiated tumors. In the lamina propria of the colon the content of collagen and elastin was almost the same with a slight predominance of collagen elements. Stroma of colorectal adenocarcinomas differed by shift of this ratio towards elastin prevalence, more prominent in well-differentiated tumors.

The opposite trend is noted in comparison of structure of normal breast tissue with its infiltrating carcinoma, namely, reduction of elastin content relative to normal tissue can be observed in neoplasm. Similar to adenocarcinomas of the colon, we detected blurring of the contours of membrane structures of cells and tumor complexes. In normal mammary gland we identified various content and distribution of collagen and elastin in its structural and functional elements. Thus, in parts of acinar lobules we detected considerably larger collagen content compared to interlobular connective tissue, where the prevalence of elastin was noted.

In the study of a lymph node using nonlinear LSM we noted visualization of the inspected object structural elements: the germinal centers of the follicles, mantle zone, and interfollicular areas. At the same time, the structure of myelinated cords, sinuses and capsule of the node were not clearly distinguished, which requires special attention in further studies. In the lymph node with metastasis of cancer (colon adenocarcinoma) we revealed complete destruction of the structure with displacement of the lymphoid tissue with carcinoma metastases. Collagen and elastin content in metastatic complexes was equal to that in the tumor node (in the colon).

In the elastin detection channel the local signals of high intensity were found from individual cells. Since the excitation was performed at a wavelength of 800 nm while fluorescence was detected in the range of 480-554nm, this range also includes the signal from the leukocyte and macrophage lysosomes. In the study of lymph node with metastasis of cancer, such cells were found in smaller amount, which allows us to conclude on the possible development of the immune response block due to tumor growth (specific influence of tumor on the response of lymphoid tissue).

To conclude, currently we have shown that:

– Technique of using multiphoton excitation followed by spectral selection of fluorescence and backscattering SHG combines high spatial resolution, the minimal time requirement, and no need to pre-staining of histological samples;

– Different collagen and elastin content in different tumor types allows differentiating not only between benign and malignant tumors, but also carcinomas of various degrees of differentiation;

– Employment of the technique allowed to determine the signs of blocking the immune response of lymph node tissue in case of metastasis, which potentially can be used for early diagnosis of metastases not visible by conventional methods of morphological, and requires further investigation.

Thus, selective visualization and further evaluation of collagen and elastin condition are of interest for the diagnosis of cancers and their lymphogenous metastases in course of intraoperative rapid biopsies. LSM visualization of endogenous fluorophores for detection of malignant tumors and their biological features requires further study.

Acknowledgements

The work was supported by grant from the Russian Foundation for Basic Research (No. 15-42-02572 and 15-42-02658).

References

1. Rodolfo Laucirica, *Arch Pathol Lab Med.*, 2005, **129**, 1565-1574.
2. W.B. Amos and J.G. White, *Biology of the Cell*, 2003, **95**, 335-342.
3. F. Helmchen and W. Denk, *NatMethods*, 2005, **2**(12), 932-40.
4. Laiho et al., *J Biomed Opt*,. 2005, **10**(2), 024016.
5. J. Leppert, et al., *Neurosurgery*, 2006, **58**(4), 759-67.
6. J. Mertz and L. Moreaux, *OptCommun*, 2001, **196**, 325-330.

Invited

THE STUDY OF RADIATION-INDUCED DAMAGE OF HUMAN RECTUM AFTER PREOPERATIVE RADIATION THERAPY BY OPTICAL METHODS

A.V. Maslennikova[1,2], M.V. Kochueva[1], S.S. Kuznetsov[1], V.V. Dudenkova[2,3,1], E.B. Kiseleva[1], and **K.V. Babak[2]**

[1] Nizhny Novgorod State Medical Academy, 10/1 Minina Sq., Nizhny Novgorod, Russian Federation
maslennikova.anna@gmail.com
[2] N.I. Lobachevsky Nizhny Novgorod State University, 23 Gagarina Pr., Nizhny Novgorod, Russian Federation
[3] Institute of Applied Physics of RAS, 46 Uljanova St., Nizhny Novgorod, Russian Federation

Abstract. The work objective was studying the dynamics of radiation-induced changes of normal tissues by multiphoton microscopy (MPM). MPM is based on non-linear processes such as two photon-excited fluorescence (TPEF) from endogenous fluorophores and second harmonic generation (SHG) from non-centrosymmetric molecules (collagen). Fourteen patients (12 underwent preoperative radiation therapy for rectal cancer in a total dose of 40 Gy or 50.4 Gy, single dose 2 Gy, and two patients who underwent only surgery were enrolled. Surgery was performed in 4–6 weeks after completing the radiation therapy. MPM-imaging of normal rectal tissue was performed by LSM 510 Meta (Carl Zeiss, Germany) with femtosecond Ti-Sa laser MAI TAI HP (Spectra Physics, USA). MPM-images of rectal tissue after irradiation were characterized by irregularity and blurring of collagen fibers and bundles, the decrease of number of collagen-bearing structures and other signs reflecting the processes of collagen degradation. MPM microscopy allows evaluating radiation-induced changes of normal tissues after ionizing radiation and gets information in addition to standard and special histological staining.

Radiotherapy, like all other cancer treatment modalities, not only results in beneficial effects with regard to tumor control, but also is associated with side effects in disease-free normal tissues. One of the crucial mechanisms of the development of late radiation adverse events is the activation of the synthesis of the excessive amount of collagen in irradiated tissues that can lead to radiation induced fibrosis. That is why the study of the processes of radiation induced damage and subsequent remodeling of collagen in organs that were included into planning treatment volume is of great importance. Organs that are frequently affected by pelvic radiotherapy are the urinary bladder and the rectum, as they are included in the treatment field of a wide variety of tumors, namely malignancies of prostate, uterus/cervix etc. New optical tools that provide information about structure and function of biological tissues open the opportunity of studying the processes of radiation-induced damage and consequent remodeling. MPM is based on non-linear processes such as two photon-excited fluorescence (TPEF) from endogenous fluorophores and second harmonic generation (SHG) from non-centrosymmetric molecules. The main endogenous fluorophores are NADH, NAD(P)H, flavoproteins, lipofuscin, elastin, melanin and metal-free porphyrins. Our work objective was to study if MPM may give additional information about radiation-induced changes in normal tissues that were included into the treatment volume in the course of radiation therapy.

From February 2014 to October 2014, fourteen patients were enrolled into the study. Twelve patients underwent preoperative radiation therapy (PRT) for rectal cancer in a total dose of 40 Gy or 50.4 Gy, single dose 2 Gy. Two patients underwent surgery only for the disease. Surgery was performed in 4–6 weeks after completing the radiation therapy. Samples of normal rectal tissue were fixed in 10% neutral formalin and embedded in paraffin. Paraffin-embedded material was sectioned on the slices 10 μm thick and the slices were deparaffinized and studied by LSM 510 Meta (Carl Zeiss, Germany) with femtosecond Ti-Sa laser MAI TAI HP (Spectra Physics, USA). The study was performed with following settings: excitation wavelength 800 nm, registration at two wavelength ranges: 362–415 nm for detecting SHG signals from collagen fibers and 512–576 nm for detecting two photon-excited fluorescence from elastin. The excitation light was focused onto the sample using 40x (NA 1.3) objective with oil immersion. The same material was prepared using Van Gieson (for collagen) staining. This staining is a standard method of estimation of tissue collagen and was used as a method of comparing with LSM images.

MPM-images of non-irradiated rectum demonstrated a stratified structure with well-delineated epithelium, basal membrane and lamina propria and an accurate border between epithelium and submucosa. Collagen and elastin structures formed smooth bundles of various thickness situated in one direction. All structures are clearly determined. Crypts are of the same size, form and location. A basal membrane presents a thin smooth line of the same thickness with an ordered fiber's structure on all its extent. Lamina propria presents a combination of smooth muscle fibers and connective tissue fibers. Muscle fibers have equal size, form and direction (Fig. 1).

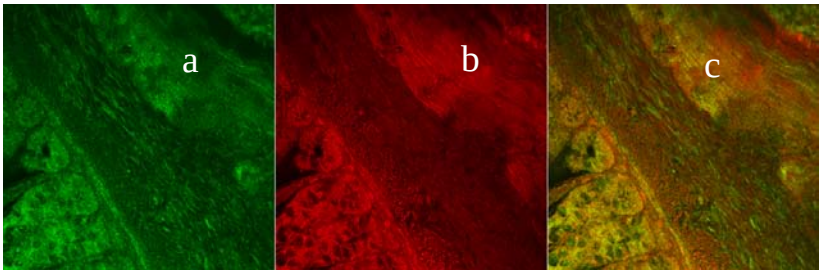

Fig. 1. MPM-images of non-irradiated rectum. Image size 202x202 μm.
a – SHG signals from collagen fibers, b – 2PEF signals from elastin, c – merged image

In 4–6 weeks after RT completing MPM-images of rectal tissue demonstrated essential disorders of normal structure reflecting first of all the processes of collagen and elastin degradation and disorganization (Fig. 2). We observed a loss of stratified mucosal structure, changes of epithelial cells, and a decrease of epithelial layer thickness. The basal membrane was thickened due to tissue edema. Muscle fibers became gyros and thickened, there were foci of fiber's breaks and replacement of damaged bundles by connective tissue. Collagen and elastin fibers demonstrated a loss of ordered structure and direction with a decrease of number of connective tissue structures. The contours of collagen and elastin fibers became blurred and unclear, the fibers were of variable thickness, the thickened fibers prevailed because of continued edema and swelling. Besides, instead of ordered bundles and fibers we observed a chaotic fibers distribution, essentially in the submucosa layer. The disorganization, fragmentation and disorientation of smooth muscle fibers and bundles was observed too. In general, all this manifestations reflect the processes of local degradation of extracellular matrix.

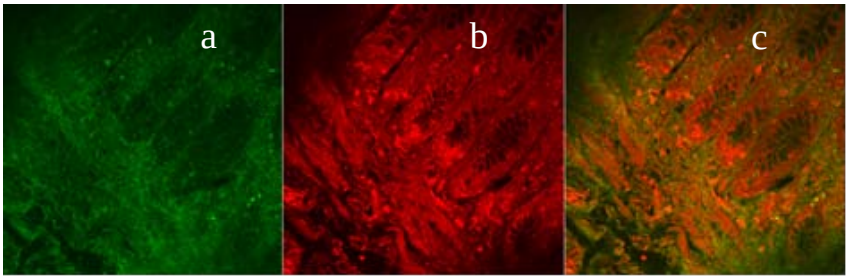

Fig. 2. MPM-images of rectum in 4 weeks after RT in a dose of 40 Gy. Image size 202x202 μm,
a – SHG signals from collagen fibers, b – 2PEF signals from elastin, c – merged image

Acknowledgements

Russian Foundation for Basic Research (## 13-02-00436 and 15-42-02658) for financial support.

References

1. K.-R. Trott, W. Doerr, A. Facoetti, J. Hopewell, et al., "Biological mechanisms of normal tissue damage: Importance for the design of NTCP models", *Radiotherapy & Oncology*, 2012, **105**(1), 79–85.
2. J.W. Denham and M. Hauer-Jensen, "The radiotherapeutic injury – a complex 'wound", *Radiotherapy & Oncology*, 2002, **63**(2), 129-145.
3. A. Alex, J. Weingast, M. Weinigel, et al., "Three-dimensional multiphoton/optical coherence tomography for diagnostic applications in dermatology", *J. Biophotonics*, 1–12 (2012)/ DOI 10.1002/jbio.201200085.

PDT IN ENDOSCOPY: PILOT CLINICAL STUDY

A.A. Mitrakov[1], R.S. Alieva[1], N.A. Razina[1], M.N. Kuzin[1], E.I. Efimova[1], N.N. Mitrakova[2], S.V. Gamayunov[1,3], and **N.M. Shakhova[3,4]**

[1] Regional Oncological Hospital, Nizhny Novgorod, Russia
alexandr_mit@mail.ru
[2] Republic Clinical Hospital, Cheboksary, Russia
[3]State Medical Academy, Nizhny Novgorod, Russia
[4]Institute of Applied Physics RAS, Nizhny Novgorod, Russia

Abstract. Photodynamic therapy (PDT) is a modern technique that can be employed for treatment of localized and advanced forms of cancer in situations when standard treatment is unacceptable. PDT can serve as a basic or supplementary treatment, and as a radical or palliative method. Results of PDT of lung, esophageal, laryngeal and gastric cancer are shown in this study. Our first results of endoscopic PDT demonstrated good tolerance of this technique, absence of complications and side effects. None of patients with localized cancer has died because of primary tumor progression. In advanced cancer the quality of life was improved and lifetime was increased. Endoscopic PDT requires further investigation and optimization.

Lung, gastric, esophageal and laryngeal cancers are the leading cause of death among oncological diseases [1]. Photodynamic therapy (PDT) is a modern technique that can be employed for treatment of both localized and advanced forms of cancer [2, 3]. In some cases standard treatment like surgery, radiotherapy or chemotherapy is unacceptable for many reasons: advanced age, severe comorbidity, or multiple tumors. PDT is an alternative treatment technique in such situations. PDT can serve as a basic or supplementary treatment, and as a radical or palliative method [4].

PDT of lung, esophageal, laryngeal and gastric cancer has been introduced into practice in the Nizhny Novgorod Regional Oncological Hospital since October 2012. 26 patients have undergone PDT with total of 48 PDT procedures (22 repeated procedures). Patient cohort included 9 patients with gastric cancer (7 localized, 2 advanced), 9 patients with esophageal cancer (3 localized, 6 advanced), 6 patients with lung cancer (one localized, 5 advanced), 2 patients with laryngeal cancer. Photoditazin (with absorption peak at 662 nm) was used as a photosensitizer for PDT. Photoditazin was administered intravenously in dose of 1 mg/kg followed in 1.5–2.0 hours by endoscopic illumination using 662 nm laser. Depending on type and localization of a tumor cylindrical or front light illumination mode was selected with power density of 300 mW/cm^2, and corresponding energy density of 150–300 J/cm^2. Local anesthesia was applied. After the procedure patients followed less-light regimen during two days.

Follow-up period varied from 2 to 26 months. Endoscopy examination was used for monitoring of PDT results in survived patients once in 2 months. The results were evaluated using following criteria: endoscopic data, mortality, complications, patient treatment satisfaction, symptom relief and survival.

Two patients with advanced gastric cancer died, survival period after PDT was 13 and 21 months. One patient with localized gastric carcinoma died because of advanced tumor of other localization (lung cancer). Six patients with localized gastric carcinoma remain alive with good quality of life (QOL) and without signs of progression, with follow up period varying from 5 to 26 months.

In group with esophageal cancer (follow up period from 2 to 12 months): 4 patients are alive with good quality of life and without signs of progression, 5 patients died (1 patient with localized form died of advanced laryngeal carcinoma, 4 patients with advanced form had survival periods 2, 5, 8 and 12 months after PDT with satisfactory QOL).

In lung cancer group: 3 patients died in 4, 5 and 6 months after PDT, 3 patients are alive with good quality of life and without signs of progression for up to 18 months.

The period of observation in laryngeal cancer patients ranged from 8 to 24 months, both patients are alive.

No mortality or complications associated with PDT were registered. All patients expressed satisfaction with treatment. All survived patients (15 patients in total) did not reveal functional disorders. In radical treatment there are no signs of stenosis, in cases of palliative treatment (tumor recanalization) quality of life became significantly better compared to that before PDT.

The first results of endoscopic application of PDT demonstrated good tolerance of this technique, absence of complications and side effects. None of patients with localized cancer has died because of primary tumor progression during the period from 5 to 26 month. In cases of advanced cancer the

quality of life was improved and lifetime was increased after PDT comparing to average survival period [5]. Endoscopic PDT requires further investigation and optimization. More accurate assessment of tumor invasion is desirable to improve PDT outcomes. Technological approaches we are working to solve concern increasing the accuracy of dosimetry and development of real time monitoring.

Acknowledgements

The authors thank the Russian Basic Research Foundation (14-02-00753) and the Ministry of Education and Science of Russian Federation (project RFMEFI60414X0027, contract № 14.B25.31.0015) for the financial support of this work. The authors are also grateful to the staff and management of the Nizhny Novgorod Regional Oncological Hospital for the possibility to conduct this study.

References

1. http://www.cancer.org/research/cancerfactsstatistics/cancerfactsfigures 2014.
2. T. Yano, K. Hatogai, H. Morimoto, Y. Yoda, and K. Kaneko, "Photodynamic therapy for esophageal cancer", *Ann Transl Med*., 2014, **2**(3), 29.
3. C.B. Simone and K.A. Cengel, "Photodynamic therapy for lung cancer and malignant pleural mesothelioma", *SeminOncol*., 2014, **41**(6), 820-30.
4. T. Nakamura, H. Fukui, M. Fujita, T. Fujimori, and Y. Ishii, "Photodynamic therapy (PDT) combined with tumor reduction for advanced gastric cancer", *Gastrointestinal Endoscopy*, 2000, **51**(4), Part 2, AB258.
5. M.J. Aarts, B.E. van den Borne, B Biesma, J.S. Kloover, J.G. Aerts, and V.E. Lemmens, "Improvement in population-based survival of stage IV NSCLC due to increased use of chemotherapy", *Int J Cancer*, 2015, **136**(5), E387-95.

THE ROLE OF OPTICAL DIFFUSE SPECTROSCOPY AND ULTRASONOGRAPHY IN COMPLEX EVALUATION OF PREOPERATIVE POLYCHEMOTHERAPY EFFICIENCY IN PATIENTS WITH BREAST CANCER

M.V. Pavlov[1], **M.A. Gorozhantseva**[2], **P.V. Subochev**[3], **G.Yu. Golubyatnikov**[3], **A.G. Orlova**[3], **I.S. Shumskaya**[5], **N.M. Shakhova**[3], and **A.V. Maslennikova**[2,4]

[1] Regional Oncological Clinic, Nizhny Novgorod, Russia
pavlov.med@mail.ru
[2] Nizhny Novgorod State Medical Academy, Nizhny Novgorod, Russia
[3]Institute of Applied Physics RAS, Nizhny Novgorod, Russia
[4]N.I.Lobachevsky State University, Nizhny Novgorod, Russia
[5] Medical center "Pryoksky", Nizhny Novgorod, Russia

Abstract. Modern standards of breast cancer (BC) treatment suggest extensive use of preoperative hormone therapy and chemotherapy; however, techniques for prediction of individual tumor response to treatment are not currently available. The aim of the study was to analyze the response to treatment in patients with breast cancer at stage II-IV, who received neoadjuvant chemotherapy (NACT). Another aim was to propose approach to the early assessment of NACT efficiency. One hundred seven patients were enrolled; tumor response to chemotherapy was assessed in respect to age, stage, tumor immunophenotype and chemotherapy protocols. To develop a technique for predicting tumor response to preoperative treatment, a combined use of optical diffusion spectroscopy (ODS) and ultrasonography was proposed. ODS technique allowed to determine the dynamics of tumor oxygenation in course of NAPCT, while ultrasound examination was used to assess the dynamics of blood flow in neoplasms.

Breast cancer is a polymorphic disease from the point of view of morphology and pathogenetics, characterized by a spectrum of different biological features. Due to the extensive use of preoperative chemotherapy, it is important to find criteria to predict the sensitivity of breast cancer to drug exposure. The main criteria, which reflect changes in the neoplasms metabolism, are its oxygenation level and vascular channel features [1, 2]. The aim of the study was the analysis of tumor response in patients treated with NACT, and the study of potential of complementary application of optical diffuse spectroscopy and ultrasonography for monitoring of preoperative chemotherapy in patients with breast cancer.

The first part of the study included analysis of 107 clinical cases of patients with breast cancer at stage II-IV who received NACT. Tumor response was evaluated in respect to age, stage of disease, immunohistochemical characteristics and NACT protocol by means of statistical processing engine SPSS with Spearman rank correlation. The second part of the study included a pilot clinical study of the response of breast cancer tumors to preoperative chemotherapy basing on data oxygenation level changes. Experiments were performed on the experimental setup with parallel plane geometry and single source and detector pair created at the Institute of Applied Physics RAS (Nizhny Novgorod, Russia). Three laser fibers coupled in a single bundle illuminate the studied volume at 684 nm, 794 nm, and 850 nm. The images were acquired by simultaneous scanning of source and detector facing each other. During DOS imaging, subjects were placed in a prone position on a padded examination platform with the breast to be imaged pendant between to plates; this setup is similar to the imaging geometry used in prone breast biopsy. The plates were moved into contact with the breast and breast was compressed lightly to maintain a homogeneous imaging volume during each imaging session. Obtained images were processed with MathCad, and concentrations of main indicators, influencing tissue oxygenation (oxygemoglobin, deoxygemoglobin, total hemoglobin and oxygen saturation) were reconstructed. The region of interest (tumor zone) was countered manually with ImageJ program according to previous mammograms.

Blood flow dynamics in course of NACT was studied by ultrasonography. Scanning was performed employing "Medison Accuvix-V20" setup (Samsung, Korea) using multifrequency linear sensor with range of 5.0–13.0 MHz in power Doppler mode.

The retrospective study did not reveal close correlation between tumor response to treatment and age ($r = 0.010$; $p = 0.000$), tumor stage ($r = 0.064$; $p = 0.006$), NACT protocol ($r = 0.116$; $p = 0.016$) and tumor immunophenotype ($r = 0.172$; $p = 0.003$). (Fig. 1).

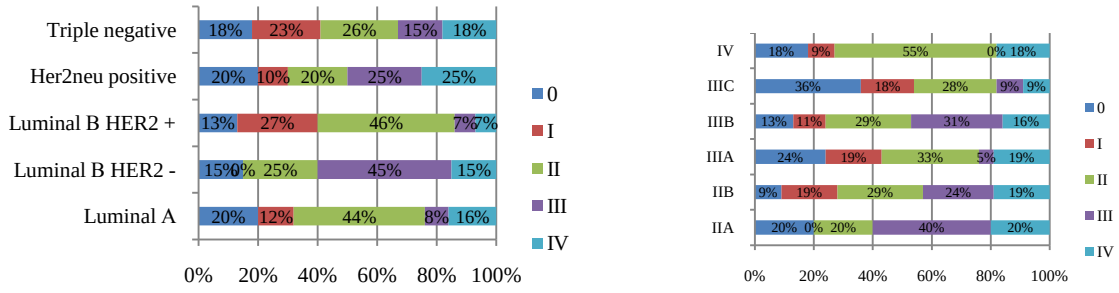

a) r = 0.172 b) r = 0.064

Fig. 1. Tumor response to treatment depending on tumor immunophenotype:
no correlation (a), Tumor response to treatment depending on tumor stage: weak correlation (b)

In the ODS study of the oxygenation level dynamics were identified (8 clinical cases were included in the analysis). Dynamics of tumor oxygen state (comparison between an oxygenation trend and pathomorphologic response) was evaluated. The main predictive criterion allowing evaluating chemotherapy effectiveness appeared to be a trend of tumor oxygenation changes. Complete response (necrosis, the absence of viable cells) correlated with an increase of tumor oxygenation comparing with its initial level after the first cycle of chemotherapy. Incomplete response correlated with a decreased or stable tumor oxygenation.

Original protocol of ultrasound inspections was developed to determine the blood flow dynamics in tumor in course of NAPCT. Scanning of the tumor and peripheral zone was performed with transversal step of 50 mm in mutually perpendicular planes. The obtained images were processed in the Matlab environment, which allowed calculating the ratio of the number of colored pixels to the total number of pixels in the selected volume. This allowed to correctly comparing data on tumor blood supply before treatment and in course of NAPCT (Figure 2).

Fig. 2. Tumor in B-mode (a), Tumor in power Doppler mode (b),
Numerical processing in Matlab environment (c)

Our studies show that such parameters as patient age, tumor stage and immunophenotype cannot be used as predictors of tumor response. Tumor response to chemotherapy is correlated with the dynamics of tumor oxygenation in course of treatment which can be employed to predict the effects of therapeutic procedures. Evaluation of the potential of ultrasonography for predicting the NAPCT efficiency basing on the dynamics of tumor blood supply and blood flow requires further studies.

Acknowledgements

The authors thank the Foundation for Assistance to Small Innovative Enterprises in the scientific and technical sphere and Russian Foundation for Basic Research (#15-42-02528) for the financial support, as staff of Nizhny Novgorod Oncology Clinic for making this study possible.

References

1. P. Vaupel, "Hypoxia and Aggressive Tumor Phenotype: Implications for Therapy and Prognosis", *The Oncologist*, 2008, **13**(3), 21–26.
2. B.J. Tromberg, A. Cerussi, N. Shah, et al., "Imaging in breast cancer: Diffuse optics in breast cancer: detecting tumors in pre-menopausal women and monitoring neoadjuvant chemotherapy", *Breast Cancer Res*., 2005, **7**, 279–285.

Invited

SPECTRAL MONITORING DURING ALA-BASED IPDT

A. Rühm, H. Stepp, W. Beyer, M. Hermwille, J. Rudrof, R. Sroka

Laser-Forschungslabor, LIFE-Zentrum, Klinikum der Universität München, München, Germany,
Adrian.Ruehm@med.uni-muenchen.de

Abstract. Spectral monitoring of inter-fiber signals during iPDT reveals a variety of behaviors of transmitted excitation light, autofluorescence and PPIX fluorescence. The time and distance dependence of these signals were investigated.

Objective

The success of fluorescence guided resection (FGR) for the treatment of malignant glioma [1–4] has also stimulated research efforts to utilize the underlying biophysical effects therapeutically by means of interstitial photodynamic therapy (iPDT) [5–7]. Being able to identify potential responders of such kind of treatment in advance would be highly desirable [8–10].

Materials and Methods

During iPDT treatment of glioblastoma based on 5-aminolevulinic acid (5-ALA) induced protoporphyrin IX (PpIX), light applicators are stereotactically placed into the tumor region after careful dosimetry planning [5–7]. The applicators can be used for light delivery to the tumor, but also for light collection and detection [11]. The light propagating from each applicator to each other applicator can thus be recorded before and after the PDT treatment for monitoring purposes. Using a spectrometer for detection allowed to separately analyze a) the excitation light of 633 nm wavelength which is simply transmitted between two applicators and b) the PpIX fluorescence light of ~704 nm wavelength which predominantly arises from the vital tumor regions illuminated in each case. In order to identify relevant information with regard to treatment response [8-10], the obtained spectral data were processed and analyzed in different ways.

Results

In all cases the PpIX fluorescence was bleached completely after the PDT treatment. The transmission of the treatment light usually decayed to some extent during PDT. The transmission of the treatment light and the fluorescence intensity measured between each applicator pair did not show a monotonous decay with increasing applicator distance (Fig. 1). The comparison of the data with model calculations points to local inhomogeneities of the optical properties within the treated tissue region. Based on simplifying assumptions, the mean value of the effective attenuation coefficient μ_{eff} within the tissue as well as local deviations of the absorption coefficient μ_{a} from the corresponding mean value could be derived.

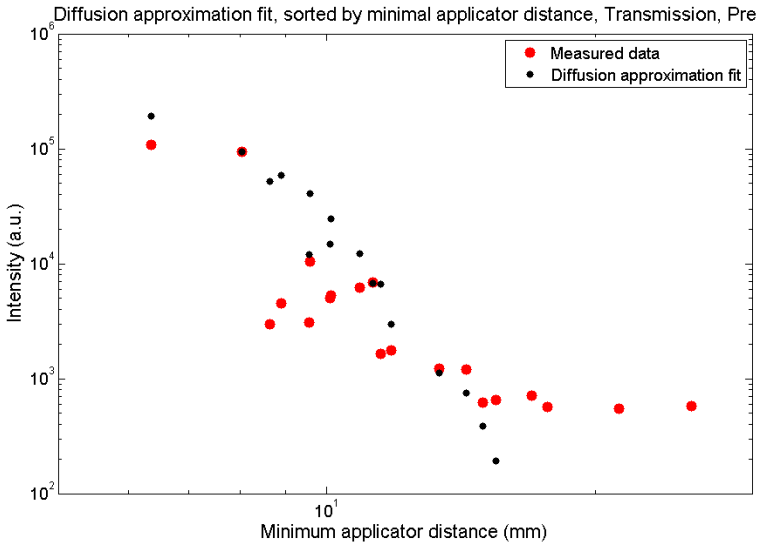

Fig. 1 Transmitted excitation light intensity measured between applicator pairs, plotted as a function of the minimum distance between the two applicators in each case

Conclusion

The obtained spectral data provides novel additional information which might be suitable to describe individual treatment conditions. Further analysis of the distance dependence of such data might allow to characterize the distribution of the treatment light within an inhomogeneous tissue volume in advance. This information could eventually be used to optimize the treatment planning for the benefit of the treatment outcome on an individual basis.

References

1. W. Stummer, A. Novotny, H. Stepp, C. Goetz, K. Bise, and H.-J. Reulen, *J. Neurosurg.*, 2000, **93**(6), 1003-1013.
2. W. Stummer, U. Pichlmeier, T. Meinel, O. D. Wiestler, F. Zanella, H.-J. Reulen, and the ALA-Glioma Study Group, *Lancet Oncol.*, 2006, **7**(5), 392-401.
3. H. Stepp and W. Stummer, In: *Optical Methods and Instrumentation in Brain Imaging and Therapy*, S. Madsen (Ed.), Springer, 2013, 173-205.
4. J. T. Liu, D. Meza, and N. Sanai, *Neurosurgery*, 2014, **75**(1), 61-71.
5. T. J. Beck, F.-W. Kreth, W. Beyer, J. H. Mehrkens, A. Obermeier, H. Stepp, W. Stummer, and R. Baumgartner, *Lasers Surg. Med.*, 2007, **39**(5), 386-393.
6. A. Johansson, H. Stepp, T. Beck, W. Beyer, T. Pongratz, R. Sroka, T. Meinel, W. Stummer, F.-W. Kreth, J.-C. Tonn, and R. Baumgartner, *Proc. SPIE 7380: Photodynamic Therapy: Back to the Future*, David H. Kessel (Ed.), Seattle, USA, 2009, 73801D.
7. A. Johansson, F.-W. Kreth, W. Stummer, and H. Stepp, *IEEE J. Sel. Topics in Quantum Electron.*, 2010, **16**(4), 841-853.
8. A. Johansson, F.-W. Kreth, A. Ardeshiri, W. Stummer, O. Schnell, J. Herms, G. Palte, W. Beyer, and H. Stepp, *Proc. SPIE 7715: Biophotonics: Photonic Solutions for Better Health Care II*, J. Popp, W. Drexler, V. V. Tuchin; D. L. Matthews (Eds.), Brussels, Belgium, 2010, 77151M.
9. A. Johansson, G. Palte, O. Schnell, J.-C. Tonn, J. Herms, and H. Stepp, Photochem. Photobiol., 2010, **86**(6), 1373-1378.
10. A. Johansson, F. Faber, G. Kniebühler, H. Stepp, R. Sroka, R. Egensperger, W. Beyer, and F.-W. Kreth, *Lasers Surg. Med.*, 2013, **45**(4), 225-234.
11. A. Rühm, H. Stepp, W. Beyer, G. Hennig, T. Pongratz, R. Sroka, O. Schnell, J.-C. Tonn, and F.-W. Kreth, *Proc. SPIE 8928: Optical Techniques in Neurosurgery, Neurophotonics, and Optogenetics*, H. Hirschberg, S. J. Madsen, E. D. Jansen, Q. Luo, S. K. Mohanty, N. V. Thakor (Eds.), San Francisco, United States, 2014, 89280E.

ANALYSIS OF DIFFERENT LASERS APPLICATION FOR ENT PATHOLOGY

M.A. Shakhova[1], A.B. Terentyeva[1], V.I. Kochenov[1], D.A. Sapunov[2], L.B. Snopova[1], V.I. Bredikhin[3], V.A. Kamensky[3], and **A.V. Shakhov[1]**

[1] State Medical Academy, Nizhny Novgorod, Russia, maha-shakh@yandex.ru
[2] Regional Hospital, Nizhny Novgorod, Russia
[3] Institute of Applied Physics RAS, Nizhny Novgorod, Russia

Abstract. Laser surgery is a method of choice for treatment of several ENT pathologies. In this paper we overview our 30 years of experience in laser surgery in ENT. Total of 850 clinical cases were analyzed. The following devices were employed for laser surgery: CO_2 laser "Romashka 2", YAG:Nd laser at 1.06 μm and 1.32/1.44 μm, diode laser at 1.56 μm, Alta®-ST at 0.98 μm. Continuous wave mode with variable power up to 10 W was applied. Results of study show that Proper selection of regimes and techniques for laser scalpel applications depending on morphologic and functional object features are the key to a good clinical outcomes.

In recent decades employment of laser radiation as a factor of physical action in otorhinolaryngology became a perspective direction. Laser surgery is a method of choice for treatment of several pathologies, in particular, early forms of malignant tumors. This choice is governed by the following features of laser application: minimizing intraoperative blood loss, prevention of secondary infection and adherence to the basic principle of oncology – ablastics [1]. The proper choice of laser radiation parameters is the key for optimal clinical outcome. Morphological and functional features of ENT determine the possibility of complications in case of improper choice of laser surgery mode [2].

In Russia laser technologies are employed in ENT practice since 1970s for treatment of a wide range of pathological states: hypertrophic rhinitis, recurrent epistaxis, hypertrophic pharyngitis, chronic sub- and decompensated tonsillitis, scar deformation of the trachea and larynx, disorders of larynx innervation, benign and malignant tumors [3]. In this paper we overview our 30 years of experience in laser surgery in ENT [4].

The study is performed at the ENT Department of Regional Clinic and Medical Academy. Analysis of laser surgery experience since 1982 is conducted .The following devices were employed for laser surgery: CO_2 laser "Romashka 2", YAG:Nd laser at 1.06 μm and 1.32/1.44 μm (IAP RAS, Russia), diode laser at 1.56 μm (IRE-Polus, Russia), Alta®-ST at 0.98 μm (Dental Photonics, Inc) in continuous wave mode with variable power up to 10 W applied.

Total of 850 clinical cases were analyzed within the frames of the study including following pathologies: otitis media with effusion, chronic sub- and decompensated tonsillitis, hypertrophic pharyngitis, hypertrophic rhinitis, laryngeal and tracheal stenosis, disorders of larynx innervation, benign tumors of the nasal cavity, pharynx and larynx, laryngeal carcinoma.

CO_2 laser "Romashka 2" was employed in our clinic since the beginning of 1980s for optimization of larynx carcinoma surgery in frames of complex approach in combination with cryosurgery.

The laser scalpel was employed for surgical access in course of laryngectomy to minimize blood loss and for laser vaporization of the tumor in case of unilateral lesion of the larynx (35 cases). This allowed to optimize the immediate (two-fold reduction in the number of postoperative complications) and long-term (two to five fold reduction in the number of recurrences depending on the stage) results of larynx cancer treatment. Complications of laser surgery (mainly, the destruction of cartilage) were registered at advanced cancer stages and amounted to no more than 10%. The disadvantage of the CO_2 scalpel "Romashka 2" was the impossibility to use it in endoscopic procedures.

The appearance of YAG: Nd laser at 1.06 μm in the clinic in the early 1990s allowed to expand the indications for laser surgery due to the possibility of fiber delivery of laser radiation to the sites with difficult accessibility. Since that time the development of such surgical procedures as the removal of benign and malignant tumors of the nasal cavity and pharynx, lacunotomy in case of chronic tonsillitis has been started. Introduction of fiber delivery of laser radiation at a wavelength of 1.06 μm also provided a minimally invasive access for surgery of the larynx for removal of benign and malignant tumors.

However, weak absorption at the wavelength of 1.06 μm resulted in development of such complications as perforation of the nasal septum, expressed collateral inflammatory reaction, laringeal stenosis. The total number of complications of laser surgery during 2 years of using YAG: Nd laser at 1.06 μm reached 14%, including 10% which required surgical correction (tracheostomy, reconstruc-

tion of defects of the nasal septum, surgical hemostasis, excision of the scar deformations), in 4% therapeutic correction (anti-inflammatory treatment) was effective.

The advanced setup modality employing variable wavelength of 1.32 μm /1.44 μm provided more efficient laser cut which allowed not only to reduce the incidence of complications associated with cartilage damage, but also apply laser surgery to correct these complications. However, weak absorption of this radiation in blood required additional hemostasis. Complications of this period (6.5%) were mainly related to the intra-operative bleeding which required ligation of the large vessels in three cases (1.5%). Another drawback of the YAG: Nd system was its ergonomic characteristics: dimensions and requirement for water cooling.

The experience gained allowed for more frequent use of laser surgery in routine clinical practice for a wide range of pathologies. A portable and user-friendly diode laser with the wavelength of 1.56 μm was introduced into practice. During this period laser tympanotomy for treatment of exudative otitis media was learnt. Immediate and long-term results of using this setup are comparable with the use of the setup at 1.32 μm /1.44 μm.

Currently a portative intellectual laser system Alta®-ST at 0.98 μm with functional properties optimized due to computer-controlled tip initiation is employed in the clinic. Due to relatively small amount of clinical results only preliminary conclusions concerning its safety, efficiency and usability can be made. Conducted experiments with biotissues (both ex vivo and in vivo) demonstrate efficient laser cut with minimal zone of collateral tissues damage (up to 350 μm). Results of chronic experiment indicate optimization of healing processes.

Development and improvement of laser systems and techniques for radiation delivery allows to design new laser based medical technologies. In recent decades, photodynamic therapy was introduced into ENT, which may substitute laser surgery, for example, in such cases as laryngeal papillomatosis, as PDT is able to significantly reduce the number or even eradicate specific microbial pathogens [5].

However, it is worth mentioning that laser surgery remains the method of choice in wide range of ENT pathologies. Proper selection of regimes and techniques for laser scalpel applications depending on morphologic and functional object features are the key to good laser surgery outcomes.

Acknowledgements

The authors thank the Russian Science Foundation (grant “The Use of Laser Induced Nonequilibrium Processes in Medical Technologies” No. 14-15-00840) for the financial support of this work and the hospital staff and management for the possibility to conduct this study.

References

1. S.M. Zeitels, J.A. Burns, G. Lopez-Guerra, R.R. Anderson, and R.E. Hillman, *Ann Otol Rhinol Laryngol Suppl.,* 2008, **199**, 3-24.
2. Y. Yan, A.E. Olszewski, M.R. Hoffman, P. Zhuang, Ch.N. Ford, S.H. Dailey, and J.J. Jiang, *J Voice,* 2010, **24**(1), 102-109.
3. V.P. Minaev, *Quantum Electronics,* 2005, **35**(11), 976-983.
4. A.V. Shakhov, A.B. Terentjeva, V.A. Kamensky, et al., *J. of Surg. Oncology,* 2001, **77**(4), 253-58.
5. M.G. Bredell, E. Besic, C. Maake, H. Walt, *J Photochem Photobiol,* 2010, **101**(3), 185-90.

Invited

INTERSTITIAL TECHNIQUES IN BIOPHOTONIC

R. Sroka, N. Markwardt, G. Scheib, B. Hollnburger, N. Dominik, A. Rühm, and **H. Stepp**

LIFE-Center, University Hospital of Munich, Munich, Germany
herbert.stepp@med.lmu.de

Abstract. Clinical laser light application in bulky tissue is often related to interstitial techniques which require specific characterization of the light emitting system. In case of receiving light information from inside of bulky tissue knowledge about light detection characteristics is recommended. Three approaches are presented related to specific questions. First the emission and detection characteristic of cylindrical diffusers are investigated with the aim to use inter-diffusor signals for light dosimetry during interstitial PDT. Second the potential of interstitial measurement using side-detecting fibers to derive optical properties of tissue are investigated. Finally investigations on fluorescence guidance during interstitial biopsy extraction are presented.

Introduction

Interstitial Photodynamic Therapy (iPDT) using cylindrical diffusors, as shown in figure 1, looks promising for treatment of this disease. In order to make this kind of treatment as safe, accurate and reliable as possible a couple of precondition should be taken into consideration prior to, during and after treatment and should be included in confident treatment concept. With regard to this question about the safety of a trajectory a cylindrical diffusor is positioned or biopsy should be taken may arise. In addition to this it should be confirmed that the tumor accumulated the photosensitizer. For treatment planning the emission characteristics of diffusors should be taken into account to perform an ideal distribution of several fibers for adequate and uniform illumination. During iPDT information from signals of inter-fiber crosstalk may give hints about bleeding and bleaching effects, which in addition needs information about the optical properties of the tissue in between [1, 2]. This presentation showed efforts and approaches to receive such signal to potentially improve this kind of treatment.

Investigations

Emission characteristics of commercial available cylindrical diffusors were measured and simulated to derive the optical properties of the specific diffusor. In fig. 1 (left) a summary of such an investigation is shown. It can be derived that measured and simulated emission characteristic are nearly identical, showing also light at unintended positions, e.g. nearby the tip of the fiber. Based upon these information in the following step the detection characteristic are measured and simulated which is a prerequisite to start with inter-diffusor crosstalk investigation, as shown in fig. 1 (right).

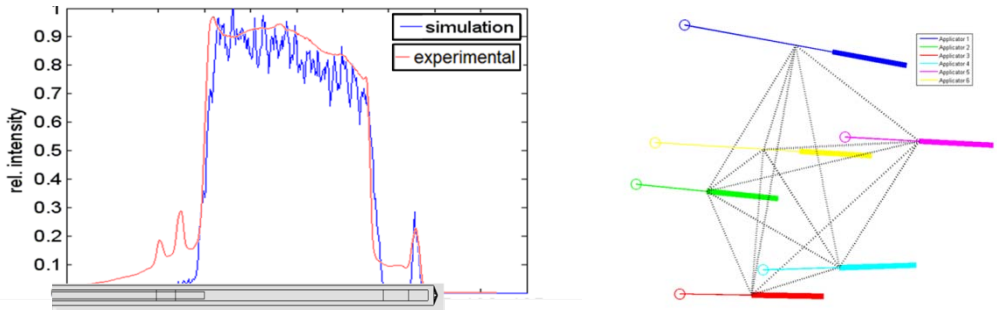

Fig. 1. *Left*: Measured and simulated emission characteristic of a commercial available cylindrical diffusor. *Right*: Sketch of inter-diffusor cross-talk [2]

Minimally invasive investigation of tissue optical properties within the tissue can be performed by turning a side-detecting fiber placed interstitially while light is emitted from an interstitial light source [3]. In a first approach this technique was tested in liquid phantoms (Fig. 2 left) and optical parameters were derived using theory proposed in the literature (Fig. 2 right) and compared to known values [4].

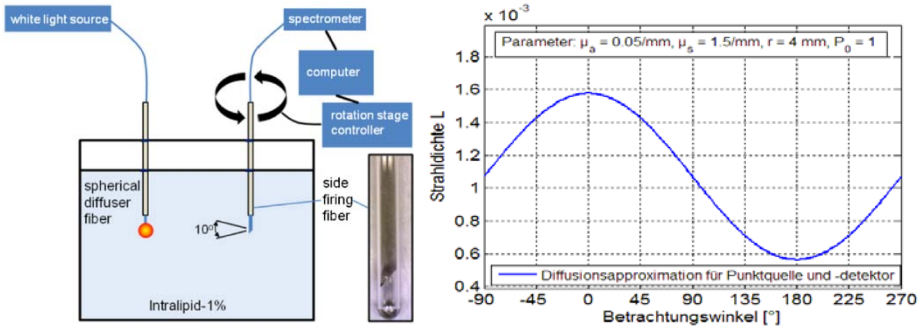

Fig. 2. Left: Experimental set-up to investigate optical properties by use of a side-detecting fiber. Right: Sinusoidal signal detection as function of the turning angle from which the optical parameter can be derived

A fiber-based mechano-optical device for stereotactic biopsies is developed (Fig. 3) [4, 5]. Two different fluorophores are employed to improve its safety and reliability. The fluorescence of intravenously applied indocyanine green (ICG) facilitates the recognition of blood vessels and thus helps minimize the risk of cerebral hemorrhages. 5-aminolevulinic-acid-induced protoporphyrin IX (PpIX) fluorescence is used to localize vital tumor tissue. ICG fluorescence detection using a 2-fiber probe turned out to be an applicable method to recognize blood vessels about 1.5 mm ahead of the fiber tip during a brain tumor biopsy. Moreover, the suitability of two different PpIX excitation wavelengths regarding practical aspects was investigated: While PpIX excitation in the violet region (at 405 nm) allows for higher sensitivity, red excitation (at 633 nm) is noticeably superior with regard to blood layers obscuring the fluorescence signal.

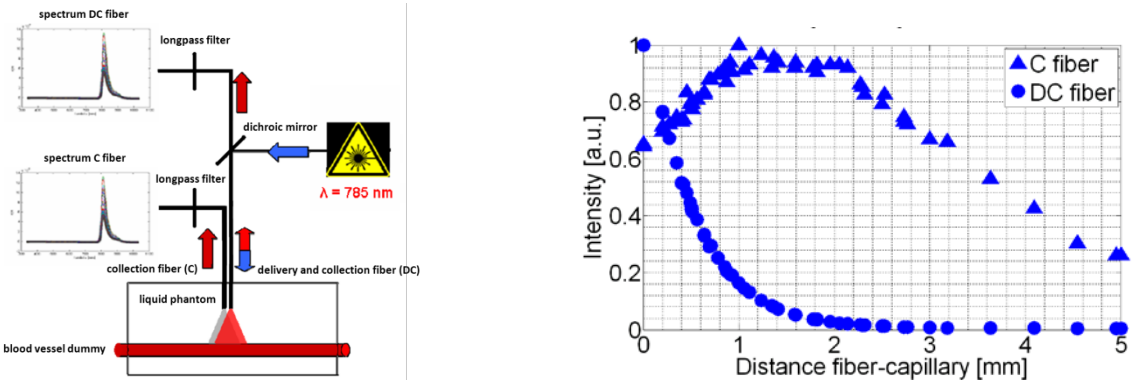

Fig. 3. Left: Principle of 2-fiber-probe device for interstitial fluorescence detection.
Right: Detected signals of C and DC fiber as function of the distance of fluorescence occurrence

References

1. A. Rühm, H. Stepp, W. Beyer, G. Hennig, T. Pongratz, R. Sroka, O. Schnell, J.-C. Tonn, and F.-W. Kreth, "5-ALA based photodynamic management of glioblastoma", *Proc. SPIE*, 8928; *Optical Techniques in Neurosurgery, Neurophotonics, and Optogenetics*, 89280E; doi:10.1117/12.2040268.
2. A. Rühm, H. Stepp, W. Beyer, M. Hermwille, J. Rudrof, R. Sroka, and F.-W. Kreth, "Spectral monitoring of stereotactic interstitial PDT of glioblastoma", *Part of European Conferences on Biomedical Optics. Medical Laser Application and Tissue Interaction*, 2015 Munich.
3. A. Liemert and A. Kienle, "A novel analytical solution for the radiance in an anisotropically scattering medium," *Applied Optics*, 2015, **54**(8), 1963-1964.
4. T. Beck, et al., "Clinical determination of tissue optical properties in vivo by spatially resolved reflectance measurements," *Proc. SPIE, Photon Migration and Diffuse-Light Imaging*, 2003, **5138**.
5 H. Stepp, W. Beyer, D. Brucker, A. Ehrhardt, S. Fischer, W. Goebel, M. Goetz, B. Guenther, G. Hennig, J. Herms, K.-M. Irion, A. Johansson, Y. Kienast, G. Kniebuehler, P. Li, A. Ruehm, and S. Sandner, "Fluorescence guidance during stereotactic biopsy", *Proc. SPIE 8207, Photonic Therapeutics and Diagnostics VIII*, 82074H; doi:10.1117/12.915751.
6 N. Markwardt, A. von Berg, S. Fiedler, M.-H. Goetz, N. Haj-Hosseini, C. Polzer, H. Stepp, P. Zelenkov, and A. Rühm, "Optical spectroscopy for stereotactic biopsy of brain tumors", *Part of European Conferences on Biomedical Optics. Medical Laser Application and Tissue Interaction*. 2015 Munich.

RISK OF URINARY TRACT INFECTION IN LASER LITHOTRIPSY

O.S. Streltsova[1], D.P. Pochtin[2], T.P. Katalagina[2], and **V.A. Kamensky[3]**

[1]State Medical Academy, Nizhny Novgorod, Russia, strelzova_uro@mail.ru
[2] Regional Hospital, Nizhny Novgorod, Russia,
[3]Institute of Applied Physics RAS, Nizhny Novgorod, Russia

Abstract. In this paper we perform comparative analysis of infection risk in course of lithotripsy of concrements. The *in vitro* analysis includes mechanical fragmentation in a liquid, laser fragmentation in a liquid, and laser fragmentation in the air. We show that laser lithotripsy fight again infection much more efficiently comparing to mechanical fragmentation. We also show that in laser lithotripsy covering the distal end of the fiber with strongly absorbing layer will allow to employ different laser systems without custom selection of the wavelength, which can make the procedure of laser lithotripsy more cost-effective.

Percutaneous nephrolithotripsy (PCNL) with the high-power lasers is an effective and safe treatment for patients with large renal stones. It is demonstrated to be more efficient for large size of the stones in the upper urinary tract compared to shockwave lithotripsy (SWL) [1, 2]. Nevertheless, postoperative complications are probable; one of the serious complications is life-threatening infection, which can be triggered by dissemination of microorganisms due to fragmentation [3–5]. The essential mechanism determining the efficiency of the procedure is the photothermal mechanism leading to chemical decomposition of urinary calculi [6], which in its turn depends of proper laser choice for particular calculi chemical composition. The most common modality is holmium:yttrium-aluminium-garnet (Ho: YAG) lithotripsy. The erbium:yttrium-aluminium-garnet laser is suspected to be more efficient, however there is a problem with the fibers for delivery of radiation with corresponding wavelength [5]. Thus, the study of the potential of various laser devices for increase of lithotripsy efficacy, decrease of complications rate and optimization of equipment costs is of importance. The aim of this work is the search for laser lithotripsy technique allowing for effective fragmentation of renal calculi in combination with a minimal microbial dissemination.

The study was performed at the Urology Clinic of Nizhny Novgorod State Medical Academy in collaboration with Institute of Applied Physics RAS. Ex vivo lithotripsy of the stones obtained by nephro-litho-extraction was performed. A total of 22 procedures were performed with stones of different chemical composition with a density up to 1200 H by Hounsfield scale and up to 2 cm in size. In 10 cases (45%) the objects before fragmentation were infected: in 6 cases by E.coli, in 2 cases by Enterococcus faecalis, and in 2 cases by Ps.aeruginosa. Three regimes of action were employed: mechanical fragmentation in a liquid, laser fragmentation in a liquid, and laser fragmentation in the air.

Mechanical fragmentation was performed using a lithotriptor. Laser fragmentation was performed using the iAlta®-ST device (980 ± 10 nm, output power up to 25 W) with a computer-controlled tip initiation. Lithotripsy was performed in a Petri dish in the presence of a sterile liquid (saline solution), thereby reproducing the model of fragmentation in the natural liquid medium (urine). In case of laser fragmentation in air the fragments were placed in a saline solution after crushing. For comparative evaluation of microbial dissemination due to fragmentation bacteriological examination of the liquids containing the fragments after lithotripsy was conducted. A total of 22 bacteriological examinations were conducted (10 after mechanical fragmentation, 7 after laser fragmentation in a liquid medium, and 5 after laser fragmentation in the air).

Efficient fragmentation of concrements with formation of a large number of small fragments was achieved both under mechanical and laser action. In course of laser lithotripsy the concrements fragments were smaller (1–2 mm) and more uniform in size compared to mechanical lithotripsy, while laser fragmentation in the air was accompanied by melting effect.

Bacteriological examinations revealed that "urine infection" occurred in all 10 cases after mechanical fragmentation: in a liquid a pronounced growth of the microorganism, by which the concrement was infected before fragmentation, was observed, microbial titer ranged from 10^2 to 10^6 colony-forming units (CFU / ml). After laser fragmentation in a liquid dissemination of microorganisms occurred, however, in 5 out of the 7 cases the degree of microbial contamination is lower than that in the case of mechanical fragmentation of the same concrements, the titer ranged from 10^1 to 10^4 CFU / ml. In case of laser fragmentation in the air the melting effect was probably accompanied by initial microorganism inactivation; bacterial growth was not detected in any of the considered cases.

The experiment showed that the effective fragmentation can be achieved by employing lasers with the wavelength different from common systems (Ho: YAG) due to initiation of the distal end of the fiber with strongly absorbing chemical. This leads to heating of the fiber end, and destruction occurs due to thermal energy. Concomitant physical and chemical processes may contribute to inactivation of microorganisms through several mechanisms: direct exposure to high temperatures, generation of high-frequency ultrasound in a place of fiber-concrement interaction, formation of hydrogen peroxide as a result of dissociation of 0.01% of the water molecules to hydrogen and hydroxyl radicals during heating within the bubbles formed [7]. However, this aspect requires further studies.

Our results allow making preliminary conclusions. The technology of covering the distal end of the fiber with strongly absorbing layer will allow to employ different laser systems for lithotripsy without custom selection of the wavelength, which can make the procedure of laser lithotripsy more cost-effective. The potential of the proposed technique with respect to the prevention of microorganism dissemination and inflammatory complications requires further study.

Acknowledgements

The authors thank the Russian Science Foundation (grant "The Use of Laser Induced Nonequilibrium Processes in Medical Technologies" No. 14-15-00840) for the financial support of this work and the hospital staff and management for the possibility to conduct this study.

References

1. Y. Sun, X. Gao, T. Zhou, et al., *J Endourol.*, 2009, **23**(10), 1687-91.
2. S.S. Bapat, K.V. Pai, S.S. Purnapatre, et al., *J Endourol.*, 2007, **21**(12), 1425-7.
3. Y.C. Jou, C.H. Shen, M.C. Cheng, et al., *Urology*, 2007, **69**(1), 22-5; discussion 25-6.
4. Y.C. Jou, J.H. Shen, M.C. Cheng, et al., *Urology*, 2005, **65**(3), 454-8.
5. J.M. Teichman, *Curr Opin Urol.*, 2002, **12**(4), 305-9.
6. K.F. Chan, G.J. Vassar, T.J. Pfefer, et al., *Lasers Surg Med*, 1999, **25**(1), 22-37.
7. V.I. Yusupov, V.M. Chudnovskii, and V.N. Bagratashvili, *Laser Physics*, 2011, **21**(7), 1230-1234.

LASER-BASED METHODS FOR NONINVASIVE OUTCOME PROGNOSIS OF SURGICAL TREATMENT OF VESICO-VAGINAL FISTULA

O.S. Streltsova[1], V.N. Krupin[1], M.V. Mamonov[2], and **A.S. Vorobyova[2]**

[1] State Medical Academy, Nizhny Novgorod, Russia, strelzova_uro@mail.ru
[2] Regional Hospital, Nizhny Novgorod, Russia

Abstract. In this paper we report on employment of optical diagnostic techniques for monitoring the outcome of vesico-vaginal fistula treatment. Cross-polarization optical coherence tomography (CP OCT) and laser Doppler flowmetry (LDF) were employed for monitoring of surrounding tissues allowing to monitor inflammatory processes and evolution of blood microcirculation. The combination of CP OCT and LDF demonstrated high potential to become the aims for complementary assessment of the readiness of bladder tissues for surgery, which will personalize and objectify prediction of the results of surgical treatment and to optimize the timing of the surgical correction of vesico-vaginal fistula.

Vesico-vaginal fistula is a severe complication of pelvic cellulitis, radiation therapy, or gynecologic surgery [1]. In patients with recurrent fistulas plastics of fistula is performed not earlier than 6–8 months after the formation of a fistula, which significantly worsens the patient's life quality. Cystoscopic visual evaluation of tissues around the fistula fails to adequately assess their condition, justify the need for therapeutic preparation and optimal timing of surgical treatment. In this respect, the development of additional diagnostic techniques for this pathology is required [2, 3]. The aim of present study is to develop approaches to non-invasive diagnostics of tissues of vesico-vaginal fistula in order to define criteria for readiness for surgical treatment.

In Urology Department of Regional Hospital 26 surgical treatment procedures on vesico-vaginal fistula were performed in the last 7 years. Recurrences of fistula in the early postoperative period were observed in 15.4% of cases (4 out of 26). In order to reduce the recurrence rate the diagnostics of tissues surrounding the fistula using a combination of cross-polarization optical coherence tomography (CP OCT) and laser Doppler flowmetry (LDF) techniques was proposed.

Totally 6 patients were enrolled in the study employing combination of techniques and 10 patients were enrolled in LDF study. For OCT inspection the "OCT 1300 U" system (IAP RAS, Nizhny Novgorod, Russia) was used with following parameters: probing central wavelength of 1300 nm, image acquisition time of 2 sec, spatial resolution of 20–25 μm, and imaging depth up to 2 mm. In the course of endoscopic manipulations the flexible probe (outer diameter of 2.7 mm) was inserted into the instrumental channel 8Ch of a cystoscope and pressed under visual control to the bladder area of interest.

Inspection of microcirculation around the fistula was performed employing laser analyzer of capillary blood flow "LAKK-02" (SPE "LAZMA", Russia) at the wavelength of 0.63 μm with exposition time of 2 minutes. LDF provides data averaged over a large number of erythrocytes, analyze hemodynamics in real time, and to evaluate the contribution of active and passive mechanisms of microcirculation. Blood flow was analyzed near the edges of the defect from the bladder side and in 1.5–2 cm away from the fistula, as well as in unaltered bladder wall. The following parameters of microcirculation were evaluated: modulation of blood flow in the microvasculature, standard deviation (σ) and variation coefficient characterizing the ratio of the tissue perfusion to its variability (K_v) and calculated by the formula

$$K_v = \sigma / \text{ПМ} \times 100\%$$

A total of 24 CP OCT images were obtained, followed analysis revealed zones of local inflammatory process in all studied patients. Typical changes in the CP OCT images indicated the presence of exudative and proliferative cystitis, and atrophy of the epithelial layer at the border of fistula. Analysis of microcirculation showed that the most pronounced changes were revealed at the edge of the fistula. Recovery of the microcirculation to the level of the intact areas was observed in 2 cm from the edge. Along with the study of the level of tissue blood perfusion the oxygen saturation level in tissue was recorded. Following disorders of microcirculation were revealed in fistulas and surrounding tissues: reduction of PM and σ at the background of Kv exceeding that of unaltered tissues, indicating the in-

creased neurogenic tonus of arterioles and arterioles-venular anastomoses, and, hence, deep metabolic disorders.

The revealed alterations became the reason for anti-inflammatory therapy. After finishing the treatment noninvasive monitoring of tissue condition was performed by CP OCT and LDF techniques. Upon registering appropriate characteristics of the tissues around the fistula the surgical treatment was carried on. In case when the noninvasive techniques indicated preserving of alterations the pre-operative treatment continued. In the presence of persistent inflammatory changes revealed by the CP OCT and / or LDF the possible recurrence was predicted.

Thus, the CP OCT technique allowed for noninvasive real-time visualization of structural disorders of the bladder and the vagina tissues, to differentiate local inflammatory alterations, and monitor conservative preparation and readiness of tissues for surgical intervention. The LDF technique allowed for real-time assessment of microcirculation, which is also a criterion of readiness for surgical correction of a vesico-vaginal fistula.

Currently, a number of factors, including the size of the fistula, are treated as predictors of the surgical correction efficiency [4]. However, this parameter does not allow to optimize the timing of surgical treatment. The combination of CP OCT and LDF demonstrated high potential to become the aims for complementary assessment of the readiness of bladder tissues for surgery, which will personalize and objectify prediction of the results of surgical treatment and to optimize the timing of the surgical correction of vesico-vaginal fistula.

Acknowledgements

The authors thank the Russian Science Foundation (grant No. 14-15-00538) for the financial support of this work and the hospital staff and management for the possibility to conduct this study.

References

1. T.H. Hsu, R.R. Rackley, J.B. Abdelmalak, S. Madjar, and S.P. Vasavada, *Urology*, 2002, **59**(4), 597-9.
2. C. Andreoni, H. Bruschini, J.C. Trazzi, R. Simmetti, and M. Srougi, *J Urol*, 2003, **170**, 2330-2332.
3. J. Stoker, E. Rociu, W.R. Schouten, and J.S. Laméris, *AJR Am J Roentgenol***,** 2002, **178**, 737-741.
4. J.L. Ockrim, T.J. Greenwell, C.L. Foley, D.N. Wood, and P.J.R. Shah, *BJU*, 2009, **103**, 1122-1126.

WORKSHOPS

Tumor and Stem Cells Biology

Chairs

Igor Adameyko
Karolinska Institutet, Sweden

Lothar Lilge
Princess Margaret Cancer Centre, University of Toronto, Canada

Angelika Rűck
Universitat Ulm, Germany

Invited

INDIVIDUAL ECTOMESENCHYMAL CLONES ORGANIZE THE FACE BY LOCAL MULTILINEAGE DIFFERENTIATION WITHOUT SIGNIFICANT MIGRATION

I. Adameyko

Karolinska Institutet, Stockholm, Sweden
igor.adameyko@ki.se

Abstract

Facial region represents highly integrated and still enigmatic compartment that demonstrates high degree of coordination between different cellular sources and differentiating structures during embryonic development. Building up the skeletal elements, especially in the head, has been extensively studied in the past. However, no consensus exists today about how embryos control precise and complex geometries of their cartilages, bones and joints. Our hypothesis implies that controlled allocations of the organized polarized cellular micro-domains provide precise sculpting and scaling up various cartilaginous structures in the body. We clearly see similar logic in activity of dental mesenchymal stem cells and cell fate choice in populations of pulp cells and odontoblast during teeth development and continuous growth. Relatively small geometrically simple or complex clonal envelopes serve as tissue units that can be increased in numbers or in size to scale up the structure without shape loss or drastic distortion. At the moment we succeeded with mathematical model simulating shape-related aspects of morphogenesis in 3D. In this model we can place progenitor cells anywhere in the virtual tissue, we can introduce migration, change cell division speed and allocation of daughter cells, use gradients of attractants and orienteers etc. The best feature of the model includes clonal analysis in 3D+ time with mathematical assessment of order and geometry in the whole resulting tissue that is comparable to the experimental natural tissue dynamics. Understanding tissue dynamics during development and regeneration is a key for much future advancement. For example, hundreds of human mutations leading to congenital abnormalities have been identified. However, in most cases we are missing the understanding of what is happening between the gene and the phenotype, i.e. how the collective cellular behavior is translated into morphofunctional outcome. We are filling fill this conceptual niche through understanding cellular behavior and mechanisms in shape-making. In general, we utilize multiple transgenic animals allowing us to dissect the role of different signaling pathways in shape-making of skeletal elements. To experimentally address our hypothesis we also use advanced genetics tracing with multicolor reporters, single cell transcriptomics, mathematical modelling and 3D-imaging of the entire developing skeletal structures in the context of the whole body using micro-computed tomography (CT). At the moment we develop and upgrade techniques for high contrast micro-CT imaging that allows us segmenting cartilage and mesenchymal condensations with 50 micrometer resolution. In a pilot experiment we developed a novel approach of contrasting embryos with salts of tungsten acid that provides significantly improved contrast. We also do microsurgery and grafting, live imaging of zebrafish as well as *ex vivo* organoid cultures with microfluidics-based artificial gradients to understand the logic of the fate induction and deposition of cartilaginous elements in space.

THE STUDY OF INTRACELLULAR HYDROGEN PEROXIDE LEVEL AND CELL DEATH MECHANISMS IN HELA CELLS UNDER CISPLATIN TREATMENT

A.S. Belova[1,2], A.G. Orlova[1,2,3], I.V. Balalaeva[2], N.N. Razumkova[2], A.V. Maslennikova[1,3], N.M. Mishina[3,4], N.M. Shakhova[1,3], E.V. Zagaynova[3], and **V.V. Belousov[3,4]**

[1] Institute of Applied Physics of the Russian Academy of Sciences, Nizhny Novgorod, Russia
belova-as@mail.ru
[2] Lobachevsky State University of Nizhni Novgorod, Nizhni Novgorod, Russia
[3] N. Novgorod State Medical Academy, Nizhny Novgorod, Russia
[4] Shemyakin-Ovchinnikov Institute of Bioorganic Chemistry, Moscow, Russia

Abstract. The goal of the study was the investigation of the level of hydrogen peroxide in tumor cells *in vitro* after exposing them with cisplatin. Cell line of human cervical carcinoma HeLa Kyoto, expressing the cytosolic sensor for hydrogen peroxide HyPer2 was used. Sensor reaction has been estimated using flow cytometry after 24-hours incubation with drug in different concentrations. In parallel staining of cisplatin-treated cells with dye on apoptosis and vital dye was performed. Increase of the intracellular hydrogen peroxide amount as well as percentage of apoptotic cells was detected. We can conclude that H_2O_2 take part in HeLa Kyoto response on cisplatin exposure. Detected response was not the consequence of cell death.

Introduction

Chemotherapy is one of the main methods of treatment of malignant tumors. Some of the methods are based on the sensitivity of cancer cells to oxidative stress; reactive oxygen species play a crucial role in the implementation of the cytotoxic action of anticancer drugs. One of the most interesting forms of ROS is hydrogen peroxide (H_2O_2), which is a signaling molecule. Cisplatin - a chemotherapeutic drug used in clinical practice for the treatment of a wide range of tumors. This medicine is not only causes DNA damage [1], but also induces the production of reactive oxygen species (ROS) that can initiate tumor cell death [2, 3]. In our study we checked whether hydrogen peroxide participate in cell death process under cytotoxic effect of cisplatin.

Materials and Methods

Experiments were performed on cell line of human cervical cancer HeLa Kyoto transfected with cytoplasmic sensor of hydrogen peroxide – HyPer2 (HeLa Kyoto-HyPer2) [4]. Taking into account pH sensitivity of HyPer2 we made additional experiments with H_2O_2-insensitive analog of HyPer2 – sensor of pH HyPer2-C199S (HeLa Kyoto-HyPer2-C199S cell line) [5].

In our experiments concentrations of cisplatin causing loss of viability of 50% of cells (IC50) for both cultures were determined and were statistically indistinguishable. So for both cell lines we used the same concentrations of cisplatin: IC50 – 2.5 μg/ml, 4 × IC50 – 10.0 μg/ml, 10 × IC50 – 25 μg/ml. Incubation time with medicine was 24 hours.

For flow cytometry Phycoerythrin (PE) Annexin V and 7-Amino-actinomycin (7-AAD) were taken. Annexin V conjugated with PE is a marker of apoptosis. 7-AAD is a vital dyes that stain dead cells only. This combination allows identify viable cells (PE Annexin V negative and 7-AAD negative); early apoptotic cells (PE Annexin V positive and 7-AAD negative), cells in late apoptosis, necrosis or dead cells (both PE Annexin V and 7-AAD positive, PE Annexin V positive and 7-AAD negative). Wavelengths of lasers used for excitation of dyes were 488 and 635 nm. Fluorescence of PE Annexin V and 7-AAD was measured with a 585/42 nm filter and a 670 LP filter. HyPer2 reaction assessment was performed using data on changes of fluorescence intensity under excitation at single wavelength – 488 nm [4].

Results

We observed that in both cell lines percentage of early apoptotic cells rise with increase of concentration of cisplatin. The highest number of cells in early apoptosis was detected upon effect of drug concentration corresponded to 4 × IC50. After incubation with 10 × IC50 almost all cells were dead (fig. 1). Treatment with cisplatin caused two types of HyPer2 reaction: appearance of population of cells with low HyPer2 fluorescence and increase of HyPer2 emission intensity in cells from initial, fluorescent population (fig. 2, left histogram). According to PE Annexin V and 7-AAD staining, low-fluorescent cells belong to dead cells group while fluorescent cells – to group of cells that survived. Fluorescence of HyPer2 of viable cells increased with increasing concentrations of the drug till the

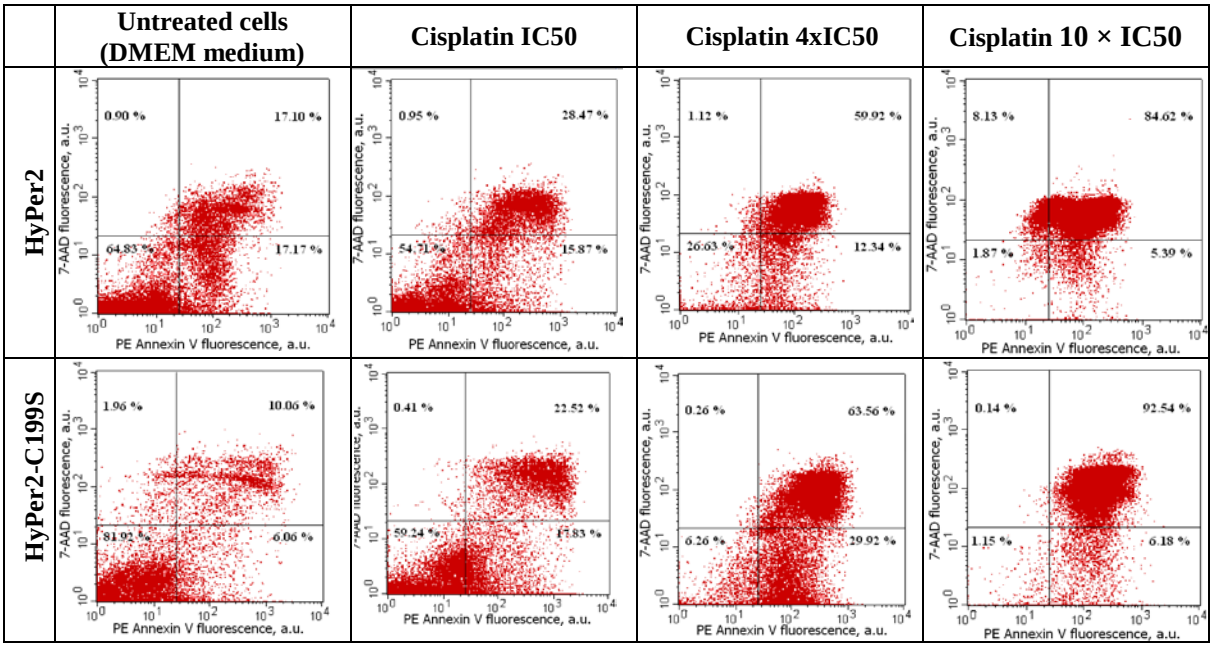

Fig. 1. Results of flow cytometry with PE Annexin V and 7-AAD

concentration 4 × IC50, under that fluorescence of almost all cells was significantly reduced. It is important to note that fluorescence intensity of H_2O_2 insensitive sensor HyPer2-C199S in population of survived cells remains unchanged (fig. 2, right histogram), therefore the observed HyPer2 reaction does not related to pH changes and can be associated with H_2O_2 concentration changes only.

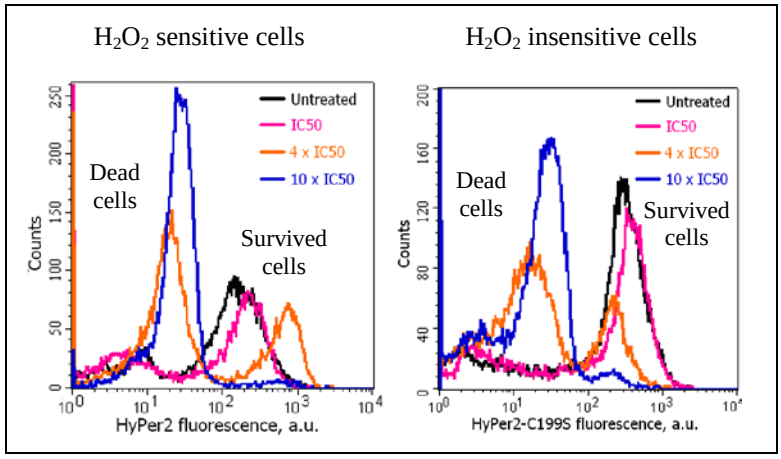

Fig. 2. Fluorescence of HyPer2 and HyPer2-C199S after 24 hours of incubation with different concentrations of cisplatin

Conclusion

Increasing fluorescence of HyPer2 with almost constant level of fluorescence of HyPer2-C199S allows suggest that increasing the concentration of the cisplatin leads to an increase of the amount of hydrogen peroxide. Taking into account that HyPer2 reaction was observed only for viable, non-apoptotic cells, detected response was not the consequence of cell death.

Acknowledgements

This work was supported the Russian Science Foundation, project 14-25-00129.

References

1. K.A. Conklin, *Integrative Cancer Therapies*, 2004, **3**(4), 294-300.
2. G. Manda, M.T. Nechifor, and T.-M. Neagu, *Cur. Chem. Biol.*, 2009, **3**, 342-366.
3. T.P. Szatrowski and C.F. Nathan, *Cancer Res.*, 1991, 5, 794-798.
4. K.N. Markvicheva, D.S. Bilan, N.M. Mishina, A.Yu. Gorokhovatsky, L.M. Vinokurov, S. Lukyanov, and V.V. Belousov, *Bioorganic & Medicinal Chemistry*, 2011, **19**, 1079–1084.
5. D. Poburko, J. Santo-Domingo, and N. Demaurex, *The Journal of Biological Chemistry*, 2011, **286**(13), 11672–11684.
6. K.N. Markvicheva, E.A. Bogdanova, D.B. Staroverov, S. Lukyanov, and V.V Belousov, *Methods in Molecular Biology, Redox-Mediated Signal Transduction - Methods and Protocols*, John T. Hancock (ed.) 2009, **476**, 79-86.

Invited

PHARMACOLOGICAL INHIBITION OF LYSOSOMES STIMULATES LONGITUDINAL GROWTH, AND ACTIVATES THE mTORC1 SIGNALING PATHWAY IN A CHONDROCYTE-SPECIFIC MANNER

P.T. Newton[1,2], K.K. Vuppalapati[1], Th. Bouderlique[1], and **A.S. Chagin**[1,2]

[1] Department of Physiology and Pharmacology, Karolinska Institutet, SE- 17177, Stockholm, Sweden
andrei.chagin@ki.se
[2] Department of Women's and Children's Health, Astrid Lindgren Children's Hospital, Karolinska University Hospital, SE- 17176, Stockholm, Sweden

Key words: mTOR; bafilomycin; chondrocyte; bone; autophagy; lysosome; mTORC1

Mechanistic target of rapamycin complex 1 (mTORC1) is a protein signaling complex at the fulcrum of anabolic (protein synthesis) and catabolic (macro-autophagy) processes, which acts depending on wide-ranging environmental cues. The most important activators of mTORC1 are amino acids. In response to amino acids mTORC1 promotes protein synthesis (via phosphorylation of ribosomal proteins) and simultaneously inhibits autophagy-dependent catabolic activity (via Ulk1/2 kinases). Thus, mTORC1 serves as a intracellular controller of amino acids availability and, in connection to that it adjusts cellular metabolism toward catabolic or anabolic stage.

It is widely accepted that mTORC1 is activated on the surface of lysosomes functional where sensing of amino acids occurs. Furthermore, it is activation by amino acids requires a v-ATPase proton pump, which is downstream of amino acid signal. The exact interaction between v-ATPase and mTORC1 signaling is not precisely evaluated, but it involves interaction between v-ATPase and Ragulator complex on lysosomal membrane. This interaction is amino acids-dependent, and determines activity of Ragulator. In presence of amino acids flux v-ATPase binding with Ragulator is weakened, which allows Ragulator to activated Rag proteins, which in turn acitivate mTORC1. At the same time v-ATPase activity is required for mTORC1 activation and blocking of v-ATPase blocks mTORC1.

However, we found that inhibition of lysosomal activity in chondrocytes (by v-ATPase inhibitors bafilomycin A1 or concanamycin A) potently activated mTORC1 signaling. Activity of mTORC1 was visualized by phosphorylated forms of S6 and 4E-BP1, two well-known downstream targets of mTORC1. Maximal S6 phosphorylation was observed at 48 hours treatment and reached as high as a 12-fold increase ($p<0.018$). Furthermore, in bone organ culture bafilomycin promoted potent stimulation of longitudinal growth associated with the activation of mTORC1 ($p<0.001$). Unwanted cellular material is delivered to lysosomes via macro-autophagy and bafilomycin blocks autophagic flux. We found that lysosomal inhibition activated mTORC1 in autophagy-deficient bones (from Atg5 knockout mice), suggesting a macro-autophagy-independent mechanism of mTORC1 activation. Furthermore, mTORC1 activation was also insensitive to nutrition levels and occurs even in the absence of serum or decreased levels of amino acids.

Thus, our data show that interaction of between mTORC1 and v-ATPase is more complex than it was believed and can involve v-ATPase-dependent inhibition of mTORC1. Furthermore, our data suggest that regulation of mTORC1 pathway can be achieved in a tissue-specific manner.

ASSESSMENT OF FUNCTIONAL ACTIVITY OF CHANG LIVER CELL CULTURE IN BLOOD SERUM OF PATIENTS WITH LIVER DISEASES OF VARIOUS ETIOLOGY

E.I. Cherkasova[1], M.S. Murtazaliyeva[2], T.N. Gorshkova[2], I.L. Novozhilov[1], A.V. Meleshina[3], V.E. Zagainov[3], and **E.V. Zagaynova[3,1]**

[1]Lobachevsky State University of Nizhni Novgorod, Nizhny Novgorod, Russian Federation, e-mail: cherkasova.el@yandex.ru
[2]Volga District Medical Centre under Federal Medical and Biological Agency of Russia, Nizhny Novgorod, Russian Federation;
[3]Nizhny Novgorod State Medical Academy, Nizhny Novgorod, Russian Federation

Abstract. Immortalized cell culture of hepatocytes, Chang liver, is one of the candidates for the use in "bioartificial liver" systems. The aim of the investigation was to evaluate the possibility of using the Chang liver cell culture as a bioreactor cell kit making a complex study of biochemical parameters of its effect on the blood serum of patients with liver diseases of various etiology. The results of complex assessment can be used to determine the efficacy of applying various cell cultures as a model system in the development of "bioartificial liver" systems. Chang liver cell culture, according to the complex assessment results, is most active relative to the blood sera of the "cirrhosis" group of patients with impairments of synthetic and detoxifying liver functions.

At present, the most effective method of treating hepatic failure is liver transplantation: either of the whole organ from the postmortem donor or its fragment from the living relative or postmortem donor, suggesting its future hypertrophy in the post-operative period. To reduce the mortality rate among the patients with liver insufficiency, effective extracorporeal systems are being developed to maintain the liver functions till the time of transplantation, which are capable to perform not only detoxifying [1, 2], but metabolic, synthetic and regulatory functions as well [3, 4]. In this connection, since 80-ies of the last century supporting systems, combining functions of blood/plasma perfusion and cell technologies, have been worked out.

Liver support systems using live hepatocyte cultures — "artificial liver" bioreactors — have been developed. Cultures of hepatocyte-like cells in these systems enrich patient's plasma and blood with the synthesis products (albumin, bile acids, clotting factors and so on) and are capable of partial detoxification. In order to perform effectively bioregulatory and synthetic functions cells must meet several criteria: to perform the functions of a normal liver hepatocyte (detoxification, synthesis of biologically active substances), actively proliferate (accumulating minimum 400 g of biomass volume) in the composition of bioreactor, function in the continuous contact with the plasma of patients having acute liver failure [5].

The aim of the investigation was to evaluate the possibility of using Chang liver cell culture as a cell kit for a bioreactor by a complex study of biochemical parameters of its effect on the blood serum of patients with hepatic diseases of various etiology.

Chang liver cell line (ATCC®CCL-13™; Scientific Research Institute of Virology of Russian Academy of Medical Sciences, Russia) was used in the work. The cells were cultured under standard conditions. Blood sera samples were examined for two groups of patients with hepatic ailments of various etiology. Samples of blood serum from two groups of patients were investigated: patients with obstructive jaundice were included in group 1 "jaundice" (n=9), group 2 "cirrhosis" (n=10) comprised patients with hepatic cirrhosis and hepatocellular jaundice. To study the effect of the cultured Chang liver cells on the patients' blood serum, confluent monolayer of the cells was incubated with serum samples at 37°C in a 5% CO_2 atmosphere with the ratio of $(2.0\text{-}2.1)\cdot 10^5$ cells per 0.105 ml of serum during 12 hours. The maximum time of incubation was chosen for the cells not to lose their metabolic functions [6]. On completion of the process, the values of the main biochemical parameters of synthetic (albumin, urea, transthyretin) and detoxifying (total bilirubin fraction) functions were determined, as well as markers of cell destruction (hepatic transaminases, lactate dehydrogenases).Viability cell changes after exposure to the serum were defined by MTT test. The experimental data were statistically processed using Microsoft Excel and Graf Pad software. The results are presented as $M\pm\sigma$ (SD). Statistical significance of the mean differences was determined by Mann–Whitney criterion.

Statistically significant rise of the albumin level was found to occur in three serum samples of the "cirrhosis" group, but the normal value of albumin was not reached in any case. Elevation of the urea level was noted in three samples, and the level of transthyretin was increased in one sample. Notably,

a positive dynamics of a synthetic function was found in culturing the cells only with the patients' sera of group "cirrhosis", while in sera of group "jaundice" only statistically significant reduction of biochemical values of the synthetic function was observed.

In relation to the detoxifying activity of Chang liver culture, statistically significant reduction of the total bilirubin level was established in four serum samples from group "jaundice". And in three samples positive alterations in the percent composition of its fraction were noted: simultaneous increase of conjugated bilirubin level and reduction of unconjugated one. Similar dynamics of bilirubin fractions together with the reliable reduction of the total bilirubin level was noted in five samples from "cirrhosis" group. Notably, the decrease of the total bilirubin level in the sera after the cell culture effect does not depend on the initial value of this parameter — the reduction occurs both in the samples with low values of the total bilirubin level and with the levels sharply exceeding the norm.

Biochemical components of the sera, in their turn, also influenced hepatocyte vital activity. Sera of the both groups were found to inhibit the life activity of the cells, and the most prominent negative effect was made by the sera of the "cirrhosis" group: the LDG level rose in the samples of all patients, the AlAT one increased in half the cases. Sera from the group "jaundice" did not affect significantly and negatively the cell culture. Besides, the change of vital activity of the cells after their exposure to the sera samples of both groups was determined by MTT-test. Statistically significant reduction of cell vital activity was established to occur after incubation with five of the nine samples from the "jaundice" group, and with six of the ten samples from the group "cirrhosis".

In our work complex evaluation of the biochemical parameters of the synthetic and detoxifying functions, exhibited by Chang liver culture, was used, being highly informative for the assessment of the effect of the cells on the blood sera, and determination of viability of the sells themselves. This model helped investigate the activity of the cell culture relative to the blood serum samples from the patients with hepatic failure. Chang liver culture shows synthetic activity in the sera of the patients of the group "cirrhosis", while the sera of the group "jaundice" do not stimulate the synthetic function of the culture cells.

Detoxifying activity of the Chang liver culture, manifesting itself in the decrease of the total bilirubin level and positive dynamics of its fractions, is observed in both groups, but is most evident in the group "cirrhosis", as it occurs in half the cases. Sera are found to inhibit the viability of the cells in 50% of cases in each group.

Thus, the obtained data led to the conclusion, that Chang liver cell culture is most active in relation to the blood sera of the patients from the group "cirrhosis", where originally significant fall of albumin level and lower values of bilirubin and its fractions were observed.

The results of complex assessment of the main biochemical blood sera parameters can be used to determine the efficacy of application of various cell cultures as a model in the development of "bioartificial liver" systems, and for evaluation of the cell condition within a bioreactor. Immortalized Chang liver cell culture of hepatocytes is one of the candidates for the use in the composition of the artificial systems such as "bioartificial liver".

Acknowledgements

This research was supported by the Ministry of Education and Science of Russia within the state task to perform work in the field of scientific work (basic part) № 2014/134 (Project 2460).

References

1. H.B. Stockmann and J.N. Jzermans, *Eur. J. Gastroenterol. Hepatol.,* 2002, **14**(2), 195–203.
2. I. Sauer, K. Zeilinger, G. Pless, D. Kardassis, et al., *J. Hepatol.*, 2003, **39**(4), 649–653.
3. V.E. Ryabinin, S.I. Grobovoy, S.I. Tkachev, and I.E. Kravchuk, *Vestnik RAMN*, 2002, **3**, 21–24.
4. V.E. Ryabinin, V.I. Suprun, and S.I. Tkachev, *Application of artificial life support systems and cellular technologies in hepatotherapy*, Chelyabinsk, 2007, p. 304.
5. X.-P. Pan and L.-J. Li, *Hepatobiliary. Pancreat. Dis. Int.*, 2012, **11**(6), 594–605.
6. É. Török, C. Vogel, M. Lütgehetmann, et al., *Tissue Eng.*, 2006, **12**(7), 1881–1890.

INVESTIGATION OF pH AND HYDROGEN PEROXIDE IN LIVING CANCER CELLS WITH GENETICALLY ENCODED SENSORS

I. Druzhkova[1], M. Shirmanova[1], M. Lukina[1], V. Dudenkova[1,2], T. Sergeeva[1], V. Belousov[1,3], S. Lukyanov[1,3], and **E. Zagaynova[1,2]**

[1] Nizhny Novgorod State Academy, Nizhny Novgorod, Russia, danirin@yandex.ru
[2] Lobachevsky Nizhny Novgorod State University, Nizhny Novgorod, Russia
[3]Shemyakin-Ovchinnikov Institute of Bioorganic Chemistry RAS, Moscow, Russia

Abstract. The aim of this work is to develop a new approach to register intracellular pH and hydrogen peroxide level with genetically encoded ratiometric sensors. Cancer cells were investigated in monoculture and co-cultures with fibroblasts. The data about changes of pH and hydrogen peroxide level under these conditions were analyzed. pHi mapping of tumors in vivo was performed.

Introduction

It is well known that tumor is a complex tissue consisted of cancer cells, stroma cells, tumor-infiltrated leucocytes, vessels etc. It is generally accepted that cancer cells and cancer-associated fibroblasts (CAF) can change their metabolism to maintain tumor progression and adapt cancer cells to unfavourable conditions [1]. The role of intracellular pH (pHi) and hydrogen peroxide level in the tumor-normal cell interaction is not well understood because their evaluation is a challenge.

Intra-extracellular pH gradients are different in cancer cells and normal cells. Extracellular pH (pHe) of normal tissue is slightly more alkaline than pHi and lies in the range 7.3–7.4, while in tumor tissue it is more acidic (6.2–6.9). It has been hypothesized that such reversed pH gradient is one of the reasons of neoplastic growth and cancer progression [2, 3]. Measuring of pHi in cancer cells and tumor microenvironment can be important for monitoring of cancer progression and response to various treatments [1].

It was shown that hydrogen peroxide works as “fertilizer” to promote tumor growth, progression and metastasis [4].

The aim of this work is to develop a new approach to register intracellular pH and hydrogen peroxide level with genetically encoded ratiometric sensors and to analyze the role of these parameters in cancer-normal cell interactions.

Materials and methods

In this work new genetically encoded sensors, SypHer2 for pHi and HyPer2 for hydrogen peroxide, were used. These proteins belong to the GFP family. They were constructed on the base of yellow fluorescent protein cpYFP and have two excitation picks at 420 nm and 500 nm and an emission pick at 516 nm [5]. Registration of pHi and H2O2 with is based on calculating the ratio of fluorescence intensities I500/I420.

HeLa Kyoto cells, stably transducted with SypHer2 or HyPer2 genes, and human fibroblasts were used. Human fibroblasts were obtained from healthy volunteer and kindly provided by Koltzov Institute of Developmental Biology RAS (Russia). The cells were cultured under standard conditions. The experiments were performed on monolayer cell cultures, 3D tumor spheroids and tumors xenografts. To investigate pHi and hydrogen peroxide level under conditions of interaction of cancer cells with fibroblasts, experiments on co-cultures were performed. The protocol for co-culturing of cancer cells and fibroblasts was modified from Ref. [7].

Calibration of the ratiometric signal for quantitative assay of pHi was made using buffer solutions (130 mM KGluconate, 2 mM $CaCl_2$, 1mM $MgCl_2$, 10 μM nigericin and 30 mM MOPS) [6]. Fluorescence microscopy was performed using an inverted Nikon Eclipse TI N-STORM microscope (Nikon, Japan) or LSM 710 laser scanning confocal microscope (Carl Zeiss, Germany). For *in vivo* imaging of tumors IVIS-Spectrum system (Caliper Life Sciences, USA) was used.

Fluorescence images were processed with ImageJ 1.39p software (NIH, USA). Background signal taken from an empty region was subtracted from the measurements, and the ratio of emission intensity resulting from excitation at two wavelengths was calculated (I500/I420).

Results

Among a variety of methods for investigation of intracellular parameters optical methods that use genetically encoded sensors have many advantages. These methods are noninvasive, do not require exogenous introduction of fluorescent probes and allow conducting observation of dynamic processes.

Dependence of SypHer2 signal on pHi value was studied on monolayer HeLa-SypHer2 cell culture and calibration curve was constructed. As expected, fluorescence ratio I500/I420 increased with pH. Using the calibration curve, the value of pHi in HeLa-SypHer2 cells in standard cultivation conditions *in vitro* was determined to be 7.35±0.11.

The data about pHi and hydrogen peroxide level changes in conditions of co-culture HeLa cells with fibroblasts were obtained. It was found that under conditions of co-culturing pHi and hydrogen peroxide level in cancer cells have some modifications in comparison with appropriate mono-cultures. In particular, we showed that pHi of tumor cells in co-cultures is more acidic than pHi of tumor cells in monoculture, that can be explained by higher production of lactate in this conditions. At the same time, hydrogen peroxide level in cancer cells under co-culture conditions was much higher than in monoculture, and maximum of hydrogen peroxide level was observed on the day 2nd. The possible reason for hydrogen peroxide increase is interaction of cancer cells with fibroblasts for driving the Warburg effect.

The experiments on HeLa-SypHer2 tumor spheroids and tumor xenografts *in vivo* showed that SypHer2 ratiometric signal across the tumor nodule is heterogeneous, which indicates the presence of the zones with different pHi.

Conclusions

New method for analysis of intracellular pH and hydrogen peroxide level with genetically encoded ratiometric sensors SypHer2 and HyPer2 was developed. Our data indicate that in HeLa monoculture pHi is more alkaline, and H_2O_2 level is lower, whereas in co-culture with fibroblasts more acidic pHi and higher H_2O_2 level was observed in tumor cells. The possibility of pHi mapping in tumor spheroids and xenografts was demonstrated for the first time.

Acknowledgements

This work was supported by the Russian Science Foundation (project # 14-15-00646).

References

1. C.W. Song, R. Griffin, and H.J. Park, "Influence of tumor pH on therapeutic response", Chapter 2 in: *Cancer drug discovery and development: cancer drug resistance*, Edited by: B. Teicher, 2006, Humana Press Inc., Totowa, NJ.
2. M. Damaghi, J.W. Wojtkowiak, and R.J. Gillies, "pH sensing and regulation in cancer", *Front Physiol*., 2013, **4**, 370.
3. B.A. Webb, M. Chimenti, M.P. Jacobson, and D.L. Barber, "Dysregulated pH: a perfect storm for cancer progression", *Nat. Rev. Cancer*., 2011, **11**, 671-677.
4. M.P. Lisanti, U-E. Martinez-Outschoorn, Z. Lin, S. Pavlides, D. Whitaker-Menezes, R.G. Pestell, A. Howell, and F.Sotgia, "Hydrogen peroxide fuels aging, inflammation, cancer metabolism and metastasis", *Cell Cycle*, 2011, **10**(15), 2440-2449.
5. K.N. Markvicheva, D.S. Bilan, N.M. Mishina, A.Yu. Gorokhovatsky, L.M. Vinokurov, S. Lukyanov, and V.V. Belousov, "A genetically encoded sensor for H_2O_2 with expanded dynamic range", *Bioorganic & Medicinal Chemistry*, 2011, **19**, 1079-1084.
6. J.A. Thomas, R.N. Buchsbaum, A. Zimniak, and E. Racker, "Intracellular pH measurements in Ehrlich ascites tumor cells utilizing spectroscopic probes generated *in situ*", *Biochemistry*, 1979, **10**, 2210-2218.
7. U.E. Martinez-Outschoorn, Z. Lin, C. Trimmer, N. Flomenberg, C. Wang, S. Pavlides, R.G. Pestell, A. Howell, F. Sotgia, and M.P. Lisanti, "Cancer cells metabolically “fertilize” the tumor microenvironment with hydrogen peroxide, driving the Warburg effect. Implications for PET imaging of human tumors", *Cell Cycle*, 2011, **10**, 2504-2520.

Invited

NERVE-DEPENDENT MORPHOGENESIS THROUGH PROVIDING MULTIPOTENT CELLS TO THE INNERVATED TISSUES

V. Dyachuk[1,2] and **I. Adameyko**[1]

[1]Karolinska Institutet, Department of Physiology and Pharmacology, Stockholm, Sweden
slava.dyachuk@ki.se
[2]A.V. Zhirmunsky Institute of Marine Biology FEB RAS, Vladivostok, Russia

Abstract. Embryonic development is a highly sophisticated process whereby different cell types are produced in the correct spatio-temporal order and then organized into tissues of the growing embryo. As complexity of the developing embryo increases with time, different mechanisms have evolved at different times of development for generating cellular elements and positioning them in the correct spatial and cellular context. Formation of the vertebrate peripheral nervous system (PNS) is an elegant example of how evolution has solved the logistical problem related to producing and positioning central nervous system (CNS)-derived cells far away from any CNS structures using nerves as intermediates. Other important roles of the peripheral nerves include producing and delivering our pigment cells - melanocytes as well as generating a subpopulation of mesenchymal stem cells in embryonic head.

Peripheral nerve system represents a transporting system where the multipotent cells are hosted and necessary for development of the visceral organs of the body. These multipotent Schwann cell precursors (SCP) originate from neural crest cells and are recruited to the innervated tissues. As previously shown, SCPs are able to differentiate into melanocytes [1] and mesenchymal stem cells (Kauka et al., 2014). Unexpectedly, our genetic fate-mapping experiments showed that glial SCP positioned along the nerves may differentiate into parasympathetic neurons. These precursors initially express transcriptional factors Sox10, Phox2b, and ErbB3. They migrate along the cranial nerves and reach the target tissues, after that they differentiate into both glial cells and parasympathetic neurons. The expression of neuronal markers such as Phox2b and Mash1 correlated with glial markers (Sox10, Erbb3), which suggested a switch from SCPs to parasympathetic neuron development. ErbB3 and Mash1 KO mice do not possess parasympathetic NS and support SCP-dependent origin of parasympathetic ganglia. Experiments with Confetti mouse strain allowed for the identification of individual clones originating from single glial cells. These data confirmed that parasympathetic neurons arise from bi-potent glial progenitors that generate both glia and neurons. These findings are novel and improve our understanding of parasympathetic nervous system origin and give another unexpected example of the plasticity of stem-like glial progenitors. Elucidating the molecular mechanisms involved may result in novel strategies for treatment of pathological conditions.

References

1. I. Adameyko, F. Lallemend, J. B. Aquino, J. A. Pereira, P. Topilko, T. Muller, N. Fritz, A. Beljajeva, M. Mochii, I. Liste, et al., "Schwann cell precursors from nerve innervation are a cellular origin of melanocytes in skin", *Cell*, 2009, **139**, 366-379.
2. N. Kaukua, M. Shahidi, C. Konstantinidou, V. Dyachuk, M. Kaucka, A. Furlan, et al., "Glial origin of mesenchymal stem cells in a tooth model system", *Nature*, 2014 , **513**(7519), 551-4.

THE STUDY OF TUMOR RESPONSE TO DIFFERENT TREATMENT BY MULTIPHOTON TOMOGRAPHY

V.V. Elagin[1], M.M. Karabut[1], N.L. Buyanova[1], M.A. Sirotkina[1], S.S. Kuznetsov[1], L.B. Snopova[1], N.D. Gladkova[1], A. Vitkin[1,2], and **E.V. Zagaynova[1]**

[1] Nizhny Novgorod State Medical Academy, Nizhny Novgorod, Russia
elagin.vadim@gmail.com
[2] University of Toronto, Toronto, Canada

Abstract. Multiphoton tomography is a new, non-invasive technique enabling study the skin diseases at a cellular and subcellular level, which is based on autofluorescence. This innovative technique can be applied to the study of tumor response to therapy. It was shown that tumor cells without chemotherapy had irregular shape and dark nuclei. After treatment, necrosis developed in tumor tissue. It appeared as area with lost the fluorescence signals. Stromal component was damaged only in necrosis areas. Chemotherapy leads to decrease of mitosis amount in field of view in two times as compared to the control.

Introduction. The Gold Standard for diagnosis and investigation of tumor response is histopathology based on resection of tumor so it do not allow to make continuous monitoring. Multiphoton laser tomography, (MPT) provides real-time imaging of living investing tissue at a cellular and subcellular level [1]. Autofluorescence of endogenous fluorophores and second harmonic generation (SHG) from collagen matrix are used for functional and structural imaging by MPT [2].

Therefore, the purpose of the research was to assess the capabilities of MPT for the study of tumor response to therapy.

Materials and Methods. Mouse colon carcinoma cell line (CT-26) were subcutaneously injected to auricle of Balb/C mice. Two hundred thousand cells in 20 µl of phosphate-buffered saline were inoculated. Irinotecan was diluted in sterile saline and 20 mg/kg were intraperitoneal administered daily for 5 days starting on the 10 day of tumor growth. Monitoring of tumor response was carried out by MPT flex (JenLab, Germany) on days 10, 12, 17, 18. Autofluorescence and SHG was stimulated by tunable femtosecond Ti:Sapphire laser at 740 nm wavelength. The power was increased up to 40 mW to obtain stronger signals from deeper regions. In all the figures, autofluorescence signals were displayed in green and SHG signals were displayed in red. In addition, finding results were confirmed by histopathological analysis. Mice without Irinotecan were kept as a control.

Results. MPT images of different layers of tumor node acquired sequentially from the dorsal auricle. Control mice had tumor nodes covered by several layers of epidermis (stratum corneum, stratum granulosum, stratum spinosum). Tumor cell were invaded into epidermis and located at a depth of 40 µm. The tumor cells appeared as irregular shape areas with dark oval nuclei and strong autofluorescence from cytoplasm. The major portion of field of view represent by tumor cells. Stromal component appeared scarce fibers. It should be noted, that histopathological analysis did not reveal areas of necrosis in tumor tissue without chemotherapy. Moreover, cells with irreversible damage were absent.

Mice from group with Irinotecan had tumor located at 30 µm. Area of necrosis with stroma and parenchyma destruction was find at the same depth. In other sites, stromal component was similar to control and represented by not interlacing scarce fibers. Histopathological analysis confirmed this fact and revealed one more area of necrosis. Moreover, 10% – 20% cells outside of necrosis area displayed irreversible damage of nuclei and cytoplasm. Chemotherapy led to decrease of mitosis amount in field of view in two times as compared to the control. Tumor regression grade was 3-4 (by Mandard).

Conclusions. In conclusion, we have shown that MPT may be used for study of tumor response to chemotherapy. After treatment, we find necrosis area in tumor tissue. Moreover, autofluorescence signals allowed to get information about condition of cells (shape, nucleocytoplasmic ratio, necrosis formation, cell density). Stromal component did not change after chemotherapy. Therefore, the next stage of our research will be focused on identify morphological features of tumor after treatment.

Acknowledgements. This work was supported by the Ministry of education and science of the Russian Federation (project № 14.B25.31.0015).

References

1. K. Konig and I. Riemann, *Journal of Biomedical Optics*, 2003, **8**(3), 432–439.
2. K. Konig, *Journal of Biophotonics*, 2008, **1**(1), 13–23.

AMINOALKYLAMIDE DERIVATIVES OF CHLORIN E6 AS ADVANCED PHOTOSENSITIZERS FOR ANTICANCER AND ANTIMICROBIAL PHOTODYNAMIC THERAPY

A.A. Ignatova[1], **O.I. Gushchina**[2], **A.F. Mironov**[2], and **A.V. Feofanov**[1]

[1] Shemyakin-Ovchinnikov Institute of Bioorganic Chemistry of the Russian Academy of Sciences, Moscow, Russian Federation, aignatova_83@mail.ru

[2] Lomonosov Moscow State University of Fine Chemical Technologies, Moscow, Russian Federation

Abstract. We report on structural modifications of chlorin e6 that make it highly efficient photosensitizer with extended range of applications. We demonstrate that N-alkylamine derivative of 13-carbamoylchlorin e6 possesses advanced intracellular accumulation in cancer cells and high cytotoxicity upon irradiation with red light. Methylation of the terminal aminogroup does not impair the photodynamic properties of the compound. Furthermore, both amino and dimethylamino derivatives have significant photoinduced bactericidal activity against gram-positive bacteria. Thus, these derivatives can be considered as promising universal agents for anticancer and antimicrobial photodynamic therapy.

Photodynamic therapy (PDT) becomes widely used in oncology and other fields of medicine including ophthalmology, dentistry, cosmetology and antimicrobial therapy [1, 2]. The development of improved photosensitizers remains an important task for PDT.

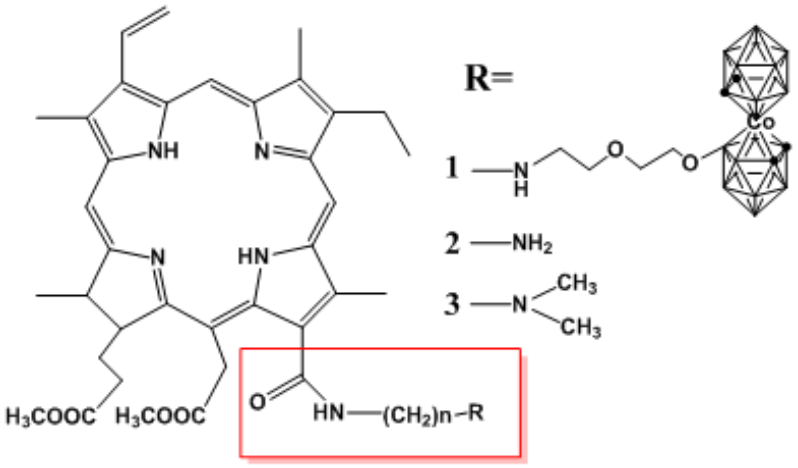

Fig. 1. The structure of studied chlorin e6 derivatives

Previously, we have found that chlorin e6 conjugated with cobalt bis(dicarbollide) by means of aminoalkylamide linker (Fig. 1, **1**) possessed extremely high intracellular accumulation and photocytotoxic effect [3, 4]. We have supposed that such advanced properties of the conjugate **1** arose due to favorable combination of the structure of chlorin e6 and aminoalkylamide linker. To check this hypothesis we have synthesized aminoalkylamide derivatives of chlorin e6 (Fig. 1, 2 and 3) and studied their properties. It was found that novel compounds interact with cancer cells very similar to the previously studied conjugate **1**. They accumulate effectively in cytoplasm of rat glioma C6 cells but do not penetrate into the nucleus (Fig. 2). In cytoplasm **2**, **3** have a similar granular-diffuse distribution. As shown with confocal laser scanning microscopy most of these intracellular granules are lysosomes.

Compounds **2**, **3** have high quantum yields of singlet oxygen generation (0,79–0,85), but do not form hydroxyl radicals. Efficient generation of $^1O_2$ in combination with high intracellular accumulation result in enhanced photoinduced cytotoxicity of compounds **2**, **3**. Photoinduced concentration-dependent killing of cells is observed at nanomolar concentrations of **2** and **3** (IC_{50} = 50 nM). In the absence of light irradiation, these compounds are non-toxic for cells up to 10 μM.

Furthermore it is found that derivatives **2** and **3** possess photoinduced bactericidal activity against Gram-positive bacteria *Staphylococcus aureus* 209P and *Bacillus subtilis* B-501, but do not affect the growth of Gram-negative bacteria *Pseudomonas aeruginosa* PAO1. Using a modified broth dilution assay combined with light irradiation it was measured that for Gram-positive bacteria the minimal bactericidal concentration of **2** and **3** was the same and equal to 60 nM.

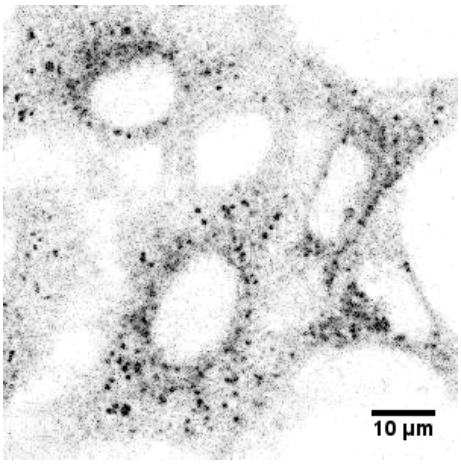

Fig. 2. Typical distribution of **2** and **3** in rat glioma C6 cells

Comparison of properties of **2** and **3** indicates that modification of the terminal amino group affects weakly the functional activities of aminoalkylamide derivatives of chlorin e6.

In conclusion, novel chlorin e_6 derivatives **2** and **3** are prospective photosensitizers for anticancer and antimicrobial PDT.

Acknowledgements

The research was supported by RFBR grant 13-04-00670.

References

1. R. Allison, *Future Oncol.*, 2014, **10**(1), 123-4.
2. A. Rkein and D. Ozog, *Dermatol Clin.*, 2014, **32**(3), 415-25.
3. A.V. Efremenko, A.A. Ignatova, M.A. Grin, A.F. Mironov, V.I. Bregadze, I.B. Sivaev, and A.V. Feofanov, *In: Current microscopy contributions to advances in science and technology. Méndez-Vilas A., Ed.; Formatex Research Center: Badajoz*, 2012, 84-90.
4. A.V. Efremenko, A.A. Ignatova, M.A. Grin, I.B. Sivaev, A.F. Mironov, V.I. Bregadze and A.V. Feofanov, *Photochem. Photobiol. Sci.*, 2014, **13**, 92-102.

Invited

OPTICAL TOOLS TO ASSESS THE ROLE OF CARDIAC FUNCTION IN THE DEVELOPMENT OF CONGENITAL HEART DEFECTS

M.W. Jenkins

Case Western Reserve University, Cleveland, U.S.
mwj5@case.edu

Abstract

The role of cardiac function in early embryonic development is poorly understood. In order to successfully assess the impact of cardiac function on development, we need to monitor and perturb function, and quantify resultant effects on morphology. Here, we describe our latest progress in developing optical pacing to perturb hemodynamics and optical coherence tomography for measuring hemodynamics and resultant morphology. Our results indicate that abnormal regurgitant flow at the atrioventricular junction during cardiac looping leads to abnormal cardiac cushions (valve precursors) and valve leaflets. Pacing-induced defects produce similar phenotypes as found in our fetal alcohol syndrome and velo-cardio-facial syndrome/Digeorge models.

SIMULTANEOUS FLIM AND PLIM IMAGING FOR METABOLIC MAPPING

S. Kalinina, **D. Bisinger**, **J. Breymayer**, and **A. Rück**

University of Ulm, Core Facility Confocal and Multiphoton Microscopy, Germany,
sviatlana.kalinina@uni-ulm.de

Abstract. Monitoring of autofluorescence of reduced nicotinamide adenine dinucleotide (NADH) with fluorescence lifetime imaging microscopy (FLIM) is successfully used to control the balance between oxidative phosphorylation and glycolysis of living cells and tissues. We present a setup for simultaneous monitoring of NADH-FLIM and intracellular pO_2 by using phosphorescence lifetime imaging microscopy (PLIM) and tris-bipyridine ($Ru(bpy)_3^{2+}$) as an oxygen sensor. The setup is based on two-photon microscopy and multi-dimensional time-correlated single-photon-counting (TCSPC). With the two-channel FLIM/PLIM system we investigated human oral squamous carcinoma cells (SCC) in the monolayer culture and SCC that were grown on chick chorio-allantoic membrane (CAM) of fertilized eggs.

Fluorescence lifetime imaging microscopy (FLIM) of living cells and tissues among others is successfully used for monitoring autofluorescence of nicotinamide adenine dinucleotide (NADH), the metabolic coenzyme, controlling the balance between oxidative phosphorylation and glycolysis [1]. Reduced NAD (NADH) possesses emission with maximum around 440 - 470 nm depending on its state[2]. Fluorescence lifetime of NADH, which is bound to proteins, typically is reported as 2 - 3 ns, whereas the free enzyme possesses a remarkable shorter fluorescence lifetime [2, 3]. Thus, spectrally resolved FLIM is successfully used for evaluation of relative intracellular concentrations of free and protein-bound NADH and consequently for characterizing the metabolic state of cells.

Metabolic reactions are strongly dependent on the intracellular oxygen level. One of the promising methods for oxygen sensing in biomedical samples is phosphorescence lifetime imaging microscopy (PLIM). The oxygen-dependent quenching of phosphorescence of some compounds can be used to measure oxygen partial pressure (pO_2) within the physiological range [4]. We present a setup for simultaneous monitoring of NADH-FLIM and intracellular pO_2 by using tris-bipyridine ($Ru(bpy)_3^{2+}$) as an oxygen sensor. The setup is based on two-photon microscopy and multi-dimensional time-correlated single-photon-counting (TCSPC). With the two-channel FLIM/PLIM system we were able to show that pO_2 is investigated simultaneously with different metabolic parameters in living cells.

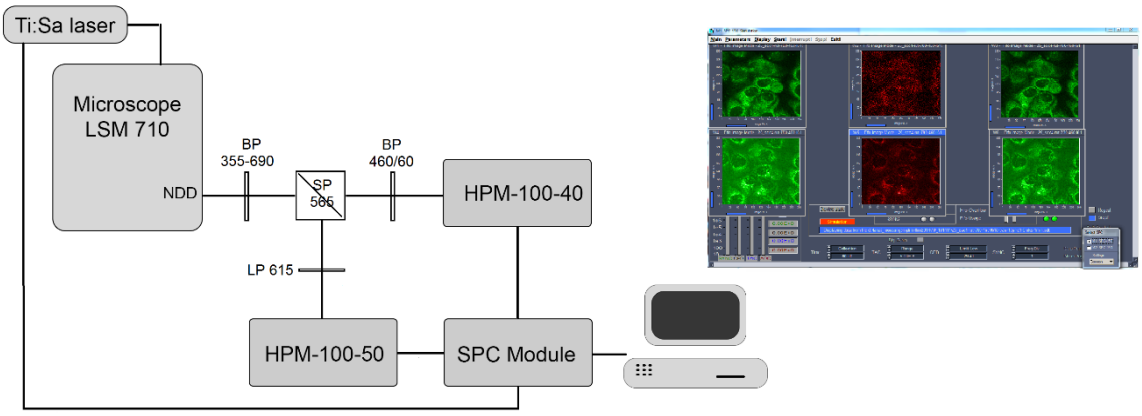

Fig. 1. System for simultaneous detection of FLIM and PLIM

Human oral squamous carcinoma cells (SCC) were metabolically mapped with simulations monitoring of the intracellular oxygen level. To evaluate a redox status of the cells SPCImage software (Becker & Hickl GmbH, Berlin, Germany) was used. The lifetime of NADH fluorescence, which was measured on the NADH-FLIM channel, was estimated with a two-exponential fitting procedure to reveal the contributions of the free and the protein-bound enzyme. A mean lifetime was calculated as

$$\tau_{mean} = (a_1 \tau_1 + a_2 \tau_2) / (a_1 + a_2) \quad (1)$$

τ_1 and τ_2 are lifetimes of the short and long component, respectively, and a_1 and a_2 are their relative contributions. As the short lifetime is correlated to the free NADH and the longer lifetime to the protein-bound compound, a ratio a_1/a_2 reasonable reveals the balance between glycolysis and oxidative phosphorylation.

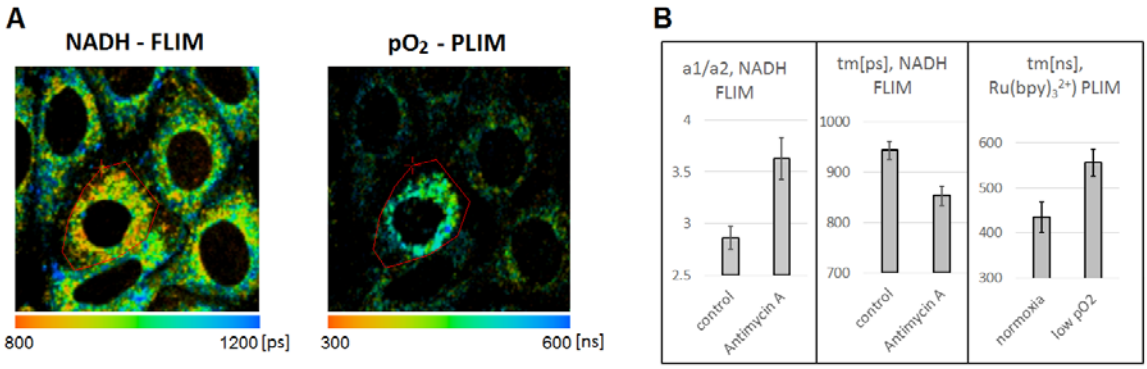

Fig. 2. (A) Distribution of mean lifetimes of simultaneously measured NADH fluorescence and $Ru(bpy)_3^{2+}$ luminescence for the monolayer SCC culture. (B) The parameters of NADH fluorescence and $Ru(bpy)_3^{2+}$ luminescence for monolayer SCC culture

Both main parameters of NADH autofluorescence – the mean lifetime and the ratio a_1/a_2 – are remarkable changed in the presence of modulators of cell respiration. For example, respiratory chain inhibitor antimycin A induces a shift to glycolysis, and this effect strongly depends on previous status of the cells at normal conditions. Investigations of monolayer cell culture were compared with results for SCC that were grown on chick chorio-allantoic membrane (CAM) of fertilized eggs. CAM-model realizes a more realistic *in vivo* situation allowing to investigate the cells in the tissue.

A two-photon excitation at 780 nm was used to induce fluorescence of intracellular NADH as well as luminescence of $Ru(bpy)_3^{2+}$. The lifetime of $Ru(bpy)_3^{2+}$ luminescence depends on an oxygen level changing at used conditions within the range from 400 ns (at normal pO_2) till 600 ns (at low pO_2). To calibrate the measurements we used the oxygen scavenger sodium sulfite (Na_2SO_3) in different concentrations.

Acknowledgements

This work was carried out with financial support by the Ministry of Financial Affairs of Germany, FKZ order: KF2122510AK2 (“PLIMOX”) and of the Ministry of Research and Development, FKZ order: 13N12942 (“METAPHOR”).

References

1. V.K. Ramanujan, J.A. Jo, G. Cantu, and B.A. Herman, *J. Microsc*, 2008, **230**(Pt 3), 329-38.
2. J.R. Lakowicz, H. Szmacinski, K. Nowaczyk, and M.L. Johnson, *Proc. Natl. Acad. Sci. USA*, 1992, **89**(4), 1271-1275.
3. A. Rück, C. Hauser, S. Mosch, and S. Kalinina, *J. Biomed. Opt.*, 2014, **19**(9), 96005.
4. I. Okura, *Photosensitization of Porphyrins and Phthalocyanines*, Gordon & Breach Science Publishers Ltd., Amsterdam, 2001, 175-177.

DUAL USE OF NOVEL PORPHYRAZINE MOLECULAR ROTORS AS SENSITIZERS AND VISCOSITY MARKERS IN PHOTODYNAMIC THERAPY

L.G. Klapshina[1, 3], **M.A. Izquierdo**[2], **A. Vyšniauskas**[2], **S.A. Lermontova**[1], **I.S. Grigoryev**[1], **N.Y. Shilyagina**[3], **I.V. Balalaeva**[3], and **M.K. Kuimova**[2]

[1] Institute of Organometallic Chemistry of the RAS, Nizhny Novgorod, Russia,
E-mail: klarisa@iomc.ras.ru
[2] Department of Chemistry, Imperial College London, Exhibition Road, London SW7 2AZ, UK
[3] Lobachevsky State University, Nizhny Novgorod, Russia

Abstract. Here we presented a new cyano-porphyrazine molecular rotor which works as an excellent dual agent, allowing a simultaneous PDT treatment and the monitoring of its progress and the mechanism by fluorescence lifetime imaging. The phasor analysis of FLIM data allowed us to detect at least two domains of high viscosity in cells, of 50 and 5000 cP, and the formation of the latter was promoted by PDT. While the main focus of this study was to improve our fundamental understanding of the light-induced processes in the irradiated cell, we also believe that these result can have practical significance to PDT treatment of cancer.

Molecular rotors are a group of fluorophores in which fuorescence depends on the rate of intramolecular rotation. In media of high viscosity, intramolecular rotation is inhibited resulting in signifcant increases of the emission intensity and the fluorescence lifetime. The development of fluorescence lifetime-based sensors is desirable, because they can be used in imaging experiments as concentration independent probes to monitor the viscosity in heterogeneous systems such as cells, with organelles exhibiting a broad range of viscosity values. Very importantly, dynamic imaging with molecular rotors allows us to monitor viscosity changes upon perturbation, if the time scale of a change is slower than the time required for image acquisition. For example, it has been previously reported changes in viscosity during light induced cell death in photodynamic therapy (PDT) of cancer, utilising a fluorescent molecular rotor, which allowed a concentration independent ratiometric detection [1].

Porphyrazines have recently emerged as a very important class of tetrapyrroles suitable for PDT which is a clinical treatment for several types of cancer and relies on the excitation of a photoactive drug, which subsequently produces short-lived cytotoxic species, such as singlet oxygen.

One of the important challenges in PDT is the correct light dosimetry, to achieve the most favourable treatment outcome. Herein, we report a new red-emitting viscosity-sensitive porphyrazine molecular rotor that is suitable for quantitative measurements of viscosity in a large dynamic range. We also demonstrate a new approach to the PDT dosimetry, based on fluorescence lifetime measurements of porphyrazine. PDT in cells using porphyrazine is accompanied by cell death and a significant viscosity change, as measured by its fluorescence lifetime. Thus we demonstrate that photoinduced changes in viscosity could be used as a new diagnostic tool during PDT treatments and could be indicative of the treatment outcome (Fig. 1).

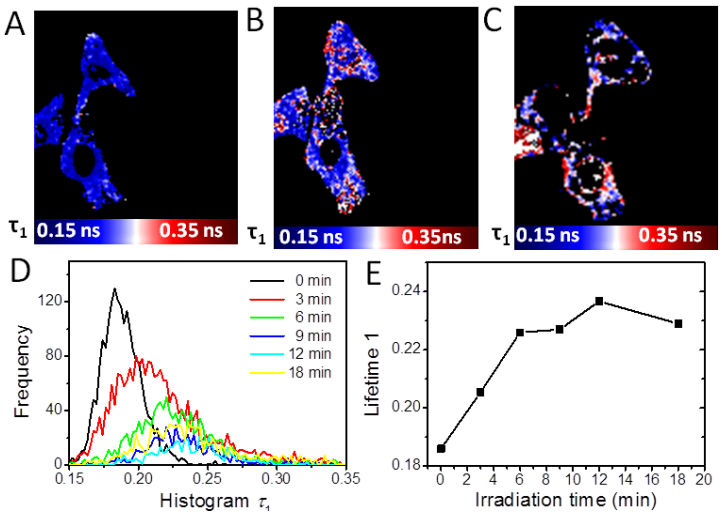

Fig. 1. (A-C) FLIM images of SK-OV-3 cells incubated with 4 μM solution of porphyrazine for 30 min (λ_{exc} = 800 nm, λ_{em} = 600 – 750 nm).
(A) Before, (B) after 3 min and (C) after 18 min irradiation (λ_{exc} = 561). (D) FLIM histogram of τ_1 obtained after different irradiation times. (E) Plot of τ_1 *vs* irradiation time

The FLIM data of SK-OV-3 cells incubated with porphyrazine before and after initial irradiation (Figs. 2 A-C) were analysed using the phasor approach (Figs. 2 D-F) in order to simplify the analysis of FLIM images.

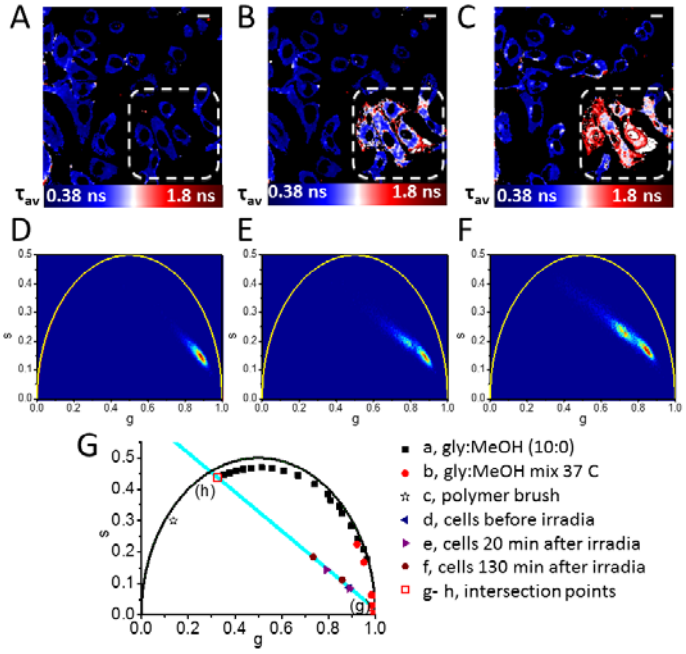

Fig. 2. (A-C) FLIM images and (D-F) phasor plots of SK-OV-3 cells incubated with 4 μM solution of porphyrazine obtained following 800 nm pulsed excitation and (600-750) nm fluorescence detection. (A, D) Before and (B, E) 20 min and (C, F) 130 min after selective irradiation of the cells included within the dashed rectangle (irradiation conditions λ_{exc} = 561 nm, 5 min). A seismic colour scale is used to assign the lifetimes in the FLIM images. (G) Phasor plot including (a) calibrations of porphyrazine in glycerol at varied temperatures, (b) calibrations of porphyrazine in glycerol:MeOH at 37 °C, (c) a polymer brush, (d-f) the centroids of the clustering of points corresponding to graphs D-F, (g-h) intersection points corresponding to viscosities of 51 cP and > 5000 cP. Scale bar is 20 μm.

Thus, we presented a new type of porphyrazine dye which works as an excellent dual agent, allowing a simultaneous PDT treatment and the monitoring of its progress and the mechanism by fluorescence lifetime imaging. The phasor analysis of FLIM data allowed us to detect at least two domains of high viscosity in cells, of 50 and 5000 cP, and the formation of the latter was promoted by PDT. While the main focus of this study was to improve our fundamental understanding of the light induced processes in the irradiated cell, we also believe that these results can have practical significance to PDT treatment of cancer. Further research is required to elucidate exact links between viscosity in individual cells and the mechanism of lesion death (*i.e.* apoptosis and necrosis).

Acknowledgements

MKK is thankful to the EPSRC for the Career Acceleration Fellowships. This work was partially supported by the European Commission in the form of Marie Curie individual Fellowship to MAI. AV thanks the EPSRC for the Prize Studentship. LGK is thankful to the Ministry of Education and Science of Russian Federation grant (Contract 14.Z50.31.0022). LGK, SAL and IVB are thankful to the Russian Foundation for Basic Research (RFBR, Contracts 13-04-40228-H, 14-03-31130, 15-02-05468). We are thankful to the Royal Society Exchanges (UK) – RFBR (Russia) joint grant to MKK and LGK for facilitating bilateral visits.

References

1. M.K. Kuimova, S.W. Botchway, A.W. Parker, M. Balaz,H.A. Collins, H.L. Anderson, K. Suhling, and P.R. Ogilby, *Nat. Chem.*, 2009, **1**, 69–73.

ASSESSMENT OF PROLIFERATION AND VIABILITY OF STROMAL CELLS WITH TURBOFP635 ON THE SURFACE SELECTIVE LASER SINTERED SCAFFOLDS

D.S. Kuznetsova[1, 2], P.S. Timashev[3], V.V. Dudenkova[1, 2], V.N. Bagratashvili[3], and **E.V. Zagaynova[1,2]**

[1] Nizhny Novgorod State Medical Academy, Russia, daria.s.kuznetsova@gmail.com
[2] Lobachevsky State University of Nizhni Novgorod, Russia
[3] Institute of Laser and Information Technologies, Troitsk, Russia

Abstract. Surface selective laser sintering is one of the novel methods of polymer scaffold fabrication using modern approaches combining the lack of influence of the high temperatures and organic solvents. This method enables to use a wide spectrum of heat-labile bioactive compounds and polymers. The purpose of this work was to obtain the polylactide scaffolds with and without nanoscale hydroxyapatite by surface selective laser sintering and study the proliferation and viability of mesenchymal stromal cells expressing the fluorescence protein TurboFP635 on the derived scaffolds.

Introduction

The current standard for the treatment of bone defects of a critical size is an autologous graft [1, 2]. But this approach is limited by the amount of available donor tissue and necessitates a second injury site resulting in additional trauma to the patient and associated risks [3]. There are alternative approaches in regenerative medicine based on the use of bioactive scaffolds, cell-seeded scaffolds and autologous bone grafts grown in vitro [1]. Conventional technologies of polymeric scaffolds synthesis for bone regeneration are based on the use of organic solvents or high temperatures. One of the methods of rapid prototyping - surface selective laser sintering (SSLS) is a novel method of polymer scaffolds synthesis using modern approaches combining the lack of influence of high temperatures and organic solvents [4, 5]. The purpose of this work was to obtain the polylactide scaffolds with and without nanoscale hydroxyapatite (HA) by surface selective laser sintering and study the proliferation and viability of mesenchymal stromal cells (MSC) on the derived scaffolds.

Materials and Methods

The scaffolds were obtained by surface selective laser sintering in Institute of Laser and Information Technologies (Troitsk, Russia). Internal structure of scaffolds was observed by scanning electron microscopy. Uniform distribution of hydroxyapatite inside the scaffold was shown by Raman spectroscopy. To test the scaffolds we used MSC from human adipose tissue stably labeled with red fluorescent protein TurboFP635. Such cells need no additional staining for observation. The proliferation of MSC was studied on days 5-20 of cell culturing by laser scanning confocal fluorescence microscopy. The viability of the cells was analyzed using specific dyes for apoptosis Annexin V-FITC and necrosis Propidium Iodide.

Results

By day 5 large cell clusters were identified in pores of both scaffold types. On days 10-15, the number of MSC significantly increased in all the samples. According to a newly developed protocol of data processing based on the fluorescence signal of TurboFP635 the scaffolds with HA had more cells than those without HA. Moreover, MSC penetrated deeper from the surface of all samples into the pores. By day 20 MSC colonized all volume of both scaffold types. The cells were found on the back side of the scaffold. The assessment of MSC viability showed the lack of large necrotic and apoptotic areas. All scaffolds presented the structure filled with viable cells. Therefore, the polylactide scaffolds obtained by surface selective laser sintering with and without HA showed good properties for MSC migration and proliferation. The scaffolds with HA had more cells and can be considered as more perspective material for bone regeneration.

Acknowledgements

This work was supported by the Russian Foundation for Basic Research (№ 13-02-12101 ofi_m).

References

1. T.W. Bauer and G.F. Muschler, *Clin Orthop Relat Res*, 2000, 10–27.
2. D.S. Kuznetsova, P.S. Timashev, et al., *STM*, 2014, 201–212.
3. S. Bhumiratana and G. Vunjak-Novakovic, *Stem Cells Transl Med*, 2012, **1**(1), 64–69.
4. E.N. Antonov, V.N. Bagratashvili, et al., *Adv Mater*, 2005, **17**(3), 327–330.
5. T.B. Bukharova, E.N. Antonov, et al., *Bull Exp Biol Med*, 2010, **149**(1), 148–153.

Invited

OPTICAL COHERENCE TOMOGRAPHY OF REPRODUCTIVE AND DEVELOPMENTAL EVENTS IN MAMMALIAN MODELS

I.V. Larina

Department of Molecular Physiology and Biophysics, Baylor College of Medicine,
One Baylor Plaza, Houston, Texas 77030, USA
larina@bcm.edu

The mouse model is essential for our understanding of normal human reproduction, development and congenital defects. Live dynamic imaging of mouse developmental events is a challenging task; imaging depth and resolution are interdependent, and a significant improvement in one of these parameters usually comes at the expense of the other. Because early mouse embryos go through rapid and dramatic morphological changes, there is no single imaging modality, which would allow for visualization of all these events at high resolution. Our research focuses on developing methods for live imaging and dynamic characterization of reproductive and early embryonic developmental events and using them in mouse models of human diseases. Using multidisciplinary methods: optical coherence tomography (OCT), fluorescence microscopy, live mouse embryo manipulations and static embryo culture, molecular biology, advanced image processing and computational modeling we aim to understand developmental processes. We have developed a series of OCT based approaches to live analysis of reproductive and developmental processes including:

(1) three-dimensional imaging and tracking of murine oocytes as they exit the ovary and migrate through the oviduct to the uterus;

(2) live imaging of early mouse embryos (E8.5 – E9.5) cultured on an imaging stage and visualization of developmental events with a spatial resolution of a few micrometers (less than the size of an individual cell) and a frame rate of up to hundreds of frames per second;

(3) reconstruction of cardiodynamics in 4D (3D+time);

(4) *in utero* embryonic imaging of different organ systems including limbs, brain and eye. We are now using these methods to study how specific mutations affect organogenesis.

Acknowledgements

This work was supported by the NIH (1R01HL120140, U54 HG006348) and the Optical Imaging and Vital Microscopy (OIVM) Core at the Baylor College of Medicine.

Invited

THE USE OF TRANSFERRIN Ru(II) PHOTOSENSITIZERS AS TUMOUR TARGETING STRATEGY

L. Lilge[1], S. Forward[1], P. Kaspler[2], S. Lazio[2], Ya. Arenas[2], and **A. Mandel[2]**

[1] Princess Margaret Cancer Centre, University Health Network, Toronto, Canada
lothar.d.lilge@gmail.com
[2] Theralase Inc., Toronto Canada

Abstract. Photosensitizers based on metal-complexes are of interest due to the ability to modify absorption and chemical binding properties separately via the use of different ligands. Ru^{2+} based photosensitizers are known to be Photodynamic Therapy (PDT) agents against bacteria, whereas use for oncological indications *in vivo* has not been demonstrated. We present *in vitro* and *in vivo* data showing that premixing a Ru^{2+}-based photosensitizer, TLD1433, with transferrin increased the molar extinction coefficient, particularly at longer activation wavelengths, reduced photobleaching rates, and reduced the toxicity of the complex. Considering that the transferrin receptor is upregulated in the majority of malignancies, premixing of the Ru^{2+} complex with transferrin will convert the active pharmaceutical ingredient TLD1433 into a drug of potentially considerable clinical usage.

Introduction

Attributes of particular Ru^{2+} complexes are their controllable design, preparation, isolation or purification and a potentially high $^1O_2$ quantum yields, whereas Coordination complexes are of interest as they may not require oxygen to exert a cytotoxic effect. The pseudo-octahedral complexes provided by Ru^{2+} allow design option for ligands providing affinity for DNA binding, overall stability, and solubility. Drug transport through tissue for these Ru^{2+} complexes is however an issue limiting their testing *in vivo* and also for subsequent clinical translation.

In the vast majority of cancers the transferrin receptor (Tf-R) is upregulated to boost Fe^{3+} stores. Expression of Tf-R correlates with tumor grade, stage, progression and metastasis and investigating the Tf-R as a transport mechanism for PDT has been ongoing for the past decade.

Here, we report on the effects of the $[Ru^{2+}$ (4,4'-dimethyl-2,2'-bipyridine (dmb))$_2$(2-(2',2":5",2"'-terthiophene)-imidazo[4,5-f][1,10] phenanthroline)$]^{2+}$ complex known as TLD1433 following binding with Tf, whereby the TLD1433-Tf complex is termed Rutherrin.

Results

Figure 1 shows the gain in molar extinction coefficient by Rutherrin over Tf or TLD1433 across the visible and NIR optical spectrum. The increased Rutherrin absorption was reflected by increased luminescence emission compared to TLD1433 albeit at a lesser gain so the luminescence is weak. One formed at pH 7.5 the Rutherrin complex is maintained even at a pH of 4.8. Additionally an improved photostability over TLD1433 is noted, resulting in in less than 50% absorption loss for 2 10^{19} hυcm^{-3} 525 nm photons absorbed by the photosensitizer.

Figure 2 show the TLD1433 and Rutherrin fluorescence after 150 minutes loading in AY29 cells showing a marked.

Figure 3 shows reduced dark toxicity at low photosensitizer concentration and some increase in PDT mediated cell kill in AY29 cells this leads particular for 8–16μM concentration of the active ingredient to a marked increase in therapeutic index.

The reduced dark toxicity seen in vitro was also noted in vivo where the maximum tolerated dose for the photosensitizer was increased almost 2 fold. Particular through the gains in NIR absorption by Rutherrin over TLD1433 the efficacy for Rutherrin mediated PDT in vivo was improved as shown in figure 4.

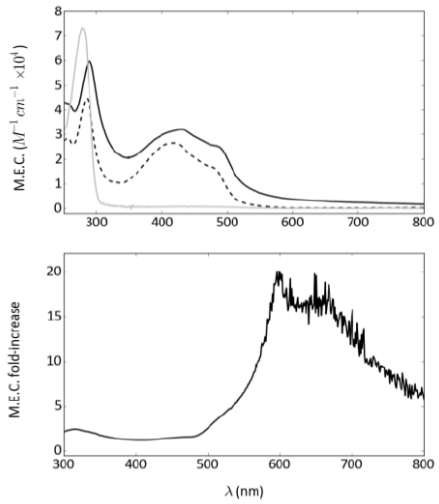

Fig. 1. Molar extinction coefficient following premixing with Tf. (*Top*) b-Tf (light grey), 10µM TLD1433 (dashed black), 10µM b-Rutherrin (2.5µM b-TF) in PBS. (*Buttom*) Ratio of 10µM Rutherrin over 10µM TLD1433 MECs

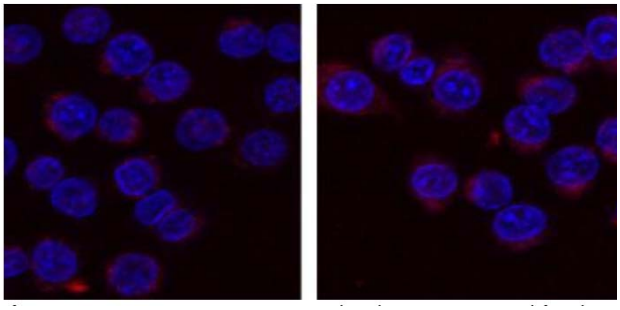

Fig. 2. Fluorescence by TLD1433 (*left*) and Rutherrin (*right*) in Ay29 cells

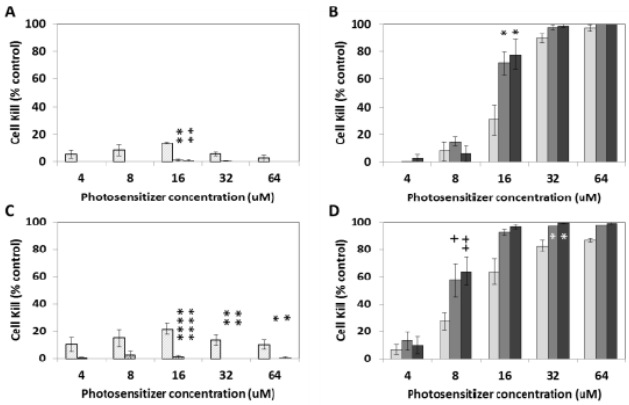

Fig. 3. Concentration dependent TLD1433 and 4-64µM Rutherrin Dark toxicity and PDT mediated induced cell kill in rat AY27 cells following (**A, B**) 30 minutes or (**C, D**) 90 minutes incubation. (**A, C**) Dark toxicity, (**B, D**) following 625nm light (119mW/cm^{-2}, 90Jcm-2) mediated PDT for TLD1433 (light grey) and Rutherrin (5 µM Tf) (grey) or Rutherrin (10µM Tf) (black). Asterisks indicate significant effect of h-Tf (*.P<0.05, **.P<0.01, ****.P<0.0001), crosses show significant effect of incubation time (+.P<0.05, ++.P<0.01, N = 3 all)

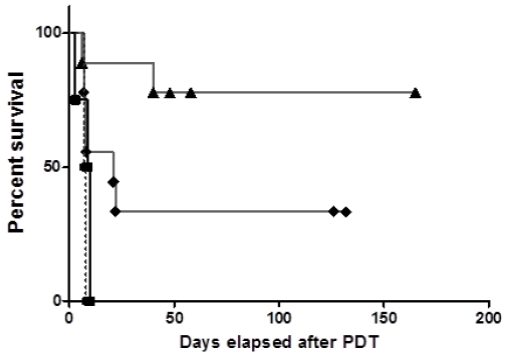

Fig. 4. Tumor free survival after 50mg/kg TLD1433 or m-Rutherrin (12.5µM Tf) mediated PDT in the CT26.CL25 subcutaneous tumor model. For NIR PDT 5x5 mm tumors were treated with 600Jcm^{-2} radiant exposure of 808nm light. Light only (square), TLD1433 only (circle), TLD1433 PDT (rhombus), Rutherrin PDT (triangle)

Conclusions

Our findings suggest Rutherrin as preferred PDT PS drug over TLD14433 Predominant generation of hydroxyl radical is an indication for use in low oxygen environment present in solid tumors. The combination of Tf mediated transport and PDT activity in low oxygen concentration are interesting aspects towards targeting cancer stem cells.

STUDY OF NADH AND FAD IN CANCER AND NORMAL CELLS IN VITRO USING FLIM

M.M. Lukina[1, 2], **V.V. Dudenkova**[1, 2], **M.V. Shirmanova**[1], and **E.V. Zagaynova**[1]

[1] Nizhny Novgorod State Medical Academy, Russia, kuznetsova.m.m@yandex.ru
[2] Lobachevsky State University of Nizhny Novgorod, Russia

Abstract. Fluorescence metabolic imaging measures lifetimes from nicotinamide adenine dinucleotide (NADH) and flavin adenine dinucleotide (FAD). The purpose of our work was to investigate metabolic activity of normal and cancer cells *in vitro* by Fluorescence Lifetime Imaging (FLIM). NADH and FAD were analyzed in monocultures and co-culture of cancer cells and fibroblasts. It was found that cancer cells shift metabolism from OXPHOS on glycolysis in the presence of fibroblasts.

Introduction

Cell metabolism is the sum of the chemical reactions taking place within each cell and providing energy for vital processes [1, 2]. Most mammalian cells use oxidative phosphorylation (OXPHOS) for energy supply, whereas a metabolic switch from OXPHOS to glycolysis is often observed in cancer cells, even in the presence of oxygen (Warburg effect) [3]. NADH and FAD are the main metabolic cofactors that work as electron acceptors and donors in the electron transport chain of mitochondria. Since these co-factors have capability for fluorescence, their relative content and state (free or bound) can be assessed using time-resolved fluorescence microscopy. Recently, NADH and FAD fluorescence lifetime measurements have been used to monitor cell metabolic activities, based on the lifetime changes and the ratio of relative contributions of two major lifetime components [4, 5, 6]. The advantage of fluorescence lifetime measurement over intensity measurement is a sensitivity to the changes between free and bound form [5, 6, 7, 8].

The purpose of our work was to investigate metabolic activity of normal and cancer cells *in vitro* by Fluorescence Lifetime Imaging (FLIM).

Materials and Methods

In these experiments different cell lines, including colon carcinoma and fibroblasts, were used. The cells were cultured in DMEM containing 100 μg/ml penicillin, 100 μg/ml streptomycin sulfate and 5% fetal bovine serum (FBS) at 37 °C in a humidified atmosphere with 5% CO_2. For fluorescence imaging 300×10^3 cells were plated on 25 mm glass-bottomed dishes in DMEM Life (without phenol red). Fluorescence lifetimes were measured in 24 h.

Fluorescence lifetime images were collected using the fluorescence laser-scanning microscope LSM 710 (Carl Zeiss, Germany) equipped with time-correlated single photon counting (TCSPC) electronics (Becker & Hickle GmbH, Germany). The images were acquired through a water immersion objective 40x, 1.2 NA. NADH and FAD fluorescence was excited by a femtosecond Ti:sapphire laser with a repetition rate of 80MHz at the wavelength of 750 nm or 900 nm and recorded using 455-500 nm or 500-550 nm bandpass filters, respectively. The analysis of the FLIM data was performed using SPCImage software (Becker & Hickl GmbH, Germany).

Results

As expected, NADH and FAD fluorescence decay curves were best fit to a double-exponential decay model with the first (short, τ_1) components corresponded to free NADH and protein-bound FAD, and the second (long, τ_2) components corresponded to protein-bound NADH and free FAD. The results of lifetime measurements showed that in the mouse fibroblasts the fluorescence lifetimes did not differ from cancer cells, but the relative contributions of the lifetime components were different, indicating that the fibroblasts display more OXPHOS metabolism than cancer cells in monoculture conditions. It is interesting that in monocultures of human cancer and normal cells fluorescence lifetime parameters did not differ significantly. In co-culture conditions an increase of the relative contribution of free NADH was detected in the cancer cells, while in the fibroblasts it decreased indicating a shift to more glycolytic metabolism in cancer cells and to more oxidative metabolism in the fibroblasts.

Conclusion

In summary, FLIM technique showed great opportunities for metabolic imaging in living cells. The differences in a cell metabolism were detected between mouse cancer cells and fibroblasts, as well as between mouse and human cancer cells in monocultures. Co-culturing of human cancer and normal cells led to metabolic switch to glycolysis in cancer cells, similar to that characteristic for most real tumors.

Acknowledgements

The study has been financially supported by the Russian Scientific Foundation, project # 14-15-00646. The authors are grateful to Dr. Vladislav Shcheslavskiy (Becker & Hickl GmbH, Germany) for helpful consultations in FLIM.

References

1. R.A. Cairns, I.S. Harris, and T.W. Mak, *Nature Reviws Cancer*, 2011, 85-95.
2. J.M. Calderon-Montano, E. Burgos-Moron, C. Perez-Guerrero, et al., *WebmedCentral*, 2011.
3. B.A. Webb, M.l. Chimenti, M.P. Jacobson, and D.L. Barber, *Nature Reviws Cancer*, 2011, **11**, 671-677.
4. Han-Wen Guo, Chien-Tsun Chen, Yau-Huei Wei, et al, *JBO*, 2008, **13**(5), 054011-1 – 054011-9.
5. J.R. Lakowicz, H. Szmacinski, K. Nowaczyk, and M.L. Johnson, *PNAS*, 1992, **89,** 1271-1275.
6. M.C. Skala, G.M. Palmer, K.M. Vrotsos, A. Gendron-Fitzpatrick, and N. Ramanujam, *Optics Express*, 2007, 7863-7875.
7. M.C. Skala and N. Ramanujam, *Methods Mol Biol*, 2010, **594**, 155-162.
8. M.C. Skala, K.M. Riching, A. Gendron-Fitzpatrick, et al., *PNAS*, 2007, 1949-1999.

METABOLIC TRAJECTORY INVESTIGATION OF MESENCHYMAL STEM CELLS DIFFERENTIATION USING FLUORESCENCE LIFETIME MICROSCOPY

A.V. Meleshina[1,2], **V.V. Dudenkova**[1], **A.S. Bystrova**[1], **E.I. Cherkasova**[1,2], and **E.V. Zagainova**[1,2]

[1] Nizhny Novgorod State University, Nizhny Novgorod, Russia, almele@ya.ru
[2] Nizhny Novgorod State Medical Academy, Nizhny Novgorod, Russia

Abstract. The non-invasive imaging of cell metabolism within tissues to assess the efficacy of stem cell therapy and understanding the tissue development is of great interest. In this study we investigated metabolic trajectory of the mesenchymal stem cell (MSC) differentiation on the change of the fluorescence lifetime of free and bound forms of the nicotinamide adenine dinucleotide (NADH) and flavin adenine dinucleotides (FAD) using Fluorescence Lifetime Microscopy. Undifferentiated, adipogenically and osteogenically differentiated human MSCs were imaged with a Zeiss 710 microscope coupled to a FLIM system. Short and long NADH, FAD lifetime fluorescence and ratio of free and bound NADH and FAD were shown to increase in differentiated cells.

Introduction

Currently the investigation of the stem cell's metabolic state, differentiation state and cell-lineage commitment is sure to be of great interest. At the same time fluorescence lifetime microscopy (FLIM) allows non-invasively and for a longer time to study the functional changes that underlie cellular metabolism. FLIM measures the time-decay characteristics of the cell and allows to identify a molecular localization of intrinsic fluorophores and endogenous proteins such as collagen, flavins, nicotinamide adenine dinucleotide (NADH).

Materials and methods

Cell culture

We used human bone marrow mesenchymal stem cell (MSC). Differentiation of the MSCs was induced by incubating attached MSCs in the adipogenic and osteogenic induction medium. Before and on day 21 after the induction of adipogenic and osteogenic differentiation, the samples of cells were imaged.

The fluorescence lifetime images are acquired with a Zeiss 710 microscope coupled to a Ti:Sapphire laser system and a FLIM system. The intrinsic fluorescence of NADH and FAD was excited at 750 nm and 900 nm respectively.

Results and discussions

The representative images of the NADH fluorescence lifetime of the undifferentiated MSCs, differentiated adipocytes and osteoblasts on day 21 were received. Each pixel represents short and long fluorescence which corresponds to lifetimes of free and bound NADH and was color-coded. Apparently, these images exhibited an NADH fluorescence lifetime shift color changed toward higher values during the MSC differentiation. The changes in the NADH fluorescence lifetime from the undifferentiated MSCs to the differentiated adipocytes and osteoblasts were confirmed in a series of samples. Short and long NADH, FAD lifetime fluorescence were increased in the differentiated adipocytes and osteoblasts. Besides, the rise of free and bound NADH and FAD ratio was shown. The increase of this ratio indicates the change ratio of free and bound NADH and FAD in differentiated MSCs adipocytes and osteoblasts. This is the evidence of changes in the ways of the hydrolytic cleavage of macromolecules in the cells. Our results about the increase of short and long NADH, FAD lifetime fluorescence as well as were the change ratio of free and bound NADH and FAD in the differentiation process confirmed by the data of other researchers [1].

Conclusion

The results suggest that the change in the ratio of free and bound forms of NADH and FAD in undifferentiated and differentiated adipocytes and osteoblasts indicates a switching pathway of the glycolysis and oxidative phosphorylation in the differentiation process.

Acknowledgements

The work is carried out with the support of Russian Science Foundation (grants No. 14-15-00536) and by Ministry of Education and Science of the Russian Federation in the framework of the state order № 2014/134 (project No. 2460).

References

1. H.-W. Guo, et al., *Journal of Biomedical Optics,* 2008, **13**(50), 1-3.

Invited

IMAGING HYPOXIA IN 3D TISSUE MODELS USING PHOSPHORESCENT O_2 NANOSENSORS

D.B. Papkovsky, R.I. Dmitriev, and **A.V. Zhdanov**

School of Biochemistry and Cell Biology, University College Cork, Cork, Ireland;
d.papkovsky@ucc.ie

Abstract. Molecular oxygen (O_2) plays important roles in cell and tissue function. Quenched phosphorescence detection allows non-invasive quantification of O_2 in respiring samples using solid-state sensors or soluble nanosensor probes. Here we demonstrate the O_2 imaging PLIM-TCSPC method with different 3D tissue models: cancer and stem cell spheroids, explants of brain, colon, bladder tissue, cultured organoids. This approach allows visualisation of hypoxia with sub-cellular resolution, and studies of stem cell development and metabolic responses of cancer cells to drug treatment.

Introduction

Quenched-phosphorescence detection allows quantification of cell and tissue O_2 by means of dedicated indicator dyes and sensor materials on their basis [1]. Pt(II)-porphyrins, which display long-lived emission (lifetimes 10-100 μs), high brightness [2], can be incorporated in solid matrices (e.g. polystyrene scaffold) or nanoparticle structures, which shield them from interferences (pH, ionic strength, proteins, etc.), improve biocompatibility and provide optimal sensitivity to O_2. Cell-penetrating O_2 probes can also be designed from small molecule and nanoparticle structures. The O_2 nanosensors of new generation [3] provide efficient staining of monolayer and 3D cell cultures in 1-16 h and high-resolution imaging of tissue O_2 in multiple detection modalities (ratiometric intensity or lifetime based O_2 sensing under one or two-photon excitation). Phosphorescent O_2 imaging can be multiplexed with many other conventional fluorescent probes, proteins and antibody stains, to correlate tissue hypoxia and O_2 dynamics with other physiological parameters of the cell or tissue sample. Tumor spheroids are now widely used to study cancer *in vitro* [4]. In this 3D tissue model cell-cell contacts and mass exchange conditions have close resemblance to *in vivo* conditions. Due to their size (> 100 μm), gradients of nutrients and metabolites such as O_2 and niche regions, such as necrotic cores are formed. The main challenges with imaging of tumor spheroids are limited in-depth staining with extrinsic probes (nanoparticles, fluorescent proteins), and limited light penetration depth.

Imaging of intra- and pericellular O_2 in 3D tissue models

Recently, we have developed new ultra-bright nanoparticle O_2 probes with improved cell staining ability, tunable surface charge and spectral characteristics (two emission spectra variants: blue-red and green-infrared). Using optimised procedure, we achieved almost 100% in-depth staining and intracellular distribution of the probe in 200–300 μm spheroids, thus allowing their imaging on a confocal one-photon TCSPC-PLIM microscope. Fig. 1A shows examples of staining of tumor spheroids from HCT116 cell with nanoparticles (red) and corresponding phosphorescence lifetime (PLIM) image informing on its oxygenation state. To relate the oxygenation with number of dead cells, spheroids can be co-stained with fluorescent live cell dyes such as CellTox Green [5].

As an alternative to cell staining, we also designed phosphorescent O_2–sensitive scaffolds, where the standard microporous polystyrene scaffold for 3D cell culture was impregnated with an O_2-sensitive indicator dye to allow sensing of peri-cellular O_2 concentration [6]. Fig. 1B shows distribution of HCT116 cells in the scaffold, and dependence of oxygenation on cell density (reflected as higher phosphorescence lifetime values).

These O_2 imaging approaches – cell-penetrating nanoparticle probes and phosphorescent O_2 sensitive scaffolds – are now actively used in several detailed physiological studies with 3D models of stem and cancer cells.

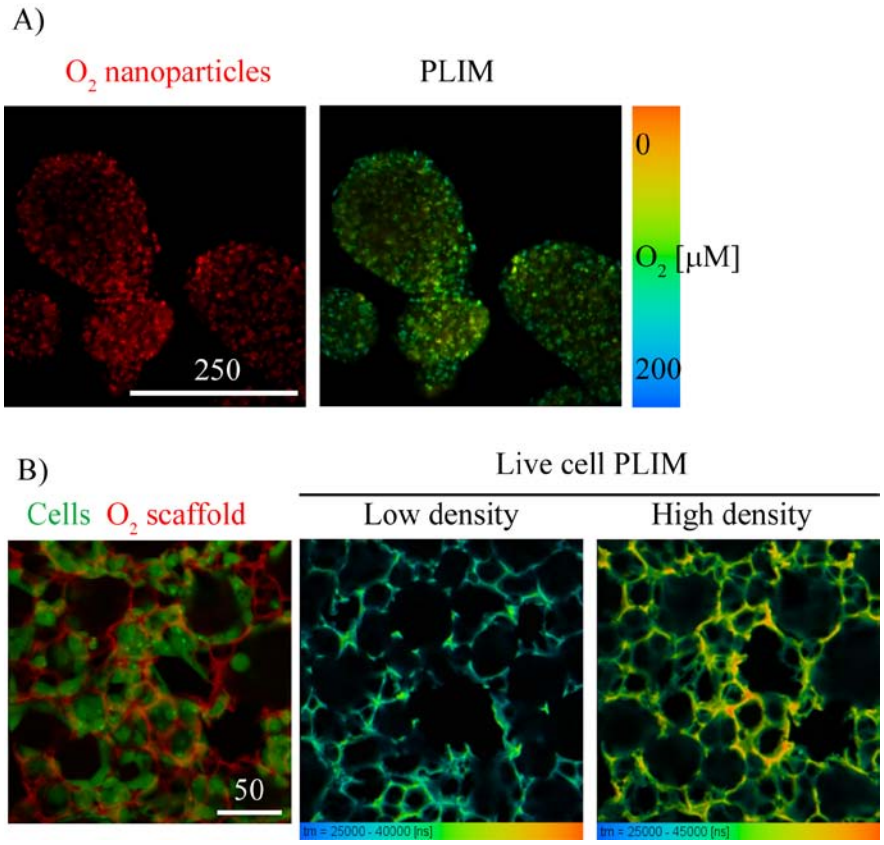

Fig. 1. A: Images of HCT116 cell spheroids stained with the nanoparticle O_2 probe. B: Imaging of local oxygenation of cells seeded at low and high density in the phosphorescent O_2-sensitive scaffold. False-color scales reflect distribution of phosphorescence lifetime or O_2 concentration. Scale bars are in μm

Acknowledgments

Financial support of this work by Science Foundation Ireland, grants 13/SIRG/2144 and 12/RC/2276, is gratefully acknowledged.

References

1. D.B. Papkovsky and R. I. Dmitriev, *Chemical Society Reviews*, 2013, **42**, 8700-8732.
2. M. Quaranta, S.M. Borisov, and I. Klimant, *Bioanalytical reviews*, 2012, **4**, 115-157.
3. R. Dmitriev and D. Papkovsky, *Methods and Applications of Fluorescence*, 2015 (*in press*).
4. G. Mehta, A.Y. Hsiao, M. Ingram, G.D. Luker, and S. Takayama, *Journal of Controlled Release*, 2012, **164**, 192-204.
5. R.I. Dmitriev, S.M. Borisov, J. Jenkins, and D.B. Papkovsky, in *SPIE BiOS, International Society for Optics and Photonics*, 2015, 932806-932808.
6. J. Jenkins, R.I. Dmitriev, K. Morten, K.W. McDermott, and D.B. Papkovsky, *Acta Biomaterialia*, 2015, **16**, 126-135.

Invited

INVESTIGATION OF CELL METABOLISM BY FLIM AND PLIM

A. Rück[1], J. Breymayer[1], D. Bisinger[1], E.M. Schneider[2], P. Schäfer[3], L. Merthan[3], B. von Einem[3], C.A.F. von Arnim[3], and **S. Kalinina[1]**

[1]University Ulm, Core Facility Confocal and Multiphoton Microscopy, N24, Albert-Einstein-Allee 11, 89081 Ulm, Germany, angelika.rueck@uni-ulm.de
[2]Section Experimental Anesthesiology, University Hospital Ulm, Albert Einstein Allee 23, 89081 Ulm, Germany
[3]Dept. of Neurology, University Hospital Ulm, Oberer Eselsberg 45, 89081 Ulm, Germany

Abstract. Glycolysis and oxidative phosphorylation are key players in energy conserving mechanisms. It is accepted that both reactions go along with changes of the fluorescence lifetime of NADH and FAD. FLIM of NADH and FAD are therefore achieving increased interest in fluorescence guided diagnosis of various diseases. However, as observed in a variety of investigations, the situation is complex and the result is influenced by other parameters like oxidative stress. Moreover, oxygen tension has to be taken into account in order to understand the underlying reasons for metabolic alterations. Phosphorescence lifetime imaging (PLIM) is a new method to observe oxygen tension.

Cell metabolism in general and energy content in greater detail can be determined by the analysis of chemical reactions providing ATP, FAD+ and NAD(P)H. Glycolysis and oxidative phosphorylation (OXPHOS) are the key players in energy conserving mechanisms. It is well accepted that both reactions go along with changes of the fluorescence lifetime of NADH and FAD. The time resolved fluorescence characteristics of NADH and FAD are therefore achieving increased interest in fluorescence guided diagnosis of various diseases. However, as observed in a variety of investigations, the situation is complex and the result is influenced by other parameters like oxidative stress or tissue architecture. In this context, the observation of a "negative" Warburg effect is just one example [1]. Consecutively, fluorescence lifetime measurements (FLIM) addressed by imaging of NADH and FAD does not always correlate with cell metabolism. Moreover, oxygen tension has to be taken into account in order to understand the underlying reasons for metabolic alterations. Importantly, phosphorescence lifetime imaging (PLIM) is a new method to observe oxygen tension (see figure 1).

Within this presentation the basic mechanisms and relations of FLIM, PLIM and cell metabolism will be discussed and clinically relevant applications will be demonstrated. This includes investigations on tumour diagnosis, Alzheimers related disease as well as the transition of SIRS (severe inflammatory response syndromes) to sepsis.

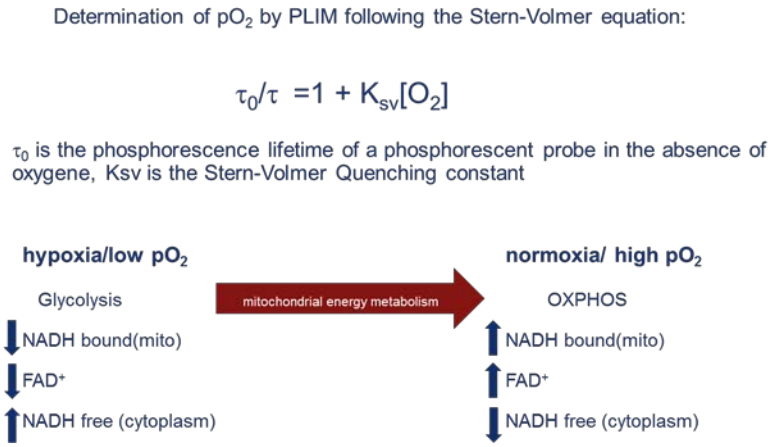

Fig. 1. Possible correlation between pO_2 (PLIM) and cell metabolism (FLIM)

Acknowledgements

This work was carried out with financial support by the Ministry of Financial Affairs of Germany, FKZ order: KF2122510AK2 ("PLIMOX"), FKZ order: IGF 18239 N/3 ("MITOSKOPIE") and of the Ministry of Research and Development, FKZ order: 13N12942 ("METAPHOR").

References

1. A. Rück, C. Hauser, S. Mosch, and S. Kalinina, "Spectrally resolved fluorescence lifetime imaging to investigate cell metabolism in malignant and nonmalignant oral mucosa cells", *Journal of Biomedical Optics*, 2014, **19**(9), 096005.

STUDY OF APOPTOSIS IN CANCER CELLS USING A NEW GENETICALLY ENCODED FRET-BASED SENSOR FOR CASPASE-3

T.F. Sergeeva[1], M.V. Shirmanova[1], V.V. Dudenkova[1,2], O.A. Zlobovskaya[3], E.V. Zagaynova[1], and **K.A. Lukyanov[1,3]**

[1]Nizhny Novgorod State Medical Academy, Nizhny Novgorod, Russia,
prazina@yandex.ru
[2] Nizhny Novgorod State University, Nizhny Novgorod, Russia
[3]Shemyakin-Ovchinnikov Institute of Bioorganic Chemistry, Moscow, Russia

Abstract. Apoptosis is known to be an important cellular event that plays a key role during treatment of many diseases. Caspase-3 is a cysteine protease involved in the «execution» phase of a programmed cell death. This study was aimed at the development of method of detection of caspase-3 activation using a new genetically encoded FRET-based sensor consisted of a red and near-infrared proteins fused through a DEVD linker. The possibility of analysis of a caspase-3 activity in cancer cells *in vitro* by means of the sensor and fluorescence lifetime imaging was shown for the first time.

Introduction

Apoptosis is a cellular process that plays an important role in tissue homeostasis, pathophysiology and treatment of many diseases. Several mechanisms through mitochondria or outer membrane receptors are known to be involved into apoptosis induction [1–3]. The execution of apoptosis is mediated by the members of the caspase family, which can be subdivided into initiator and effector caspases. Caspase-3 is believed to be the primary executioner of a programmed cell death. Inhibition of this enzyme can block apoptosis. Measurement of caspase-3 activity is essential, for example, for anti-cancer drug design and screening [4, 5].

The use of biosynthetic fluorescent sensors based on Forster resonance energy transfer (FRET) is an important approach for imaging apoptosis. FRET is a quantum mechanical process between two fluorophores whereby energy from an excited donor molecule is transferred to the acceptor molecule. This results in a reduction in donor fluorescence emission and lifetime, at the same time, an increase in acceptor fluorescence emission. It is known that the lifetime of a donor protein is elevated in caspase-3 activation. Therefore, FRET technique can be used to monitor the dynamics of caspase-3 activation in living cells in real time [5–7].

The aim of this study was to develop the method of caspase-3 activity detection in cancer cells *in vitro* using a new genetically encoded FRET-based sensor.

Materials and Methods

CT26 (murine colon carcinoma) cell line and CT26 stably expressing the sensor for caspase-3 were cultured in DMEM with 10% FCS, 1% glutamine, 10 units/mL penicillin and 10 μg/mL streptomycin. Cell cultures were maintained at 37 °C in a humidified 5% CO_2 incubator.

CT26 cells were transiently transfected with mKate2 plasmid cDNA. Transfection of the plasmid into CT26 cells was carried out by using X-tremeGENE 9 DNA Transfection Reagent (Roche Diagnostics GmbH, Germany). After 24-48 hours fluorescence signal was examined by Fluorescence Lifetime Imaging (FLIM).

For apoptosis induction, CT26 cells stably expressing the sensor for caspase-3 were plated 24 hours before the experiment and then treated with 5 μg/ml staurosporine (STS) immediately before fluorescence imaging. Detection of caspase-3 activation was performed during 3 hours post-induction of apoptosis using the FLIM system.

FLIM was performed on the Laser Scanning Confocal Microscope LSM 710 (Carl Zeiss, Germany) with FLIM module (Becker&Hickl GmbH., Germany). C-Apochromat 63x/1.2 W Korr objective was used for all measurements. The donor protein was excited with a Ti:Sa short-impulse femtosecond laser ChameleonVisionII (Coherent) at 1000 nm. Fluorescence was detected with 595–670 nm emission filter. FLIM sequences were obtained at 37 °C at a modulation frequency of 80 MHz. he FLIM data were processed using the SPCImage software (Becker&Hickl GmbH, Germany). The fluorescence lifetime of the donor alone as well as in the presence of the acceptor were measured.

Results

A new genetically encoded FRET-based sensor for caspase-3 was constructed by fusing of the far-red protein mKate2 (donor) and the near-infrared protein iRFP (acceptor) with a specialized linker that contains a caspase-3 recognition and cleavage sequence, DEVD. Activation of caspase-3 leads to the cleavage of a linker DEVD between a donor and acceptor proteins, effectively reducing the FRET.

The onset of apoptosis in CT26 cells expressing mKate2-DEVD-iRFP sensor was observed after STS treatment. STS is supposed to be a powerful inducer of apoptosis in a variety of cell types [7, 8]. It was used as a positive control on caspase-3 activation. In the experiment the treatment with STS led to activation of caspase-3 and appearance of morphologically apoptotic, disintegrated cells. Caspase-3-dependent cleavage of the DEVD motif decreased energy transfer from a donor protein mKate2 to the acceptor iRFP and resulted in FRET loss.

Analysis of fluorescence lifetime in CT26 cells expressing mKate2-DEVD-IRFP after STS treatment revealed an increase in mKate2 lifetime. In the cells expressing mKate2 alone, the mean fluorescence lifetime of mKate2 was 2045±44 ps. In comparison, the mean fluorescence lifetime of mKate2 in the cells stably expressing mKate2-DEVD-iRFP sensor was 1759±49 ps. After STS treatment the lifetime of the donor increased to 2064±37 ps and corresponded to the lifetime of mKate2 in the cells expressing this protein alone. Consequently, a new genetically encoded FRET-based sensor of a caspase-3 activity, mKate2-DEVD-iRFP, can be used to provide a measurement of the caspase-3 activation in tumor cells.

In conclusion, the possibility of analysis of a caspase-3 activity in cancer cells *in vitro* by means of the new FRET-based sensor and fluorescence lifetime imaging was shown for the first time. This method can be used to monitor activation of caspase-3 during anti-tumor treatment to provide rapid assessment of apoptosis induction for improvement chemotherapy efficacy.

Acknowledgements

This work was financially supported by the Russian Science Foundation (project # 14-25-00129).

References

1. F. Zhou, D. Xing, S. Wu, and W.R. Chen, *Mol Imaging Biol*, 2010, **12**, 63-70.
2. R.S.Y. Wong, *Journal of Experimental & Clinical Cancer Research*, 2011, **30**, 87-101.
3. K. Kominami, T. Nagai, T. Sawasaki, et al., *PLOS ONE*, 2012, **7**(11), 1-18.
4. M. Keese, V. Yagublu, K. Schwenke, et al., *IJC*, 2010, **126**, 104-113.
5. Y. Lu, T. Chen, J. Qu, et al., *Journal of Biomedical Science*, 2009, **16**, 16-31.
6. M. Seervi, P.K. Sobhan, K.A. Mathew, et al., *Apoptosis*, 2014, **19**, 269-284.
7. W. Pan, J. Qu, T. Chen, et al., *Eur Biophys J*., 2009, **38**, 447-456.
8. L. Wang, T. Chen, J. Qu, and X. Wie, *Micron*, 2009, **40**, 811-820.

Invited

TWO-PHOTON LIGHT-SHEET MICROSCOPY IN DEVELOPMENTAL BIOLOGY AND NEUROSCIENCES

W. Supatto

Ecole Polytechnique, Laboratory for Optics and Biosciences, CNRS, Inserm, Palaiseau, France,
willy.supatto@polytechnique.edu

Abstract. We report on recent developments in two-photon light-sheet microscopy to perform multicolor and fast imaging deep inside live organisms. The principle, implementation and advantages of two-photon light-sheet microscopy are discussed. With live imaging of fly and zebrafish embryos and larvae, we demonstrate its performance in maintaining good signal and high spatial resolution deep inside biological tissues, as well as high acquisition speed and low phototoxicity. In addition, we present a strategy based on wavelength mixing to perform optimal and simultaneous two-photon excitation of three chromophores with distinct absorption spectra. These approaches open new opportunities for live imaging in developmental biology and neurosciences, including the investigation of cardiac development or the brain-wide functional imaging.

Multiscale and multidimensional study of biological processes tremendously benefits from recent advances in live microscopy [1]. In the past decade, light-sheet microscopy has gained widespread recognition due to its distinct advantages for imaging live organisms. Indeed, the ability to carry out fast, three-dimensional optical sectioning with both an extended field of view and limited photodamage is a unique advantage of light-sheet microscopy. However, the imaging speed performance of light-sheet microscopy comes with several limitations for live imaging, including a limited imaging depth. On the other hand, two-photon excited fluorescence microscopy achieves high imaging depth into scattering tissues with limited acquisition speed and challenging multicolor excitation. To overcome these limitations, we report on the development of two-photon light-sheet microscopy, which combines two-photon excited fluorescence with orthogonal illumination. First, we will introduce the principle of two-photon light-sheet microscopy and demonstrate its performance in maintaining high spatial resolution deep inside biological tissues, as well as high acquisition speed and low phototoxicity [2]. In addition, we will present a strategy based on wavelength mixing to perform optimal and simultaneous two-photon excitation of three chromophores with distinct absorption spectra. We show this approaches open new opportunities for live, multicolor, multidimensional and multiscale imaging in developmental biology and neurosciences. We illustrate these potentials by imaging fly development, and recording fast and multicolor images of the beating heart in zebrafish embryos with negligible photodamage and sufficient spatio-temporal resolution for 3D-cell tracking during a cardiac cycle [3]. In addition, we show near-infrared two-photon light-sheet imaging is suitable for 3D brain-wide functional imaging in zebrafish larvae at cellular resolution [4]. This method eliminates the photostimulation associated with one-photon functional imaging. Hence, two-photon light-sheet imaging should be considered as the method of choice for whole-brain network analysis of most processes involving the visual modality or sensitive to the photic environment.

Acknowledgements

I thank all contributors of the presented work: T.V. Truong, D.S. Koos, J.M. Choi, and S.E. Fraser at Caltech (California, USA); P. Mahou, J.M. Sintes, and E. Beaurepaire at Ecole Polytechnique (France); S. Wolf, G. Debregeas, S. Kruglik, and R. Candelier at UPMC (France); & J. Vermot at IGBMC (France). This work was supported by the French Agence Nationale de la Recherche (ANR-2010-JCJC-1510-01, ANR-11-EQPX-0029), European Union Seventh Framework Programme (Marie Curie International Reintegration Grant no. 268379), Foundation Louis D de l'Institut de France.

References

1. P. Pantazis and W. Supatto, "Advances in whole-embryo imaging: a quantitative transition is underway", *Nature Reviews Molecular Cell Biology*, 2014, **15**(5), 327-339.
2. T.V. Truong, et al., "Deep and fast live imaging with two-photon scanned light-sheet microscopy", *Nature Methods*, 2011, **8**(9), 757-760.
3. P. Mahou, et al., "Multicolor two-photon light-sheet microscopy", *Nature Methods*, 2014, **11**(6), 600-601.
4. S. Wolf, et al., "Whole-brain functional imaging with two-photon light-sheet microscopy", *Nature Methods*, 2015, **12**(5), 379-380.

PHOTOTOXIC EFFECTS OF FLUORESCENT PROTEIN KILLER-RED INDUCED IN A MOUSE TUMOR BY PULSED LASER IRRADIATION

D.V. Yuzhakova[1,2], M.V. Shirmanova[1], G.S. Perelman[2], L.B. Snopova[1], P.V. Subochev[3], V.A. Kamensky[3], E.O. Serebrovskaya[4], S.A. Lukyanov[1,4,5], and **E.V. Zagaynova[1]**

[1] Nizhny Novgorod State Medical Academy, 603005 Minin and Pozharsky Sq., 10/1, Nizhny Novgorod, Russia, yuzhakova-diana@mail.ru

[2] Lobachevsky State University of Nizhny Novgorod, Gagarina Ave., 23, Nizhny Novgorod, Russia, 603950

[3] Institute of Applied Physics RAS, Ulyanov St., 46, Nizhny Novgorod, Russia, 603950

[4] Shemyakin-Ovchinnikov Institute of Bioorganic Chemistry RAS, Miklukho-Maklaya St., 16/10, Moscow, Russia, 117997

[5] Pirogov Russian National Research Medical University, Ostrovitianova St., 1, Moscow, Russia, 117997

Abstract. The development of photodynamic therapy, a promising therapeutic strategy for cancer, requires highly selective phototoxic agents. The purpose of this study was to compare the phototoxicity of the first genetically encoded photosensitizer KillerRed (KR) against mouse colon carcinoma CT26 in vivo upon continuous wave (CW) and pulsed laser irradiation. Our results showed the increased number of damaged and apoptotic cells in CT26-KR tumors after pulsed laser treatment, while in the case of CW mode there was no effect. Therefore, we report for the first time on phototoxicity of KR in a mouse tumor model upon pulsed laser irradiation.

Introduction

Photodynamic therapy (PDT) is a promising therapeutic strategy for cancer [1]. However, the development of effective PDT requires highly selective phototoxic agents. Recently, it was found that a red fluorescent protein KillerRed (KR) has pronounced phototoxic properties and can be successfully used as genetically encoded photosensitizer.

Previously the ability of KillerRed to block cell division and induce a cell death was demonstrated in cancer cell lines *in vitro* [2, 3] and HeLa tumor xenografts *in vivo* [4], but the induction of the effects required multiple laser irradiation at high light doses. To improve this approach for PDT an optimization of the laser treatment regime is needed. Recently, a comparison of continuous wave (CW) and pulsed laser irradiations has been performed on the KR-expressing tumor spheroids and higher efficiency of pulsed laser treatment for activation of apoptosis has been shown [5].

The purpose of this study was to compare the phototoxicity of the first genetically encoded photosensitizer KillerRed in mouse colon carcinoma CT26 *in vivo* upon CW and pulsed laser irradiations.

Materials and Methods

Cell line and mouse tumor model

CT26 murine colon carcinoma cell line (ATCC CRL-2638) stably expressing histone H2B-tandem KillerRed (H2B-tKR) fusion was obtained by lentiviral transduction.

The experiments were carried out on the immunocompetent Balb/c mice weighing 18–20 g. CT26 or CT26-KR tumors were induced by subcutaneous (s.c.) injection of $5 \cdot 10^5$ cancer cells suspended in 100 μL PBS into the mouse leg.

All the experiments conducted on animals were approved by the Institutional Ethical Committee (Nizhny Novgorod State Medical Academy, Russia).

Laser treatment

A diode pumped solid state yellow laser (MGL, Changchun New Industries Optoelectronics Tech. Co., Ltd. (CNI) P.R. China), 593 nm, was used for CW laser treatment. In the case of pulsed mode tumors were irradiated by a tunable pulsed laser (LS-2214PC, LOTIS TII, Belarus), 584 nm, 15 ns, 10 Hz. To perform PDT mice were treated for 30 min at 150 mW/cm^2, 260 J/cm^2 for CW laser or 225 mW/cm^2, 337 J/cm^2 for pulsed laser on the 6, 7, and 8th days of the tumor growth. During the irradiation photobleaching of KR in tumors *in vivo* was assessed based on fluorescence whole-body imaging. 24 h after the last treatment tumors were surgically removed for histological analysis (H&E).

Results

The evaluation of photobleaching of KR in CT26-KR tumors showed a significant difference between the CW and pulsed mode. The CW laser irradiation at 150 mW/cm^2 resulted in 35% fluores-

cence decrease and temperature increase by 1-2°C. Maximum fluorescence decrease 45% was obtained at the power density of 260 mW/cm^2, but there was an undesirable temperature increase by 4-5°C in that case. Pulsed laser treatment demonstrated higher fluorescence decrease (60%) at lower power density (225 mW/cm^2) and no temperature changes.

An analysis of phototoxicity of KR after PDT with CW (150 mW/cm^2, 30 min, x3) laser displayed no effect on tumor tissue (Fig. 1). There was no difference in histopathology between treated and untreated CT26-KR tumors. In contrast, PDT with pulsed laser (225 mW/cm^2, 337 J/cm^2, x3) caused pronounced dystrophic changes in tumor cells (Fig. 1). It was found that the portion of damaged cells was 23.2% and 43.8% in untreated and treated CT26-KR tumors respectively. The dystrophic changes included vacuolated cytoplasm, swollen or irregular hyperchromic nuclei and chromatin condensation.

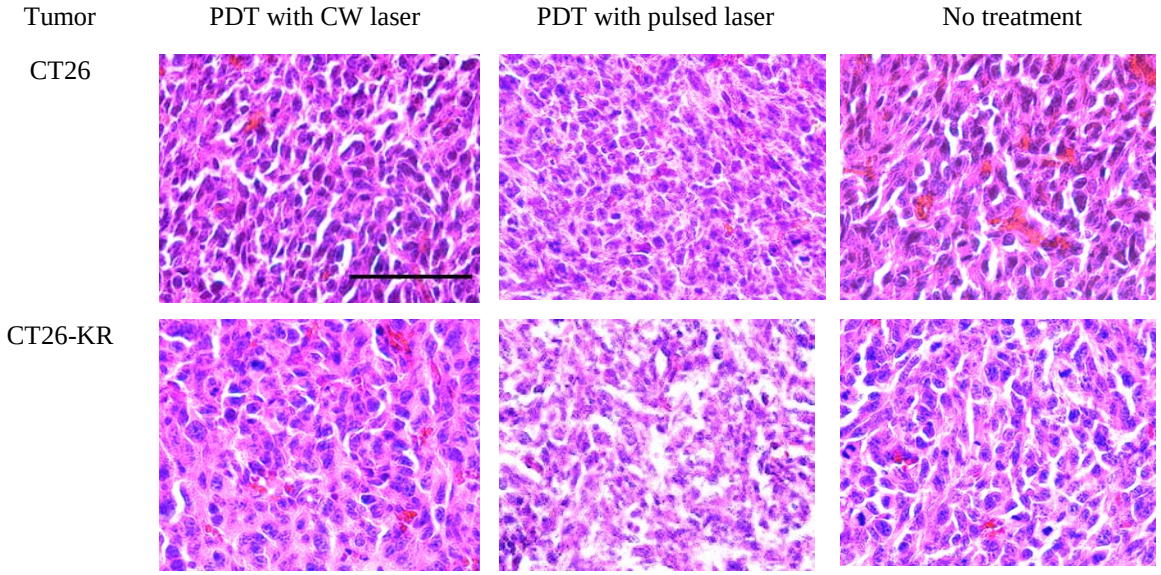

Fig. 1. A histological view of CT26 and CT26-KR tumors.
Representative tissue sections stained with H&E are shown. Scale bar is 100 μm

In summary, we present the first report on a phototoxicity of KillerRed as a genetically encoded photosensitizer a mouse tumor model upon pulsed laser irradiation. We show that pulsed mode is more preferable for animal studies due to the absence of temperature effect, and induces more pronounced photobleaching and phototoxicity of KillerRed.

Acknowledgements

This work was supported by the Ministry of Education and Science of the Russian Federation (project #11.G34.31.0017) and the Russian Foundation for Basic Research (grants # 14-04-01185A, 14-02-00860).

References

1. A.P. Castano, P. Mroz, and M.R. Hamblin, *Nature Reviews Cancer*, 2006, **6**, 535-545.
2. E.O. Serebrovskaya, T.V. Gorodnicheva, G.V. Ermakova, et al., *Biochem. J.*, 2011, **435**, 65-71.
3. M.E. Bulina, K.A. Lukyanov, O.V. Britanova, et al., *Nat. Protoc*., 2006, **1**, 947-53.
4. M.V. Shirmanova, E.O. Serebrovskaya, K.A. Lukyanov, et al., *J. Biophotonics*., 2013, **6**, 283-90.
5. D.S. Kuznetsova, M.V. Shirmanova, V.V. Dudenkova, et al., *J. Biophotonics*, 2015, **2015**, 1–9.

Invited

INVESTIGATION OF TUMOR METABOLIC STATUS USING GENETICALLY ENCODED SENSORS AND FLUORESCENCE IMAGING

E. Zagaynova[1], M. Shirmanova[1], I. Druzhkova[1], M. Lukina[1], V. Dudenkova[1,2], L. Shimolina[2], M. Kuimova[4], V. Shcheslavsky[5], and **V. Belousov[1,3]**

[1] Nizhny Novgorod State Academy, Nizhny Novgorod, Russia
ezagaynova@gmail.com
[2] Lobachevsky Nizhny Novgorod State University, Nizhny Novgorod, Russia
[3] Shemyakin-Ovchinnikov Institute of Bioorganic Chemistry RAS, Moscow, Russia
[4] Imperial College London, London, Great Britain
[5] Becker&Hickl GmbH, Berlin, Germany

Abstract. We report here on some results about the specific tumor cells parameters obtained by the fluorescence microscopy techniques (one-photon and two-photon microscopy, FLIM) and fluorescence whole-body imaging. A few parameters that potentially can change as a result of cancer transformation were studied – intracellular pH (pHi), hydrogen peroxide level, metabolic status and microviscosity.

New genetically encoded ratiometric biosensors SypHer2 [1] and HyPer2 [2] based on the fluorescent protein cpYFP were used to detect pHi and hydrogen peroxide, correspondingly. Cell metabolism was analyzed by NADH and FAD fluorescence lifetime [3]. The study was performed on monolayer cell cultures, tumor spheroids and tumor xenografts. To initiate cancer-normal cell interaction, co-cultures of human cancer cells and fibroblasts were prepared.

The method of pHi mapping in tumor spheroids and tumors *in vivo* was developed. More acidic pHi in the core of the tumor nodule was demonstrated, that may be a consequence of hypoxia-induced glycolytic metabolism [4].

Metabolic imaging in living cells showed the differences in a cell metabolism between cancer cells and fibroblasts, as well as between mouse and human cancer cells in monocultures. As expected, in co-culture conditions human cancer cells switched their metabolism to glycolysis, similar to real tumors. Slight acidification of the cytoplasm of cancer cells was detected in the co-culture, whereas production of hydrogen peroxide increased significantly. These findings testify to the important role of hydrogen peroxide in cellular interactions and metabolic cooperation of cancer cells and fibroblasts for supporting carcinogenesis.

Using fluorescent Bodipy-based molecular rotors and FLIM cellular microviscosity was estimated in cancer cells and fibroblasts in vitro and tumors in vivo. We showed that microviscosity of the plasma membrane is higher than of intracellular compartments in all cell lines, and in cancer cells the plasma membrane is more viscous than in fibroblasts.

Finally, we can conclude, that all parameters are dramatically changed during cancer transformation and in the process of interaction between normal and cancer cells.

References

1. M. Matlashov et al., *BBA General Subjects*, 2015 (in press).
2. K.N. Markvicheva, D.S. Bilan, N.M. Mishina, et al., Bioorganic & Medicinal Chemistry, 2011, **19**, 1079–1084.
3. J.R. Lakowicz, H. Szmacinski, K. Nowaczyk, and M.L. Johnson, PNAS, 1992, **89**, 1271-1275.
4. M.V. Shirmanova, I.N. Druzhkova, M.M. Lukina et al., *BBA-General Subjects*, 2015 (in press).

SPONSORS

BECKER & HICKL GMBH: 22 YEARS OF MULTI-DIMENSIONAL TCSPC ADVANCES IN FLUORESCENCE LIFETIME TECHNIQUES

W. Becker

Becker & Hickl GmbH, Nahmitzer Damm 30, 12277 Berlin, Germany
E-mail: becker@becker-hickl.com

Abstract. In 1993 Becker & Hickl introduced a time-correlated single photon counting (TCSPC) technique which was 100 times faster in acquisition speed than the existing devices. Moreover, the new technique not only recorded a single waveform of a light signal but a complex photon distribution over the times of the photons in the excitation period and various other parameters, such as wavelength, spatial parameters, or the time from a stimulation of the sample. In the past 20 years, multi-dimensional TCSPC has constantly been developed, and become the basis of several key technologies of biomedical optics. We will describe the recent advances of the technique.

Development of Multi-Dimensional TCSPC

Becker & Hickl GmbH was founded in 1993 with the aim to introduce new technical principles in time-correlated single photon counting (TCSPC). The first one was a fast TAC-ADC principle which made the devices more than 100 times faster in acquisition speed without sacrificing time resolution and accuracy. The second one was a multi-dimensional recording process. It resulted from the realisation that TCSPC records a photon distribution. In classic TCSPC, this is just the distribution of the photons over the time in the excitation pulse period. In multi-dimensional TCSPC, it is a distribution over several parameters [1]. In addition to the time in the excitation pulse period, these can be the wavelength of the photons, the (variable) wavelength of an excitation source, spatial coordinates in an image area, an additional time after the start of the experiment or after a stimulation of the sample, a time within the period of an additional modulation of the laser, a voltage, or any other parameter of the experiment that can be associated to the photons [2]. These developments resulted in a variety of new techniques, instrumental principles and applications, a selection of which will be described in this paper. A few examples are shown in Fig. 1.

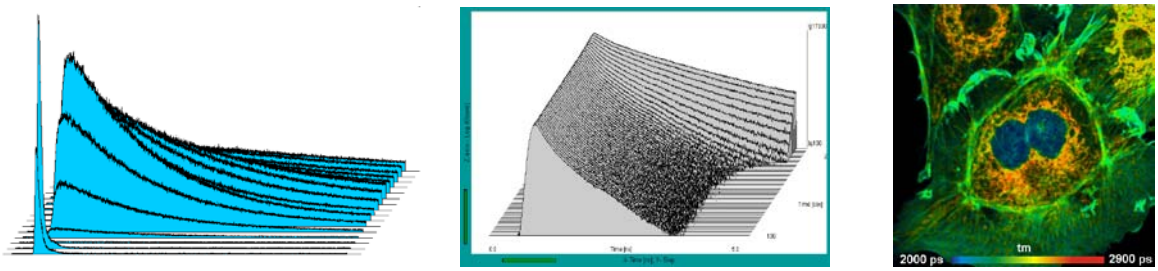

Fig. 1. Examples of multi-dimensional TCSPC. Left to right: Multi-wavelength fluorescence decay measurement, change of fluorescence lifetime of chlorophyll with time of exposure, fluorescence-lifetime image

Applications

Typical TCSPC applications in biomedical optics are time-resolved diffuse optical imaging techniques, spectroscopy of single bio-molecules, and fluorescence lifetime imaging (FLIM) [3]. Diffuse optical imaging aims at the reconstruction of internal structures and optical parameters of thick tissue via the detection of time-of-flight distributions of photons at multiple wavelength and at multiple source and detector positions. Single molecule spectroscopy resolves the function of bio-molecules by detecting photon bursts from molecules travelling through a laser focus, and detecting parameters such as wavelength, polarisation, and temporal changes within the individual bursts. FLIM detects molecular interactions between bio-molecules and their molecular environment by recording fluorescence decay functions within the pixels of an image area.

Advances

Recent advances in multi-dimensional TCSPC have been driven by a combination of new detectors and the use of 64 bit Windows technology. The large amount of memory available in the 64 bit environment provides the memory space for more complex photon distributions, and the detectors provide

the sensitivity for filling these distributions with photons. The improvements are especially apparent in FLIM. With 64 bit technology, it becomes possible to record FLIM data at mega-pixel image size [4]. More importantly, complex photon distributions can be recorded without compromising spatial resolution. These can be multi-wavelength FLIM, excitation-wavelength multiplexed FLIM, spatial mosaic FLIM, Z-stack FLIM, temporal mosaic FLIM [2], FLITS [5], FLIM combined with electrophysiology, or combined fluorescence and phosphorescence lifetime imaging [6]. An example for Ca^{++} measurement by temporal mosaic FLIM is shown in Fig. 2.

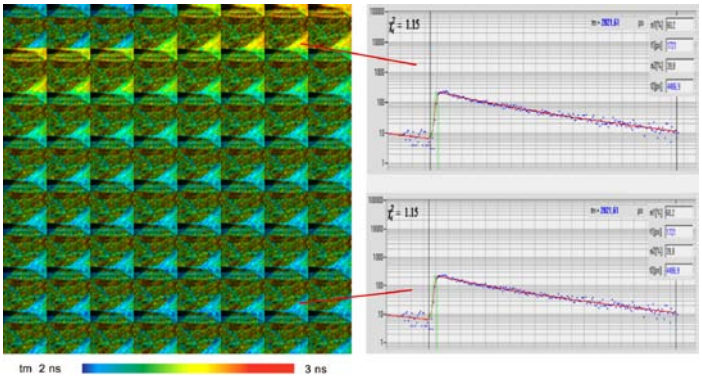

Fig. 2. Measurement of change in Ca++ concentration by temporal mosaic FLIM. Cultured neurons stained with Oregon Green, electrical stimulation. Time per mosaic element is 38 milliseconds

References

1. W. Becker, "Advanced time-correlated single-photon counting techniques", Springer, Berlin, Heidelberg New York, 2005.
2. W. Becker, "The bh TCSPC Handbook, 6th edition", Becker & Hickl GmbH, 2014.
3. W. Becker (Ed.), "Advanced time-correlated single-photon counting applications", Springer, Berlin, Heidelberg New York, 2015.
4. H. Studier and W. Becker, "Megapixel FLIM", *Proc. SPIE*, 2014, 8948.
5. W. Becker, V. Shcheslavkiy, S. Frere, and I. Slutsky, "Spatially Resolved Recording of Transient Fluorescence-Lifetime Effects by Line-Scanning TCSPC", *Microsc. Res. Techn.*, 2014, **77**, 216-224.
6. W. Becker, B. Su, A. Bergmann, K. Weisshart, and O. Holub, "Simultaneous Fluorescence and Phosphorescence Lifetime Imaging". *Proc. SPIE*, 2011, **7903**, 790320.

CURRENT TRENDS IN SUPPORTING WORKFLOW FOR BIOTECHNOLOGY-BASED DRUG DISCOVERY

T.O. Malygina

OPTEC LLC, Moscow, Russia,
malygina@optecgroup.com

Abstract. The onset of the new millennium coincides with the outbreak of new technologies in medical science and bioproduction. Current trends of medical research are distinguished for biological approaches based on molecular and cell biology. These new trends call for new research techniques and as a consequence new workflow for R&D laboratories. This paper reviews some novel instrumentation facilitating research by minimizing routine work and providing more results from a single experiment.

In drug discovery applications induced pluripotent stem cells are becoming a popular option for studying disease pathogenesis and screening drug candidates. These stem cell types have unlimited self renewal capacity can be differentiated into specific cell types and allow production of a sufficient number to investigate the disease state of interest. Current interest in cell models for drug discovery is induced by the fact that this provides a more relevant and less expensive model for active substances testing as compared with animals testing. In some cases this can be particularly useful as for example with neurological conditions, where patient brain tissue samples are rarely available in large quantities and animal models do not accurately reflect the specific human disease [1, 2]. And these new opportunities require new techniques.

MP-SPR for cell research

Surface Plasmon Resonance (SPR) is a well-known technology, which has been used to study the kinetics of bimolecular interaction of proteins and small molecules with enzymes active centers for more than 30 years. Novel Multi-Parameter SPR (MP-SPR) systems extended the applicability of this method to more complicated systems. MP-SPR instruments are based on goniometric arrangement providing a wide range of 40–78 degrees of SPR angle and recording a full SPR curve. This provides new opportunities for drug discovery as the ultimate goal is not just to look at drug-target interaction, but to get an idea, how the drug will behave in vivo. Drugs are typically encapsulated in other materials, such as cellulose and ideally, should be released slowly. MP-SPR can be used to optimize the encapsulation material in order get best efficacy – slow release of drug from the carrier material. Similarly, new implants also carry a drug to stimulate healing and decrease inflammation.

The first paper describing multi-parameter surface plasmon resonance approach for developing new types of cell-based tools for life science research aimed at improving mechanistic understanding of the type and contribution of different drug transport routes on drug absorption has been published in 2012 [3]. In this study an MP-SPR approach in combination with living cell sensing has been utilized for monitoring drug-cell interactions in real-time, under constant flow and without labels. The MP-SPR approach, i.e. surface plasmon resonance angle versus intensity plots, provided fully specific signal patterns for various cell behaviors when stimulating cells with drugs that use para- and transcellular absorption routes. Simulated full surface plasmon resonance angular spectra of cell monolayers were compared with actual surface plasmon resonance measurements performed with MDCKII cell monolayers providing better understanding the origin of the surface plasmon resonance signal responses during drug stimulation of cells. The comparison of the simulated and measured surface plasmon resonance responses allowed for better understanding and plausible explanations for the type of cellular changes, e.g. morphological or mass redistribution in cells, that were induced in the MDCKII cell monolayers during drug stimulation, and consequently to differentiate between the type and modes of drug actions. The MP-SPR approach presented in that study has layed the foundation for developing new types of cell-based tools for life science research, which should contribute to an improved mechanistic understanding of the type and contribution of different drug transport routes on drug absorption.

Long term time-lapse cells imaging

In recent years, terminal growth arrest, that is, senescence, especially therapy-induced senescence (TIS), has become a major subject in cancer research and several fields of life sciences. Senescence is characterized by a specific set of morphological and biochemical changes. However, methods that evidence senescence induction are still very limited and show large variation between individual examiners. Most notably, these assays are classical endpoint assays, and, therefore, screening for senescence is time consuming and expensive. The first challenge in studying living cells is how to maintain cells in a healthy state with normal functionality whilst being imaged for periods more than 24 h. If you want to keep cells happy for a long period of time you would always keep them in an incubator, but then multiple events will escape from your eye. Schott et al. [4] used PanSys 3000 to evaluated the cytotoxicity of heterodinucleoside phosphate analogs, their corresponding monomers ECyd and 5-FdU and combinations thereof on six metastatic melanoma cell lines and six ex vivo patient-derived melanoma cells in comparison to current standard cytostatic agents and the BRAF V600E inhibitor Vemurafenib. In vitro (real-time)-proliferation assays demonstrated that such platform is very convenient to study cytotoxic efficacy causing melanoma cell death and is helpful for searching candidates improving therapeutic success of patients afflicted with metastatic malignant melanoma and highlight the importance for prospective clinical evaluation.

Thus, these new approaches and novel instrumentation provides a basis for substantial improve and intensification of cell-based research for drug discovery.

References

1. Mattis VB and Svendsen CN, *Lancet Neurol*., 2011, **10(**4) 383-394.
2. Ito D et al., *Ann Neurol*, 2012, **72(**2) 164-174.
3. Viitala T, Granquist N., Liang H., Yliperttula M, *CRC Newsletter*, 2012, 29(6), 14-16.
4. Schott S, Niessner H et al., *Int. J. Cancer*, 2012, 131, 2165-2174.

INTEGRATED CELL CULTURE OBSERVATION SYSTEM

O.E. Sidorenko

BioVitrum Ltd, Saint-Petersburg, Russia

Abstract. With conventional cell monitoring procedures, a culture vessel has to be taken out of the incubator for microscope observation, where cells are subjected to stressful environmental changes and vibration. Researchers then have to spend additional time for repositioning the vessel to find the same observation points. Nikon's BioStation CT eliminates these problems by providing a stable environment so that the cultures don't suffer while they are being imaged and allowing for a complete trace of the same live cells, including stem cells. BioStation CT houses a microscope and a camera within the Incubator. It automatically captures images of cell cultures; there is no need to remove the vessel from the incubator and move it to the microscope.

Remote access

Configuring the imaging settings, scheduling a time-lapse experiment, and viewing the cell images are possible via a network. The captured data can be automatically down-loaded to the user's local computer. This enables users to monitor the cell status outside laboratory. When a culture environment (temperature, humidity, CO2 concentration) control error occurs, BioStation CT can notify the users of the error by e-mails.

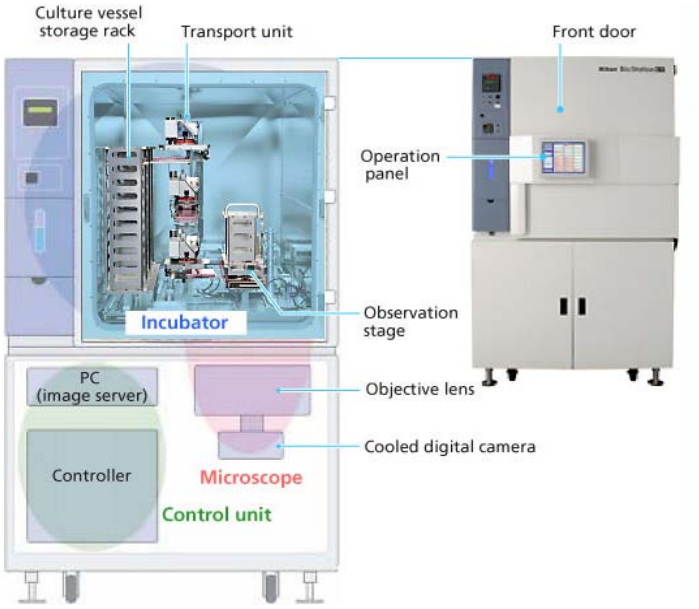

Automatic image capture

The autofocus mechanism allows capture of in-focus images. Z-stack imaging in phase contrast observation, multi-sample imaging and multi-point imaging are possible with multiple magnifications. User-configured imaging conditions that can be saved in BioStation CT support the repeatability of observations.

Automatic vessel transportation

BioStation CT incorporates a transport unit that provides stable vessel transportation within the heated and humidified incubation area. The high-precision motorized stage in the observation unit allows for automated imaging of the entire area of a well in all culturing formats.

Full-well scan imaging and highly magnified image stitching

High-resolution full-well scans are reconstructed by stitching the captured adjacent images. This enables clear detection of an iPS colony, which is difficult to detect because of its low induction efficiency, no matter where it forms in the vessel. The specified position of the vessel can be highly magnified with high resolution. BioStation CT also offers cell registration to allow for repeated visits to the same location. These time-lapse sequences can be created even when a vessel is removed from the BioStation CT for medium exchange.

Micro observation

Phase contrast and fluorescence images can be captured with a high-sensivity cooled CMOS camera. These images can be 2x, 4x, 10x, 20x and 40x magnified. Up to 40 phase contrast images can be captured along the Z axis with the Z-stack function.

Macro observation

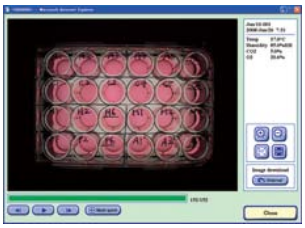

Brightfield image of the whole vessel provides users outside the Bio-Station CT with information such as handwritten information on the vessel, medium color and whether mold is growing or not. In addition, alkaline phosphatase stained cell counting is possible with optional image analysis software CL-Quant.

Fluorescence observation

Long-life and low-cost LED illuminator is employed as a light source. Up to five fluorescence filter cubes can be mounted. Up to three channels can be used with simultaneous multi-channel acquisition. The expression of fluorescence proteins such as CFP, YFP, Kusabira Orange, DsRed, Texas Red and Cy5 can be viewed effectively in fluorescence observation.

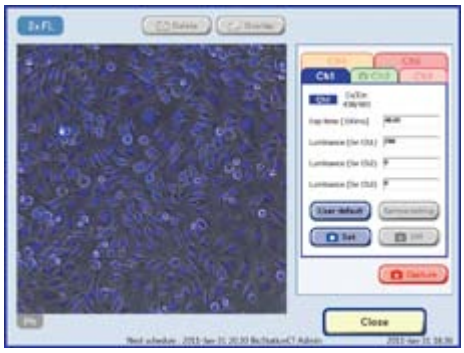

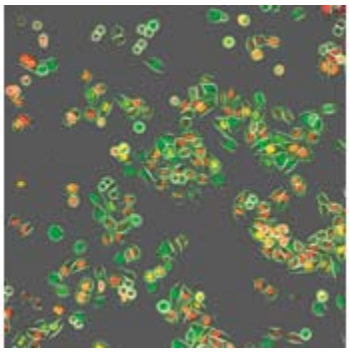

Precise temperature control

The inside temperature is directly controlled by panel heaters embedded in the incubator's six sides. This allows highly precise temperature maintenance.

Humidity control with air-flow type active aerosol spray humidifier

Distilled water is automatically sprayed inside the incubator to keep optimum humidity. Water can be supplied to the tank without opening the incubator door. This air-flow type humidifier reduces contamination risks compared to the water bath type.

Environment data recording

The culture environment is constantly monitored and recorded. The environment data can be accessed anytime.

Smooth vessel transportation

The waver of liquid surface during the transportation is less than 2 mm. The drift and stress of cells are reduced.

Reduced contamination risk

The incubator interior can be sterilized using hydrogen peroxide gas.

Reliable data management and documentation support

The obtained data is duplicated and protected using uninterruptible power supply. Observation information such as temperature, humidity and imaging date can be written and displayed on the captured image to simplify presentation document preparation.

The Government of the Russian Federation supports organization of the TPB-2015 Symposium under the program of mega-grants designed to support research projects implemented under the supervision of the world's leading scientists at Russian institutions of higher learning and research

Mega grant No. 14.B25.31.0015

Development of new technologies of optical coherence tomography for problems of individual cancer therapy

Leading Scientist – Alex Vitkin

Mega grant No. 14.Z50.31.0022

Biocompatible luminescent nanocomplexes for theranostics

Leading Scientist – Andrey Zvyagin

Mega grant No. 14.Z50.31.0007

Laboratory and numerical investigation of plasma phenomena in extreme astrophysical objects

Leading Scientist – Julien Fuchs

Organization of the International conference "Optical Bioimaging"
Project No. 15-02-20468

Organization of the International conference "Nanobiophotonics"
Project No. 15-04-20526

Organization of the International conference "Novel Laser Applications in Biomedicine", Project No. 15-02-20518

Organization of the workshop on tumor and stem cells biology
Agreement No. 4132603

Skolkovo Institute of Science and Technology (Skoltech) supports organization of the TPB-2015 Symposium within the framework of the Skoltech/MIT Initiative 203-MRA

2015 Nizhny Novgorod regional grant in science and technologies

Organization and holding of the International Symposium "Topical Problems of Biophotonics-2015"
Agreement No. 7

STANFORD
COMPUTER
OPTICS

Superior imaging intensified CCD cameras

XXRapidFrame

Multiframing ICCD camera

Up to 8 channels

Up to 100 billion frames per second

Based on 4 Picos or 4 Quik E ICCD camera technology

Optional UV enhanced system

Contact
Europe/Asia
Paul Hoess KG.
81541 Muenchen, Germany
Phone: +49 (0)89 652029
europe@stanfordcomputeroptics.com

USA/Canada
Stanford Computer Optics, Inc.
Berkeley, CA 94708, USA
Phone: +1(510) 527-3516
Info@stanfordcomputeroptics.com

www.stanfordcomputeroptics.com

BioVitrum
www.biovitrum.ru

Your reliable partner in Russia

Nikon incubation microscopy

When imaging living cells, tissues and organisms, it is essential to maintain cells in an optimal environment, wl1ich as closely as possible mimics the in vivo environment to obtain results that reflect real life processes. Failure to control the environment, especially during long term time lapse studies may result in unhealthy cells that fail to divide or exhibit abnormal morphologies confounding the interpretation of the results. A constant environment also helps to define the effects of experimental variables more accurately, and provides more consistent and reliable results.

BioStation is a combined incubator and imaging system that provides a user specified automatically maintained environment for cells during culture and imaging. Potential cell stress from environmental changes and physical disturbance, when transferring culture vessels from incubator to microscope for imaging, is eliminated. With cell friendly phase and fluorescence imaging, Biostation IM-Q (for up to four concurrent studies) and BioStation CT (for multiuser/-multistudies) are ideal for determining the effects of morphogens, performing protein localisation studies, monitoring the effects of gene knockout and knockdown, etc. while minimising cell stress.

«BioVitrum» Ltd.
Saint-Petersburg (HQ)
199106, Russia, Saint-Petersburg
V.O., Bolshoi pr., 68/A
Tel.\fax: (812) 305-06-06
www.biovitrum.ru

«BioVitrum» Ltd.
Moscow
127287, Russia, Moscow
2-nd Khutorskaya st., 38 A, build. 8, floor 7
Tel.\fax: +7 (495) 787-40-46
www.biovitrum.ru

Regional offices
Novosibirsk
Rostov-on-Don
Astana (Kazakhstan)
Kazan
Krasnodar
Nizhnyi Novgorod
Vladivostok
Ekaterinburg

Becker & Hickl GmbH

Time-Correlated Single Photon Counting

Fluorescence Lifetime Imaging

FCS, Single Molecule Spectroscopy

Near-Infrared Spectroscopy

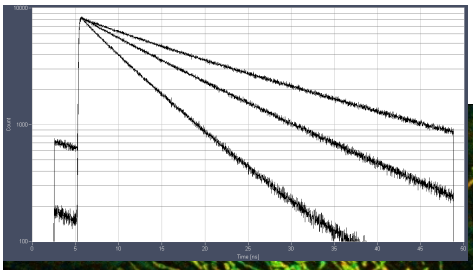

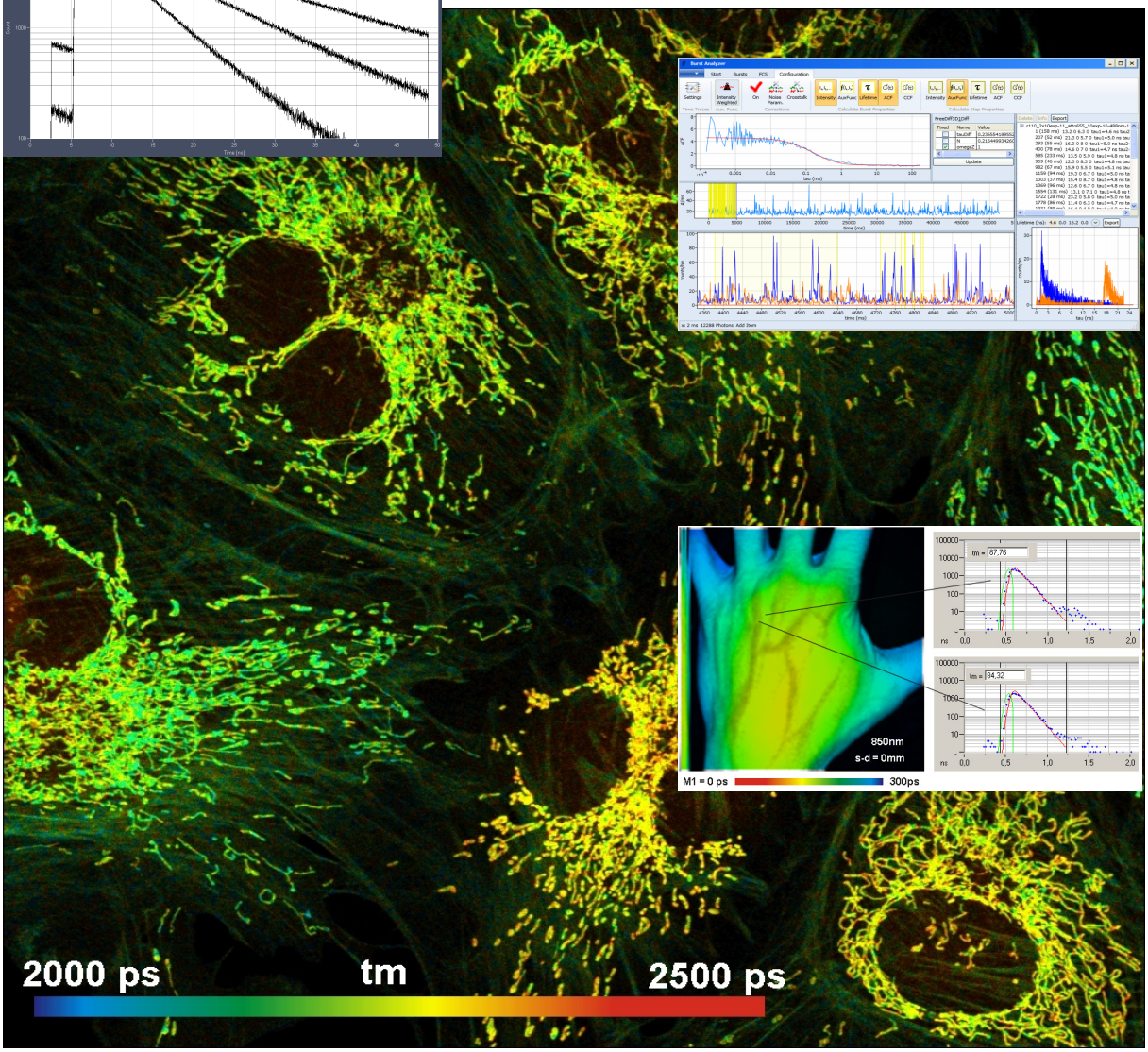

TCSPC Systems Detectors FLIM Systems Laser Scanning Systems ps Diode Lasers

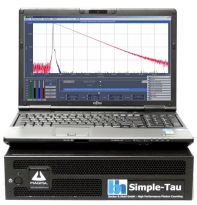

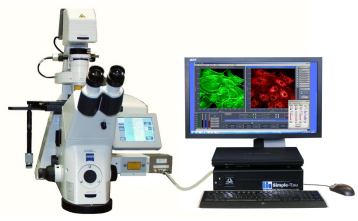

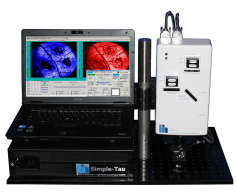

22 Years Technology Leader in TCSPC

Becker & Hickl GmbH

Fibre-Probe System for *in vivo* Fluorescence Decay Measurements

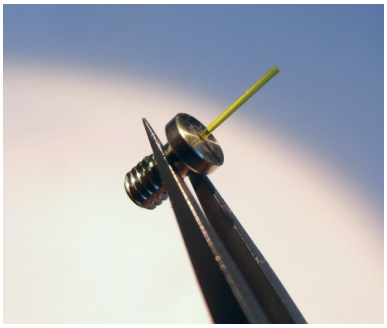

Single-mode excitation fibre
Multi-mode detection fibre
Small-size implantable fibre tip
Tip removable from fibre system by miniature fibre connector
Input compatible with bh ps diode lasers
Output compatible with all bh TCSPC detectors
Excellent sensitivity down to µW excitation power

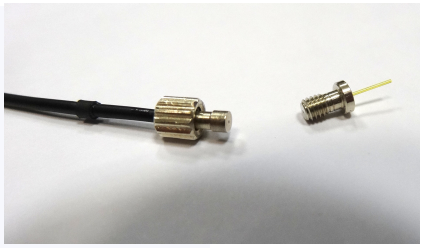

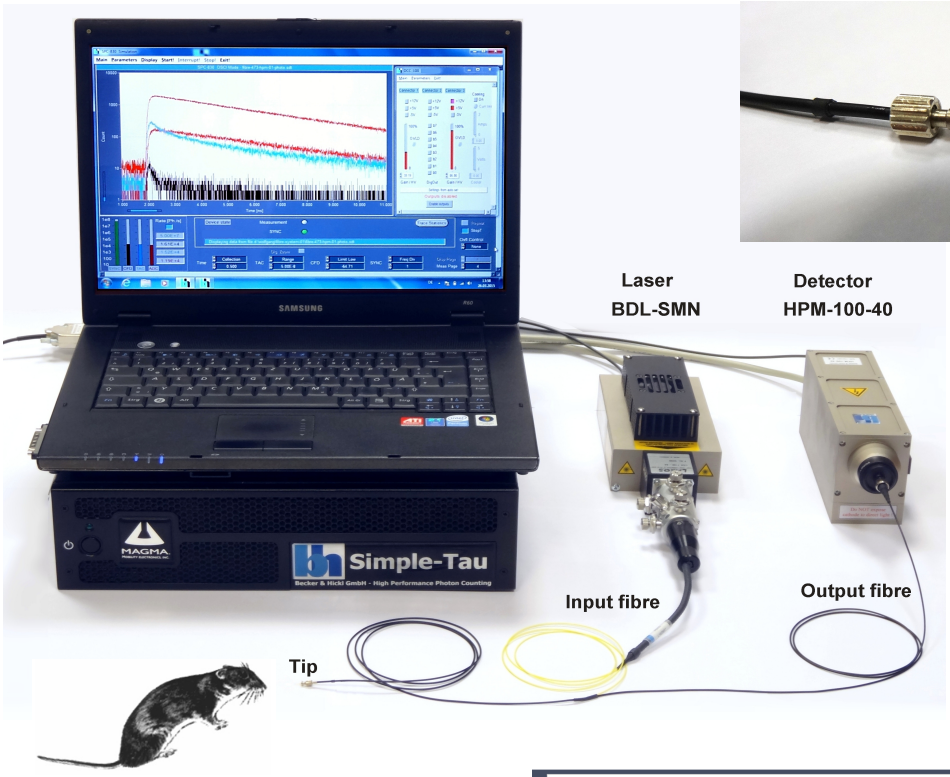

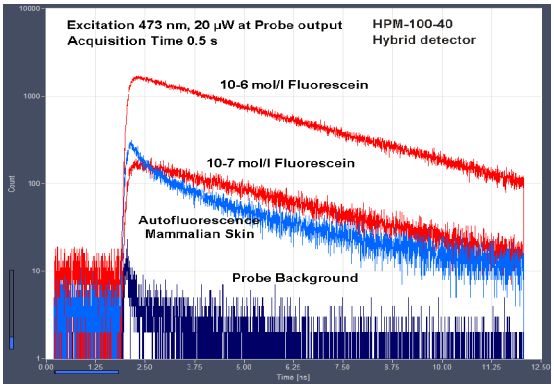

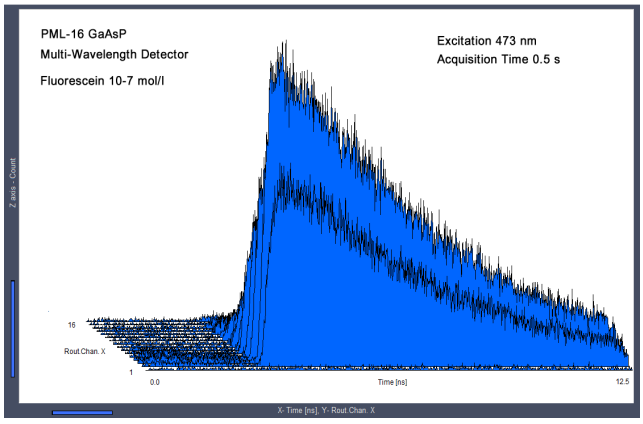

22 Years Technology Leader in TCSPC

Becker & Hickl GmbH

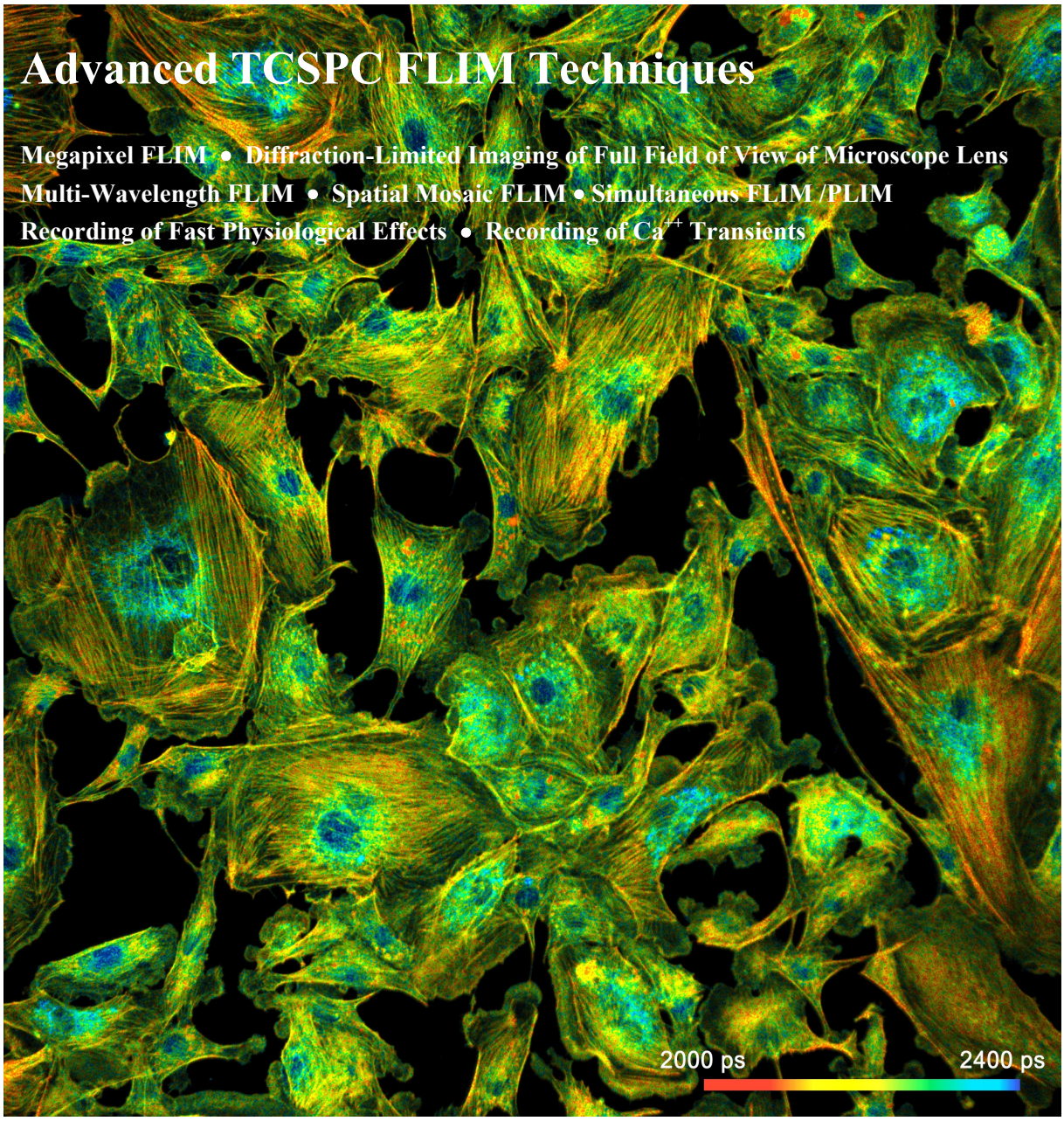

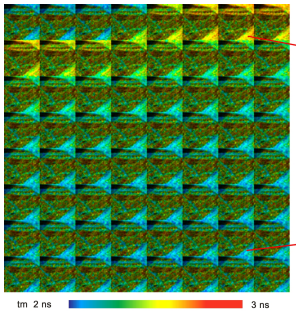

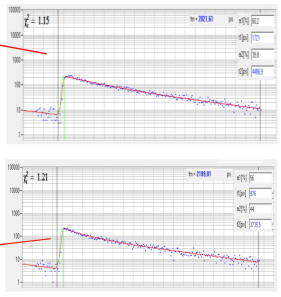

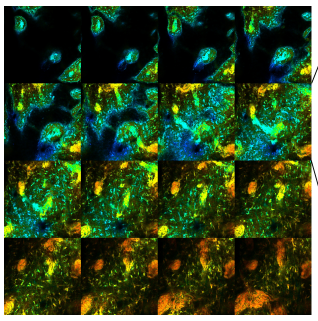

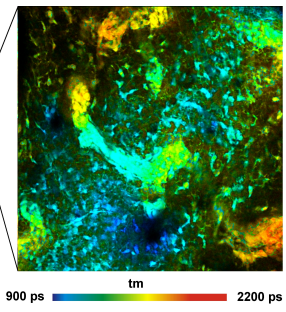

22 Years Technology Leader in TCSPC

Chameleon Discovery

Specification	
Output A	
Wavelength range (nm)	680 - 1300
Output power	
700 mW	1300 nm
800 mW	1400 nm
900 mW	1300 nm
1000 mW	1100 nm
1200 mW	800 nm
1300 mW	600 nm
Repetition rate	80±0,5 MHz
Power stability	±1%
Pulse Duration	100 fs
Beam Mode at 800 nm	M^2< 1,2
Output B	
Wavelength 1040 nm	>1500 mW

Highest average power	More than 1.4 W at peak enables deepest in vivo imaging
Short pulses delivered to the sample plane	pulses 100 fs with GDD precompensation enables efficient excitation and brightest SHG/THG imaging
Powerful second output	Two lasers in one! More than 1.5 W at 1040 nm for multicolour excitation, CARS and optogenetics applications.
Handsfree operation and simple integration	Compact size and backwards compatible software and beam parameters to other Chameleon Family lasers

LaserTrack is official representative of Coherent Inc. in CIS.

lasertrack@lasertrack.ru; www.lasertrack.ru; +7(495) 775 38 63

Решения для клеточных центров

ОПТЭК
Объединяя решения

Контроль моноклональности

Разработка протокола культивирования

Биопроцессинг

Поиск активных молекул

Розлив в криопробирки

Криохранение

Микроскопия

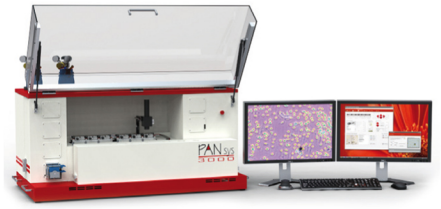

Разработка протокола культивирования

ЭКСПАНСИЯ

Адгезивные клеточные культуры

ДИФФЕРЕНЦИАЦИЯ

NSC, MSC,RPE, кератиноциты, меланоциты, мышечные клетки

V INTERNATIONAL SYMPOSIUM

TOPICAL PROBLEMS of BIOPHOTONICS 2015

TPB 2015

Nizhny Novgorod
Russia
20 – 24 July, 2015

NIZHNY NOVGOROD was founded in 1221. The dominating feature of the city skyline is the grand *Kremlin* (1500-11), with its red-brick towers. The only ancient edifice left within the kremlin walls is the hip-roofed *Archangel Cathedral* (1624-31). Other notable landmarks are two great medieval abbeys. *The Pechersky Monastery* features the austere five-domed cathedral (1632) and two rare churches surmounted by hipped roofs, dating from the 1640s. *The Annunciation Monastery*, likewise surrounded by strong walls, has another five-domed cathedral (1649) and the *Assumption Church* (1678).

Panorama of Pechersky Monastery

The most original church – *the Nativity Church* (1719) was built by *the Stroganovs* in the nascent baroque style. In 1817, *the Makariev fair*, one of the liveliest in the world, was transferred to Nizhny Novgorod, which thereupon started to attract millions of visitors annually. By the mid-XVII century, the city on the Volga was firmly established as the trade capital of the Russian Empire.

Nizhny Novgorod is the birthplace of the Russian writer *Maxim Gorky*. The city was renamed Gorky following his return to the USSR in 1932 and was known as such until 1991. All that time the city was closed to foreigners for security of the Soviet military research.

The Nobel laureate *Andrei Sakharov* was exiled here to live in banishment until 1986 to limit his contacts. The names of many other scientists including *N.Lobachevsky, N.Bogolyubov,* and *A.Andronov* are associated with Nizhny Novgorod.

Today's Nizhny Novgorod is one of the largest scientific, industrial and cultural centres of Russia with population of about 1.3 million. The city industry includes aircraft, automobile, electronics, ship building.

Panorama of Nizhny Novgorod: Kremlin, Upper-Volga Embankment, Chkalovskaya Staircase and Steam-boat «Hero» monument.

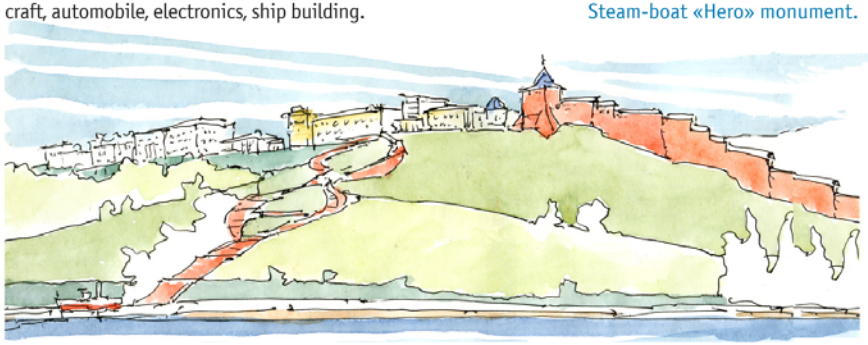

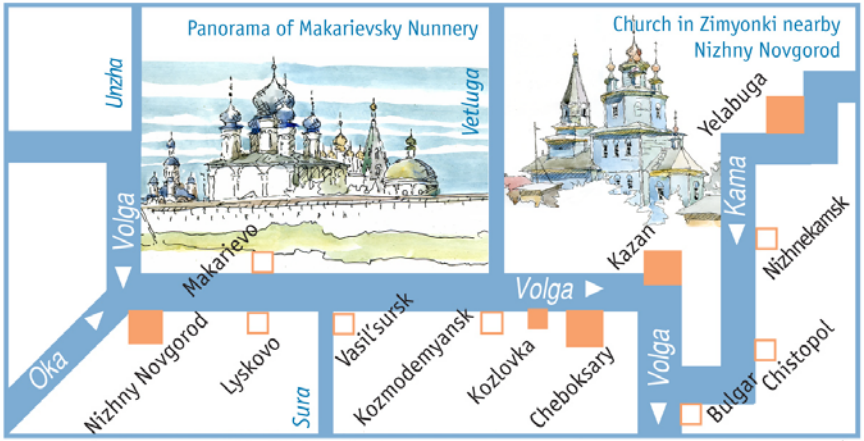

Nizhny Novgorod: the Nativity Church and Rozhdestvenskaya St.

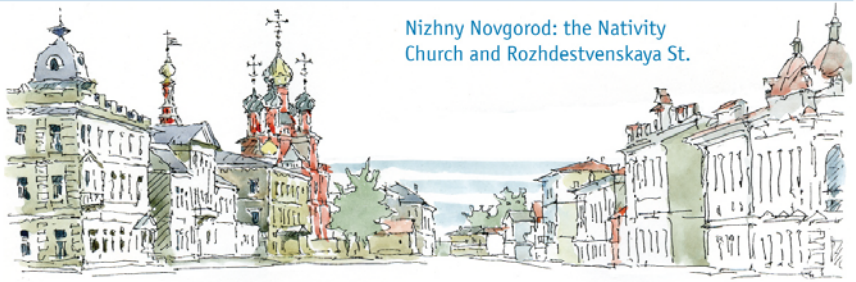

CHEBOKSARY was first mentioned in the chronicles in 1469. In the old part of the modern city one can see *Vvedensky Cathedral* (1651), *Assumption* (1763) and *Resurrection* (1702) *churches of Trinity Monastery*. Old buildings blend well with the modern embankment decorated with railings with national ornaments. Cheboksary has four theatres, art, literature and history museums, and a museum of beer.

Church of 17th century in Cheboksary

The local art gallery situated in an art-noveau building has an amazing collection of Russian paintings dating back to the middle of the XIX and the beginning of the XX century including a rich collection of *Nikolay Feshin's* works.

Street in Cheboksary: church and Art Museum

Cheboksary is a beautiful and hospitable city visited by numerous tourists, especially during the summer period.

Volga near Cheboksary

Old Tatar suburbs near the Bulak stream

KAZAN was founded by Volga Bulgars. In the XV century, it became the capital of the militant Kazan khanate, and in 1552 Ivan the Terrible annexed it to Russia. The characteristic image of Kazan is the mixture of the Russian and Eastern styles. In the old Tatar suburbs beyond the Bulak stream one can see craftsmen's shops, old houses of rich Tatars, and mosques with tall minarets at the corners of city quarters.

The white walls of the Kazan Kremlin have been girding the city for more than four centuries. Here one can see *Peter and Paul's Cathedral*, a masterpiece of the XVIII century architecture. *Mardjani* (1767) and *Azimov* (1887) *mosques* add to the uniqueness of the cityscape.

Numerous churches have survived here: *churches of Epiphany* (1731-1756), *St. Nicholas* (1885), *Pokrov* (1703), the buildings of *the John the Baptist Monastery*, *Zilant Monastery*, and *Raifa Monastery*. The historical centre of the city has many buildings and the so-called «income houses» in the styles of eclecticism and art-noveau.

The walls of the famous *Kazan University* founded in 1804 remember the names of mathematician *N.Lobachesky*, chemist *A.Butlerov* and poet *V.Khlebnikov*. Kazan today has about 1.2 million inhabitants. It is the capital of the Tatar Republic and a major centre of business and industry, including aircraft, chemical engineering, and medical equipment.

18th century mosque in Kazan

Anatomical Theatre in Kazan University built by architect Michail Korinfsky in the 1830-s

18th century mosque in Old Tatar suburbs

Panorama of the Kaban Lake in Kazan

YELABUGA is a small old town nestled in the woods on the right bank of the Kama River. This town with a panorama of churches with ancient stone mansions is a unique example of the architecture of the XIX century.

The history of Yelabuga dates back to VIII-V BC. The mysterious Tower of Yelabuga «Devil» settlement witnessed the tumultuous events of the Middle Ages. Legends, traditions and historical facts are associated with the great names of Temir-ak-Saka, Ivan the Terrible, Pugachev, and Empress Catherine II, by whose highest decree in 1780 the village Trekhsvyatskoye was granted the status of a town and got the name of Yelabuga.

Old street with merchants' houses in Yelabuga

The nature of the surrounding area was immortalized by the Russian landscape painter Ivan Shishkin, born in Yelabuga. The museum devoted to his memory is not far from the Bell Tower. Another museum is that of Nadezhda Durova, the legendary heroin of the Patriotic War of 1812.

Also of interest is the museum of district medicine named after the great physiologist and psychotherapist Vladimir Bekhterev. Yelabuga was the last refuge of the famous Russian poet Marina Tsvetaeva. Every name, every place keeps a lot of well-known and still unread pages of history.

Cathedral and Bell-tower of Yelabuga

Merchants' houses in Kozlovka

KOZLOVKA is a Chuvash town located on the right bank of the Volga River, near the borders with the Mari El Republic and the Republic of Tatarstan.

River port in Chuvashiya

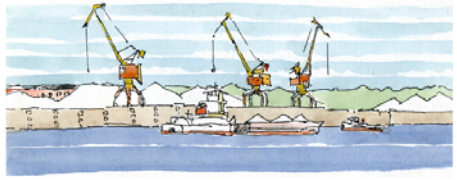

The first settlement at the site of the modern town was founded in 1671. In the middle of the XIX century it was a large Volga landing place and a rich fishery and woodworking center. A few samples of merchants' houses can still be seen on the Volga embankment.

Volga near Kozlovka

Also preserved is the manor-house of the outstanding geometrician Nikolay Lobachevsky, where he spent his summers. Lobachevsky was not only a remarkable scientist, pedagogue and administrator, but also a good contriver. He had in his manor a stable, a farm-yard, a bee-garden, a vegetable garden, and an orchard.

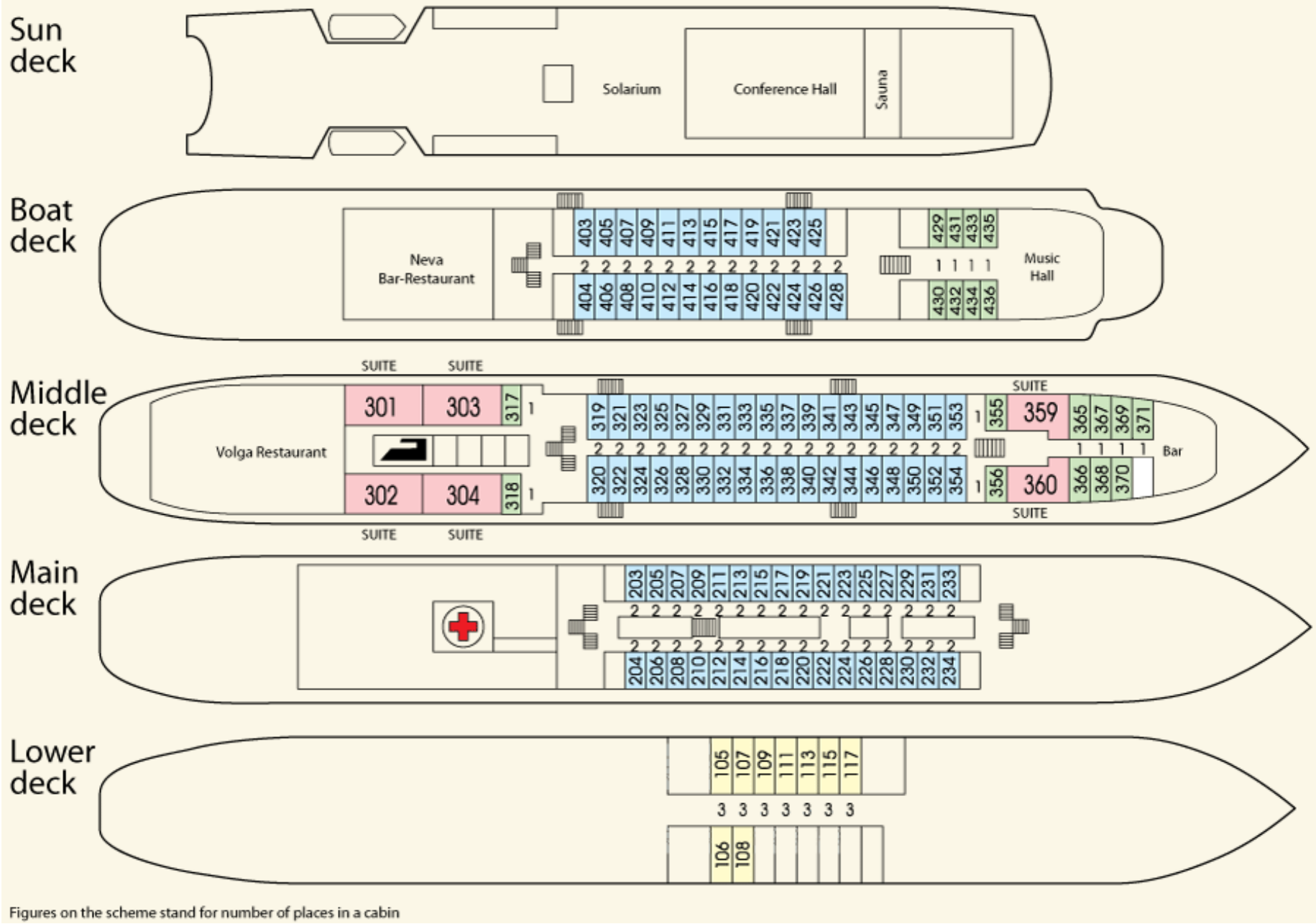

Figures on the scheme stand for number of places in a cabin

INDEX OF AUTHORS

The electron version of the TPB-2015 Symposium materials was prepared
at the Institute of Applied Physics of the Russian Academy of Sciences,
46 Ulyanov Str., 603950 Nizhny Novgorod, Russia